



Dipl.-Ing. Reinmar J. Kobler, BSc

**M/EEG-based kinematics de- and encoding in visuomotor and
oculomotor tasks**

DOCTORAL THESIS

to achieve the university degree of
Doktor der technischen Wissenschaften

submitted to

Graz University of Technology

Supervisor

Gernot R. Müller-Putz, Univ.-Prof. Dr.techn. Dipl.-Ing.
Institute of Neural Engineering
Laboratory of Brain-Computer Interfaces

Graz, September 2020

Colophon

This document was typeset with the help of KOMA-Script and L^AT_EX using the kaobook class.

AFFIDAVIT

I declare that I have authored this thesis independently, that I have not used other than the declared sources/resources, and that I have explicitly indicated all material which has been quoted either literally or by content from the sources used. The text document uploaded to TUGRAZonline is identical to the present doctoral thesis.

Date, Signature

Abstract

A device that records and simultaneously translates brain activity into a control signal is denoted brain-computer interface (BCI). A central research direction, namely, movement control has already been pursued since the last century. One strategy to implement low-level movement control is to design BCIs that directly decode movement information from brain activity and use it to control end-effectors rather than relying on potentially impaired neuromuscular activity. This strategy has been explored in non-human primates and later also in human patients and case-studies in paralyzed humans whose electrophysiological brain activity was recorded with implanted electrodes. In these case studies, paralyzed individuals could continuously control the trajectory of computer cursors and make robotic arms or via neuroprostheses their paralyzed arms reach and grasp objects. Key to these impressive results was the discovery that neural spiking and population activity in motor cortex is tuned to the kinematics of executed and also intended movements. For about a decade, increasing evidence suggests that population activity recorded non-invasively in the form of electroencephalography (EEG) and magnetoencephalography (MEG) encodes also kinematic information. Unlike invasively recorded brain activity, EEG and MEG suffer from co-varying motion and eye artifacts which has so far impeded their application in studying kinematics related effects in visuomotor tasks that require eye-hand coordination.

This PhD thesis provides multiple contributions to functional neuroimaging tools that can disentangle co-varying eye and other artifacts from kinematics-related effects in low-frequency M/EEG. Using this new tools allowed us to corroborate and extend the understanding of kinematics related effects in the low-frequency M/EEG in discrete and continuous movement tasks. In discrete movements, we identified that sensorimotor cortex (SMC) encoded directional information during a visuomotor task but not during an oculomotor task. Whereas parieto-occipital cortex (POC) encoded directional information in both tasks and consistent across participants. In continuous tracking movements, similar large scale cortical networks were active. In the tracking task, we observed velocity tuning in SMC (visuomotor task) and POC (visuomotor and oculomotor tasks). At the same time, we found that SMC was additionally tuned to the length of the velocity vector (i.e., speed) during the visuomotor task. The methodological and conceptual advances were eventually combined to implement a proof-of-concept, EEG-based, kinematics decoding BCI for continuous movement control. In two feasibility studies with healthy users, we demonstrated that the proposed BCI can be used to control a robotic arm with moderate accuracy. Further research is necessary to improve the accuracy and transfer the system to paralyzed users.

Kurzfassung

Ein System, das Gehirnaktivität aufzeichnet und gleichzeitig in ein Steuersignal umwandelt, wird als Gehirn-Computer-Schnittstelle (Englisch: Brain-Computer Interface, BCI) bezeichnet. Ein zentrales Thema in der BCI-Forschung ist die Steuerung von Bewegungen. Eine Strategie besteht darin BCIs zu entwerfen, die Bewegungsinformationen direkt aus der Gehirnaktivität dekodieren und diese zur Steuerung von Endeffektoren wie Computer Cursors oder robotischen Armen verwenden, anstatt sich auf potenziell beeinträchtigte neuromuskuläre Aktivität zu verlassen. Diese Strategie wurde an Primaten und später auch an Patienten und in Fallstudien an gelähmten Menschen untersucht. Mittels implantierter Elektroden wird elektrophysiologische Hirnaktivität aufgezeichnet und in Steuersignale umgewandelt. In den Fallstudien konnten gelähmte Personen die Trajektorie von Computer Cursors kontinuierlich steuern und robotische Arme oder mittels Neuroprothesen ihre gelähmten Arme dazu bringen nach Objekten zu reichen und diese zu ergreifen. Die Grundlage für diese beeindruckenden Ergebnisse war die Entdeckung, dass neuronale Aktionspotenziale und Hirnaktivität im motorischen Kortex Information über die kinematischen Parameter ausgeführter und auch beabsichtigter Bewegungen codieren. Seit etwa einem Jahrzehnt deuten zunehmende Studienergebnisse darauf hin, dass nicht-invasiv, in Form von Elektroenzephalographie (EEG) und Magnetoenzephalographie (MEG), aufgezeichnete Hirnaktivität auch kinematische Information codiert. Im Gegensatz zur invasiv aufgezeichneten Hirnaktivität zeichnen EEG und MEG gleichzeitige Bewegungs- und Augenartefakte auf, was ihre Anwendung bei der Untersuchung kinematischer Effekte während visuomotorischer Aufgaben, die Auge-Hand-Koordination erfordern, bisher behindert hat.

Diese Doktorarbeit präsentiert Methoden, die es ermöglichen kovariierende Augenartefakte von kinematischen Effekten im niederfrequenten M/EEG zu trennen. Mittels der neuen Methoden konnte diese Doktorarbeit zu einem besseren Verständnis kinematischer Effekte im niederfrequenten M/EEG während diskreter und kontinuierlicher Bewegungen beitragen. In zielgerichteten, diskreten Bewegungen wurde festgestellt, dass der sensomotorische Kortex (SMC) Richtungsinformation während einer visuomotorischen Aufgabe, jedoch nicht während einer okulomotorischen Aufgabe codiert. Der parieto-okzipitale Kortex (POC) codierte Richtungsinformation in beiden Aufgaben. Bei zielgerichteten, kontinuierlichen Bewegungen waren ähnliche kortikale Areale aktiv. Während dieser Bewegungen codierte SMC (visuomotorisch) und POC (visuomotorisch und okulomotorisch) Information über die vektorielle Geschwindigkeit. Gleichzeitig stellten wir fest, dass SMC zusätzlich Information über die Länge des Geschwindigkeitsvektors codierte. Die methodischen und konzeptionellen Fortschritte wurden schließlich kombiniert, um ein EEG-basiertes BCI für die Bewegungssteuerung zu implementieren. In zwei Machbarkeitsstudien mit gesunden Menschen wurde gezeigt, dass das EEG-basierte BCI zur Steuerung eines robotischen Arms mit mäßiger Genauigkeit verwendet werden kann. Weitere Forschung ist erforderlich, um die Genauigkeit zu verbessern und die Übertragbarkeit der Ergebnisse an gelähmten Menschen zu testen.

Acknowledgments

Pursuing a PhD degree is an adventure. At the beginning, things are unclear – the environment is unknown, the concepts and jargon are unfamiliar, and the stream of papers seems endless. Having a supervisor that provides guidance whenever one loses track and at the same time gives space to explore is an invaluable asset. **Gernot**, thank you so much for being such an asset for me. Let me also thank you for giving me the opportunity in the first place, trusting me and my abilities, and taking time to discuss various matters – even in the early mornings or late afternoons, not to say evenings. Seeing your tireless effort and enthusiasm about BCIs and neural engineering in general was truly inspirational.

To me, an adventure without company does not seem worthwhile. Knowing already Reini, Andi and David from my master's degree and time at the Graz BCI racing team, I was eager to start my PhD adventure at the institute of neural engineering (INE). **Reini**, thank you for seeing my potential as well as your guidance during my masters's degree and beyond. Working and discussing with you has been a pleasure. I admire your easy-going nature paired with your critical view on various matters. **David** and **Andi**, thank you for infecting me with the BCI virus, taking time to explain me stuff and your critical way of thinking.

During a new adventure, one inevitably encounters strangers, gets to know them as they walk along a shared path, and after the paths have split, looks back on shared memories. I gratefully acknowledge the EU for financially supporting my PhD adventure via the ERC consolidator grant 681231 "Feel Your Reach". Working within this project, gave me the chance to meet **Andreea, Joana, Catarina** and **Lea**. In countless discussions, meetings, retreats and off-work activities you turned from strangers into friends. I could not be more grateful for having you as my colleagues; working and spending time with you guys has always been a pleasure. I am also very grateful for having had the chance to meet and work with visiting students. A special thanks goes to **Inês, Liza, Valeria** and **Victor** who "chose" to work with me. I consider our joint research activities as one of the most productive and joyful times during my PhD. Thanks for all the hard work, in-depth discussions and mostly your patience with me. **Valeria**, let me also thank you for your inspiring work attitude that has motivated me to go the extra mile, and becoming a wonderful colleague and friend. I also want to thank current and former INE lab members as well as BCI racing team members for valuable discussions and their support. I further want to thank **Hirata-sensei, Hashimoto-sensei, Dowaki-san** and the other members of the Hirata lab for making my research stay at Osaka University a wonderful and highly productive chapter of my PhD adventure.

Every adventure - however wonderful it may be - has a start and an end. Without the support of my family and friends, reaching the start and enduring this adventure would not have been possible. Thank you for your unconditional support. **Dad**, thank you for showing me that working hard and having a joyful life are not mutually exclusive. **Erich**, you are the best. Thank you for your utter friendship during our childhood, youth and young adulthood. My dearest **Ai**, I could not be more grateful for having you in my life. Thank you so much for the priceless moments that we have shared together, your incredible patience with me and agreeing to spend the rest of our lives together. I cannot wait to start our new adventure together in Japan.

Contents

Abstract	v
Kurzfassung	vii
Acknowledgments	ix
Contents	x
Acronyms	xiii
1 Introduction	1
1.1 The long-term Vision	1
1.2 Organization of the Thesis	2
1.3 Physiology of the Acting Brain	3
Cortical Control of Action	4
1.4 How to measure Brain Activity?	5
Micro-scale – APs and LFP	6
Macro-scale – EEG and MEG	6
Meso-scale – ECoG	9
1.5 Neural Correlates of Movement	9
Direction of discrete Movements	10
Movement initiation	10
Velocity and Position	12
1.6 What is a Brain-Computer Interface?	12
Components of a BCI	13
Feedback	16
2 Motivation and Related Work	17
2.1 Control Strategies	17
2.2 Invasive BCIs for Movement Control	18
Neural Spiking Activity	18
Population Activity	20
2.3 Non-invasive BCIs for Movement Control	21
Motor Imagery	21
2.4 Towards direct, non-invasive BCIs for Movement Control	22
State of the Art	22
Limitations	26
3 Aim of this Thesis	28
3.1 A proof-of-concept direct BCI for Movement Control	28
3.2 Neurophysiology of executed and observed Movements	29
3.3 Encoding Model	30
3.4 Workplan	31
Online Eye Artifact Correction	31
Neural Correlates of Movement	31
Decoding Accuracy Improvement	31
Proof-of-concept direct BCI	32

4	Methods and Results	33
4.1	Online Artifact Correction	33
	Evaluation of Algorithms for online Eye Artifact Correction	33
	Correction of CRD and Eyelid Artifacts in EEG and MEG	35
	Online Detection and Correction of transient high-variance Artifacts	37
4.2	Neural Correlates of Movement	39
	Discrete Movements in different Directions	39
	Continuous Tracking Movements	42
	Simultaneous Decoding of Velocity and Speed	44
4.3	Decoding Accuracy Improvement	46
	Distance- and speed-informed Kinematics Decoding	46
4.4	Proof-of-concept direct BCI	48
	Online robotic Arm Control with a linear Decoder	48
	Online robotic Arm Control with a non-linear Decoder	50
5	Discussion	52
5.1	Methodological Progress	52
	Eye Artifacts	52
	Motion Artifacts	53
	Transient high-variance Artifacts	54
	Decoding Algorithms	54
	Comparison with SoA	55
5.2	Conceptual Progress	56
	Directional and non-directional Kinematics	57
	Executed and observed Movements	57
	Continuous and discrete Movements	58
5.3	Limitations	59
6	Conclusion	61
6.1	Outlook	61
	Bibliography	63
	APPENDIX	83
A	Author Contributions	84
A.1	Primary Publications	84
A.2	Secondary Publications	85
B	Primary Publications	86
C	Secondary Publications	147

List of Figures

1.1 Hierarchy of the human motor control system	3
1.2 Human brain regions implicated in actions	4
1.3 Components of a BCI	14
4.1 Eye artifact calibration paradigm	33
4.2 Eye artifact correction example	34
4.3 Eye artifact correction results	36
4.4 Pop and drift artifact correction results for simulated data.	37
4.5 Examples of pop, drift and muscle artifacts.	38
4.6 Experimental setup and paradigm to study discrete and continuous movements	40
4.7 Neural correlates of movements in different directions	41
4.8 Neural correlates of continuous tracking movements	43
4.9 Experimental setup and paradigm to study continuous index finger movements	44
4.10 Neural correlates of 2D velocity and speed in LFTD MEG activity.	45
4.11 Qualitative distance- and speed-informed decoding results.	47
4.12 Quantitative distance- and speed-informed decoding results.	47
4.13 Overview of the online decoding experiment.	48
4.14 Results of the online, linear decoding experiment.	49

List of Tables

4.1 Results for the online, non-linear decoding experiment.	51
---	----

Acronyms

A

- aIPS** anterior intra-parietal sulcus. 4
- ALS** amyotrophic lateral sclerosis. 1
- ASR** artifact subspace reconstruction. 37, 54
- AT** assistive technology. 1

B

- BCI** brain-computer interface. 2, 12–23, 26–29, 31, 32, 37, 49, 50
- BP** Bereitschaftspotential. 11

C

- CAR** common average reference. 15
- CNS** central nervous system. 1, 3, 13
- CRD** corneo-retinal dipole. 8, 33–35
- CSP** common spatial patterns. 15

D

- DoF** degree of freedom. 22
- DRS** dorsal reach system. 4

E

- ECG** electrocardiography. 8
- ECoG** electrocorticography. 9–12, 20–22, 44
- EEG** electroencephalogram. 6, 9, 11–15, 21–26, 28, 29, 31–33, 35, 36
- EMG** electromyography. 8
- EOG** electrooculography. 8, 33, 36
- EP** evoked potential. 6, 13, 15
- ERD** event-related desynchronization. 11
- ERDS** event-related de-/synchronization. 11, 15, 16, 21
- ERP** event-related potential. 6, 11, 13, 15, 16
- ErrP** error potential. 36
- ERS** event-related synchronization. 11

F

- FEF** frontal eye field. 4
- FIR** finite impulse response. 15

G

- GEYESUB** generalized eye artifact subspace subtraction algorithm. 35

H

- HEAR** high-variance electrode artifact removal algorithm. 37, 38, 54

I

- ICA** independent component analysis. 15, 23, 35
- IIR** infinite impulse response. 15, 49

K

KF Kalman filter. 19, 20, 46

KRR kernel ridge regression. 25

L

LFP local field potential. 6, 10, 11, 20, 22

LFTD low-frequency time-domain. 10, 12, 20, 22–30, 37, 39, 44

LGS lateral grasp system. 4

M

M1 primary motor cortex. 3, 4, 9, 10, 12, 18–20

MEG magnetoencephalogram. 7, 10, 12, 21–25, 29, 31, 35, 44

MI motor imagery. 21, 22

MRCP movement-related cortical potential. 11, 26, 31, 36, 39

MS multiple sclerosis. 1

MUA multi-unit activity. 6, 19, 20

N

NHP non-human primate. 3, 4, 18, 20, 32

O

OAS oculomotor intention and attention system. 4

oHEAR online high-variance electrode artifact removal algorithm. 37

P

PCA principal component analysis. 15

PEF parietal eye field. 4

PLS partial least squares regression. 46

PM premotor cortex. 3, 9, 10

PMd dorsal premotor cortex. 4, 10, 19, 20

PMv ventral premotor cortex. 4

POC parieto-occipital cortex. 39–44

PPC posterior parietal cortex. 4, 19, 23, 24, 27, 39, 42, 44

PSP post-synaptic potential. 5–7

PTT pursuit tracking task. 12

R

RPCA robust principal component analysis. 37, 54

S

S1 primary somatosensory cortex. 3, 4

SCI spinal cord injury. 1, 17, 21, 23

SGEYESUB sparse generalized eye artifact subspace subtraction algorithm. 35, 53

sLDA shrinkage linear discriminant analysis. 15, 16

SMC sensorimotor cortex. 10–12, 20, 23, 24, 27, 30, 39–44

SMR sensorimotor rhythm. 21, 22

SNR signal to noise ratio. 13, 15, 17, 19, 22, 23, 28, 37

SP saccadic spike potential. 8

SPOC superior parieto-occipital cortex. 4

SUA single-unit activity. 6, 19, 20

U

UKF unscented Kalman filter. 19, 31, 46, 50

W

WF Wiener filter. 19, 21, 24, 25, 43, 46

1.1 The long-term Vision

Paralysis, defined as the loss of motor function in one or more muscles, can be caused by stroke, by traumatic damages to the central nervous system (CNS) like spinal cord injury (SCI) or by neurodegenerative diseases like multiple sclerosis (MS) or amyotrophic lateral sclerosis (ALS). Nearly 1 in 50 persons live with some form of paralysis in the US [1], rendering paralysis not only a challenge for the individual but also for society.

Individuals with a permanent loss of upper-limb function are faced with a dramatic loss in quality of life and independence. The primary cause for a permanent loss of upper- and lower-limb function, denoted tetraplegia, is SCI. The incidence rate of SCI ranges from 15 million in Western Europe to 39 million per year in the US [2]. As of 2020, an estimated 294,000 persons with SCI live in the US with 47% diagnosed incomplete and 12% complete tetraplegia [3]. For individuals with high tetraplegia (i.e., spinal cord injury at cervical levels C1-C4), the average cost for health care and living expenses are about 1,000,000 USD in the first year and 200,000 USD in each subsequent year. Their daily lives depend on the assistance provided by their caregivers - often family members or friends serve as their primary caregivers.

Assistive technology (AT) can help the individuals to regain some aspects of independence. AT aims to replace or restore some of the lost function to increase the ability to perform daily life activities. In the case of high tetraplegia commonly used ATs are speech recognition systems, eye trackers or head or tongue operated joysticks [4]. An alternative to using residual muscular function is to directly interface with the brain - the topic of this thesis. In fact, a survey among 156 persons with cervical SCI in the US showed that they would be likely to adopt a technology that uses brain activity to directly control upper-limb function, including grasping and to some degree also reaching [5]. Other priorities were high speed typing and fast robot arm control.

Now, picture the following: a person with tetraplegia would like to reach and grasp towards an object; let's assume an apple. Wouldn't it be great if she would just think or attempt to perform the action (of reaching and grasping the apple) and a smart system that monitors her brain activity detects her intention and translates it into commands for a neuroprosthesis to move her own, paralyzed arm or for a robotic arm to execute the action for her. Is this an engineering or neuroscience problem? Well, it is both. It turns out that such a simple thought of reaching and grasping an apple is not trivial to execute. Even in healthy people who can seamlessly put the thought into action, the brain needs to process a myriad of information to accomplish the task. It has to identify movement goals (e.g., the apple), their spacial location with respect to the body and hand,

1.1 The long-term Vision	1
1.2 Organization of the Thesis	2
1.3 Physiology of the Acting Brain	3
Cortical Control of Action	4
1.4 How to measure Brain Activity?	5
Micro-scale – APs and LFP	6
Macro-scale – EEG and MEG	6
Meso-scale – ECoG	9
1.5 Neural Correlates of Movement	9
Direction of discrete Movements	10
Movement initiation	10
Velocity and Position	12
1.6 What is a Brain-Computer Interface? 12	
Components of a BCI	13
Feedback	16

plan a trajectory, transform it into muscle activations, and incorporate somatosensory and visual feedback. A symbiosis of engineering in the form of developing tools that can measure and detect neural activity, and movement neuroscience in the form of associating neural activity with behavior has considerably advanced our understanding of how the brain controls goal-directed movements. This multidisciplinary symbiosis has moved the vision of restoring or replacing lost function closer to reality. Within the last two decades we have seen case studies demonstrating that paralyzed volunteers can use so called brain-computer interfaces (BCIs) to replace [6, 7] or restore [8, 9] lost movement function.

1.2 Organization of the Thesis

The remainder of this chapter briefly outlines basic concepts to establish the necessary background knowledge. Topics that will be covered are the neurophysiological aspects of movement with a focus on the neural substrates involved in the control of action, techniques to measure brain activity within the body (invasive) and from outside the body (non-invasive), the neural correlates of movement and a definition of the term brain-computer interface (BCI).

The second chapter starts with an introduction of control strategies that have been used to replace and restore lost upper-limb function in BCI research. The chapter then continues with a review of related work in the invasive and non-invasive domains. The focus of the review is set to non-invasive approaches that decoded the kinematics of executed movement trajectories – the primary research topic of this thesis. The chapter ends with a brief account of the limitations of current non-invasive kinematics decoding approaches.

In chapter three, the general and specific aims of this thesis as well as the underlying encoding model are introduced and elaborated. The chapter ends with a workplan that outlines the research activities and key milestones.

Chapter four summarizes the methods and findings of primary and secondary publications in the context of this thesis. The chapter covers four topics (i) online artifact correction, (ii) neural correlates of movement, (iii) improving decoding accuracy and (iv) a proof-of-concept direct BCI.

The fifth chapter relates the findings reported in the primary and secondary publication with each other, explains how they contribute to methodological and conceptual progress, and discusses the achievements in the context of other works in the literature. The chapter ends with an account of remaining limitations.

In the last chapter, the main achievements of this thesis are summarized and future research directions are outlined.

1.3 Physiology of the Acting Brain

Movements like reaching towards an object require the participation of four highly interactive subsystems of the CNS [10]. Figure 1.1 outlines an overview of the involved subsystems and the major pathways. The first subsystem is located within the gray matter in the spinal cord and brainstem. These areas include the lower motor neurons which directly innervate the muscles and some local circuits. All movement commands either reflexive or voluntary are transmitted to the muscles via the lower motor neurons. The local circuits receive sensory input and commands from higher centers. As such, the local circuits are mainly involved in the coordination between different muscle groups.

The second subsystem comprises upper motor neurons which are located in the brainstem and cortex. They either directly project to lower motor neurons or more likely to the associated local circuits. The upper motor neuron pathways which arise in the cortex are essential for initializing voluntary movements and to control complex sequences of skilled movements [11, 12]. Particularly primary motor cortex (M1) and premotor cortex (PM) are important for planning, initiating and directing voluntary movements. Descending pathways from upper motor neurons located in the brain stem are responsible for basic navigational movements (i.e., orienting of eyes, head and body) and posture control. Ascending pathways via the spinal cord, brain stem and thalamus relay sensory inputs and feedback to the primary somatosensory cortex (S1) and the cerebellum.

The other two subsystems do not directly modulate the lower motor neurons or associated local circuits. They control movement by modulating the activity of upper motor neurons. One of these two subsystems is the cerebellum. It has been implicated in the detection of discrepancies between the intended movement and the actually performed one. This information is used to mediate real-time and long-term reductions in movement errors. The other subsystem is the basal ganglia. They are located in the forebrain and have been implicated in the suppression of undesired movements and priming of upper motor neurons to initiate voluntary movements.

A hierarchic organization of the motor system is also supported by the findings of lesion studies in mammals [13]. It seems incredible that substantial parts of the CNS can be removed while significant functionality is preserved. In spinalized preparations, the spinal cord can control some multi-joint movements and integrate somatosensory feedback in central pattern generators to generate repetitive movement such as walking [14]. At the brain stem level much knowledge was obtained from decerebration experiments. With an intact brainstem, cats can retain the ability to walk spontaneously. At the subcortical level, studies based on decortication (i.e., removal of the cortex without damage to the basal ganglia) showed that cats, dogs and rodents exhibit superficially normal behavior after a recovery period [15]. Upon closer inspection of the behavior, clear deficits become apparent. They are more dramatic in non-human primates (NHPs) that reach and exhibit dexterous finger movements. Focal lesions in the motor cortex of NHPs result in a transient paralysis, followed by substantial recovery except for fine motor skills [16]. In humans, lesions in the motor cortex are often followed by permanent paralysis or impaired movement of the

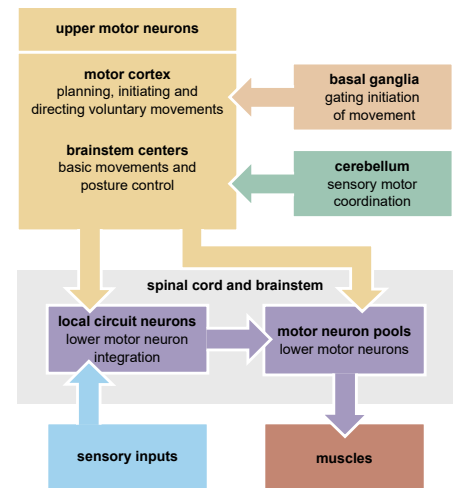


Figure 1.1: Hierarchy of the neural subsystems involved in the control of movement. Four subsystems make important and complementary contributions. The lower motor neurons and circuits are the direct interface to muscles and sensory feedback. Descending pathways from upper motor neurons in the motor cortex and brainstem drive the local circuits in the brainstem and spinal cord. The cerebellum and basal ganglia modulate the activity of the upper motor neurons. Ascending pathways that relay sensory inputs to the cortex and cerebellum are not shown. Figure adapted from [10].

contra-lateral limb [17]. This suggests that the cortex, in particular the motor cortex, is critical in mediating sensory rich control to produce dexterous movements and, in turn, renders the cortex the right area to study the neural correlates of actions.

Cortical Control of Action

Although the motor cortex has been studied for more than a century, it remains unclear how its activity reflects upper-limb movements and how sensory information is integrated to produce movement [18]. From a systems neuroscience perspective the primary- and premotor cortex, containing upper-motor neurons, are regarded as the output hubs of cortical networks involved in movement control [19, 20]. To produce goal-directed movements in space, the cortex integrates high-level visual information about movement goals and the end-effector (e.g., hand) with other sensory information (e.g., proprioception), computes a movement plan and transforms it into low-level control commands that can be transmitted to the lower motor neurons.

Starting from vision, Ungerleider and Mishkin discovered that visual processing diverges in the cortex into two large-scale networks denoted ventral stream, sensitive to object features, and dorsal stream, sensitive to spatial relationships [21]. The dominant role of the dorsal stream is to mediate visually guided behavior, since it is sensitive to spatial information that is required to specify the parameters of potential and ongoing actions [22]. The posterior parietal cortex (PPC) is a central part within the dorsal stream. Information from the spatial senses (vision and proprioception) converges in PPC, where it is integrated and transformed from high-level reference frames (e.g., eye- or head centered coordinates) to motor relevant reference frames (e.g., body centered coordinates) [23]. This information is transmitted to the premotor cortex where it is integrated with information from prefrontal cortex about action goals and the current contexts and together with the primary motor cortex translated into low-level movement commands that are relayed via the cortico-spinal tract [20]. As the movement commands are executed by the muscles, somatosensory feedback is transmitted to S1, where it is directly relayed to the motor cortex or indirectly via PPC, which integrates somatosensory and visual feedback [24].

Anatomical and functional connectivity in NHPs [25–27] and humans [19, 20, 28] suggests that the dorsal stream can be divided into three partially overlapping pathways (Figure 1.2). The dorso-medial pathway, also denoted dorsal reach system (DRS), includes superior parieto-occipital cortex (SPOC) and dorsal premotor cortex (PMd), and has been implicated in arm reaching and online corrections. The dorso-lateral pathway, referred as lateral grasp system (LGS), includes anterior intra-parietal sulcus (aIPS) and ventral premotor cortex (PMv), and has been implicated in hand grasping and action understanding. The third pathway, denoted oculomotor intention and attention system (OAS), includes the parietal eye field (PEF) and frontal eye field (FEF), and has been implicated in eye movement control.

All three systems are active during visuomotor tasks that require eye hand coordination [28]. For natural and well learned manual tasks, the

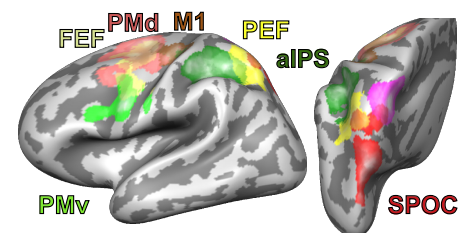


Figure 1.2: Human brain regions implicated in actions. Lateral (left) and posterior (right) views of the left hemisphere of the cortical surface. Frontal and parietal areas involved in hand and eye movement control are highlighted. Frontal areas include the primary motor cortex (M1), dorsal premotor cortex (PMd), ventral premotor cortex (PMv) and the frontal eye field (FEF). Parietal areas include the superior parieto-occipital cortex (SPOC), anterior intra-parietal sulcus (aIPS) and parietal eye field (PEF). They form fronto-parietal networks associated with reaching (SPOC and PMd), grasping (aIPS and PMv) and oculomotion (PEF and FEF). Figure adapted from [20].

typical human behavior starts with a gaze shifts towards the target and the hand moving to the target location [29]. Interestingly, the hand attracts also visual attention. If the hand is present in field of view, visual attention is biased towards it, resulting in lower reaction times to targets close to the hand [30] and stronger activation of SPOC for targets within reach [31].

In NHP neurophysiology studies, it has been shown that the dorsal stream can represent multiple competing actions simultaneously, while more information is accumulated to bias the competing actions until a remaining action is initiated [12, 32]. This suggests that the preparation of potential actions and deciding which action to initiate are parallel processes and involve similar fronto-parietal networks [12] which are biased towards specific actions by prefrontal cortex and the basal ganglia [32]. Human movement behavior also indicates that movement preparation and initiation are parallel processes [33]. Goal-directed discrete reaching movements are typically initiated between 200 ms to 300 ms after a target has been presented. However, ongoing movements can be adjusted within approx. 100 ms to compensate a target perturbation, indicating the presence of additional mental processes, associated with movement initiation, that delay the response in discrete movements.

In summary, the human cortex especially the dorsal stream specifies potential and orchestrates ongoing actions. In anatomically and functionally overlapping fronto-parietal networks hand and eye movements are planned and executed. In parallel, the same networks contribute to the decision process of which action to initiate among all potential ones. Before specific neural correlates of movements are discussed in section 1.5, the next section establishes how brain activity can be measured.

1.4 How to measure Brain Activity?

The primary cells that perform computations within the brain are neurons [10, 34]. They form highly interconnected networks. The human brain contains approx. 10^{10} neurons with 10^{14} connections or synapses in between them. Within the networks, each neuron integrates information from its inputs, denoted dendrites. If the integrated information exceeds a threshold, the neuron elicits an action potential, which is transferred via its axon to synapses. Synapses are directed links that connect a pre-synaptic and a post-synaptic neuron. The transmission is implemented via electrochemical processes that manipulate the post-synaptic neuron's membrane potential with respect to the extracellular space. Depending on the synapse, the pre-synaptic neuron's action potentials can either depolarize or hyperpolarize the post-synaptic neuron's membrane potential. These changes are termed excitatory (depolarization) and inhibitory (hyperpolarization) post-synaptic potentials (PSPs).

In this section, the focus is set to recording techniques that directly measure the electric processes either directly in terms of action potentials at the microscale or spatially integrated population activity at the micro-, meso- or macroscale [35]. Another class of recording techniques measures the neural activity indirectly either via a mechanism known

as neurovascular coupling or via changes in metabolism. Each recording technique has specific advantages and disadvantages in terms of invasiveness, spatiotemporal resolution and cost – for reviews see [36, 37].

Micro-scale – Action Potentials and Local Field Potentials

Electrodes in the vicinity of the neurons can detect the action potentials but also the extracellular potential changes due to the PSPs. The superposition of both signals is denoted local field potential (LFP) [35]. Action potentials and uncorrelated signals are quickly attenuated in neural tissue. The spatial reach is typically below 20 cm [38]. To record action potentials, the electrodes need to be inserted into the brain during a surgical procedure. Within the LFP, the action potentials can be separated in terms of their spectral properties. The action potential related activity is mainly reflected in the higher frequencies above 300 Hz, while the PSPs dominate the lower frequencies [35]. Action potentials or so called spikes are typically detected by applying a high-pass filter (> 300 Hz) and a threshold. The obtained spike traces are called multi-unit activity (MUA) since an electrode can record the action potentials of a single or more neurons. Knowing that the spikes of each neuron have a characteristic shape [39], the spikes of specific neurons can be inferred via clustering. This process is called spike sorting [40] and the resulting spike traces per neuron are denoted single-unit activity (SUA). In the context of movement control, small electrode arrays are typically inserted in M1 and other areas along the dorsal stream [41].

Macro-scale – Electroencephalography and Magnetoencephalography

In 1924, Hans Berger was the first to record human brain activity with electrodes placed at the scalp. He denoted the recorded signals electroencephalogram (EEG) [42]. Within the EEG he described different neural oscillations. He observed that the so called alpha rhythm - a prominent oscillation at around 7 Hz to 14 Hz - is suppressed and substituted with faster beta waves when the eyes are opened. In addition to the oscillatory activity the EEG also captures transient responses [43]. The transient responses are separated in evoked potentials (EPs) and event-related potentials (ERPs). EPs are early responses that reflect the processing of simple sensory stimuli, while ERPs reflect endogeneous responses to more complex stimuli. The transient responses are typically masked by the ongoing oscillatory activity and can be recovered by averaging responses across repetitions or trials.

Genesis of EEG and MEG

The EEG is essentially a modified version of the LFP generated in the brain [35]. Two effects dominate the modification. First, the electric field decays with the square of the distance from the source. Second, volume conduction of the head tissues (brain, cerebral fluid, skull, scalp) have a smoothing effect over an area of approx 10 cm^2 . The attenuation

and smoothing effects limit the sensitivity of electrodes at the scalp to detect only correlated activity of large brain areas. Due to the parallel organization of pyramidal neurons in the cortex and their segregation in apical and basal dendrites, correlated PSPs can result in the formation of dipoles with similar orientation over large patches which are sufficiently strong to project to the scalp [44]. The cortical alpha rhythm is a prominent example.

The electric dipoles result in a current flow in the extracellular fluid, giving rise to a magnetic field perpendicular to the current flow. The magnetic field is also attenuated with the square of the distance to the source. At the scalp the magnetic flux, denoted magnetoencephalogram (MEG), can be measured with superconducting quantum interference device magnetometers [45] or more recently also with optically pumped magnetometers [46]. The MEG is not distorted by the different conductive properties of the tissue layers. Since the electric and magnetic fields are perpendicular to each other MEG and EEG sensors are more sensitive to different sources. EEG is more sensitive to radial sources (i.e., sources located at the gyri), while MEG is more sensitive to tangential sources (i.e., sources located in the sulci).

Linear mixture of sources model

The electric and magnetic fields propagate from the sources to the sensors via the various tissue layers instantaneously [44]. In essence, the bioelectric processes during the propagation of the signals from n sources $\mathbf{s}[t]$ to m sensors $\mathbf{x}[t]$ can be summarized with a linear transformation. Under some assumptions, the linear transformation, can reasonably assumed to be stationary during the course of an experiment and represented as a $m \times n$ forward model \mathbf{A} . At each time-point t the sensor activity is given by a linear mixture of the active sources plus some measurement noise $\mathbf{n}[t]$:

$$\mathbf{x}[t] = \mathbf{A} \mathbf{s}[t] + \mathbf{n}[t] \quad (1.1)$$

Reconstructing the source signals from the measurements forms an ill-posed problem, since the number of sensors is much smaller than the number of sources ($n \gg m$). There are two approaches to estimate the source activity [47]. In the data driven approach, machine learning techniques are used to disentangle the activity of specific or various sources by their statistical properties either in an unsupervised or supervised fashion. In the model driven approach, also known as M/EEG source imaging [48] the forward model \mathbf{A} is computed given measurements or assumptions about the head geometry, sensor locations and the conductivity of various tissue layers. Using the forward model and assumptions about the sources, an associated inverse model can be computed and used to infer the source activity.

M/EEG and Artifacts

The sensors at the scalp are sensitive to all electric (magnetic) sources that project to the sensor location. In this thesis, all sources that do

not reflect brain activity are considered as artifacts. Potential artifact sources are typically separated in technical and biological origin [43]. Prominent technical artifacts are power line noise at 50/60 Hz, and electrode pops or drifts. Among the biological artifacts, the most prominent artifacts are caused by electromyography (EMG), electric activity of the muscles, electrooculography (EOG), electric activity of the eyes, and electrocardiography (ECG), electric activity of the heart.

M/EEG analysis is concerned to a great deal with strategies to cope with artifacts because the temporal and spectral properties can considerably overlap with the ones of typical M/EEG sources. This starts with the experimental design where the experimenter asks participants to avoid certain types of artifacts (e.g., eye movements), goes on to the recording hardware that attenuates noise sources, and ends with dedicated artifact removal or detection algorithms acting upon the recorded signals. In the context of this thesis eye movement and motion artifacts are particularly important because they can co-vary with the kinematics of goal-directed movements.

Eye Movement Artifacts

Movements of the eye and eyelid create bioelectric potentials that are commonly referred to as EOG, or eye artifacts in the case of M/EEG analysis. There are three main physiological sources of eye artifacts [49, 50]: the corneo-retinal dipole (CRD), the eyelid and the saccadic spike potential (SP). The CRD models the potential difference between the positively charged cornea with respect to the retina [51]. The CRD orientation changes as the eyeball rotates, which introduces artifacts that co-vary with the eye movements. Eyelid movements occur during vertical eye movements and blinks. As the eyelid slides across the cornea, a potential/field is introduced [52]. Contractions of the extraocular muscles around the onset of eye movements give rise to the SP [53]: a transient potential/field in the 20 - 90 Hz range [50].

The exact effect of the eye artifacts to the potential/field at each sensor depends on various factors such as the sensor location with respect to the head, head geometry, conductances of the various tissue layers and the scalp-electrode interface. As these factors inherently vary across participants and sessions, the eye artifact related potential/field at each sensor needs to be estimated for each experiment. Within a session and a large visual workspace (visual angle $\leq 20^\circ$) it can be assumed that the artifact contributions are linear [54] and time-invariant [55]. Eye artifact correction approaches are typically based on independent component analysis (ICA) [54, 56, 57] or linear regression [58–60].

Motion Artifacts

The term motion or movement artifacts is typically used to summarize a class of artifacts related to sensor/cable/head movements [61]. First, if the skin is pressed or stretched, potential differences between the inner and outer skin layers can introduce an artifact. This artifact can be significantly reduced by abrading the skin [62]. Second, motion of the electrodes in relation to the skin alters the electrical double layer and

thereby causes a voltage change. This can be reduced via minimizing the impedance and the electrode movement velocity [63]. Third, cable movements or movements in the participant's vicinity can introduce trielectric noise. In the case of cable movements, it is caused by friction and mechanical deformation of the insulator. Immediate pre-amplification reduces this effect [64]. The introduced artifacts are typically linear for small movements [65].

Motion artifacts can be problematic if they co-vary with the dependent variables (e.g., arm movements). Philips et al. showed that they can confound the results and lead to misinterpretations [66]. The experimental setup can greatly reduce motion artifacts. Active electrodes are suitable to attenuate cable motion artifacts, chin-clips reduce the artifacts during arm movements compared to chest-belts and minimizing the electrode-scalp impedance further attenuates potential motion artifacts. The best long-term recording stability is achieved with sintered Ag/AgCl electrodes, salty (Cl^-) electrolytes and skin abrasion [67].

Meso-scale – Electrocorticography

If the recording electrodes are placed underneath the skull above or below the dura mater the electric signals are denoted as electrocorticography (ECoG) [43]. The electrodes are typically mounted on flexible stripes or grids with distances below 2 cm. Compared to EEG, ECoG has a higher spatial resolution, is less affected by volume conduction, and depending of the choice of reference also by eye and motion artifacts. These properties make ECoG a viable clinical tool to monitor and localize epileptic foci in epilepsy patients [68]. In a typical procedure the human patients undergo two surgeries. In a first surgery the electrodes are implanted and after some days the electrodes and pathological tissue are removed. In the meantime the participants are invited to participate in studies to address basic or applied research questions.

1.5 Neural Correlates of Movement

In the cortex, contra-lateral M1 and PM are regarded as central hubs in the generation and control of upper-limb movements. Both areas have direct connections to the spinal cord and their stimulation elicits complex multi-joint movements [69, 70]. Generally, movements can be described by two groups of parameters, namely kinetics (forces and muscle activity) and kinematics (motion in space). While there is not yet a consensus on how the motor areas control movement [18], there is evidence that they encode information about both groups of parameters [71, 72]. The remainder of this section reviews kinematics-related effects.

Kinematics describe the spatial aspect of motion. Their neural correlates are studied in discrete point-to-point movements with static direction of motion, and continuous movements with varying position and velocity. Unlike continuous movements, discrete movements are also accompanied with movement initiation processes.

Direction of discrete Movements

In a classic center-out task, Georgopoulos et al. were the first to report directional tuning of neural spiking activity in M1 neurons of NHPs [71]. In the center-out task, the NHPs moved from a center location to one of 8 equidistant target locations in a cue guided paradigm. They observed that the neurons' firing rates exhibited a cosine tuning curve - with a maximal firing rate during movements in the neurons' preferred direction. Most of the tuned neurons reached their maximal firing rate 100 ms before the movement onset. For each direction modulated neuron, they created a vector that pointed in the preferred direction of the neuron; the instantaneous firing rate defined the vector's length. Summing all these vectors they obtained the famous population vector [73] with which they could reconstruct the arm movements. The population vector had a high congruence to the hand movement trajectories [73], even if the movements were made in different parts of the workspace [74]. Later directional tuning effects have also been observed in other tasks [75, 76] and cortical regions along the dorsal stream [77–80].

Apart from neural spiking activity, there is also evidence of directional tuning effects in invasively recorded population activity. Mehring et al. reported directional tuning in the low-pass filtered LFP activity [81] and later also in power modulations in different frequency bands (<4 Hz, 6-13 Hz and >60 Hz) [82]. The low-pass filtered LFP activity tuning started 100 ms before and peaked 250 ms after the movement onset. Human ECoG studies, also showed directional tuning effects in low-frequency time-domain (LFTD) activity in sensorimotor cortex (SMC) and power modulations >60 Hz [83, 84]. Ball et al. showed that in addition to M1 also PM and lateral prefrontal cortex encoded information in the LFTD activity and power modulations (<2 Hz and >50 Hz) [85]. In both types of features they observed the strongest tuning effects in motor cortex (M1 and PM); the tuning started around 250 ms before and peaked 500 ms after the movement onset.

The direction related tuning effects in LFP and ECoG, raised the question whether movement direction related effects can also be observed in the EEG and MEG. In a study with simultaneously recorded EEG and MEG, Waldert et al. showed that LFTD activity originating in SMC indeed encoded information about movement direction [86]. Movement direction was expressed strongest within the interval 0 ms to 500 ms after the movement onset. At around the same time Hammon et al. reported that the direction of the movement goal can also be detected from EEG activity in the planning period before the movement onset [87].

Movement initiation

Apart from direction related effects, the largest response ($\geq 50\%$ of the variance in spiking rates) of neurons in M1 and PMd is a condition (or direction) independent response time-locked to movement initiation [88]. Kaufman et al. found that the response predicted the reaction times of discrete reaching movements with high accuracy; approx. 150 ms before the movement onset, the firing rates suddenly increased. In previous works that studied center-out tasks, the effect was reported as omnidirectional [73] or speed-tuned [89]. The presence of a condition

independent effect supports the idea that the decision to act is made within the same sensorimotor circuits that are responsible for preparing and executing the associated actions [12, 90]. However, initiating a movement in response to a new goal takes about 200 ms to 300 ms, while an ongoing movement can be adjusted to accommodate a perturbed target within 100 ms, suggesting that movement preparation is temporally dissociated from the decision making process [33].

At the population level, prominent movement onset time-locked responses have been observed in LFP [91, 92], ECoG [83] and also non-invasively in EEG [93, 94] and MEG [95]. In the case of EEG, voluntary movements are accompanied with two time-locked phenomena. The movement onset is accompanied with a phase-locked negative ERP denoted movement-related cortical potential (MRCP) [96–98]. Before the movement onset, during the movement and after the movement offset the relative band-power of neural oscillations is changed. These relative power changes are denoted event-related de-/synchronization (ERDS) [94, 99].

The MRCP was first described by Kornhuber and Deecke [93]. They reported a negative ERP before the onset of hand and finger movements and a series of shorter ERPs thereafter. The post movement onset ERPs were similar to those of passive movements. In subsequent studies several components were identified [96, 97]. One prominent component is the Bereitschaftspotential (BP). It starts around 2.0 s before the movement onset and is bilaterally symmetric over pre- and post-central regions [100]. About 500 ms before the movement onset the BP intensifies and becomes stronger at contra-lateral motor areas [96]. The MRCP is modulated by attention [93], briskness [97] or speed [100–102], force [100, 102, 103] and the type of movement (finger, arm, foot) [104]. Apart from executed movements, MRCPs can also be elicited by imagined [101, 105–107] and attempted [108–110] movements.

Movements are also accompanied with relative power changes in neural oscillations. In their original publication, Pfurtscheller and Aranibar described a relative power decrease in the mu rhythm activity in central areas starting 2 s prior to voluntary movements that was maintained during the movement [94]. Mu rhythms typically display two distinct event-related desynchronization (ERD) patterns [111]. The lower mu rhythm (8 - 10 Hz) ERD occurs during almost any kind of movement and is widespread across SMC. The higher mu rhythm (10 - 13 Hz) ERD is topographically and functionally specific. Typically, the mu ERD is accompanied with a more localized beta rhythm (14 - 30 Hz) ERD and broadband gamma (> 40 Hz) event-related synchronization (ERS) in contra-lateral SMC [99]. After a movement, the mu rhythm power returns to baseline. In the beta band often a rebound is seen in the first post movement second [112]. A localized mu and beta ERD associated to specific movements (e.g., right hand movement) is typically accompanied with simultaneous ERS in neighboring cortical areas [113]. The focal-ERD/surrounding-ERS phenomenon might reflect a mechanism to direct attention to a specific sensorimotor module or effector and inhibit others [114]. The somatotopically organized ERD and ERS effects associated to distinct limb movements allow to infer the type of movement from the recorded EEG activity. What is more, mere imagination of distinct

limb movements activates SMC in a similar fashion as during the pre-movement phase of executed movements [115–117] even in participants with impaired motor function [118].

Velocity and Position during continuous Movements

In the classic center-out task, position and velocity are highly correlated which limits the chance to attribute directional effects to either kinematic variable. Wang et al. studied consecutive reaches to random targets and observed that the spiking activity of M1 neurons encoded information about both position and velocity as well as about speed [119]. One third of the studied neurons were tuned to velocity, about 10% to position and about 20% to a mixture of both parameters. Paninski et al. studied a pursuit tracking task (PTT) to identify position and velocity related effects during continuous movements [120]. In their PTT, the instantaneous position and velocity vectors were decorrelated. They also observed tuning of M1 neurons to both velocity and position; the majority of velocity tuned neurons predicted the upcoming velocity by 100 ms. Human ECoG studies that studied consecutive movements to random targets [121] or continuous movements [122–124] suggest that SMC encodes velocity and position information in LFTD activity and power modulations (> 50 Hz). Hammer et al. found that speed was more clearly represented in SMC than velocity and position [124]. The authors argue that the difference in encoding of velocity and speed between neural spiking activity and the population activity recorded with ECoG could be attributed to the spatial integration; speed tuned effects may be summed up, while direction related effects could cancel each other.

In non-invasive recordings, the tuning characteristics are under debate - mainly due to the potential presence of confounding eye and motion artifacts [66] and the use of outdated methods to study encoding effects [125]. Bradberry et al. were the first to infer velocity information from MEG [126] and EEG [127]. In self-chosen, continuous movements, Ofner et al. reported that information about both velocity and position could be inferred [128]. Jerbi et al. found a coherent representation of movement speed in the LFTD MEG activity generated in M1 [129]. Subsequent studies could extend the coherence between LFTD MEG activity and the magnitude of various other movement parameters [130, 131].

Many of the works that studied the neural correlates of upper-limb kinematics during continuous and discrete movements, were driven by the idea of decoding the trajectories of executed, imagined or attempted movements in real-time. If possible, the decoded trajectories could be used as control signal in a brain-computer interface (BCI). Before state of the art approaches are reviewed in the next chapter, the remainder of this chapter gives a formal definition of a BCI and the underlying concepts.

1.6 What is a Brain-Computer Interface?

This chapter started with a long-term vision that outlined a system that detects the user's intention and translates it into an action without the

person moving. Such a system is denoted brain-computer interface (BCI) or sometimes also brain-machine interface (BMI).

A BCI is formally defined as a *system that measures CNS activity and converts it into artificial output that replaces, restores, enhances, supplements or improves natural CNS output and thereby changes the ongoing interactions between the CNS and its external or internal environment* [132]. A system that only monitors brain activity or analyzes recorded brain activity is not a BCI. In addition to monitoring brain activity in real-time, a BCI is required to simultaneously translate the brain activity to an artificial control signal for an application. The application can either directly provide feedback about the brain activity to the BCI user [133] or indirectly in the case of passive BCIs [134]. From the definition it also immediately follows that a BCI is a closed-loop system; the feedback provided by an application potentially influences the CNS activity which in turn influences the application via the derived control signal. It also directly follows that the user, who modulates his/her CNS activity, is an integral part of the BCI.

The primary goal of BCI research and development is to support paralyzed people with severe disabilities that prevent them from using conventional neuromuscular forms of communication or interaction with the environment [133]. In this thesis we focus on interactions with the environment, and in particular on EEG-based BCIs. From the previous sections we know that the recorded neural activity and the signal to noise ratio (SNR) differ in among recording modalities. However, from a BCI perspective the underlying concepts are identical [132].

Building a BCI requires knowledge about two domains. First, one needs to understand how a particular brain activity is modulated by the users actions or intentions. Second, one needs technical knowledge about how the brain signals can be measured, specific modulations detected and finally transformed into a control signal for an application. The previous section established how brain activity is modulated during voluntary movements. The next chapter introduces the neural correlates of intentions to act and how they have been used in BCIs. In the remainder of this chapter, the focus lies on the technical aspects - particularly the components of a BCI.

Components of a BCI

Figure 1.3 outlines the basic BCI design. The design distinguishes four aspects, namely, the user, signal-acquisition, signal translation and the application which provides feedback [132].

User

From the perspective of the user, BCIs can be categorized into active, reactive and passive [133, 134]. Active BCIs use voluntary modulations of spontaneous brain activity. They do not require any type of external stimulus. Reactive BCIs detect EPs and ERPs and, therefore, require the user to focus their attention to external stimuli. Passive BCIs do not require any active interaction of the user. They work implicitly in the background with the aim to improve human-computer interaction.

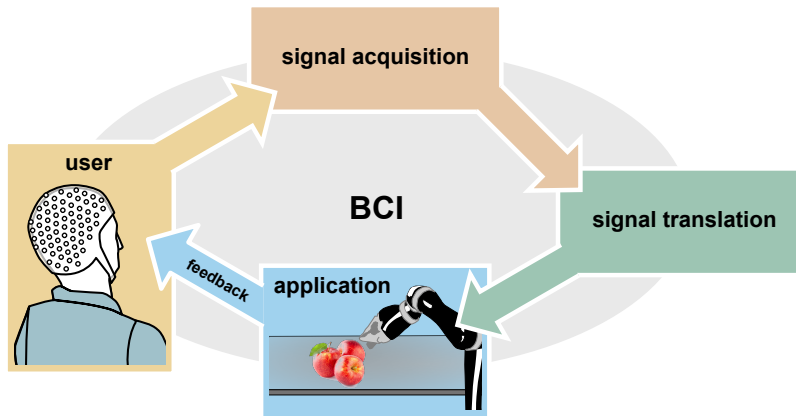


Figure 1.3: Components of a BCI. A BCI is a closed-loop system. It consists of a user, which modulates his/her brain activity, signal acquisition hardware, which digitizes (electro-)physiological activity, signal translation software, which extracts features and detects control commands, and eventually an application, which provides feedback to the user.

BCIs are also categorized according to how the user can control an application. The control paradigms are categorized in *synchronized*, *system-paced*, *constantly engaged* and *self-paced* [135, 136]. In a synchronized BCI, the user can use the BCI periodically, however, there is no non-control state. This is typically the case during training paradigms. A non-control state is defined as periods during which the user willingly chooses not to use the system. A system-paced BCI is periodically available and offers a non-control state. In a constantly engaged BCI, the BCI is continuously available; the user has to actively perform certain mental activity so that the BCI does not trigger actions. Finally, a self-paced BCI is continuously available and offers a non-control state.

Signal Acquisition

The first step during BCI operation is the acquisition and digitization of the brain signals. EEG-based BCIs rely on electrodes placed on the scalp - typically at standard locations [137]. The quality of the detected signals depends considerably on the electrode-scalp interface. To date, the best long-term recording stability is achieved with sintered Ag/AgCl electrodes and salty (Cl⁻) electrolyte gels [67]. Electrodes are also typically categorized in active and passive. Active electrodes come with an integrated pre-amplifier and are therefore less prone to motion artifacts introduced by cable movements compared to passive electrodes. Via the cables few or up to several hundreds of electrodes are connected to biosignal amplifiers. The biosignal amplifier designs belong to the class of instrumentation amplifiers. They detect and amplify voltages between each electrode and a dedicated reference electrode. A high input impedance and a high common mode rejection ratio enable them to attenuate environment noise common to all electrodes and to amplify small voltages in the μV range.

Signal Translation

Once the brain activity is digitized the signals need to be translated to control commands. This process is classically divided into pre-processing, feature extraction and classification [133]. Due to advances in machine learning, pattern recognition and the availability of larger datasets, the signal translation problem starts to be seen as one integrated problem

that can be addressed with deep learning methods [138]. Still, successful deep learning models incorporate the domain knowledge of EEG analysis in the network design. Moreover, for particular sub topics in BCI there is only little data available, which necessitates manual pre-processing and feature extraction.

As in many other electrophysiological signals, pre-processing typically starts with high-pass filtering to attenuate drifts and notch filtering to attenuate line noise [139]. Then spatial filtering is applied to counteract the effects of volume conduction. Because of volume conduction, the electrodes integrate activity of approx. 10 cm^2 . Thus, neighboring electrodes pick up activity of similar sources. The most basic spatial filters are bipolar, Laplace and common average reference (CAR) filters [43]. Bipolar filters compute the difference between pairs of electrodes, and Laplace filters between a center electrode and the surrounding electrodes - typically 4 or 8. A CAR filter computes the average voltage across all channels and subsequently subtracts this new reference signal. More elaborate filters can further improve the SNR but need to be fitted to recorded data. Examples are principal component analysis (PCA), independent component analysis (ICA) and common spatial patterns (CSP). Spatial filters extracted via ICA or regression algorithms are often used to attenuate artifacts [140]. Given that the frequency range is adequate, temporal filtering can further improve the SNR. Finite impulse response (FIR) and infinite impulse response (IIR) filters are popular. Both have advantages and disadvantages in online operation. IIR filters introduce different delays across frequencies, causing distortions. They offer a steep transition between the pass- and stop-bands for a given delay. FIR filters do not introduce distortions at the cost of poor attenuation in the stop-band.

Given the pre-processed signals, feature extraction describes the process of isolating specific modulations in the brain activity that reflect a certain task performed by the user. Common modulations in the EEG activity are EPs, ERPs and ERDS. In the case of EPs and ERPs, epochs are extracted. Epochs are segments of pre-processed EEG, time-locked to certain events. The features for subsequent classification can be the signal during the entire epoch or specific time points. In the case of ERDS, the power of specific oscillations is modulated. Logarithmic bandpower features are the most widespread type of feature used to detect ERDS. The features are computed by squaring the signal and applying a moving average filter. The resulting signal corresponds to the time-varying power which follows a χ^2 distribution. Many of the subsequently used classifiers assume that the features are approximately Gaussian. To make the distribution of the band-power features more Gaussian, they are log-transformed.

Classification describes the process of inferring the label of an observation which is characterized by a set of features [141]. The labels can be up, right, left and down for arm movements in these directions, for example. A classifier assigns labels to observations based on its model parameters. The model parameters are fit to calibration data so that the number of errors in held out data is minimized. A classification model can either linearly or non-linearly transform the features to infer the labels. Various classifiers have been applied in a BCI setting [142]. Shrinkage linear discriminant analysis (sLDA) is the gold standard in BCI due to its simplicity and robustness [143]. If the features follow a Gaussian

distribution and have the same covariance matrix for all classes, sLDA is an optimal classifier in the sense that it minimizes the classification error. Blankertz et al. showed that these two assumptions typically hold for ERPs [143].

If the goal is to infer a continuous quantity given a set of features, the problem is considered a regression problem [141]. The continuous quantity can, for example, be the trajectory of an arm movement. As before, a linear or non-linear regression model transforms the features so that the errors between the observed data and the model's predictions are minimal. If the features consist of repeated measurements at a certain rate up to the current time, the regression problem is also called filtering. In the BCI literature it is common to use the term decoder instead of the terms regression model or filter [144].

Feedback

The classifier or decoder output is mapped to control signals of an application. The mapping depends considerably on the mode of operation (synchronous, self-paced, etc.). Applications can be software like spelling programs, assistive devices like wheelchairs or even neuroprostheses or robotic arms. In either case, the application provides feedback, which closes the BCI loop outlined in Figure 1.3. The feedback component is of high relevance to facilitate learning or adaptation of the user [145, 146]. Feedback training has been demonstrated to increase the strength of ERDS effects during various mental tasks [147]. To facilitate learning the task should be intuitive and engaging for the user, which necessitates clear instructions by the experimenter [145].

This chapter starts with a brief overview of strategies that have been used in BCIs to address the long-term vision of controlling end-effectors like computer cursors, robotic arms and neuroprostheses. Then, BCIs for movement control based on invasively and non-invasively recorded brain activity are reviewed. Recently, the dominant control strategy of invasive BCIs - the decoding of kinematics - has been successfully tested non-invasively in several offline analyses. Advances and current limitations in this research direction are summarized at the end of this chapter.

2.1 Control Strategies

The strategies used to control end-effector movements are categorized as direct and indirect [148] or sometimes also as natural and artificial [149].

In indirect movement control BCIs the user learns to perform one or several mental tasks that result in distinct modulations of his/her brain activity. In this context one also distinguishes between active and reactive BCIs. An active BCI detects voluntary induced modulations and, upon detection, changes the state of an end-effector. These state changes can be opening or closing of an hand orthosis [150], advancing in a certain direction [151] or changing the mode of control of a neuroprosthesis [152]. In active BCIs the mental tasks are arbitrarily mapped to movements of the end-effector. For example, a user with SCI was trained to imagine feet movements to close a hand orthosis [150]. Due to the arbitrary mapping, the BCI user needs substantial training until the mapping becomes intuitive [150, 151]. The reactive BCIs use external stimuli and covert or overt attention shifts to establish a control signal. They offer system-paced and incremental state transitions of an end-effector [153, 154] or a very high-level forms of control [155]. For example, in a high-level form of control a user could choose that his/her wheel-chair drives to the kitchen or living room. In this case, the user would have no influence on the path.

Direct motor control BCIs utilize the neural correlates of voluntary movements to infer executed and intended movement trajectories [148, 149]. They are intuitive in the sense that the user does not need to perform another mental task other than attempting to move the end-effector in the desired fashion.

Due to a high SNR of neural correlates of movement, there is a preference to use direct approaches in invasive recording techniques [7, 148, 156, 157]. However, there are some works that used indirect control strategies [84, 158]. Due to a limited SNR and only recent advances in the understanding of the expression of kinematic information in non-invasive brain activity,

2.1 Control Strategies	17
2.2 Invasive BCIs for Movement Control	18
Neural Spiking Activity	18
Population Activity	20
2.3 Non-invasive BCIs for Movement Control	21
Motor Imagery	21
2.4 Towards direct, non-invasive BCIs for Movement Control	22
State of the Art	22
Limitations	26

indirect control strategies have been dominantly used in non-invasive BCIs for movement control [149].

2.2 Invasive BCIs for Movement Control

Neural Spiking Activity

In the late 1960s Fetz and colleagues were the first to present a spiking activity based BCI [159]. They showed that NHPs could learn to control a meter needle to obtain a reward by modulating the spiking activity of single neurons in M1. Breakthroughs in the area of multi-channel neuronal recording technology in the 1990s allowed to simultaneously record neural spiking activity from multiple cortical areas in rodents and NHPs. At the end of the 1990s a BCI could reconstruct continuous lever movements based on the spiking activity of several neurons [160]. The authors observed that after the animals learned to operate the lever with the BCI, the animals would occasionally not execute the conditioned movement but still produce the neural activity to obtain a reward.

Later the same and other groups demonstrated that NHPs learned to control computer cursors [161, 162] and robotic arms [78, 163]. Carmena et al. also observed that after the BCI was used to control a cursor, the arm and cursor movements became dissociated and eventually the NHPs ceased to produce overt movements [78]. They also reported that the transition from overt movement to BCI control altered the directional tuning properties of approx. two thirds of the tuned neurons in all considered fronto-parietal areas. This direct evidence of directional tuning of neurons to movements of an artificial end-effector paved the way for experiments with paralyzed humans.

Hochberg and colleagues demonstrated that a human study participant with tetraplegia could control two-dimensional cursor movements [7]. They inserted an electrode array in the hand knob areas of M1 and asked the participant to imagine a series of movements. The observed modulations in firing rates were largely consistent with the ones observed in NHPs and contained selective neurons that were modulated by specific actions such as hand opening or closing and non-specific neurons that coded the onset of any imagined action. Due to the lack of overt movements, they fit the decoder to calibration data during which a technician controlled a cursor and the participant imagined to manually track the moving cursor. After training for several months, the user could track the technician's movements with high correlations ($r^2 = 0.5$) and perform center-out movements to specific target locations with high accuracy (>75%, mean time to target 2.5 s). Based on this experimental approach and recording technology, more recent works demonstrated successful control of increasingly complex end-effectors like robotic arms with multiple degrees of freedom [164, 165].

Unfortunately, the inserted electrode arrays suffer from bio-compatibility issues [166, 167]. This can lead to tissue lesions and then into an encapsulation of the electrodes with glia cells in an inflammatory reaction. The whole process results in a reduction of detectable spiking activity over time, making the system unusable to detect spikes after several months or

years [168]. Due to a lack of systems with improved bio-compatibility the electrode arrays have so far been used in the majority of human clinical trials.

Among the potential areas, M1 is the most commonly used [7, 78, 164] because a considerable fraction of the spiking activity is clearly correlated with different movement parameters [71, 89]. In addition, PMd [78, 169] and PPC [78, 170] have been targeted. Recall that they are important areas within the fronto-parietal networks for upper-limb movement control. The group around Andersen demonstrated that the intended movement goals, types and even trajectories could be decoded from spiking activity in human PPC [170].

Several algorithms have been proposed to decode executed and intended movements [171]. The first decoding algorithm was the renowned population vector method. The population vector is created in three simple steps. First, the preferred direction of each neuron is identified. Second, the unit vector, pointing in the preferred direction, is multiplied with the current spiking activity. Third, the vectorial sum of all tuned neurons is the population vector. Despite its theoretical importance in the understanding of neural tuning and success in simple repetitive movements, the approach suffers from a number of limitations. The fitting procedure does not consider any criterion to minimize errors, the neurons' tuning properties can differ across tasks and conditions, and the method requires time-consuming spike sorting to extract SUA.

The most widespread used decoder is the Wiener filter (WF) and its regularized variants. The WF assigns weights to the features so that the mean-squared error between the target signal and its prediction are minimal [172]. The features are the spiking rates of several units (SUA or MUA) during one or several preceding time-points, called lags. Typically the preceding 300 ms to 1000 ms in steps of 50 ms or 100 ms are considered. With an increasing number of units and lags compared to the amount of data the risk of overfitting due to the curse of dimensionality increases. Recent works used regularization methods to reduce overfitting to calibration data [164, 165, 170].

Another commonly used algorithm is the Kalman filter (KF) [173]. Similarly to the WF, the KF transforms multiple features into predictions of several outputs. In the KF, the outputs are denoted states that cannot be directly observed and the features are denoted measurements. Once the model is fitted to calibration data, the filter computes new estimates of the states in two steps. In the first step, called prediction, the previous state and a state transition model are used to provide an estimate of the new state. In the second step, called update, the estimated state and an encoding model are used to estimate the measurements (e.g., firing rates). Then the error between the estimated measurements and the actually observed ones is computed and the estimated state is adjusted resulting in the final estimate of the new state. Knowing that spiking activity exhibits tuning to direction and speed [89] and that they are nonlinearly related, Li et al. [174] proposed to use an unscented Kalman filter (UKF), a variant of the KF that can handle non-linear relations between the states and/or the measurements [175]. They found that the UKF outperformed a WF and KF in offline simulations and in BCI-based control of computer cursors. A 10^{th} -order UKF decoded 2D velocity trajectories with SNRs of

1.15 dB (center-out task) and 1.46 dB (tracking task) and correlations of 0.5 (center-out task) and 0.55 (tracking task).

Population Activity

In addition to SUA and MUA, the intracortical electrodes also record synaptic transmissions which are the primary sources in the lower frequencies (<300 Hz) of the LFP. Direct LFP-based BCIs for movement control have been primarily evaluated in NHPs and offline simulations [81, 82, 176].

In the same paper where Mehring et al. reported the tuning of time-domain LFP activity to movement direction, they also reported the results of offline decoding simulations [81]. In a 2D center-out task, they reported average correlations of approx. 0.7 using LFP and slightly higher correlations using MUA. O'Leary and Hatsopoulos reported that the low-frequency (<10 Hz) time-domain LFP activity in M1 and PMd was modulated strongest by the target direction [177]. Using the LFTD features, they predicted the target in a 8 direction center-out task with moderate accuracies (up to 50 %). In a more recent offline study, Aggarwal et al. compared the decoding performance of LFP and MUA in a reach and grasp task [176]. The grand average correlations between the actual and decoded kinematics were 0.76 for MUA, 0.61 for high-frequency LFP power features (100 Hz to 175 Hz) and 0.58 for LFTD features. They additionally found that LFP and MUA predicted the various stages during the paradigm (baseline, reaction, movement and hold) with moderate accuracies (73% MUA, 62% LFTD features and 59% power features). The first successful demonstration of a direct LFP-based BCI in NHPs was presented in a 2D random-target pursuit task [157]. In [157], the NHPs used both LFP and MUA based BCI over several months without recalibration.

Other studies in NHPs used ECoG to reconstruct movement trajectories. The group around Fujii decoded goal-directed 3D arm movements in offline simulations using subdural [178] and epidural [179] ECoG grids. They studied power modulations and reported that the decoders utilized modulations in higher-frequencies (>60 Hz) and recent lags (<500 ms). The grand average correlations between the actual and decoded 3D trajectories were 0.72 (subdural) and 0.57 (epidural).

Successful offline decoding of executed 2D and 3D arm and finger movements has also been reported in human ECoG studies [84, 85, 121, 122, 124, 180, 181]. Several groups investigated which regions and features were most informative. Overall, electrodes above SMC were most useful for decoding trajectories. Regarding the features, power-modulations at high frequencies (>60 Hz) and LFTD features contained most information about the trajectories.

Using LFTD features, Schalk et al. predicted positions and velocities with correlations of 0.49 in a 2D continuous tracking task [180]. Using similar features, Pistohl et al. predicted cursor trajectories with a linear KF (correlation = 0.33 for 6 participants; correlation = 0.43 for 3 participants with ECoG grids covering hand/arm areas) in a 2D continuous random target reaching task [121]. Nakanishi et al. studied a 3D continuous reaching and grasping task in 3 participants [122]. They decoded wrist

and elbow positions as well as elbow and shoulder joint angles with moderate congruence. For example, the correlation for 3D wrist position was 0.51. Ball et al. investigated self-paced center-out reaching movements [85]. They could predict the movement direction before the movement onset with moderate accuracy (45 % for 4 directions). Shortly after the movement onset the accuracy peaked at 76 %.

Most of the human ECoG studies reported here used decoders that belong to the class of WFs. Although the offline simulation results indicate a potential use of ECoG based direct BCIs for movement control, so far only one feasibility study demonstrated online BCIs operation [182], while the majority relied on indirect control strategies based on imagination of distinct movements [84, 158, 180]. With the help of feedback training many of the indirect BCIs users could improve their motor imagery skill. After successful training, they could continuously control computer cursors with moderate accuracy in 1D [84], 2D [180] and 3D [158] environments.

2.3 Non-invasive BCIs for Movement Control

The vast majority of EEG and MEG based movement control BCIs used indirect control strategies, and among them most utilized ERDS effects in sensorimotor rhythms (SMRs) during motor imagery (MI) [132]. An emerging alternative to the MI strategy is inspired by the success of direct strategies in invasive BCIs for motor control. The remainder of this section will review the progress of indirect, MI-based BCIs and their limitations, while the next section summarizes the progress and state of the art of direct approaches.

Motor Imagery

Feasibility studies in healthy people and people with SCI demonstrated discrete control [8, 150] as well as continuous control [6, 151, 183, 184] of various end-effectors.

In continuous control tasks, the strategy of continued mutual adaptation of the user to the BCI and the BCI to the user proved successful [151, 183]. Starting with user-specific SMR patterns during distinct MI tasks, an initial BCI is calibrated. Based on this BCI, the user receives feedback which supports him to gradually improve his/her SMR control. In a new iteration, the new data is used to recalibrate the BCI. As this process proceeds, the BCI usage becomes automatized much like a well-learned skill, rendering the deliberate act of MI less important [6, 183]. Already in 1991, Wolpaw et al. described a mu rhythm based BCI used for 1D cursor control [151]. The users reported a variety of MI strategies (running, shooting baskets, etc.) to make a computer cursor move up or down. As the cursor control improved, the imagery became less important for the users.

Later it was demonstrated that people could learn to modulate two SMRs simultaneously which allowed them to control 2D cursor movements [6]. Remarkably, the reported control accuracy was comparable with the accuracy reported in the first invasive, direct BCI that demonstrated 2D cursor control [7]. More recently, it was demonstrated that three SMRs

can be simultaneously modulated, enabling 3D cursor [183] and robotic arm control [184].

Unlike SMR-based BCIs, the number of simultaneously controllable degrees of freedom (DoFs) has drastically increased in direct, invasive BCIs in recent years [164, 165]. This highlights the fundamental limitation of the indirect, MI-based control strategy. Increasing the number of mental tasks is feasible [185] but requires substantially more training time to detect the patterns with reasonable accuracy. In addition, the coarse spatial resolution of EEG and MEG limits the number of distinct patterns that can be detected [149]. As a remedy, many non-invasive approaches traded the continuous control of multiple DoFs for several sequential operations with lower DoFs. Although this sequential operation strategy was demonstrated to be feasible in 3D robotic arm [184, 186], orthosis [150] and neuroprosthesis [8, 152] control, the time to complete complex movements substantially increases.

2.4 Towards direct, non-invasive BCIs for Movement Control

SMRs in the mu and beta band are associated with a general movement activity [99], which is exploited in MI-based BCIs, but they have consistently been reported to contain little information about the direction and the trajectory of limb movements [85, 86, 124, 129].

From the previous sections we know that LFTD activity and high-gamma power modulations (>50 Hz) carry most information about movement trajectories in invasively recorded population activity (LFP and ECoG). Compared to the LFP and ECoG, the SNR of kinematics related effects can be assumed to be lower in MEG and EEG [187]. The limited spatial extent of sources in the gamma band and the low SNR of gamma oscillations in the MEG and EEG render a single trial detection impractical. However, there is a growing amount of evidence that the kinematics related effects in LFTD are detectable at the single-trial level [86, 87, 126–128]. Still, the sub field of decoding kinematics from M/EEG is relatively new with many open questions to be answered before direct BCIs for movement control can become an alternative to the traditional indirect, MI-based BCIs. Central topics have been elimination of potentially confounding motion and eye artifacts [66, 188], classification of movement direction, decoding of entire movement trajectories and a transfer to imagined, observed or attempted movements.

State of the Art

Classification of Movements in different Directions

Movements in discrete directions have been studied predominantly in variants of the classical visually guided center-out task. The variants include non-delayed executed movements [87, 189], delayed movements after imperative go cues [190–192] or self chosen moments [86, 193] and imagined movements [189]. Some studies analyzed the pre-movement period after the appearance of direction cues [190, 191], others investigated

effects in the peri-movement period around the movement onset [86, 192, 193] and some considered both aspects [87, 189]. The pre-movement period contains activity associated with movement intention. Movement intention can be defined as an early plan to move and represents a high level state which specifies the goals of movements rather than the low level details (e.g., exact muscle activations) required for execution. Consequently, peri-movement activity is associated with the formation and execution of low level movement plans. There is evidence that the direction can be inferred from LFTD M/EEG activity during both periods. For BCIs, the pre-movement period is particularly interesting because effects related to the intended movement direction do not reflect somatosensory feedback that is unavailable in persons with SCI.

Hammon et al. were the first to decode the intended movement direction from EEG activity [87]. In 4 participants and 3 movement directions, they observed a similar classification accuracy in the pre-movement period (average accuracy of 59 %) and movement period (63 %). Their classifier used LFTD and band-power features. The participants performed arm and eye movements during the task, introducing eye and motion artifacts. They attenuated them with an extensive ICA cleaning procedure. Later, Li et al. and Kuo et al. corroborated and extended their findings in similar tasks with more participants [190, 191]. Both studies restricted the analysis to the pre-movement period and LFTD features. They reported moderate average accuracies of 65 %, in two directions [190] and 60 % in three directions [191]. The discriminative sources were primarily located in PPC, which is consistent with direction related effects in invasive studies [80, 170].

In the peri-movement phase SMC has been implicated in the encoding of information about movement direction. Waldert et al. investigated the classification of directions from MEG and EEG activity during self-paced hand movements in 4 directions [86]. Using LFTD features they obtained a peak accuracy of 60 % (MEG) and 55.0 % (EEG) about 500 ms after the movement onset. The primary discriminative sources were located in contralateral and medial SMC. Robinson et al. 2013 also studied reaching movements in 4 directions [192]. Using more sophisticated feature extraction methods, classification algorithms and a ± 1 -s window around the movement onset, they obtained an average accuracy of 80 % in 7 participants. The discriminative sources were located in SMC and PPC and had highest SNR around 500 ms after the movement onset. In contrast to the findings of [86, 192], Lew et al. reported a similar accuracy in the pre-movement and post-movement periods in 5 participants (3 stroke patients) and a delayed reaching task [193]. On a closer look, one cannot rule out that their classifier was compromised by residual artifacts, since their eye artifact correction approach attenuated the artifacts in frontoparietal channels only moderately [194]. Using MEG and a paradigm that did not force the participants to delay movements, Wang et al. could classify movements in four directions with an average accuracy (5 participants) of 80 % around 250 ms after the movement onset and 67 % shortly before the movement onset. They also asked the participants to imagine the previously executed movements and analyzed the data aligned to the direction cue. The average accuracy (63 %) was comparable to the pre-movement period of executed movements. In a second group (4 participants), Wang et al. introduced a forced delay period with an

imperative go cue. The obtained accuracy in this group was lower in executed (62 %) and imagined (50 %) movements.

In summary, several groups have studied the decoding of (intended) movement direction from LFTD M/EEG activity. Although the individual studies contained few participants, the combined findings suggest that up to 4 directions can be inferred with moderate accuracy in pre-movement and movement periods. In the pre-movement period PPC was repeatedly reported to encode directional information, while in the movement period SMC activity was reported. This suggests the presence of two direction related effects in the LFTD M/EEG - one high-level effect that reflects movement intention (pre-movement, mainly PPC) and one low-level effect that reflects movement execution (movement, mainly SMC). Moreover, the findings presented in [189] indicate that the time-locking point might have a strong effect on the classification accuracy - in particular if the movements are imagined rather than executed. To date, this has not been systematically studied yet.

Decoding Movement Trajectories

Shortly after the first groups reported the successful classification of movements into different directions, several groups tested whether the LFTD activity encoded information about the movement trajectory to the targets. The group around Contreras-Vidal were the first that demonstrated a successful decoding of velocity trajectories during 2D center-out reaching movements from MEG [126] and 3D center-out reaching movements from EEG [127]. They obtained the best results with a WF that considered the last 200 ms (100 ms in the EEG study) and channels covering SMC and PPC. The congruence between the decoded and recorded trajectories were higher in the MEG study (approx. 0.45, 5 participants) than in the EEG study (approx. 0.3, 5 participants). Toda et al. studied 2D center-out movements in 8 directions without visual feedback during the movement [195]. They analyzed LFTD MEG activity around the movement onset (± 1 s) in source space and decoded position and velocity trajectories with a regularized WF. In the source space, they decoded position and velocity with correlations of 0.77 and 0.52 (5 participants). The decoding model accuracy dropped significantly if the decoding model was fit and evaluated in sensor space. In a visually guided 3D center-out task, Yeom et al. reported correlations of approx. 0.7 (9 participants) for a linear velocity decoder [196]. Their decoding model did not use peripheral channels, which seemed to be affected by movement and muscle artifacts during the movement task. Residual movement and muscle artifacts could have contributed to the activity at central channels, and in turn to the high decoder accuracy. Robinson et al. studied EEG during a visually guided center-out task in two-dimensions [197]. They reported average correlations of approx. 0.6 (7 participants) for linear velocity and position decoders.

Antelis et al. challenged the significance of the previously presented results [198]. They tried to decoded velocity trajectories from LFTD EEG activity during a self-paced, 3D center-out task to 8 targets. Although they used comparable pre-processing and decoding algorithms as the works before, their simulation results revealed that the correlations achieved with linear decoders were not significant. An important take

home message from their work is the importance of a realistic significance level estimation. The significance level for the correlation metric depends on various parameters. For example, it is likely to observe high spurious correlations for short time-windows and if both the true and decoded kinematic signal have a low frequency. In their study the time-windows were particularly short (1s or less), which increases the probability of observed high correlations due to chance. Taken together, short (center-out) movements are not well suited to determine how well kinematics can be decoded from LFTD activity.

Several groups have investigated kinematics decoding during continuous movement tasks and reported moderate to high correlations between the actually executed and decoded trajectories. Already in 2005, Georgopoulos et al. reported that they inferred the position trajectories of 2D pentagon drawing movements from LFTD MEG activity with high congruence (0.85 correlation, 10 participants) [199]. They did not provide any results of the contributing sources, rendering a judgment whether motion or eye artifacts contributed to the impressive results impossible. Lv et al. decoded velocity trajectories of a 2D drawing task, which was essentially a sequence of visually guided reaching tasks in 4 directions [200]. They used LFTD EEG activity as well as power features in their decoding model and reconstructed the trajectories with an average correlation of 0.3 (5 participants). A feature importance analysis revealed that the LFTD activity and power modulations in the 24 Hz to 28 Hz band of central, parietal and occipital channels contributed most to the results. Ofner and Müller-Putz studied executed continuous, 3D arm movements with varying speed [128]. Using LFTD features, they decoded 3D position and velocity trajectories with high correlations of 0.7 on average (5 participants, 3 dimensions). In another EEG study, Úbeda et al. studied a continuous 2D tracking task [201]. They tested various levels of difficulty and observed a strong effect of the tracking accuracy (i.e., how accurately the participants could track a target stimulus) on the decoding accuracy (i.e., correlation between the decoded and recorded trajectories). When the participants could accurately track the target, the correlations were moderate (0.4). As the difficulty increased, the correlations decreased.

Apart from decoding executed movement trajectories, some groups have also studied imagined movements. For example, Kim et al. asked their study participants to make continuous 3D arm movements in one condition and in another condition to imagine making the same movements while they observed a robotic arm perform the movements [202]. Using a WF, they obtained average (10 participants, 3 dimensions) correlations of 0.4 and 0.3 during executed and imagined/observed movements. They compared the decoding performance of the WF to a nonlinear kernel ridge regression (KRR) decoder. The correlations of the KRR decoder were on average 0.1 higher in both conditions, which suggests that the EEG also encoded information that was non-linearly related to the velocity trajectories. They also emphasized that although the participants were instructed to avoid eye movements, there were still residual eye movement artifacts present in the EEG activity. To rule out the contribution of eye artifacts, Ofner and Müller-Putz came up with a paradigm that avoided any visual stimuli that co-varied with the imagined movement [188]. The participants imagined rhythmic arm

movements either in the vertical or horizontal plane. The rhythm of the movement was paced by a metronome (0.5 Hz). They could infer the single trial movement plane (vertical or horizontal) with an accuracy of 64 % and obtained correlations of 0.3 between the system paced rhythm and the decoded trajectories. Despite the low performance, the results demonstrated that even in the complete absence of any direction stimuli and overt movement, the direction of the intended movement can be inferred from LFTD EEG. Very recently Úbeda et al. studied visually guided imaginations of 2D center-out movements to 8 targets in 5 healthy participants [203]. They tried to decode the position and velocity trajectories of a visual stimuli that guided the movements. They could only decode the horizontal component of the velocity trajectories with a low, yet significant correlation of 0.25. The results for the vertical velocity component as well as for the position trajectories were not significant. They also tried to classify between different targets, but were only successful to discriminate between two targets (e.g., left vs. right and up vs. down) with a low, yet significant classification accuracy of approx. 60 %.

Although most studies investigated whether information about the intended/imagined movement direction can be inferred, Farina and colleagues studied the expression of speed. They found that the MRCP is modulated by the speed of imagined wrist movements [204]. Later they also showed that the speed of an ensuing movement already modulates the pre-movement part of the MRCP [102].

Altogether, the evidence presented by several groups suggests that the LFTD M/EEG activity carries information about the movement trajectories of executed and imagined/observed movements. In the case of executed movements, it is not clear how well the trajectories can be inferred. Some studies reported high correlations [128, 196, 199], while others reported moderate correlations in comparable tasks [127, 200]. In the case of imagined/observed movements, the reported correlations were moderate to low [188, 201, 202].

Limitations

Due to the susceptibility of M/EEG activity to motion and eye artifacts, the disagreement in the reported correlations between studies could be at least partially explained by residual artifacts that might have led to overly optimistic results. For example, the usage of a chest band and passive electrodes can introduce large motion artifacts in central channels that co-vary with the movement kinematics [66]. While active electrodes and chin clips can mitigate motion artifacts, they have no effect on eye artifacts.

Avoiding eye movements does not seem to be a solution. This strategy strongly limits the types of tasks that can be studied to either simple discrete movements or repetitive continuous movements. Kim et al. reported that even though the study participants were instructed to avoid eye movements, they still moved their eyes slightly and the introduced artifacts led to a higher decoder performance [202]. The potential BCI users want to perform goal-directed actions and freely orient their gaze, much like in direct BCIs based on spiking activity [5]. The best

alternative strategy is to attenuate eye movements. Several methods have been proposed. Some studies simply excluded pre-frontal and frontal channels [198, 203], while others used artifact attenuation methods [87, 200, 202]. Each method has its advantages and disadvantages in terms of attenuation quality and online applicability. A systematic evaluation is missing.

A better understanding of the brain sources that encode kinematic information in the M/EEG could help to disentangle the relevant brain sources from artifact sources. While there seems to be a common understanding that areas along the dorsal stream - particularly SMC and PPC - encode kinematic information during discrete and continuous movements, many studies investigated the decoder weights which are optimized for decoding but should not be interpreted to infer the contributing sources [125]. A more detailed analysis of the sources utilized by the linear decoding models could contribute to a better understanding of the involved areas and their spatiotemporal dynamics.

Although linear decoders like Wiener and Kalman filters can be readily interpreted, some recent works obtained a higher decoding accuracy with non-linear models [202, 205]. This suggests that more information about the movements is encoded than what linear position/velocity decoders can extract. With sufficient taps, Wiener and Kalman filters can integrate and differentiate positions and velocities and transform coordinate spaces [149]. However, they cannot model non-linear relationships like between velocity and speed. There is evidence that information about both is encoded in the LFTD M/EEG activity. This could at least partially explain why non-linear decoders outperformed linear ones.

Among all limitations of the sub-field, the most critical one is that it remains unclear whether an M/EEG-based direct BCI can be used online. There is a single study that reported continuous 2D cursor control based on imagined arm movements [206]. However, later it was shown that a randomly moving cursor could achieve similar performance [207]. All the other previous works analyzed the data offline.

The central aim of this thesis is to develop a direct BCI that decodes the movement trajectories of healthy volunteers from LFTD EEG activity during goal-directed movements. To complement the research towards the central aim, this thesis also explores the neural correlates of movements during different volitional states and tasks, ranging from discrete center-out movements to continuous goal-directed hand and eye movements. Since eye movements strongly contaminate the LFTD M/EEG activity, a considerable part of the thesis will focus on the correction of eye artifacts.

The correction of eye artifacts will allow us to study the neural correlates of natural human movement behavior during actions, in contrast to previous non-invasive works. In previous works, the dominant strategy was to avoid eye movements with limited success in the suppression of eye artifacts [202] and decoding performance [188]. Knowing that the cortex is strongly involved in the control of goal-directed movements and that M/EEG signals primarily detect cortical activity, we expect that the decoding performance will be higher during natural movement behavior.

In this thesis we will also use high density M/EEG recordings, which provide access to the population activity of the whole brain. High-density recordings during natural movement behavior will enable us to study the tuning characteristics of LFTD activity to different kinematic variables in a similar fashion as it has been done with neural spiking activity [71, 120] and invasive population activity [82, 85]. Although the SNR will be lower compared to the invasive approaches, we will have access to all relevant brain areas along the dorsal stream.

Another important difference to previous works is that in this thesis we will conduct experiments during different volitional states. This will allow us to identify cortical networks that encode kinematic information in a specific volitional state (e.g., executed movements) and others that encode kinematic information in multiple volitional states (e.g., executed and observed movements).

3.1 A proof-of-concept direct BCI for Movement Control

A direct BCI for movement control should be able to infer information about the kinematics from the EEG activity in real-time so that the user can control an end-effector to accomplish a certain task. With this clear aim in mind, we specified several constraints that should be fulfilled:

- The BCI should allow the user to continuously control an end-effector in multiple dimensions over several tens of seconds. Longer

3.1 A proof-of-concept direct BCI for Movement Control	28
3.2 Neurophysiology of executed and observed Movements	29
3.3 Encoding Model	30
3.4 Workplan	31
Online Eye Artifact Correction	31
Neural Correlates of Movement	31
Decoding Accuracy Improvement	31
Proof-of-concept direct BCI	32

periods of continuous control allow a more realistic estimate of the decoder accuracy, since the chance of observing spuriously high correlations is reduced. It is sufficient to demonstrate simultaneous 2D control. Nonetheless, an extension to 3D control should be straightforward.

- ▶ The BCI user can use the system to make goal-directed movements. We set the focus to tracking tasks. They are goal directed and continuous. In such tasks, a target stimulus would be moving and the user would try to follow the target with an end-effector.
- ▶ The direct BCI has to be invariant to eye and motion artifacts. Residual eye and motion artifacts can result in spuriously high decoder performance. It is critical to disentangle kinematics related brain activity and the potentially co-varying artifacts. We will rely on eye artifact correction and source analysis methods to demonstrate that the decoding algorithms access brain activity.
- ▶ The BCI operation has to be safe. This seems to be trivially satisfied in non-invasive BCIs. However, if the end-effector is a robotic arm, the system must ensure that the robotic arm does not accidentally collide with the user or objects. Large jerky robotic arm movements could be the result of transient artifacts within the EEG activity. To ensure safe operation and predictable end-effector movement behavior, the system has to detect transient artifacts, ideally correct them or if not possible return to a safe state.
- ▶ The processing delay introduced by the system should be low. Short delays between the intended (and executed arm) movements and the decoded movements that drive the end-effector are desirable for two reasons. First, short delays allow the completion of movements with higher accuracy, which seems to be also beneficial for movement decoding [201, 208]. Second, the shorter the introduced delay is the smaller is the temporal coupling between a movement update and its consequence. Generally, a tight coupling between actions and their consequences facilitates learning.
- ▶ Lastly, the proof-of-concept system should achieve a sufficient decoding accuracy so that the BCI users are convinced that they can improve the task performance with training.

3.2 Neurophysiology of executed and observed Movements

As already pointed out, many of the previous studies analyzed the decoder weights to identify sources that encoded information about the kinematics. However the weights do not only extract the encoded information they also suppress uninformative noise. Sources that encode information about the kinematics can be identified by either fitting an encoding model or computing the patterns associated to the weights [125, 209]. A combined extraction of the encoding sources and eye artifact correction will make EEG and MEG suitable functional neuroimaging techniques to study the dynamics of natural movement behavior. In this thesis, we plan to use these tools to investigate three research questions:

- ▶ How is the LFTD activity spatiotemporally tuned to the kinematics of executed upper-limb movements? The results of previous studies

agree that kinematic information of different dimensions (e.g., horizontal, vertical) is encoded in similar cortical patches. In the case of spiking activity the firing rates of neurons in SMC are preferentially tuned to velocity rather than position [120]. Does this transfer to the LFTD M/EEG activity?

- ▶ How do the kinematics-related tuning characteristics change across volitional states? Does the LFTD activity originating in SMC encode information about observed movements? How about other areas along the dorsal stream?
- ▶ How similar/different are the kinematics-related tuning characteristics of discrete and continuous goal-directed movements? Do the same areas that encode information about the kinematics of continuous movements also encode information about the direction of discrete movements? Previous studies classified the movement direction time-locked to the movement onset [86] or to the cues [87, 190] and observed movement direction related effects in different cortical areas. This raises the question whether the movement onset or cue time-locked effects are more similar to the kinematics-related effects in continuous movements.

3.3 Encoding Model

Similar to previous works [81, 86, 126–128, 180] we assume that the kinematics $\mathbf{k}[t]$ (e.g., 2D position, 2D velocity or speed) during goal-directed movements are linearly encoded in the LFTD M/EEG activity $\mathbf{x}[t]$. As defined in equation 1.1, $\mathbf{x}[t]$ contains a linear mixture of various sources $\mathbf{s}[t]$. Some of the brain sources encode kinematic information $\mathbf{s}_{brain}^{(k)}[t]$, while others reflect non-task relevant brain and noise sources $\mathbf{n}[t]$. Knowing that the sensors capture not only brain activity but potentially also motion and eye artifacts $\mathbf{n}_{art}^{(k)}[t]$ that co-vary with the kinematics $\mathbf{k}[t]$, we consider the model

$$\mathbf{x}[t] = \mathbf{A} \mathbf{s}[t] + \mathbf{n}[t] = \mathbf{B} \mathbf{s}_{brain}^{(k)}[t] + \mathbf{C} \mathbf{n}_{art}^{(k)}[t] + \mathbf{n}[t] \quad (3.1)$$

where the desired kinematics encoding brain sources $\mathbf{s}_{brain}^{(k)}[t]$ and undesired artifact sources $\mathbf{n}_{art}^{(k)}[t]$ are projected to the sensors $\mathbf{x}[t]$ with the mixing matrices \mathbf{B} and \mathbf{C} . Similar to previous works that used linear filters, we assume that the brain and artifact sources are a linear transformed and filtered combination of the kinematic state $\mathbf{k}[t]$ at the current t , previous $t - \tau$ and future $t + \tau$ time-points

$$\mathbf{s}_{brain}^{(k)}[t] = \sum_{\tau} \mathbf{D}[\tau] \mathbf{k}[t - \tau] = (\mathbf{D} * \mathbf{k})[t] \quad (3.2)$$

$$\mathbf{n}_{art}^{(k)}[t] = (\mathbf{E} * \mathbf{k})[t] \quad (3.3)$$

summarized with the linear operators \mathbf{D} and \mathbf{E} with which $\mathbf{k}[t]$ is convolved¹. The central aim of this thesis it then to infer the kinematic state (e.g., 2D position and velocity) $\mathbf{k}[t]$ online from the LFTD EEG $\mathbf{x}[t]$ without using co-varying artifact sources $\mathbf{n}_{art}^{(k)}[t]$.

1: The $(\delta * \chi)[t]$ operator indicates a convolution of the signal $\chi[t]$ with the filter δ across time.

3.4 Workplan

Answering the stated research questions and reaching the central aim will require to conduct several studies. The key milestones and our plan to get there are outlined in the next paragraphs.

Online Eye Artifact Correction

To assure that the direct BCI relies on brain activity rather than artifacts during goal-directed movements, the artifacts need to be removed before the BCI is calibrated. We will test how well state of the art eye artifact correction algorithms can estimate the artifact mixing matrix \mathbf{C} and sources $\mathbf{n}_{art}^{(k)}[t]$ from calibration data during which $\mathbf{s}_{brain}^{(k)}[t]$ are inactive. During goal-directed movements, the corrected signals $\mathbf{x}_c[t]$ are then

$$\mathbf{x}_c[t] = \mathbf{x}[t] - \hat{\mathbf{C}} \hat{\mathbf{n}}_{art}^{(k)}[t] \cong \mathbf{B} \mathbf{s}_{brain}^{(k)}[t] + \mathbf{n}[t] \quad (3.4)$$

where the $\hat{\cdot}$ -modifier is used to indicate the estimates of the true, unknown sources signal and mixing matrix. If current state of the art algorithms are insufficient to attenuate the artifacts, we will develop and test a new algorithm.

Neural Correlates of Movement

In a parallel line of research, we will explore the neural correlates of movement in a series of EEG and MEG studies. In single experiments we will study multiple conditions and tasks. In discrete movement tasks, we will analyze whether and how strongly the MRCP is modulated by movements in different directions. In continuous movement tasks, we will analyze how kinematic information is encoded in the corrected M/EEG activity $\mathbf{x}_c[t]$, and how well linear models can infer the kinematic information. Following the approach of previous non-invasive decoding studies, we will first investigate velocity and position related effects. Motivated by recent findings of several groups, we will later also investigate effects related to the length of the velocity and position vectors, namely, speed and distance.

Decoding Accuracy Improvement

If the results indicate that information about directional (velocity, position) and non-directional (speed, distance) kinematics can be simultaneously detected with linear decoders, we will explore ways to integrate the information to improve the decoding accuracy. In the invasive domain, UKFs have proven successful in combining directional and non-directional information encoded in spiking activity [174].

Proof-of-concept direct BCI

We will eventually use the insights from the offline analyses to design an EEG-based direct BCI to continuously control the movements of a robotic arm. Similar to the tests of direct BCIs in NHPs, we will test the EEG-based system in a group of healthy participants and executed movements.

4.1 Online Artifact Correction

Evaluation of Algorithms for online Eye Artifact Correction

Reference # 210

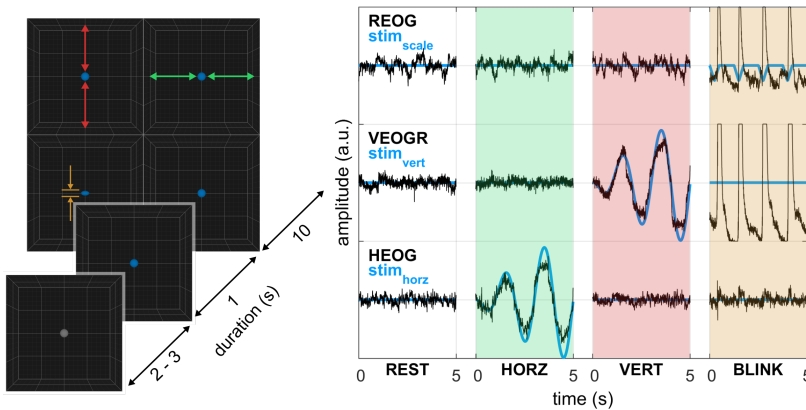
A comparison of ocular artifact removal methods for block design based EEG experiments

Kobler R.J., Sburlea A.I., and Müller-Putz G.R.

Proceedings of the 7th Graz Brain-Computer Interface Conference, 2017

DOI: 10.3217/978-3-85125-533-1-44

In accordance with the aims of this thesis, the first study was designed to test how well state of the art correction algorithms could attenuate eye artifacts in the LFTD EEG. In the LFTD EEG activity, eye movement artifacts are mainly caused by blinks and displacements of the CRD during gaze shifts [50]. The CRD and blink related artifact contributions to the potentials at the EEG electrodes can be assumed to be linear [54]. However, during a visuomotor task, one cannot assume that the artifacts introduced by the CRD are uncorrelated with the activity of brain sources that encode directional information.



- 4.1 Online Artifact Correction 33
 - Evaluation of Algorithms for online Eye Artifact Correction 33
 - Correction of CRD and Eyelid Artifacts in EEG and MEG 35
 - Online Detection and Correction of transient high-variance Artifacts 37
- 4.2 Neural Correlates of Movement . . 39
 - Discrete Movements in different Directions 39
 - Continuous Tracking Movements . 42
 - Simultaneous Decoding of Velocity and Speed 44
- 4.3 Decoding Accuracy Improvement . 46
 - Distance- and speed-informed Kinematics Decoding 46
- 4.4 Proof-of-concept direct BCI 48
 - Online robotic Arm Control with a linear Decoder 48
 - Online robotic Arm Control with a non-linear Decoder 50

Figure 4.1: Eye artifact calibration paradigm. The left panel visualizes the sequence of events during a trial, directed by a blue stimulus on the screen. The stimulus color and movement guided the participants eye movements. The right panel shows the stimulus' movement (blue traces) during the first 5 s of condition specific tasks. The paradigm considered four conditions: REST, HORZ, VERT and BLINK. Additionally horizontal, vertical and radial EOG derivatives for selected trials of a study participant are plotted (black traces).

As in [60], we decided to temporarily disentangle the artifact and brain sources by using a block based experimental design. Figure 4.1 displays the visually guided paradigm that was used to record eye artifacts in a controlled fashion. If the brain sources, encoding directional information $\mathbf{s}_{brain}^{(k)}[t]$, are "silent" during an eye artifact calibration block and sufficiently distant from the eye artifact sources, one should be able to learn spatial filters that remove the contribution of the eye artifact sources and maintain brain activity during a visuomotor task. This approach assumes time-invariant contributions of the eye artifacts to the potentials at the electrodes. In this pilot study (5 participants), we used the data of

a second eye artifact block, recorded approx. 60 minutes after the first one, to answer two questions:

- ▶ Is the time-invariance assumption reasonable?
- ▶ Which correction algorithm performs best in this block based approach?

Contribution to the Thesis

Among the 5 algorithms that we compared, one algorithm based on artifact subspace subtraction, achieved the best trade-off between attenuating eye artifacts and maintaining resting brain activity - see Figure 4.2 for an example. In the evaluation data, recorded approx. 60 minutes after the calibration data, the algorithm could still attenuate blink and CRD related eye artifacts to chance level ($|r| < 0.1$). This result confirmed that the calibration block based approach, suggested in [60], is a feasible approach for online eye artifact correction. Unlike the subspace subtraction algorithm, the regression algorithm proposed in [60] could not effectively attenuate the eye artifacts during blinks and vertical eye movements.

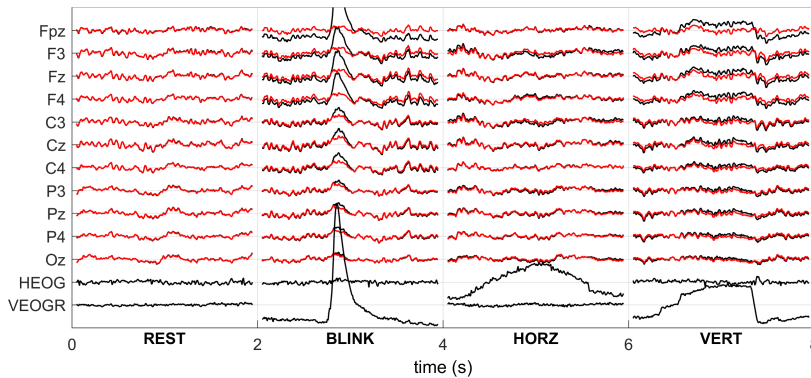


Figure 4.2: Representative examples for the eye artifact correction on the second eye artifact block. For each condition, the traces visualize short periods of the activity at 11 channels before (black traces) and after correction with the best performing algorithm (red traces).

Correction of CRD and Eyelid Artifacts in EEG and MEG

Reference # 211

Corneo-retinal-dipole and eyelid-related eye artifacts can be corrected offline and online in EEG and MEG signals

Kobler R.J., Sburlea A.I., Lopes-Dias C., Schwarz A., Hirata M. and Müller-Putz G.R.

NeuroImage, 218 (2020)

DOI: 10.1016/j.neuroimage.2020.117000

During the course of this thesis, we used the paradigm and correction approach presented in [210] in several studies. To test whether the findings in the small pilot dataset generalize to different EEG recording systems, channel configurations or even MEG, we analyzed the data of 5 studies which contained recordings of a total of 69 participants.

Based on the success of the subspace subtraction algorithm in [210], we proposed a modified algorithm which we denoted sparse generalized eye artifact subspace subtraction algorithm (SGEYESUB). The key differences to its predecessor, denoted GEYESUB here, is that SGEYESUB removes the minimal amount of subspaces that are necessary to correct CRD and eyelid artifacts, and that it adds a sparsity constraint to the optimization problem. The minimal number of artifact subspaces is 3 during eye movements in a 2D workspace; blinks and the vertical and horizontal CRD components have distinct topographies [54]. The sparsity constraint pushes the solution to have few non-zero weights close to the artifact sources. Hence, any source along the dorsal stream which was not active during the eye artifact calibration paradigm would contribute negligibly to the artifact subspace and consequently would not be removed during (online) correction. As outlined in Figure 4.3, we fitted the parameters to data of an eye artifact block recorded at the beginning of an experiment and tested the performance with the data of a second block recorded between 10 to 115 minutes later.

For the EEG data (Figure 4.3c), the results were generally similar to [210]. Compared to state of the art ICA and regression based algorithms, SGEYESUB achieved the best trade-off between correcting eye artifacts, maintaining resting brain activity as well as event-related potentials. We did not see any effect of time on the algorithms' performance, validating the feasibility of the block based approach in online artifact correction.

The results observed in the EEG data generally transferred to the MEG data (Figure 4.3b). For MEG data SGEYESUB marginally, yet significantly improved the correction performance upon GEYESUB for vertical eye movements. We also observed a marginal correction performance decrease with time, which could be attributed to small shifts of the head position in relation to the sensors across time.

Contribution to the Thesis

In this publication we presented and thoroughly tested the tools to correct eye artifacts in EEG and MEG in online experiments. After fitting SGEYESUB to calibration data, the algorithm can correct the artifacts for at least 1.5 hours. The method is fully data driven, tested with different recording hardware and channel configurations, and does not require

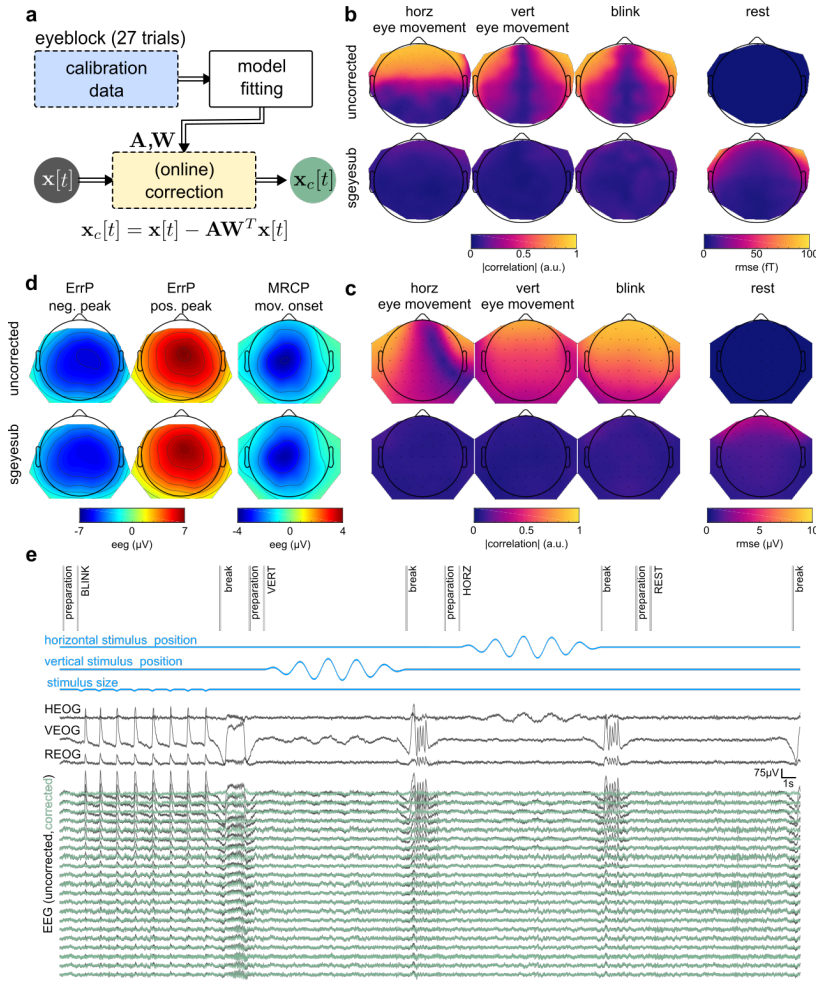


Figure 4.3: Eye artifact correction results. **a**, Outline of the block based approach. The parameters (W and A) of linear correction algorithms are fit to calibration data and used to subsequently correct the M/EEG signals ($x[t]$). **b**, Topographic plots summarize the performance metrics for the MEG dataset. **c**, As in **b** for the EEG datasets. **d**, Topographic distribution of the negative and positive peaks of an error potential (ErrP) as well as an MRCP at the movement onset. **e**, Exemplary visualization of the stimulus (blue traces), EOG and uncorrected EEG (black traces) and corrected EEG (green traces) during BLINK, VERT, HORZ and REST trials.

computationally expensive hyper-parameter tuning when applied in a new experiment. It takes about 15 minutes to obtain a fitted model which includes briefing of the participant, data acquisition and model fitting. As we will see in the next sections, the novel tools enable an efficient and effective (online) disentanglement of eye artifact and brain sources, even if the artifacts co-vary with task relevant brain activity as defined in equation 3.1.

Online Detection and Correction of transient high-variance Artifacts

Reference # 212

HEAR to remove pops and drifts: the high-variance electrode artifact removal (HEAR) algorithm

Kobler R.J., Sburlea A.I., Mondini V. and Müller-Putz G.R.

Proceedings of the 41st Conference of the IEEE EMBC, 2019

DOI: 10.1109/EMBC.2019.8857742

Apart from eye and motion artifacts, M/EEG signals are also affected by other types of artifacts [43, 140]. Transient, high-variance artifacts such as pops, drifts and muscle artifacts strongly contaminate the M/EEG signals and thereby also the decoded movement trajectory and feedback received by a BCI user. Moreover, if the end-effector is a robotic arm the transient artifacts could result in unpredictable and jerky movements causing a safety risk. To assure safe robotic arm control based on LFTD M/EEG activity, the transient, high-variance artifacts should be corrected or at least detected. In the low-frequencies, electrode pops and drifts have a large contribution. They typically affect single or few electrodes. In [212], we proposed the high-variance electrode artifact removal algorithm (HEAR) which monitors the variance of each channel. HEAR continuously computes the probability that a channel is currently affected by an artifact via comparing the time-varying variance to the variance of previously recorded resting data. This probability is then used to weigh the amount of linear interpolation of the channel by its neighboring channels. If multiple channels are affected, HEAR can at least detect that the artifact cannot be corrected.

We compared the performance of HEAR to two state-of-the-art transient artifact correction algorithms [213, 214]. In the case of simulated data, where the ground truth is known, the application of HEAR and its online variant oHEAR had little impact on the SNR during artifact-free periods and could improve the SNR during pop and drift artifacts by 25 dB (Figure 4.4). For real data, HEAR could also strongly attenuate pops and drifts as well as detect transient muscle artifacts introduced during swallowing – see Figure 4.5 for examples. As a consequence, significantly fewer trials had to be rejected.

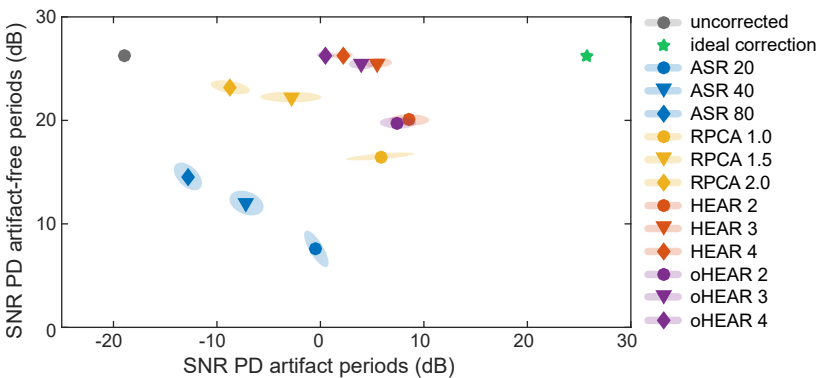


Figure 4.4: Pop and drift artifact correction results for simulated data. The plot shows the SNR of the simulated EEG signals during pop and drift artifact periods (x-axis) and artifact-free periods (y-axis). HEAR and oHEAR were compared to two other algorithms, namely, artifact subspace reconstruction (ASR) and robust principal component analysis (RPCA). The algorithms are color-coded and the symbols indicate the performance for different algorithm-specific hyper-parameters. The SNR for uncorrected (gray) and perfectly corrected (green) data are also indicated.

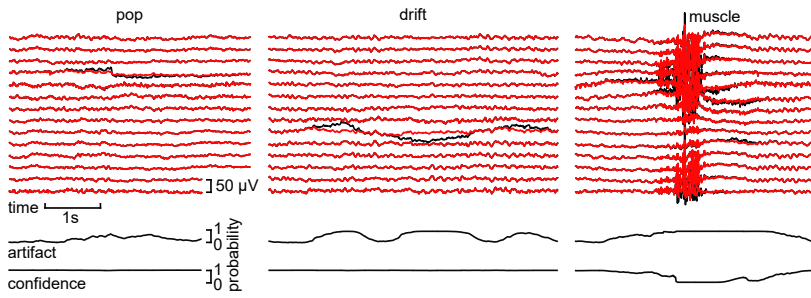


Figure 4.5: Examples of pop, drift and muscle artifacts (black traces) and the results after HEAR was applied (red traces). Below the EEG traces, the maximum artifact probability of all channels is plotted as well as the confidence of HEAR. The pop (left panel) and drift (central panel) could be strongly attenuated with a high confidence. HEAR failed to correct the muscle artifact (right panel) and reported a confidence of 0.

Contribution to the Thesis

The objective of this publication was to drastically attenuate transient, high-variance artifacts which can affect the LFTD activity based trajectory decoders and pose a safety risk in robotic arm control. In simulated data with pop and drift artifacts, HEAR outperformed state-of-the-art methods. In a real EEG dataset, HEAR reduced the fraction of outlier trials by half and maintained the waveform of event-related potentials. In the case of BCI training, HEAR can improve the reliability of the feedback a user receives through attenuating a potential negative impact of transient artifacts. Moreover, if HEAR cannot sufficiently attenuate a transient artifact because several neighboring channels are affected, it reports low confidence in the correction result. The BCI can detect these cases and return to a safe state if the EEG activity is used to control a robotic arm.

4.2 Neural Correlates of Movement

Discrete Movements in different Directions

Reference # 215

Distinct cortical networks for hand movement initiation and directional processing: an EEG study

Kobler R.J.[✉], Kolesnichenko E.[✉], Sburlea A.I. and Müller-Putz G.R.

NeuroImage, 220 (2020)

DOI: 10.1016/j.neuroimage.2020.117076

Previous studies investigated movement direction related effects in the LFTD M/EEG time-locked to the movement onset or to the cues and observed effects in different cortical areas. Aligned to the cues, PPC was repeatedly reported to encode directional information during the pre-movement period [87, 190]. Aligned to the movement onset, the encoding of directional information in SMC peaked after the movement onset [86, 189]. These time-locking-dependent observations suggest the presence of two direction related effects in the LFTD M/EEG - one high-level effect that reflects movement preparation (pre-movement period, mainly PPC) and one low-level effect that reflects movement execution (movement period, mainly SMC). The presence of two distinct networks for movement preparation and execution (or initiation) is also suggested by a recent behavioral study that investigated the response times during non-forced and forced delay reaching movements [33]. In this study, we had the aim to identify the two networks and test which one encodes more information about the movement direction.

In a trial based paradigm, we studied center-out and tracking movements in two conditions, denoted execution and observation (Figure 4.6). Depending on the condition, the participants either performed a visuomotor (execution) or oculomotor (observation) task. In the execution condition, they controlled a cursor in a virtual 2D environment via right arm movements. In the observation condition, we replayed previous, matching cursor trajectories so that the visual input and feedback would be similar in both conditions. The participants were instructed to keep their gaze fixated at a target stimulus in either condition. After a condition cue, the target smoothly moved into one of four directions for 0.5 s and then waited for the cursor. While the participants moved their eyes to keep the moving target fixated in either condition, they also moved their right arm in the corresponding direction in the execution condition. Once the cursor hit the target, a 1-s fixation period elapsed before a tracking task started. In this study, we analyzed the LFTD EEG activity of 15 healthy participants during the center-out task.

As expected, we observed an MRCP phase-locked to the cursor movement onset in the execution condition (Figure 4.7a). Using a general liner model, we could identify condition and direction related effects. The MRCP in execution condition was generated in SMC and marginally affected by the eye artifact correction (Figure 4.7b). More interestingly, we observed a consistent representation of direction in parieto-occipital cortex (POC) that was maintained after eye artifact correction. When we contrasted the direction encoding results between conditions, we additionally observed that SMC encoded more information about the

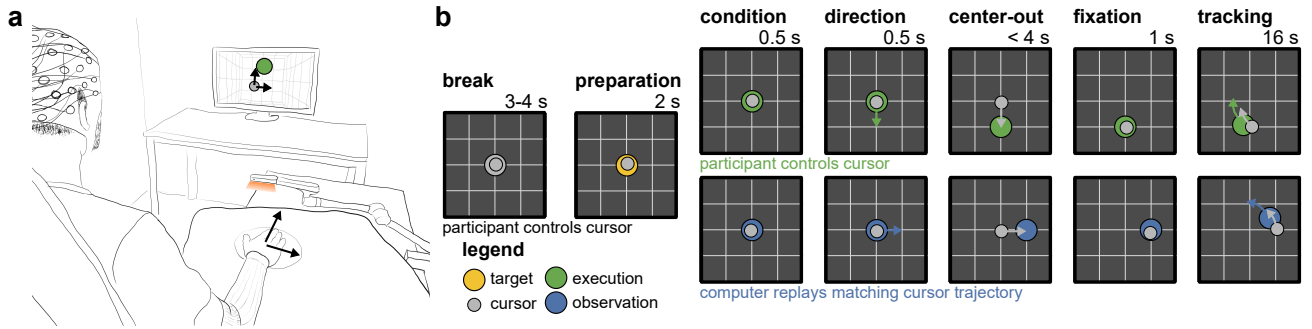


Figure 4.6: Experimental setup and paradigm to study discrete and continuous movements. **a**, Experimental setup. The participants used their right hand to control a cursor in a virtual 2D environment. **b**, The trial based paradigm considered two conditions - execution and observation. In execution condition trials, the participants controlled the cursor, while in observation condition trials, matching cursor movements were replayed. We considered two tasks. In a center-out task, a target moved for 0.5 s in one direction and stopped. After the cursor reached and resided at the target's position for 1 s, a 16-s pursuit tracking task started.

direction in the execution condition (Figure 4.7c). The effect in SMC was inconsistent in the sense that it was present at the level of voxel norms (dipole orientations are ignored), but vanished at the level of voxel components (dipole orientations matter). We furthermore found in a classification analysis (Figure 4.7) that the movement direction could be inferred with higher accuracy if the data was aligned to the cues rather than the movement onset. We obtained the highest accuracy (55.9%) in the execution condition and aligned to the cues.

Contribution to the Thesis

In this study we could demonstrate that the proposed eye artifact correction approach, defined in equation 3.4, is successful in disentangling correlated brain and artifact sources. After correcting the artifacts, we could classify the movement direction with similar accuracies as previous studies that used similar features and models [86, 87, 190]. We could confirm the presence of two direction related effects during executed movements. The movement onset-aligned effect in SMC was participant-specific, peaked after the movement onset and specific to the execution condition. Whereas, the cue-aligned effect in POC was consistent across participants, peaked around the movement onset and present in both conditions. The combined results suggest that the effect in POC encoded significantly more information about the movement direction than the effect in SMC; the difference in classification accuracy was on average 5.3%. This study shows that the time-locking strategy plays a critical role in inferring the direction of discrete, goal-directed movements.

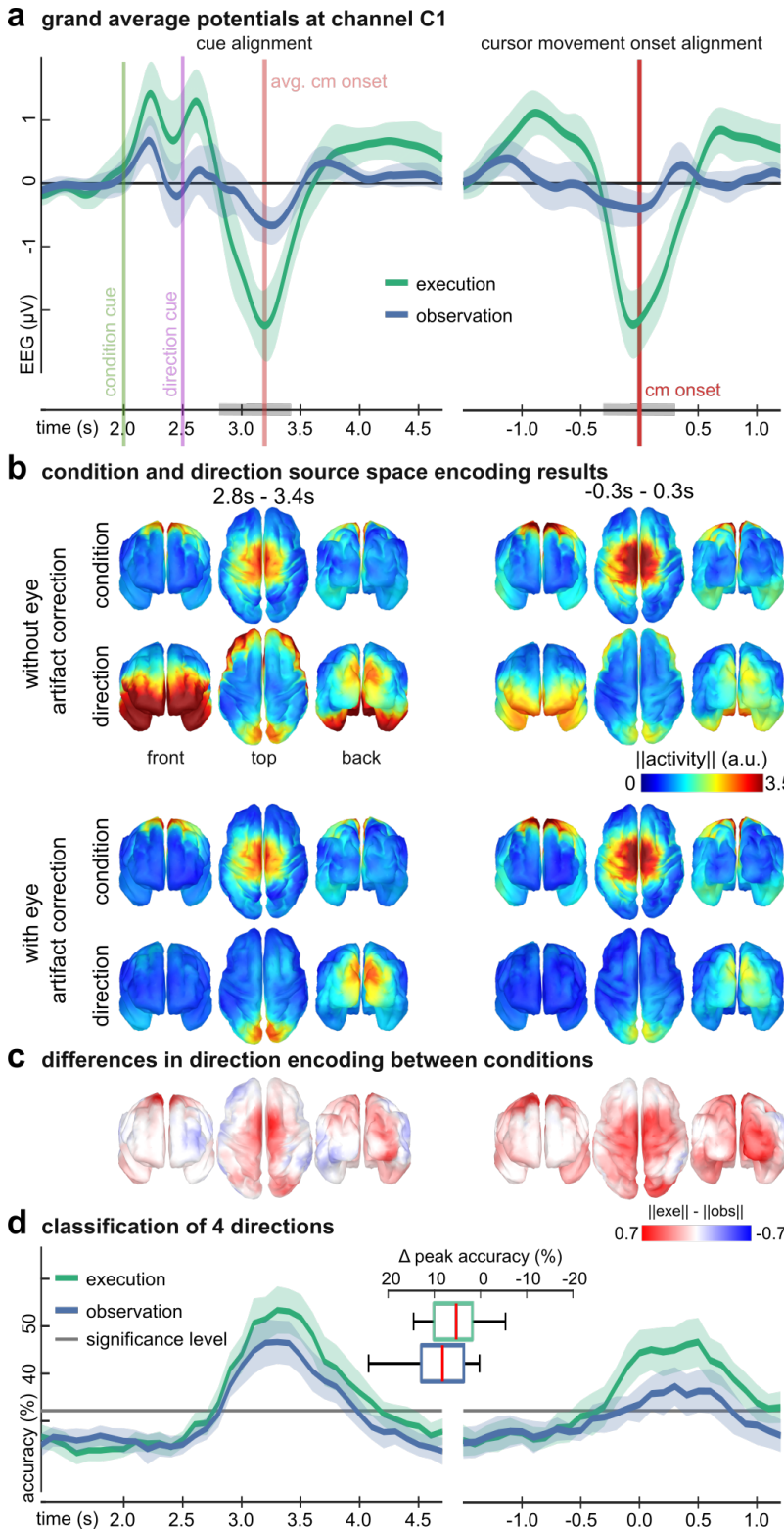


Figure 4.7: Neural correlates of movements in different directions. **a**, Grand average potentials time-locked to the cues (left panel) and the cursor movement onset (right panel). Shaded areas indicate the confidence interval. The conditions are color-coded. **b**, Source space plots visualize the grand average encoding results of condition and direction without (top) and with (bottom) eye artifact correction. For each alignment, the plots show the average absolute condition or direction related activity around the movements onset. The strongest effect of condition was in SMC, phase locked to the movement onset and marginally affected by eye artifact correction. The strongest effect of direction was in POC, phase locked to the cues. The effect of eye artifact correction was negligible on the direction related activity in POC. **c**, Source space plots that show differences in the encoding of directional information between conditions. A positive difference (red color) indicates stronger encoding in the execution condition. **d**, Grand average direction classification results in terms of accuracy curves for both conditions and alignments. Shaded areas indicate the confidence interval. A gray horizontal line indicates the significance level. Boxplots summarize the difference in peak classification accuracy between alignments (cue - movement onset). The differences were significant for both conditions.

Continuous Tracking Movements

Reference # 216

Tuning characteristics of low-frequency EEG to positions and velocities in visuomotor and oculomotor tracking tasks

Kobler R.J., Sburlea A.I. and Müller-Putz G.R.

Scientific Reports, 8(1) (2018)

DOI: 10.1038/s41598-018-36326-y

The aim of this publication was to identify the spatiotemporal tuning characteristics of LFTD EEG activity to arm movement position and velocity. To avoid transient movement initiation related effects like an MRCP, we decided to study a continuous tracking task. In the invasive domain, tracking tasks proved suitable to identify position and velocity related effects in neural spiking activity [120]. The tracking task was part of the first EEG experiment and succeeded a center-out movement in every second trial (Figure 4.6). As in [120], we implemented the tracking task so that the position and velocity signals were decorrelated at lag 0 – see Figure 4.8a. We targeted accurate smooth, two-dimensional tracking movements and created the target trajectories accordingly. The 2D trajectories were created so that the kinematics of the horizontal component were decorrelated with the ones of the vertical component. Due to constraints in workspace size and bandwidth, the cross-correlation between position and velocity of the same component increased over lags. (Figure 4.6b). As a consequence, we had to consider the auto-/cross-correlation curves when we interpreted the decoding results.

We observed four effects in the tuning curves in Figure 4.8b. First, the results were significantly higher than chance ($r_{chance} \leq 0.13$) for all kinematic variables, lags and conditions. POC encoded most information about the movement trajectories in either condition - see Figure 4.8c. Second, in the observation condition the tuning curves were modulated according to the auto-/cross correlation with the target position, indicating that the target position was most relevant in the observation condition. We observed the third and fourth effect in the difference between execution and observation condition tuning curves (dash-dotted lines in Figure 4.8b). The difference was modulated according to the auto-/cross-correlation with cursor velocity, suggesting that LFTD EEG encoded more information about the cursor velocity (both dimensions) in the execution condition. Looking at the differences in decoder patterns, we could attribute the effect to stronger velocity related activity in SMC – see Figure 4.8c. For the vertical component (right panel), we additionally observed a smaller, constant effect of condition. The differences in vertical velocity decoder patterns indicated that this effect could be explained by PPC activity.

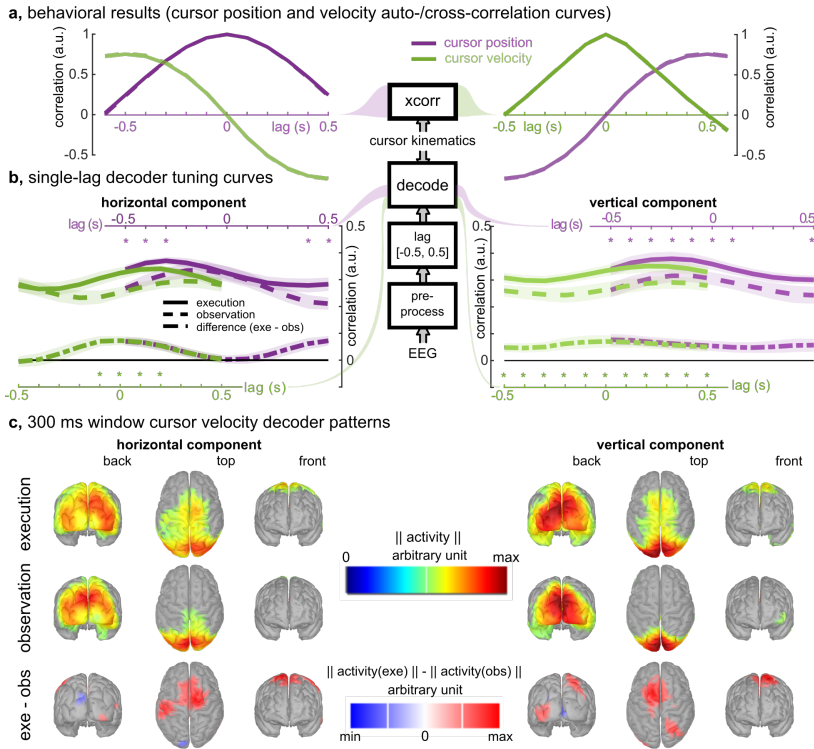


Figure 4.8: Neural correlates of cursor position and velocity during continuous tracking movements. **a**, Auto- and cross-correlation curves for the cursor position (violet) and velocity (green). **b**, Position and velocity decoder tuning curves for execution (solid lines) and observation (dashed lines) conditions. Each curve summarizes the group level test set correlation between recorded and decoded signals. Each decoder estimated the kinematic variable at lag 0 using the LFTD EEG activity at a single lag. The kinematic variables are color-coded. The left and right panel present the results for the horizontal and vertical components. **c**, Source space plots of decoder patterns for Wiener filters that decoded the horizontal (left panel) or vertical (right panel) cursor velocity using a 300-ms window of preceding LFTD EEG activity.

Contribution to the Thesis

In this publication we could confirm that EEG can be used to detect movement trajectory related effects during continuous goal-directed movements. While POC predicted the 2D movement trajectories in both conditions, SMC encoded significantly more information about the 2D cursor velocity in execution condition. Using a regularized WF [188] to decode the velocity trajectories, we obtained moderate correlations for both components. They were 0.4 in the execution condition and 0.35 in the observation condition. Furthermore, in this study we support and generalize the presence of two cortical networks encoding directional information. As in discrete center-out movements, we identified a condition specific representation in SMC and a condition invariant representation in POC.

Simultaneous Decoding of Velocity and Speed

Reference # 217

Simultaneous decoding of velocity and speed during executed and observed tracking movements: an MEG study

Kobler R.J., Hirata M., Hashimoto H., Dowaki R., Sburlea A.I. and Müller-Putz G.R.

Proceedings of the 8th Graz Brain Computer Interface Conference, 2019

DOI: 10.3217/978-3-85125-682-6-19

After two recent ECoG studies reported simultaneous decoding of arm movement velocity and speed from LFTD activity [124, 181] and previous M/EEG studies reported either speed or velocity related effects, we wondered whether speed and velocity information could be simultaneously detected in non-invasive recordings as well. To address this question, we conducted an MEG study during which 19 healthy participants performed a tracking task (Figure 4.9). The paradigm and tracking task dynamics were generally similar to the previous study. Due to the susceptibility of MEG to motion artifacts, we switched from arm movements to index finger movements. Our custom motion capture system introduced a 200 ms delay between the hand and cursor movements.

Offline, we computed the tuning curves for the horizontal and vertical cursor velocity and cursor speed – see Figure 4.10. Since there were only negligible cross-correlations between the individual kinematic variables, we could study the tuning curves in isolation. As before, the 2D velocity tuning curves were above the significance level in both conditions. We could confirm our hypothesis because the speed tuning curve was also above the significance level for all participants in the execution condition and for the majority in the observation condition. Moreover, the cursor speed tuning curve exhibited a distinct peak at the lags -0.3 s and -0.2 s in the execution condition. The patterns revealed that the peak can be attributed to speed related activity in contralateral SMC. Although speed and velocity were uncorrelated, the velocity patterns were also stronger in SMC in the execution condition – especially for the vertical component. The differences between conditions indicate that the effect also peaked at the lags -0.3 s and -0.2 s.

Contribution to the Thesis

This study shows that LFTD MEG activity can be used to simultaneously detect 2D velocity and speed information of continuous tracking movements. The tuning curves and patterns confirm and extend the previous observation that SMC encodes information about the velocity and speed of executed movements. We observed the tuning peaks in SMC about -300 ms to -200 ms which suggests that the effects in SMC were phase-locked to the finger rather than the cursor movement*. Apart from the execution condition specific effect in SMC, the patterns also suggest that PPC and POC encoded velocity and speed information in both conditions. In contrast to the previous EEG study, the representation of velocity in PPC and POC was weaker than the one in SMC. The different findings could be attributed to differences in the movement task (finger

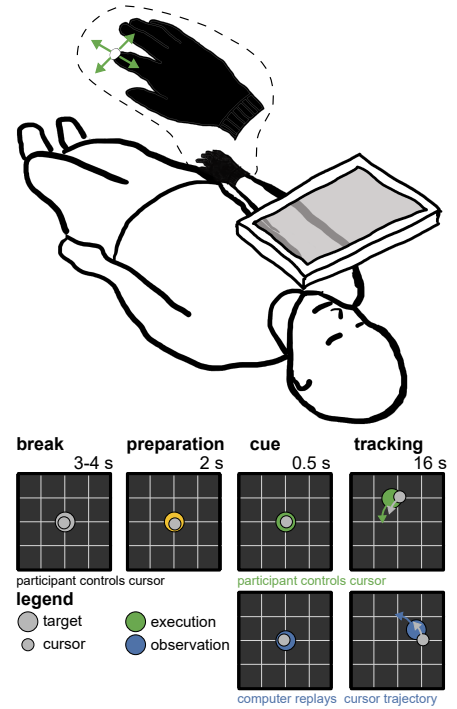


Figure 4.9: Experimental setup and paradigm to study continuous tracking movements in MEG. **a**, Experimental setup. The participants used their right index finger to control a cursor in virtual 2D environment, while they were lying inside an MEG scanner. **b**, The trial based paradigm was similar to the previous study.

* There was a 200 ms delay between the finger and cursor movements

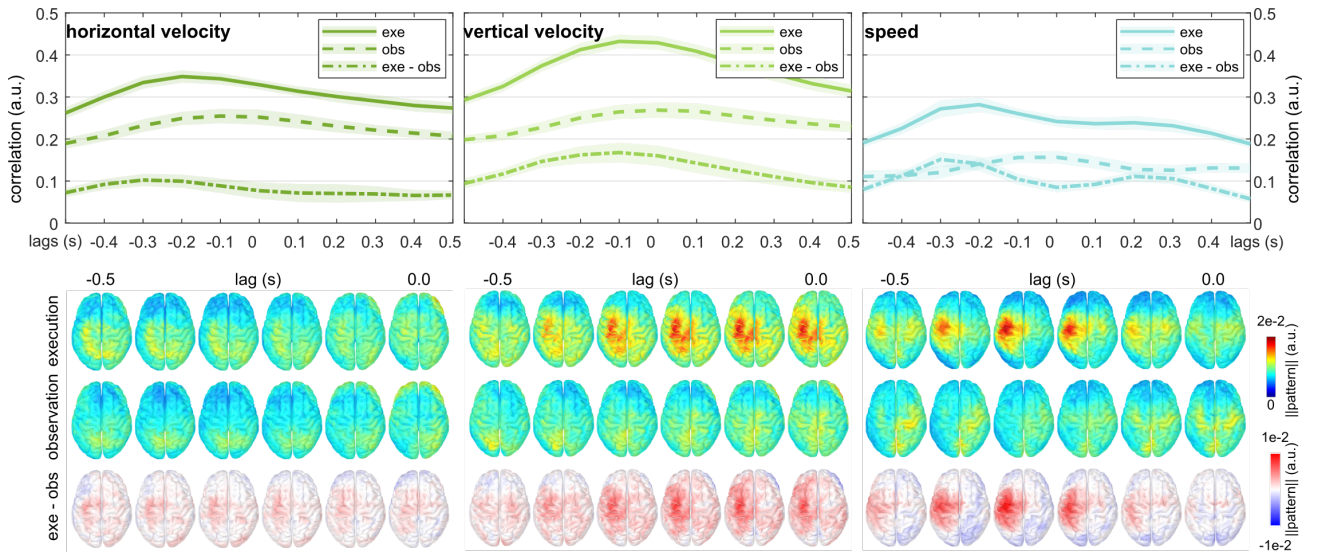


Figure 4.10: Neural correlates of 2D velocity and speed in LFTD MEG during continuous tracking movements. The plots in the top panel visualize the tuning curves of velocity and speed in both conditions. The source space plots in the bottom show the patterns associated to the tuning curves for negative lags.

vs. hand), delays between hand/finger and cursor movements and the recording modality (EEG vs. MEG).

4.3 Decoding Accuracy Improvement

Distance- and speed-informed Kinematics Decoding

Reference # 218

Distance- and speed-informed kinematics decoding improves M/EEG based upper-limb movement decoder accuracy

Kobler R.J., Sburlea A.I., Mondini V., Hirata M. and Müller-Putz G.R.

Journal of Neural Engineering, 2020

DOI: 10.1088/1741-2552/abb3b3

The LFTD M/EEG activity encodes information about directional (e.g., velocity) and non-directional (e.g., speed) kinematics [102, 129, 212]. Linear models that decode movement trajectories cannot integrate both types of kinematics due to the inherent non-linear relationship. Studies that compared linear and non-linear methods reported a higher decoder accuracy for the non-linear methods [202, 205], suggesting that the LFTD activity encodes information that is non-linearly related to the velocity/position trajectories. A drawback of general purpose non-linear methods is the lack of interpretability of the models. In this study we surmised that the decoding accuracy can be improved and interpretability retained if the non-linear relationship is explicitly modeled. This should also alleviate the mismatch in amplitudes between the decoded and recorded trajectories that several previous studies observed [198, 216, 219].

In this work we proposed to use an UKF. The state space model considered the directional kinematics as the hidden state and the LFTD M/EEG activity as the noisy measurements that linearly encoded the directional kinematics and the length of the position and velocity vectors, i.e. distance and speed. In the invasive domain, UKFs have proven successful in combining directional and non-directional information encoded in spiking activity [174].

In an offline analysis, we used the previously recorded EEG and MEG data during the continuous tracking tasks [216, 217], and compared the UKF with two linear decoders, a KF and a WF. We used partial least squares regression (PLS) as a supervised dimensionality reduction technique [220] for the state space filters and to fit the regression coefficients of the WF. Across experiments, the correlations of the recorded and UKF decoded trajectories were 0.49 in the execution and 0.36 in the observation condition. Compared to the linear KF, the UKF improved the decoder accuracy qualitatively (Figure 4.11) and quantitatively (Figure 4.12) in both conditions and experiments. Utilizing information about the non-directional kinematics, encoded within the LFTD M/EEG activity, the UKF could significantly improve the SNR upon the KF and at the same time reduce the amplitude mismatch between recorded and decoded trajectories to a minimum. Compared to the WF, the UKF achieved significantly higher correlations, while the WF achieved the highest SNR at the cost of a large amplitude mismatch. Both state space models (UKF and KF) could significantly improve the correlations upon the WF.

Contribution to the Thesis

In this study, we could demonstrate that directional and non-directional kinematic information is simultaneously detectable in LFTD M/EEG

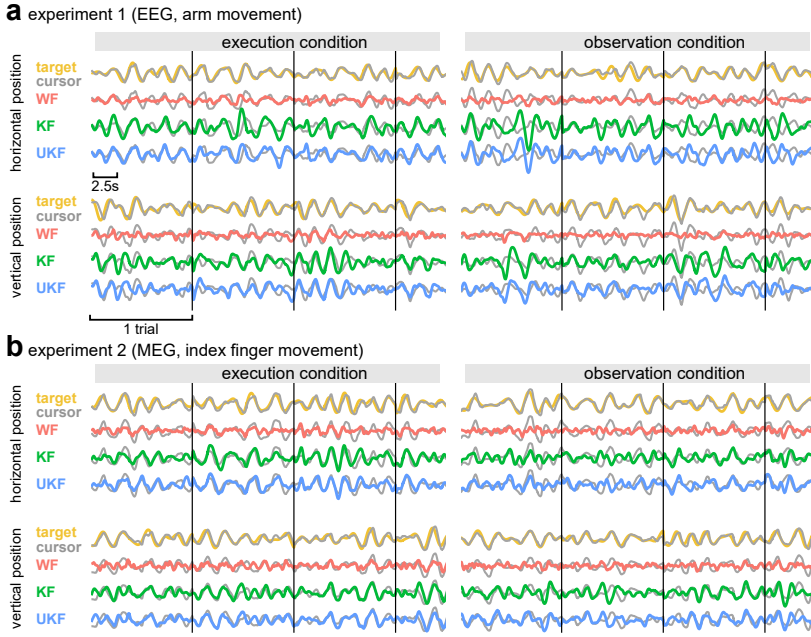


Figure 4.11: Qualitative distance- and speed-informed decoding results. **a**, Experiment 1. Example of test set trajectories (recorded and decoded) during the tracking task for a representative participant. Recorded target (yellow) and cursor (gray) position trajectories for the horizontal (top) and vertical (bottom) component. The decoded cursor trajectories are plotted on top of the recorded cursor trajectories (gray) and are color-coded (WF in red, KF in green, UKF in blue). **b**, As in **a** for the second experiment.

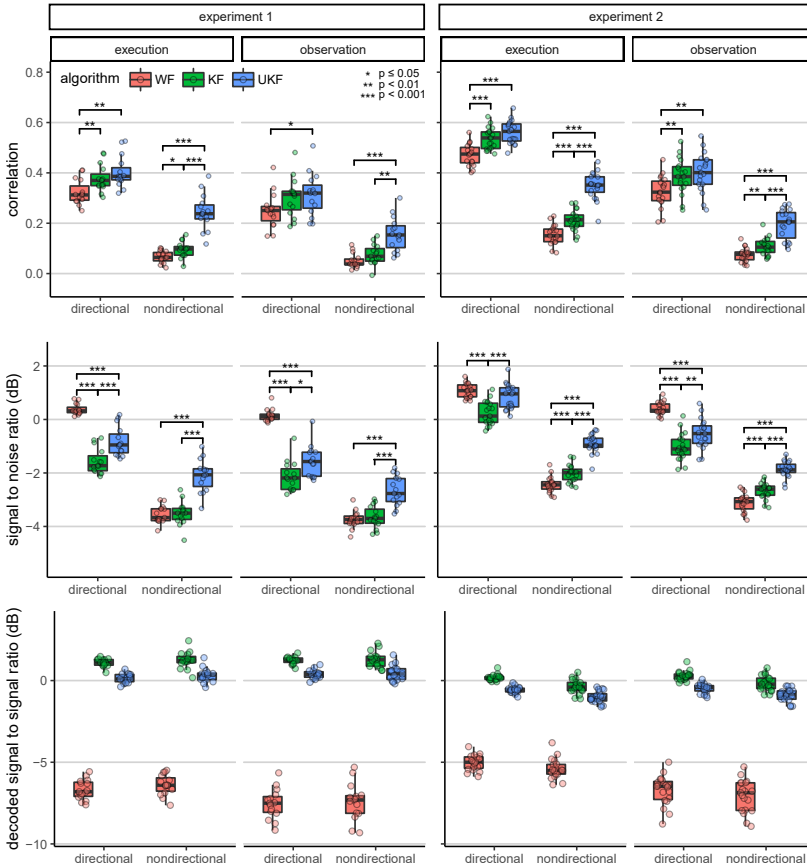


Figure 4.12: Quantitative distance- and speed-informed decoding results. The kinematics are summarized by grouping them into directional (horizontal position, horizontal velocity, vertical position, vertical velocity) and non-directional (distance, speed). The results for the first experiment 1 (EEG, 15 participants) are summarized in the left panel. The top plot shows boxplots that summarize the correlation between the recorded and decoded kinematics for execution (left) and observation (right) conditions. The algorithms are color-coded. Each dot summarizes the average cross-validation test set correlation of a participant. Significant differences between the algorithms are highlighted. The middle plot summarizes the results for the SNR, and the bottom one for the DSSR. The DSSR quantifies the amplitude mismatch. A DSSR of 0 dB is equivalent to matching amplitudes. For the DSSR, all differences were significant. The right panel summarizes the results for the second experiment (MEG, 19 participants).

signals. Moreover, movement trajectories could be reconstructed with higher accuracy with a decoder that integrated both types of kinematics compared to standard linear models. The obtained decoder correlations were within the range of previously reported results of studies that decoded executed movement trajectories from population activity in comparable, continuous movement tasks [121, 122, 180, 202, 205].

4.4 Proof-of-concept direct BCI

Online robotic Arm Control with a linear Decoder

Reference # 221

Continuous low-frequency EEG decoding of arm movement for closed-loop, natural control of a robotic arm

Mondini V.[✉], Kobler R.J.[✉], Sburlea A.I. and Müller-Putz G.R.

Journal of Neural Engineering, 2020

DOI: 10.1088/1741-2552/aba6f7

After we could demonstrate that the LFTD can be used to decode the movement trajectories of executed tracking movements with moderate accuracy [216], we designed this study to explore to which degree the results obtained offline translate to an online setting. Our strategy was to record calibration data during which the study participants tracked a moving target stimulus with a robotic arm – see Figure 4.13a. The calibration data was used to fit a linear decoder. Subsequently, the robotic arm control was gradually switched from the actual, and delayed hand movements to the decoded hand movements (Figure 4.13b). We had to delay the actual hand movements to accommodate the delays introduced by the EEG processing pipeline (approx. 250 ms). The robotic arm added another approx. 350 ms, resulting in a total delay of 600 ms between the hand and robotic arm movements. Still, the 10 participants could complete the tracking task with reasonable accuracy in the calibration data and shared control conditions (Figure 4.14c). In the 0% EEG control condition, the correlation between the target stimulus and robotic arm was on average 0.8 and 0.6 for the horizontal and vertical components, suggesting that it was more difficult to control the vertical dimension.

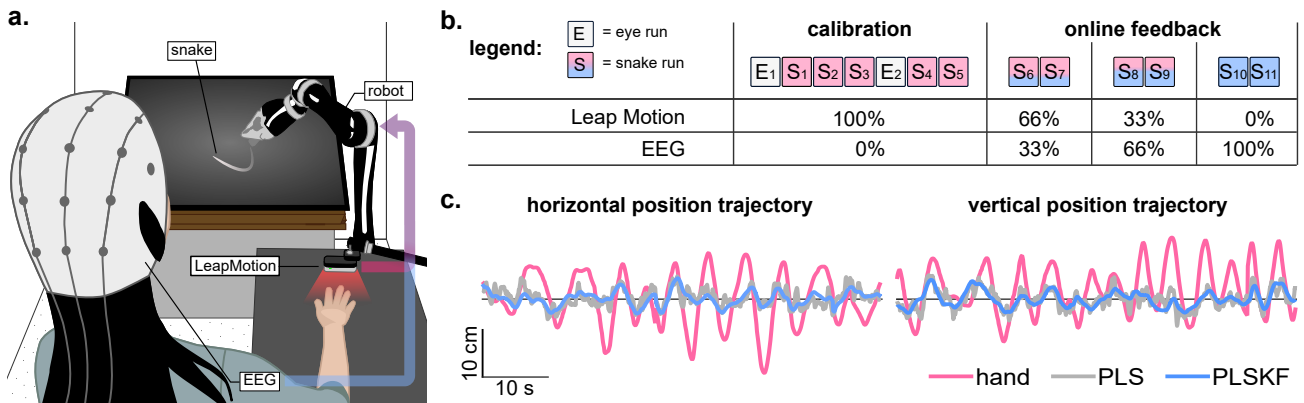


Figure 4.13: Overview of the online decoding experiment. **a.** Experimental setup. Each participant tracked a moving target stimulus, denoted snake, with a robotic arm on a 2D surface. **b.** The experimental paradigm considered four conditions. In the first condition (0% EEG control) the participant controlled the robotic arm via moving the right hand. After a decoder was calibrated, the manual control was reduced in three steps up to 100% EEG control. **c.** Sample position trajectories of a representative participant in the 33% EEG control condition. In this condition, the robotic arm trajectory was the weighted sum of the hand (66%, pink traces) and PLSKF decoded (33%, blue traces) trajectories. The gray traces show the trajectories of a PLS based WF.

As in [218], we used PLS regression as a supervised dimensionality reduction technique to compress the kinematic information, encoded in the LFTD EEG activity within the last 300 ms and compute regression weights for a WF. A Kalman filter was then used to smooth the estimates of the WF. The combined model is referred to as PLSKF. In the online experiment the PLSKF model decoded the delayed hand movement trajectories with moderate correlations of 0.27 for the positions and

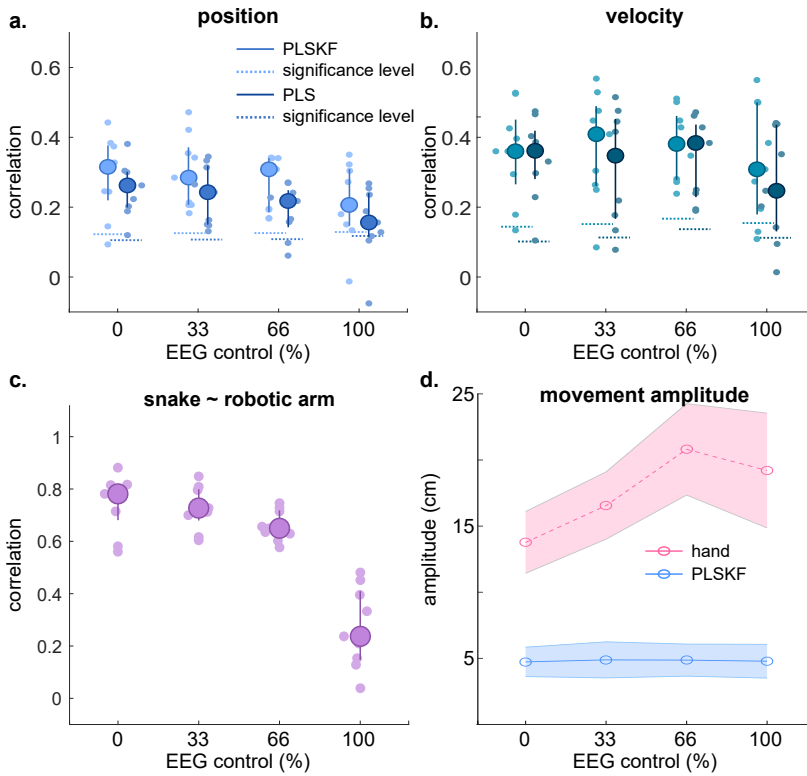


Figure 4.14: Results of the online, linear decoding experiment. Only the results for the horizontal component are displayed (a-c). The decoding results for the vertical component were generally similar. **a**, Correlation between the recorded and decoded position trajectories for each condition. The results for the 0% EEG control condition were estimated offline with a cross-validation approach. The algorithms are color-coded. Each dot marks the result for one participant. **b**, As in **a** for the velocity. **c**, Task performance across conditions in terms of correlation between the snake and robotic arm trajectories. **d**, Size of the recorded (pink) and decoded (blue) hand movements for each condition.

0.39 for the velocities during shared control (Figure 4.14a,b; 33 % and 66 % EEG control), and slightly lower correlations during 100 % EEG control (0.24 for the positions and 0.35 for the velocities). The moderate correlations transferred to a low task performance in the 100 % EEG-based control condition (Figure 4.14c). Moreover, the PLSKF decoded trajectories were consistently estimated too small by the PLSKF – see Figures 4.13c and 4.14d. Offline, we simulated the experiment with the WF; the accuracy was significantly lower (Δ correlation 0.05 for position and 0.06 for velocity).

Contribution to the Thesis

Despite a low task performance, we could show that a LFTD EEG-based, direct BCI for movement control is feasible. Yet, there was a mismatch between the amplitudes of the recorded and decoded movements, limiting closed-loop BCI operation.

We gained two critical insights. First, the PLSKF model could decode the velocity trajectories nearly as well as in the previous offline study [216]. If the same PLS based WF as in [216] was used, the difference in terms of decoder correlations was on average 0.07. This difference can be attributed to the EEG preprocessing pipeline. To achieve a delay of 250 ms, we had to reduce the order of the IIR filters, which in turn reduced the SNR of the LFTD features. The PLSKF as a state space model could almost compensate the drop in correlation. Second, the amplitude mismatch of the linear decoders manifested as a critical limitation in the online experiment. During the shared control conditions, the participants made larger movements (Figure 4.14d) and could thereby compensate the decoder output (Figure 4.14c). This issue needs to be overcome, before feedback training with this type of BCI becomes feasible.

Online robotic Arm Control with a non-linear Decoder

Reference # 222

Non-linear online low-frequency EEG decoding of arm movements during a pursuit tracking task

Martínez-Cagigal V., Kobler R.J., Mondini V., Hornero R. and Müller-Putz G.R.

Proceedings of the 42nd Conference of the IEEE EMBC, 2020

DOI: 10.1109/EMBC44109.2020.9175723

In this pilot study with 5 participants the focus was to test how an UKF decoder that integrates directional and non-directional kinematic information performs in an online experiment. Compared to the previous online experiment we introduced two major changes:

- ▶ The linear PLSKF was replaced with an UKF that decoded positions, velocities and integrated speed information.
- ▶ As in [218] the parameters of the UKF were fit to calibration data.

The paradigm was identical, while we made two small modifications in the experimental setup. First, rather than using the robotic arm's gripper as end-point, we used a stick with a dedicated tip as end-point. This reduced ambiguity of the end-point and occlusions caused by the robotic arm. Second, hand movements were mapped to twice as large robotic arm movements. In the previous experiment the mapping was 1:1.

In contrast to the previous experiment, where the recorded trajectories were three times larger than the decoded ones, the grand-average amplitude ratio was 1.07 in this experiment. In the 5 participants we obtained moderate correlations in the 0% EEG condition – see Table 4.1. They were on average 0.43 and 0.47 for the position and velocity, while the ones of the previous experiment were 0.28 and 0.39 [221]. In this study, we observed that the decoder accuracy declined as the EEG control increased. This effect was small for the horizontal velocity (Δ correlation = 0.05) and considerable for the horizontal position (Δ correlation = 0.15). The effect was similar for the vertical component of 2 participants; for the other 3 participants the correlations declined below the significance level in the 100% EEG control condition.

Contribution to the Thesis

In congruence with the previous offline analysis [218], the UKF decoder alleviated the amplitude mismatch that we observed in our previous online experiment with a linear decoder [221] and the decoder accuracy in terms of correlations were higher for the horizontal component.

The transition from hand manual control to EEG control had a negative effect on the decoder accuracy. This suggests that the feedback provided by the BCI alters the behavior and therefore also the brain signals. Since the decoder was fit to another condition, a performance decrease can be expected. A co-adaptive approach could help to mitigate this performance decrease.

For three participants the negative effect was stronger for the vertical component, especially in the 66% and 100% EEG control conditions, resulting in correlations close to or below the significance level. This

Table 4.1: Results for the online, non-linear decoding experiment. Each row summarizes the correlations between recorded and decoded trajectories of a participant. The columns indicate the kinematic variable and the condition. The conditions are additionally color-coded.

variable	% EEG control	horizontal position				horizontal velocity				vertical position				vertical velocity			
		0	33	66	100	0	33	66	100	0	33	66	100	0	33	66	100
participant	1	0.53	0.52	0.47	0.39	0.53	0.53	0.55	0.48	0.39	0.26	0.29	0.35	0.42	0.30	0.37	0.36
	2	0.63	0.52	0.42	0.34	0.68	0.66	0.54	0.48	0.42	0.21	0.13	0.09	0.44	0.37	0.22	0.19
	3	0.47	0.43	0.37	0.20	0.51	0.47	0.44	0.42	0.37	0.17	0.14	0.00	0.40	0.23	0.12	0.06
	4	0.37	0.41	0.41	0.38	0.42	0.47	0.52	0.47	0.51	0.41	0.36	0.35	0.55	0.53	0.53	0.44
	5	0.27	0.22	0.11	0.22	0.33	0.24	0.24	0.32	0.38	0.23	-0.03	-0.04	0.41	0.32	0.16	0.09
mean		0.45	0.42	0.36	0.31	0.50	0.47	0.46	0.43	0.41	0.25	0.18	0.15	0.44	0.35	0.28	0.23
SD		0.14	0.12	0.14	0.09	0.13	0.15	0.13	0.07	0.06	0.09	0.15	0.19	0.06	0.11	0.17	0.17

stronger effect could be attributed to the experimental setup. As in the previous experiment the 2D surface was tilted by approx. 45 degrees to ease the movements of the robotic arm along the vertical dimension. The end-point was additionally hovering above the screen with a safety distance of a few centimeters. These differences made the perception of the robotic arm's movements along the vertical component more ambiguous than along the horizontal one. It seems like the decoder accuracy can be strongly affected by such ambiguities. Altogether, with this study we have laid the foundation for direct, EEG-based BCIs for movement control. Further longitudinal closed-loop studies are required to explore and quantify the effects of feedback training.

The central aim of this thesis was to develop a direct, LFTD EEG-based BCI that decodes movement trajectories of goal-directed movements. To do so, it was necessary to achieve progress towards de-/encoding tools which are sensitive to movement trajectory related effects in the LFTD EEG activity and invariant to co-varying eye artifacts. The availability of such tools enables the application of M/EEG as functional neuroimaging tools in a new class of tasks that require eye-hand coordination. In order to explore and characterize movement trajectory related effects in this class of tasks, we studied discrete and continuous movements in different volitional states. In the following, the achievements of this thesis along these two aspects are discussed.

- 5.1 Methodological Progress 52
 - Eye Artifacts 52
 - Motion Artifacts 53
 - Transient high-variance Artifacts 54
 - Decoding Algorithms 54
 - Comparison with SoA 55
- 5.2 Conceptual Progress 56
 - Directional and non-directional Kinematics 57
 - Executed and observed Movements 57
 - Continuous and discrete Movements 58
- 5.3 Limitations 59

5.1 Methodological Progress – towards an EEG-based direct BCI for Movement Control

Unlike invasive recording modalities, EEG and MEG suffer from potentially co-varying (eye) artifacts, which have so far impeded their application to study the neural correlates of goal-directed movements which require eye-hand coordination. This work provides multiple contributions towards decoding tools that suppress eye and other artifacts, and combine the neural correlates of several kinematic parameters to improve the accuracy of decoded movement trajectories.

Eye Artifacts

The strategy in this thesis was to first remove the potentially co-varying eye artifacts and then analyze the remaining brain sources that co-varied with the upper-limb movements. Based on previous work of our group [60] we proposed to temporarily disentangle the eye artifact sources from the brain sources [210]. At the beginning of each experiment, the participants were asked to make repetitive eye movements according to a visually guided paradigm. This approach assumes that the brain sources, which are active in visuomotor control, are inactive during this calibration block. We demonstrated that this assumption holds since brain sources encoding directional information in SMC and PPC were retained after eye artifact correction [215–217, 221, 222].

In [210, 211] we compared several state-of-the-art eye artifact correction algorithms for their performance in this block based approach. The regression-based algorithms, proposed in [58, 60] either removed too little artifact activity or too much brain activity. Eye artifact specific [54, 223] and general purpose [224] artifact correction algorithms based on ICA suffered from a poor decomposition into independent components

because we restricted the calibration data; one eyeblock contained merely 5 minutes of data. Since ICA estimates up to as many sources as there are channels, the decomposition algorithm needs to estimate more parameters which makes the curse of dimensionality more severe. We found that for the limited amount of data, subspace subtraction algorithms - in particular SGEYESUB - achieved the best performance in CRD and eyelid artifact attenuation and preservation of brain activity in EEG and MEG [211].

In the same work we showed that the eye artifacts can be assumed to be stationary for at least 1.5 hours, extending the findings of previous works [55] and validating that the proposed block based approach is not only feasible for offline correction but also in BCI experiments. So far our group has tested the practicality of the approach and algorithms in several experiments [215–217, 221, 222, 225, 226]. Participant briefing and data recording took on average 5 minutes each. Model fitting takes another 5 minutes but can be done while other, task-specific data is recorded. To facilitate further algorithmic improvements, we published the algorithms* and a large EEG dataset containing eye artifact data of 50 participants†.

Motion Artifacts

In this work we employed two strategies to avoid and minimize motion artifacts. The first strategy concerned the hardware and recording techniques. Active electrodes were used to attenuate cable swing artifacts [64]. The skin was abraded to improve the impedance and thereby attenuate artifacts introduced by electrode movements [62]. Electrode caps were fixed with a chip clip, since a previous study demonstrated that arm movements can induce large movement artifacts if the electrode cap is fixed with a chest belt [66]. The second strategy concerned the experimental tasks. Unlike previous decoding studies [126–128, 196, 198, 202], we asked the participants to make small movements with radii ranging from 1.5 cm [217] to 15 cm [221]. The hand movements were mapped 1:1 [221], 1:2 [222] and 1:3 [216] to end-effector (cursor or robotic arm) movements in the EEG experiments and 1:10 in the MEG experiment [217]. Moreover, a 2D surface defined the movement plane and supported the hand and arm, leading to little activation of shoulder and neck muscles to stabilize the head.

Despite the two strategies, the hand/arm movement resulted in small head movements in the EEG experiments, raising the question to which extent motion artifacts contributed to the decoding results in the visuo-motor tasks. Because the induced artifact at an electrode can be assumed to be linearly related to the causing motion [65], we should have obtained a higher decoding accuracy in the experiments with larger hand movements. When we used similar pre-processing methods and decoding algorithms, we did not observe any effect of the absolute movement size on the decoder accuracy. Apart from demonstrating that motion artifacts played a negligible role, this also suggests that the LFTD EEG encodes little information about the absolute size of the hand movements.

* <https://github.com/graz-bci/eyeartifactcorrection>

† <https://doi.org/10.17605/OSF.IO/2QGRD>

Transient high-variance Artifacts

As long as there are few transient high-variance artifacts, they have little effect on the experimental findings, since the compromised trials can be simply rejected. In a BCI experiment this is different - especially if the participant receives feedback derived from the brain signals. The artifacts can severely deteriorate feedback quality which impedes learning in closed-loop BCI training and poses a safety risk in robotic arm control.

An alternative to detecting and rejecting compromised trials offline or aborting trials online is to attenuate the artifacts. Previous works have used PCA-based methods [216, 227, 228], specifically ASR [213] and RPCA [214]. While RPCA is limited to offline analyses, ASR requires high-pass filtered data at cut-off frequencies around 0.5 Hz to 2 Hz, rendering it inapplicable for movement decoding from LFTD activity; in continuous movements, frequencies at and slightly below 0.5 Hz contribute considerably to the decoding accuracy of linear decoders. In [212] we proposed the HEAR algorithm and showed that it outperforms ASR and RPCA in correcting single-electrode pops and drifts – the dominant artifacts in LFTD activity. Due to its design, HEAR cannot correct artifacts that affect multiple neighboring electrodes simultaneously. Still, the artifacts can be detected. In [221, 222], we decided to abort trials if HEAR could not correct a transient artifact. As intended, the robotic arm did not exhibit jerky, large amplitude movements during shared and EEG control conditions, suggesting that HEAR was successful in attenuating the transient single-channel artifacts. About 10% of the trials had to be aborted, mainly due artifacts introduced by swallowing and sweating. HEAR[‡] and the simulated dataset[§] as well as the code to generate the dataset are open source and publicly available.

Decoding Algorithms

Due to concern in the field about whether and to which degree LFTD EEG can be used to detect kinematics related effects in brain activity [66, 198], we decided to rely on linear decoders whose sources can be readily interpreted [125, 209]. Based on the work of Ofner et al. [106, 188], we combined decoder pattern analysis [125] and M/EEG source imaging [48] which allowed us to attribute kinematics related effects within the LFTD activity to cortical regions.

There is growing evidence that the SMC encodes speed and velocity information at various spatial scales, starting from spiking activity [89, 229] via ECoG [181] up to M/EEG [217, 218]. The non-linear relation between speed and velocity impedes linear decoders to extract and integrate the neural correlates of both kinematic variables, explaining the advantage of non-linear decoders over linear ones [174, 202, 218, 230, 231].

Rather than using general purpose, non-linear machine learning algorithms to decode movement trajectories [202, 231], we explicitly modeled the relation between the directional and non-directional kinematics, and let a UKF non-linearly combine the linearly encoded information.

[‡] <https://github.com/graz-bci/hear>

[§] <https://doi.org/10.6084/m9.figshare.7718966>

Previously, Li et al. demonstrated that directional and non-directional kinematics, encoded in neural spiking activity, could be successfully combined with a UKF [174]. In the non-invasive domain, Yeom et al. separately decoded the direction and length (speed) of the velocity vector with a linear Kalman filter and combined them non-linearly to reconstruct the velocity trajectory [230].

More sophisticated decoding algorithms and feature extraction techniques might be able to further improve the decoder accuracy. In our studies we used LFTD signals as features for the decoding algorithms. Hammer et al. used time and frequency resolved phase and power features derived from LFTD ECoG and reported approx. 0.1 higher correlations compared to merely band-pass filtered LFTD signals [123]. Another ECoG study extended the PLS regression algorithm to incorporate a smoothness constraint of the decoded trajectories [232].

Comparison with the State-of-the-Art

The proposed UKF reconstructed the movement trajectories offline [218] and online [222] with moderate congruence and negligible amplitude mismatch. In [218], the grand average correlations between the decoded and recorded position and velocity trajectories were 0.4 (EEG) and 0.56 (MEG) in the execution condition; the SNR was -0.8 dB (EEG) and 0.9 dB (MEG). In the online pilot study [222], the manual control condition (= 0% EEG-based decoding) was most similar to the offline analysis. In this condition, the correlations were 0.45. Because the experimental tasks were similar in both experiments, a comparison of the obtained correlations is appropriate. They suggest that replacing zero-phase spectral filters with low-order causal ones has little impact on the decoder accuracy. However, the decoding results in [222] should be interpreted with caution since the sample size was small in the pilot study (5 participants).

So far, other non-invasive works that decoded movement trajectories during continuous upper-limb movements from LFTD activity were limited to offline analyses. The EEG studies that used motion artifact resistant setups (active electrodes, chin clips) could reconstruct the continuous movement trajectories with moderate congruence; the average decoder correlations ranged from 0.3 to 0.5 [200–202]. This suggests that after eye artifact correction, the decoder accuracy obtained in this thesis is within the range of previous studies.

Recent studies with implanted electrodes obtained higher decoder accuracies [233–235]. One study demonstrated BCI operation based on LFTD features during a continuous random target task [233]. They recorded LFTD LFP activity of two NHPs with intracortical electrode arrays in M1 and PMd. Analyzing the calibration period, when the monkeys controlled the end-effector with their arm movements, the decoder correlations were approx. 0.8. This corresponds to a higher accuracy compared to non-invasive techniques; the gap in terms of correlation ranges from 0.24 to 0.4. When the monkeys used the BCI to control the end-effector, they could acquire the random targets in almost all trials. Although the NHPs controlled the end-effector with the BCI, they continued to move their arms.

Still, the task performance based on intracortical, direct BCIs is below the one of manual control [233, 236]. Since the decoders do not perfectly match the executed/intended movements, the NHPs typically adjust their movement behavior, affecting the neural dynamics and thereby rendering the fitted decoder parameters inefficient [237]. A successful strategy to cope with this issue is to refit the decoder periodically on the intended movement trajectories during BCI usage [238]. The intended movement trajectories are assumed to be the shortest path from the end-effector to the target [239]. These advances in intracortical decoder designs can also aid the transition from manual control to EEG-based control and thereby reduce the decline in decoder accuracy that we observed in [222].

In this thesis, we studied executed and observed goal-directed movements in a population of healthy volunteers. To which extent the obtained results might transfer to individuals with tetraplegia remains an open question. Since the participants did not move their arms in the observation condition, the findings could be used to anticipate a baseline decoder accuracy in individuals with tetraplegia. If they use a movement attempt strategy rather than mere observation, a similar performance to execution condition should be within reach [240, 241]. Using intracortical BCIs, individuals with tetraplegia achieved similar decoding accuracy in attempted movements as NHPs in executed movements [7]. Nonetheless, the moderate decoding accuracy obtained in this work is not sufficient to accurately control an end-effector.

Learning via feedback training could be a strategy to improve the accuracy. Using motor imagery of distinct movements and band-power features, Wolpaw and McFarland demonstrated that 2D cursor control could be significantly improved with feedback training [6]. After training for several weeks, the study participants could control a cursor in a 2D center-out task with average correlations of 0.63. Edelman et al. used a similar control strategy and reported that the participants could improve the control skill significantly faster in a 2D tracking task compared to a center-out task [242]. After skill acquisition within 10 sessions, some participants could track the target with moderate accuracy (average correlation of 0.4). Although there is evidence that individuals can learn to voluntarily modulate low-frequency activity with feedback training [243], it remains unclear whether, how fast and to which degree the kinematics decoding accuracy can be improved with feedback training.

5.2 Conceptual Progress – Neurophysiology of executed and observed Movements

Apart from a proof-of-concept direct BCI, this thesis also focused on the analysis of kinematics related effects in LFTD M/EEG activity during goal-directed movements. Unlike previous M/EEG studies, we could explore and characterize kinematics related effects isolated from co-varying eye artifacts [215–217]. Previous invasive electrophysiology and fMRI literature implicated contralateral SMC in particular M1 and PMd as well as PPC in particular SPOC in the encoding of kinematic information during goal-directed hand movements [27, 244, 245]. Using EEG source

imaging, different volitional states and tasks with decorrelated kinematic variables, we demonstrated that kinematics related effects in SMC and PPC can be also detected in LFTD M/EEG activity.

Directional and non-directional Kinematics

Movements can be described in Cartesian (e.g., velocity) and polar coordinates (e.g, direction and speed) and viewed from different reference points (retina, head, body, etc.). To generate complex movements, the brain needs to represent movements in various coordinate systems so that it can transform and integrate visual and sensory feedback as well as generate motor outputs. Previous works that studied executed, goal-directed movements reported direction [71, 85, 86], speed [89, 129], velocity [120, 126] and position [120, 128] effects.

In the continuous tracking tasks, we observed a consistent representation of speed in contralateral M1 and S1 phase-locked to the hand and finger movements [217, 218]. The speed-related activity was consistent across participants in terms of source location and polarity. Contralateral SMC simultaneously encoded information about 2D hand/finger velocity [216, 217] in the tracking task and direction in the center-out task [215]. This effect was consistent in terms of location; the polarity varied across participants. Since the spatial distribution of directionally tuned neurons in SMC is subject specific and varies on a small scale [233, 246], it is unlikely to observe consistent effects in the population activity with sensors that integrate the activity of large cortical patches [124]. Recently, it was shown that a large fraction of the neurons that are modulated by velocity are also modulated by speed [229]. With increasing speed the spike rates of the vast majority of modulated neurons increased as well. This correlated encoding of speed in a large number of SMC neurons renders the observation of speed related effects in LFTD M/EEG activity likely.

Unlike in contralateral SMC, we found velocity and direction to be consistently encoded in PPC across participants [215, 218]. In the EEG experiments the sources were located in POC and in the MEG experiment slightly anterior in the superior parietal lobule and intra-parietal sulcus. Because POC forms a gyrus and MEG is more sensitive to sources in the sulci, stronger source activity in EEG can be expected. POC has been identified as the human homologue of V6 and V6a in NHPs [247]. It is active during visual reaching [28, 248], pointing [248] and eye movements [28], modulated by movement direction [249, 250] and has a retinotopic organization [251]. These properties support the detection of direction related effects during visuomotor and oculomotor tasks in the LFTD EEG.

Executed and observed Movements

The volitional state, namely, whether one executes, observes or attempts a movement can considerably affect the neural representation of kinematic information [240, 250]. In the healthy population that we studied in this thesis, we considered executed (visomotor tasks) and observed (oculomotor tasks) movements. POC encoded directional information

in both volitional states, whereas the effects in contralateral SMC were specific to executed movements. A recent fMRI study observed similar effects in reaching and saccadic movements [250]. They reported that POC encoded movement direction during arm and eye movements, indicating that POC plays a role in integrating goal information across different effectors. Increasing evidence suggests that the spatial goal for a movement is primarily encoded in POC, while more rostral, anterior parietal regions encode reach vectors from the initial hand position during reaching movements [252].

In a continuous tracking task, the changing spatial goal is determined by the target's velocity, if the participants try to keep the target foveated. The model of POC would then suggest that the strongest direction tuning effect should be phase-locked to the target velocity trajectories. In our experiments, the target and cursor velocity trajectories were tightly coupled because the participants could accurately track the target. Consequently, we observed the predicted POC effects phase-locked to the cursor velocity [218, 221].

Our findings show that LFTD M/EEG activity provides access to the direction of goal-directed movements twofold. Activity in POC is modulated by the direction of the movement goal in executed and observed movements [215, 218]. The representation is consistent across participants. Activity in SMC and more anterior, rostral PPC is modulated by the directional kinematics of the moving hand and is participant-specific.

Continuous and discrete Movements

In this thesis, continuous and discrete goal-directed movements were studied, mainly with the aim to classify the direction of discrete center-out movements and decode the trajectories of continuous tracking movements. Previous non-invasive studies asked the participants to perform either discrete or continuous movements in a single experiment. We studied center-out and continuous tracking movements in a single experiment [215, 216].

With regard to the representation of directional information, we observed similar effects in the LFTD EEG activity. We found a consistent representation in POC during the pre-movement and movement periods time-locked to the cues and again later in the tracking task time-locked to the cursor(/target) velocity trajectories. In the execution condition, ipsi- and contralateral PMd encoded more information about the direction around the movement onset and later in the tracking task about the cursor velocity. Our findings suggest that directional effects during continuous and discrete goal-directed movements share common neural representations, and that they are time-locked to the velocity in the continuous case and direction cue in the discrete case. Cue aligned effects in POC seem likely since POC is implicated in the encoding of the spatial goal [252]. Moreover, POC and PMd are part of the dorsal reach system, with direct projections from POC to PMd [26], indicating that POC provides directional information that other PPC and motor areas transform into low-level commands.

In discrete movements, bilateral SMC generated an MRCP phase-locked to the movement onset [215]. Moreover, SMC was modulated by the

time-varying movement speed during the continuous tracking task [218]. Recent neurophysiological findings suggest that movement initiation related activity in PMd and M1 is modulated by the vigor (or speed) of an ensuing movement [12, 253]. In the context of M/EEG, previous studies demonstrated that the MRCP waveform is modulated by speed [102, 204], and that the time-varying speed of continuous movements is encoded in SMC [129]. Our findings suggest that speed related effects in discrete and continuous movements share a common neural representation.

5.3 Limitations

Directional Effects in SMC

Since the movements in different directions involved different sets of joints and muscle groups in our experiments, and it was shown that distinct joint movements modulate the LFTD EEG activity in SMC [106], the participant-specific representation of direction, observed in this thesis, could be attributed to joint angle or muscle synergistic effects. Disentanglement of the co-varying kinematic and kinetic variables that can describe movement poses a challenge. Still, it is now accepted that kinematic information can be inferred from neural activity in SMC.

Decoder Accuracy

The proposed distance- and speed-informed trajectory decoder resolved the amplitude mismatch, and decoded executed movement trajectories with moderate accuracy offline and online. Still, correlations around 0.4 and SNRs around 0 dB are insufficient for accurate, continuous end-effector control. Moreover, feedback based on the decoder, which was fitted to executed movements, resulted in a decline in decoding accuracy [222]. Similar effects have been previously observed in NHPs and spiking activity [237]. One strategy to improve the initially moderate performance of direct BCIs is to facilitate neural adaptation. This strategy proved useful in invasive direct BCIs in NHPs and impaired humans [237]. Using a fixed decoder that predicts the movement trajectories initially with moderate accuracy [254] or occasionally adapting the decoder [255] can help to facilitate neural adaptation and improve task performance across few sessions. In [254] NHPs could considerably improve the control skill within 10 recording sessions and retained a high-accuracy control in subsequent sessions.

Decoder Calibration

At this stage, feedback training based on a LFTD EEG-based decoder is limited by the lengthy calibration process. Recording calibration data and fitting the model took on average two thirds of the recording time [221, 222]. Ideally feedback training could be started right away with a decoder that is transferred from previous sessions or even subjects [254].

A challenge in transferring decoders is that brain signals inherently vary across time and subjects. In the case of EEG, these variations or drifts can have physical or mental origin. Physical variations include misalignment of the EEG electrodes across sessions, changes in the electrode scalp interface within or across sessions, and different head shapes of subjects. Mental variations are caused by non-task relevant brain activity due to different mental conditions. The combined variations can considerably deteriorate BCI performance. In indirect, motor-imagery BCIs, feature normalization strategies were successfully used to reduce the performance drop between sessions and subjects [256] and to implement a plug-and-play BCI [257]. Whether and with which accuracy a LFTD EEG-based decoder transfers across sessions and subjects remains an open question. The consistent group-level representation of movement direction in POC indicates that inter-subject transfer might be feasible. The accuracy of a transferred decoder will likely be lower than a session specific one, since the directional information encoded in SMC is participant-specific.

Transfer to 3D Movements

The focus of this thesis was on 2D movements along with the vast majority of invasive and non-invasive trajectory decoding studies – see [144, 245] for recent reviews. Some LFTD activity decoding studies investigated 3D movements [127, 128, 258]. A transition from 2D to 3D movements would require additional components in the decoding and eye artifact correction algorithms. During eye movements in depth, the eyeballs move in different directions, requiring an additional component to describe corneo-retinal dipole artifact in M/EEG signals. The presented eye artifact approach could be extended to correct this additional component, if a depth condition is included in the experimental paradigm and the associated artifact subspace is subtracted.

At the beginning of this thesis, I outlined a long-term vision of BCI research; a paralyzed individual makes dexterous movements with an end-effector by simply attempting a desired action. A direct BCI would detect the neural correlates of the attempted actions and transform them into control commands for the end-effector. Although there are many remaining challenges to overcome, I consider this thesis to make three major contributions towards using non-invasive functional neuroimaging techniques like EEG and MEG to implement this vision.

In several studies we showed that co-varying eye artifacts can be disentangled from LFTD M/EEG activity that encodes directional information. The achievements in artifact correction enabled the second contribution, namely, whether and how the kinematics of goal-directed movements are represented in LFTD M/EEG activity during different movement tasks and volitional states. We corroborated and extended the findings of previous works by identifying and characterizing two cortical networks that encode directional and non-directional kinematic information during discrete and continuous movements. At last, the methodological and conceptual advances were combined to implement a proof-of-concept, LFTD EEG-based, direct BCI for movement control. In two feasibility studies, we demonstrated that the direct BCI can decode executed movement trajectories with moderate congruence in real-time.

6.1 Outlook

As already mentioned, there are many remaining challenges and open questions. From the BCI perspective the most critical one is how the decoder accuracy could be improved. We have seen that allowing eye movements and removing the associated artifacts did not improve the accuracy upon previous studies that asked the users to avoid eye movements. I see three strategies that could contribute to improving the accuracy.

First, I surmise that the user could learn to improve the accuracy during longitudinal feedback training sessions. Kübler et al. demonstrated that healthy and paralyzed volunteers can learn to modulate slow-cortical potentials [243]. Moreover, accuracy improvements due to neural adaptation have been reported in invasive, direct BCIs [237]. During BCI operation, the provided feedback can alter the control strategy, rendering a decoder which was fitted to executed movements suboptimal. Indeed, we observed that the decoder accuracy declined once feedback was provided by the direct BCI, a problem that has also been reported for direct, invasive BCIs [161, 162] and addressed via intention estimation methods [238, 239].

The second strategy concerns methodological aspects. To compensate inter-session variations in electrode positioning and montage, EEG source

imaging could be used as a pre-processing step, ideally with a participant-specific head model. Recently, Edelman et al. demonstrated for an indirect, motor imagery-based BCI for movement control that a decoder fitted in source space outperformed the same decoder fitted in sensor space [242]. EEG source imaging also helped to identify power-modulations in the beta band that were phase-locked to the movement rhythm [259], length of the acceleration vector [131] and direction [219]. Combining the LFTD and spectral features might further improve the decoder accuracy. In an ECoG study, Hammer et al. transformed the LFTD activity into a time-frequency representation and reported that phase features were particularly informative [123].

The third strategy is motivated from the user perspective. To control an end-effector, it seems irrational to exclude the information encoded in the eye movement behavior. EEG and EOG activity could be combined to implement a hybrid BCI [260, 261]. Unlike an eye tracker, a hybrid BCI could detect if the user is merely moving the eyes to explore the environment, or engaged in controlling an end-effector.

Beyond improving the decoder accuracy of executed movements, future studies will also have to determine to which degree the results in healthy volunteers transfer to paralyzed users. Attempted movements seem to be the most promising mental strategy, since the decoder accuracy is typically higher than in observed or imagined movements [240, 241].

Bibliography

- [1] B. S. Armour, E. A. Courtney-Long, M. H. Fox, H. Fredine, and A. Cahill, 'Prevalence and Causes of Paralysis—United States, 2013,' *American Journal of Public Health*, vol. 106, no. 10, pp. 1855–1857, 2016. doi: 10.2105/AJPH.2016.303270 (cited on page 1).
- [2] R. Thietje and S. Hirschfeld, 'Epidemiology of Spinal Cord Injury,' in *Neurological Aspects of Spinal Cord Injury*, N. Weidner, R. Rupp, and K. E. Tansey, Eds., Cham: Springer International Publishing, 2017, pp. 3–17, ISBN: 978-3-319-46291-2. doi: 10.1007/978-3-319-46293-6_1 (cited on page 1).
- [3] NSCSC, 'Spinal cord injury facts and figures at a glance,' *Birmingham, AL: University of Alabama at Birmingham*, vol. 14, 2020 (cited on page 1).
- [4] H. A. Caltenco, B. Breidegard, B. Jönsson, and L. N. Andreasen Struijk, 'Understanding Computer Users With Tetraplegia: Survey of Assistive Technology Users,' *International Journal of Human-Computer Interaction*, vol. 28, no. 4, pp. 258–268, 2012. doi: 10.1080/10447318.2011.586305 (cited on page 1).
- [5] C. H. Blabe, V. Gilja, C. A. Chestek, K. V. Shenoy, K. D. Anderson, and J. M. Henderson, 'Assessment of brain-machine interfaces from the perspective of people with paralysis,' *Journal of Neural Engineering*, vol. 12, no. 4, 2015. doi: 10.1088/1741-2560/12/4/043002 (cited on pages 1, 26).
- [6] J. R. Wolpaw and D. J. McFarland, 'Control of a two-dimensional movement signal by a noninvasive brain-computer interface in humans,' *Proceedings of the National Academy of Sciences*, vol. 101, no. 51, pp. 17 849–17 854, 2004. doi: 10.1073/pnas.0403504101 (cited on pages 2, 21, 56).
- [7] L. R. Hochberg, M. D. Serruya, G. M. Friehs, J. A. Mukand, M. Saleh, A. H. Caplan, A. Branner, D. Chen, R. D. Penn, and J. P. Donoghue, 'Neuronal ensemble control of prosthetic devices by a human with tetraplegia,' *Nature*, vol. 442, no. 7099, pp. 164–71, 2006. doi: 10.1038/nature04970 (cited on pages 2, 17–19, 21, 56).
- [8] G. R. Müller-Putz, R. Scherer, G. Pfurtscheller, and R. Rupp, 'EEG-based neuroprosthesis control: A step towards clinical practice,' *Neuroscience Letters*, vol. 382, no. 1-2, pp. 169–174, 2005. doi: 10.1016/j.neulet.2005.03.021 (cited on pages 2, 21, 22).
- [9] A. B. Ajiboye, F. R. Willett, D. R. Young, W. D. Memberg, B. A. Murphy, J. P. Miller, B. L. Walter, J. A. Sweet, H. A. Hoyen, M. W. Keith, P. H. Peckham, J. D. Simeral, J. P. Donoghue, L. R. Hochberg, and R. F. Kirsch, 'Restoration of reaching and grasping movements through brain-controlled muscle stimulation in a person with tetraplegia: A proof-of-concept demonstration,' *The Lancet*, vol. 389, no. 10081, pp. 1821–1830, 2017. doi: 10.1016/S0140-6736(17)30601-3 (cited on page 2).
- [10] D. Purves, G. Augustine J., D. Fitzpatrick, W. C. Hall, LaMantia,, Anthony-Samuel, McNamara, James O., and Williams, Mark S., Eds., *Neuroscience*, 3rd edition. Sunderland, Massachusetts, USA: Sinauer Associates, Inc, 2004, ISBN: 978-0-87893-725-7 (cited on pages 3, 5).
- [11] I. Q. Wishaw, 'Loss of the innate cortical engram for action patterns used in skilled reaching and the development of behavioral compensation following motor cortex lesions in the rat,' *Neuropharmacology*, vol. 39, no. 5, pp. 788–805, 2000. doi: 10.1016/S0028-3908(99)00259-2 (cited on page 3).

- [12] P. Cisek and J. F. Kalaska, 'Neural Mechanisms for Interacting with a World Full of Action Choices,' *Annual Review of Neuroscience*, vol. 33, no. 1, pp. 269–298, 2010. doi: 10.1146/annurev.neuro.051508.135409 (cited on pages 3, 5, 11, 59).
- [13] J. Merel, M. Botvinick, and G. Wayne, 'Hierarchical motor control in mammals and machines,' *Nature Communications*, vol. 10, no. 1, p. 5489, 2019. doi: 10.1038/s41467-019-13239-6 (cited on page 3).
- [14] S. Grillner and P. Zangger, 'On the central generation of locomotion in the low spinal cat,' *Experimental Brain Research*, vol. 34, no. 2, 1979. doi: 10.1007/BF00235671 (cited on page 3).
- [15] P. Whelan, 'Control of locomotion in the decerebrate cat,' *Progress in Neurobiology*, vol. 49, no. 5, pp. 481–515, 1996. doi: 10.1016/0301-0082(96)00028-7 (cited on page 3).
- [16] W. G. Darling, M. A. Pizzimenti, and R. J. Morecraft, 'Functional recovery following motor cortex lesions in non-human primates experimental implications for human stroke patients,' *Journal of Integrative Neuroscience*, vol. 10, no. 03, pp. 353–384, 2011. doi: 10.1142/S0219635211002737 (cited on page 3).
- [17] G. Kwakkel, B. J. Kollen, J. van der Grond, and A. J. Prevo, 'Probability of Regaining Dexterity in the Flaccid Upper Limb: Impact of Severity of Paresis and Time Since Onset in Acute Stroke,' *Stroke*, vol. 34, no. 9, pp. 2181–2186, 2003. doi: 10.1161/01.STR.0000087172.16305.CD (cited on page 4).
- [18] M. Omrani, M. T. Kaufman, N. G. Hatsopoulos, and P. D. Cheney, 'Perspectives on classical controversies about the motor cortex,' *Journal of Neurophysiology*, vol. 118, no. 3, pp. 1828–1848, 2017. doi: 10.1152/jn.00795.2016 (cited on pages 4, 9).
- [19] J. C. Culham and K. F. Valyear, 'Human parietal cortex in action,' *Current Opinion in Neurobiology*, vol. 16, no. 2, pp. 205–212, 2006. doi: 10.1016/j.conb.2006.03.005 (cited on page 4).
- [20] J. P. Gallivan and J. C. Culham, 'Neural coding within human brain areas involved in actions,' *Current Opinion in Neurobiology*, vol. 33, pp. 141–149, 2015. doi: 10.1016/j.conb.2015.03.012 (cited on page 4).
- [21] M. Mishkin, L. G. Ungerleider, and K. A. Macko, 'Object vision and spatial vision: Two cortical pathways,' *Trends in Neurosciences*, vol. 6, pp. 414–417, 1983. doi: 10.1016/0166-2236(83)90190-X (cited on page 4).
- [22] M. A. Goodale and A. Milner, 'Separate visual pathways for perception and action,' *Trends in Neurosciences*, vol. 15, no. 1, pp. 20–25, 1992. doi: 10.1016/0166-2236(92)90344-8 (cited on page 4).
- [23] C. A. Buneo and R. A. Andersen, 'The posterior parietal cortex: Sensorimotor interface for the planning and online control of visually guided movements,' *Neuropsychologia*, vol. 44, no. 13, pp. 2594–2606, 2006. doi: 10.1016/j.neuropsychologia.2005.10.011 (cited on page 4).
- [24] B. Kolb, I. Q. Whishaw, and G. C. Teskey, *An introduction to brain and behavior*, 6th ed. McMillan Learning, 2019, ISBN: 978-1-319-10737-6 (cited on page 4).
- [25] G. Rizzolatti and M. Matelli, 'Two different streams form the dorsal visual system: Anatomy and functions,' *Experimental Brain Research*, vol. 153, no. 2, pp. 146–157, 2003. doi: 10.1007/s00221-003-1588-0 (cited on page 4).
- [26] R. Caminiti, E. Borra, F. Visco-Comandini, A. Battaglia-Mayer, B. B. Averbeck, and G. Luppino, 'Computational Architecture of the Parieto-Frontal Network Underlying Cognitive-Motor Control in Monkeys,' *eNeuro*, vol. 4, no. 1, 2017. doi: 10.1523/ENEURO.0306-16.2017 (cited on pages 4, 58).
- [27] A. Battaglia-Mayer, 'A Brief History of the Encoding of Hand Position by the Cerebral Cortex: Implications for Motor Control and Cognition,' *Cerebral Cortex*, pp. 1–16, 2018. doi: 10.1093/cercor/bhx354 (cited on pages 4, 56).

- [28] F. Filimon, 'Human cortical control of hand movements: Parietofrontal networks for reaching, grasping, and pointing.,' *The Neuroscientist*, vol. 16, no. 4, pp. 388–407, 2010. doi: 10.1177/1073858410375468 (cited on pages 4, 57).
- [29] S. Neggers and H. Bekkering, 'Ocular Gaze is Anchored to the Target of an Ongoing Pointing Movement,' *Journal of Neurophysiology*, vol. 83, no. 2, pp. 639–651, 2000. doi: 10.1152/jn.2000.83.2.639 (cited on page 5).
- [30] C. L. Reed, J. D. Grubb, and C. Steele, 'Hands up: Attentional prioritization of space near the hand.,' *Journal of Experimental Psychology: Human Perception and Performance*, vol. 32, no. 1, pp. 166–177, 2006. doi: 10.1037/0096-1523.32.1.166 (cited on page 5).
- [31] J. P. Gallivan, C. Cavina-Pratesi, and J. C. Culham, 'Is That within Reach? fMRI Reveals That the Human Superior Parieto-Occipital Cortex Encodes Objects Reachable by the Hand,' *Journal of Neuroscience*, vol. 29, no. 14, pp. 4381–4391, 2009. doi: 10.1523/JNEUROSCI.0377-09.2009 (cited on page 5).
- [32] P. Cisek, 'Cortical mechanisms of action selection: The affordance competition hypothesis,' *Philosophical Transactions of the Royal Society B: Biological Sciences*, vol. 362, no. 1485, pp. 1585–1599, 2007. doi: 10.1098/rstb.2007.2054 (cited on page 5).
- [33] A. M. Haith, J. Pakpoor, and J. W. Krakauer, 'Independence of Movement Preparation and Movement Initiation,' *Journal of Neuroscience*, vol. 36, no. 10, pp. 3007–3015, 2016. doi: 10.1523/JNEUROSCI.3245-15.2016 (cited on pages 5, 11, 39).
- [34] E. R. Kandel, Schwartz, James H., Jessell, Thomas M., Siegelbaum, Steven A., and Hudspeth, A. J., Eds., *Principles of neural science*, 5th ed. New York: McGraw-Hill, 2013, ISBN: 978-0-07-139011-8 (cited on page 5).
- [35] G. Buzsáki, C. A. Anastassiou, and C. Koch, 'The origin of extracellular fields and currents-EEG, ECoG, LFP and spikes,' *Nature Reviews Neuroscience*, vol. 13, no. 6, pp. 407–420, 2012. doi: 10.1038/nrn3241 (cited on pages 5, 6).
- [36] B. He and Z. Liu, 'Multimodal Functional Neuroimaging: Integrating Functional MRI and EEG/MEG,' *IEEE Reviews in Biomedical Engineering*, vol. 1, pp. 23–40, 2008. doi: 10.1109/RBME.2008.2008233 (cited on page 6).
- [37] F. Biessmann, S. Plis, F. C. Meinecke, T. Eichele, and K.-R. Müller, 'Analysis of Multimodal Neuroimaging Data,' *IEEE Reviews in Biomedical Engineering*, vol. 4, pp. 26–58, 2011. doi: 10.1109/RBME.2011.2170675 (cited on page 6).
- [38] H. Lindén, T. Tetzlaff, T. C. Potjans, K. H. Pettersen, S. Grün, M. Diesmann, and G. T. Einevoll, 'Modeling the Spatial Reach of the LFP,' *Neuron*, vol. 72, no. 5, pp. 859–872, 2011. doi: 10.1016/j.neuron.2011.11.006 (cited on page 6).
- [39] C. Gold, D. A. Henze, C. Koch, and G. Buzsáki, 'On the Origin of the Extracellular Action Potential Waveform: A Modeling Study,' *Journal of Neurophysiology*, vol. 95, no. 5, pp. 3113–3128, 2006. doi: 10.1152/jn.00979.2005 (cited on page 6).
- [40] M. Abeles and M. Goldstein, 'Multispikes train analysis,' *Proceedings of the IEEE*, vol. 65, no. 5, pp. 762–773, 1977. doi: 10.1109/PROC.1977.10559 (cited on page 6).
- [41] M. A. Lebedev and M. A. L. Nicolelis, 'Brain-Machine Interfaces: From Basic Science to Neuroprostheses and Neurorehabilitation,' *Physiological Reviews*, vol. 97, no. 2, pp. 767–837, 2017. doi: 10.1152/physrev.00027.2016 (cited on page 6).
- [42] H. Berger, 'Über das elektroencephalogramm des menschen,' *European Archives of Psychiatry and Clinical Neuroscience*, vol. 87, no. 1, pp. 527–570, 1929 (cited on page 6).
- [43] D. L. Schomer and F. H. Lopes da Silva, *Niedermeyer's Electroencephalography: basic principles, clinical applications, and related fields*. 7th ed. Lippincott Williams & Wilkins, 2018, ISBN: 978-0-19-022848-4 (cited on pages 6, 8, 9, 15, 37).
- [44] P. L. Nunez and R. Srinivasan, *Electric Fields of the Brain*. Oxford University Press, 2006, ISBN: 978-0-19-505038-7 (cited on page 7).

- [45] D. Cohen, 'Magnetoencephalography: Evidence of Magnetic Fields Produced by Alpha-Rhythm Currents,' *Science*, vol. 161, no. 3843, pp. 784–786, 1968. doi: 10.1126/science.161.3843.784 (cited on page 7).
- [46] E. Boto, S. S. Meyer, V. Shah, O. Alem, S. Knappe, P. Kruger, T. M. Fromhold, M. Lim, P. M. Glover, P. G. Morris, R. Bowtell, G. R. Barnes, and M. J. Brookes, 'A new generation of magnetoencephalography: Room temperature measurements using optically-pumped magnetometers,' *NeuroImage*, vol. 149, pp. 404–414, 2017. doi: 10.1016/j.neuroimage.2017.01.034 (cited on page 7).
- [47] M. X. Cohen, *Analyzing neural time series data: theory and practice*, ser. Issues in clinical and cognitive neuropsychology. Cambridge, Massachusetts: The MIT Press, 2014, ISBN: 978-0-262-01987-3 (cited on page 7).
- [48] C. M. Michel, M. M. Murray, G. Lantz, S. Gonzalez, L. Spinelli, and R. Grave De Peralta, 'EEG source imaging,' *Clinical Neurophysiology*, vol. 115, no. 10, pp. 2195–2222, 2004. doi: 10.1016/j.clinph.2004.06.001 (cited on pages 7, 54).
- [49] T. W. Picton, P. van Roon, M. L. Armilio, P. Berg, N. Ille, and M. Scherg, 'The correction of ocular artifacts: A topographic perspective,' *Clinical Neurophysiology*, vol. 111, no. 1, pp. 53–65, 2000. doi: 10.1016/S1388-2457(99)00227-8 (cited on page 8).
- [50] A. S. Keren, S. Yuval-Greenberg, and L. Y. Deouell, 'Saccadic spike potentials in gamma-band EEG: Characterization, detection and suppression,' *NeuroImage*, vol. 49, no. 3, pp. 2248–2263, 2010. doi: 10.1016/j.neuroimage.2009.10.057 (cited on pages 8, 33).
- [51] O. H. Mowrer, T. C. Ruch, and N. E. Miller, 'The corneo-retinal potential difference as the basis of the galvanometric method of recording eye movements,' *American Journal of Physiology-Legacy Content*, vol. 114, no. 2, pp. 423–428, 1935. doi: 10.1152/ajplegacy.1935.114.2.423 (cited on page 8).
- [52] M. Iwasaki, C. Kellinghaus, A. V. Alexopoulos, R. C. Burgess, A. N. Kumar, Y. H. Han, H. O. Lüders, and R. J. Leigh, 'Effects of eyelid closure, blinks, and eye movements on the electroencephalogram,' *Clinical Neurophysiology*, vol. 116, no. 4, pp. 878–885, 2005. doi: 10.1016/j.clinph.2004.11.001 (cited on page 8).
- [53] F. Riemsлаг, G. Van der Heijde, M. Van Dongen, and F. Ottenhoff, 'On the origin of the presaccadic spike potential,' *Electroencephalography and Clinical Neurophysiology*, vol. 70, no. 4, pp. 281–287, 1988. doi: 10.1016/0013-4694(88)90046-6 (cited on page 8).
- [54] M. Plöchl, J. P. Ossandón, and P. König, 'Combining EEG and eye tracking: Identification, characterization, and correction of eye movement artifacts in electroencephalographic data,' *Frontiers in Human Neuroscience*, vol. 6, no. October, pp. 1–23, 2012. doi: 10.3389/fnhum.2012.00278 (cited on pages 8, 33, 35, 52).
- [55] R. J. Croft and R. J. Barry, 'Removal of ocular artifact from the EEG: A review,' *Clinical Neurophysiology*, vol. 30, no. 1, pp. 5–19, 2000. doi: 10.1016/S0987-7053(00)00055-1 (cited on pages 8, 53).
- [56] T.-P. Jung, S. Makeig, C. Humphries, T.-W. Lee, M. J. McKeown, V. Iragui, and T. J. Sejnowski, 'Removing electroencephalographic artifacts by blind source separation,' *Psychophysiology*, vol. 37, no. 2, pp. 163–178, 2000. doi: 10.1111/1469-8986.3720163 (cited on page 8).
- [57] L. Pion-Tonachini, K. Kreutz-Delgado, and S. Makeig, 'ICLabel: An automated electroencephalographic independent component classifier, dataset, and website,' *NeuroImage*, vol. 198, pp. 181–197, 2019. doi: 10.1016/j.neuroimage.2019.05.026 (cited on page 8).
- [58] R. J. Croft and R. J. Barry, 'EOG correction of blinks with saccade coefficients: A test and revision of the aligned-artefact average solution,' *Clinical Neurophysiology*, vol. 111, no. 3, pp. 444–451, 2000. doi: 10.1016/S1388-2457(99)00296-5 (cited on pages 8, 52).

- [59] G. Gratton, M. G. Coles, and E. Donchin, 'A new method for off-line removal of ocular artifact,' *Electroencephalography and Clinical Neurophysiology*, vol. 55, no. 4, pp. 468–484, 1983. doi: 10.1016/0013-4694(83)90135-9 (cited on page 8).
- [60] A. Schlögl, C. Keinrath, D. Zimmermann, R. Scherer, R. Leeb, and G. Pfurtscheller, 'A fully automated correction method of EOG artifacts in EEG recordings,' *Clinical Neurophysiology*, vol. 118, no. 1, pp. 98–104, 2007. doi: 10.1016/j.clinph.2006.09.003 (cited on pages 8, 33, 34, 52).
- [61] J. G. Webster, 'Reducing Motion Artifacts and Interference in Biopotential Recording,' *IEEE Transactions on Biomedical Engineering*, vol. 31, no. 12, pp. 823–826, 1984. doi: 10.1109/TBME.1984.325244 (cited on page 8).
- [62] H. Tam and J. G. Webster, 'Minimizing Electrode Motion Artifact by Skin Abrasion,' *IEEE Transactions on Biomedical Engineering*, vol. BME-24, no. 2, pp. 134–139, 1977. doi: 10.1109/TBME.1977.326117 (cited on pages 8, 53).
- [63] S. Ödman and P. Åke Öberg, 'Movement-induced potentials in surface electrodes,' *Medical & Biological Engineering & Computing*, vol. 20, no. 2, pp. 159–166, 1982. doi: 10.1007/BF02441351 (cited on page 9).
- [64] J. A. J. Klijn and M. J. G. M. Kloprogge, 'Movement artefact suppressor during ECG monitoring,' *Cardiovascular Research*, vol. 8, no. 1, pp. 149–152, 1974. doi: 10.1093/cvr/8.1.149 (cited on pages 9, 53).
- [65] A. Cömert and J. Hyttinen, 'Investigating the possible effect of electrode support structure on motion artifact in wearable bioelectric signal monitoring,' *BioMedical Engineering OnLine*, vol. 14, no. 1, p. 44, 2015. doi: 10.1186/s12938-015-0044-2 (cited on pages 9, 53).
- [66] G. R. Philips, M. K. h. Hazrati, J. J. Daly, and J. C. Principe, 'Addressing low frequency movement artifacts in EEG signal recorded during center-out reaching tasks,' in *Proceedings of the 36th Annual International Conference of the IEEE Engineering in Medicine and Biology Society (EMBC)*, 2014, pp. 6497–6500. doi: 10.1109/EMBC.2014.6945116 (cited on pages 9, 12, 22, 26, 53, 54).
- [67] P. Tallgren, S. Vanhatalo, K. Kaila, and J. Voipio, 'Evaluation of commercially available electrodes and gels for recording of slow EEG potentials,' *Clinical Neurophysiology*, vol. 116, no. 4, pp. 799–806, 2005. doi: 10.1016/j.clinph.2004.10.001 (cited on pages 9, 14).
- [68] W. Penfield and H. H. Jasper, *Epilepsy and the functional anatomy of the human brain*. Boston: Little, Brown, 1954, ISBN: 978-0-316-69833-7 (cited on page 9).
- [69] W. Penfield and E. Boldrey, 'Somatic motor and sensory representation in the cerebral cortex of man as studied by electrical stimulation,' *Brain*, vol. 60, no. 4, pp. 389–443, 1937. doi: 10.1093/brain/60.4.389 (cited on page 9).
- [70] M. S. Graziano, C. S. Taylor, and T. Moore, 'Complex Movements Evoked by Microstimulation of Precentral Cortex,' *Neuron*, vol. 34, no. 5, pp. 841–851, 2002. doi: 10.1016/S0896-6273(02)00698-0 (cited on page 9).
- [71] A. P. Georgopoulos, J. F. Kalaska, R. Caminiti, and J. T. Massey, 'On the relations between the direction of two-dimensional arm movements and cell discharge in primate motor cortex,' *J. Neurosci.*, vol. 2(11), no. 11, pp. 1527–1537, 1982. doi: citeulike-article-id: 444841 (cited on pages 9, 10, 19, 28, 57).
- [72] J. F. Kalaska, D. Cohen, M. Hyde, and M. Prud'homme, 'A comparison of movement direction-related versus load direction-related activity in primate motor cortex, using a two-dimensional reaching task,' *The Journal of Neuroscience*, vol. 9, no. 6, pp. 2080–2102, 1989. doi: 10.1523/JNEUROSCI.09-06-02080.1989 (cited on page 9).

- [73] A. P. Georgopoulos, A. Schwartz, and R. Kettner, 'Neuronal population coding of movement direction,' *Science*, vol. 233, no. 4771, pp. 1416–1419, 1986. doi: 10.1126/science.3749885 (cited on page 10).
- [74] R. Caminiti, P. B. Johnson, C. Galli, S. Ferraina, and Y. Burnod, 'Making arm movements within different parts of space: The premotor and motor cortical representation of a coordinate system for reaching to visual targets.,' *Journal of Neuroscience*, vol. 11, no. 5, pp. 1182–97, 1991 (cited on page 10).
- [75] A. B. Schwartz, R. E. Kettner, and A. P. Georgopoulos, 'Primate motor cortex and free arm movements to visual targets in three-dimensional space. I. Relations between single cell discharge and direction of movement,' *Journal of Neuroscience*, vol. 8, no. August, pp. 2913–2927, 1988 (cited on page 10).
- [76] A. B. Schwartz and D. W. Moran, 'Motor Cortical Activity During Drawing Movements: Population Representation During Lemniscate Tracing,' *Journal of Neurophysiology*, vol. 82, no. 5, pp. 2705–2718, 1999. doi: 10.1152/jn.1999.82.5.2705 (cited on page 10).
- [77] J. F. Kalaska, R. Caminiti, and A. P. Georgopoulos, 'Cortical mechanisms related to the direction of two-dimensional arm movements: Relations in parietal area 5 and comparison with motor cortex,' *Experimental Brain Research*, vol. 51, no. 2, pp. 247–260, 1983. doi: 10.1007/BF00237200 (cited on page 10).
- [78] J. M. Carmena, M. A. Lebedev, R. E. Crist, J. E. O'Doherty, D. M. Santucci, D. F. Dimitrov, P. G. Patil, C. S. Henriquez, and M. A. L. Nicolelis, 'Learning to control a brain-machine interface for reaching and grasping by primates,' *PLoS Biology*, vol. 1, no. 2, 2003. doi: 10.1371/journal.pbio.0000042 (cited on pages 10, 18, 19).
- [79] R. A. Andersen, L. H. Snyder, D. C. Bradley, and J. Xing, 'Multimodal representation of space in the posterior parietal cortex and its use in planning movements,' *Annual Review of Neuroscience*, vol. 20, no. 1, pp. 303–330, 1997. doi: 10.1146/annurev.neuro.20.1.303 (cited on page 10).
- [80] C. A. Buneo, M. R. Jarvis, A. P. Batista, and R. A. Andersen, 'Direct visuomotor transformations for reaching.,' *Nature*, vol. 416, no. 6881, pp. 632–6, 2002. doi: 10.1038/416632a (cited on pages 10, 23).
- [81] C. Mehring, J. Rickert, E. Vaadia, S. Cardoso de Oliveira, A. Aertsen, and S. Rotter, 'Inference of hand movements from local field potentials in monkey motor cortex.,' *Nature Neuroscience*, vol. 6, no. 12, pp. 1253–1254, 2003. doi: 10.1038/nn1158 (cited on pages 10, 20, 30).
- [82] J. Rickert, S. C. D. Oliveira, E. Vaadia, A. Aertsen, S. Rotter, and C. Mehring, 'Encoding of Movement Direction in Different Frequency Ranges of Motor Cortical Local Field Potentials,' *Journal of Neuroscience*, vol. 25, no. 39, pp. 8815–8824, 2005. doi: 10.1523/JNEUROSCI.0816-05.2005 (cited on pages 10, 20, 28).
- [83] C. Mehring, M. P. Nawrot, S. C. de Oliveira, E. Vaadia, A. Schulze-Bonhage, A. Aertsen, and T. Ball, 'Comparing information about arm movement direction in single channels of local and epicortical field potentials from monkey and human motor cortex,' *Journal of Physiology-Paris*, vol. 98, no. 4-6, pp. 498–506, 2004. doi: 10.1016/j.jphysparis.2005.09.016 (cited on pages 10, 11).
- [84] E. C. Leuthardt, G. Schalk, J. R. Wolpaw, J. G. Ojemann, and D. W. Moran, 'A brain-computer interface using electrocorticographic signals in humans,' *Journal of Neural Engineering*, vol. 1, no. 2, pp. 63–71, 2004. doi: 10.1088/1741-2560/1/2/001 (cited on pages 10, 17, 20, 21).
- [85] T. Ball, A. Schulze-Bonhage, A. Aertsen, and C. Mehring, 'Differential representation of arm movement direction in relation to cortical anatomy and function.,' *Journal of neural engineering*, vol. 6, no. 1, p. 016006, 2009. doi: 10.1088/1741-2560/6/1/016006 (cited on pages 10, 20–22, 28, 57).

- [86] S. Waldert, H. Preissl, E. Demandt, C. Braun, N. Birbaumer, A. Aertsen, and C. Mehring, 'Hand movement direction decoded from MEG and EEG,' *Journal of Neuroscience*, vol. 28, no. 4, pp. 1000–8, 2008. doi: 10.1523/JNEUROSCI.5171-07.2008 (cited on pages 10, 22, 23, 30, 39, 40, 57).
- [87] P. Hammon, S. Makeig, H. Poizner, E. Todorov, and V. De Sa, 'Predicting Reaching Targets from Human EEG,' *IEEE Signal Processing Magazine*, vol. 25, no. 1, pp. 69–77, 2008. doi: 10.1109/MSP.2008.4408443 (cited on pages 10, 22, 23, 27, 30, 39, 40).
- [88] M. T. Kaufman, J. S. Seely, D. Sussillo, S. I. Ryu, K. V. Shenoy, and M. M. Churchland, 'The Largest Response Component in the Motor Cortex Reflects Movement Timing but Not Movement Type,' *eNeuro*, vol. 3, no. 4, 2016. doi: 10.1523/ENEURO.0085-16.2016 (cited on page 10).
- [89] D. W. Moran and A. B. Schwartz, 'Motor Cortical Representation of Speed and Direction During Reaching,' *Journal of Neurophysiology*, vol. 82, no. 5, pp. 2676–2692, 1999. doi: 10.1152/jn.1999.82.5.2676 (cited on pages 10, 19, 54, 57).
- [90] P. Cisek and J. F. Kalaska, 'Neural correlates of reaching decisions in dorsal premotor cortex: Specification of multiple direction choices and final selection of action,' *Neuron*, vol. 45, no. 5, pp. 801–814, 2005. doi: 10.1016/j.neuron.2005.01.027 (cited on page 11).
- [91] O. Donchin, A. Gribova, O. Steinberg, H. Bergman, C. de Oliveira, and E. Vaadia, 'Local field potentials related to bimanual movements in the primary and supplementary motor cortices,' *Experimental Brain Research*, vol. 140, no. 1, pp. 46–55, 2001. doi: 10.1007/s002210100784 (cited on page 11).
- [92] J. N. Sanes and J. P. Donoghue, 'Oscillations in local field potentials of the primate motor cortex during voluntary movement.,' *Proceedings of the National Academy of Sciences*, vol. 90, no. 10, pp. 4470–4474, 1993. doi: 10.1073/pnas.90.10.4470 (cited on page 11).
- [93] H. H. Kornhuber and L. Deecke, 'Hirnpotentialänderungen bei Willkürbewegungen und passiven Bewegungen des Menschen: Bereitschaftspotential und reafferente Potentiale,' *Pflügers Archiv für die Gesamte Physiologie des Menschen und der Tiere*, vol. 284, no. 1, pp. 1–17, 1965. doi: 10.1007/BF00412364 (cited on page 11).
- [94] G. Pfurtscheller and A. Aranibar, 'Evaluation of event-related desynchronization (ERD) preceding and following voluntary self-paced movement,' *Electroencephalography and Clinical Neurophysiology*, vol. 46, no. 2, pp. 138–146, 1979. doi: 10.1016/0013-4694(79)90063-4 (cited on page 11).
- [95] T. Nagamine, M. Kajola, R. Salmelin, H. Shibasaki, and R. Hari, 'Movement-related slow cortical magnetic fields and changes of spontaneous MEG- and EEG-brain rhythms,' *Electroencephalography and Clinical Neurophysiology*, vol. 99, no. 3, pp. 274–286, 1996. doi: 10.1016/0013-4694(96)95154-8 (cited on page 11).
- [96] L. Deecke, P. Scheid, and H. H. Kornhuber, 'Distribution of readiness potential, pre-movement positivity, and motor potential of the human cerebral cortex preceding voluntary finger movements,' *Experimental Brain Research*, vol. 7, no. 2, pp. 158–168, 1969. doi: 10.1007/BF00235441 (cited on page 11).
- [97] H. Shibasaki, G. Barrett, E. Halliday, and a. M. Halliday, 'Components of the movement-related cortical potential and their scalp topography.,' *Electroencephalography and clinical neurophysiology*, vol. 49, no. 3-4, pp. 213–226, 1980. doi: 10.1016/0013-4694(80)90216-3 (cited on page 11).
- [98] N. Birbaumer, T. Elbert, A. Canavan, and B. Rockstroh, 'Slow potentials of the cerebral cortex and behavior.,' *Physiological Reviews*, vol. 70, no. 1, pp. 1–41, 1990. doi: 10.1152/physrev.1990.70.1.1 (cited on page 11).
- [99] G. Pfurtscheller and F. H. Lopes Da Silva, 'Event-related EEG/MEG synchronization and desynchronization: Basic principles,' *Clinical Neurophysiology*, vol. 110, pp. 1842–1857, 1999. doi: 10.1016/S1388-2457(99)00141-8 (cited on pages 11, 22).

- [100] H. Shibasaki and M. Hallett, 'What is the Bereitschaftspotential?' *Clinical Neurophysiology*, vol. 117, no. 11, pp. 2341–2356, 2006. doi: 10.1016/j.clinph.2006.04.025 (cited on page 11).
- [101] Jankelowitz S. and Colebatch J., 'Movement-related potentials associated with self-paced, cued and imagined arm movements,' *Experimental Brain Research*, vol. 147, no. 1, pp. 98–107, 2002. doi: 10.1007/s00221-002-1220-8 (cited on page 11).
- [102] M. Jochumsen, I. K. Niazi, N. Mrachacz-Kersting, D. Farina, and K. Dremstrup, 'Detection and classification of movement-related cortical potentials associated with task force and speed,' *Journal of Neural Engineering*, vol. 10, no. 5, 2013. doi: 10.1088/1741-2560/10/5/056015 (cited on pages 11, 26, 46, 59).
- [103] O. F. do Nascimento, K. D. Nielsen, and M. Voigt, 'Relationship between plantar-flexor torque generation and the magnitude of the movement-related potentials,' *Experimental Brain Research*, vol. 160, no. 2, pp. 154–165, 2005. doi: 10.1007/s00221-004-1996-9 (cited on page 11).
- [104] H. G. Vaughan, L. D. Costa, and W. Ritter, 'Topography of the human motor potential,' *Electroencephalography and Clinical Neurophysiology*, vol. 25, no. 1, pp. 1–10, 1968. doi: 10.1016/0013-4694(68)90080-1 (cited on page 11).
- [105] R. Beisteiner, P. Höllinger, G. Lindinger, W. Lang, and A. Berthoz, 'Mental representations of movements. Brain potentials associated with imagination of hand movements,' *Electroencephalography and Clinical Neurophysiology/Evoked Potentials Section*, vol. 96, no. 2, pp. 183–193, 1995. doi: 10.1016/0168-5597(94)00226-5 (cited on page 11).
- [106] P. Ofner, A. Schwarz, J. Pereira, and G. R. Müller-Putz, 'Upper limb movements can be decoded from the time-domain of low-frequency EEG,' *Plos One*, vol. 12, no. 8, e0182578, 2017. doi: 10.1371/journal.pone.0182578 (cited on pages 11, 54, 59).
- [107] J. Pereira, A. I. Sburlea, and G. R. Müller-Putz, 'EEG patterns of self-paced movement imaginations towards externally-cued and internally-selected targets,' *Scientific Reports*, vol. 8, no. 1, p. 13394, 2018. doi: 10.1038/s41598-018-31673-2 (cited on page 11).
- [108] I. K. Niazi, N. Jiang, O. Tiberghien, J. F. Nielsen, K. Dremstrup, and D. Farina, 'Detection of movement intention from single-trial movement-related cortical potentials,' *Journal of Neural Engineering*, vol. 8, no. 6, p. 066009, 2011. doi: 10.1088/1741-2560/8/6/066009 (cited on page 11).
- [109] M. Jochumsen, I. Khan Niazi, D. Taylor, D. Farina, and K. Dremstrup, 'Detecting and classifying movement-related cortical potentials associated with hand movements in healthy subjects and stroke patients from single-electrode, single-trial EEG,' *Journal of Neural Engineering*, vol. 12, no. 5, p. 056013, 2015. doi: 10.1088/1741-2560/12/5/056013 (cited on page 11).
- [110] P. Ofner, A. Schwarz, J. Pereira, D. Wyss, R. Wildburger, and G. R. Müller-Putz, 'Attempted Arm and Hand Movements can be Decoded from Low-Frequency EEG from Persons with Spinal Cord Injury,' *Scientific Reports*, vol. 9, no. 1, p. 7134, 2019. doi: 10.1038/s41598-019-43594-9 (cited on page 11).
- [111] G. Pfurtscheller, C. Neuper, and G. Krausz, 'Functional dissociation of lower and upper frequency mu rhythms in relation to voluntary limb movement,' *Clinical Neurophysiology*, vol. 111, no. 10, pp. 1873–1879, 2000. doi: 10.1016/S1388-2457(00)00428-4 (cited on page 11).
- [112] G. Pfurtscheller, 'Central beta rhythm during sensorimotor activities in man,' *Electroencephalography and Clinical Neurophysiology*, vol. 51, no. 3, pp. 253–264, 1981. doi: 10.1016/0013-4694(81)90139-5 (cited on page 11).

- [113] P. Suffczynski, Pijn, J. M.P., Pfurtscheller, G., and Lopes da Silva, F. H., 'Event-related dynamics of alpha band rhythms: A neuronal network model of focal ERD/surround RS,' in *Event-related desynchronization and related oscillatory phenomena of the brain*. Pfurtscheller, G. and Lopes da Silva, F.H., Eds., 1999 (cited on page 11).
- [114] G. Pfurtscheller, A. Stancák, and C. Neuper, 'Event-related synchronization (ERS) in the alpha band — an electrophysiological correlate of cortical idling: A review,' *International Journal of Psychophysiology*, vol. 24, no. 1-2, pp. 39–46, 1996. doi: 10.1016/S0167-8760(96)00066-9 (cited on page 11).
- [115] G. Pfurtscheller and C. Neuper, 'Motor imagery activates primary sensorimotor area in humans,' *Neuroscience Letters*, vol. 239, no. 2-3, pp. 65–68, 1997. doi: 10.1016/S0304-3940(97)00889-6 (cited on page 12).
- [116] G. Pfurtscheller, C. Brunner, A. Schlögl, and F. Lopes da Silva, 'Mu rhythm (de)synchronization and EEG single-trial classification of different motor imagery tasks,' *NeuroImage*, vol. 31, no. 1, pp. 153–159, 2006. doi: 10.1016/j.neuroimage.2005.12.003 (cited on page 12).
- [117] K. J. Miller, G. Schalk, E. E. Fetz, M. den Nijs, J. G. Ojemann, and R. P. N. Rao, 'Cortical activity during motor execution, motor imagery, and imagery-based online feedback,' *Proceedings of the National Academy of Sciences*, vol. 107, no. 9, pp. 4430–4435, 2010. doi: 10.1073/pnas.0913697107 (cited on page 12).
- [118] C. Neuper, G. R. Müller-Putz, R. Scherer, and G. Pfurtscheller, 'Motor imagery and EEG-based control of spelling devices and neuroprostheses,' in *Progress in Brain Research*, vol. 159, Elsevier, 2006, pp. 393–409, ISBN: 978-0-444-52183-5. doi: 10.1016/S0079-6123(06)59025-9 (cited on page 12).
- [119] W. Wang, S. S. Chan, D. A. Heldman, and D. W. Moran, 'Motor cortical representation of position and velocity during reaching,' *Journal of neurophysiology*, vol. 97, pp. 4258–70, 2007. doi: 10.1152/jn.01180.2006 (cited on page 12).
- [120] L. Paninski, M. R. Fellows, N. G. Hatsopoulos, and J. P. Donoghue, 'Spatiotemporal tuning of motor cortical neurons for hand position and velocity,' *Journal of neurophysiology*, vol. 91, no. 1, pp. 515–32, 2004. doi: 10.1152/jn.00587.2002 (cited on pages 12, 28, 30, 42, 57).
- [121] T. Pistohl, T. Ball, A. Schulze-Bonhage, A. Aertsen, and C. Mehring, 'Prediction of arm movement trajectories from ECoG-recordings in humans,' *Journal of Neuroscience Methods*, vol. 167, no. 1, pp. 105–114, 2008. doi: 10.1016/j.jneumeth.2007.10.001 (cited on pages 12, 20, 47).
- [122] Y. Nakanishi, T. Yanagisawa, D. Shin, R. Fukuma, C. Chen, H. Kambara, N. Yoshimura, M. Hirata, T. Yoshimine, and Y. Koike, 'Prediction of Three-Dimensional Arm Trajectories Based on ECoG Signals Recorded from Human Sensorimotor Cortex,' *PLoS ONE*, vol. 8, no. 8, 2013. doi: 10.1371/journal.pone.0072085 (cited on pages 12, 20, 47).
- [123] J. Hammer, J. Fischer, J. Ruescher, A. Schulze-Bonhage, A. Aertsen, and T. Ball, 'The role of ECoG magnitude and phase in decoding position, velocity, and acceleration during continuous motor behavior,' *Frontiers in Neuroscience*, vol. 7, 2013. doi: 10.3389/fnins.2013.00200 (cited on pages 12, 55, 62).
- [124] J. Hammer, T. Pistohl, J. Fischer, P. Kršek, M. Tomášek, P. Marusič, A. Schulze-Bonhage, A. Aertsen, and T. Ball, 'Predominance of Movement Speed over Direction in Neuronal Population Signals of Motor Cortex: Intracranial EEG Data and A Simple Explanatory Model,' *Cerebral Cortex*, vol. 26, no. 6, pp. 2863–2881, 2016. doi: 10.1093/cercor/bhw033 (cited on pages 12, 20, 22, 44, 57).
- [125] S. Haufe, F. Meinecke, K. Görgen, S. Dähne, J. D. Haynes, B. Blankertz, and F. Bießmann, 'On the interpretation of weight vectors of linear models in multivariate neuroimaging,' *NeuroImage*, vol. 87, pp. 96–110, 2014. doi: 10.1016/j.neuroimage.2013.10.067 (cited on pages 12, 27, 29, 54).

- [126] T. J. Bradberry, F. Rong, and J. L. Contreras-Vidal, 'Decoding center-out hand velocity from MEG signals during visuomotor adaptation,' *NeuroImage*, vol. 47, no. 4, pp. 1691–1700, 2009. doi: 10.1016/j.neuroimage.2009.06.023 (cited on pages 12, 22, 24, 30, 53, 57).
- [127] T. J. Bradberry, R. J. Gentili, and J. L. Contreras-Vidal, 'Reconstructing Three-Dimensional Hand Movements from Noninvasive Electroencephalographic Signals,' *Journal of Neuroscience*, vol. 30, no. 9, pp. 3432–3437, 2010. doi: 10.1523/JNEUROSCI.6107-09.2010 (cited on pages 12, 22, 24, 26, 30, 53, 60).
- [128] P. Ofner and G. R. Müller-Putz, 'Decoding of velocities and positions of 3D arm movement from EEG,' *Proceedings of the Annual International Conference of the IEEE Engineering in Medicine and Biology Society, EMBS*, pp. 6406–6409, 2012. doi: 10.1109/EMBC.2012.6347460 (cited on pages 12, 22, 25, 26, 30, 53, 57, 60).
- [129] K. Jerbi, J.-P. Lachaux, K. N'Diaye, D. Pantazis, R. M. Leahy, L. Garnero, and S. Baillet, 'Coherent neural representation of hand speed in humans revealed by MEG imaging.,' *Proceedings of the National Academy of Sciences*, vol. 104, no. 18, pp. 7676–7681, 2007. doi: 10.1073/pnas.0609632104 (cited on pages 12, 22, 46, 57, 59).
- [130] M. Bourguignon, V. Jousmäki, M. Op de Beeck, P. Van Bogaert, S. Goldman, and X. De Tiège, 'Neuronal network coherent with hand kinematics during fast repetitive hand movements,' *NeuroImage*, vol. 59, no. 2, pp. 1684–1691, 2012. doi: 10.1016/j.neuroimage.2011.09.022 (cited on page 12).
- [131] B. Marty, M. Bourguignon, V. Jousmäki, V. Wens, M. Op de Beeck, P. Van Bogaert, S. Goldman, R. Hari, and X. De Tiège, 'Cortical kinematic processing of executed and observed goal-directed hand actions,' *NeuroImage*, vol. 119, pp. 221–228, 2015. doi: 10.1016/j.neuroimage.2015.06.064 (cited on pages 12, 62).
- [132] J. R. Wolpaw and E. Wolpaw, *Brain-Computer Interfaces: Principles and Practice*. Oxford University Press, 2011, ISBN: 978-0-19-538885-5 (cited on pages 13, 21).
- [133] J. R. Wolpaw, N. Birbaumer, D. J. McFarland, G. Pfurtscheller, and T. M. Vaughan, 'Brain-computer interfaces for communication and control.,' *Clinical neurophysiology : official journal of the International Federation of Clinical Neurophysiology*, vol. 113, pp. 767–791, 2002. doi: doi:10.1016/s1388-2457(02)00057-3 (cited on pages 13, 14).
- [134] T. O. Zander and C. Kothe, 'Towards passive brain–computer interfaces: Applying brain–computer interface technology to human–machine systems in general,' *Journal of Neural Engineering*, vol. 8, no. 2, p. 025005, 2011. doi: 10.1088/1741-2560/8/2/025005 (cited on page 13).
- [135] S. Mason, J. Kronegg, J. Huggins, M. Fatourehchi, and A. Schlögl, 'Evaluating the performance of self-paced brain-computer interface technology,' *Neil Squire Society*, 2006 (cited on page 14).
- [136] S. G. Mason, A. Bashashati, M. Fatourehchi, K. F. Navarro, and G. E. Birch, 'A comprehensive survey of brain interface technology designs,' *Annals of biomedical engineering*, vol. 35, no. 2, pp. 137–169, 2007. doi: 10.1007/s10439-006-9170-0 (cited on page 14).
- [137] R. Oostenveld and P. Praamstra, 'The five percent electrode system for high-resolution EEG and ERP measurements,' *Clinical Neurophysiology*, vol. 112, no. 4, pp. 713–719, 2001. doi: 10.1016/S1388-2457(00)00527-7 (cited on page 14).
- [138] Y. Roy, H. Banville, I. Albuquerque, A. Gramfort, T. H. Falk, and J. Faubert, 'Deep learning-based electroencephalography analysis: A systematic review,' *Journal of Neural Engineering*, vol. 16, no. 5, p. 051001, 2019. doi: 10.1088/1741-2552/ab260c (cited on page 15).
- [139] N. Bigdely-Shamlo, T. Mullen, C. Kothe, K.-M. Su, and K. A. Robbins, 'The PREP pipeline: Standardized preprocessing for large-scale EEG analysis,' *Frontiers in Neuroinformatics*, vol. 9, no. June, p. 16, 2015. doi: 10.3389/fninf.2015.00016 (cited on page 15).

- [140] J. A. Urigüen and B. Garcia-Zapirain, 'EEG artifact removal-state-of-the-art and guidelines,' *Journal of Neural Engineering*, vol. 12, no. 3, p. 31001, 2015. doi: 10.1088/1741-2560/12/3/031001 (cited on pages 15, 37).
- [141] C. Bishop, *Pattern Recognition and Machine Learning*. Springer, 2006, vol. 4, ISBN: 978-0-387-31073-2 (cited on pages 15, 16).
- [142] F. Lotte, M. Congedo, A. Lécuyer, F. Lamarche, and B. Arnaldi, 'A review of classification algorithms for EEG-based brain-computer interfaces,' *Journal of Neural Engineering*, vol. 4, R1–R13, 2007. doi: 10.1088/1741-2560/4/2/R01 (cited on page 15).
- [143] B. Blankertz, S. Lemm, M. Treder, S. Haufe, and K.-R. Müller, 'Single-trial analysis and classification of ERP components—a tutorial,' *NeuroImage*, vol. 56, no. 2, pp. 814–825, 2011. doi: 10.1016/j.neuroimage.2010.06.048 (cited on pages 15, 16).
- [144] N. Robinson and A. Vinod, 'Noninvasive Brain-Computer Interface: Decoding Arm Movement Kinematics and Motor Control,' *IEEE Systems, Man, and Cybernetics Magazine*, vol. 2, no. 4, pp. 4–16, 2016. doi: 10.1109/MSMC.2016.2576638 (cited on pages 16, 60).
- [145] F. Lotte, F. Larrue, and C. Mühl, 'Flaws in current human training protocols for spontaneous Brain-Computer Interfaces: Lessons learned from instructional design,' *Frontiers in Human Neuroscience*, vol. 7, 2013. doi: 10.3389/fnhum.2013.00568 (cited on page 16).
- [146] F. Lotte and C. Jeunet, 'Towards improved BCI based on human learning principles,' in *The 3rd International Winter Conference on Brain-Computer Interface*, Gangwon-Do, South Korea: IEEE, 2015, pp. 1–4, ISBN: 978-1-4799-7494-8. doi: 10.1109/IWW-BCI.2015.7073024 (cited on page 16).
- [147] C. Neuper and G. Pfurtscheller, 'Neurofeedback Training for BCI Control,' in *Brain-Computer Interfaces*, B. Graimann, G. Pfurtscheller, and B. Allison, Eds., Berlin, Heidelberg: Springer Berlin Heidelberg, 2009, pp. 65–78, ISBN: 978-3-642-02090-2. doi: 10.1007/978-3-642-02091-9_4 (cited on page 16).
- [148] J. P. Donoghue, 'Connecting cortex to machines: Recent advances in brain interfaces,' *Nature Neuroscience*, vol. 5, no. S11, pp. 1085–1088, 2002. doi: 10.1038/nn947 (cited on page 17).
- [149] G. R. Müller-Putz, A. Schwarz, J. Pereira, and P. Ofner, 'From classic motor imagery to complex movement intention decoding: The noninvasive Graz-BCI approach,' in *Brain-Computer Interfaces: Lab Experiments to Real-World Applications*, ser. Progress in Brain Research, D. Coyle, Ed., vol. 228, Elsevier, 2016, pp. 39–70. doi: 10.1016/bs.pbr.2016.04.017 (cited on pages 17, 18, 22, 27).
- [150] G. Pfurtscheller, C. Guger, G. Müller, G. Krausz, and C. Neuper, 'Brain oscillations control hand orthosis in a tetraplegic,' *Neuroscience Letters*, vol. 292, no. 3, pp. 211–214, 2000. doi: 10.1016/S0304-3940(00)01471-3 (cited on pages 17, 21, 22).
- [151] J. R. Wolpaw, D. J. McFarland, G. W. Neat, and C. A. Forneris, 'An EEG-based brain-computer interface for cursor control,' *Electroencephalography and clinical neurophysiology*, vol. 78, pp. 252–259, 1991. doi: 10.1016/0013-4694(91)90040-B (cited on pages 17, 21).
- [152] M. Rohm, M. Schneiders, C. Müller, A. Kreilinger, V. Kaiser, G. R. Müller-Putz, and R. Rupp, 'Hybrid brain-computer interfaces and hybrid neuroprostheses for restoration of upper limb functions in individuals with high-level spinal cord injury,' *Artificial Intelligence in Medicine*, vol. 59, no. 2, pp. 133–142, 2013. doi: 10.1016/j.artmed.2013.07.004 (cited on pages 17, 22).
- [153] M. Palankar, K. De Laurentis, R. Alqasemi, E. Veras, R. Dubey, Y. Arbel, and E. Donchin, 'Control of a 9-DoF Wheelchair-mounted robotic arm system using a P300 Brain Computer Interface: Initial experiments,' in *2008 IEEE International Conference on Robotics and Biomimetics*, Bangkok: IEEE, 2009, pp. 348–353, ISBN: 978-1-4244-2678-2. doi: 10.1109/ROBIO.2009.4913028 (cited on page 17).

- [154] R. Prueckl and C. Guger, 'A Brain-Computer Interface Based on Steady State Visual Evoked Potentials for Controlling a Robot,' in *Bio-Inspired Systems: Computational and Ambient Intelligence*, J. Cabestany, F. Sandoval, A. Prieto, and J. M. Corchado, Eds., vol. 5517, Berlin, Heidelberg: Springer Berlin Heidelberg, 2009, pp. 690–697, ISBN: 978-3-642-02477-1. doi: 10.1007/978-3-642-02478-8_86 (cited on page 17).
- [155] I. Iturrate, J. Antelis, A. Kubler, and J. Minguez, 'A Noninvasive Brain-Actuated Wheelchair Based on a P300 Neurophysiological Protocol and Automated Navigation,' *IEEE Transactions on Robotics*, vol. 25, no. 3, pp. 614–627, 2009. doi: 10.1109/TR0.2009.2020347 (cited on page 17).
- [156] M. A. Nicolelis, 'Actions from thoughts,' *Nature*, vol. 409, no. 6818, pp. 403–407, 2001. doi: 10.1038/35053191 (cited on page 17).
- [157] R. D. Flint, Z. A. Wright, M. R. Scheid, and M. W. Slutzky, 'Long term, stable brain machine interface performance using local field potentials and multiunit spikes,' *Journal of Neural Engineering*, vol. 10, no. 5, 2013. doi: 10.1088/1741-2560/10/5/056005 (cited on pages 17, 20).
- [158] W. Wang, J. L. Collinger, A. D. Degenhart, E. C. Tyler-Kabara, A. B. Schwartz, D. W. Moran, D. J. Weber, B. Wodlinger, R. K. Vinjamuri, R. C. Ashmore, J. W. Kelly, and M. L. Boninger, 'An Electrographic Brain Interface in an Individual with Tetraplegia,' *PLoS ONE*, vol. 8, no. 2, pp. 1–8, 2013. doi: 10.1371/journal.pone.0055344 (cited on pages 17, 21).
- [159] E. Fetz, 'Operant Conditioning of Cortical Unit Activity,' *Science*, vol. 163, no. 3870, pp. 955–958, 1969. doi: 10.1126/science.163.3870.955 (cited on page 18).
- [160] J. K. Chapin, K. A. Moxon, R. S. Markowitz, and M. A. Nicolelis, 'Real-time control of a robot arm using simultaneously recorded neurons in the motor cortex,' *Nature Neuroscience*, vol. 2, no. 7, pp. 664–670, 1999. doi: 10.1038/10223 (cited on page 18).
- [161] M. D. Serruya, N. G. Hatsopoulos, L. Paninski, M. R. Fellows, and J. P. Donoghue, 'Instant neural control of a movement signal,' *Nature*, vol. 416, no. 6877, pp. 141–142, 2002. doi: 10.1038/416141a (cited on pages 18, 61).
- [162] D. M. Taylor, 'Direct Cortical Control of 3D Neuroprosthetic Devices,' *Science*, vol. 296, no. 5574, pp. 1829–1832, 2002. doi: 10.1126/science.1070291 (cited on pages 18, 61).
- [163] J. Wessberg, C. R. Stambaugh, J. D. Kralik, P. D. Beck, M. Laubach, J. K. Chapin, J. Kim, S. J. Biggs, M. A. Srinivasan, and M. A. Nicolelis, 'Real-time prediction of hand trajectory by ensembles of cortical neurons in primates,' *Nature*, vol. 408, no. 6810, pp. 361–365, 2000. doi: 10.1038/35042582 (cited on page 18).
- [164] J. L. Collinger, B. Wodlinger, J. E. Downey, W. Wang, E. C. Tyler-Kabara, D. J. Weber, A. J. McMorland, M. Velliste, M. L. Boninger, and A. B. Schwartz, 'High-performance neuroprosthetic control by an individual with tetraplegia,' *The Lancet*, vol. 381, no. 9866, pp. 557–564, 2013. doi: 10.1016/S0140-6736(12)61816-9 (cited on pages 18, 19, 22).
- [165] B. Wodlinger, J. E. Downey, E. C. Tyler-Kabara, A. B. Schwartz, M. L. Boninger, and J. L. Collinger, 'Ten-dimensional anthropomorphic arm control in a human brain-machine interface: Difficulties, solutions, and limitations,' *Journal of Neural Engineering*, vol. 12, no. 1, p. 016011, 2015. doi: 10.1088/1741-2560/12/1/016011 (cited on pages 18, 19, 22).
- [166] D. Edell, V. Toi, V. McNeil, and L. Clark, 'Factors influencing the biocompatibility of insertable silicon microshafts in cerebral cortex,' *IEEE Transactions on Biomedical Engineering*, vol. 39, no. 6, pp. 635–643, 1992. doi: 10.1109/10.141202 (cited on page 18).
- [167] E. Fernández, B. Greger, P. A. House, I. Aranda, C. Botella, J. Albisua, C. Soto-Sánchez, A. Alfaro, and R. A. Normann, 'Acute human brain responses to intracortical microelectrode arrays: Challenges and future prospects,' *Frontiers in Neuroengineering*, vol. 7, 2014. doi: 10.3389/fneng.2014.00024 (cited on page 18).

- [168] C. A. Chestek, V. Gilja, P. Nuyujukian, J. D. Foster, J. M. Fan, M. T. Kaufman, M. M. Churchland, Z. Rivera-Alvidrez, J. P. Cunningham, S. I. Ryu, and K. V. Shenoy, 'Long-term stability of neural prosthetic control signals from silicon cortical arrays in rhesus macaque motor cortex,' *Journal of Neural Engineering*, vol. 8, no. 4, p. 045005, 2011. doi: 10.1088/1741-2560/8/4/045005 (cited on page 19).
- [169] G. Santhanam, S. I. Ryu, B. M. Yu, A. Afshar, and K. V. Shenoy, 'A high-performance brain-computer interface,' *Nature*, vol. 442, no. 7099, pp. 195–198, 2006. doi: 10.1038/nature04968 (cited on page 19).
- [170] T. Aflalo, S. Kellis, C. Klaes, B. Lee, Y. Shi, K. Pejsa, K. Shanfield, S. Hayes-Jackson, M. Aisen, C. Heck, C. Liu, and R. Andersen, 'Decoding motor imagery from the posterior parietal cortex of a tetraplegic human,' *Science*, vol. 348, no. 6237, pp. 906–910, 2015. doi: 10.7910/DVN/GJDUTV (cited on pages 19, 23).
- [171] S.-P. Kim, J. C. Sanchez, Y. N. Rao, D. Erdogmus, J. M. Carmena, M. A. Lebedev, M. A. L. Nicolelis, and J. C. Principe, 'A comparison of optimal MIMO linear and nonlinear models for brain-machine interfaces,' *Journal of Neural Engineering*, vol. 3, no. 2, pp. 145–161, 2006. doi: 10.1088/1741-2560/3/2/009 (cited on page 19).
- [172] N. Wiener, *Extrapolation, Interpolation, and Smoothing of Stationary Time Series*. Cambridge: MIT Press, 1964, ISBN: 978-0-262-23002-5 (cited on page 19).
- [173] R. E. Kalman, 'A New Approach to Linear Filtering and Prediction Problems,' *Journal of Basic Engineering*, vol. 82, no. 1, pp. 35–45, 1960. doi: 10.1115/1.3662552 (cited on page 19).
- [174] Z. Li, J. E. O'Doherty, T. L. Hanson, M. A. Lebedev, C. S. Henriquez, and M. A. L. Nicolelis, 'Unscented Kalman Filter for Brain-Machine Interfaces,' *PLoS ONE*, vol. 4, no. 7, e6243, 2009. doi: 10.1371/journal.pone.0006243 (cited on pages 19, 31, 46, 54, 55).
- [175] E. Wan and R. Van Der Merwe, 'The unscented Kalman filter for nonlinear estimation,' in *Proceedings of the IEEE 2000 Adaptive Systems for Signal Processing, Communications, and Control Symposium*, Lake Louise, Alta., Canada: IEEE, 2000, pp. 153–158, ISBN: 978-0-7803-5800-3. doi: 10.1109/ASSPCC.2000.882463 (cited on page 19).
- [176] V. Aggarwal, M. Mollazadeh, A. G. Davidson, M. H. Schieber, and N. V. Thakor, 'State-based decoding of hand and finger kinematics using neuronal ensemble and LFP activity during dexterous reach-to-grasp movements,' *Journal of Neurophysiology*, vol. 109, no. 12, pp. 3067–3081, 2013. doi: 10.1152/jn.01038.2011 (cited on page 20).
- [177] J. G. O'Leary and N. G. Hatsopoulos, 'Early Visuomotor Representations Revealed From Evoked Local Field Potentials in Motor and Premotor Cortical Areas,' *Journal of Neurophysiology*, vol. 96, no. 3, pp. 1492–1506, 2006. doi: 10.1152/jn.00106.2006 (cited on page 20).
- [178] Z. Chao, Y. Nagasaka, and N. Fujii, 'Long-term asynchronous decoding of arm motion using electrocorticographic signals in monkey,' *Frontiers in Neuroengineering*, vol. 3, no. March, 2010. doi: 10.3389/fneng.2010.00003 (cited on page 20).
- [179] K. Shimoda, Y. Nagasaka, Z. C. Chao, and N. Fujii, 'Decoding continuous three-dimensional hand trajectories from epidural electrocorticographic signals in Japanese macaques,' *Journal of Neural Engineering*, vol. 9, no. 3, p. 036015, 2012. doi: 10.1088/1741-2560/9/3/036015 (cited on page 20).
- [180] G. Schalk, J. Kubánek, K. J. Miller, N. R. Anderson, E. C. Leuthardt, J. G. Ojemann, D. Limbrick, D. Moran, L. A. Gerhardt, and J. R. Wolpaw, 'Decoding two-dimensional movement trajectories using electrocorticographic signals in humans,' *Journal of Neural Engineering*, vol. 4, no. 3, p. 264, 2007. doi: 10.1088/1741-2560/4/3/012 (cited on pages 20, 21, 30, 47).

- [181] D. T. Bundy, M. Pahwa, N. Szrama, and E. C. Leuthardt, 'Decoding three-dimensional reaching movements using electrocorticographic signals in humans,' *Journal of Neural Engineering*, vol. 13, no. 2, p. 026 021, 2016. doi: 10.1088/1741-2560/13/2/026021 (cited on pages 20, 44, 54).
- [182] T. Milekovic, J. Fischer, T. Pistohl, J. Ruescher, A. Schulze-Bonhage, A. Aertsen, J. Rickert, T. Ball, and C. Mehring, 'An online brain-machine interface using decoding of movement direction from the human electrocorticogram,' *Journal of neural engineering*, vol. 9, no. 4, p. 046 003, 2012. doi: 10.1088/1741-2560/9/4/046003 (cited on page 21).
- [183] D. J. McFarland, W. A. Sarnacki, and J. R. Wolpaw, 'Electroencephalographic (EEG) control of three-dimensional movement,' *Journal of Neural Engineering*, vol. 7, no. 3, p. 036 007, 2010. doi: 10.1088/1741-2560/7/3/036007 (cited on pages 21, 22).
- [184] J. Meng, S. Zhang, A. Bekyo, J. Olsoe, B. Baxter, and B. He, 'Noninvasive Electroencephalogram Based Control of a Robotic Arm for Reach and Grasp Tasks,' *Scientific Reports*, vol. 6, no. November, p. 38 565, 2016. doi: 10.1038/srep38565 (cited on pages 21, 22).
- [185] E. V. Friedrich, R. Scherer, and C. Neuper, 'Long-term evaluation of a 4-class imagery-based brain-computer interface,' *Clinical Neurophysiology*, vol. 124, no. 5, pp. 916–927, 2013. doi: 10.1016/j.clinph.2012.11.010 (cited on page 22).
- [186] G. R. Müller-Putz, R. Scherer, G. Pfurtscheller, and C. Neuper, 'Temporal coding of brain patterns for direct limb control in humans,' *Frontiers in Neuroscience*, 2010. doi: 10.3389/fnins.2010.00034 (cited on page 22).
- [187] S. Waldert, T. Pistohl, C. Braun, T. Ball, A. Aertsen, and C. Mehring, 'A review on directional information in neural signals for brain-machine interfaces,' *Journal of Physiology Paris*, vol. 103, no. 3-5, pp. 244–254, 2009. doi: 10.1016/j.jphysparis.2009.08.007 (cited on page 22).
- [188] P. Ofner and G. R. Müller-Putz, 'Using a noninvasive decoding method to classify rhythmic movement imaginations of the arm in two planes,' *IEEE Transactions on Biomedical Engineering*, vol. 62, no. 3, pp. 972–981, 2015. doi: 10.1109/TBME.2014.2377023 (cited on pages 22, 25, 26, 28, 43, 54).
- [189] W. Wang, G. P. Sudre, Y. Xu, R. E. Kass, J. L. Collinger, A. D. Degenhart, A. I. Bagic, and D. J. Weber, 'Decoding and cortical source localization for intended movement direction with MEG,' *Journal of neurophysiology*, vol. 104, no. 5, pp. 2451–2461, 2010. doi: 10.1152/jn.00239.2010 (cited on pages 22–24, 39).
- [190] J. Li, Y. Wang, L. Zhang, and T.-P. Jung, 'Combining ERPs and EEG spectral features for decoding intended movement direction,' in *34th Annual International Conference of the IEEE Engineering in Medicine and Biology Society.*, San Diego, CA: IEEE, 2012, pp. 1769–1772, ISBN: 978-1-4577-1787-1. doi: 10.1109/EMBC.2012.6346292 (cited on pages 22, 23, 30, 39, 40).
- [191] C.-c. Kuo, J. L. Knight, C. A. Dressel, A. W. L. Chiu, J. L. Knight, C. A. Dressel, A. W. L. Chiu, B. Engineering, and U. States, 'Non-Invasive BCI for the Decoding of Intended Arm Reaching Movement in Prosthetic Limb Control,' *American Journal of Biomedical Engineering*, vol. 2, no. 4, pp. 155–162, 2012. doi: 10.5923/j.ajbe.20120204.02 (cited on pages 22, 23).
- [192] N. Robinson, C. Guan, A. P. Vinod, K. Keng Ang, and K. Peng Tee, 'Multi-class EEG classification of voluntary hand movement directions,' *Journal of Neural Engineering*, vol. 10, no. 5, 2013. doi: 10.1088/1741-2560/10/5/056018 (cited on pages 22, 23).
- [193] E. Y. Lew, R. Chavarriaga, S. Silvoni, and J. d. R. Millán, 'Single trial prediction of self-paced reaching directions from EEG signals,' *Frontiers in Neuroscience*, vol. 8, no. August, pp. 1–13, 2014. doi: 10.3389/fnins.2014.00222 (cited on pages 22, 23).

- [194] E. Y. L. Lew, R. Chavarriaga, S. Silvoni, and J. D. R. Millán, 'Detection of self-paced reaching movement intention from EEG signals,' *Frontiers in Neuroengineering*, vol. 13, 2012. doi: 10.3389/fneng.2012.00013 (cited on page 23).
- [195] A. Toda, H. Imamizu, M. Kawato, and M.-a. Sato, 'Reconstruction of two-dimensional movement trajectories from selected magnetoencephalography cortical currents by combined sparse Bayesian methods,' *NeuroImage*, vol. 54, no. 2, pp. 892–905, 2011. doi: 10.1016/j.neuroimage.2010.09.057 (cited on page 24).
- [196] H. G. Yeom, J. S. Kim, and C. K. Chung, 'Estimation of the velocity and trajectory of three-dimensional reaching movements from non-invasive magnetoencephalography signals,' *Journal of neural engineering*, vol. 10, no. 2, p. 026006, 2013. doi: 10.1088/1741-2560/10/2/026006 (cited on pages 24, 26, 53).
- [197] N. Robinson, C. Guan, and A. P. Vinod, 'Adaptive estimation of hand movement trajectory in an EEG based brain-computer interface system,' *Journal of Neural Engineering*, vol. 12, no. 6, p. 66019, 2015. doi: 10.1088/1741-2560/12/6/066019 (cited on page 24).
- [198] J. M. Antelis, L. Montesano, A. Ramos-Murguialday, N. Birbaumer, and J. Minguez, 'On the Usage of Linear Regression Models to Reconstruct Limb Kinematics from Low Frequency EEG Signals,' *PLoS ONE*, vol. 8, no. 4, 2013. doi: 10.1371/journal.pone.0061976 (cited on pages 24, 27, 46, 53, 54).
- [199] A. P. Georgopoulos, F. J. P. Langheim, A. C. Leuthold, and A. N. Merkle, 'Magnetoencephalographic signals predict movement trajectory in space,' *Experimental Brain Research*, vol. 167, no. 1, pp. 132–135, 2005. doi: 10.1007/s00221-005-0028-8 (cited on pages 25, 26).
- [200] J. Lv, Y. Li, and Z. Gu, 'Decoding hand movement velocity from electroencephalogram signals during a drawing task,' *Biomedical engineering online*, vol. 9, no. 1, p. 64, 2010. doi: 10.1186/1475-925X-9-64 (cited on pages 25–27, 55).
- [201] A. Úbeda, E. Hortal, E. Iáñez, C. Perez-Vidal, and J. M. Azorín, 'Assessing Movement Factors in Upper Limb Kinematics Decoding from EEG Signals,' *Plos One*, vol. 10, no. 5, e0128456, 2015. doi: 10.1371/journal.pone.0128456 (cited on pages 25, 26, 29, 55).
- [202] Kim, Jeong-Hun, F. Biessmann, and Lee, Seong-Whan, 'Decoding three-dimensional trajectory of executed and imagined arm movements from electroencephalogram signals,' *IEEE Transactions on Neural Systems and Rehabilitation Engineering*, vol. 23, no. 5, pp. 867–876, 2015. doi: 10.1109/TNSRE.2014.2375879 (cited on pages 25–28, 46, 47, 53–55).
- [203] A. Úbeda, J. Azoín, R. Chavarriaga, and J. D. R. Millán, 'Evaluating decoding performance of upper limb imagined trajectories during center-out reaching tasks,' in *2016 IEEE International Conference on Systems, Man, and Cybernetics*, 2016, pp. 252–257, ISBN: 978-1-5090-1897-0 (cited on pages 26, 27).
- [204] Y. Gu, K. Dremstrup, and D. Farina, 'Single-trial discrimination of type and speed of wrist movements from EEG recordings,' *Clinical Neurophysiology*, vol. 120, no. 8, pp. 1596–1600, 2009. doi: 10.1016/j.clinph.2009.05.006 (cited on pages 26, 59).
- [205] A. Korik, N. Siddique, R. Sosnik, and D. Coyle, '3D Hand Movement Velocity Reconstruction using Power Spectral Density of EEG Signals and Neural Network,' in *35th Annual International Conference of the IEEE Engineering in Medicine and Biology Society, Milan*, 2015, pp. 8103–8106, ISBN: 978-1-4244-9270-1 (cited on pages 27, 46, 47).
- [206] T. J. Bradberry, R. J. Gentili, and J. L. Contreras-Vidal, 'Fast attainment of computer cursor control with noninvasively acquired brain signals,' *Journal of Neural Engineering*, vol. 8, no. 3, p. 036010, 2011. doi: 10.1088/1741-2560/8/3/036010 (cited on page 27).
- [207] R. Poli and M. Salvaris, 'Comment on 'Fast attainment of computer cursor control with noninvasively acquired brain signals',', *Journal of Neural Engineering*, vol. 8, no. 5, p. 058001, 2011. doi: 10.1088/1741-2560/8/5/058001 (cited on page 27).

- [208] J. P. Cunningham, P. Nuyujukian, V. Gilja, C. A. Chestek, S. I. Ryu, and K. V. Shenoy, 'A closed-loop human simulator for investigating the role of feedback control in brain-machine interfaces,' *Journal of Neurophysiology*, vol. 105, no. 4, pp. 1932–1949, 2011. doi: 10.1152/jn.00503.2010 (cited on page 29).
- [209] L. C. Parra, C. D. Spence, A. D. Gerson, and P. Sajda, 'Recipes for the linear analysis of EEG,' *NeuroImage*, vol. 28, no. 2, pp. 326–341, 2005. doi: 10.1016/j.neuroimage.2005.05.032 (cited on pages 29, 54).
- [210] R. J. Kobler, A. I. Sburlea, and G. R. Müller-Putz, 'A comparison of ocular artifact removal methods for block design based electroencephalography experiments,' in *Proceedings of the 7th Graz Brain-Computer Interface Conference*, 2017, pp. 236–241, ISBN: 978-3-85125-533-1. doi: 10.3217/978-3-85125-533-1-44 (cited on pages 33, 35, 52, 85).
- [211] R. J. Kobler, A. I. Sburlea, C. Lopes-Dias, A. Schwarz, M. Hirata, and G. R. Müller-Putz, 'Corneo-retinal-dipole and eyelid-related eye artifacts can be corrected offline and online in electroencephalographic and magnetoencephalographic signals,' *NeuroImage*, vol. 218, p. 117 000, 2020. doi: 10.1016/j.neuroimage.2020.117000 (cited on pages 35, 52, 53, 84).
- [212] R. J. Kobler, A. I. Sburlea, V. Mondini, and G. R. Müller-Putz, 'HEAR to remove pops and drifts: The high-variance electrode artifact removal (HEAR) algorithm,' in *Proceedings of the 41st Annual International Conference of the IEEE Engineering in Medicine and Biology Society (EMBC)*, Berlin, Germany: IEEE, 2019, pp. 5150–5155, ISBN: 978-1-5386-1311-5. doi: 10.1109/EMBC.2019.8857742 (cited on pages 37, 46, 54, 85).
- [213] C. Kothe and T.-P. Jung, 'Artifact removal techniques with signal reconstruction,' 2014 (cited on pages 37, 54).
- [214] E. J. Candes, X. Li, Y. Ma, and J. Wright, 'Robust Principal Component Analysis?' *Journal of the ACM*, vol. 58, no. 3, p. 11, 2011. doi: 10.1145/1970392.1970395 (cited on pages 37, 54).
- [215] R. J. Kobler, E. Kolesnichenko, A. I. Sburlea, and G. R. Müller-Putz, 'Distinct cortical networks for hand movement initiation and directional processing: An EEG study,' *NeuroImage*, vol. 220, p. 117 076, 2020. doi: 10.1016/j.neuroimage.2020.117076 (cited on pages 39, 52, 53, 56–58, 84).
- [216] R. J. Kobler, A. I. Sburlea, and G. R. Müller-Putz, 'Tuning characteristics of low-frequency EEG to positions and velocities in visuomotor and oculomotor tracking tasks,' *Scientific Reports*, vol. 8, no. 1, p. 17713, 2018. doi: 10.1038/s41598-018-36326-y (cited on pages 42, 46, 48, 49, 52–54, 56–58, 84).
- [217] R. J. Kobler, M. Hirata, H. Hashimoto, R. Dowaki, A. I. Sburlea, and G. R. Müller-Putz, 'Simultaneous decoding of velocity and speed during executed and observed tracking movements: An MEG study,' in *Proceedings of the 8th Graz Brain Computer Interface Conference 2019*, Graz, 2019. doi: 10.3217/978-3-85125-682-6-19 (cited on pages 44, 46, 52–54, 56, 57, 85).
- [218] R. J. Kobler, A. I. Sburlea, V. Mondini, M. Hirata, and G. R. Müller-Putz, 'Distance- and speed-informed kinematics decoding improves M/EEG based upper-limb movement decoder accuracy,' *Journal of Neural Engineering*, 2020. doi: 10.1088/1741-2552/abb3b3 (cited on pages 46, 48, 50, 54, 55, 57–59, 84).
- [219] R. J. Kobler, I. Almeida, A. I. Sburlea, and G. R. Müller-Putz, 'Using machine learning to reveal the population vector from EEG signals,' *Journal of Neural Engineering*, vol. 17, no. 2, p. 026 002, 2020. doi: 10.1088/1741-2552/ab7490 (cited on pages 46, 62).
- [220] S. de Jong, 'SIMPLS: An alternative approach to partial least squares regression,' *Chemometrics and Intelligent Laboratory Systems*, vol. 18, no. 3, pp. 251–263, 1993. doi: 10.1016/0169-7439(93)85002-X (cited on page 46).

- [221] V. Mondini, R. J. Kobler, A. I. Sburlea, and G. R. Müller-Putz, 'Continuous low-frequency EEG decoding of arm movement for closed-loop, natural control of a robotic arm,' *Journal of Neural Engineering*, 2020. doi: 10.1088/1741-2552/aba6f7 (cited on pages 48, 50, 52–54, 58, 59, 85).
- [222] V. Martínez-Cagigal, R. J. Kobler, V. Mondini, R. Hornero, and G. Müller-Putz, 'Non-linear online low-frequency EEG-based decoding of hand movements during a pursuit tracking task,' in *Proceedings of the 42st Annual International Conference of the IEEE Engineering in Medicine and Biology Society (EMBC)*, Montréal, Canada: IEEE, 2020. doi: 10.1109/EMBC44109.2020.9175723 (cited on pages 50, 52–56, 59, 85).
- [223] M. A. Klados, C. Papadelis, C. Braun, and P. D. Bamidis, 'REG-ICA: A hybrid methodology combining Blind Source Separation and regression techniques for the rejection of ocular artifacts,' *Biomedical Signal Processing and Control*, vol. 6, no. 3, pp. 291–300, 2011. doi: 10.1016/j.bspc.2011.02.001 (cited on page 52).
- [224] I. Winkler, S. Brandl, F. Horn, E. Waldburger, C. Allefeld, and M. Tangermann, 'Robust artifactual independent component classification for BCI practitioners,' *Journal of Neural Engineering*, vol. 11, no. 3, p. 035013, 2014. doi: 10.1088/1741-2560/11/3/035013 (cited on page 52).
- [225] A. Schwarz, J. Pereira, R. Kobler, and G. R. Müller-Putz, 'Unimanual and Bimanual Reach-and-Grasp Actions Can Be Decoded From Human EEG,' *IEEE Transactions on Biomedical Engineering*, pp. 1–1, 2019. doi: 10.1109/TBME.2019.2942974 (cited on page 53).
- [226] C. Lopes-Dias, A. I. Sburlea, and G. R. Müller-Putz, 'Online asynchronous decoding of error-related potentials during the continuous control of a robot,' *Scientific Reports*, vol. 9, no. 1, p. 17596, 2019. doi: 10.1038/s41598-019-54109-x (cited on page 53).
- [227] C. Y. Chang, S. H. Hsu, L. Pion-Tonachini, and T. P. Jung, 'Evaluation of Artifact Subspace Reconstruction for Automatic Artifact Components Removal in Multi-channel EEG Recordings,' *IEEE Transactions on Biomedical Engineering*, pp. 1242–1245, 2019. doi: 10.1109/TBME.2019.2930186 (cited on page 54).
- [228] H. Tanaka, M. Miyakoshi, and S. Makeig, 'Dynamics of directional tuning and reference frames in humans: A high-density EEG study,' *Scientific Reports*, vol. 8, no. 1, p. 2016, 2018. doi: 10.1038/s41598-018-26609-9 (cited on page 54).
- [229] Y. Inoue, H. Mao, S. B. Suway, J. Orellana, and A. B. Schwartz, 'Decoding arm speed during reaching,' *Nature Communications*, vol. 9, no. 1, p. 5243, 2018. doi: 10.1038/s41467-018-07647-3 (cited on pages 54, 57).
- [230] H. G. Yeom, W. Hong, D.-Y. Kang, C. K. Chung, J. S. Kim, and S.-P. Kim, 'A Study on Decoding Models for the Reconstruction of Hand Trajectories from the Human Magnetoencephalography,' *BioMed Research International*, vol. 2014, pp. 1–8, 2014. doi: 10.1155/2014/176857 (cited on pages 54, 55).
- [231] S. Nakagome, T. P. Luu, Y. He, A. S. Ravindran, and J. L. Contreras-Vidal, 'An empirical comparison of neural networks and machine learning algorithms for EEG gait decoding,' *Scientific Reports*, vol. 10, no. 1, p. 4372, 2020. doi: 10.1038/s41598-020-60932-4 (cited on page 54).
- [232] A. Eliseyev and T. Aksenova, 'Penalized Multi-Way Partial Least Squares for Smooth Trajectory Decoding from Electrocorticographic (ECoG) Recording,' *PLOS ONE*, vol. 11, no. 5, D. Zhang, Ed., 2016. doi: 10.1371/journal.pone.0154878 (cited on page 55).
- [233] S. D. Stavisky, J. C. Kao, P. Nuyujukian, S. I. Ryu, and K. V. Shenoy, 'A high performing brain-machine interface driven by low-frequency local field potentials alone and together with spikes,' *Journal of Neural Engineering*, vol. 12, no. 3, p. 036009, 2015. doi: 10.1088/1741-2560/12/3/036009 (cited on pages 55–57).

- [234] Y. Nakanishi, T. Yanagisawa, D. Shin, H. Kambara, N. Yoshimura, M. Tanaka, R. Fukuma, H. Kishima, M. Hirata, and Y. Koike, 'Mapping ECoG channel contributions to trajectory and muscle activity prediction in human sensorimotor cortex,' *Scientific Reports*, vol. 7, no. March, p. 45486, 2017. doi: 10.1038/srep45486 (cited on page 55).
- [235] J. G. Makin, J. E. O'Doherty, M. M. Cardoso, and P. N. Sabes, 'Superior arm-movement decoding from cortex with a new, unsupervised-learning algorithm,' *Journal of Neural Engineering*, vol. 15, no. 2, 2018. doi: 10.1088/1741-2552/aa9e95 (cited on page 55).
- [236] D. Sussillo, S. D. Stavisky, J. C. Kao, S. I. Ryu, and K. V. Shenoy, 'Making brain-machine interfaces robust to future neural variability,' *Nature Communications*, vol. 7, no. 1, p. 13749, 2016. doi: 10.1038/ncomms13749 (cited on page 56).
- [237] K. V. Shenoy and J. M. Carmena, 'Combining decoder design and neural adaptation in brain-machine interfaces,' *Neuron*, vol. 84, no. 4, pp. 665–680, 2014. doi: 10.1016/j.neuron.2014.08.038 (cited on pages 56, 59, 61).
- [238] V. Gilja, P. Nuyujukian, C. A. Chestek, J. P. Cunningham, B. M. Yu, J. M. Fan, M. M. Churchland, M. T. Kaufman, J. C. Kao, S. I. Ryu, and K. V. Shenoy, 'A high-performance neural prosthesis enabled by control algorithm design,' *Nature Neuroscience*, vol. 15, no. 12, pp. 1752–7, 2012. doi: 10.1038/nn.3265 (cited on pages 56, 61).
- [239] F. R. Willett, B. A. Murphy, D. Young, W. D. Memberg, C. H. Blabe, C. Pandarinath, B. Franco, J. Saab, B. L. Walter, J. A. Sweet, J. P. Miller, J. M. Henderson, K. V. Shenoy, J. D. Simeral, B. Jarosiewicz, L. R. Hochberg, R. F. Kirsch, and A. B. Ajiboye, 'A Comparison of Intention Estimation Methods for Decoder Calibration in Intracortical Brain-Computer Interfaces,' *IEEE Transactions on Biomedical Engineering*, vol. 65, no. 9, pp. 2066–2078, 2018. doi: 10.1109/TBME.2017.2783358 (cited on pages 56, 61).
- [240] C. E. Vargas-Irwin, J. M. Feldman, B. King, J. D. Simeral, B. L. Sorice, E. M. Oakley, S. S. Cash, E. N. Eskandar, G. M. Friehs, L. R. Hochberg, and J. P. Donoghue, 'Watch, Imagine, Attempt: Motor Cortex Single-Unit Activity Reveals Context-Dependent Movement Encoding in Humans With Tetraplegia,' *Frontiers in Human Neuroscience*, vol. 12, p. 450, 2018. doi: 10.3389/fnhum.2018.00450 (cited on pages 56, 57, 62).
- [241] A. Rastogi, C. E. Vargas-Irwin, F. R. Willett, J. Abreu, D. C. Crowder, B. A. Murphy, W. D. Memberg, J. P. Miller, J. A. Sweet, B. L. Walter, S. S. Cash, P. G. Rezaii, B. Franco, J. Saab, S. D. Stavisky, K. V. Shenoy, J. M. Henderson, L. R. Hochberg, R. F. Kirsch, and A. B. Ajiboye, 'Neural Representation of Observed, Imagined, and Attempted Grasping Force in Motor Cortex of Individuals with Chronic Tetraplegia,' *Scientific Reports*, vol. 10, no. 1, p. 1429, 2020. doi: 10.1038/s41598-020-58097-1 (cited on pages 56, 62).
- [242] B. J. Edelman, J. Meng, D. Suma, C. Zurn, E. Nagarajan, B. S. Baxter, C. C. Cline, and B. He, 'Noninvasive neuroimaging enhances continuous neural tracking for robotic device control,' *Science Robotics*, vol. 4, no. 31, 2019. doi: 10.1126/scirobotics.aaw6844 (cited on pages 56, 62).
- [243] A. Kübler, B. Kotchoubey, T. Hinterberger, N. Ghanayim, J. Perelmouter, M. Schauer, C. Fritsch, E. Taub, and N. Birbaumer, 'The thought translation device: A neurophysiological approach to communication in total motor paralysis,' *Experimental Brain Research*, vol. 124, no. 2, pp. 223–232, 1999. doi: 10.1007/s002210050617 (cited on pages 56, 61).
- [244] J. P. Gallivan, K. S. Barton, C. S. Chapman, D. M. Wolpert, and J. Randall Flanagan, 'Action plan co-optimization reveals the parallel encoding of competing reach movements.,' *Nature Communications*, vol. 6, no. May, p. 7428, 2015. doi: 10.1038/ncomms8428 (cited on page 56).
- [245] M. P. Branco, L. M. de Boer, N. F. Ramsey, and M. J. Vansteensel, 'Encoding of kinetic and kinematic movement parameters in the sensorimotor cortex: A Brain-Computer Interface perspective,' *European Journal of Neuroscience*, no. November 2018, pp. 1–18, 2019. doi: 10.1111/ejn.14342 (cited on pages 56, 60).

- [246] B. Amirikian and A. P. Georgopoulos, 'Directional tuning profiles of motor cortical cells,' *Neuroscience Research*, vol. 36, no. 1, pp. 73–79, 2000. doi: 10.1016/S0168-0102(99)00112-1 (cited on page 57).
- [247] S. Pitzalis, P. Fattori, and C. Galletti, 'The human cortical areas V6 and V6A,' *Visual Neuroscience*, vol. 32, E007, 2015. doi: 10.1017/S0952523815000048 (cited on page 57).
- [248] C. Cavina-Pratesi, J. D. Connolly, S. Monaco, T. D. Figley, A. D. Milner, T. Schenk, and J. C. Culham, 'Human neuroimaging reveals the subcomponents of grasping, reaching and pointing actions,' *Cortex*, vol. 98, pp. 128–148, 2018. doi: 10.1016/j.cortex.2017.05.018 (cited on page 57).
- [249] S. Fabbri, A. Caramazza, and A. Lingnau, 'Tuning Curves for Movement Direction in the Human Visuomotor System,' *Journal of Neuroscience*, vol. 30, no. 40, pp. 13 488–13 498, 2010. doi: 10.1523/JNEUROSCI.2571-10.2010 (cited on page 57).
- [250] C. Magri, S. Fabbri, A. Caramazza, and A. Lingnau, 'Directional tuning for eye and arm movements in overlapping regions in human posterior parietal cortex,' *NeuroImage*, vol. 191, pp. 234–242, 2019. doi: 10.1016/j.neuroimage.2019.02.029 (cited on pages 57, 58).
- [251] A. Tosoni, S. Pitzalis, G. Committeri, P. Fattori, C. Galletti, and G. Galati, 'Resting-state connectivity and functional specialization in human medial parieto-occipital cortex,' *Brain Structure and Function*, vol. 220, no. 6, pp. 3307–3321, 2014. doi: 10.1007/s00429-014-0858-x (cited on page 57).
- [252] M. Vesia and J. D. Crawford, 'Specialization of reach function in human posterior parietal cortex,' *Experimental Brain Research*, vol. 221, no. 1, pp. 1–18, 2012. doi: 10.1007/s00221-012-3158-9 (cited on page 58).
- [253] M. A. Carland, D. Thura, and P. Cisek, 'The Urge to Decide and Act: Implications for Brain Function and Dysfunction,' *The Neuroscientist*, vol. 25, no. 5, pp. 491–511, 2019. doi: 10.1177/1073858419841553 (cited on page 59).
- [254] K. Ganguly and J. M. Carmena, 'Emergence of a Stable Cortical Map for Neuroprosthetic Control,' *PLoS Biology*, vol. 7, no. 7, J. Ashe, Ed., e1000153, 2009. doi: 10.1371/journal.pbio.1000153 (cited on page 59).
- [255] A. L. Orsborn, H. G. Moorman, S. A. Overduin, M. M. Shanechi, D. F. Dimitrov, and J. M. Carmena, 'Closed-Loop Decoder Adaptation Shapes Neural Plasticity for Skillful Neuroprosthetic Control,' *Neuron*, vol. 82, no. 6, pp. 1380–1393, 2014. doi: 10.1016/j.neuron.2014.04.048 (cited on page 59).
- [256] P. Zanini, M. Congedo, C. Jutten, S. Said, and Y. Berthoumieu, 'Transfer Learning: A Riemannian Geometry Framework With Applications to Brain-Computer Interfaces,' *IEEE Transactions on Biomedical Engineering*, vol. 65, no. 5, pp. 1107–1116, 2018. doi: 10.1109/TBME.2017.2742541 (cited on page 60).
- [257] R. J. Kobler and R. Scherer, 'Restricted Boltzmann Machines in Sensory Motor Rhythm Brain-Computer Interfacing: A study on inter-subject transfer and co-adaptation,' in *2016 IEEE International Conference on Systems, Man, and Cybernetics, SMC 2016 - Conference Proceedings*, 2016, pp. 469–474, ISBN: 978-1-5090-1897-0. doi: 10.1109/SMC.2016.7844284 (cited on page 60).
- [258] A. Korik, R. Sosnik, N. Siddique, and D. Coyle, 'Decoding Imagined 3D Hand Movement Trajectories From EEG: Evidence to Support the Use of Mu, Beta, and Low Gamma Oscillations,' *Frontiers in Neuroscience*, vol. 12, no. March, pp. 1–16, 2018. doi: 10.3389/fnins.2018.00130 (cited on page 60).
- [259] M. Seeber, R. Scherer, J. Wagner, T. Solis-Escalante, and G. R. Müller-Putz, 'High and low gamma EEG oscillations in central sensorimotor areas are conversely modulated during the human gait cycle,' *NeuroImage*, vol. 112, pp. 318–326, 2015. doi: 10.1016/j.neuroimage.2015.03.045 (cited on page 62).

- [260] G. Pfurtscheller, B. Allison, G. Bauernfeind, C. Brunner, T. Solis Escalante, R. Scherer, T. Zander, G. Müller-Putz, C. Neuper, and N. Birbaumer, 'The hybrid BCI,' *Frontiers in Neuroscience*, vol. 4, p. 3, 2010. doi: 10.3389/fnpro.2010.00003 (cited on page 62).
- [261] G. R. Müller-Putz, R. Leeb, M. Tangermann, A. Kübler, F. Cinotti, D. Mattia, R. Rupp, K.-R. Müller, and J. D. R. Millán, 'Towards Noninvasive Hybrid Brain – Computer Interfaces : Framework , Practice , Clinical Application , and Beyond,' *Proceedings of the IEEE*, vol. 103, no. 6, pp. 926–943, 2015. doi: 10.1109/JPROC.2015.2411333 (cited on page 62).

APPENDIX

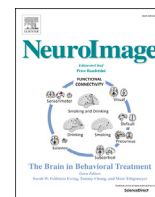
A.1 Primary Publications

reference	author	work (%)	contributions
[211]	Kobler R.J.	75	idea, analysis, interpretation, writing
	Sburlea A.I.	5	interpretation, editing
	Lopes-Dias C.	5	analysis, editing
	Schwarz A.	5	analysis, editing
	Hirata M.	5	supervision, editing
	Müller-Putz G.R.	5	supervision, interpretation, editing
[215]	Kobler R.J.	50	idea, study design, recording, analysis, interpretation, writing
	Kolesnichenko E.	40	analysis, interpretation, writing
	Sburlea A.I.	5	study design, interpretation, editing
	Müller-Putz G.R.	5	supervision, study design, interpretation, editing
[216]	Kobler R.J.	90	idea, study design, recording, analysis, interpretation, writing
	Sburlea A.I.	5	study design, interpretation, editing
	Müller-Putz G.R.	5	supervision, study design, interpretation, editing
[218]	Kobler R.J.	80	idea, analysis, interpretation, writing
	Sburlea A.I.	5	interpretation, editing
	Mondini V.	5	interpretation, editing
	Hirata M.	5	supervision, interpretation, editing
	Müller-Putz G.R.	5	supervision, interpretation, editing

A.2 Secondary Publications

reference	author	work (%)	contributions
[210]	Kobler R.J.	90	idea, study design, recording, analysis, interpretation, writing
	Sburlea A.I.	5	study design, interpretation, editing
	Müller-Putz G.R.	5	supervision, study design, interpretation, editing
[212]	Kobler R.J.	85	idea, study design, recording, analysis, interpretation, writing
	Sburlea A.I.	5	interpretation, editing
	Mondini V.	5	analysis, interpretation, editing
	Müller-Putz G.R.	5	supervision, interpretation, editing
[217]	Kobler R.J.	75	idea, study design, recording, analysis, interpretation, writing
	Hirata M.	5	supervision, study design, interpretation, editing
	Hashimoto H.	5	study design, recording, editing
	Dowaki R.	5	study design, recording
	Sburlea A.I.	5	interpretation, editing
	Müller-Putz G.R.	5	supervision, interpretation, editing
[221]	Mondini V.	50	study design, recording, analysis, interpretation, writing
	Kobler R.J.	40	study design, recording, analysis, interpretation, editing
	Sburlea A.I.	5	study design, interpretation, editing
	Müller-Putz G.R.	5	idea, supervision, study design, interpretation, editing
[222]	Martinez-Cagigal V.	30	study design, recording, analysis, interpretation, writing
	Kobler R.J.	30	idea, study design, recording, analysis, interpretation, writing
	Mondini V.	30	study design, recording, analysis, interpretation, editing
	Hornero R.	1	supervision
	Müller-Putz G.R.	9	idea, supervision, interpretation, editing

Primary Publications | **B**



Corneo-retinal-dipole and eyelid-related eye artifacts can be corrected offline and online in electroencephalographic and magnetoencephalographic signals



Reinmar J. Kobler^a, Andreea I. Sburlea^a, Catarina Lopes-Dias^a, Andreas Schwarz^a, Masayuki Hirata^{b,c}, Gernot R. Müller-Putz^{a,*}

^a Institute of Neural Engineering, Graz University of Technology, Graz, 8010, Styria, Austria

^b Department of Neurological Diagnosis and Restoration, Osaka University Graduate School of Medicine, Suita, Osaka, Japan

^c Department of Neurosurgery, Osaka University Graduate School of Medicine, Suita, Osaka, Japan

ARTICLE INFO

Keywords:

Electroencephalography
Magnetoencephalography
Eye artifact
Electrooculography
Event-related potential
Brain-computer interface

ABSTRACT

Eye movements and blinks contaminate electroencephalographic (EEG) and magnetoencephalographic (MEG) activity. As the eye moves, the corneo-retinal dipole (CRD) and eyelid introduce potential/field changes in the M/EEG activity. These eye artifacts can affect a brain-computer interface and thereby impinge on neurofeedback quality. Here, we introduce the sparse generalized eye artifact subspace subtraction (SGEYESUB) algorithm that can correct these eye artifacts offline and in real time. We provide an open source reference implementation of the algorithm and the paradigm to obtain calibration data. Once the algorithm is fitted to calibration data (approx. 5 min), the eye artifact correction reduces to a matrix multiplication. We compared SGEYESUB with 4 state-of-the-art algorithms using M/EEG activity of 69 participants. SGEYESUB achieved the best trade-off between correcting the eye artifacts and preserving brain activity. Residual correlations between the corrected M/EEG channels and the eye artifacts were below 0.1. Error-related and movement-related cortical potentials were attenuated by less than 0.5 μV . Our results furthermore demonstrate that CRD and eyelid-related artifacts can be assumed to be stationary for at least 1–1.5 h, validating the feasibility of our approach in offline and online eye artifact correction.

1. Introduction

Human eye movements and blinking activity carry rich information about mental processes (Hoffman and Subramaniam, 1995; Kahneman and Beatty, 1966; Wilson, 2002). Yet eye movements and blinks contaminate electroencephalographic (EEG) and magnetoencephalographic (MEG) activity in the form of electrooculographic (EOG) and magnetooculographic (MOG) artifacts (Gratton et al., 1983; Katila et al., 1981). Given the relative strength of EOG and MOG artifacts - commonly referred to as eye artifacts - compared to EEG and MEG activity, they can severely confound experimental findings, clinical diagnosis, or neurofeedback in the case of brain-computer interfaces (BCIs).

There are three major physiological sources generating eye artifacts (Keren et al., 2010; Picton et al., 2000). They comprise the corneo-retinal dipole (CRD), the eyelid and extraocular muscles (Gawne et al., 2017; Keren et al., 2010). The CRD models the positive charge of the cornea

with respect to the retina (Mowrer et al., 1935). As the eyeball rotates, the dipole orientation changes, which in turn results in a potential/field change at the M/EEG sensors. The CRD-related artifact's amplitude declines approximately with the square of the distance to the CRD (Croft and Barry, 2000a). Eyelid movements occur during blinks and vertical gaze shifts. As the eyelid slides across the positively charged cornea, a high amplitude potential/field is introduced (Iwasaki et al., 2005). Contraction of the extraocular muscles at a saccade onset results in the saccadic spike potential (Riemslog et al., 1988): a transient potential in the 20–90 Hz range (Keren et al., 2010).

At frequencies below 20 Hz, CRD and eyelid induced artifacts dominate (Keren et al., 2010). Their exact effect on the potential/field at each sensor depends on various factors such as the sensor location with respect to the head, the head geometry, conductances of the various tissue layers and the scalp-electrode interface. As these factors inherently vary across participants and sessions, the eye artifact related potential/field at each

* Corresponding author.

E-mail address: gernot.mueller@tugraz.at (G.R. Müller-Putz).

<https://doi.org/10.1016/j.neuroimage.2020.117000>

Received 17 January 2020; Received in revised form 18 May 2020; Accepted 26 May 2020

Available online 1 June 2020

1053-8119/© 2020 Graz University of Technology. Published by Elsevier Inc. This is an open access article under the CC BY-NC-ND license (<http://creativecommons.org/licenses/by-nc-nd/4.0/>).

<http://creativecommons.org/licenses/by-nc-nd/4.0/>

sensor needs to be re-estimated for each experiment. Within a large visual workspace (visual angle $\leq 20^\circ$) it can be assumed that the artifact contributions are linear (Plöchl et al., 2012). Offline, the eye artifacts are commonly modeled to be linear and time-invariant within a recording session (Croft and Barry, 2000a; Urigüen and Garcia-Zapirain, 2015). Eye artifact correction approaches are typically based on independent component analysis (ICA) (Jung et al., 2000; Mannan et al., 2016; Pion-Tonachini et al., 2019; Plöchl et al., 2012; Winkler et al., 2014) or linear regression (Croft and Barry, 2000b; Gratton et al., 1983). Regression approaches typically use pre-defined (bipolar) spatial filters to estimate the eye artifact activity from EOG channels. This poses a limitation, since residual brain activity within the estimated eye artifact activity is removed. Berg and Scherg introduced a subspace subtraction approach to address this limitation (Berg and Scherg, 1994). The correction uses calibration data to first estimate the eye artifact source from EEG and EOG channels and then regress their contribution from the EEG channels (Lins et al., 1993a).

In neurofeedback and brain-computer interface (BCI) studies, the eye artifacts have to be corrected in real-time. Assuming a stationary eye artifact model, Schlögl et al. proposed to record a short period of eye movements and blinks at the beginning of an experiment (calibration data), then fit parameters of a correction model to the calibration data, and use the fitted model to correct EEG signals online (Schlögl et al., 2007). Given that an experimenter aims to maximize the time of BCI or neurofeedback operation, the time to record calibration data is typically limited. We recently presented a 5-min paradigm to record eye artifact calibration data in a controlled fashion and showed that CRD and eyelid-related artifacts could be attenuated to the noise level up to 1 h after calibration (Kobler et al., 2017).

Here, we present a new CRD and eyelid-related artifact correction algorithm based on artifact subspace subtraction (Berg and Scherg, 1994; Parra et al., 2005). We compare its performance in terms of attenuating eye artifacts and preserving brain activity to four representative correction algorithms, using five datasets with 78 recording sessions in total. For all datasets, we recorded at least two blocks containing 5 min of resting and eye artifact activity. The two blocks were separated by up to

100 min, allowing us to additionally investigate whether a time-invariant model is sufficient to describe the eye artifacts in the M/EEG channels.

2. Materials and methods

We performed an offline analysis using 5 datasets which contain 78 recordings of 69 participants. Eye artifacts were recorded during 2–4 dedicated experimental blocks according to the paradigm presented in Fig. 1a. The trial based paradigm distinguished 4 conditions, namely, REST, HORZ, VERT and BLINK. Depending on the condition, the participants were instructed to keep their eyes open and focus their gaze (REST) on a stimulus located in the center of the screen, track the moving stimulus along a horizontal/vertical axis (HORZ/VERT), or slide their eyelid down and up once as if they would blink involuntarily whenever the stimulus' size reduces (BLINK). Fig. 1b displays the stimulus' trajectories and the behavior of a representative participant, inferred from EOG activity, during the 4 conditions. The stimulus moved with a frequency of 0.5 Hz during HORZ/VERT trials and reduced its size 8 times during BLINK trials.

If not stated otherwise, each experimental block (eye block) consisted of 27 trials (9 REST and 6 HORZ/VERT/BLINK), and lasted for approx. 5 min. We provide a reference implementation (Kobler et al., 2019) using Matlab (Matlab, 2015b; Mathworks, USA), Psychtoolbox (Brainard, 1997; Pelli, 1997) and labstreaminglayer (Kothe et al., 2019).

The 5 datasets analyzed here were recorded at Graz University of Technology (EEG datasets) and Osaka University (MEG dataset) to study different aspects of neural correlates of M/EEG activity in behaving healthy humans. In all datasets, the experimental procedure conformed to the declaration of Helsinki and was approved by local ethics committees. After the participants were informed about the purpose and the procedure of each study, they gave their written consent.

2.1. EEG dataset 1 (EEGDS1)

The dataset comprised 15 participants and was recorded to investigate the expression of directional information in low-frequency EEG

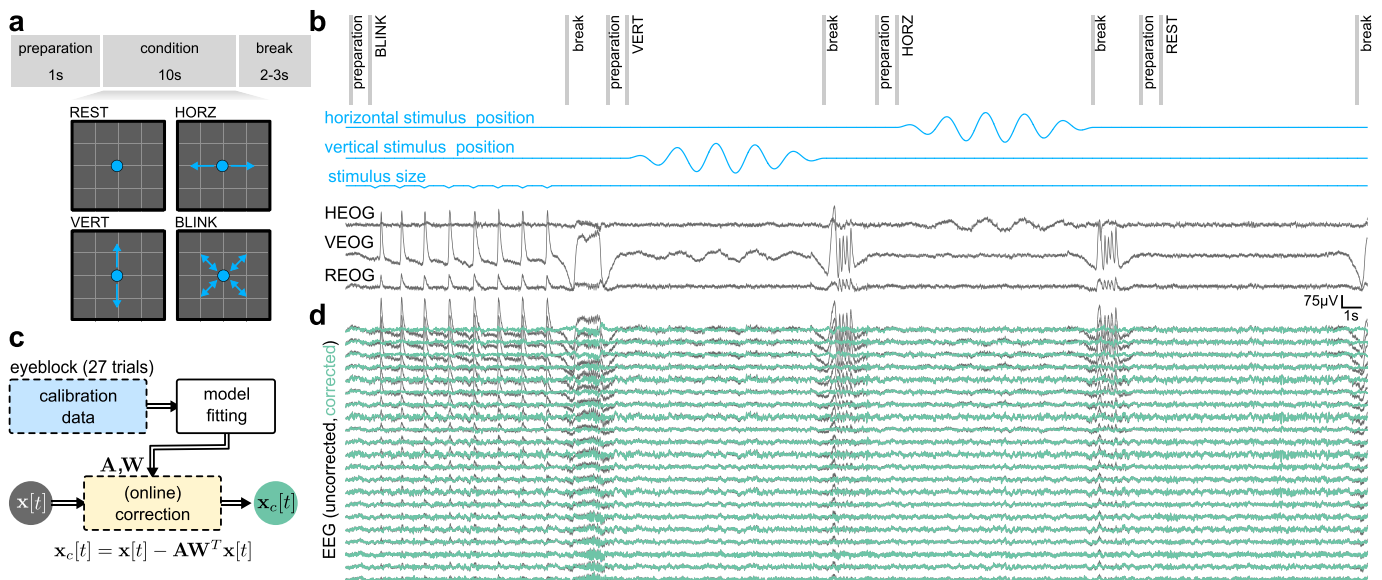


Fig. 1. Experimental approach to correct eye artifacts in M/EEG signals. **a**, Experimental paradigm. Each trial started with a 1-s preparation period, followed by a 10-s task depending on the condition and a short break. The position and size of a stimulus coded the four experimental conditions. Blue arrows indicate movement, or a decrease in size during BLINK trials. **b**, Blue traces indicate the stimulus position and size during four consecutive trials. The behavior, inferred from EOG activity (horizontal, vertical, radial), of a typical participant is displayed below. **c**, One eye block (27 trials) was used to fit eye artifact correction model parameters (A, W). New samples of EOG and M/EEG activity ($x[t]$) were corrected by subtracting the eye artifact subspace. **d**, Uncorrected (black) and corrected (green) EEG activity for a representative participant.

activity during continuous tracking movements (Kobler et al., 2018) and movement-related cortical potentials (MRCs) during center-out movements (Kobler et al., in revision). We extended the dataset by including 5 pilot measurements, which we presented in (Kobler et al., 2017). EEG activity was recorded at 64 (58 in the pilot) electrodes placed according to the 10-10 system, with the reference at the right mastoid and ground at AFz. EOG activity was recorded at 6 electrodes placed next to the outer canthi, infra orbital and superior orbital. EEG and EOG activity was captured synchronously using active electrodes (actiCAP, Brain Products GmbH, Germany) and a biosignal amplifier system (BrainAmp, Brain Products GmbH, Germany). We recorded 2 eye artifact blocks - one at the beginning of the experiment and one at the end. They were separated by 134 min, on average.

2.2. EEG dataset 2 (EEGDS2)

We recorded this dataset to study the online control of a robotic arm using a low-frequency EEG-based kinematics decoder (Mondini et al., in review). The dataset comprised 10 participants. We used the same EEG and EOG setup and equipment as in EEGDS1, and recorded 2 eye artifact blocks - one at the beginning of the experiment and another one approximately 34 min later.

2.3. EEG dataset 3 (EEGDS3)

This dataset was recorded to study the online detection of error-related potentials (ErrPs) during robotic arm control (Lopes-Dias et al., 2019). It comprises 15 participants. The EEG and EOG recording equipment was the same as in EEGDS1. The electrode layout differed slightly; EEG and EOG signals were recorded with 61 and 3 electrodes respectively. The 3 EOG electrodes were placed below the outer canthi and above the nasion. We recorded 2 eye artifact blocks at the beginning of the experiment. They were separated by 9 min on average.

2.4. EEG dataset 4 (EEGDS4)

In this dataset, we explored EEG correlates of unimanual and bimanual reach and grasp actions (Schwarz et al., 2019). It contains recordings of 15 participants. EEG activity was recorded with 58 electrodes covering frontal, central, parietal and temporal areas according to the layout described in (Oostenveld and Praamstra, 2001). The reference electrode was placed on the right earlobe, ground on position AFF2h. EOG activity was recorded with 6 active electrodes positioned next to the outer canthi, infra orbital and superior orbital to the left and right eye. EEG and EOG signals were recorded simultaneously using active electrodes (g.GAMMAsys/g.LADYbird, g.tec GmbH, Austria) and four biosignal amplifiers (g.USBamp, g.tec GmbH, Austria). We recorded 3 eye artifact blocks - one at the beginning of the experiment, one in the middle and one at the end. Each block had 27 trials (18 REST, 3 HORZ, 3 VERT, 3 BLINK). They were separated by 60 min on average. In this dataset, BLINK trials were indicated with the text 'BLINK' appearing on the screen. The text stayed visible during the trial. We instructed the participants to blink with a rate of 1–2 Hz. We excluded the data of one participant due to large cross-talk between the vertical and horizontal EOG derivatives, limiting the detection of upward/downward/leftward/rightward eye movements.

2.5. MEG dataset (MEGDS)

This dataset was recorded to study the joint decoding of upper-limb movement speed and velocity from low-frequency MEG activity (Kobler et al., 2019). It contains data of 19 participants. MEG activity was recorded with 160 gradiometers. As in (Kobler et al., 2019), we used 129 channels for the analysis. EOG activity was recorded using 4 electrodes placed next to the outer canthi of both eyes and inferior and superior orbital to the left eye. The MEG and EOG signals were recorded

synchronously with an MEG system (MEGvision NEO, RICOH Ltd., Japan) and a biosignal amplifier (Neurofax EEG 1200, Nihon Koden Corp., Japan). We recorded 4 eye artifact blocks - two at the beginning of the experiment and two at the end. They were separated by 100 min on average.

2.6. EEG pre-processing

The EEG datasets shared a common pre-processing pipeline implemented with Matlab 2015b (MathWorks Inc., USA) and EEGLAB (version 14.1.1) (Delorme and Makeig, 2004). First, the EEG and EOG signals were resampled at 200 Hz, then a notch filter (Butterworth filter, 2nd order, 49 and 51 Hz cut-off frequencies) and a high-pass filter (Butterworth filter, 2nd order, 0.4 Hz cut-off frequency) were applied bidirectionally to attenuate line noise and drifts. We visually inspected the data for bad channels, which were spherically interpolated using spherical spline interpolation in EEGLAB (Delorme and Makeig, 2004). Next, we used the EOG channels to compute vertical, horizontal and radial EOG derivatives. The horizontal EOG (HEOG) derivative was the difference between the signals of the electrodes placed next to the outer canthi of both eyes; the vertical EOG (VEOG) derivative was the difference between the superior and inferior orbital electrodes; the radial EOG derivative was the average of all EOG electrodes. For EEGDS3 only three EOG electrodes were available. As in (Schlögl et al., 2007), we set the VEOG derivative to the mean of the differences between the electrode above the nasion and the ones below the outer canthi. The EOG derivative signals were subsequently low-pass filtered (Butterworth filter, 2nd order, 5Hz cut-off frequency, filter applied bidirectionally). We then extracted 8s long epochs, starting 1s after the condition cue. Finally, we visually inspected the epoched data and rejected epochs contaminated by muscular artifacts or electrode pops and drifts. On average, 14% (1% standard-error of the mean, SEM) epochs were rejected.

2.7. MEG pre-processing

As in (Kobler et al., 2019), we applied two additional pre-processing steps to attenuate effects of small head movements and technical artifacts in the MEG dataset. First, we spherically interpolated the MEG sensors to their average position with respect to the participants' head, using Brainstorm toolbox (version 05-Jun-2018) (Tadel et al., 2011). Second, we applied ICA to identify and reject technical and spatially stationary artifacts introduced by the experimental equipment and other appliances in the hospital. In detail, we applied the extended Infomax algorithm to decompose the MEG signals into independent components (ICs) that explained 99.9% of the variance. We visually inspected and marked on average 8.6 (0.2 SEM) out of 63.5 (0.1 SEM) ICs for rejection.

2.8. Eye-movement and blink detection

We used the low-pass filtered EOG derivative signals to extract periods of eye-movements and blinks from the epoched data. In BLINK epochs, a blink was detected if the vertical EOG derivative exceeded a threshold of 75 μ V for at least 25 ms. In VERT epochs, upwards/downwards eye movements were detected, if the vertical EOG derivative exceeded ± 10 μ V for at least 200 ms. In HORZ epochs, rightwards/leftwards eye movements were detected, if the horizontal EOG derivative exceeded ± 10 μ V for at least 200 ms. If we detected a blink in REST, HORZ, VERT epochs, the affected samples were considered as outliers. In detail, a sample was considered as an outlier, if the V/HEOG derivative exceeded 100 μ V (150 μ V for the VEOG derivative in VERT epochs) for at least 200 ms.

For each block, we concatenated the periods during which we detected rest/blink/right/left/up/down activity. Each sample within these periods was assigned the corresponding label, resulting in an $n_{channels} \times n_{samples}$ matrix X and an $n_{channels} \times 1$ vector y containing the labels.

2.9. Proposed algorithm

Similar to (Kobler et al., 2017; Parra et al., 2005), the proposed algorithm removes the subspaces that explain the variance introduced by CRD and eyelid movements from the M/EEG activity. This is done in a two step procedure. First, the subspace activity $s[t]$ at each time-point t , represented as an $n_{subspaces} \times 1$ vector, is estimated from the M/EEG and EOG activity, represented as an $n_{channels} \times 1$ vector $x[t]$

$$s[t] = W^T x[t] \quad (1)$$

using an $n_{channels} \times n_{subspaces}$ unmixing matrix W . Second, the corrected activity $x_c[t]$ is obtained by subtracting the contribution of the subspaces

$$x_c[t] = x[t] - As[t] \quad (2)$$

using an $n_{channels} \times n_{subspaces}$ mixing matrix A . The mixing matrix A corresponds to the patterns associated with the unmixing matrix W (Haufe et al., 2014). The least squares solution for A is

$$A = \Sigma_x W \Sigma_s^{-1} \quad (3)$$

with covariance matrices Σ_x and Σ_s . The subspace signal covariance matrix Σ_s can be computed using the channel covariance matrix Σ_x and the unmixing matrix W :

$$\Sigma_s = W^T \Sigma_x W \quad (4)$$

We computed Σ_x using the samples and analytical shrinkage regularization (Schäfer and Strimmer, 2005). Fig. 1c summarizes the correction approach.

The central difference to previous artifact subspace subtraction methods (Kobler et al., 2017; Parra et al., 2005) lies in the computation of the unmixing matrix W . Since each subspace, defined by an $n_{channels} \times 1$ unmixing vector w , is associated with one artifact dimension (horizontal eye movements, vertical eye movements or blinks), we split the matrix estimation problem into $n_{subspaces} = 3$ vector estimation problems. For example, in the case of horizontal eye movements we used the samples labeled as left and right to find the subspace that best separates them. We modeled this classification problem as a logistic regression optimization problem with weighted elastic net regularization. The optimization problem is defined as

$$w^*, b^* = \arg \min_{w,b} \sum_t \log \left(1 + e^{-y[t](w^T x[t] + b)} \right) + \frac{\alpha}{2} \|w\|_{\Sigma_x^{(rest)}}^2 + \beta \|w\|_1 \quad (5)$$

with labels $y[t] \in \{-1, 1\}$ (representing left and right, for example), regularization parameters α and β , and channel covariance matrix during resting periods $\Sigma_x^{(rest)}$. The L1 norm in (5) drives w to be sparse. The term $\|w\|_{\Sigma_x^{(rest)}}^2$ denotes the weighted L2 norm of w defined as

$$\|w\|_{\Sigma_x^{(rest)}}^2 = w^T \Sigma_x^{(rest)} w \quad (6)$$

Minimizing (6) ensures minimal subspace activity during resting periods, which is equivalent to maximizing the preservation of brain activity during eye artifact free periods. Our motivation for the sparsity constraint was mainly to improve the generalization to new data with potentially different configurations of active brain sources. The sparsity constraint forces the solution to have most of the weights equal to zero at occipital, parietal and central channels and to have few nonzero weights at prefrontal and anterior temporal channels because they are closest to the artifact sources. Hence, activity of sources in occipital, parietal and central areas that might not have been active in the calibration data would contribute negligibly to the artifact subspaces, and, thereby, would not be removed.

We solved the optimization problem in (5) with a Nesterov accelerated proximal gradient descent algorithm (Beck and Teboulle, 2009). The

proposed artifact correction algorithm first removes the two subspaces ($A_{eye} W_{eye}^T$) related to horizontal and vertical eye movements, and then removes from the residual signals the subspace associated with eye blinks ($a_{blink} w_{blink}^T$). In detail, (5) is used to compute the unmixing vectors for horizontal w_{horz} and vertical w_{vert} eye movements. Then they are combined to form W_{eye} . Using (3), A_{eye} is computed. Then (2) is used to remove the two subspaces. The residual activity during blinks and resting data is used in (5) to estimate w_{blink} . As before, (3) and (2) are used to compute and to correct the M/EEG signals. The pseudocode for fitting the artifact correction model is provided in Supplementary Listing 1. It outputs a one step correction matrix C that combines equations (1) and (2) into a single matrix multiplication, which is computationally inexpensive.

$$x_c[t] = C x[t] \quad (7)$$

with

$$C = (I - a_{blink} w_{blink}^T) C_{eye} \text{ and } C_{eye} = I - A_{eye} W_{eye}^T \quad (8)$$

We additionally provide an open source and freely available reference implementation in Matlab (Kobler, 2019). Using the open source implementation, the process of recording the calibration data and fitting the model took on average 10 min and up to 15 min if the briefing of participants is included.

2.10. Algorithm evaluation

We compared the proposed algorithm to four representative correction algorithms. The first one was originally proposed by Schlögl et al. and is denoted EYEREG here. EYEREG requires the horizontal and vertical EOG derivative signals and solves a regression problem for each EEG channel (Schlögl et al., 2007). The second algorithm, EYEEEG, works in the independent component space. For each IC, the variance is computed during eye artifacts (eye movements and blinks) and rest. If the variance during eye artifacts is larger than the variance during rest, an IC is classified as eye artifact related and rejected (Plöchl et al., 2012). Plöchl et al. proposed to classify ICs as artifactual, if the respective variance ratio was larger than 1.1. We tested a variety of thresholds (Supplementary Figure 7) and found that a threshold of 2.0 resulted in the best trade-off between eye artifact correction and preservation of brain activity. The third algorithm is a representative of the subspace subtraction algorithms and is publicly available as an EEGLAB plugin named EYESUBTRACT (Zhou et al., 2005). We designed the fourth algorithm based on the ideas of Parra et al. (2005) and presented it in (Kobler et al., 2017). To distinguish it from EYESUBTRACT, we denote it here as generalized eye artifact subspace subtraction (GEYESUB) algorithm. In contrast to EYESUBTRACT, it also considers resting data in the optimization problem. This allows a trade-off between eye artifact correction and preservation of brain activity.

We evaluated the correction quality of the algorithms with a causal evaluation approach. All algorithms were fitted to the first eye block (first and second for EEGDS4 and MEGDS), while the second (third for EEGDS4; third and fourth for MEGDS) eye block was used to evaluate the algorithms. Depending on the algorithm, the fitting procedure comprised the computation of ICA or regression weights.

As in (Kobler et al., 2017), we computed 3 evaluation metrics. To assess the CRD and blink artifact correction quality, we computed Pearson correlation coefficients between the EOG derivative and the corrected M/EEG channels; for the HORZ epochs, we used the HEOG derivative, and for the VERT and BLINK epochs, the VEOG derivative. To assess the preservation of brain activity, we computed the root mean squared error (RMSE) between the corrected and uncorrected signal at each M/EEG channel during REST epochs. To assess the impact on the spectral domain, we computed the power spectral density (PSD) ratio between corrected and uncorrected signals during REST trials. We used Welch's method with a 2-s window (1 s overlap) to compute the PSDs for

frequencies in the range from 0 to 30 Hz.

We also computed MRCPs for EEGDS1 and ErrPs for EEGDS2 before and after eye artifact correction, using data of the main experimental blocks. The paradigms and pre-processing procedures to obtain the MRCPs and ErrPs are described in (Kobler et al., in revision) and (Lopes-Dias et al., 2019).

We tested for significant differences across algorithms with permutation paired t-tests (Maris and Oostenveld, 2007; Nichols and Holmes, 2002) and controlled the false discovery rate (FDR) according to (Benjamini and Yekutieli, 2001). We also computed confidence intervals across recording sessions. The confidence intervals were estimated, from the mean and standard error of the mean (SEM), with a confidence level of 0.05, assuming a Student's t distribution.

2.11. Hyperparameter estimation

The proposed algorithm (SGEYESUB) has two hyperparameters α and β , defined in equation (5). We used a grid search to determine α and β with the goal to minimize the RMSE during REST epochs and residual correlations during HORZ/VERT/BLINK epochs of the second block on EEGDS1 (20 participants). The set of candidate values was {0.001, 0.01, 0.1, 1, 10} for α and {0.00001, 0.0001, 0.001, 0.01, 0.1} for β . The combination of $\alpha = 1$ and $\beta = 0.01$ resulted in the best performance across the participants within EEGDS1.

We fitted the hyperparameters of GEYESUB with the same grid search approach. GEYESUB has two hyperparameters. One weighs the L2 norm in a penalized logistic regression classifier. It was varied in the range {0.0001, 0.001, 0.01, 0.1, 1, 10, 100} and fixed to 100. The second hyperparameter was used to shrink the unmixing matrix towards identity. It was varied in the range {0.000001, 0.00001, 0.0001, 0.001, 0.01, 0.1, 1} and fixed to 0.001. Since both eye blocks of EEGDS1 were used to fit the hyperparameters of GEYESUB and SGEYESUB, we excluded the eye block data of EEGDS1 from the final evaluation.

2.12. Model evaluation

As a last analysis step, we investigated whether the assumption of a stationary model in equations (1) and (2) holds for a 1–1.5 h long experiment. If the contribution of eye artifacts to the M/EEG sensors varied over time, the performance of the eye artifact correction algorithms would decrease. To test whether a stationary model is sufficient, we compared the performance of the correction algorithms between the first and second block. To get an unbiased estimate of the evaluation metrics for the first block, we applied a leave-one-trial-out cross-validation scheme. In detail, we fitted the correction algorithms to all but one trial of the first block, and computed the evaluation metric for the held out trial and a randomly selected trial with the same condition from the second block. After each trial of the first block was tested once, we computed the mean of the evaluation metrics across the trials of each block.

We fitted a regression line with the difference in the evaluation metric between the first and second block as a dependent variable and the duration between the first and second block as a predictor. We tested the significance of the slope of the regression line with permutation tests (Maris and Oostenveld, 2007; Nichols and Holmes, 2002). In 10,000 permutations, we randomly flipped the sign of the differences in the evaluation metrics before fitting the regression model. We set the p-value as the fraction of random models whose absolute value of the slope was larger than the absolute value of the observed slope. Regarding multiple comparisons, we controlled the false discovery rate (FDR) according to (Benjamini and Yekutieli, 2001).

2.13. Data and code availability statement

Reference implementations of SGEYESUB, the other algorithms and the experimental paradigm are provided on GitHub (Kobler, 2019). The

repository also provides code to demonstrate how the algorithms were fitted and applied to M/EEG data.

The pre-processed EEG datasets are publicly available on OSF (Kobler et al., 2020). The raw EEG datasets are available upon request to the corresponding author and require a formal data sharing agreement. The authors do not have the permission to share the MEG dataset (MEGDS).

3. Results

The grand average eye artifact correction results of the EEG datasets are displayed in Fig. 2. The figure displays topographic plots (Fig. 2a–d) and barplots for the average channel (Fig. 2e and f). The topographic plots in the top row of Fig. 2a show the correlations of the EEG channels with the eye artifacts for uncorrected data. Compared to uncorrected data, all algorithms attenuated the CRD and eyelid-related artifacts. All algorithms except EYEREG achieved a rather uniform attenuation to residual correlations below 0.1 across channels. EYEREG failed to correct vertical eye movements; the residual correlations at pre-frontal, posterior and occipital channels were considerably larger (approx. 0.2) compared to the other algorithms. This effect was significant for the average channel (Fig. 2e). The residual correlation with the VEOG derivative was 0.2 on average, compared to 0.1 for EYEEG and below 0.1 for the subspace subtraction algorithms. The differences between EYEEG and the subspace algorithms was also significant. We did not observe any other significant difference in the correction quality of the algorithms during eye movement and blink epochs.

The topographic distribution of the RMSE during rest epochs is summarized in Fig. 2b. We observed a gradient with largest RMSE at pre-frontal channels and smallest RMSE at occipital channels. EYESUBTRACT removed considerably more activity than EYEEEG, which in turn removed more activity than EYEREG, GEYESUB and SGEYESUB. The differences were significant for the average EEG channel (Fig. 2f). The significance tests also revealed that EYEREG (1.2 μ V) removed significantly less activity than GEYESUB (1.5 μ V) and SGEYESUB (1.5 μ V). The size of this effect was small (0.3 μ V).

In addition to resting data, we also estimated the effect of the correction approaches on ErrPs and MRCPs. The grand average topographic distributions of the positive and negative peaks of the ErrP, and the MRCP at movement onset are displayed in Fig. 2c and d, respectively. Compared to the uncorrected potentials, the application of EYESUBTRACT not only resulted in a strong attenuation, but also in a change of the topographic distribution. The other algorithms attenuated both potentials slightly (Supplementary Figures 2,3). SGEYESUB attenuated the ErrP peaks at electrode FCz and the MRCP at electrode Cz by 0.5 μ V (0.1 μ V SEM) and 0.3 μ V (0.1 μ V SEM). Overall, the effects on the potentials are in agreement with the effects on the RMSE during rest periods (Fig. 2b).

Fig. 3 summarizes the PSD ratio during rest epochs for frontal, central and parietal channels. Similarly to the RMSE during rest epochs (Fig. 2b), we observed a gradient from frontal to parietal channels. For all algorithms the attenuation was strongest for frequencies below 5 Hz. The attenuation for frequencies above 10 Hz was negligible for all algorithms except for EYESUBTRACT.

The causal evaluation results for the MEG dataset are summarized in Fig. 4. The subspace subtraction algorithms achieved a rather uniform attenuation of the eye artifacts to residual correlations below 0.1 across channels (Fig. 4a). The residual correlations of EYEEEG and EYEREG at fronto-temporal channels were considerably larger during vertical eye movements (approx. 0.3). The observations of the topographic distributions manifested in significant differences for the average channel (Fig. 4c). For vertical eye movements, EYEEEG (0.12) and EYEREG (0.15) performed significantly worse than the other algorithms. EYESUBTRACT (0.06) and SGEYESUB (0.07) achieved significantly lower residual correlations than GEYESUB (0.08). For horizontal eye movements, EYESUBTRACT achieved significantly lower residual correlations ($|\text{correlation}| = 0.06$) than the other algorithms. For blinks, EYESUBTRACT (0.09) outperformed EYEREG

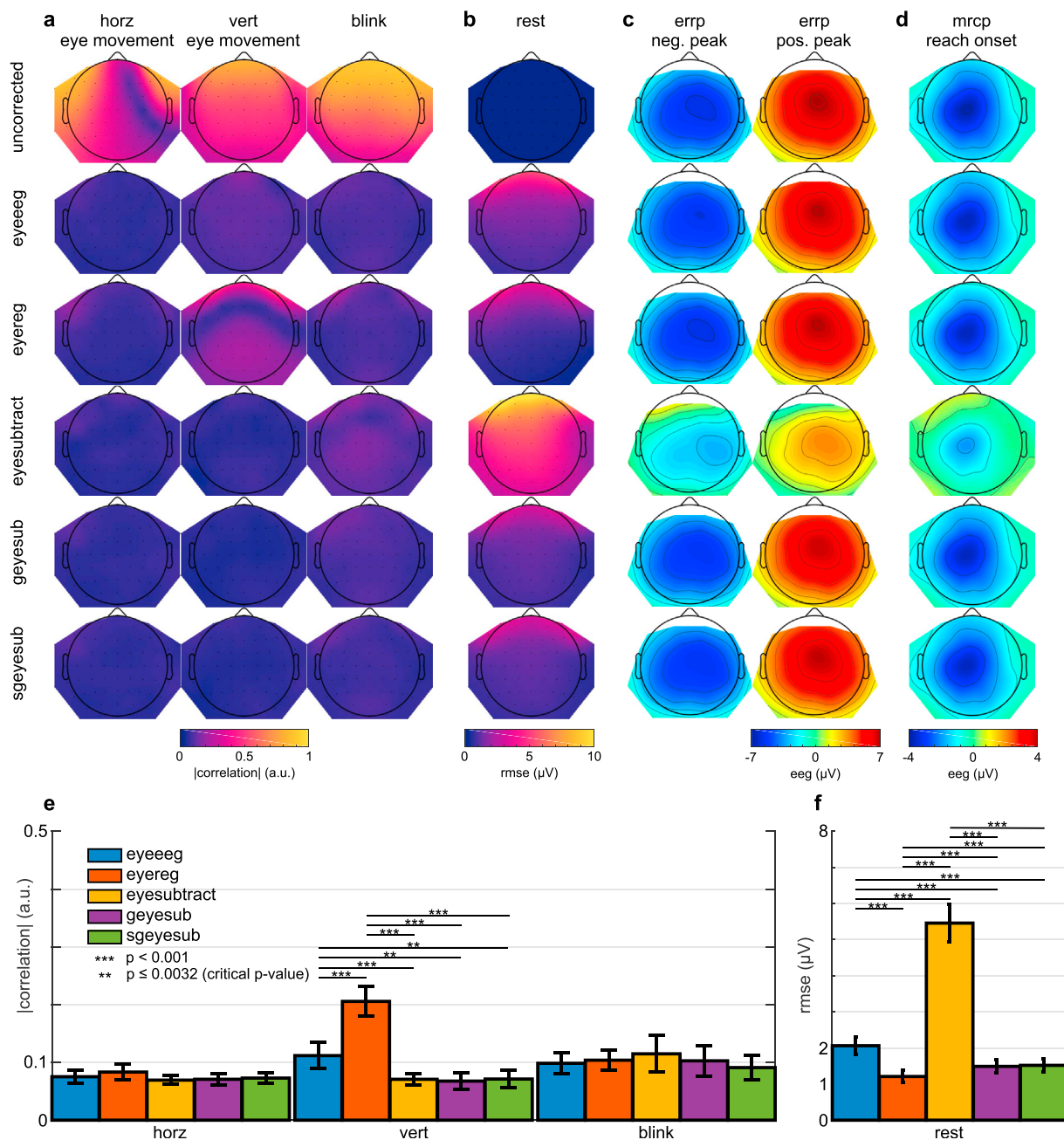


Fig. 2. EEG datasets. Grand average test set eye artifact correction results. **a**, Topographic plots summarize the residual correlation between each EEG channel and the associated EOG derivative during horizontal/vertical eye movements and blinks (columns) for all algorithms (rows) and the datasets EEGDS2 and EEGDS3 (25 recordings). **b**, As in **a** for the RMSE during rest epochs. **c**, Topographic distribution of the negative and positive peak of the ErrP before and after correction for EEGDS3 (15 recordings). **d**, As in **c** for the MRCP at the movement onset for EEGDS1 (15 recordings). **e**, Average residual correlation for the EEG channels of EEGDS2, EEGDS3 and EEGDS4 (39 recordings). Error bars indicate the 95% confidence interval of the mean. Significant differences are highlighted (asterisks and horizontal line connecting the two algorithms). **f**, As in **e** for the RMSE during rest epochs. Significant differences in **e** and **f** were identified with two-sided, paired permutation t-tests (10,000 permutations, $df = 38$). We controlled the false discovery rate for 40 tests at a significance level of 0.05, resulting in a critical p-value of 0.0032.

(0.11) and GEYESUB (0.12). For the RMSE during rest epochs (Fig. 4b,d), the results were generally similar to the EEG dataset results. EYESUBTRACT removed most resting activity (58 fT) across the MEG channels followed by EYEEEG (31 fT), GEYESUB (18 fT), SGEYESUB (18 fT) and EYEREG (15 fT). EYEREG outperformed all other algorithms in this regard.

The PSD ratio between the corrected and uncorrected MEG signals are summarized in Fig. 5 for frontal, central and parietal channels. The confidence intervals indicate that EYESUBTRACT attenuated all frequencies significantly stronger at frontal channels, while the attenuation of EYEEEG, EYEREG, GEYESUB and SGEYESUB for frequencies above 5 Hz was negligible.

In addition to the causal algorithm evaluation, we also investigated whether a stationary model was sufficient to attenuate eye artifacts during the course of the experiments. Using leave-one-trial-out cross-validation, we computed the evaluation metrics for the correction algorithms on the first and second block. In Fig. 6, we show the differences between the first and second block as a function of time (EEG datasets). The timespan between the first and second block ranged from 8 to 72 min. We did not observe any significant slope. That is, the residual correlations during eye movements and blinks, and the RMSE during rest epochs did not change significantly as time progressed.

For the MEG dataset the timespan between the first and third block

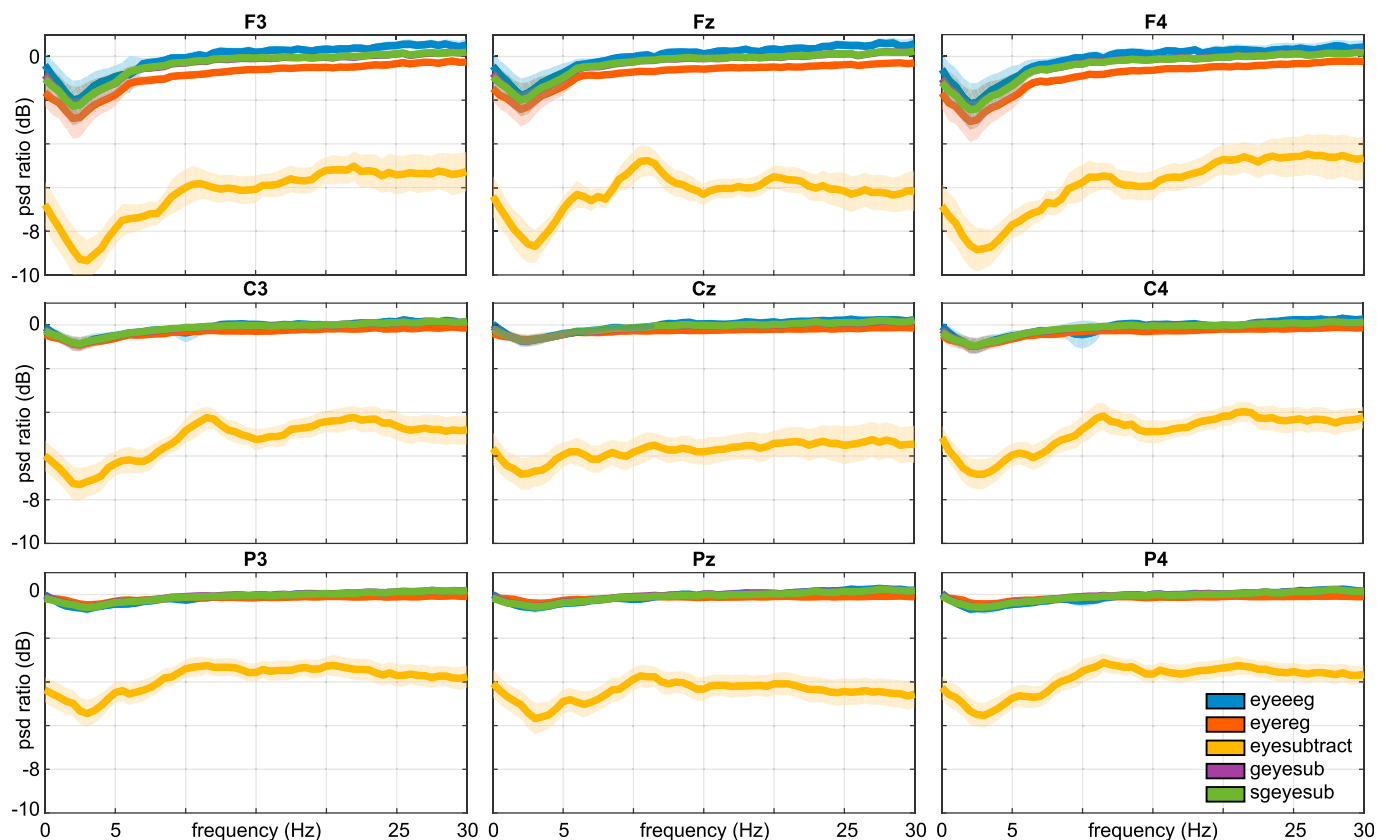


Fig. 3. EEG datasets (EEGDS2, EEGDS3, EEGD4). Grand average attenuation of resting brain activity across frequencies at frontal (top), central (middle) and parietal (bottom) electrodes. The attenuation is measured with the power spectral density (PSD) ratio, defined as the PSD of the uncorrected activity over the corrected activity. A PSD ratio of 0 dB indicates that the correction did not attenuate resting brain activity. The algorithms are color coded. Solid lines summarize the mean across the recordings and shaded areas its 95% confidence interval (39 recordings). The traces of GEYESUB (violet) and SGEYESUB (green) are overlapping in all of the plots; they also overlap with the traces of EYEREG (orange) and EYEEEG (blue) for central and parietal channels.

ranged from 93 to 117 min (Fig. 7). The regression analysis revealed significant slopes of the differences in residual correlations during horizontal eye movements for all algorithms. For example, the slope for SGEYESUB was $1.96e-4 \text{ min}^{-1}$, corresponding to an increase in residual correlation of 0.02 after 100 min. During vertical eye movements, the slopes of GEYESUB and SGEYESUB were significant, while the p-values of EYEEEG, EYEREG and EYESUBTRACT were close to the critical p-value. The slopes during blinks were significant for EYEEEG, GEYESUB and SGEYESUB. Considering the results of all algorithms, a stationary eye artifact model was insufficient to describe the artifacts. However, the non-stationarity was low; for SGEYESUB, the increase in residual correlation after 60 min would have been approximately 0.01.

In Figs. 8 and 9 we report the dependency of the algorithms on the amount of calibration data. We fitted the algorithms to an increasing amount of calibration data starting with 10% of the first block, and evaluated their performance on the second block. For the EEG datasets, the residual correlations and the RMSE of SGEYESUB declined quickly as the amount of calibration data increased to 40% (Fig. 8). From 40 to 100% the performance improved gradually. For the MEG dataset, we only observed a gradual improvement (Fig. 9).

4. Discussion

We have shown that the proposed algorithm (SGEYESUB) was successful in attenuating CRD and eyelid-related artifacts for both EEG and MEG data. Compared to the other algorithms, it achieved the best trade-off between attenuating the eye artifacts and maintaining brain activity. The grand average residual correlations between the corrected M/EEG

activity and the eye artifacts were below 0.1, the root mean squared error between corrected and uncorrected resting activity was below $1.5 \mu\text{V}$ and 18 fT, and event-related potentials (ErrPs, MRCPs) were attenuated by less than $0.5 \mu\text{V}$. We could also show that a stationary model was sufficient to effectively attenuate the eye artifacts for at least 1–1.5 h.

If eye artifacts were not corrected, eye movements and blinks would contaminate the signal of all EEG channels (Fig. 2a, top row), while parietal and occipital MEG channels would be marginally affected (Fig. 4a, top row). These MEG channels were likely to be affected less because the MEG was acquired with axial gradiometers, which attenuate distant sources (Taulu et al., 2014). For both modalities, the differences in topography between horizontal and vertical eye movements were apparent (Figs. 2a and 4a, top row), while the differences in topography between vertical eye movements and blinks were subtle. For example, in the EEG datasets (Fig. 2a, top row) the blink topography exhibited a gradient from frontal to occipital electrodes. Whereas the topography of vertical eye movements additionally exhibited a gradient from central to lateral electrodes.

These three distinct topographies confirmed that the artifacts during eye movements and blinks arise from 3 physiological sources (Lins et al., 1993b; Plöchl et al., 2012; Schlögl et al., 2007). Thus, one source is not sufficient to model CRD and eyelid-related artifacts during blinks and vertical eye movements. Since EYEREG used only the horizontal and vertical EOG derivatives (2 sources), it failed to correct CRD and eyelid-related artifacts (Fig. 2a,e and Fig. 4a,c). This is consistent with our previous findings in a smaller EEG dataset (Kobler et al., 2017). GEYESUB, SGEYESUB and EYESUBTRACT estimate 3 to 4 sources, which is sufficient to describe the CRD and eyelid-related artifacts in the M/EEG

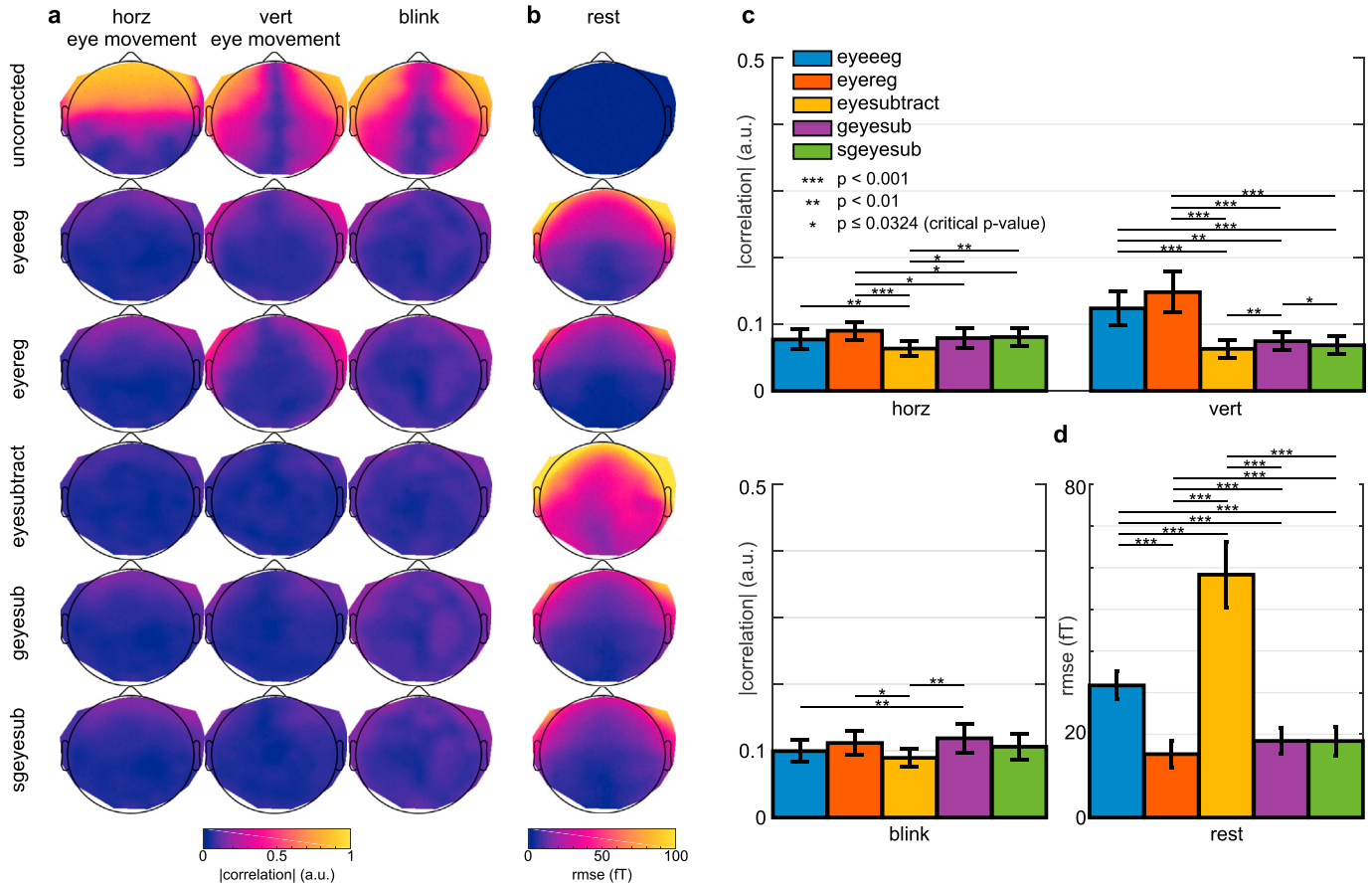


Fig. 4. MEG dataset. Grand average test set eye artifact correction results. **a**, Topographic plots summarize the correlation between each MEG channel and the associated EOG derivative (19 recordings). **b**, As in **a** for the RMSE during rest epochs. **c**, Average residual correlation for the MEG channels. Error bars indicate the 95% confidence interval of the mean. **d**, As in **c** for the RMSE during rest epochs. Significant differences in **c** and **d** were identified with two-sided, paired permutation t-tests (10,000 permutations, $df = 18$). We controlled the false discovery rate for 40 tests at a significance level of 0.05, resulting in a critical p-value of 0.0324. Significant differences are highlighted (asterisks and horizontal line connecting the two algorithms).

channels.

Croft and Barry introduced another regression algorithm, denoted revised artifact-aligned average (RAAA) algorithm (Croft and Barry, 2000b). It uses the REOG derivative as a third component. Supplementary Figures 5 and 6 summarize its performance for the EEG and MEG datasets. We observed that all regression algorithms were inferior to one another in at least one performance metric (Supplementary Figures 5b and 6b). The residual correlations of RAAA were lower than EYEREG during horizontal and vertical eye movements but higher during blinks. Compared to EYEREG, RAAA also removed slightly more resting activity. This indicates the cost of using the REOG derivative; residual brain activity within the REOG derivative is removed.

EYEEEG classified ICs as eye artifact-related based on the variance ratio between periods of rest and eye movements. For a variance ratio threshold of 2.0 we observed significantly higher residual correlations during vertical eye movements and a higher RMSE during rest periods compared to SGEYESUB (Figs. 2 and 4). At this threshold, EYEEEG rejected on average 5.6 (2.3 standard-deviation, SD) ICs out of 46.6 (6.6 SD) ICs for the EEG dataset and 2.6 (0.7 SD) out of 63.5 (2.9 SD) ICs for the MEG dataset. Plöchl et al. rejected on average 5.3 out of 64 ICs across participants with a threshold of 1.1 (Plöchl et al., 2012). At this threshold the RMSE during resting periods would have almost doubled for the EEG and MEG datasets, while the residual correlations would have reduced marginally (Supplementary Figure 7). With an increasing threshold more brain activity could be preserved at the cost of lower artifact correction performance (Supplementary Figure 7). Since EYEEEG works in IC space, it also depends on the result of ICA. An ICA algorithm needs to estimate

$O(n_{\text{channels}}^2)$ parameters, while the other algorithms need to estimate only $O(n_{\text{channels}} \cdot n_{\text{subspaces}})$ parameters with the number of subspaces being 4 or less. When using little calibration data, the performance of EYEEEG dropped (Figs. 8 and 9), indicating that the ICA estimates of the eye artifact sources were likely not as close to the true sources as the other algorithm ones.

EYESUBTRACT removed more than double of the resting brain activity compared to the other algorithms (Fig. 1b,f, Fig. 2b,d, Figs. 3 and 4). This manifested in attenuated ErrPs (Supplementary Figure 1) and MRCPs (Supplementary Figure 2) and altered topographic distributions (Fig. 2c and d). The objective of EYESUBTRACT is to minimize CRD and eyelid-related artifacts, while resting brain activity is not considered. This resulted in excellent artifact correction performance at the cost of removing a large amount of brain activity.

GEYESUB and SGEYESUB also consider the resting periods in their objective criteria and could, therefore, maximize both the attenuation of eye artifacts and preservation of brain activity. SGEYESUB differed from GEYESUB in three ways. First, SGEYESUB removed only 3 subspaces compared to 4 for GEYESUB. Second, the objective function of SGEYESUB in equation (5) contains two penalties that enforced sparsity (L1 penalty) and orthogonality to resting data (weighted L2 penalty). Note that the L1 penalty pushed the solution to use few channels that carry most information about the artifacts (mainly EOG channels). This means that it pushed the solution closer to the ones of regression algorithms, which use only EOG derivatives. The advantage of SGEYESUB over the regression algorithms is that the additional weighted L2 penalty enforced orthogonality to resting data. Third, GEYESUB and SGEYESUB differed in their

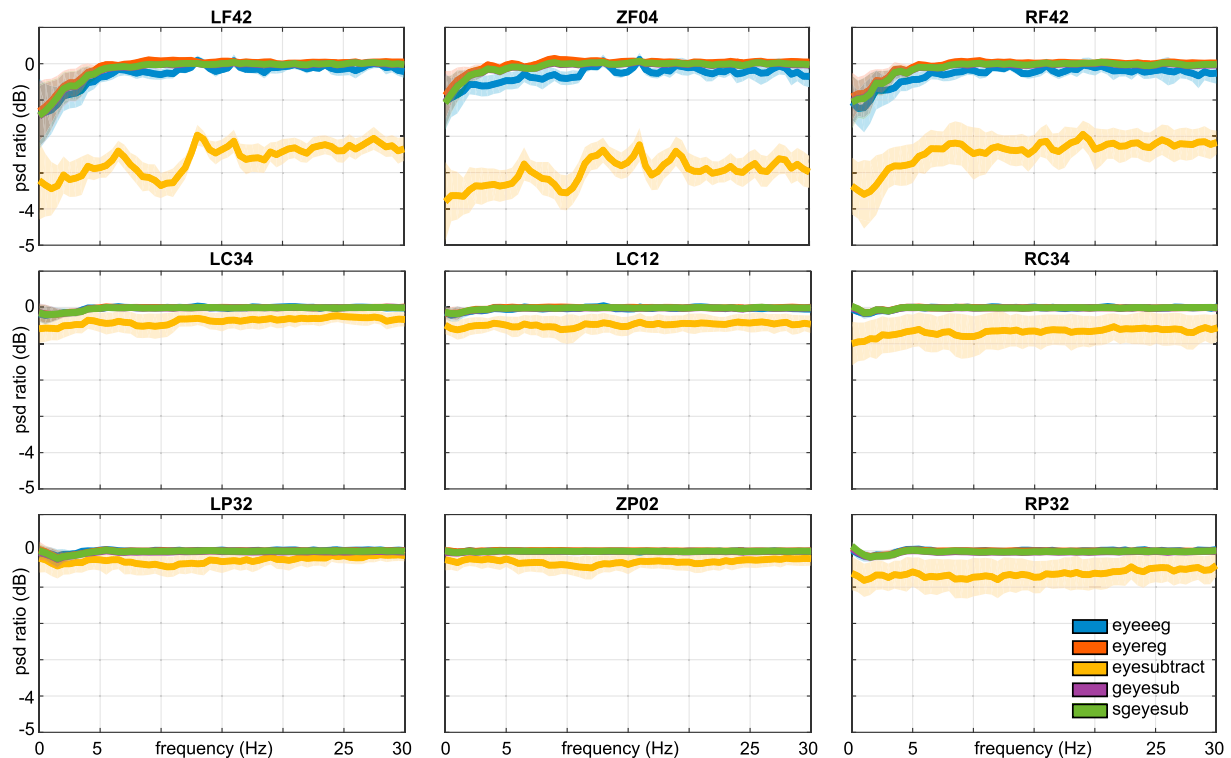


Fig. 5. MEG dataset. Grand average attenuation of resting brain activity across frequencies at frontal (top), central (middle) and parietal (bottom) channels. The attenuation is measured with the power spectral density (PSD) ratio, defined as the PSD of the uncorrected activity over the corrected activity. A PSD ratio of 0 dB indicates that the correction did not attenuate resting brain activity. The algorithms are color coded. Solid lines summarize the mean across the recordings and shaded areas its 95% confidence interval (19 recordings). The traces of EYEREG (orange), GEYESUB (violet) and SGEYESUB (green) are overlapping in all of the plots, they also overlap with the trace of EYEEEG (blue) at central and parietal channels.

fitting procedure. For SGEYESUB, we estimated the weight matrix W in two steps. First, we corrected the artifacts during horizontal and vertical eye movements and, subsequently, the residual artifacts during blinks. In GEYESUB, logistic regression with a standard L2 penalty was used to estimate the initial weight vector u for each of the 4 subspaces. Next, the mixing vector a associated with the weight vector u was computed. A refined weight matrix V was then estimated via regularized least squares based on the mixing matrix A (concatenated mixing vectors) and the covariance during resting data. This procedure implicitly implemented the weighted L2 penalty but added an additional level of complexity. We surmised that the same or even better performance could be achieved by directly specifying the orthogonality to resting data in the objective function. The results suggest that the performance of SGEYESUB and GEYESUB was similar for the EEG datasets (Figs. 2 and 3), while SGEYESUB outperformed GEYESUB for vertical eye movements in the MEG dataset (Figs. 4 and 5) by a small margin - the difference in residual correlation was low (0.01). Taken together, SGEYESUB, which removes the minimal number of subspaces, marginally improved the CRD and eyelid correction performance upon GEYESUB.

Since GEYESUB and SGEYESUB do not explicitly require EOG channels/derivatives to estimate A and W , we investigated whether the performance would drop, if the EOG channels were excluded from the fitting procedure (Supplementary Figures 3,4). For both algorithms, the RMSE during rest epochs would increase significantly from 1.5 μ V to 3.9 μ V in the case of EEG (Supplementary Figure 3d) and from 18 fT to 34 fT in the case of MEG (Supplementary Figure 4c). GEYESUB would also fail to attenuate horizontal eye movements at frontal and central MEG channels (Supplementary Figure 4a), resulting in significantly higher residual correlations for the average MEG channel. The results suggest that if no EOG channels were available, both algorithms would remove more brain

activity, but still less than EYESUBTRACT. Regarding the residual correlations with the eye artifacts, SGEYESUB would be more robust to excluding EOG channels in the experimental setup than GEYESUB.

In all experiments, we used sintered Ag/AgCl EEG electrodes and salty gels. They provide good long term recording stability (Tallgren et al., 2005). We did not detect any effect of time on the correction performance within 1 h for the EEG datasets (Fig. 6), suggesting that the CRD and blink-related artifacts were stationary. For the MEG dataset, we observed a significant increase in residual correlations over time (Fig. 7). This effect can be due to the MEG sensors not being attached to the participants. It is likely that the relative position between the participants' head and sensors varies over time. The slopes of the residual correlations were low for SGEYESUB ($\Delta|\text{correlation}| \leq 0.01/\text{hour}$), indicating that the effect was negligible for approximately 1.5 h.

SGEYESUB is a plug-and-play method; it generalizes to new datasets without any hyperparameter tuning or expert knowledge. Our results show that the performance of SGEYESUB was robust to a reduction in the amount of calibration data and the number of EOG channels. If half of the calibration data were used to fit the algorithm, the performance decrease was marginal (Figs. 8 and 9). A reduction in the amount of calibration data would be highly desirable, since more time could be spent on BCI/neurofeedback training.

Despite the promising results, there remain a number of limitations that need to be addressed in future research. We have developed and evaluated SGEYESUB particularly for BCI and neurofeedback applications. Beyond that, we envision its application in a clinical setting (e.g., epilepsy monitoring). Before SGEYESUB can become a viable tool in clinical practice, further research is required - particularly its impact on source imaging and dipole fitting methods needs to be assessed. Another limitation of the current study is that the workspace was limited to two

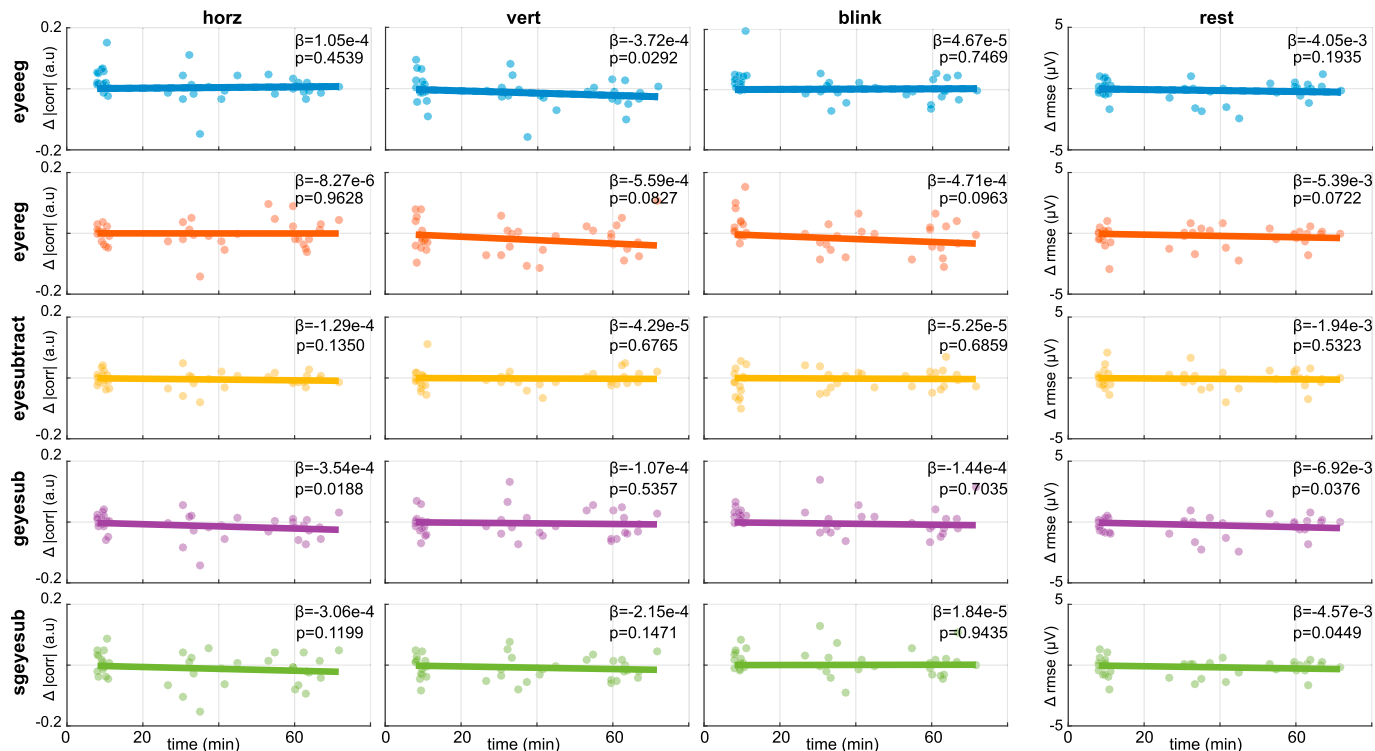


Fig. 6. EEG datasets (EEGDS2, EEGDS3, EEGDS4). Eye artifact correction quality over time. The plots are arranged in rows (algorithms) and columns (conditions). The condition specific evaluation metrics were computed using leave-one-trial-out cross-validation. Each dot corresponds to one recording. It summarizes the difference in an evaluation metric between the first and second block. A positive difference indicates a larger value in the second block compared to the first one. The trend is summarized with a regression line. Its slope β is displayed in the top right corner. We did not observe significant slopes (two-sided, permutation tests with 10,000 permutations, $df = 38$, $\alpha = 0.05$, 20 tests, FDR correction).

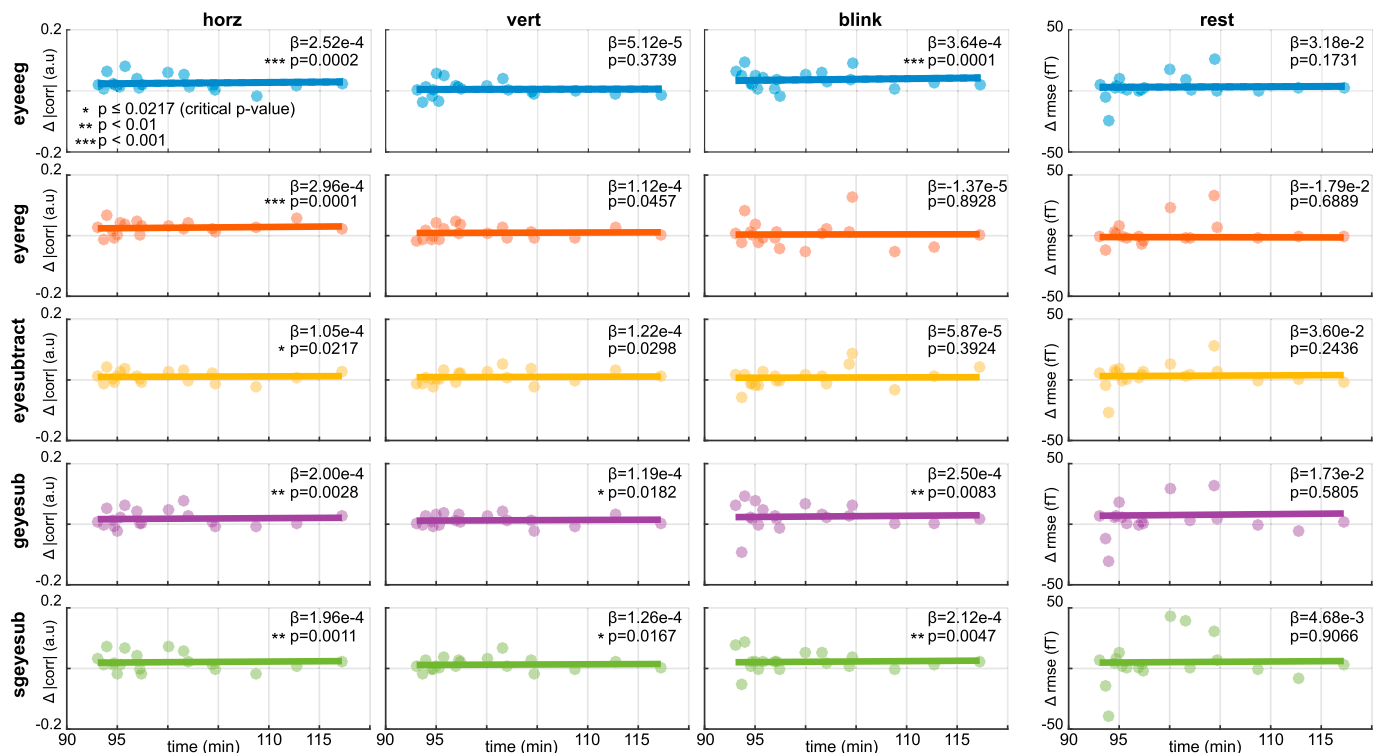


Fig. 7. MEG dataset. Eye artifact correction quality over time. The plots are arranged in rows (algorithms) and columns (conditions). The condition specific evaluation metrics were computed using leave-one-trial-out cross-validation. Each dot corresponds to one recording. It summarizes the difference in an evaluation metric between the first and second block. The trend is summarized with a regression line. Its slope β is displayed in the top right corner. Significant slopes were identified with two-sided, permutation tests (10000 permutations, $df = 18$). We controlled the false discovery rate for 20 tests at a significance level of 0.05, resulting in a critical p-value of 0.0217.

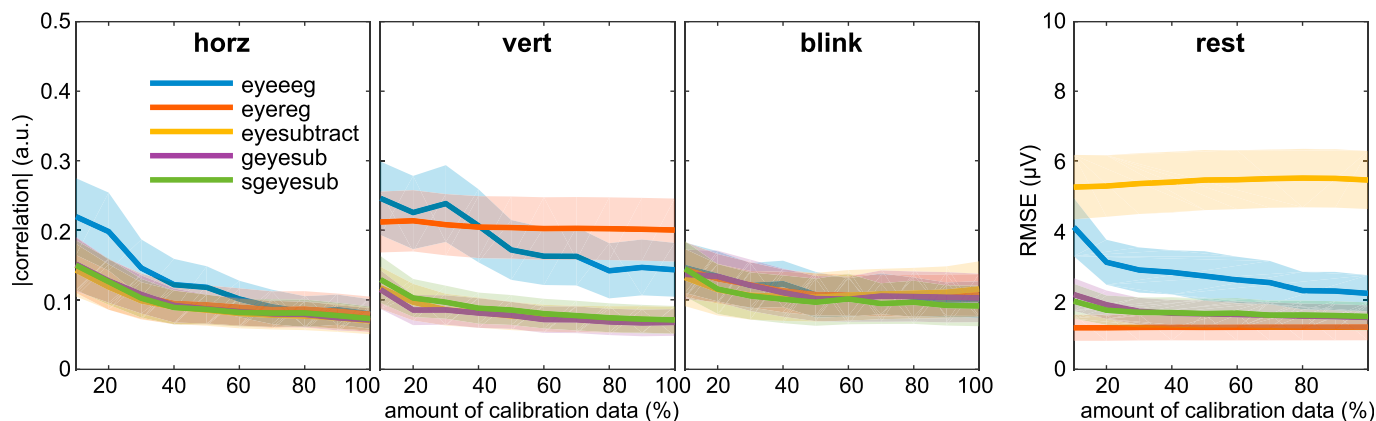


Fig. 8. EEG datasets (EEGDS2, EEGDS3, EEGDS4; 39 recordings). Dependency of the eye artifact correction algorithms on the amount of calibration data. The conditions are summarized in individual plots. The algorithms were fitted to the first 10, 20, ..., 100% of the calibration data and evaluated on the second eye block (causal evaluation). Each line summarizes the grand average performance for one algorithm. Shaded areas indicate the 95% confidence interval of the mean.

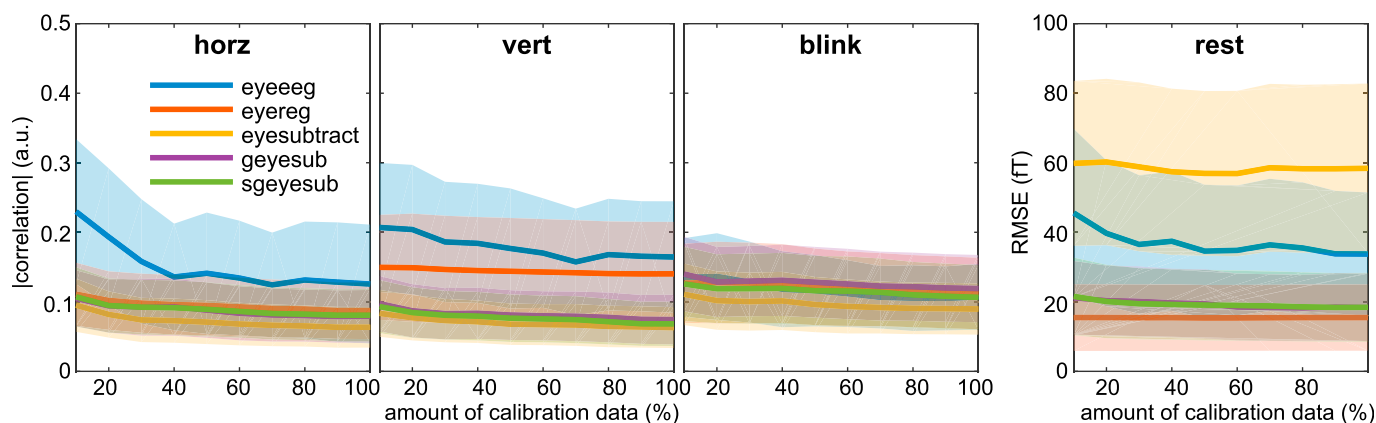


Fig. 9. MEG dataset (19 recordings). Dependency of the eye artifact correction algorithms on the amount of calibration data. The conditions are summarized in individual plots. The algorithms were fitted to the first 10, 20, ..., 100% of the calibration data and evaluated on the second eye block (causal evaluation). Each line summarizes the grand average performance for one algorithm. Shaded areas indicate the 95% confidence interval of the mean.

dimensions (horizontal and vertical). Vergence eye movements allow us to additionally focus our gaze in depth. During vergence eye movements, the eyeballs, and thereby also the CRDs, move in different directions, requiring an additional depth component to describe the CRD artifact in M/EEG signals. The presented approach could be extended to correct this additional component and, therefore, generalize to real-life scenarios, if a depth condition is included in the experimental paradigm and the associated artifact subspace is subtracted.

5. Conclusion

In a comprehensive analysis, including EEG and MEG data of 69 participants, we have evaluated 5 eye artifact correction algorithms with regard to their attenuation of corne-retinal dipole (CRD) and eyelid-related artifacts. We have shown that the proposed algorithm (SGEYESUB) effectively attenuates both types of artifacts and at the same time removes little brain activity from EEG and MEG signals. The other algorithms were inferior to SGEYESUB in the sense that they either removed more brain activity or failed to correct the artifacts in one or both recording modalities. Moreover, our results indicate that a stationary model is sufficient to describe the CRD and eyelid artifacts for at least 1–1.5 h, validating the feasibility of our approach in online eye artifact correction. Once the model is fitted, the CRD and eyelid artifact correction is reduced to a matrix multiplication. An effective and efficient eye artifact correction approach will prove useful beyond neurofeedback and brain-computer interface studies.

CRedit authorship contribution statement

Reinmar J. Kobler: Funding acquisition, Conceptualization, Investigation, Formal analysis, Software, Writing - original draft, Writing - review & editing, Visualization. **Andreea I. Sburlea:** Conceptualization, Writing - review & editing. **Catarina Lopes-Dias:** Investigation, Writing - review & editing. **Andreas Schwarz:** Investigation, Writing - review & editing. **Masayuki Hirata:** Resources, Writing - review & editing, Supervision, Data curation. **Gernot R. Müller-Putz:** Funding acquisition, Conceptualization, Resources, Writing - review & editing, Supervision, Data curation.

Acknowledgements

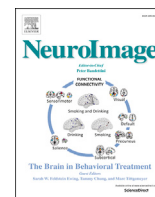
The authors acknowledge Joana Pereira, Valeria Mondini and Philipp Raggam for their valuable comments. This work has received funding from the European Research Council (ERC) under the European Union's Horizon 2020 research and innovation programme (Consolidator Grant 681231 'Feel Your Reach'). R.J.K. received additional funding from Graz University of Technology through its research abroad program (grant number O-940600008).

Appendix A. Supplementary data

Supplementary data to this article can be found online at <https://doi.org/10.1016/j.neuroimage.2020.117000>.

References

- Beck, A., Teboulle, M., 2009. A fast iterative shrinkage-thresholding algorithm for linear inverse problems. *SIAM J. Imag. Sci.* 2, 183–202. <https://doi.org/10.1137/080716542>.
- Benjamini, Y., Yekutieli, D., 2001. The control of the false discovery rate in multiple testing under dependency. *Ann. Stat.* 29, 1165–1188. <https://doi.org/10.1214/aos/1013699998>.
- Berg, P., Scherg, M., 1994. A multiple source approach to the correction of eye artifacts. *Electroencephalogr. Clin. Neurophysiol.* 90, 229–241. [https://doi.org/10.1016/0013-4694\(94\)90094-9](https://doi.org/10.1016/0013-4694(94)90094-9).
- Brainard, D.H., 1997. The psychophysics toolbox. *Spatial Vis.* 10, 433–436. <https://doi.org/10.1163/156856897X00357>.
- Croft, R.J., Barry, R.J., 2000a. Removal of ocular artifact from the EEG: a review. *Clin. Neurophysiol.* 30, 5–19. [https://doi.org/10.1016/S0987-7053\(00\)00055-1](https://doi.org/10.1016/S0987-7053(00)00055-1).
- Croft, R.J., Barry, R.J., 2000b. EOG correction of blinks with saccade coefficients: a test and revision of the aligned-artefact average solution. *Clin. Neurophysiol.* 111, 444–451. [https://doi.org/10.1016/S1388-2457\(99\)00296-5](https://doi.org/10.1016/S1388-2457(99)00296-5).
- Delorme, A., Makeig, S., 2004. EEGLAB: an open source toolbox for analysis of single-trial EEG dynamics including independent component analysis. *J. Neurosci. Methods* 134, 9–21. <https://doi.org/10.1016/j.jneumeth.2003.10.009>.
- Gawne, T.J., Killen, J.F., Tracy, J.M., Lahti, A.C., 2017. The effect of saccadic eye movements on the sensor-level magnetoencephalogram. *Clin. Neurophysiol.* 128, 397–407. <https://doi.org/10.1016/j.clinph.2016.12.013>.
- Gratton, G., Coles, M.G.H., Donchin, E., 1983. A new method for off-line removal of ocular artifact. *Electroencephalogr. Clin. Neurophysiol.* 55, 468–484. [https://doi.org/10.1016/0013-4694\(83\)90135-9](https://doi.org/10.1016/0013-4694(83)90135-9).
- Haufe, S., Meinecke, F., Görgen, K., Dähne, S., Haynes, J.D., Blankertz, B., Bießmann, F., 2014. On the interpretation of weight vectors of linear models in multivariate neuroimaging. *Neuroimage* 87, 96–110. <https://doi.org/10.1016/j.neuroimage.2013.10.067>.
- Hoffman, J.E., Subramanian, B., 1995. The role of visual attention in saccadic eye movements. *Percept. Psychophys.* 57, 787–795. <https://doi.org/10.3758/BF03206794>.
- Iwasaki, M., Kellinghaus, C., Alexopoulos, A.V., Burgess, R.C., Kumar, A.N., Han, Y.H., Lüders, H.O., Leigh, R.J., 2005. Effects of eyelid closure, blinks, and eye movements on the electroencephalogram. *Clin. Neurophysiol.* 116, 878–885. <https://doi.org/10.1016/j.clinph.2004.11.001>.
- Jung, T.-P., Makeig, S., Humphries, C., Lee, T.-W., McKeown, M.J., Iragui, V., Sejnowski, T.J., 2000. Removing electroencephalographic artifacts by blind source separation. *Psychophysiology* 37, 163–178. <https://doi.org/10.1111/1469-8986.3720163>.
- Kahneman, D., Beatty, J., 1966. Pupil diameter and load on memory. *Science* 154, 1583–1585. <https://doi.org/10.1126/science.154.3756.1583>.
- Katila, T., Maniewski, R., Poutanen, T., Varpula, T., Karp, P.J., 1981. Magnetic fields produced by the human eye. *J. Appl. Phys.* 52, 2565–2571. <https://doi.org/10.1063/1.329000>.
- Keren, A.S., Yuval-Greenberg, S., Deouell, L.Y., 2010. Saccadic spike potentials in gamma-band EEG: characterization, detection and suppression. *Neuroimage* 49, 2248–2263. <https://doi.org/10.1016/j.neuroimage.2009.10.057>.
- Kobler, R.J., 2019. Sparse generalized eye artifact subspace subtraction (SGEYESUB) reference implementation [WWW Document]. URL: <https://github.com/rkobler/eyearifactcorrection>.
- Kobler, R.J., Hirata, M., Hashimoto, H., Dowaki, R., Sburlea, A.I., Müller-Putz, G.R., 2019. Simultaneous decoding of velocity and speed during executed and observed tracking movements: an MEG study. In: Proceedings of the 8th Graz Brain Computer Interface Conference 2019. Graz. <https://doi.org/10.3217/978-3-85125-682-6-19>.
- Kobler, R.J., Kolesnichenko, E., Sburlea, A.I., Müller-Putz, G.R., in revision. Distinct cortical networks for hand movement initiation and directional processing: an EEG study. *Neuroimage*.
- Kobler, R.J., Sburlea, A.I., Lopes-Dias, C., Schwarz, A., Mondini, V., Müller-Putz, G.R., 2020. EEG Eye Artifact Dataset. Open Sci. Foundation. <https://dx.doi.org/10.17605/OSF.IO/2QGRD>.
- Kobler, R.J., Sburlea, A.I., Müller-Putz, G.R., 2018. Tuning characteristics of low-frequency EEG to positions and velocities in visuomotor and oculomotor tracking tasks. *Sci. Rep.* 8, 17713. <https://doi.org/10.1038/s41598-018-36326-y>.
- Kobler, R.J., Sburlea, A.I., Müller-Putz, G.R., 2017. A comparison of ocular artifact removal methods for block design based electroencephalography experiments. In: Proceedings of the 7th Graz Brain-Computer Interface Conference, pp. 236–241. <https://doi.org/10.3217/978-3-85125-533-1-44>.
- Kothe, C., Medine, D., Boulay, C., Grivich, M., Stenner, T., 2019. Lab Streaming Layer (LSL) - a software framework for synchronizing a large array of data collection and stimulation devices [WWW Document]. URL: <https://github.com/sccn/labstreaminglayer>.
- Lins, O.G., Picton, T.W., Berg, P., Scherg, M., 1993a. Ocular artifacts in recording EEGs and event-related potentials II: source dipoles and source components. *Brain Topogr.* 6, 65–78. <https://doi.org/10.1007/BF01234128>.
- Lins, O.G., Picton, T.W., Berg, P., Scherg, M., 1993b. Ocular artifacts in EEG and event-related potentials I: scalp topography. *Brain Topogr.* 6, 51–63. <https://doi.org/10.1007/BF01234127>.
- Lopes-Dias, C., Sburlea, A.I., Müller-Putz, G.R., 2019. Online asynchronous decoding of error-related potentials during the continuous control of a robot. *Sci. Rep.* 9, 17596. <https://doi.org/10.1038/s41598-019-54109-x>.
- Mannan, M.M.N., Jeong, M.Y., Kamran, M.A., 2016. Hybrid ICA—regression: automatic identification and removal of ocular artifacts from electroencephalographic signals. *Front. Hum. Neurosci.* 10, 1–17. <https://doi.org/10.3389/fnhum.2016.00193>.
- Maris, E., Oostenveld, R., 2007. Nonparametric statistical testing of EEG- and MEG-data. *J. Neurosci. Methods* 164, 177–190. <https://doi.org/10.1016/j.jneumeth.2007.03.024>.
- Mondini, V., Kobler, R.J., Sburlea, A.I., Müller-Putz, G.R., in review. Online EEG-Based Decoding of Arm Movement for the Natural Control of an Assistive Robotic Arm. *J. Neural. Eng.*
- Mowrer, O.H., Ruch, T.C., Miller, N.E., 1935. The corneo-retinal potential difference as the basis OF the galvanometric method OF recording eye movements. *Am. J. Physiol. Leg. Content* 114, 423–428. <https://doi.org/10.1152/ajplegacy.1935.114.2.423>.
- Nichols, T., Holmes, A., 2002. Nonparametric permutation tests for functional neuroimaging: a primer with examples. *Hum. Brain Mapp.* 15, 1–25. <https://doi.org/10.1016/B978-012264841-0/50048-2>.
- Oostenveld, R., Praamstra, P., 2001. The five percent electrode system for high-resolution EEG and ERP measurements. *Clin. Neurophysiol.* 112, 713–719. [https://doi.org/10.1016/S1388-2457\(00\)00527-7](https://doi.org/10.1016/S1388-2457(00)00527-7).
- Parra, L.C., Spence, C.D., Gerson, A.D., Sajda, P., 2005. Recipes for the linear analysis of EEG. *Neuroimage* 28, 326–341. <https://doi.org/10.1016/j.neuroimage.2005.05.032>.
- Pelli, D.G., 1997. The VideoToolbox software for visual psychophysics: transforming numbers into movies. *Spatial Vis.* 10, 437–442. <https://doi.org/10.1163/156856897X00366>.
- Picton, T.W., van Roon, P., Armiljo, M.L., Berg, P., Ille, N., Scherg, M., 2000. The correction of ocular artifacts: a topographic perspective. *Clin. Neurophysiol.* 111, 53–65. [https://doi.org/10.1016/S1388-2457\(99\)00227-8](https://doi.org/10.1016/S1388-2457(99)00227-8).
- Pion-Tonachini, L., Kreuz-Delgado, K., Makeig, S., 2019. ICLLabel: an automated electroencephalographic independent component classifier, dataset, and website. *Neuroimage* 198, 181–197. <https://doi.org/10.1016/j.neuroimage.2019.05.026>.
- Plöchl, M., Ossandón, J.P., König, P., 2012. Combining EEG and eye tracking: identification, characterization, and correction of eye movement artifacts in electroencephalographic data. *Front. Hum. Neurosci.* 6, 1–23. <https://doi.org/10.3389/fnhum.2012.00278>.
- Riemsagel, F.C.C., Van der Heijde, G.L., Van Dongen, M.M.M.M., Ottenhoff, F., 1988. On the origin of the presaccadic spike potential. *Electroencephalogr. Clin. Neurophysiol.* 70, 281–287. [https://doi.org/10.1016/0013-4694\(88\)90046-6](https://doi.org/10.1016/0013-4694(88)90046-6).
- Schäfer, J., Strimmer, K., 2005. A shrinkage approach to large-scale covariance matrix estimation and implications for functional genomics. *Stat. Appl. Genet. Mol. Biol.* 4. <https://doi.org/10.2202/1544-6115.1175>.
- Schlögl, A., Keirnath, C., Zimmermann, D., Scherer, R., Leeb, R., Pfurtscheller, G., 2007. A fully automated correction method of EOG artifacts in EEG recordings. *Clin. Neurophysiol.* 118, 98–104. <https://doi.org/10.1016/j.clinph.2006.09.003>.
- Schwarz, A., Pereira, J., Kobler, R., Müller-Putz, G.R., 2019. Unimanual and bimanual reach-and-grasp actions can be decoded from human EEG. *IEEE Trans. Biomed. Eng.* 1–1. <https://doi.org/10.1109/TBME.2019.2942974>.
- Tadel, F., Baillet, S., Mosher, J.C., Pantazis, D., Leahy, R.M., 2011. Brainstorm: a user-friendly application for MEG/EEG analysis. *Comput. Intell. Neurosci.* <https://doi.org/10.1155/2011/879716>, 2011.
- Tallgren, P., Vanhatalo, S., Kaila, K., Voipio, J., 2005. Evaluation of commercially available electrodes and gels for recording of slow EEG potentials. *Clin. Neurophysiol.* 116, 799–806. <https://doi.org/10.1016/j.clinph.2004.10.001>.
- Taulu, S., Simola, J., Nenonen, J., Parkkonen, L., 2014. In: Supek, S., Aine, C.J. (Eds.), *Novel Noise Reduction Methods, Magnetoencephalography*. Springer Berlin Heidelberg, Berlin, Heidelberg, pp. 35–71. https://doi.org/10.1007/978-3-642-33045-2_2.
- Urigüen, J.A., Garcia-Zapirain, B., 2015. EEG artifact removal-state-of-the-art and guidelines. *J. Neural. Eng.* 12, 31001. <https://doi.org/10.1088/1741-2560/12/3/031001>.
- Wilson, G.F., 2002. An analysis of mental workload in pilots during flight using multiple psychophysiological measures. *Int. J. Aviat. Psychol.* 12, 3–18. https://doi.org/10.1207/S15327108IJAP1201_2.
- Winkler, I., Brandl, S., Horn, F., Waldburger, E., Allefeld, C., Tangermann, M., 2014. Robust artifactual independent component classification for BCI practitioners. *J. Neural. Eng.* 11, 035013 <https://doi.org/10.1088/1741-2560/11/3/035013>.
- Zhou, X., Gerson, A.D., Parra, L.C., Sajda, P., 2005. EEGLAB plugin EYESUBTRACT [WWW Document]. URL: <http://sccn.ucsd.edu/eeGLAB/plugins/eyesubtract1.0.zip> (accessed 12.3.19).



Distinct cortical networks for hand movement initiation and directional processing: An EEG study



Reinmar J. Kobler^{a,1}, Elizaveta Kolesnichenko^{a,b,1}, Andreea I. Sburlea^a,
Gernot R. Müller-Putz^{a,c,*}

^a Institute of Neural Engineering, Graz University of Technology, Graz, Styria, 8010, Austria

^b Swammerdam Institute for Life Sciences–Center for Neuroscience, University of Amsterdam, Amsterdam, North Holland, 1098XH, the Netherlands

^c BioTechMed, Graz, 8010, Styria, Austria

ARTICLE INFO

Keywords:

EEG
Movement-related cortical potential
Movement direction
Sensorimotor cortex
Parieto-occipital cortex
Visuomotor task

ABSTRACT

Movement preparation and initiation have been shown to involve large scale brain networks. Recent findings suggest that movement preparation and initiation are represented in functionally distinct cortical networks. In electroencephalographic (EEG) recordings, movement initiation is reflected as a strong negative potential at medial central channels that is phase-locked to the movement onset - the movement-related cortical potential (MRCP). Movement preparation describes the process of transforming high level movement goals to low level commands. An integral part of this transformation process is directional processing (i.e., where to move). The processing of movement direction during visuomotor and oculomotor tasks is associated with medial parieto-occipital cortex (PO) activity, phase-locked to the presentation of potential movement goals. We surmised that the network generating the MRCP (movement initiation) would encode less information about movement direction than the parieto-occipital network processing movement direction. Here, we studied delta band EEG activity during center-out reaching movements (2D; 4 directions) in visuomotor and oculomotor tasks. In 15 healthy participants, we found a consistent representation of movement direction in PO 300–400 ms after the direction cue irrespective of the task. Despite generating the MRCP, sensorimotor areas (SM) encoded less information about the movement direction than PO. Moreover, the encoded directional information in SM was less consistent across participants and specific to the visuomotor task. In a classification approach, we could infer the four movement directions from the delta band EEG activity with moderate accuracies up to 55.9%. The accuracies for cue-aligned data were significantly higher than for movement onset-aligned data in either task, which also suggests a stronger representation of movement direction during movement preparation. Therefore, we present direct evidence that EEG delta band amplitude modulations carry information about both arm movement initiation and movement direction, and that they are represented in two distinct cortical networks.

1. Introduction

Whenever a reaching movement is made, a series of processes occur in the brain that include cue processing, extraction of high level movement goals, computation of low-level details (Battaglia-Mayer, 2018; Kalaska and Crammond, 1992) and deciding to initiate the movement (Cisek and Kalaska, 2010; Rizzolatti and Luppino, 2001). Recent evidence from behavioral studies with humans and spiking activity in non-human primates suggests that preparation and initiation of movements are reflected by parallel neural processes (Carland et al., 2019;

Haith et al., 2016). Movement preparation involves a series of processes related to cue perception, determination of high-level movement goals (e.g., where to move), and their translation to low-level movement commands, whereas movement initiation reflects decision processes dealing with the commitment to move to a particular movement goal (e.g., when to move) and the vigor of the ensuing movement (Carland et al., 2019; Haith et al., 2016). Movement initiation is typically accompanied with strong activity in sensorimotor areas and basal ganglia phase-locked to the movement onset (Carland et al., 2019; Kaufman et al., 2016; Pfurtscheller and Lopes Da Silva, 1999; Shibasaki et al.,

* Corresponding author. Institute of Neural Engineering, Graz University of Technology, Graz, Styria, 8010, Austria.

E-mail address: gernot.mueller@tugraz.at (G.R. Müller-Putz).

¹ These authors contributed equally.

<https://doi.org/10.1016/j.neuroimage.2020.117076>

Received 26 November 2019; Received in revised form 15 June 2020; Accepted 17 June 2020

Available online 22 June 2020

1053-8119/© 2020 The Authors. Published by Elsevier Inc. This is an open access article under the CC BY license (<http://creativecommons.org/licenses/by/4.0/>).

1980), while movement preparation is associated with fronto-parietal network activity, transforming high-level movement goals to low-level commands (Cavina-Pratesi et al., 2018; Cisek and Kalaska, 2010; Fabbrì et al., 2010; Ledberg et al., 2007; Perry and Fallah, 2017). It is established that spiking activity in primary sensorimotor areas carries information about movement direction at the movement onset (Georgopoulos et al., 1982). It is not clear whether macroscopic activity in terms of electroencephalographic (EEG) signals carry directional information phase-locked to the movement onset.

Within the EEG activity, time-domain amplitude modulations in the delta band that start prior to the movement onset have been reported to be predictive for movement initiation (Bierbaumer et al., 1990; Deecke et al., 1969; Shibasaki and Hallett, 2006). In the context of a motor task, slow potentials in the EEG activity phase-locked to the movement onset are known as movement-related cortical potentials (MRCPs) (Deecke et al., 1969). MRCPs have been investigated in relation to lower-limb movements, such as isometric dorsiflexion (Xu et al., 2014) or walking (do Nascimento et al., 2005; Jiang et al., 2015; Sburlea et al., 2015), as well as in upper-limb movements (Ibáñez et al., 2014; López-Larraz et al., 2014; Niazi et al., 2011). Several studies involving different types of movement have shown that amplitude and phase information encoded in the time-domain delta band are predictive of movement initiation (Sburlea et al., 2017; Sun et al., 2017).

Apart from encoding the initiation of executed (Lew et al., 2012), attempted (Ofner et al., 2019) and imagined (Pereira et al., 2018) upper-limb movements, MRCPs have also been reported to encode information about goal-directedness (Pereira et al., 2017), speed (Gu et al., 2009), force (Jochumsen et al., 2013), grasp types (Schwarz et al., 2018), other movements of the upper limb (Ofner et al., 2019, 2017) and movement direction (Li et al., 2012; Waldert et al., 2008). The representation of directional information within the MRCP is typically studied during center-out reaching tasks and aligned to the response (Robinson and Vinod, 2016). The employed experimental paradigms often force the participants to respond after a go cue which leads to considerable phase locking between the direction cue and the response (Waldert et al., 2008). Moreover, higher classification accuracies for movement direction can be obtained if the participants are allowed to move immediately after target presentation rather than a forced random delay period (Wang et al., 2010).

Since movement initiation and preparation are likely to be independent processes in the brain (Haith et al., 2016), it is not clear if the time-domain amplitude modulations encode information about movement direction phase-locked to the movement onset (movement initiation) or to the cue (movement preparation). Knowing that directional processing is an integral part of movement preparation, we surmise that delta band EEG activity has a stronger representation of movement direction during movement preparation (i.e., phase-locked to the cue) than during movement initiation (i.e., phase-locked to the movement onset). If this is the case, a classifier should predict the movement direction with higher accuracy in the cue aligned case compared to the movement onset aligned case. To test our hypothesis, we conducted an EEG study with healthy participants. Our experimental paradigm comprised a center-out task to identify cortical regions encoding directional information, and two experimental conditions to identify cortical regions generating the MRCP associated with arm movements. In the first condition (observation), the participants moved their eyes; in the second condition (execution), they also moved their right arm.

2. Materials and methods

2.1. Participants

Fifteen healthy participants were recruited for this study (23.8 (mean) \pm 2.8 (standard deviation, SD) years, 9 female). Eleven participants had already participated at least once in an EEG experiment before. All participants had normal or corrected to normal vision, and self-

reported to be right handed. The study was carried out in accordance with the Declaration of Helsinki and was approved by the ethics committee of the Medical University of Graz. All participants were instructed about the purpose and procedure of the study, after which they signed an informed consent form. All received monetary compensation for their participation.

2.2. Experimental set-up

During the course of the experiment, the participants were sitting in a comfortable chair, positioned 1.4 m away from a computer screen (Fig. 1a). An armrest supported the left arm, while the right arm was supported by a table at the same height. To reduce friction between the right arm and the table, participants were asked to wear a sleeve and place their hand on a circular pad. A LeapMotion controller (LeapMotion Inc., San Francisco, USA), placed 20 cm above the hand, was used to record the right hand's palm position. After each participant found a comfortable resting position, the palm position was mapped to the origin of a virtual environment (center of the screen). In analogy to the interaction with a computer by using a computer mouse, we decided to map rightward/forward hand movements to rightward/upward cursor movements. We mapped a circle with a 5-cm radius around the resting position to a circle with a 16-cm radius on the screen. The limits of the circle on the screen were indicated by the bounds of a virtual grid. For instance, a right hand movement 5 cm to the right would make the cursor touch the grid on the right side.

2.3. Experimental procedure

The experimental procedure consisted of 4 blocks, and lasted 3 h in total. In the first block, we asked the participants to familiarize themselves with the paradigm (approx. 10 min). In the second and fourth blocks, eye artifacts (blinks and eye movements) and resting activity were recorded (approx. 5 min each). The detailed procedure is described in Kobler et al. (2017). In the third block, participants performed the main experimental task according to the paradigm illustrated in Fig. 1b. Each trial implemented a two dimensional (2D), visually guided center-out reaching task (COT). In half of the trials, the COT was followed by a pursuit tracking task (PTT), which we used to study the tuning characteristics of low-frequency EEG signals to end-effector positions and velocities (Kobler et al., 2018).

A trial started if a target stimulus (large sphere) changed its color to yellow. This triggered the participants to focus their gaze upon the target and to keep their hand in the resting position and, thereby, the cursor (small gray sphere) in the center of the screen. Our paradigm distinguished between two conditions: observation (obs) and execution (exe). The conditions were indicated by a visual cue (change in target color; pseudo-randomly distributed across trials). After a period of 0.5 s, the target started to move in one of four directions (up, right, down, left; pseudo-randomly distributed across trials). After the target moved for 0.5 s, it stopped at a distance of 5 cm and waited for the approaching cursor. As soon as the distance to the cursor was smaller than a threshold, the fixation period (1 s duration) started. In the execution condition (green target), the participants tracked the target visually and controlled the cursor by moving their right hand (visuomotor task). In the observation condition (blue target), the participants tracked the target only visually while their right hand was resting (oculomotor task). We replayed previous, matching cursor trajectories to obtain similar visual dynamics during both conditions. The replay procedure was implemented in an adaptive fashion that ensured similar cursor movements within a participant, and that the participants could neither predict the condition nor the direction of the next trial. The detailed procedure is described in (Kobler et al., 2018).

We asked the participants to make a single smooth, continuous reaching movement towards the target and stop at the target position during the execution condition. If a participant did not move for 4 s after

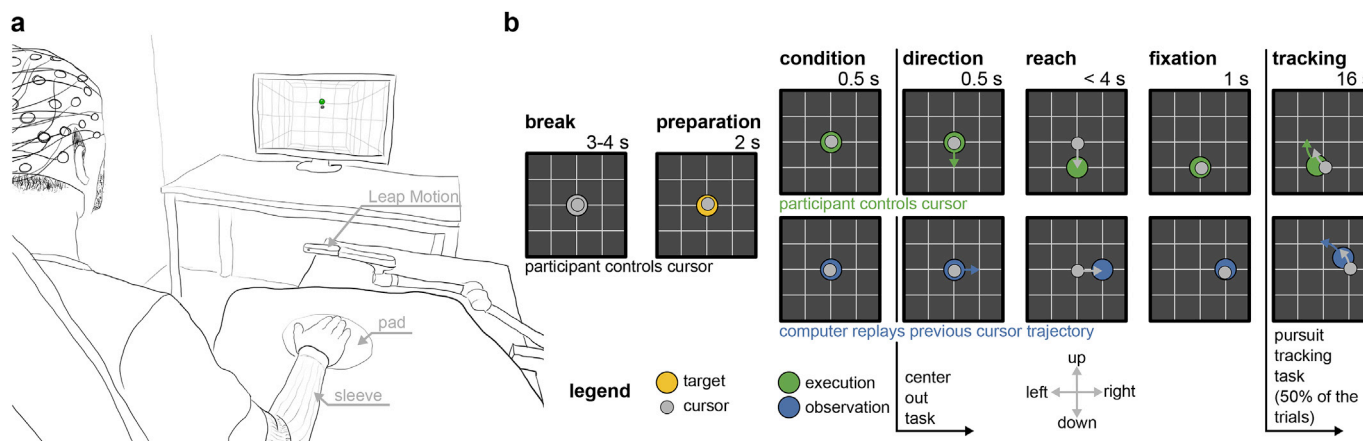


Fig. 1. Experimental setup and paradigm. **a**, During the experiment, the participants sat in a comfortable chair in front of a computer screen. Both arms were supported at the same height. Right arm movements were recorded with a LeapMotion controller. Forward/backward hand movements on the table were mapped to upward/downward cursor movements on the screen. **b**, Diagram of the experimental paradigm. A visual cue indicated the condition, either execution (green target) or observation (blue target), followed by a 2D center-out task in four directions. The direction was indicated by the target movement (0.5 s duration; arrows visualize movement in the individual images). After 1 s of fixation, a pursuit tracking task was performed for 16 s (50% of the trials). In the execution condition the participants controlled the cursor, while in the observation condition, the computer replayed a previously executed cursor trajectory that matched the current target trajectory.

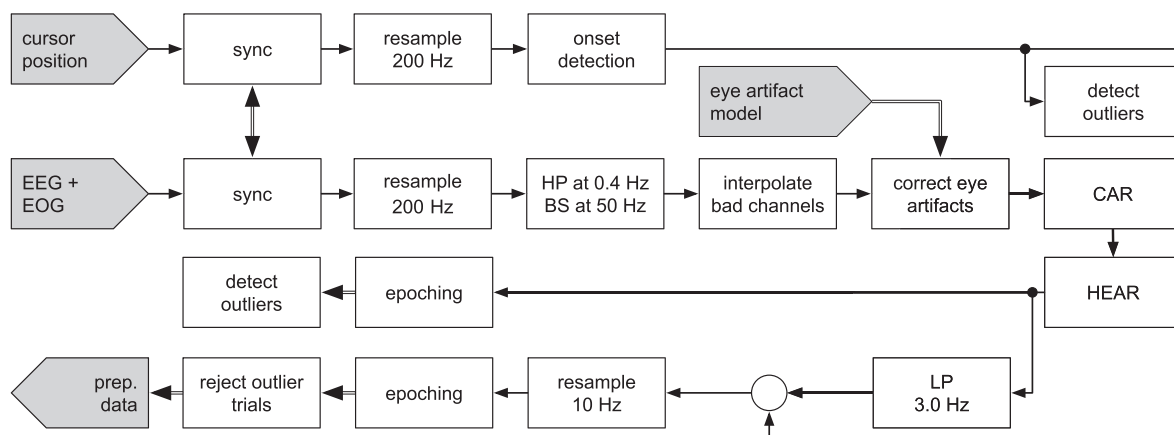


Fig. 2. Pre-processing pipeline. After synchronization, EEG and EOG signals were resampled, high-pass and notch filtered; bad channels were spherically interpolated. Next, eye artifacts were corrected. The corrected EEG signals were re-referenced to the common average reference. Then, HEAR was applied to remove transient, single electrode outliers. A subsequent low-pass filter was applied to extract delta band EEG signals. After synchronization, the movement onset was detected using the Euclidean distance between the cursor and the origin. Outlier trials were automatically detected based on the movement onsets and the epoched broadband EEG signals. The final pre-processed dataset comprised the delta band EEG signals during non-outlier trials.

the direction cue the trial was aborted. A participant did not move, if the distance between the cursor and the origin was smaller than a threshold (1 cm). A trial was also aborted, if the threshold was exceeded while the target was still moving, or during the entire COT in the observation condition. Aborted trials were appended to a queue of trials. A total of 360 trials (180 per condition, pseudo randomly distributed) were recorded in 20 runs with short breaks in between. We recorded only 192 trials for participant 1.

2.4. EEG recording

We placed 64 active electrodes (actiCAP, Brain Products GmbH, Gilching, Germany) on the scalp according to the 10–10 system. The reference and ground electrodes were positioned at the right mastoid and AFz, respectively. Six additional active electrodes were placed at the superior, inferior and outer canthi of the right and left eyes to record

electrooculographic (EOG) activity. [Supplementary Fig. 1](#) visualizes the locations of all 70 electrodes. After the electrodes were placed on the scalp, their 3D positions and the positions of anatomical landmarks (nasion, left-/right preauricular points) were recorded with an ultrasound based digitizer (ELPOS, Zebis Medical GmbH, Isny, Germany). EEG and EOG signals were recorded at 1 kHz (BrainAmp, Brain Products GmbH, Gilching, Germany). The paradigm was implemented in Python 2.7 based on the simulation and neuroscience application (SNAP) platform (Kothe, 2012) and the 3D engine Panda3D (Goslin and Mine, 2004). The screen position signals of the visual stimuli (cursor, target) were recorded at 60 Hz. All signals (EEG, EOG and stimuli) were recorded using the lab streaming layer (LSL) protocol (Kothe et al., 2019) and synchronized offline using a photodiode signal, which captured an impulse on the screen at the start of each trial. All signals were then resampled to 200 Hz.

2.5. Pre-processing

The recorded data was analyzed offline using Matlab (Matlab 2015b, Mathworks Inc., Natick, USA) and the open source software EEGLAB (Delorme and Makeig, 2004) version 14.1.1. Fig. 2 outlines the pre-processing pipeline. The EEG signals were high-pass filtered (0.4 Hz cut-off frequency, Butterworth filter, fourth order, zero-phase). Data cleaning was initiated by a spherical interpolation of channels with poor signal quality (visual inspection). We interpolated 2.1 channels on average (Supplementary Table 1). Eye movements and blinks were attenuated by applying the sparse generalized eye artifact subspace subtraction algorithm (Kobler et al., 2020b). The algorithm was fitted to calibration data, recorded during the experimental blocks 2 and 4. The EEG channels were subsequently converted to a common average reference (CAR). We applied the high-variance electrode artifact removal (HEAR) algorithm to attenuate occasional, single electrode pops and low-frequency drifts (Kobler et al., 2019). HEAR monitors the variance of each EEG channel. If the variance increases drastically (e.g., 3 times the variance of calibration data), the probability of an artifact contaminating the signal rises. This artifact probability is then used to weigh the amount of linear interpolation by neighboring channels. Next, a low-pass filter (3.0 Hz cut-off frequency, Butterworth filter, fourth order, zero-phase) was applied to the broadband EEG signals to extract delta band activity, before the signals were resampled at 10 Hz.

The cursor position signal was used to detect the onset of the reaching movements. For each trial, the cursor movement onset was calculated based on the Euclidean distance between the cursor and the origin. A distance equal to 0 corresponded to the origin (i.e., center position), while a distance equal to 1 indicated the position of the circle bounded by the virtual grid (Fig. 1). During the preparation period the distance was not exactly zero because the resting position was controlled by the participant (Fig. 1b). To remove these trial-to-trial fluctuations, we subtracted the average distance during the last second of the preparation period. The first time-point at which the cursor distance exceeded a threshold of 0.05 served as an initial estimate for the movement onset. It was refined using a window that captured the smoothed (moving average finite impulse response filter, triangular window, 63 filter taps, zero-phase) cursor distance of the preceding 1.75 s. For each time-point within the window, the derivative was estimated by computing finite differences. For the time-point with the maximal derivative, we computed the tangent. We defined the time-point at which the tangent intersected with the zero-line along the time axis as the final estimate of the cursor movement onset.

We set the cursor movement offset to the time-point at which the distance between the cursor and final target position became smaller than 0.1 (corresponding to 1.6 cm on the screen). The movement duration was then the difference between the estimated offset and onset. Trials with abnormal movement onset or duration were marked as outliers. Abnormal trials were detected if the cursor movement onset relative to the start of a trial (i.e., target turned yellow) or the movement duration were improbable (i.e., larger than 2.5 standard deviations around the mean). The underlying distribution's mean and standard deviation were computed using robust estimates. In detail, the mean and standard deviation were estimated as the median and 1.4826 times the median absolute deviation among all trials (Leys et al., 2013).

To detect outliers within the EEG signals, we epoched the broadband (0.4–100 Hz) EEG signals according to two alignment cases: start of trial aligned and cursor movement onset aligned. In the start of trial aligned case, we extracted epochs in the [0.75, 4.75] s interval after the start of the trial. Whereas in the cursor movement onset aligned case, we extracted epochs in the [-2, 1.25] s interval around the cursor movement onset. In either case, epochs were marked as outliers if the EEG signal of any channel exceeded a threshold of ± 200 μV or had an abnormal probability, kurtosis or variance (i.e., larger than x standard deviations around the mean across trials, where x equals 6 in the case of probability or kurtosis, and 5 in the case of variance). We applied the joint

probability, kurtosis and variance rejection criteria twice to detect gross outliers in the first iteration, and subtle outliers in the second iteration. Finally, the union of detected outlier epochs was rejected from the low-pass filtered and epoched EEG activity.

2.6. Behavioral analysis

In order to understand behavioural dynamics of the participants and eliminate differences of visual stimuli dynamics across conditions or directions as confounds, we analyzed the cursor movement onsets and movement durations. To identify group level effects of condition (execution, observation) and direction (right, left, up, down) in the cursor movement onset time-points, a two-way repeated measures analysis of variance (ANOVA) was performed. The same two-way repeated measures ANOVA was also performed for the cursor movement duration. For both ANOVAs, we computed Mauchly's tests to identify if the sphericity assumption was violated; q-q-plots were used to inspect if the cursor movement onset and duration followed a Gaussian distribution.

In addition to the reach dynamics, we calculated the onsets of the eye movements. Eye movements typically start with a catch up saccade, as a target stimulus starts moving. To identify the catch up saccade timing, vertical and horizontal EOG derivatives were calculated from the broadband EEG data; the difference between right and left outer canthi was computed for the horizontal EOG derivative, and the difference between left/right superior and inferior electrodes was computed for the vertical EOG left/right derivative. We then computed the average across trials with the same direction. The threshold for the direction specific eye movement onset was the time-point at which the EOG derivative, associated with the direction, exceeded the trial baseline activity (1–1.5 s) by 3 standard deviations.

2.7. Encoding of condition and direction

To identify EEG activity that encodes information about condition and direction, we fitted a general linear model (GLM) to the recordings of each participant. The GLM contained the factors condition, direction and intercept. We split the direction information into two orthogonal factors (horizontal, vertical), equalized the number of trials per condition and direction, and finally z-scored the factors. The factors were identical for all time-points within a trial, and could be expressed as a $4 \times n_{\text{trials}}$ matrix S

$$S = [s_{\text{cond}}; s_{\text{dir,horz}}; s_{\text{dir,vert}}; 1] \quad (1)$$

with $1 \times n_{\text{trials}}$ vectors s_{cond} , $s_{\text{dir,horz}}$ and $s_{\text{dir,vert}}$ coding the factors and a constant intercept term. For each time-point i , the GLM can be defined as

$$X^{(i)} = A^{(i)} S + E^{(i)} \quad (2)$$

with an $n_{\text{channels}} \times n_{\text{trials}}$ matrix $X^{(i)}$ reflecting the EEG activity, an $n_{\text{channels}} \times 4$ matrix $A^{(i)}$ reflecting the regression coefficients and an $n_{\text{channels}} \times n_{\text{trials}}$ matrix $E^{(i)}$ containing the residuals which are assumed to follow a Gaussian distribution. The regression coefficients for the intercept term correspond to the average across all trials. The least squares estimate of $A^{(i)}$ is

$$\hat{A}^{(i)} = C_{XS}^{(i)} \cdot C_{SS}^{-1} \quad (3)$$

with an $n_{\text{channels}} \times 4$ cross-covariance matrix $C_{XS}^{(i)}$ between the pre-processed EEG activity and the predictors, and a 4×4 covariance matrix C_{SS} between the factors. We used analytical shrinkage regularization to estimate C_{SS} (Schäfer and Strimmer, 2005). The predicted EEG activity is then

$$\hat{X}^{(i)} = \hat{A}^{(i)} S \quad (4)$$

Given (2) and (4), the residuals $E^{(i)}$ are

$$E^{(i)} = X^{(i)} - \hat{X}^{(i)} \quad (5)$$

We used them to inspect if the GLM assumptions were met. In detail, we plotted the residuals of each channel against the predicted feature activity $\hat{X}^{(i)}$ to check whether the homoscedasticity and linearity assumptions of the GLM were met; q-q-plots were used to check if the residuals followed a Gaussian distribution.

2.8. EEG source imaging

We applied EEG source imaging (Michel et al., 2004) to map the EEG signals from the channels to the cortical surface and, thereby, ease neurophysiological interpretation. We used the ICBM152 template boundary element (BEM) head model (Fonov et al., 2011). The BEM comprised three layers (cortex, skull, scalp) with relative conductivities (1, 0.008, 1). The cortex layer was modeled with 5011 voxels. We co-registered the BEM and the digitized EEG electrode positions (Supplementary Fig. 1b) using the three anatomical landmarks (nasion, left and right preauricular points). To compensate deviations between participant and template anatomy, we finalized the co-registration by projecting floating electrodes to the scalp layer. OpenMEEG (Gramfort et al., 2010) was used to compute the forward model for 15033 sources (3 sources per voxel) on the cortical surface. sLORETA (Pascual-Marqui, 2002) was used to estimate the inverse solution. To reduce the effect of sensor noise in the inverse solution, 3 min of resting data (similar preprocessing as the reaching data; recorded during experimental blocks 2 and 4) were used to estimate a sensor noise covariance matrix (shrinkage regularization with 10% of the average eigenvalue).

After we projected the subject specific EEG signals to the cortical surface, we normalized them by the global field power (GFP) (Kobler et al., 2020a). We estimated the GFP by randomly selecting a sample from each trial, averaging these samples, and computing the standard deviation across sources. This procedure was repeated 10,000 times. The final subject-specific GFP estimate was set to the median of the 10,000 repetitions. After GFP normalization, we computed group level averages of the activity and regression coefficients on the cortical surface.

We tested the regression coefficients for significant group level activation using permutation tests (Maris and Oostenveld, 2007; Nichols and Holmes, 2002). We used 10,000 permutations to obtain a random distribution. In each permutation, we randomly sign flipped the regression coefficients of the participants before the group averages of the 15,033 sources were computed and the norm for each of the 5011 voxels was extracted. A voxel's p value was then set to the percentage of random voxel norms that were larger than the observed voxel norm.

To reduce the number of tests and obtain a single representation for the direction factor, we added the voxel norms of the regression coefficients associated with the horizontal and vertical factors. This allowed us to identify voxels that code information about the vertical and/or horizontal factor. For the tests we considered the time-points within the interval spanned by the cue associated with each factor (i.e., condition cue for the condition factor) and the cursor movement offset. The number of tests was $461,012 = 3$ (factors) * 2 (alignments) * 5011 (voxels) * 15.3 (average number of time-points).

We also investigated differences in the encoding of direction between the conditions in 8 regions of interest (ROIs) along the dorsal reaching system (Gallivan and Culham, 2015). The ROIs are displayed in Fig. 5a; they covered parieto-occipital cortex (PO), superior parietal lobule (SPL), premotor cortex (PM) and primary sensorimotor cortex (SM1) of both hemispheres. Before the differences were computed and averaged across participants, each voxel's norm was extracted. In doing so, we identified voxels which encoded more directional information in one condition, irrespective of the participants' dipole orientations. We used two-sided,

permutation (10,000), paired t-tests to identify significant differences. The number of tests was $16 = 8$ (ROIs) * 2 (alignments). We controlled the false discovery rate (FDR) at a significance level of 0.05 for a total of 461,028 tests (Benjamini and Yekutieli, 2001).

2.9. Classification of condition and direction

We used the pre-processed EEG signals to classify conditions (execution vs. observation) using two-class shrinkage regularized linear discriminant analysis (sLDA) (Blankertz et al., 2011). sLDA is an optimal classifier in the sense that it minimizes the classification error, if the features follow a Gaussian distribution and have the same covariance matrix for all classes. Blankertz et al. showed that these two assumptions typically hold for event-related potential data (Blankertz et al., 2011). The pre-processed EEG signals were split into train and test sets using a leave-one-trial-out cross-validation (CV) scheme. In this scheme, if N is the number of trials, the classifier was trained on N-1 trials, and tested on the held-out trial. The process was repeated over the N folds, so that each trial was tested once.

We fitted and evaluated a classifier for each time-point using two approaches: single time-point and windowed. In the single time-point approach, we classified the activity of the 64 EEG channels, while in the windowed approach we classified the activity of the 64 EEG channels at the current and 5 preceding time-points (64 channels x 6 time-points = 384 features). We computed classification accuracies to summarize the performance on the held-out test sets.

For a balanced, two-class problem with an infinite amount of trials, the theoretical chance level constitutes 50%. Due to the limited number of trials, we estimated the significance level through a shuffling approach. In 1000 repetitions, we randomly permuted class labels across trials and applied the same leave-one-trial-out CV scheme. We set the significance level to the 95 percentile of the test set classification accuracies.

We further sought to determine if directional information can be decoded from low frequency time domain EEG signals. For this purpose, we fitted a 4-class sLDA classifier to discriminate between directions (up, right, down, left). We applied the same leave-one-trial-out CV scheme as for the condition classifier. To identify interaction effects, we repeated the direction classification for each condition.

We used permutation tests to identify significant group level effects (Maris and Oostenveld, 2007; Nichols and Holmes, 2002). As before, we tested time-points within the interval spanned by the cue associated with each factor (i.e., condition cue for the condition factor) and the cursor movement offset. We first tested if the observed classification accuracies were significantly different from chance, by computing one-sided, permutation (10,000 permutations), paired t-tests between the observed accuracies and the participant specific significance threshold (95 percentile of the shuffling results). The number of tests was $106 = 4$ (condition, direction, direction (exe), direction (obs)) * 2 (alignment) * 13.3 (average number of time-points). Next, we used two-sided, permutation (10,000 permutations), paired t-tests to test if the direction classification accuracy was significantly different between the conditions. The number of tests was $24 = 2$ (alignment) * 12 (time-points). Finally, we computed two-sided, permutation (10,000 permutations), paired t-tests to identify differences in the peak classification accuracy between the two types of alignments (start of the trial, cursor movement onset) in both conditions (2 tests). The total number of tests was 132. We controlled the false discovery rate at a significance level of 0.05 (Benjamini and Yekutieli, 2001).

3. Results

3.1. Behavioral results

The distribution of cursor movement onsets and offsets are presented in Fig. 3a,e and Supplementary Figs. 2 and 3. The grand average cursor

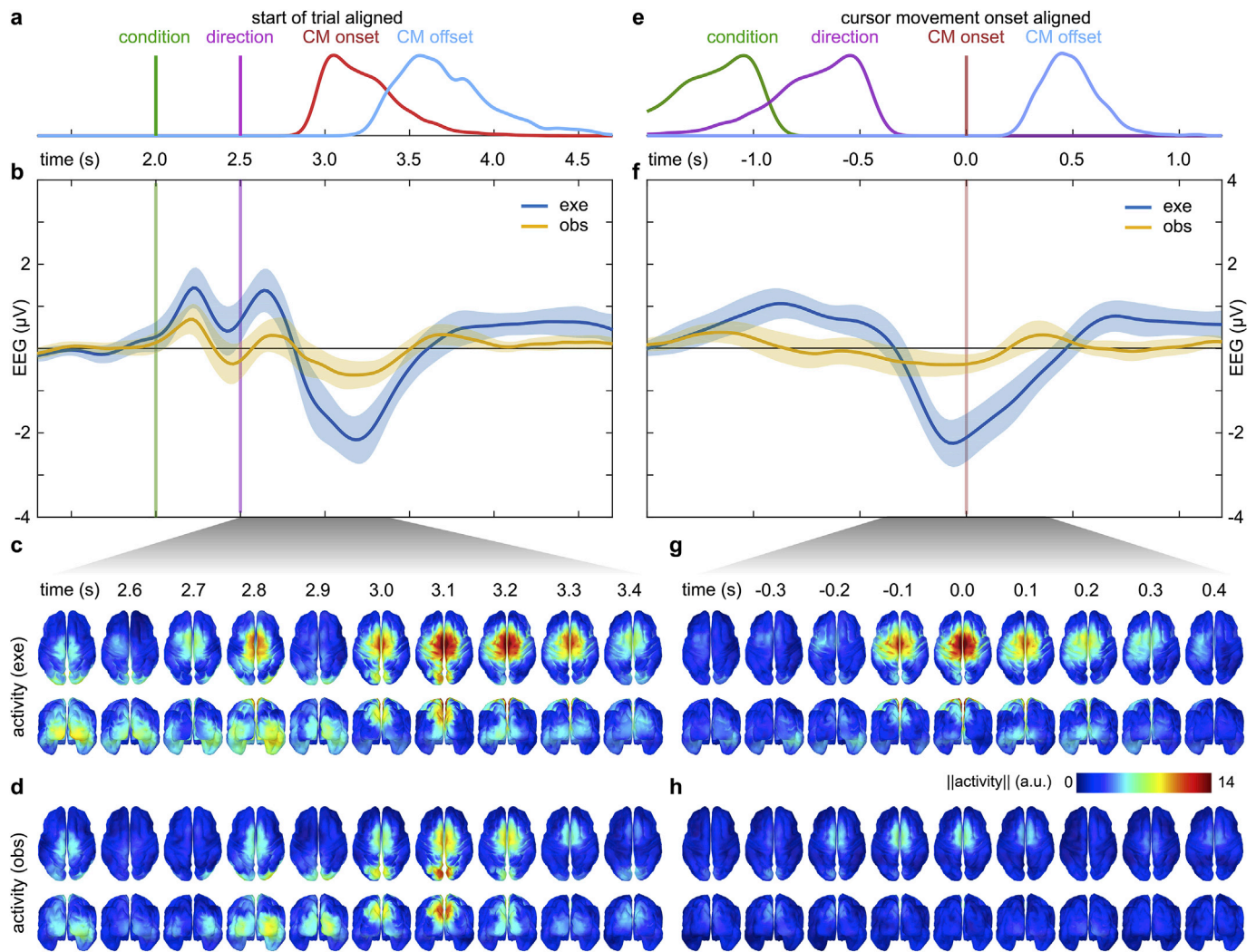


Fig. 3. Condition specific grand average activity in channel and source space for start of trial aligned (left) and cursor movement aligned (right) data. **a**, Distribution of the cues and cursor movement (CM) onsets/offsets for start of trial aligned data ($t = 0$ s). A Gaussian smoothing kernel (0.04 s bandwidth) was used to estimate the probability density from all trials and participants. The participant level distributions are summarized in [Supplementary Fig. 2](#). **b**, Grand average MRCP for start of trial aligned data at channel C1. The conditions are color-coded. Shaded areas summarize the confidence interval of the mean across participants. **c**, Grand average source space activity for execution condition and time-points around the average cursor movement onset ($t = 3.2$ s). **d**, As in **c** for observation condition. **e-h**, As in **a-d** for cursor movement onset aligned data ($t = 0$ s).

movement onset with respect to the start of a trial was 3.23 s (0.18 s SD) and the mean cursor movement duration with respect to cursor movement onset was 0.49 s (0.13 s SD). The cursor movement onset and duration were approximately normally distributed across participants. For the cursor movement onset, Mauchly's test indicated that the assumption of sphericity had neither been violated for direction ($W = 0.73$, $p > 0.05$) nor the interaction of direction and condition ($W = 0.87$, $p > 0.05$). For the cursor movement duration, the assumption of sphericity had neither been violated for direction ($W = 0.52$, $p > 0.05$) nor the interaction of direction and condition ($W = 0.71$, $p > 0.05$). The two-way repeated measures ANOVA showed no significant main effect of condition on the cursor movement onset ($F = 3.43$, $p = 0.085$, $df = 1$) and on the cursor movement duration ($F = 1.29$, $p = 0.27$, $df = 1$). There was also no significant main effect of direction on the cursor movement onset ($F = 1.58$, $p = 0.208$, $df = 3$). We identified a significant main effect of direction on the cursor movement duration ($F = 4.99$, $p = 0.047$, $df = 3$). There was no significant interaction effect between condition and direction on the cursor movement onset ($F = 1.09$, $p = 0.365$, $df = 3$) and on the cursor movement duration ($F = 0.56$, $p = 0.643$, $df = 3$).

To further investigate the main effect of direction on the cursor movement duration, post-hoc pairwise t-tests with Bonferroni correction

were performed. The mean cursor movement durations were 0.48 s (0.09 s SD) for the right direction, 0.51 s (0.10 s SD) for the left direction, 0.48 s (0.08 s SD) for the up direction and 0.49 s (0.09 s SD) for the down direction. The post-hoc tests revealed a significant difference in movement duration between the right and left directions ($p = 0.0053$), with a difference in means of 0.03 s. Despite the significant difference, the effect size remains small. We concluded that condition had no effect on the cursor dynamics, and direction had a negligible effect on the cursor movement duration.

Regarding eye movement behavior, the average time for a catch-up saccade to take place was 2.69 s (0.06 s SD). Since the target started to move 2.5 s after the start of a trial, it means that it took on average 190 ms for the eyes to catch up with the moving target. This result is in line with the typical timing of catch-up saccades (Purves et al., 2004).

3.2. Movement-related cortical potentials

To compare time-domain amplitude modulations in execution and observation conditions, we computed grand average MRCPs for channel C1 for start of trial aligned data and cursor movement onset aligned data (Fig. 3b,f). In addition to the MRCP, we also compared the source space

activity in either condition for selected time points around the cursor movement onset (Fig. 3c,d,g,h).

Looking at the results for the start of trial alignment (left panel in Fig. 3), the activity before the condition cue at 2.0 s is fluctuating around 0 μV (Fig. 3b). Following the condition cue at 2.0 s and the direction cue at 2.5 s, there are pronounced visually evoked potentials (VEPs) originating in occipital areas (Fig. 3c and d). After the second VEP, we observed an MRCP in execution condition, with a steep negative amplitude deflection (Fig. 3b) peaking in negativity at the average cursor movement onset ($-2.3 \mu\text{V}$ at 3.2 s). There was also a smaller but noticeable negative amplitude deflection in the observation condition ($-0.7 \mu\text{V}$ at 3.2 s). As expected, the execution condition-specific MRCP led to a stronger activation in contralateral and central motor areas (Fig. 3c) in comparison to the observation condition (Fig. 3d).

For the cursor movement onset alignment (right panel in Fig. 3), the cue-locked VEP effects faded at channel C1 (Fig. 3f). Within the interval -1.0 s to -0.5 s, we observed a positivity in the execution condition.

Starting at -0.4 s, there was a prominent MRCP in the execution condition. At channel C1, the MRCP amplitude peaked with a value of $-2.3 \mu\text{V}$ at -0.1 s, corresponding to 100 ms before the cursor movement onset (Fig. 3f). The negativity was generated in contralateral and central motor areas (Fig. 3g). In the observation condition, the activation in central motor areas was considerably lower (Fig. 3h). Generally, and as expected, the MRCP related to the hand movement initiation (execution condition) was phase-locked to the cursor movement onset.

3.3. Cortical sources encoding condition and direction

We used a GLM and EEG source imaging to identify cortical sources encoding information about the condition and direction. The residuals of the GLM generally followed a normal distribution and indicated that the homoscedasticity and linearity assumptions were fulfilled. Fig. 4 displays voxels with significant regression coefficients for the factors intercept, condition and direction.

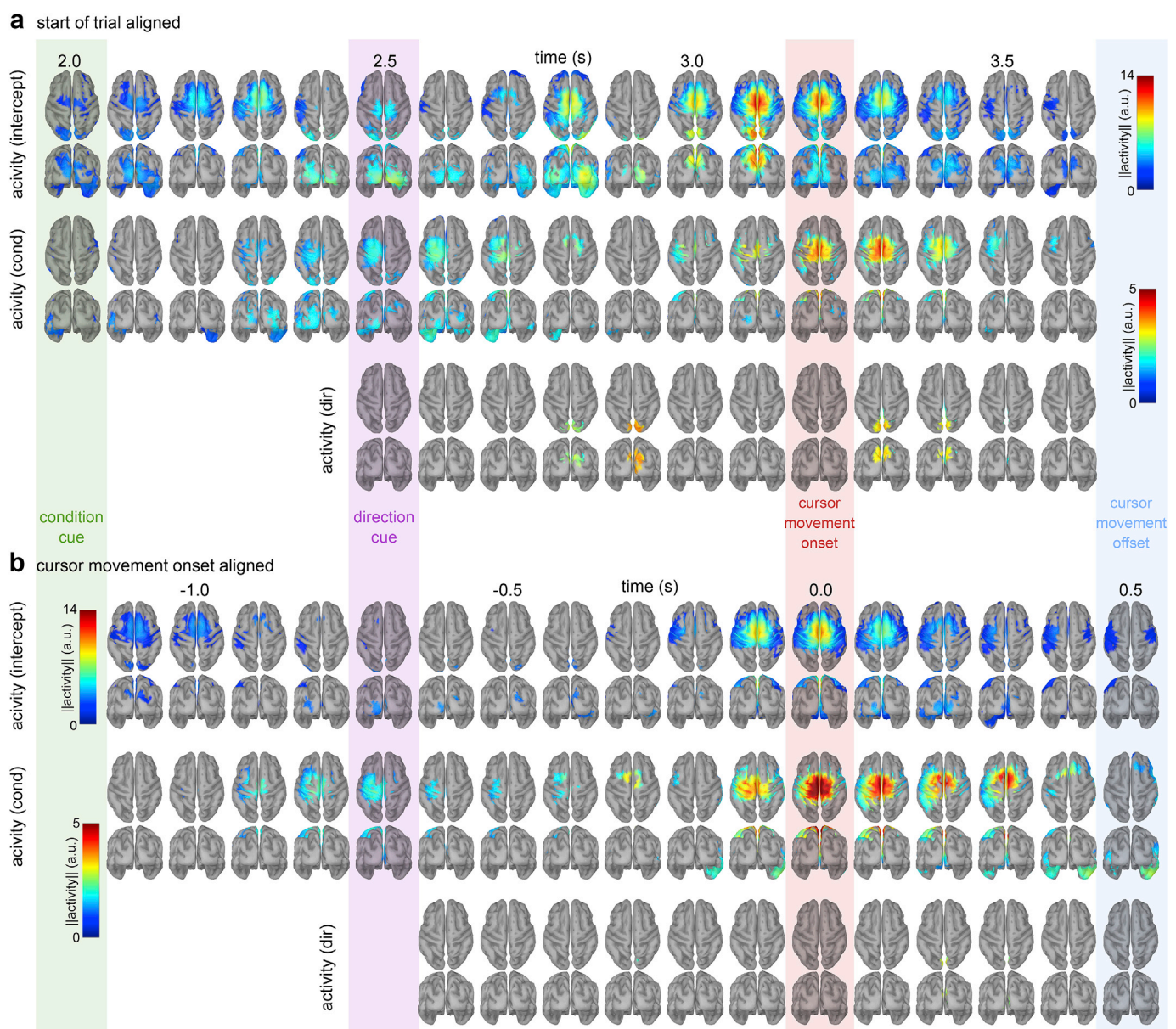


Fig. 4. Grand average source space condition and direction factor encoding results for start of trial aligned (a) and cursor movement onset aligned (b) data. Each plot states the regression coefficients of the linear encoding model at the voxel level. I.e. the activity that is explained by each factor (intercept, condition, direction). The rows summarize the factors and the columns the time-points. Only voxels with significant group level regression coefficients are shown (one-sided permutation tests, critical p -value = 0.0004, FDR corrected).

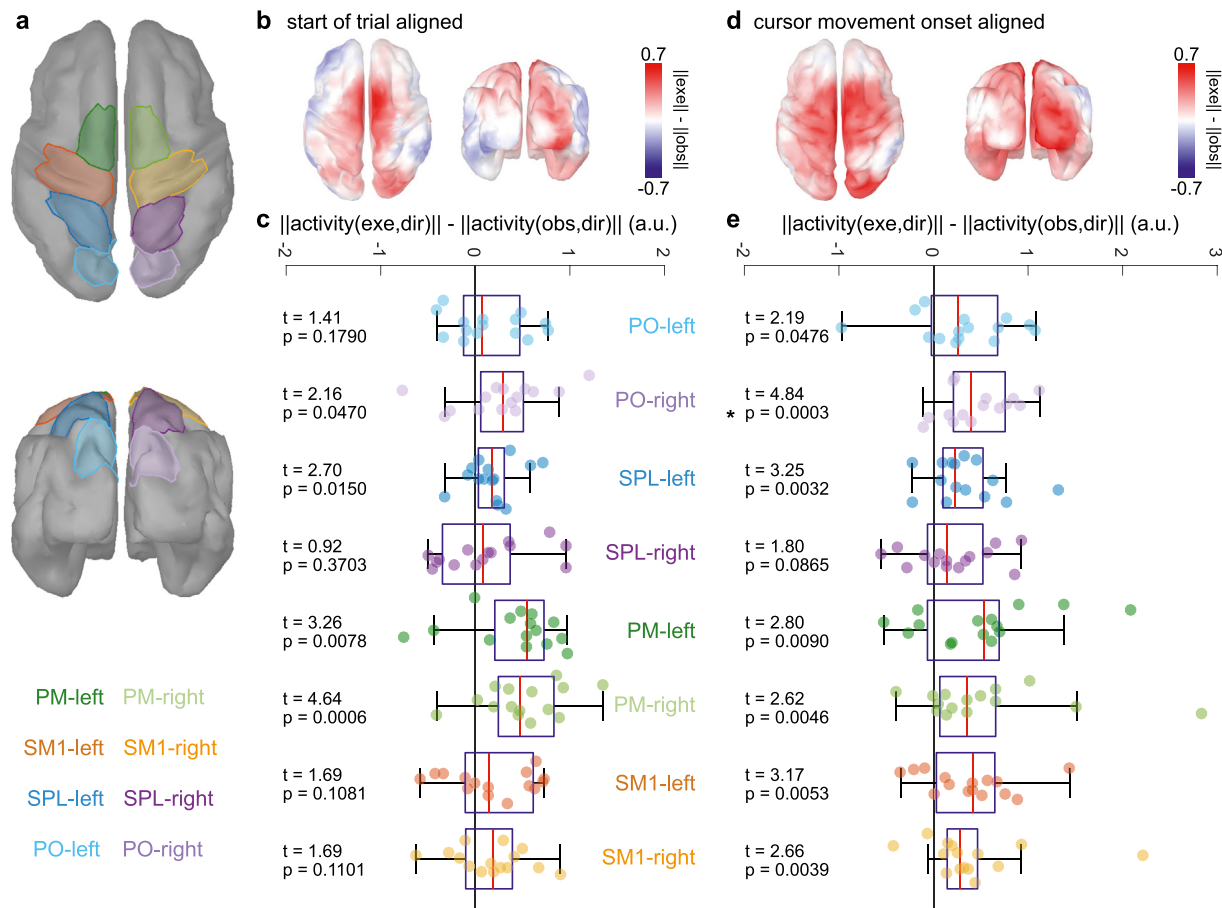


Fig. 5. Condition-specific direction encoding around the cursor movement onset. **a**, Regions of interest (ROIs). The ROIs covered parieto-occipital cortex (PO), superior parietal lobule (SPL), primary sensorimotor cortex (SM1) and premotor cortex (PM) of both hemispheres. **b**, Start of trial alignment. Grand average difference in direction-related activity between execution and observation condition. The average within the interval $t = [2.9, 3.4]$ s is displayed. Before the differences were computed and averaged across participants and time-points, each voxel's norm was extracted. As a result, voxels which encoded more directional information in one condition, irrespective of the participants' dipole orientations were identified. Red voxels indicate stronger direction related activity in the execution condition. **c**, Boxplots summarizing **b** at ROI level. Each boxplot displays the difference in direction related activity. The ROIs are color coded. Each dot marks the result of one participant. Two-sided, permutation, paired t-tests did not reveal significant differences (critical p-value = 0.0004, FDR corrected). **d-e** As in **b-c** for cursor movement onset alignment and the interval $t = [-0.3, 0.3]$ s. Significant differences are highlighted (*).

The intercept term corresponds to the grand average activity across all trials. For the start of trial alignment, it is equivalent to the average of Fig. 3c and d. We observed significant group level activations in occipital, parieto-occipital and sensorimotor areas (Fig. 4a, top row). Interpreting the intercept term is not straightforward. If there is no condition- or direction-related activity, the intercept indicates activity that is common across all trials. At $t = 3.1$ s, for example, the significant intercept term for voxels in parieto-occipital areas was due to similar activation in both conditions (Fig. 3c and d). If there are condition and/or direction-related effects, the intercept term represents the average. For example, at $t = 0.0$ s in the case of cursor movement onset alignment, the intercept (Fig. 4b, top row) and condition (Fig. 4b, middle row) terms of voxels in medial central sensorimotor areas were significant. In this case, the intercept does not reflect common neural activity; it is simply the average of both conditions (Fig. 3g and h).

For the start of trial aligned condition factor (Fig. 4a, middle row), we observed significant voxel activity in contralateral sensorimotor areas from 2.3 s (300 ms after the condition cue) to 2.7 s, and from 3.0 s to 3.6 s. In the interval 3.1 s–3.4 s the activity intensified in central sensorimotor areas with a peak close to the average cursor movement onset ($t = 3.2$ s). We additionally observed significant activity in occipital and parietal areas in the interval 2.0 s–2.8 s. For the cursor movement onset alignment (Fig. 4b, middle row), we also observed condition related activity in sensorimotor areas. The activity peaked in central

sensorimotor areas at the cursor movement onset ($t = 0.0$ s). We did not observe significant activity in occipital and parietal areas. Comparing the sensorimotor activity between the start of trial (Fig. 4a, middle row, $t = 3.2$ s) and cursor movement onset (Fig. 4b, middle row, $t = 0.0$ s) alignments, we observed a stronger effect of condition in the cursor movement onset alignment. This suggests that the sensorimotor activity, generating the hand MRCP, had a stronger phase-locking to the cursor movement onset.

For the start of trial aligned direction factor (Fig. 4a, bottom row), we observed significant voxel activity in parieto-occipital areas from 2.8 s to 2.9 s, corresponding to 300 ms–400 ms after the direction cue and 100 ms–200 ms after the average eye movement onset. The parieto-occipital cortex was again significantly activated from 3.2 s to 3.3 s, corresponding to 0 ms–100 ms after the average movement onset and 300 ms–400 ms after the target stimulus reached its final location. For the cursor movement onset aligned direction factor (Fig. 4b, bottom row), we did not observe significant activity. The lack of significant activity in the cursor movement onset alignment indicates that the parieto-occipital activity was phase-locked to the start of trial alignment.

3.4. Differences in direction encoding

We also investigated if the encoding of directional information varied between conditions. We observed a tendency that areas along the dorsal

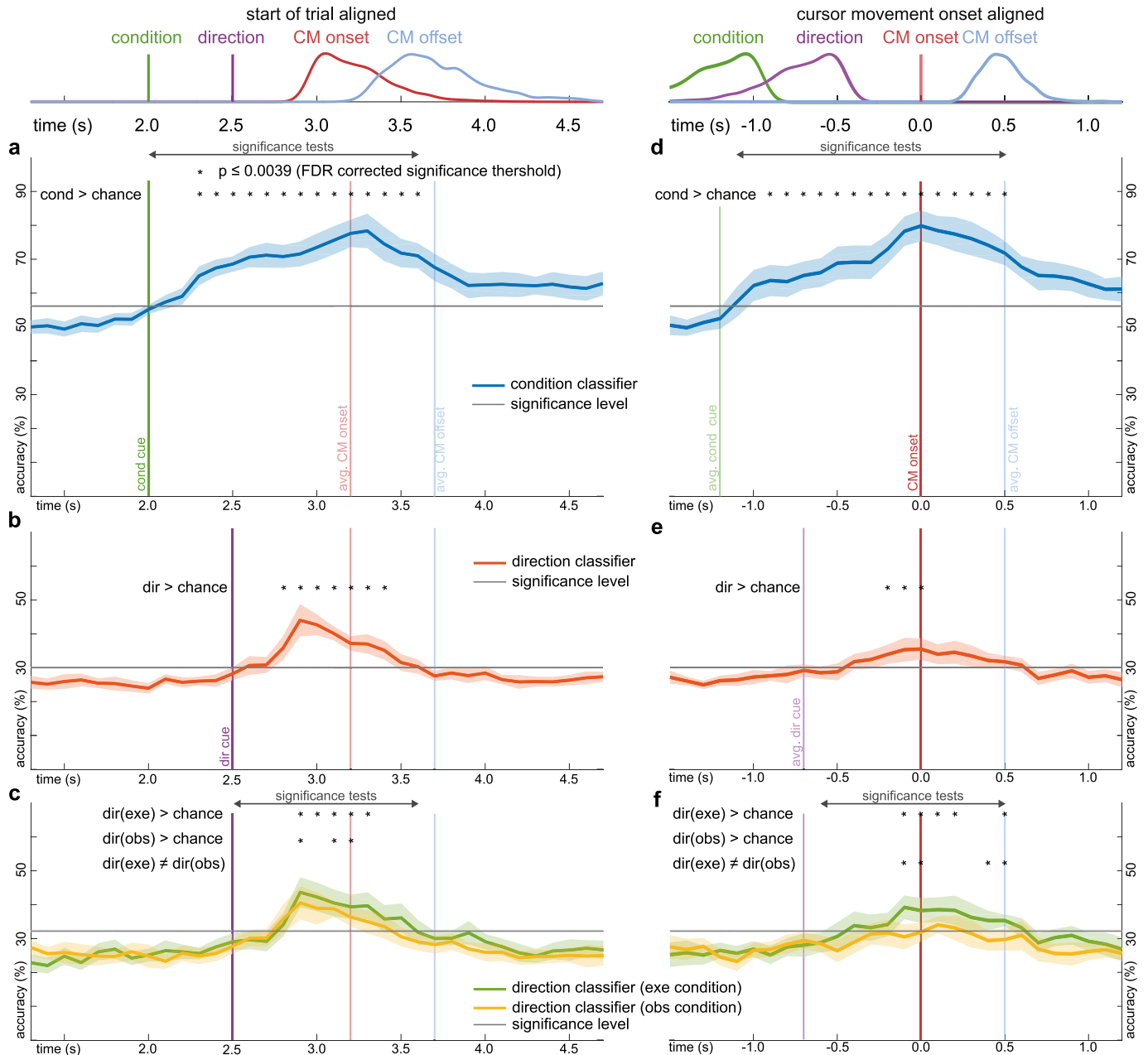


Fig. 6. Grand average condition and direction classification accuracy curves. For each time-point, an sLDA classifier was fit in a cross-validation scheme to predict condition or direction from the EEG channels. All plots show the grand average test set accuracies and their confidence intervals across participants. **a**, Condition (exe vs. obs) classification accuracy curve for start of trial aligned data. To identify significant group level effects, we computed one-sided permutation paired t-tests (critical p value = 0.0039, FDR corrected) between the test set accuracies (blue) and participant specific significance levels (gray). Significant differences are highlighted (*). **b**, As in **a** for direction (right vs. up vs. left vs. down) classification accuracy curves. **c**, Condition specific direction classification accuracy curves. In addition to one-sided tests against the significance level, we computed two-sided permutation paired t-tests between the exe and obs specific accuracy curves to identify significant interaction effects between condition and direction. **d-f**, As in **a-c** for cursor movement onset aligned data.

stream encoded more information around the cursor movement onset in the execution condition (Fig. 5b,d). For the start of trial alignment (Fig. 5b and c), we observed a weak effect in PM of both hemispheres ($t_{\text{left}} = 3.3$, $t_{\text{right}} = 4.6$); the effect did not turn significant at the ROI level (Fig. 5c). For the cursor movement onset alignment, all ROIs tended to encode slightly more directional information (Fig. 5e). The *t*-test results were not significant (except for PO-right) because of considerable variance across participants compared to the mean difference. This suggests that EEG delta band activity that originated in sensorimotor areas tended to encode more directional information in the execution condition. The size of the effect (mean difference between conditions ≤ 0.7) for the activity in sensorimotor areas was small and less consistent across

participants compared to the parieto-occipital activity present in both conditions (Fig. 4a, bottom).

3.5. Single time-point condition and direction classification

Fig. 6 shows accuracy curves (condition, direction) for single time-point classifiers and both alignment methods. We compared accuracy curves with the significance levels to identify group level effects (Fig. 6a-c,d-f), while we identified interaction effects (condition \times direction) by comparing direction classifier accuracy curves across conditions (Fig. 6c,f).

The condition classifier accuracy curves for start of trial (Fig. 6a) and

cursor movement onset aligned data (Fig. 6d) crossed the significance level threshold of 56.0% (0.6% SD) following the condition cue. The start of trial aligned accuracy reached its peak of 78.4% (9.2% SD) around the average cursor movement onset ($t = 3.3$ s); the cursor movement onset aligned peak was 79.8% (8.2% SD) at $t = 0.0$ s. In either alignment, the accuracy declined within 1 s after the peak and eventually plateaued. We observed significant group level accuracies from 2.3 s to 3.6 s for start of trial (Fig. 6a) and from -0.9 s to 0.5 s for cursor movement onset aligned data (Fig. 6d).

In Fig. 6b,e, we show accuracy curves for direction classifiers that were fit to distinguish between the four movement directions (right, up, left, down) irrespective of condition. We obtained significant group level effects for both alignments (Fig. 6b,e). The accuracies exceeded the significance level of 30.0% (0.46% SD) from 2.8 s to 3.4 s for start of trial (Fig. 6b), and from -0.2 s to 0.0 s for cursor movement onset aligned data (Fig. 6e). For each type of alignment, the accuracy peaked at 44.0% (8.6% SD) at 2.9 s and 35.5% (5.7% SD) at 0.0 s, respectively.

Lastly, we report direction classifier accuracy curves for each condition (Fig. 6c,f). We compared the group level averages with a significance level of 32.3% (0.8% SD) in execution and 32.0% (0.8% SD) in observation condition. For start of trial aligned data (Fig. 6c), the execution condition curve was above the significance level from 2.9 s to 3.3 s, while the observation condition curve was significant at 2.9 s, 3.1 s and 3.2 s. There was no significant difference between conditions (two-sided

permutation paired t-tests, $\text{dir}(\text{exe}) \neq \text{dir}(\text{obs})$). That is, there was no interaction effect. For cursor movement onset aligned data (Fig. 6f), the curves in observation condition were not significant, while in execution condition we observed significant accuracies from -0.1 s to 0.2 s and at 0.5 s. There was also a significant difference between conditions at similar time-points (two-sided permutation paired t-tests, $\text{dir}(\text{exe}) \neq \text{dir}(\text{obs})$). These results suggest that direction could be inferred from the EEG delta band activity for start of trial aligned data irrespective of condition (Fig. 6c). Whereas for cursor movement onset aligned data, information about direction could be inferred only in execution condition (Fig. 6f).

3.6. Start of trial alignment vs. cursor movement onset alignment

We used the windowed classification approach to investigate the effect of alignment on direction classification in execution condition. Fig. 7a,d shows the accuracy curves for both alignment types. The windowed classifiers achieved peak accuracies of 55.9% (8.6% SD) at 3.4 s (0.2 s SD) for the start of trial and 50.6% (7.5% SD) at 0.3 s (0.3 s SD) for the cursor movement onset aligned data. The confusion matrices for the peak accuracies indicate no bias towards one of the 4 directions for the start of trial alignment (Fig. 7f) and a small bias towards rightward movements for cursor movement onset alignment (Fig. 7f). We observed significantly higher peak accuracies for the start of trial alignment than

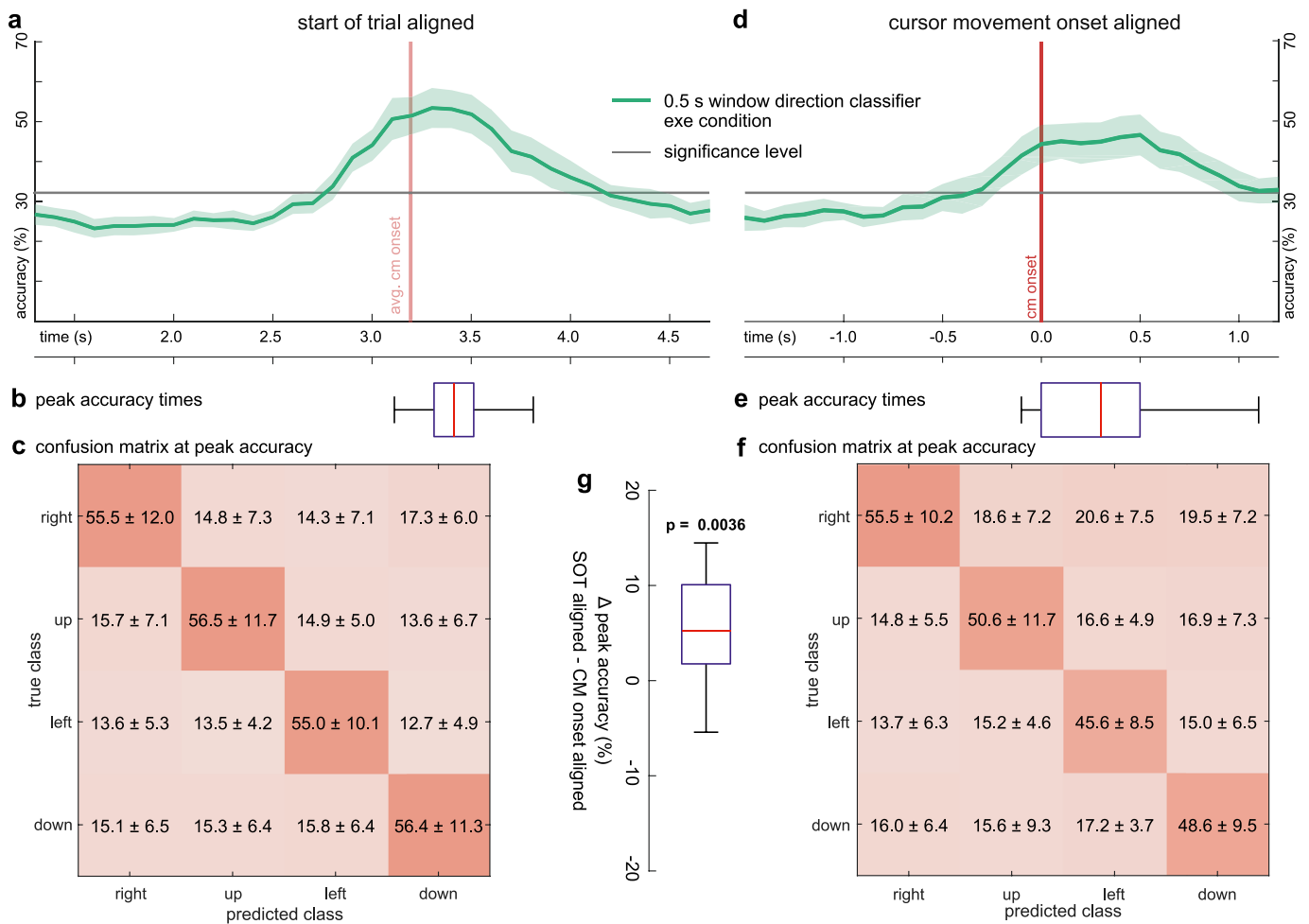


Fig. 7. Execution condition. Effect of alignment on direction classification accuracy. For each time-point, an sLDA classifier was fit to predict the direction from EEG activity at the current and 5 preceding time-points (windowed classification). **a**, Windowed classification accuracy curve for start of trial aligned data. Shaded areas indicate the confidence interval across participants. **b**, Boxplot summarizing the participants' peak accuracy time-points. **c**, Confusion matrix at the peak accuracy. **d-f**, As in **a-c** for cursor movement onset aligned data. **g**, Boxplot summarizing the paired difference in peak accuracy between the two alignments. The start of trial aligned peak accuracy was significantly higher than the cursor movement aligned one ($p = 0.0036$, critical p -value = 0.0039, FDR correction for 132 tests).

for the cursor movement onset alignment (Fig. 6g, average Δ peak accuracy 5.3%, $p = 0.0036$, two-sided, permutation, paired t -test). This result suggests that the representation of movement direction within delta band EEG activity was more consistent across trials if the data was aligned to the cues, rather than to the cursor (hand) movement onset. The same holds true for the observation condition (Supplementary Fig. 4).

4. Discussion

We have studied the relation of MRCPs and directional information in the EEG delta band activity during center-out reaching movements. Our results indicate that delta band amplitude modulations carry significantly more directional information phase-locked to the direction cue compared to the cursor movement onset. This suggests a functional dissociation between the network generating the MRCP in the execution condition (movement initiation) and the network processing directional information (movement preparation). In addition to the functional dissociation, we observed a spatial separation. The network generating the hand movement-related MRCP in the execution condition comprised contralateral and central sensorimotor areas, while the network processing directional information in both conditions comprised medial parieto-occipital areas.

In the start of trial alignment case, we could infer directional information in both conditions, suggesting an effector (hand, eye) independent representation that was consistently expressed in medial parieto-occipital cortex. We found significant direction related activation 300–400 ms after the direction cue and again 300–400 ms after the target reached its final location (Fig. 4a, bottom row). This is in agreement with the results obtained from the PTT (Kobler et al., 2018). Using a regression approach to decode directional kinematics (position and velocity) we found that the medial parieto-occipital areas encoded directional information in both conditions. The medial parieto-occipital cortex in humans is functionally equivalent to V6/V6A in non-human primate areas (Pitzalis et al., 2015). V6 (Pitzalis et al., 2006) and V6A (Tosoni et al., 2015) have a retinotopic organization in humans and are active in reaching and eye movements (Fabbri et al., 2010; Fernandez-Ruiz et al., 2007; Filimon et al., 2009; Magri et al., 2019). It is, therefore, unlikely that the direction related activity in the parieto-occipital cortex simply reflects visually evoked potentials.

For the cursor movement onset aligned data, significant directional information was present from -100 to 200 ms in the execution condition (Fig. 6f), suggesting a hand movement specific representation around the cursor movement onset. We did not observe a consistent group level representation of direction on the cortical surface during this interval (Fig. 4b, bottom row). If the voxels' dipole orientations were allowed to vary across participants, we observed slightly higher direction related activity in sensorimotor areas in execution condition in contrast to observation condition (Fig. 5d and e). This suggests that hand movement specific directional information, originating in sensorimotor areas, was present in the delta band EEG signals and that its encoding varied across participants. Other studies reported significant SM1 activity during center-out movements (Bradberry et al., 2010; Waldert et al., 2008). If single or few joint movements are used to control the cursor movement, then muscle activity and direction are strongly correlated. Since, SM1 has a somatotopic organization, different joint movements are spatially separated and a classifier can extract this information from EEG activity (Ofner et al., 2017). Despite that there is clear evidence from invasive studies that directional information is present in SM1 (Ball et al., 2009; Georgopoulos et al., 1982; Mehring et al., 2003). However, the spatial distribution of preferred directions of SM1 neurons is approximately random (Amirikian and Georgopoulos, 2000; Ben-Shaul et al., 2003). Hence, the probability of observing direction related effects at an electrode becomes lower as the number of neurons, contributing to the potential at the electrode, increases (Hammer et al., 2016). It is, therefore, unlikely to obtain a strong group-level effect of direction in the EEG activity generated in SM1.

Using the windowed approach to classify directions, we obtained peak accuracies of 55.9% (8.6% SD) for the start of trial alignment. Waldert et al. also investigated the classification of directions from EEG activity for executed hand movements in 4 directions (Waldert et al., 2008). They aligned the data to the movement onset and reported peak classification accuracies of 55.0% (SD 8.4%) 500 ms after the movement onset. Wang and Makeig used a similar paradigm to investigate movement direction in a pilot study (4 participants). They reported that EEG activity originating in PPC could predict direction (left vs. right) 200–300 ms after the direction cue with an accuracy of 80% irrespective of hand, eye or hand + eye movements (Wang and Makeig, 2009). Later (Li et al., 2012), reported an accuracy of 65.4% for the same task with a larger sample (10 participants). Wang et al. also studied a visuomotor center-out task using wrist movements (Wang et al., 2010). They predicted 4 directions from delta band MEG signals, and reported higher classification accuracies if the participants could move immediately after target presentation rather than a forced random delay period. This is in agreement with our finding that significantly higher classification accuracies could be obtained cue aligned compared to movement onset aligned (Fig. 7, Supplementary Fig. 4).

The strongest difference in EEG activity between the two experimental conditions can be attributed to the MRCP related to the hand movement initiation (Fig. 3). The MRCP waveform (Fig. 3f) and cortical activation in central sensorimotor areas (Fig. 3g) in the execution condition agree with previous EEG studies which investigated upper-limb movements (Jochumsen et al., 2013; Ofner et al., 2017). In the observation condition, we observed a slight negativity at electrode C1 (Fig. 3b, f), which was more pronounced for the start of trial alignment ($0.7 \mu\text{V}$) than for the cursor movement onset alignment ($0.2 \mu\text{V}$). The source space activity (Fig. 3d,h) indicates that central sensorimotor areas were also activated in the observation condition, but to a significantly weaker extent than in the execution condition (see condition factor encoding in Fig. 4a and b). The single-lag condition classifiers utilized this difference and reached the highest classification accuracies at the movement onset (Fig. 6a,d). We did not observe a difference in the peak accuracies between the two alignment methods.

In the classification analysis, we observed an interaction effect between the factors condition, direction and alignment. The direction classifiers aligned to the cursor movement onset in the execution condition had significantly higher accuracies around the cursor movement onset than in the observation condition (Fig. 6f). Note that the cursor was not controlled by the participant in the observation condition and, therefore, not task relevant. This could explain why the classification accuracies were at chance level in observation condition (Fig. 6f, yellow curve). The execution condition classification accuracies were significantly higher than chance level, indicating the presence of directional information around the movement onset (Fig. 6f, green curve). As pointed out above, we did not observe a consistent group level encoding of direction in the cortex for the cursor movement alignment; however, we observed a tendency that areas along the dorsal stream encoded more information in the execution condition (Fig. 5d and e). The direction classifiers utilized this participant, execution condition and cursor movement onset specific representations to achieve significant accuracies (Fig. 6f).

Since the participants were moving their eyes and right arm, artifacts could have contaminated the EEG signals. In the EEG delta band corneo-retinal dipole and blink artifacts are the dominating eye artifacts (Keren et al., 2010). Using a state of the art correction algorithm (Kobler et al., 2020b) we could remove their contribution. Supplementary Figs. 7 and 8 show the encoding results without eye artifact correction. As expected, we observed strong direction-related activity at cortical sites closest to the eyes (e.g., prefrontal and anterior temporal areas). After correction, we did not find such artifactual contributions (Fig. 4a and b; Supplementary Figs. 5 and 6). Hence, it is unlikely that eye artifacts contributed to the direction classification results. Regarding movement artifacts, the activity of the shoulder/neck muscles at the start and stop of the arm

movement could have contaminated the EEG during the execution condition. Indeed, activity in inferior temporal sites of the right hemisphere before the cursor movement onset and at the cursor movement offset (Fig. 4a and b; middle rows) could be explained by residual movement artifacts. Alternatively, the activity at these sites could reflect the activity of subcortical brain structures (e.g., cerebellum) that we did not include in our head model. It was recently demonstrated that EEG signals also contain brain activity originating in subcortical regions (Seeber et al., 2019). In either case, the activity was clearly weaker than the central sensorimotor cortex activity. Hence, we think that the hand movement initiation related MRCP mainly contributed to the condition classification.

Studying two experimental tasks could have been another potential limitation. The center-out task was succeeded by the PTT in half the trials. Since we gave the participants time to practice both tasks, and the instructions across tasks were similar, we think that the confounding effects on behavior and EEG activity were negligible. Lastly, despite using state of the art methods to detect the movement onsets from the cursor trajectories, it is not possible to detect the exact onset. This could have introduced jitter that might have attenuated effects phase-locked to the movement onset. To ensure that the jitter was minimal, we visually inspected the automatically detected onsets and fine-tuned the parameters.

In this study, we investigated delta band amplitude modulations during center-out movements. In addition to the MRCPs in the delta band, it is established that the EEG alpha and beta band power in sensorimotor areas change during movements (Pfurtscheller and Lopes Da Silva, 1999). In the last years, it has been shown that these power changes also covary with upper-limb movement rhythmicity (Seeber et al., 2016), Euclidean norm of acceleration (Marty et al., 2018) and direction (Kobler et al., 2020a; Korik et al., 2018). It is not clear whether the delta band amplitude modulations or alpha/beta band power modulations contain more directional information about executed movements. Korik et al. studied a center-out task and reported that movement direction could be decoded with moderate correlations (approx. 0.4) from alpha and beta band power features and with low correlations (approx. 0.15) from delta band amplitude features. In a circular arm movement task, we observed the contrary; movement direction was highly correlated (approx. 0.68) with delta band amplitude modulations, while the correlations with beta band power modulations were moderated (approx. 0.28). A key difference to (Kobler et al., 2020a) is that the participants moved their eyes in this study. Although we corrected for corneo-retinal dipole (CRD) and eyelid artifacts, the eye movements introduce another type of artifact – the saccadic spike potential (SP) (Keren et al., 2010). The SP reflects extraocular muscle activity, whose contribution starts at about 10 Hz and dominates the CRD and eyelid artifacts for frequencies above 20 Hz. The SP artifact also varies with eye movement direction (Keren et al., 2010), which potentially confounds direction decoding results from band-power features. Taken together, further research is required to disentangle the SP artifact and direction related band power changes.

5. Conclusions

Previous behavioral work gave indirect evidence that movement initiation and movement preparation have distinct cortical representations (Haith et al., 2016). We found direct evidence that EEG delta band amplitude modulations carry information about both arm movement initiation and directional processing, as an integral part of movement preparation, and that they are represented in two distinct cortical networks. Information about movement direction was primarily expressed in parieto-occipital area activity and was phase-locked to the direction cue. Whereas information about the arm movement initiation was reflected in the MRCP, a response phase-locked potential, originating in central sensorimotor areas. Despite generating the MRCP, the sensorimotor areas also showed a tendency to encode information about

movement direction; compared to the parieto-occipital area activity, the direction-related activity in sensorimotor areas was less consistent across participants and specific to the execution condition. Using a classification approach, we demonstrated that significantly more information about movement direction can be inferred from the EEG activity for cue aligned data. This finding may prove useful in future non-invasive brain-computer interface designs.

CRedit authorship contribution statement

Reinmar J. Kobler: Formal analysis, Writing - original draft, Writing - review & editing. **Elizaveta Kolesnichenko:** Formal analysis, Writing - original draft, Writing - review & editing. **Andreea I. Sburlea:** Writing - review & editing. **Gernot R. Müller-Putz:** Writing - review & editing.

Acknowledgments

The authors acknowledge Joana Pereira, Catarina Lopes-Dias and Lea Hehenberger for fruitful discussions. This work has received funding from the European Research Council (ERC) under the European Union's Horizon 2020 research and innovation programme (Consolidator Grant 681231 'Feel Your Reach'). E.K. received funding from ERASMUS+ (Erasmus study programme ISCED code 0510).

Appendix A. Supplementary data

Supplementary data to this article can be found online at <https://doi.org/10.1016/j.neuroimage.2020.117076>.

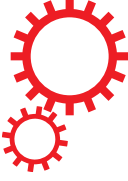
References

- Amirikian, B., Georgopoulos, A.P., 2000. Directional tuning profiles of motor cortical cells. *Neurosci. Res.* 36, 73–79. [https://doi.org/10.1016/S0168-0102\(99\)00112-1](https://doi.org/10.1016/S0168-0102(99)00112-1).
- Ball, T., Schulze-Bonhage, A., Aertsen, A., Mehring, C., 2009. Differential representation of arm movement direction in relation to cortical anatomy and function. *J. Neural. Eng.* 6, 016006. <https://doi.org/10.1088/1741-2560/6/1/016006>.
- Battaglia-Mayer, A., 2018. A brief history of the encoding of hand position by the cerebral cortex: implications for motor control and cognition. *Cerebr. Cortex* 1–16. <https://doi.org/10.1093/cercor/bhx354>.
- Benjamini, Y., Yekutieli, D., 2001. The control of the false discovery rate in multiple testing under dependency. *Ann. Stat.* 29, 1165–1188. <https://doi.org/10.1214/aos/1013699998>.
- Ben-Shaul, Y., Stark, E., Asher, I., Drori, R., Nadasdy, Z., Abeles, M., 2003. Dynamical organization of directional tuning in the primate premotor and primary motor cortex. *J. Neurophysiol.* 89, 1136–1142. <https://doi.org/10.1152/jn.00364.2002>.
- Bierbaumer, N., Elbert, T., Canavan, A., Rockstroh, B., 1990. Slow potentials of the cerebral cortex and behavior. *Physiol. Rev.* 70 (1), 1–41. <https://doi.org/10.1152/physrev.1990.70.1.1>.
- Blankertz, B., Lemm, S., Treder, M., Haufe, S., Müller, K.-R., 2011. Single-trial analysis and classification of ERP components—a tutorial. *Neuroimage* 56, 814–825. <https://doi.org/10.1016/j.neuroimage.2010.06.048>.
- Bradberry, T.J., Gentili, R.J., Contreras-Vidal, J.L., 2010. Reconstructing three-dimensional hand movements from noninvasive electroencephalographic signals. *J. Neurosci.* 30, 3432–3437. <https://doi.org/10.1523/JNEUROSCI.6107-09.2010>.
- Carland, M.A., Thura, D., Cisek, P., 2019. The urge to decide and act: implications for brain function and dysfunction. *Neuroscientist* 25, 491–511. <https://doi.org/10.1177/1073858419841553>.
- Cavina-Pratesi, C., Connolly, J.D., Monaco, S., Figley, T.D., Milner, A.D., Schenk, T., Culham, J.C., 2018. Human neuroimaging reveals the subcomponents of grasping, reaching and pointing actions. *Cortex* 98, 128–148. <https://doi.org/10.1016/j.cortex.2017.05.018>.
- Cisek, P., Kalaska, J.F., 2010. Neural mechanisms for interacting with a world full of action choices. *Annu. Rev. Neurosci.* 33, 269–298. <https://doi.org/10.1146/annurev.neuro.051508.135409>.
- Deeche, L., Scheid, P., Kornhuber, H.H., 1969. Distribution of readiness potential, pre-movement positivity, and motor potential of the human cerebral cortex preceding voluntary finger movements. *Exp. Brain Res.* 7, 158–168. <https://doi.org/10.1007/BF00235441>.
- Delorme, A., Makeig, S., 2004. EEGLAB: an open source toolbox for analysis of single-trial EEG dynamics including independent component analysis. *J. Neurosci. Methods* 134, 9–21. <https://doi.org/10.1016/j.jneumeth.2003.10.009>.
- do Nascimento, O.F., Nielsen, K.D., Voigt, M., 2005. Influence of directional orientations during gait initiation and stepping on movement-related cortical potentials. *Behav. Brain Res.* 161, 141–154. <https://doi.org/10.1016/j.bbr.2005.02.031>.
- Fabbri, S., Caramazza, A., Lingnau, A., 2010. Tuning curves for movement direction in the human visuomotor system. *J. Neurosci.* 30, 13488–13498. <https://doi.org/10.1523/JNEUROSCI.2571-10.2010>.

- Fernandez-Ruiz, J., Goltz, H.C., DeSouza, J.F.X., Vilis, T., Crawford, J.D., 2007. Human parietal "reach region" primarily encodes intrinsic visual direction, not extrinsic movement direction, in a visual-motor dissociation task. *Cerebr. Cortex* 17, 2283–2292. <https://doi.org/10.1093/cercor/bhl137>.
- Filimon, F., Nelson, J.D., Huang, R.-S., Sereno, M.I., 2009. Multiple parietal reach regions in humans: cortical representations for visual and proprioceptive feedback during on-line reaching. *J. Neurosci.* 29, 2961–2971. <https://doi.org/10.1523/JNEUROSCI.3211-08.2009>.
- Fonov, V., Evans, A.C., Botteron, K., Almi, C.R., McKinstry, R.C., Collins, D.L., 2011. Unbiased average age-appropriate atlases for pediatric studies. *Neuroimage* 54, 313–327. <https://doi.org/10.1016/j.neuroimage.2010.07.033>.
- Gallivan, J.P., Culham, J.C., 2015. Neural coding within human brain areas involved in actions. *Curr. Opin. Neurobiol.* 33, 141–149. <https://doi.org/10.1016/j.conb.2015.03.012>.
- Georgopoulos, A.P., Kalaska, J.F., Caminiti, R., Massey, J.T., 1982. On the relations between the direction of two-dimensional arm movements and cell discharge in primate motor cortex. *J. Neurosci.* 2 (11), 1527–1537. <https://doi.org/10.1523/JNEUROSCI.02-11-01527.1982>.
- Goslin, M., Mine, M.R., 2004. The Panda3D graphics engine. *Computer* 37, 112–114. <https://doi.org/10.1109/MC.2004.180>.
- Gramfort, A., Papadopoulos, T., Olivi, E., Clerc, M., 2010. OpenMEEG: opensource software for quasistatic bioelectromagnetics. *Biomed. Eng. Online* 9. <https://doi.org/10.1186/1475-925X-9-45>.
- Gu, Y., Dremstrup, K., Farina, D., 2009. Single-trial discrimination of type and speed of wrist movements from EEG recordings. *Clin. Neurophysiol.* 120, 1596–1600. <https://doi.org/10.1016/j.clinph.2009.05.006>.
- Haith, A.M., Pakpoor, J., Krakauer, J.W., 2016. Independence of movement preparation and movement initiation. *J. Neurosci.* 36, 3007–3015. <https://doi.org/10.1523/JNEUROSCI.3245-15.2016>.
- Hammer, J., Pistohl, T., Fischer, J., Kršek, P., Tomášek, M., Marušić, P., Schulze-Bonhage, A., Aertsen, A., Ball, T., 2016. Predominance of movement speed over direction in neuronal population signals of motor cortex: intracranial EEG data and a simple explanatory model. *Cerebr. Cortex* 26, 2863–2881. <https://doi.org/10.1093/cercor/bhw033>.
- Ibáñez, J., Serrano, J.I., del Castillo, M.D., Monge-Pereira, E., Molina-Rueda, F., Alguacil-Diego, I., Pons, J.L., 2014. Detection of the onset of upper-limb movements based on the combined analysis of changes in the sensorimotor rhythms and slow cortical potentials. *J. Neural. Eng.* 11, 056009. <https://doi.org/10.1088/1741-2560/11/5/056009>.
- Jiang, N., Gizzi, L., Mrachacz-Kersting, N., Dremstrup, K., Farina, D., 2015. A brain-computer interface for single-trial detection of gait initiation from movement related cortical potentials. *Clin. Neurophysiol.* 126, 154–159. <https://doi.org/10.1016/j.clinph.2014.05.003>.
- Jochumsen, M., Niazi, I.K., Mrachacz-Kersting, N., Farina, D., Dremstrup, K., 2013. Detection and classification of movement-related cortical potentials associated with task force and speed. *J. Neural. Eng.* 10. <https://doi.org/10.1088/1741-2560/10/5/056015>.
- Kalaska, J., Crammond, D., 1992. Cerebral cortical mechanisms of reaching movements. *Science* 255, 1517–1523. <https://doi.org/10.1126/science.1549781>.
- Kaufman, M.T., Seely, J.S., Sussillo, D., Ryu, S.I., Shenoy, K.V., Churchland, M.M., 2016. The largest response component in the motor cortex reflects movement timing but not movement type. *eNeuro* 3. <https://doi.org/10.1523/ENEURO.0085-16.2016>.
- Keren, A.S., Yuval-Greenberg, S., Deouell, L.Y., 2010. Saccadic spike potentials in gamma-band EEG: characterization, detection and suppression. *Neuroimage* 49, 2248–2263. <https://doi.org/10.1016/j.neuroimage.2009.10.057>.
- Kobler, R.J., Almeida, I., Sburlea, A.I., Müller-Putz, G.R., 2020a. Using machine learning to reveal the population vector from EEG signals. *J. Neural. Eng.* 17, 026002. <https://doi.org/10.1088/1741-2552/ab7490>.
- Kobler, R.J., Sburlea, A.I., Lopes-Dias, C., Schwarz, A., Hirata, M., Müller-Putz, G.R., 2020b. Corneo-retinal-dipole and eyelid-related eye artifacts can be corrected offline and online in electroencephalographic and magnetoencephalographic signals. *Neuroimage* 218, 117000. <https://doi.org/10.1016/j.neuroimage.2020.117000>.
- Kobler, R.J., Sburlea, A.I., Mondini, V., Müller-Putz, G.R., 2019. HEAR to remove pops and drifts: the high-variance electrode artifact removal (HEAR) algorithm. In: Proceedings of the 41st Annual International Conference of the IEEE Engineering in Medicine and Biology Society (EMBC). IEEE, Berlin, Germany, pp. 5150–5155. <https://doi.org/10.1109/EMBC.2019.8857742>.
- Kobler, R.J., Sburlea, A.I., Müller-Putz, G.R., 2017. A comparison of ocular artifact removal methods for block design based electroencephalography experiments. In: Proceedings of the 7th Graz Brain-Computer Interface Conference. TU Graz Publishing House, Graz, Austria, pp. 236–241. <https://doi.org/10.3217/978-3-85125-682-6-19>.
- Kobler, R.J., Sburlea, A.I., Müller-Putz, G.R., 2018. Tuning characteristics of low-frequency EEG to positions and velocities in visuomotor and oculomotor tracking tasks. *Sci. Rep.* 8, 17713. <https://doi.org/10.1038/s41598-018-36326-y>.
- Korik, A., Sosnik, R., Siddique, N., Coyle, D., 2018. Decoding imagined 3D hand movement trajectories from EEG: evidence to support the use of Mu, beta, and low gamma oscillations. *Front. Neurosci.* 12, 1–16. <https://doi.org/10.3389/fnins.2018.00130>.
- Kothe, C., 2012. Simulation and neuroscience application platform (SNAP) [WWW Document]. URL <https://github.com/scn/SNAP>.
- Kothe, C., Medine, D., Boulay, C., Grivich, M., Stenner, T., 2019. Lab Streaming Layer (LSL) - a software framework for synchronizing a large array of data collection and stimulation devices [WWW Document]. URL <https://github.com/scn/labstreaminglayer>.
- Ledberg, A., Bressler, S.L., Ding, M., Coppola, R., Nakamura, R., 2007. Large-scale visuomotor integration in the cerebral cortex. *Cerebr. Cortex* 17, 44–62. <https://doi.org/10.1093/cercor/bhj123>.
- Lew, E., Chavarriga, R., Silvoni, S., Millán, José Del R., 2012. Detection of self-paced reaching movement intention from EEG signals. *Front. Neuroeng.* 13. <https://doi.org/10.3389/fneng.2012.00013>.
- Leys, C., Ley, C., Klein, O., Bernard, P., Licata, L., 2013. Detecting outliers: do not use standard deviation around the mean, use absolute deviation around the median. *J. Exp. Soc. Psychol.* 49, 764–766. <https://doi.org/10.1016/j.jesp.2013.03.013>.
- Li, J., Wang, Y., Zhang, L., Jung, T.-P., 2012. Combining ERPs and EEG spectral features for decoding intended movement direction. In: 2012 Annual International Conference of the IEEE Engineering in Medicine and Biology Society. Presented at the 2012 34th Annual International Conference of the IEEE Engineering in Medicine and Biology Society (EMBC). IEEE, San Diego, CA, pp. 1769–1772. <https://doi.org/10.1109/EMBC.2012.6346292>.
- López-Larraz, E., Montesano, L., Gil-Agudo, Á., Minguez, J., 2014. Continuous decoding of movement intention of upper limb self-initiated analytic movements from pre-movement EEG correlates. *J. NeuroEng. Rehabil.* 11, 153. <https://doi.org/10.1186/1743-0003-11-153>.
- Magri, C., Fabbri, S., Caramazza, A., Lingnau, A., 2019. Directional tuning for eye and arm movements in overlapping regions in human posterior parietal cortex. *Neuroimage* 191, 234–242. <https://doi.org/10.1016/j.neuroimage.2019.02.029>.
- Maris, E., Oostenveld, R., 2007. Nonparametric statistical testing of EEG- and MEG-data. *J. Neurosci. Methods* 164, 177–190. <https://doi.org/10.1016/j.jneumeth.2007.03.024>.
- Marty, B., Bourguignon, M., Jousmäki, V., Wens, V., Goldman, S., De Tiège, X., 2018. Movement kinematics dynamically modulates the rolandic ~ 20-Hz rhythm during goal-directed executed and observed hand actions. *Brain Topogr.* <https://doi.org/10.1007/s10548-018-0634-y>, 0, 0.
- Mehring, C., Rickett, J., Vaadia, E., Cardoso de Oliveira, S., Aertsen, A., Rotter, S., 2003. Inference of hand movements from local field potentials in monkey motor cortex. *Nat. Neurosci.* 6, 1253–1254. <https://doi.org/10.1038/nn1158>.
- Michel, C.M., Murray, M.M., Lantz, G., Gonzalez, S., Spinelli, L., Grave De Peralta, R., 2004. EEG source imaging. *Clin. Neurophysiol.* 115, 2195–2222. <https://doi.org/10.1016/j.clinph.2004.06.001>.
- Niazi, I.K., Jiang, N., Tiberghien, O., Nielsen, J.F., Dremstrup, K., Farina, D., 2011. Detection of movement intention from single-trial movement-related cortical potentials. *J. Neural. Eng.* 8, 066009. <https://doi.org/10.1088/1741-2560/8/6/066009>.
- Nichols, T., Holmes, A., 2002. Nonparametric permutation tests for functional neuroimaging: a primer with examples. *Hum. Brain Mapp.* 15, 1–25. <https://doi.org/10.1016/B978-012264841-0/50048-2>.
- Ofner, P., Schwarz, A., Pereira, J., Müller-Putz, G.R., 2017. Upper limb movements can be decoded from the time-domain of low-frequency EEG. *PLoS One* 12, e0182578. <https://doi.org/10.1371/journal.pone.0182578>.
- Ofner, P., Schwarz, A., Pereira, J., Wyss, D., Wildburger, R., Müller-Putz, G.R., 2019. Attempted arm and hand movements can be decoded from low-frequency EEG from persons with spinal cord injury. *Sci. Rep.* 9, 7134. <https://doi.org/10.1038/s41598-019-43594-9>.
- Pascual-Marqui, R.D., 2002. Standardized low resolution brain electromagnetic tomography (sLORETA): technical details. *Methods Find. Exp. Clin. Pharmacol.* 24, 1–16.
- Pereira, J., Ofner, P., Schwarz, A., Ioana Sburlea, A., Müller-Putz, G.R., 2017. EEG neural correlates of goal-directed movement intention. *Neuroimage* 149, 129–140. <https://doi.org/10.1016/j.neuroimage.2017.01.030>.
- Pereira, J., Sburlea, A.I., Müller-Putz, G.R., 2018. EEG patterns of self-paced movement imaginations towards externally-cued and internally-selected targets. *Sci. Rep.* 8, 13394. <https://doi.org/10.1038/s41598-018-31673-2>.
- Perry, C.J., Fallah, M., 2017. Effector-based attention systems. *Ann. N. Y. Acad. Sci.* 1396, 56–69. <https://doi.org/10.1111/NYAS.13354>.
- Pfurtscheller, G., Lopes Da Silva, F.H., 1999. Event-related EEG/MEG synchronization and desynchronization: basic principles. *Clin. Neurophysiol.* 110, 1842–1857. [https://doi.org/10.1016/S1388-2457\(99\)00141-8](https://doi.org/10.1016/S1388-2457(99)00141-8).
- Pitzalis, S., Fattori, P., Galletti, C., 2015. The human cortical areas V6 and V6A. *Vis. Neurosci.* 32, E007. <https://doi.org/10.1017/S0952523815000048>.
- Pitzalis, S., Galletti, C., Huang, R.-S., Patria, F., Comitteri, G., Galati, G., Fattori, P., Sereno, M.I., 2006. Wide-field retinotopy defines human cortical visual area V6. *J. Neurosci.* 26, 7962–7973. <https://doi.org/10.1523/JNEUROSCI.0178-06.2006>.
- Purves, D., Augustine, G.J., Fitzpatrick, D., Hall, W.C., LaMantia, Anthony-Samuel, McNamara, James O., Williams, Mark S. (Eds.), 2004. *Neuroscience, third ed.* Sinauer Associates, Inc, Sunderland, Massachusetts, USA.
- Rizzolatti, G., Luppino, G., 2001. The cortical motor system. *Neuron* 31, 889–901. [https://doi.org/10.1016/S0896-6273\(01\)00423-8](https://doi.org/10.1016/S0896-6273(01)00423-8).
- Robinson, N., Vinod, A.P., 2016. Noninvasive brain-computer interface: decoding arm movement kinematics and motor control. *IEEE Syst. Man Cybern. Mag.* 2, 4–16. <https://doi.org/10.1109/MSMC.2016.2576638>.
- Sburlea, A.I., Montesano, L., Minguez, J., 2017. Advantages of EEG phase patterns for the detection of gait intention in healthy and stroke subjects. *J. Neural. Eng.* 14, 036004. <https://doi.org/10.1088/1741-2552/aa5f2f>.
- Sburlea, A.I., Montesano, L., Minguez, J., 2015. Continuous detection of the self-initiated walking pre-movement state from EEG correlates without session-to-session recalibration. *J. Neural. Eng.* 12, 036007. <https://doi.org/10.1088/1741-2560/12/3/036007>.
- Schäfer, J., Strimmer, K., 2005. A shrinkage approach to large-scale covariance matrix estimation and implications for functional genomics. *Stat. Appl. Genet. Mol. Biol.* 4. <https://doi.org/10.2202/1544-6115.1175>.



- Schwarz, A., Ofner, P., Pereira, J., Sburlea, A.I., Müller-Putz, G.R., 2018. Decoding natural reach-and-grasp actions from human EEG. *J. Neural. Eng.* 15, 016005 <https://doi.org/10.1088/1741-2552/aa8911>.
- Seeber, M., Cantonas, L.-M., Hoevens, M., Sesia, T., Visser-Vandewalle, V., Michel, C.M., 2019. Subcortical electrophysiological activity is detectable with high-density EEG source imaging. *Nat. Commun.* 10, 753. <https://doi.org/10.1038/s41467-019-08725-w>.
- Seeber, M., Scherer, R., Müller-Putz, G.R., 2016. EEG oscillations are modulated in different behavior-related networks during rhythmic finger movements. *J. Neurosci.* 36, 11671–11681. <https://doi.org/10.1523/JNEUROSCI.1739-16.2016>.
- Shibasaki, H., Barrett, G., Halliday, E., Halliday, a M., 1980. Components of the movement-related cortical potential and their scalp topography. *Electroencephalogr. Clin. Neurophysiol.* 49 (3–4), 213–226. [https://doi.org/10.1016/0013-4694\(80\)90216-3](https://doi.org/10.1016/0013-4694(80)90216-3).
- Shibasaki, H., Hallett, M., 2006. What is the Bereitschaftspotential? *Clin. Neurophysiol.* 117 (11), 2341–2356. <https://doi.org/10.1016/j.clinph.2006.04.025>.
- Sun, Y., Zeng, H., Song, A., Xu, B., Li, H., Liu, J., Wen, P., 2017. Investigation of the phase feature of low-frequency electroencephalography signals for decoding hand movement parameters. In: 2017 IEEE International Conference on Systems, Man, and Cybernetics (SMC). Presented at the 2017 IEEE International Conference on Systems, Man and Cybernetics (SMC). IEEE, Banff, AB, pp. 2312–2316. <https://doi.org/10.1109/SMC.2017.8122966>.
- Tosoni, A., Pitzalis, S., Committeri, G., Fattori, P., Galletti, C., Galati, G., 2015. Resting-state connectivity and functional specialization in human medial parieto-occipital cortex. *Brain Struct. Funct.* 220, 3307–3321. <https://doi.org/10.1007/s00429-014-0858-x>.
- Waldert, S., Preissl, H., Demandt, E., Braun, C., Birbaumer, N., Aertsen, A., Mehring, C., 2008. Hand movement direction decoded from MEG and EEG. *J. Neurosci.* 28, 1000–1008. <https://doi.org/10.1523/JNEUROSCI.5171-07.2008>.
- Wang, W., Sudre, G.P., Xu, Y., Kass, R.E., Collinger, J.L., Degenhart, A.D., Bagic, A.I., Weber, D.J., 2010. Decoding and cortical source localization for intended movement direction with MEG. *J. Neurophysiol.* 104, 2451–2461. <https://doi.org/10.1152/jn.00239.2010>.
- Wang, Y., Makeig, S., 2009. Predicting intended movement direction using EEG from human posterior parietal cortex. *Augment. Cogn.* 437–446. https://doi.org/10.1007/978-3-642-02812-0_52.
- Xu, R., Jiang, N., Mrachacz-Kersting, N., Lin, C., Prieto, G.A., Moreno, J.C., Pons, J.L., Dremstrup, K., Farina, D., 2014. A closed-loop brain–computer interface triggering an active ankle–foot orthosis for inducing cortical neural plasticity. *IEEE Trans. Biomed. Eng.* 61, 2092–2101. <https://doi.org/10.1109/TBME.2014.2313867>.

SCIENTIFIC REPORTS



OPEN

Tuning characteristics of low-frequency EEG to positions and velocities in visuomotor and oculomotor tracking tasks

Reinmar J. Kobler, Andreea I. Sburlea  & Gernot R. Müller-Putz 

Movement decoders exploit the tuning of neural activity to various movement parameters with the ultimate goal of controlling end-effector action. Invasive approaches, typically relying on spiking activity, have demonstrated feasibility. Results of recent functional neuroimaging studies suggest that information about movement parameters is even accessible non-invasively in the form of low-frequency brain signals. However, their spatiotemporal tuning characteristics to single movement parameters are still unclear. Here, we extend the current understanding of low-frequency electroencephalography (EEG) tuning to position and velocity signals. We recorded EEG from 15 healthy participants while they performed visuomotor and oculomotor pursuit tracking tasks. Linear decoders, fitted to EEG signals in the frequency range of the tracking movements, predicted positions and velocities with moderate correlations (0.2–0.4; above chance level) in both tasks. Predictive activity in terms of decoder patterns was significant in superior parietal and parieto-occipital areas in both tasks. By contrasting the two tracking tasks, we found that predictive activity in contralateral primary sensorimotor and premotor areas exhibited significantly larger tuning to end-effector velocity when the visuomotor tracking task was performed.

Access to neural activity through various recording modalities allowed us to study its tuning characteristics in upper-limb movements from microscale up to macroscale levels. At the microscale level, neural spiking activity in primary motor¹ and premotor² as well as posterior parietal³ areas is tuned to reach direction among other movement parameters⁴. By exploiting these tuning characteristics, non-human primates^{4,5} and selected humans⁶ with spinal cord injuries have been able to control artificial end-effectors in a 3D world. At the macroscale level, in terms of non-invasively accessible neural activity, spatiotemporal tuning characteristics are not yet clearly understood with regard to upper-limb movements.

The results of functional Magnetic Resonance Imaging (fMRI) studies in humans have revealed a fronto-parietal reach network comprising dorsal premotor (PMd) and medial areas of the superior parietal lobule (SPL)^{7,8}. This network is active during executed and observed reaching movements^{7,8} as well as during saccadic eye movements⁹ and exhibits directional tuning¹⁰. The fMRI findings, in conjunction with the successful decoding of positions and velocities from low-frequency electrocorticography (ECoG) signals¹¹, suggested that information about directional movement parameters might be accessible from outside the brain. Not much later, research groups reported successful classification of reach directions¹², and regression of end-effector positions and velocities¹³ on the basis of low-frequency magnetoencephalographic (MEG) and electroencephalographic (EEG) signals. Since then, research in this context has focused on regression of end-effector positions and velocities or classification of reach direction in center-out tasks with linear models¹⁴. In this paper, we focus on the regression approach.

A general limitation of studying reaching movements with a regression approach in center-out tasks is that the 2D or 3D position and velocity vectors of the end-effector point always in the same direction - the direction of the target stimulus. As a consequence, the position and velocity signals are strongly correlated during the reaching movement. For this reason, it is difficult to identify the covariate (target position, end-effector position or velocity) to which the recorded neural activity is preferentially tuned¹⁵. Alternatively, by studying continuous

Institute of Neural Engineering, Graz University of Technology, Graz, Austria. Correspondence and requests for materials should be addressed to G.R.M.-P. (email: gernot.mueller@tugraz.at)

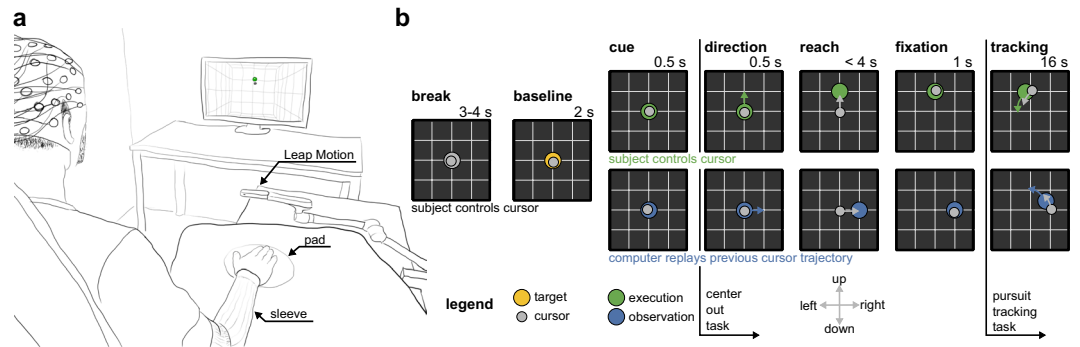


Figure 1. Experimental setup and paradigm. **(a)** Participants sat in a comfortable chair positioned 1.4 m from a computer screen. Both arms were supported at the same height. The right arm rested on a table at a comfortable position. The friction between arm and surface was reduced by a sleeve and a circular pad positioned between hand and table. Palm position movements were recorded by a LeapMotion controller (LeapMotion Inc., USA) located 20 cm above the hand. Forward/backward hand movements on the table were mapped to upward/downward cursor movements on the screen. **(b)** Each trial started with a 3–4 s break during which the target (large ball) resided in the center. A 2 s baseline period was initiated when the target turned yellow. During this period, participants were asked to keep their hand in the resting position and, thereby, the cursor in the center of the screen. A visual cue indicated the condition, either execution (green target) or observation (blue target), followed by a center-out task in four directions. The direction was indicated by the target movement (0.5 s duration; arrows visualize movement in the individual images). After 1 s of fixation, a pursuit tracking task was performed for 16 s. A colored target stimulus (yellow, green, or blue) instructed the participants to fixate and track the target with their eyes. In the execution condition the participants controlled the cursor, while in the observation condition, the computer replayed a previously executed cursor trajectory which matched to the current target trajectory. See Supplementary Video S1 for examples.

movements in a pursuit tracking task (PTT), instantaneous position and velocity can be decorrelated¹⁵. In a PTT, the goal is to track a moving target with an end-effector. This requires the brain to visually monitor the moving target stimulus in relation to the end-effector so that the end-effector movement can be updated to achieve the goal. In such a visuomotor (VM) task, the eyes naturally track the moving target stimulus¹⁶. As a consequence of this natural tracking behavior, the oculomotor network, which also spans parietal and frontal regions¹⁷, is activated at the same time as the reaching network⁹.

To facilitate natural behavior and isolate the neural activity related to the involvement of the upper-limb, a control condition can be introduced. In the control condition, participants would perform an oculomotor (OM) task by tracking a target stimulus only with their eyes^{9,18}. In the other condition (VM task), upper-limb movement is additionally involved in the tracking. By contrasting these conditions, it should be possible to infer whether low-frequency EEG carries more information about end-effector positions and velocities during the performance of the VM or OM task, and to identify where the differences are expressed at the cortical level. We hypothesized that contralateral, primary motor and premotor areas carry more information about end-effector positions and velocities when the VM task is being performed, and that activity in areas related to the reaching and oculomotor networks is tuned to positions and velocities in both tasks.

Here, we present the tuning characteristics of low-frequency EEG activity to positions and velocities during continuous tracking movements. In two conditions, participants were asked to track a pseudo-randomly moving target either visually (OM task) or by additionally controlling a cursor with their right arm (VM task). We evaluated our approach offline by examining the recordings of healthy participants. Our experimental results confirmed that low-frequency EEG carries information about target and cursor positions and velocities in both conditions. More interestingly, when contrasting conditions, we found that the low-frequency EEG carried more information about the instantaneous cursor velocity during the VM task rather than during the OM task. The differences were mainly reflected in the premotor and contralateral primary sensorimotor areas. The temporal tuning characteristics of these differences indicated that the predictive neural activity preceded cursor velocity with 150 ms. Therefore, we could show that low-frequency EEG activity, originating in premotor and primary sensorimotor areas, can at least offline be used to predict the velocities of executed upper-limb movements.

Results

To test our hypotheses, we recorded high-density EEG and electrooculography (EOG) from 15 healthy participants during a two-dimensional PTT. In every trial, the PTT was preceded by a short, visually guided, center-out reaching task. Here, we present our findings during the PTT. Figure 1 depicts the experimental setup and paradigm. The paradigm separated two conditions. In the first condition (execution, VM task), participants were asked to track a pseudo-randomly moving target with their gaze and right hand by manipulating a cursor (Fig. 1a). In the second condition (observation, OM task), participants were asked to track the moving target with their gaze, while keeping their right hand in a resting position. To obtain similar visual input and tracking dynamics in both conditions, we replayed the participant's most recent, matching, executed cursor trajectory in observation condition trials. All results presented subsequently were determined after pre-processing, correcting

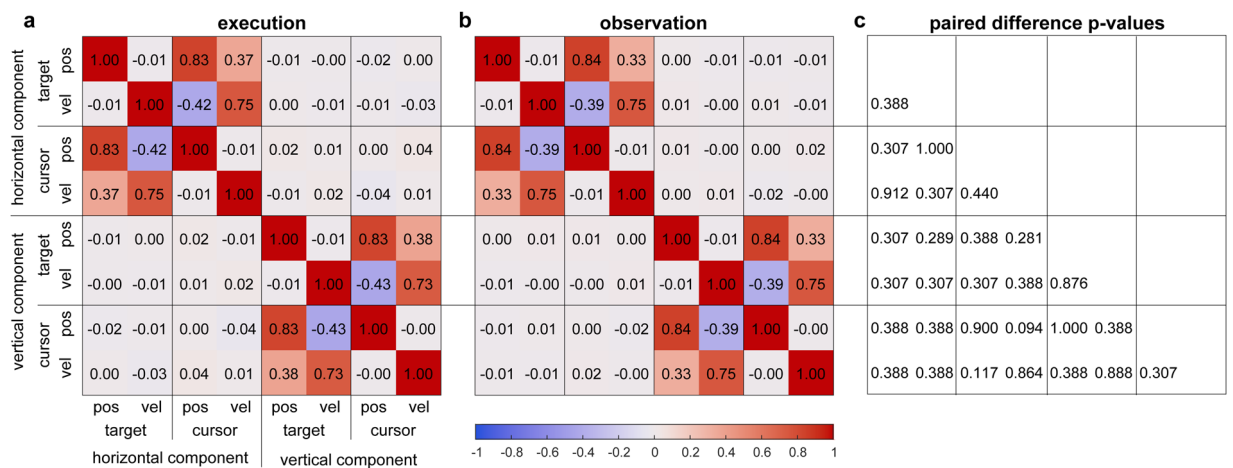


Figure 2. Group-level stimuli cross-correlations in both conditions. **(a)** Cross-correlations between the two-dimensional movement parameters (target position, target velocity, cursor position, cursor velocity) in execution condition. **(b)** Cross-correlations in observation condition. **(c)** *P*-values for paired Wilcoxon sign rank tests between conditions. *P*-values were adjusted⁵⁵ for 28 comparisons to control the false discovery rate (FDR) at a level of 0.05.

for EOG artifacts¹⁹ and downsampling the recorded data to 10 Hz (see Methods). Throughout the text, grand average results are presented in the form of the mean value and its standard error.

Tracking analysis. To analyze the tracking dynamics, we computed cross-correlations between the positions and velocities of both stimuli in execution and observation conditions. Figure 2a summarizes the grand average cross-correlations in the execution condition. The large cross-correlations ($r > 0.7$) observed between signals of the same movement parameter (e.g. target and cursor position) show that participants complied with the instruction to minimize the distance to the target. Cross-correlations between the position and velocity of the same stimulus were negligible ($|r| < 0.02$; e.g. target position and target velocity), while we observed moderate ($|r| \sim 0.4$; e.g. target position and cursor velocity) cross-correlations across stimuli. Our target trajectory generation procedure ensured decorrelated horizontal and vertical components. Hence, cross-correlations observed with any signal from the other component were negligible ($|r| < 0.05$). Figure 2b summarizes the grand average cross-correlations in observation condition. We did not detect significant differences to the execution condition results (Fig. 2c).

To estimate the temporal dependencies among the four movement parameters (target position, target velocity, cursor position, cursor velocity) per component, we computed cross-correlations over lags in the interval $[-0.5$ s, 0.5 s] in steps of 0.1 s. Figures 3a–d depict the results for the horizontal (a,b) and vertical (c,d) components. We aligned the individual figures based on the peak cross-correlations between pairs of movement parameters. For example, the origin in Figure 3b is shifted by -0.525 s compared to that in Figure 3a because the cursor velocity was maximally correlated with cursor position 0.525 s in the future. In the execution condition, the participants reacted with their hand movements (cursor trajectories) to the pseudo-random target trajectories. This means that the properties of the target trajectories (e.g. cross-correlation peak between target position and velocity) also determined the properties of the cursor trajectories.

The cross-correlation peak between target and cursor position can be used to infer information about the participants' tracking behavior. We used the lag of the cross-correlation peak to estimate the latency between the target and cursor. In the execution condition, the latency reflected the duration that a participant took to adjust the cursor movement to the pseudo-random target movement. The cross-correlation between the target and cursor position peaked at a delay of 153 ± 19 ms at group level. After accounting for a 55 ± 1 ms delay, introduced by our online processing system which transformed hand movements into cursor movements, the average latency of hand movements was approximately 100 ms. This result is in accordance with the findings of behavioral studies, which report that a minimum latency of 80–100 ms is needed for a visual or proprioceptive signal to influence an ongoing movement^{20,21}.

Movement parameter tuning curves. We estimated tuning curves for each movement parameter with a single sample, sliding-window, linear regression approach^{13,22}. The regression approach is outlined in Figure 3e. At different lags, a partial least squares (PLS)²³ estimator was used to decode each movement parameter from the EEG within the sliding window (one sample). This modelling approach implied that the relevant activity in the signal used for decoding (EEG) has to be in the same frequency range as the signal to be decoded (e.g. horizontal cursor velocity)²⁴. To extract the relevant activity in the frequency range (0.3 to 0.6 Hz) of the target and cursor trajectories, we bandpass-filtered the EEG (Supplementary Fig. S3 shows power spectral densities of the bandpass-filtered EEG and the movement parameters). In a cross-validation scheme, we computed correlations between the signals to be decoded (e.g. horizontal cursor velocity) and their estimates for each lag to generate the tuning curves.

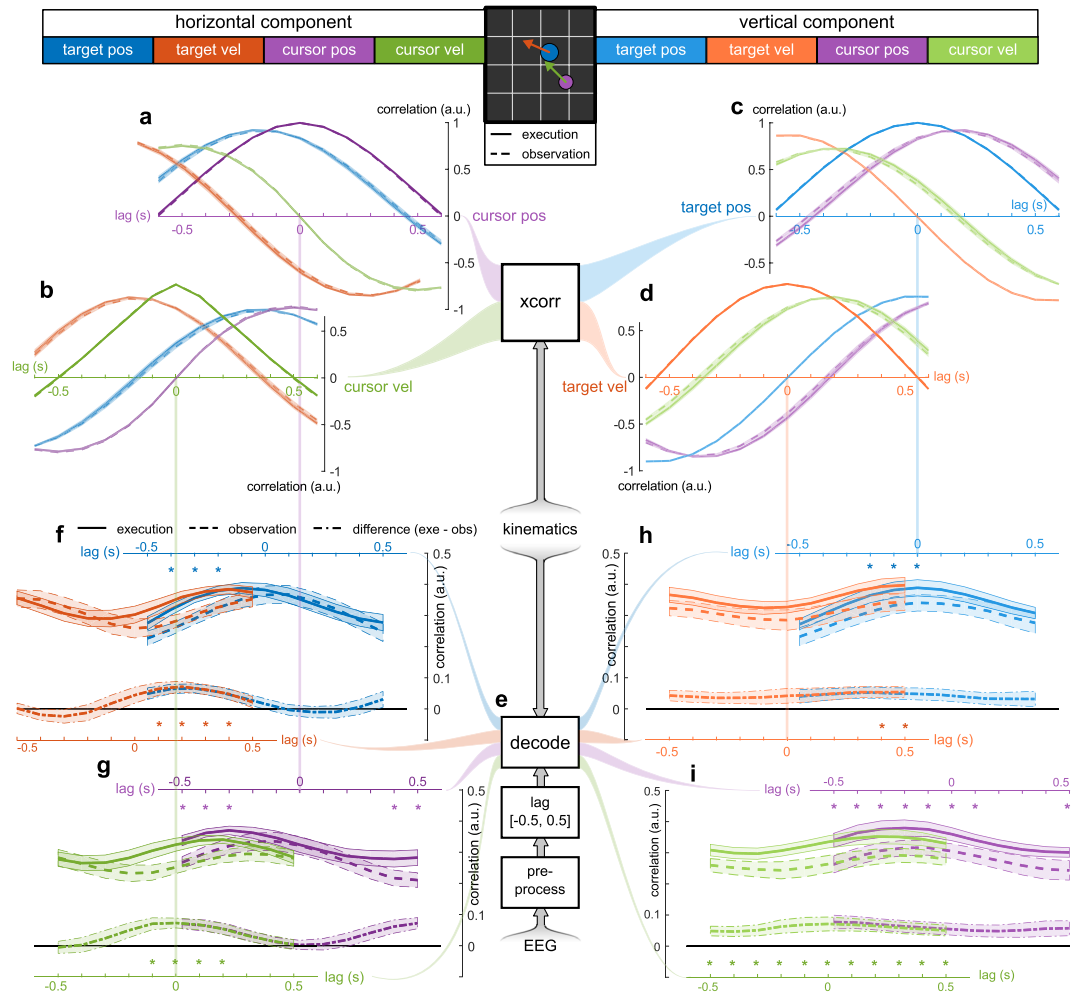


Figure 3. Grand average movement parameter auto-/cross-correlation curves, and movement parameter tuning curves. **(a–d)** Grand average stimuli auto- and cross-correlations. **(a)** Auto- and cross-correlation curves of horizontal components relative to the horizontal cursor position during execution (solid lines) and observation (dashed lines). Movement parameters are color-coded. Shaded areas represent the standard-error of the mean. Cross-correlations were evaluated for lags, ranging from -0.5 s (leading relative to cursor position) to 0.5 s (lagging) in 0.1 s steps. **(b)** Auto- and cross-correlation curves of horizontal components relative to the horizontal cursor velocity. **(c)** Auto- and cross-correlation curves of vertical components relative to the vertical target position. **(d)** Vertical target velocity. **(e)** Outline of the regression approach. After EEG preprocessing (including bandpass-filtering), a sliding window (one sample) was used to decode the movement parameters and their estimates at different lags. **(f–i)** Grand average correlations between movement parameters and their estimates at different lags (tuning curves). **(f)** Tuning curves for the horizontal target position (blue) and velocity (orange). The mean and its standard error summarize the results for execution (solid lines), observation (dashed lines) and their paired difference (dash dotted lines). Cross-correlation peaks between target position and velocity were used to align the time-lag axes. Lags with significant differences between conditions (paired Wilcoxon sign-rank tests, FDR adjustment for 88 comparisons, 0.05 significance level) are highlighted (*). **(g)** Tuning curves for horizontal cursor position (violet) and velocity (green). **(h)** Tuning curves for vertical target position (blue) and velocity (orange). **(i)** Tuning curves for vertical cursor position (violet) and velocity (green).

Figures 3f–i summarize the grand average tuning curves for both conditions. Due to the independence between the horizontal and vertical components (Fig. 2), the tuning curves in Figures 3f–i are complementary. For both components, the grand average correlations ranged from 0.2 to 0.4 . We used a shuffling approach to estimate chance levels for each participant. The chance levels were similar across components, conditions and lags (target position $r_{chance} = 0.13 \pm 0.003$, target velocity $r_{chance} = 0.12 \pm 0.002$, cursor position $r_{chance} = 0.12 \pm 0.003$, cursor velocity $r_{chance} = 0.10 \pm 0.002$). Compared to chance level, the observed correlations were significant for all participants, components, conditions, movement parameters and lags. As in Figures 3a–d, we aligned the tuning curves (Fig. 3f–i) according to the peak cross-correlations between pairs of movement parameters. After the alignment, we observed three effects.

As a first effect, we found that in the observation condition the tuning curves in Figures 3f–i (dashed lines) were modulated by the auto-/cross-correlation with target position. That is, an increase in the tuning curve of

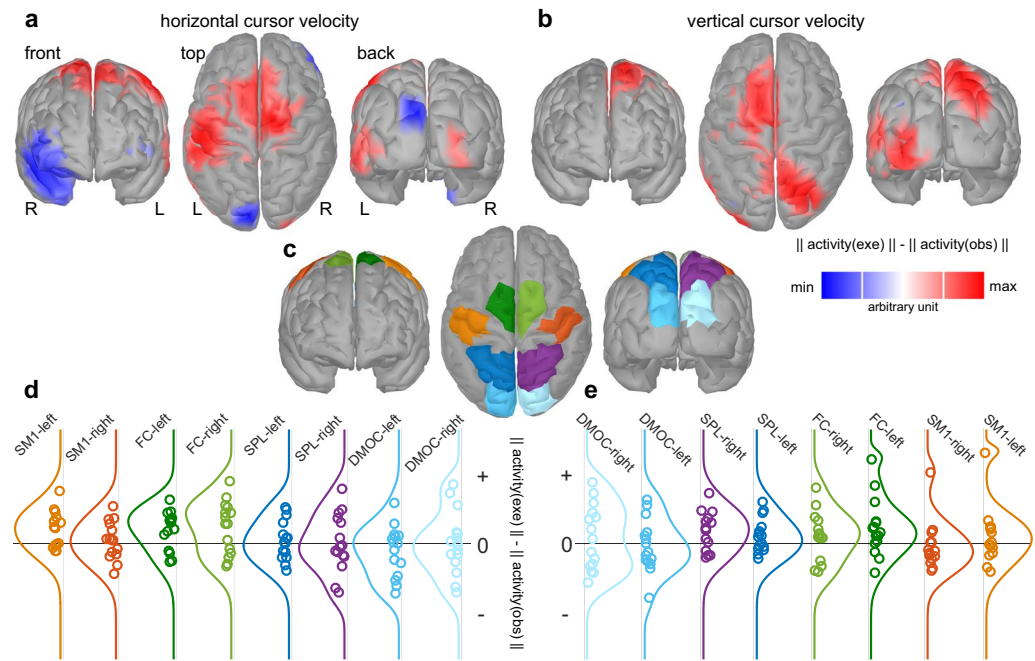


Figure 4. Grand average pattern activity difference between conditions in source space for single-lag (lag 0) cursor velocity decoder models. **(a)** Horizontal cursor velocity pattern. Voxel color indicates the sign of the difference in norms; positive (red) indicates larger pattern activity in execution. Voxels with a difference in norms less than half of the absolute maximum are shaded with gray to emphasize the sites with the largest effects. **(b)** Vertical cursor velocity pattern. **(c)** Anatomical regions of interest (ROI)s, covering dorsomedial occipital cortex (DMOC), superior parietal lobule (SPL), fronto-central (FC) and primary sensorimotor areas (SM) of both hemispheres. **(d)** Density estimates of the differences in ROI activity for participants for the horizontal cursor velocity. Each point represents one participant. Density curves follow the ROI color-coding scheme. **(e)** As in **(d)** for vertical cursor velocity.

a movement parameter coincided with an increase in the absolute auto-/cross-correlation between the movement parameter and the target position signal. We observed this effect for all movement parameters due to the dependencies between them. The dependencies are reflected in the auto-/cross-correlation curves (Fig. 3a–d). For example, the tuning curve of the vertical target position (Fig. 3h, blue dashed line) exhibited a similar waveform compared to the target position's autocorrelation curve (Fig. 3c, blue line). The tuning curve of the horizontal cursor position (Fig. 3g, violet dashed line) and its cross-correlation curve with the target position (Fig. 3a, blue line) represents another example. The size of the effect was approximately 0.1 for both components and maximal for target position. In the execution condition (solid lines), we detected the same modulation. However, it was partially masked by the other effects.

The second effect observed concerns the vertical component (Fig. 3h,i). The paired differences between execution and observation conditions (dash-dotted lines) exhibited a positive effect on all movement parameters and lags. That is, in the execution condition, the low-frequency EEG contained significantly more information about the movement parameters of the vertical component. The effect was largest for vertical cursor position and velocity with an average difference in correlation of 0.05 (Fig. 3i, violet and green dash-dotted lines).

The third effect concerned the differences in tuning curves for both components (Fig. 3f–i, dash-dotted lines). The differences were modulated by the absolute auto-/cross-correlation between a movement parameter and cursor velocity (Fig. 3a–d, green lines). The effect was prominent for the horizontal component and largely masked by the second effect for the vertical component. For example, the difference in tuning curves for the horizontal cursor position (Fig. 3g, violet dash-dotted line) resembled the absolute value of its cross-correlation curve with the horizontal cursor velocity (Fig. 3a, green line). The size of the effect was maximal (approx. 0.07) for the horizontal cursor velocity at lag 0 (Fig. 3g, green dash-dotted line). Taken together, we inferred that the extracted EEG carried significantly more information about the instantaneous (lag 0 s) cursor velocity in the execution condition.

We were also interested in assessing which brain areas encoded more information in the execution condition than in the observation condition. To determine which brain areas contributed to the third effect, we selected the cursor velocity decoder models at a lag of 0 s as representatives and computed their associated activation patterns²⁵. The patterns were subsequently mapped to the cortical surface by applying EEG source imaging^{26,27} on a template head model. In source space, we computed pairwise differences between the conditions for the Euclidean norm of each voxel (see Methods).

Figure 4 depicts the grand average difference in pattern norms for the horizontal (Fig. 4a) and vertical (Fig. 4b) cursor velocities at lag 0. We defined eight anatomical regions of interest (ROIs) to span areas related to the fronto-parietal reaching network^{7,9}. They are dorsomedial occipital cortex (DMOC), superior parietal lobule

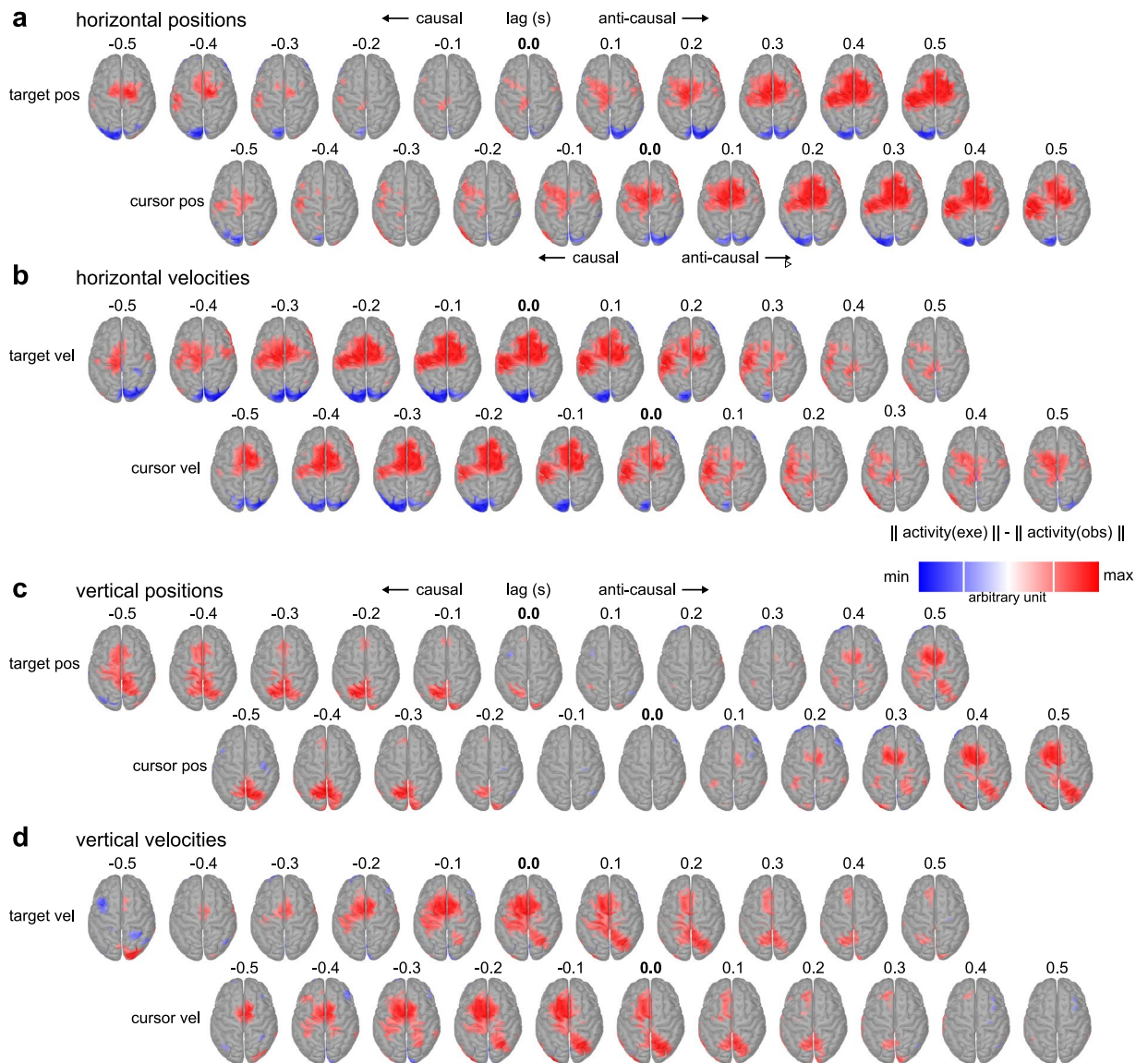


Figure 5. Grand average pattern activity differences between conditions for all single-lag decoder models. **(a)** Single-lag decoder patterns for the horizontal target (top) and cursor (bottom) positions for lags ranging from -0.5 s (brain activity leading relative to the position signals) to 0.5 s (brain activity lagging). As before, cross-correlation peaks between the target and cursor positions were used to align the time-lag axes. The red color indicates larger voxel activity in the execution condition. **(b)** Single-lag decoder patterns for the horizontal target (top) and cursor (bottom) velocities. **(c)** As in **(a)** for the vertical positions. **(d)** As in **(b)** for the vertical velocities.

(SPL), fronto-central (FC) and primary sensorimotor areas (SM) of both hemisphere (Fig. 4c). We summarized the pattern activity of each ROI as the average of its voxels. Figures 4d,e depict the distribution of both horizontal and vertical components for all participants. Regarding the horizontal component (Fig. 4d), we observed a positive effect in FC and left SM areas. For the vertical component (Fig. 4e), we observed positive effects in right SPL and both FC areas. Considering their positive sign, the results indicate that the activity in the areas contained more information about the instantaneous cursor velocity in execution condition.

In Figure 5 we show the difference in pattern norms for all single-lag models (Fig. 3f–i), to demonstrate how the differences in tuning curves are reflected on the cortical surface. Negative lags indicated leading brain activity (causal tuning), while positive lags indicated lagging brain activity (anti-causal tuning). The difference in activation patterns in fronto-central and contralateral sensorimotor areas was tuned to the horizontal and vertical cursor velocity in the $[-0.5, 0.1]$ s interval and peaked around -0.1 to -0.2 s (Fig. 5b,d; bottom rows). As before, due to the temporal dependence between the position and velocity signals (Fig. 3a–d), we also observed tuning effects for the position signals. The difference in activation patterns was anti-causally tuned to cursor position for lags in the range $[0, 0.5]$ s (Fig. 5a,c; bottom rows). Overall, the strength of the differences was more pronounced for the horizontal component. Similar to the cursor velocity pattern at lag 0 (Fig. 4b,e), we observed a positive

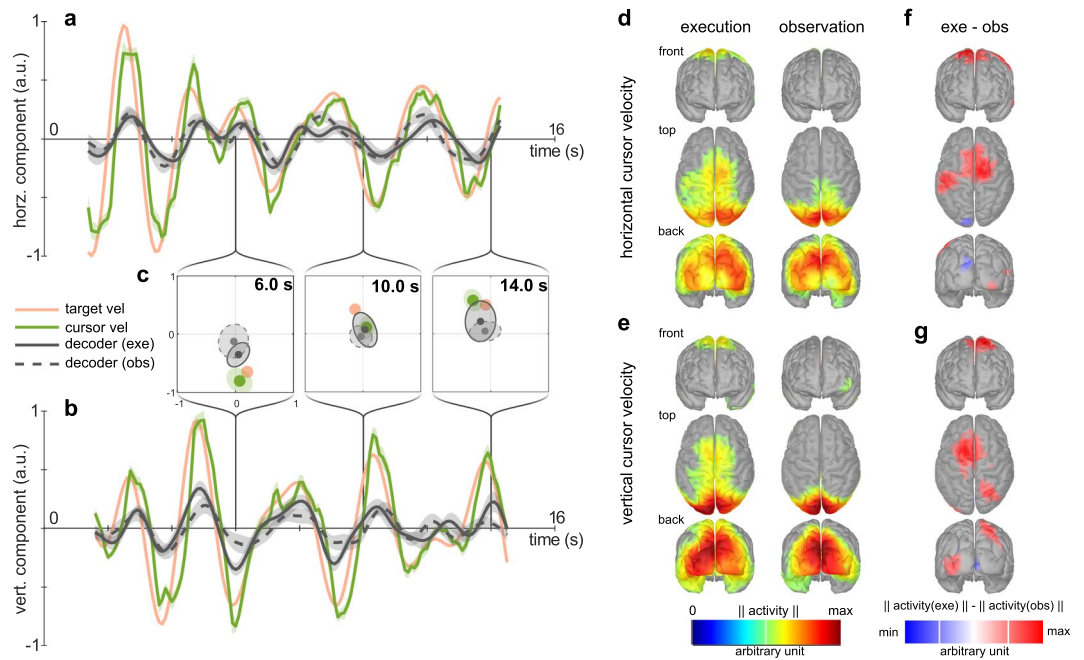


Figure 6. Grand average cursor velocity prediction for a $[-0.3, 0]$ s estimation window. **(a–c)** Illustrations of executed and decoded cursor velocities for a specific target trajectory. **(a)** Grand average horizontal target (orange line), cursor (green line) and decoded cursor velocity in execution (gray solid line) and observation (gray dashed line) conditions. Shaded areas summarize the standard error of the mean. **(b)** As in **(a)** for the vertical component. **(c)** 2D representation for single time points. Dots indicate the group-level average. Dispersion over participants is summarized by the square root of the covariance matrix. **(d–g)** Grand average multiple-lag decoder patterns. **(d)** Horizontal cursor velocity patterns in the execution (left) and observation (right) conditions. Pattern activity norms were averaged over lags. The voxel color indicates strength of activity. **(e)** Vertical cursor velocity patterns in the execution (left) and observation (right) conditions. **(f)** Difference between lag-averaged pattern norms for the horizontal component. The voxel color indicates the sign and strength of the difference in the pattern activity. **(g)** As in **(f)** for the vertical component.

effect in SPL only on the vertical component movement parameters (Fig. 5c,d). With respect to vertical cursor velocity (Fig. 5d; bottom row), the positive effect started in the right SPL at lag -0.3 s, peaked at lag 0 s, subsequently translated to the left SPL and faded at lag 0.3 s.

Multiple-lag cursor velocity prediction. To exploit the tuning of neural activity over multiple lags, we extended the feature set by using multiple samples in the sliding window, linear regression approach. We evaluated sliding windows covering the samples at lags $[-0.1, 0]$ s to $[-0.5, 0]$ s in 0.1 s steps to predict the horizontal and vertical cursor velocities. The correlations between the recorded and decoded cursor velocities initially increased, but became saturated for windows exceeding $[-0.3, 0]$ s (Fig. S4). For the $[-0.3, 0]$ s window, the grand average test set correlations were $r_{exe} = 0.40 \pm 0.02$, $r_{obs} = 0.36 \pm 0.04$ for the horizontal component and $r_{exe} = 0.41 \pm 0.03$, $r_{obs} = 0.33 \pm 0.03$ for the vertical component.

To visualize the decoded cursor velocities, we selected a representative trajectory and summarized the results over participants. Figures 6a–c show the recorded target, cursor and the decoded cursor velocities for this particular trajectory in both conditions. The small standard-error around the recorded cursor velocities (green shaded area) demonstrates that the participants were tracking the target consistently. Compared to the recorded cursor velocities, the decoded cursor velocities exhibited more variance over participants than their neural predictions (Fig. 6c). Still, the grand average decoded cursor velocities were strongly correlated for both components and conditions. The grand average correlations were $r_{exe} = 0.83 \pm 0.02$, $r_{obs} = 0.82 \pm 0.02$ on average for the 90 trajectories on the horizontal component, and $r_{exe} = 0.85 \pm 0.02$, $r_{obs} = 0.80 \pm 0.03$ on the vertical component. This reflects a 0.40 gain in correlation at the group level compared to the results at participant level.

As before, we computed activation patterns and projected them to the cortex. Figures 6d,e depict the grand average patterns (average over participants and lags), and Table 1 lists the p -values of non-parametric permutation paired t -tests for the eight ROIs. Compared to chance level, the pattern activity was significant in DMOC areas in both conditions. SPL pattern activity was significant in the execution and mainly in the observation condition; the effect on vertical cursor velocity did not reach significance in observation condition. FC pattern activity was generally larger in the execution condition (Fig. 6f,g). The differences observed between execution and observation conditions were in line with the single-lag results (Fig. 3f–i). They were significant in right FC and left SM for the horizontal component, and in right SPL for the vertical component. The effects on left FC (and right FC for the vertical component) did not reach significance.

movement parameter	condition	ROI							
		DMOC right	DMOC left	SPL right	SPL left	FC right	FC left	SM1 right	SM1 left
horizontal cursor vel	exe	0.0270	0.0096	0.0373	0.0096	0.0373	0.13	0.49	0.15
	obs	0.0096	0.0096	0.0096	0.0120	0.32	0.36	0.79	0.30
	exe - obs	0.79	0.57	0.60	0.60	0.0224	<i>0.067</i>	0.25	0.0148
vertical cursor vel	exe	0.0096	0.0120	0.0096	0.0096	<i>0.068</i>	0.11	0.74	0.72
	obs	0.0096	0.0096	<i>0.068</i>	<i>0.094</i>	0.79	0.14	0.79	0.53
	exe - obs	0.82	0.49	0.0171	0.36	<i>0.098</i>	<i>0.051</i>	0.65	0.51

Table 1. Significance of ROI activation for multiple lag cursor velocity decoders (exe vs. shuffled exe, obs vs. shuffled obs, and exe vs. obs). *P*-values were computed with two-sided non-parametric permutation paired *t*-tests (1000 permutations). Significant differences (FDR adjustment of *p*-values for 48 comparisons, 0.05 significance level) appear in bold text.

Visual tracking analysis. We examined the EOG signals to compare the visual tracking behavior between conditions by computing cross-correlations between the horizontal and vertical target position and the associated EOG derivative signals. The cross-correlations peaked at lag 0 for both conditions, indicating that the participants' gaze was focused on the target's instantaneous position. By comparing the correlation values at lag 0, we detected significant differences among conditions and components (significance levels were Bonferroni corrected from 0.05 to 0.01 for 5 two-sided paired Wilcoxon sign-rank tests). We found a slightly lower degree of correlation in the execution condition compared to the observation condition for the horizontal component ($r_{exe} = 0.88 \pm 0.01$, $r_{obs} = 0.90 \pm 0.02$, $p = 0.00537$), while the degree of correlation was higher in the execution condition for the vertical component ($r_{exe} = 0.79 \pm 0.02$, $r_{obs} = 0.70 \pm 0.04$, $p = 0.00153$). Within conditions, the degrees of correlation were higher for the horizontal component ($p_{exe} = 0.00012$; $p_{obs} = 0.00006$).

In the execution condition, the VM task required the processing of visual feedback about the cursor in relation to the moving target, while in the observation condition, the cursor was not task-relevant. Authors of previous behavioral studies have reported a reduced blink rate (BR) if more visual information was processed^{28,29}. In our study, we detected blinks by thresholding the vertical EOG derivative¹⁹. As predicted, we found a significantly lower BR in terms of blinks per second (bps) in the execution condition as compared to the observation condition ($BR_{exe} = 0.019 \pm 0.006$ bps, $BR_{obs} = 0.028 \pm 0.006$ bps, $p = 0.0015$).

Discussion

We have presented a novel paradigm, which was tailored to study the tuning characteristics of human, low-frequency EEG to target and cursor (end-effector) positions and velocities in the presence of eye movements. Our paradigm allowed us to distinguish between two conditions with similar tracking dynamics, but with different cursor-control origin. By not inhibiting eye movements during the PTT, we could study tracking movements in a natural fashion and focus on the effects related to the involvement of the upper limb. We presented evidence that this involvement indeed influences the spatiotemporal expression of information about end-effector positions and velocities in the low-frequency EEG activity.

In a PTT, participants typically manipulate an end-effector to minimize its distance to a target. Typically, task compliance results in high cross-correlations between movement parameters of the same type (e.g. position). However, the cross-correlations between positions and velocities depend on the properties of the target trajectories. We created a trade-off between task difficulty, bandwidth and steepness of the increase in correlation over lags. By using the 0.3 to 0.6 Hz band, we could study EEG in a similar frequency range as those examined in previous studies^{15,22}, and shift the peak in cross-correlation between target velocity and position to 0.55 s. After accounting for the dependence between the movement parameters by aligning the tuning curves, we determined one effect in both conditions and two effects in the difference between conditions.

The effect observed in both conditions and components concerned the modulation of the tuning curves by the amount of cross-correlation between a movement parameter and target position. This effect let us to infer that information about the instantaneous target position was encoded in the low-frequency EEG. In the observation condition, the effect was prominent, while it was partially masked by the other effects in the execution condition. The target position was particularly relevant during the PTT. In both conditions, the participants had to keep their gaze fixated on the target. The fact that a peak in the correlation between target position and EOG derivatives occurred at lag 0 confirmed that the participants were able to accomplish the task. This finding is in accordance with findings for human smooth pursuit behavior for a bandlimited pseudo-randomly moving stimulus³⁰. As a consequence, eye movement artifacts were also phase locked to the target position signal. To assess which sources contributed to the observed effect, we computed patterns for target position decoders at lag 0 and projected them to source space (Fig. S5). The grand average patterns for both conditions indicated that the contributions originated from a combination of brain activity with the largest predictive activity in parieto-occipital areas and residual eye artifacts.

As with the modulation of the tuning curves with target position in both conditions, we observed a modulation of the differences between conditions with cursor velocity. By mapping single-lag cursor velocity model patterns to source space and computing differences between conditions, we observed a stronger effect during the execution condition in both FC and contralateral SM ROIs (Fig. 5). The FC ROIs covered dorsal premotor (PMd) and supplementary motor areas (SMA). Their involvement in reaching is in accordance with the findings

of imaging studies in humans³¹. The difference in activation patterns in FC and contralateral SM ROIs was sustained over multiple lags, with its peak activity leading cursor velocity by approximately 150 ms. The delay can be reduced to about 95 ms by accounting for the 55 ms delay between the hand and cursor movement, introduced by the online processing system. The remaining 95 ms could be explained by motor output delays³². Estimating the actual motor output delay is not a straightforward task, since it depends on the task demands and the type of perturbation among other factors³². However, Paninski *et al.* studied the tuning of movement parameters in a comparable PTT¹⁵. They investigated M1 single unit activity in non-human primates and reported that neural activity was tuned to cursor velocity in a [−400, 400] ms lag range (peak at −100 ms; neural activity leading). Thus, a stronger degree of tuning of neural activity to cursor velocity in motor areas during the execution condition offers a plausible explanation. An alternative explanation would be offered by anti-causal tuning to the cursor position for lags in the range [0, 500] ms (Fig. 5a,c). Tuning to the cursor position peaked at 300 to 400 ms, which would reflect feedback processing (neural activity lagging). Experimental results on decoding movement parameters in behaving non-human primate spiking activity^{1,4} and local field potentials³³, together with results of studies on human MEG³⁴ and ECoG³⁵, show that tuning of SM activity to movement parameters yields peaking activity around 100 ms before the movement. Taken together, the differences in the activation patterns reflects more likely information about upcoming cursor velocities. Consequently, the observed effects for the cursor positions can be explained by the cross-correlations between the movement parameters (Fig. 3a–d).

The third effect observed concerned the vertical component alone. In the execution condition, we observed that the correlations of the tuning curves were generally higher (Fig. 3h,i), a 0.1 higher correlation between vertical EOG derivative and target position and a decrease in blink rate. Moreover, the activation patterns were significantly stronger in the SPL (Fig. 5b,d, Table 1). Relative decreases in the blink rate have been shown to be related to the processing of more visual information²⁸ and more demanding tasks²⁹. This reflects the difference between visuomotor (VM) and oculomotor (OM) tasks studied here. Behavioral and decoding results combined indicate greater engagement in tracking vertical component signals in the VM task. We offer two non-exclusive explanations for this phenomenon. First, unlike the horizontal component, the vertical component mapping was not congruent; this means that forward hand movements were mapped to upward cursor movements. Therefore, the increase in SPL activity could be explained by the integration of incongruent proprioceptive and visual information. Second, we studied two stimuli, moving in two uncorrelated dimensions, which meant that the oculomotor system had to keep track of both dimensions. The findings of behavioral studies³⁰ and our results show that smooth pursuit is more accurate for the horizontal component. Accurate control of the upper-limb in the VM task could require the visual system to extract more information about the vertical component and, as a side effect, improve smooth pursuit. Since the SPL is involved in smooth pursuit control³⁶, the increase in information about the vertical component could be explained.

By combining multiple lags to predict cursor velocities we could raise grand average decoder correlations by around 0.05 to 0.4 in the execution condition and to 0.35 in the observation condition. These correspond to correlations reported in previous EEG decoding studies in center-out¹³ and continuous movement tasks^{37,38}. By averaging over participants, the correlations improved drastically to 0.8. The 2D plots in Figure 6c illustrate the reason for this effect. The grand average decoded cursor velocity is frequently in the same quadrant as the recorded cursor velocity; however, the variance among participants is considerable. Thus, the individual correlations are substantially lower. We inferred that the signal to noise ratio could be drastically improved by averaging the response over participants and consequently that the low-frequency EEG strongly correlates with positions and velocities at the group level in both conditions.

The grand average multiple lag cursor velocity decoder model patterns (Fig. 6d,e) demonstrate that the contributing sources were primarily of cortical origin in both conditions. Therefore, it is unlikely that the cursor velocity decoders relied on residual eye movement artifacts. It is also unlikely that arm or neck movement artifacts contributed, considered that there was no arm movement in the observation condition, and that the difference in decoder patterns (Fig. 6f,g) were primarily located in contralateral primary sensorimotor, fronto-central and parietal areas. In both conditions and in both components, pattern activity was strongest in the parieto-occipital and parietal areas (Fig. 6d,e). The associated DMOC and SPL ROIs showed significantly stronger pattern activity compared to the patterns of shuffled data (Table 1). This is in accordance with an increase in blood oxygenation level dependent (BOLD) activity in these areas during executed and observed reaching movements³⁹. Moreover, the strong tuning of parieto-occipital and parietal areas in both conditions, reported here, is in accordance with the modulation of BOLD activity by movement direction in an fMRI adaptation study¹⁰. Since there was no significant difference in the DMOC ROIs between conditions (Table 1; exe - obs), we inferred that the predictive activity in the parieto-occipital areas was not specific to the VM task. That is, the predictive activity in parieto-occipital areas did not require the involvement of the upper-limb.

In conclusion, we demonstrated that low-frequency EEG carries information about target and cursor positions and velocities, which is primarily encoded in fronto-parietal and parieto-occipital networks. By contrasting between the decoder patterns of the VM and OM tracking tasks, we found that the degree of tuning in fronto-central and contralateral primary sensorimotor areas to the instantaneous cursor velocity was significantly larger in the VM tracking task. The temporal tuning characteristics indicate that neural activity lead cursor velocity by approximately 150 ms (hand velocity by 95 ms). Altogether, the presented results on spatial and temporal tuning characteristics of the low-frequency EEG extend the findings of previous decoding studies. Moreover, we believe that it is possible to transfer our findings to individuals with tetraplegia, since the participants in this study moved their right arm only during the VM task, but the decoder correlations were clearly above chance level in both tracking tasks. Future closed-loop studies need to investigate whether the tuning characteristics of low-frequency EEG can be exploited to control an end-effector and whether the control skill can be improved.

Methods

Participants. Fifteen people, aged 23.8 ± 0.8 years, participated in this study. All received payment to compensate for their participation. Nine of the participants were female. All participants self-reported to have normal or corrected-to-normal vision and to be right handed. Eleven participants had previously participated at least once in an EEG experiment. All signed an informed consent form after they had been instructed about the purpose and procedure of the study. The experimental procedure conformed to the declaration of Helsinki and was approved by the ethics committee of the Medical University of Graz (approval number 29-058 ex 16/17).

Experimental set-up. Figure 1a depicts the recording environment. Participants sat in a shielded room, positioned 1.4 m away from a computer screen. Their left arm was supported by an arm rest, while the right arm was supported by a planar surface at the same height. To reduce friction between the right arm and the surface, participants were asked to wear a sleeve and place their hand on a circular pad. A LeapMotion controller (LeapMotion Inc., USA), placed 20 cm above the hand, was used to record the right hand's palm position. After participants found a comfortable resting position, the right hand's palm position was mapped to the origin (center of the screen) in the virtual environment. In analogy to the interaction with a computer by using a computer mouse, we decided to map rightward/forward hand movements to rightward/upward cursor movements. In order to create a trade-off between movement range and movement/muscular artifacts in the EEG, we mapped a circle with a 5 cm radius around the resting position to a circle with a 16 cm radius on the screen. The limits of the circle on the screen were indicated by the bounds of a virtual grid. E.g. by moving their hand 5 cm to the right, the participants could make the cursor touch the grid on the right side.

Experimental procedure. The experimental procedure consisted of 4 blocks, lasting 3 hours in total. In the first block, participants were asked to familiarize themselves with the paradigm (approx. 10 min). In the second and fourth block, eye artifacts (blinks and eye movements) and resting activity were recorded for 5 min. The detailed procedure is described in¹⁹. In the third block, participants performed the main experimental task according to the paradigm illustrated in Figure 1b. Each trial implemented a center-out reaching task followed by a PTT. A yellow target stimulus marked the beginning of a trial. It triggered the participants to fixate their gaze upon the target. The paradigm distinguished between two conditions. In the observation condition (blue target), participants merely tracked the moving target visually while the computer replayed a previous cursor trajectory. In the execution condition (green target), participants additionally had to minimize the distance between the target and cursor by moving their right hand and thereby the cursor. A total of 180 trials (90 per condition, pseudo randomly distributed) were recorded in 20 runs with short breaks in between. We additionally recorded 180 short trials (90 per condition, pseudo randomly distributed with the other trials within the 20 runs). A short trial ended after the center-out task. The data recorded during short trials were not used in this analysis. Supplementary Movie S1 shows the tracking behavior of representative participants in both conditions during long (center-out + PTT) and short (center-out) trials.

Target trajectories were generated offline and were identical across participant. Twelve base target trajectories were sampled from pink noise, which was band-passed in the frequency range of 0.3 to 0.6 Hz according to the procedure described by Paninski *et al.*¹⁵. We sampled the horizontal and vertical components independently so that they were uncorrelated. The trajectory pool was extended by adding rotated (90°, 180° and 270°) and mirrored versions of the base target trajectories. This yielded a total of 96 trajectories; 90 of these were randomly distributed over the 180 trials (once per condition). This procedure ensured uncorrelated position and velocity signals at lag 0 (Fig. S1).

The results of pilot studies revealed that the tracking dynamics varied among participants and over time. To achieve similar and participant specific tracking dynamics between the conditions, we implemented an adaptive approach. In observation condition trials, the most recent cursor trajectory of all matching versions (original, rotated and/or mirrored) of the associated base target trajectory was selected for replay. Details about the cursor trajectory replay procedure are described in the supplementary methods.

Data recording and pre-processing. All data was recorded using the labstreaming layer (LSL) protocol (<https://github.com/sccn/labstreaminglayer>). 64 active electrodes (actiCAP, Brain Products GmbH, Germany) were placed on the scalp according to the 10–10 system. The reference and ground electrodes were positioned at the right mastoid and AFz. Six additional active electrodes were placed at the superior, inferior and outer canthi of the right and left eyes to record EOG. Figure S2 visualizes the locations of all 70 electrodes. EEG and EOG data were recorded at 1 kHz (BrainAmp, Brain Products GmbH, Germany). The paradigm was implemented in Python 2.7 based on the simulation and neuroscience application (SNAP) platform (<https://github.com/sccn/SNAP>) and the 3D engine Panda3D (<https://www.panda3d.org>). The screen position signals of the visual stimuli (cursor, target) were recorded via LSL at 60 Hz and synchronized offline with the EEG signals by means of a photodiode, which captured an impulse on the screen at the start of each trial. All signals were then resampled to 200 Hz.

The pre-processing pipeline is depicted in Figure 7 and was implemented in Matlab (Matlab 2015b, Mathworks Inc., USA) and the open source software EEGLAB⁴⁰ version 14.1.1. EEG data were high-pass filtered (0.25 Hz cut-off frequency, Butterworth filter, eighth order, zero-phase). Data cleaning was initiated by a spherical interpolation of channels with poor signal quality (visual inspection). We interpolated 2.1 channels on average (Table S1). Eye movements and blinks were attenuated by applying the artifact subspace subtraction algorithm (outline in subsection *eye artifact correction*). The EEG channels were subsequently converted to common average reference (CAR). We then applied robust principal component analysis (Robust PCA)⁴¹ to attenuate occasional electrode pops and low-frequency drifts. The motivation behind Robust PCA is to separate a data matrix \mathbf{X} (raw EEG) into

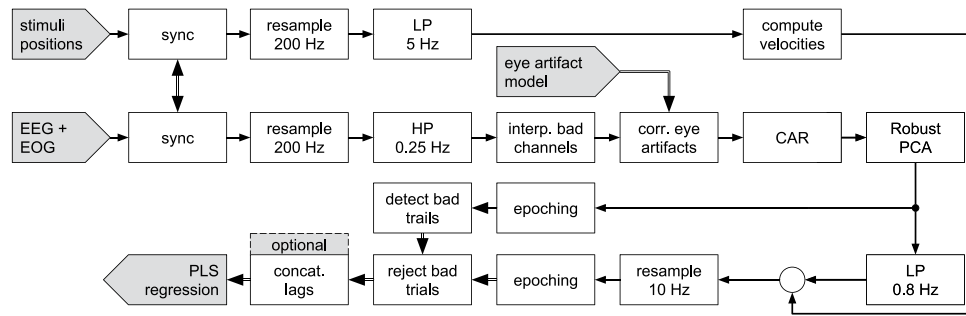


Figure 7. Signal pre-processing pipeline. After synchronization, brain signals were resampled, high-pass filtered and bad channels were spherically interpolated. Then, eye artifacts were attenuated¹⁹, followed by a conversion to a common average reference. Next, Robust PCA⁴¹ was applied to attenuate single electrode outliers. A subsequent low-pass filter was applied to extract the EEG signals in the frequency range of the target and cursor movements. Stimuli position signals were low-pass filtered before computing velocities and then concatenated to the EEG. After epoching, marked trials were rejected. Samples were optionally concatenated to extend the feature space for PLS regression.

a sum of a low rank matrix \mathbf{L} (EEG) and a sparse matrix \mathbf{S} (occasional single or few electrode outliers, e.g. pops). The optimization problem can be formulated as

$$\min \|\mathbf{L}\|_* + \lambda \|\mathbf{S}\|_1 \quad \text{s. t.} \quad \mathbf{X} = \mathbf{L} + \mathbf{S} \quad (1)$$

and solved iteratively⁴¹. We fixed the regularization parameter $\lambda = \frac{1.5}{\sqrt{N}}$ with N being the number of samples. All subsequent processing steps were applied to the extracted low rank data matrix \mathbf{L} . We epoched the data into 14 s trials, starting 1 s after tracking onset. Trials were marked for rejection if (1) the EEG signal of any channel exceeded a threshold of $\pm 200 \mu\text{V}$ or had an abnormal probability or kurtosis (more than 6 standard deviations beyond the mean), (2) the correlation of any EOG derivative (HEOG/VEOG) with the target position (horizontal/vertical) was improbable (more than 4 standard deviations beyond the mean), and (3) if a tracking error appeared (i.e. if hand tracking was lost or jerky). We applied the joint probability and kurtosis rejection criteria twice to detect gross outliers in the first iteration, and subtle outliers in the second iteration. All criteria combined marked an average of 16% of the trials for rejection. Supplementary Table S1 lists detailed information for each participant. Before actually rejecting trials, a low-pass filter (0.8 Hz cut-off frequency, Butterworth filter, fourth order, zero-phase) was used to extract EEG signals in the frequency of the target and cursor movements.

Stimuli position signals were low-pass filtered at 5 Hz (cut-off frequency, moving average finite impulse response filter, 17 filter taps, zero-phase) before velocities were extracted by computing first order, finite differences. Thereafter, the brain and stimuli signals were merged and resampled at 10 Hz. Then, the previously marked trials were rejected. Optionally, samples at various lags were concatenated to extend the feature space before fitting a regression model.

Eye artifact correction. The eye artifact correction approach is based on a block design^{19,42}. We fitted a linear eye artifact model to the recordings of blocks 2 and 4 (eye artifacts and resting brain activity) and applied the correction to the data of block 3.

The eye artifact model assumes a linear and stationary mixing of eye artifact sources $\mathbf{s}^{(a)}(t)$ ($n_{\text{artifact sources}} \times 1$) with brain activity, denoted as noise $\mathbf{n}(t)$ ($n_{\text{artifact sources}} \times 1$). The activity at the EEG and EOG channels $\mathbf{x}(t)$ ($n_{\text{channels}} \times 1$) is then

$$\mathbf{x}(t) = \mathbf{A}^{(a)} \mathbf{s}^{(a)}(t) + \mathbf{n}(t) \quad (2)$$

with a $n_{\text{channels}} \times n_{\text{artifact sources}}$ mixing matrix $\mathbf{A}^{(a)}$. The brain activity $\mathbf{x}_c(t)$ can be recovered by subtracting the eye artifact activity at each channel

$$\mathbf{x}_c(t) = \mathbf{x}(t) - \hat{\mathbf{A}}^{(a)} \hat{\mathbf{s}}^{(a)}(t) \approx \mathbf{n}(t) \quad (3)$$

if $\hat{\mathbf{A}}^{(a)}$ and $\hat{\mathbf{s}}^{(a)}(t)$ are good estimates of the unknown true mixing matrix and eye artifact sources. We applied the artifact subspace subtraction algorithm^{19,43} to compute the estimates. The algorithm estimates the source signals $\hat{\mathbf{s}}^{(a)}(t)$ by linearly combining all channels

$$\hat{\mathbf{s}}^{(a)}(t) = \mathbf{V}^{(a)} \mathbf{x}(t) \quad (4)$$

with a $n_{\text{artifact sources}} \times n_{\text{channels}}$ unmixing matrix $\mathbf{V}^{(a)}$. The correction in Equation (3) simplifies to

$$\mathbf{x}_c(t) = \mathbf{x}(t) - \hat{\mathbf{A}}^{(a)} \hat{\mathbf{s}}^{(a)}(t) = (\mathbf{I} - \hat{\mathbf{A}}^{(a)} \mathbf{V}^{(a)}) \mathbf{x}(t) \quad (5)$$

The eye artifact model parameters ($\hat{\mathbf{A}}^{(a)}$ and $\mathbf{V}^{(a)}$) were estimated in a two step approach¹⁹. First, penalized logistic regression was used to estimate each eye artifact source signal (e.g. horizontal eye movements) and its associated mixing coefficients (columns of $\hat{\mathbf{A}}^{(a)}$). Second, given the mixing matrix $\hat{\mathbf{A}}^{(a)}$ and the covariance matrix of the channels during resting brain activity \mathbf{R}_n ($n_{channels} \times n_{channels}$), the unmixing matrix $\mathbf{V}^{(a)}$ can be computed via regularized weighted least squares⁴³:

$$\mathbf{V}^{(a)} = (\hat{\mathbf{A}}^{(a)\text{T}} \mathbf{R}_n \hat{\mathbf{A}}^{(a)} + \mathbf{\Lambda})^{-1} \hat{\mathbf{A}}^{(a)\text{T}} \mathbf{R}_n \quad (6)$$

with $\mathbf{\Lambda}$ being a $n_{artifact\ sources} \times n_{artifact\ sources}$ diagonal regularization matrix. The original publication¹⁹ contains details about the model fitting procedure, choice of regularization parameters and a comparison to state of the art eye artifact correction approaches.

Movement parameter estimation. As low-frequency EEG is strongly correlated over time and space, there is considerable multicollinearity among the extracted features. An application of the partial least squares (PLS) regression⁴⁴ method is particularly suitable in this scenario. As in²², we fit one model per movement parameter, condition and participant.

Let \mathbf{X} be a $F \times N$ matrix of F predictor variables with N samples (i.e. the EEG data), and let \mathbf{y} be a $1 \times N$ vector representing the dependent variable (i.e. a particular movement parameter). The predictor variables are modelled as

$$\mathbf{X} = \mathbf{P}\mathbf{T} + \mathbf{E} \quad (7)$$

with \mathbf{T} representing a $D \times N$ matrix of latent components and \mathbf{E} , a $F \times N$ matrix of additive independent and identically distributed (iid) noise. \mathbf{P} , representing a $F \times D$ matrix, projects the latent components \mathbf{T} to the observed predictors \mathbf{X} . The goal of applying PLS regression is to find latent components \mathbf{T} that have maximal covariance with the dependent variable \mathbf{y} , while reducing the dimension from F to D . The dependent variable is then modelled as

$$\mathbf{y} = \mathbf{v}^T \mathbf{T} + \mathbf{g} \quad (8)$$

with \mathbf{v} , representing a $D \times 1$ weight vector, and additive iid noise \mathbf{g} . Here, we applied the SIMPLS algorithm²³ to estimate \mathbf{P} and \mathbf{v} for $D = 10$ latent components. The estimates can be combined to a $F \times 1$ weight vector to directly estimate the dependent variable

$$\hat{\mathbf{y}} = \hat{\mathbf{w}}^T \mathbf{X} \quad (9)$$

from the predictor variables \mathbf{X} .

The model was evaluated by applying 10 times a 5-fold cross validation (CV). That is, the data was randomly partitioned to 5 folds. Then model parameters were fit to 4 folds. Model prediction was tested on the held out fold by computing the Pearson correlation coefficient $r_{y\hat{y}}$ between \mathbf{y} and $\hat{\mathbf{y}}$. This was repeated until each fold was tested once. Thereafter, the random partitioning was repeated another 9 times, resulting in 50 estimates of $r_{y\hat{y}}$.

Chance level performance was estimated by applying the 5-fold CV to shuffled data. We broke the association between \mathbf{X} and \mathbf{y} while maintaining the correlation structure by randomly exchanging \mathbf{y} across trials. The shuffling and 5-fold CV procedure was repeated 100 times.

To interpret the extracted models, we transformed weight vectors to activation patterns²⁵. We scaled the unit-less patterns⁴⁵ with the standard-deviation of $\hat{\mathbf{y}}$ to express the patterns in terms of voltages. The scaled pattern associated with an estimated weight vector is then

$$\hat{\mathbf{a}} = \hat{\Sigma}_{\mathbf{X}} \hat{\mathbf{w}} \hat{\sigma}_{\hat{\mathbf{y}}}^{-1} \quad (10)$$

with empirical covariance matrix $\hat{\Sigma}_{\mathbf{X}}$ and standard-deviation $\hat{\sigma}_{\hat{\mathbf{y}}}$ of predictors and estimated dependent variable, respectively. Analytical shrinkage regularization⁴⁶ was applied to compute the estimate $\hat{\Sigma}_{\mathbf{X}}$. We then summarized the 50 CV models by computing the geometric median⁴⁷ across their patterns. This procedure yielded a representative pattern per movement parameter, condition and participant. To summarize the patterns obtained from chance level models, we randomly picked 50 patterns associated with 10 out of all 100 repetitions and computed their geometric median.

Pattern source mapping. We applied EEG source imaging^{26,27} to map the scaled patterns from channel space (i.e. scalp level) to source space (i.e. cortical surface). Head models were created by co-registering the ICBM152 boundary element model (BEM) template⁴⁸ with recorded electrode positions (ELPOS, Zebri Medical GmbH, Germany) using the open source software Brainstorm⁴⁹ version 19-Jan-2018. The BEM comprised three layers (cortex, skull, scalp) with relative conductivities (1, 0.008, 1). The cortex was modelled with 5001 voxels. BEM and electrode positions were co-registered by three anatomical landmarks (nasion, left and right preauricular points). Due to deviations between participant and template anatomy, we completed the co-registration by projecting floating electrodes to the scalp layer (Fig. S2b). OpenMEEG^{50,51} was used to compute the forward model; that is, to describe the propagation of the electric fields from cortex to scalp. sLORETA⁵² was applied to compute the corresponding inverse model for unconstrained sources. For unconstrained sources the activity at each voxel is described 3 components (x, y, z coordinates). We used three minutes of resting EEG, recorded during

blocks two and four, to estimate sensor noise. The pre-processing of resting EEG was conducted identically as explained above. We then estimated the noise covariance matrix by applying analytical shrinkage regularization⁴⁶.

Before mapping the regression model patterns to source space, we normalized them to alleviate participant-dependent scaling. Since the scaled patterns reflected the potential at the scalp, their magnitude reflected the magnitude of the recorded signals. However, in the EEG, the global field power can vary considerably among participants. To compensate for this effect, we normalized the patterns by the average channel power. The average channel power was estimated by taking the median of the diagonal elements of the noise covariance matrix. The inverse scalar was then applied to scale participant-specific patterns. We then projected the final channel space patterns onto source space in Brainstorm, extracted the Euclidean norm of the three components (x, y, z coordinates) per voxel and optionally averaged over lags if the model comprised multiple lags.

Source space statistics. Group level analysis was performed by computing paired differences between patterns of a movement parameter in source space. Significance was assessed at eight regions of interest (ROIs), which have consistently been associated with movement processing. The ROIs are depicted in Figure 4c and cover fronto-central, primary sensorimotor, parietal and parieto-occipital areas. Activity at each ROI was summarized by the mean of its voxels. Significant ROIs were detected by applying two-tailed non-parametric permutation paired *t*-tests^{53,54} with 1000 repetitions. Regarding multiple comparisons, we controlled the false discovery rate (FDR) at a significance level of 0.05 by adjusting the *p*-values⁵⁵.

Code availability. The codes used for data collection and analysis in this study are available from the corresponding author upon request.

Data Availability

The data that support the findings of this study are available from the corresponding author upon request.

References

- Georgopoulos, A. P., Kalaska, J. F., Caminiti, R. & Massey, J. T. On the relations between the direction of two-dimensional arm movements and cell discharge in primate motor cortex. *J. Neurosci.* **2**, 1527–1537 (1982).
- Caminiti, R., Johnson, P. B., Galli, C., Ferraina, S. & Burnod, Y. Making arm movements within different parts of space: the premotor and motor cortical representation of a coordinate system for reaching to visual targets. *J. Neurosci.* **11**, 1182–1197 (1991).
- Kalaska, J. F., Caminiti, R. & Georgopoulos, A. P. Cortical mechanisms related to the direction of two-dimensional arm movements: relations in parietal area 5 and comparison with motor cortex. *Exp. Brain Res.* **51**, 247–260 (1983).
- Carmena, J. M. *et al.* Learning to control a brain-machine interface for reaching and grasping by primates. *PLoS Biol.* **1**, E42 (2003).
- Wessberg, J. *et al.* Real-time prediction of hand trajectory by ensembles of cortical neurons in primates. *Nature* **408**, 361–365 (2000).
- Hochberg, L. R. *et al.* Neuronal ensemble control of prosthetic devices by a human with tetraplegia. *Nature* **442**, 164–171 (2006).
- Culham, J. C. & Valyear, K. F. Human parietal cortex in action. *Curr. Opin. Neurobiol.* **16**, 205–212 (2006).
- Filimon, F., Nelson, J. D., Hagler, D. J. & Sereno, M. I. Human cortical representations for reaching: mirror neurons for execution, observation, and imagery. *Neuroimage* **37**, 1315–1328 (2007).
- Filimon, F., Nelson, J. D., Huang, R.-S. & Sereno, M. I. Multiple parietal reach regions in humans: cortical representations for visual and proprioceptive feedback during on-line reaching. *J. Neurosci.* **29**, 2961–2971 (2009).
- Fabbri, S., Caramazza, A. & Lingnau, A. Tuning curves for movement direction in the human visuomotor system. *J. Neurosci.* **30**, 13488–13498 (2010).
- Schalk, G. *et al.* Decoding two-dimensional movement trajectories using electrocorticographic signals in humans. *J. Neural Eng.* **4**, 264–275 (2007).
- Waldert, S. *et al.* Hand movement direction decoded from MEG and EEG. *J. Neurosci.* **28**, 1000–1008 (2008).
- Bradberry, T. J., Gentili, R. J. & Contreras-Vidal, J. L. Reconstructing three-dimensional hand movements from noninvasive electroencephalographic signals. *J. Neurosci.* **30**, 3432–3437 (2010).
- Robinson, N. & Vinod, A. P. Noninvasive Brain-Computer Interface: Decoding Arm Movement Kinematics and Motor Control. *IEEE Systems, Man, and Cybernetics Magazine* **2**, 4–16 (2016).
- Paninski, L., Fellows, M. R., Hatsopoulos, N. G. & Donoghue, J. P. Spatiotemporal tuning of motor cortical neurons for hand position and velocity. *J. Neurophysiol.* **91**, 515–532 (2004).
- Sailer, U., Flanagan, J. R. & Johansson, R. S. Eye-hand coordination during learning of a novel visuomotor task. *J. Neurosci.* **25**, 8833–8842 (2005).
- Perry, C. J., Amarasooriya, P. & Fallah, M. An Eye in the Palm of Your Hand: Alterations in Visual Processing Near the Hand, a Mini-Review. *Front. Comput. Neurosci.* **10** (2016).
- Pereira, M., Sobolewski, A. & del R. Millán, J. Action Monitoring Cortical Activity Coupled to Submovements. *eNeuro* **4**, ENEURO.0241–17.2017 (2017).
- Kobler, R. J., Sburlea, A. I. & Müller-Putz, G. R. A Comparison of Ocular Artifact Removal Methods for Block Design Based Electroencephalography Experiments. In *Proceedings of the 7th Graz Brain-Computer Interface Conference* 236–241 (2017).
- Desmurget, M. & Grafton, S. Forward modeling allows feedback control for fast reaching movements. *Trends Cogn. Sci.* **4**, 423–431 (2000).
- Haith, A. M., Pakpoor, J. & Krakauer, J. W. Independence of Movement Preparation and Movement Initiation. *J. Neurosci.* **36**, 3007–3015 (2016).
- Ofner, P. & Müller-Putz, G. R. Using a noninvasive decoding method to classify rhythmic movement imaginations of the arm in two planes. *IEEE Trans. Biomed. Eng.* **62**, 972–981 (2015).
- de Jong, S. SIMPLS: An alternative approach to partial least squares regression. *Chemometrics Intellig. Lab. Syst.* **18**, 251–263 (1993).
- Antelis, J. M., Montesano, L., Ramos-Murguialday, A., Birbaumer, N. & Minguez, J. On the usage of linear regression models to reconstruct limb kinematics from low frequency EEG signals. *PLoS One* **8**, e61976 (2013).
- Haufe, S. *et al.* On the interpretation of weight vectors of linear models in multivariate neuroimaging. *Neuroimage* **87**, 96–110 (2014).
- Michel, C. M. *et al.* EEG source imaging. *Clin. Neurophysiol.* **115**, 2195–2222 (2004).
- Michel, C. M. & Murray, M. M. Towards the utilization of EEG as a brain imaging tool. *Neuroimage* **61**, 371–385 (2012).
- Veltman, J. A. & Gaillard, A. W. Physiological workload reactions to increasing levels of task difficulty. *Ergonomics* **41**, 656–669 (1998).
- Wilson, G. F. An Analysis of Mental Workload in Pilots During Flight Using Multiple Psychophysiological Measures. *Int. J. Aviat. Psychol.* **12**, 3–18 (2002).

30. Collewijn, H. & Tamminga, E. P. Human smooth and saccadic eye movements during voluntary pursuit of different target motions on different backgrounds. *J. Physiol.* **351**, 217–250 (1984).
31. Battaglia-Mayer, A. A Brief History of the Encoding of Hand Position by the Cerebral Cortex: Implications for Motor Control and Cognition. *Cereb. Cortex.* <https://doi.org/10.1093/cercor/bhx354> (2018).
32. Miall, R. C. & Wolpert, D. M. Forward Models for Physiological Motor Control. *Neural Netw.* **9**, 1265–1279 (1996).
33. Mehring, C. *et al.* Inference of hand movements from local field potentials in monkey motor cortex. *Nat. Neurosci.* **6**, 1253–1254 (2003).
34. Jerbi, K. *et al.* Inferring hand movement kinematics from MEG, EEG and intracranial EEG: From brain-machine interfaces to motor rehabilitation. *IRBM* **32**, 8–18 (2011).
35. Pistohl, T., Ball, T., Schulze-Bonhage, A., Aertsen, A. & Mehring, C. Prediction of arm movement trajectories from ECoG-recordings in humans. *J. Neurosci. Methods* **167**, 105–114 (2008).
36. Krauzlis, R. J. Recasting the smooth pursuit eye movement system. *J. Neurophysiol.* **91**, 591–603 (2004).
37. Lv, J., Li, Y. & Gu, Z. Decoding hand movement velocity from electroencephalogram signals during a drawing task. *Biomed. Eng. Online* **9**, 64 (2010).
38. Kim, J.-H., Bießmann, F. & Lee, S.-W. Decoding Three-Dimensional Trajectory of Executed and Imagined Arm Movements From Electroencephalogram Signals. *IEEE Trans. Neural Syst. Rehabil. Eng.* **23**, 867–876 (2015).
39. Filimon, F. Human cortical control of hand movements: parietofrontal networks for reaching, grasping, and pointing. *Neuroscientist* **16**, 388–407 (2010).
40. Delorme, A. & Makeig, S. EEGLAB: an open source toolbox for analysis of single-trial EEG dynamics including independent component analysis. *J. Neurosci. Methods* **134**, 9–21 (2004).
41. Candès, E. J., Li, X., Ma, Y. & Wright, J. Robust principal component analysis? *J. ACM* **58**, 1–37 (2011).
42. Schlögl, A. *et al.* A fully automated correction method of EOG artifacts in EEG recordings. *Clin. Neurophysiol.* **118**, 98–104 (2007).
43. Parra, L. C., Spence, C. D., Gerson, A. D. & Sajda, P. Recipes for the linear analysis of EEG. *Neuroimage* **28**, 326–341 (2005).
44. Wold, S., Sjöström, M. & Eriksson, L. PLS-regression: a basic tool of chemometrics. *Chemometrics Intellig. Lab. Syst.* **58**, 109–130 (2001).
45. Ofner, P., Schwarz, A., Pereira, J. & Müller-Putz, G. R. Upper limb movements can be decoded from the time-domain of low-frequency EEG. *PLoS One* **12**, e0182578 (2017).
46. Bartz, D. & Müller, K.-R. Covariance shrinkage for autocorrelated data. In *Advances in neural information processing systems* 1592–1600 (2014).
47. Weiszfeld, E. Sur le point pour lequel la somme des distances de n points donnés est minimum. *Tohoku Math. J.* **43**, 355–386 (1937).
48. Fonov, V. *et al.* Unbiased average age-appropriate atlases for pediatric studies. *Neuroimage* **54**, 313–327 (2011).
49. Tadel, F., Baillet, S., Mosher, J. C., Pantazis, D. & Leahy, R. M. Brainstorm: a user-friendly application for MEG/EEG analysis. *Comput. Intell. Neurosci.* **2011**, 879716 (2011).
50. Kybic, J. *et al.* A common formalism for the integral formulations of the forward EEG problem. *IEEE Trans. Med. Imaging* **24**, 12–28 (2005).
51. Gramfort, A., Papadopoulos, T., Olivi, E. & Clerc, M. OpenMEEG: opensource software for quasistatic bioelectromagnetics. *Biomed. Eng. Online* **9**, 45 (2010).
52. Pascual-Marqui, R. D. Standardized low-resolution brain electromagnetic tomography (sLORETA): technical details. *Methods Find. Exp. Clin. Pharmacol.* **24**(Suppl D), 5–12 (2002).
53. Nichols, T. E. & Holmes, A. P. Nonparametric permutation tests for functional neuroimaging: a primer with examples. *Hum. Brain Mapp.* **15**, 1–25 (2002).
54. Maris, E. & Oostenveld, R. Nonparametric statistical testing of EEG- and MEG-data. *J. Neurosci. Methods* **164**, 177–190 (2007).
55. Yekutieli, D. & Benjamini, Y. Resampling-based false discovery rate controlling multiple test procedures for correlated test statistics. *J. Stat. Plan. Inference* **82**, 171–196 (1999).

Acknowledgements

The authors acknowledge Joana Pereira, Catarina Lopes Dias, Lea Hehenberger, Martin Seeber, Patrick Ofner, Andreas Schwarz and David Steyrl for their valuable comments and Maria Höller for her support during data acquisition. This work has received funding from the European Research Council (ERC) under the European Union's Horizon 2020 research and innovation programme (Consolidator Grant 681231 'Feel Your Reach').

Author Contributions

R.J.K., A.I.S. and G.R.M. conceived the study. R.J.K. implemented the paradigm and performed the acquisition. R.J.K. conducted the analysis. R.J.K., A.I.S. and G.R.M. interpreted the data. R.J.K. created the Figures and Tables. R.J.K. wrote the draft of the manuscript. R.J.K., A.I.S. and G.R.M. edited the manuscript.

Additional Information

Supplementary information accompanies this paper at <https://doi.org/10.1038/s41598-018-36326-y>.

Competing Interests: The authors declare no competing interests.

Publisher's note: Springer Nature remains neutral with regard to jurisdictional claims in published maps and institutional affiliations.



Open Access This article is licensed under a Creative Commons Attribution 4.0 International License, which permits use, sharing, adaptation, distribution and reproduction in any medium or format, as long as you give appropriate credit to the original author(s) and the source, provide a link to the Creative Commons license, and indicate if changes were made. The images or other third party material in this article are included in the article's Creative Commons license, unless indicated otherwise in a credit line to the material. If material is not included in the article's Creative Commons license and your intended use is not permitted by statutory regulation or exceeds the permitted use, you will need to obtain permission directly from the copyright holder. To view a copy of this license, visit <http://creativecommons.org/licenses/by/4.0/>.

© The Author(s) 2018



PAPER

OPEN ACCESS

RECEIVED
7 April 2020REVISED
4 August 2020ACCEPTED FOR PUBLICATION
28 August 2020PUBLISHED
xx xx xxxxOriginal content from
this work may be used
under the terms of the
[Creative Commons
Attribution 4.0 licence](#).Any further distribution
of this work must
maintain attribution to
the author(s) and the title
of the work, journal
citation and DOI.Distance- and speed-informed kinematics decoding improves
M/EEG based upper-limb movement decoder accuracyReinmar J Kobler¹ , Andreea I Sburlea¹, Valeria Mondini¹ , Masayuki Hirata^{2,3} and
Gernot R Müller-Putz^{1,4} ¹ Institute of Neural Engineering, Graz University of Technology, Graz 8010, Styria, Austria² Department of Neurological Diagnosis and Restoration, Osaka University Graduate School of Medicine, Suita, Osaka, Japan³ Department of Neurosurgery, Osaka University Graduate School of Medicine, Suita, Osaka, Japan⁴ BioTechMed, Graz 8010, Styria, AustriaE-mail: gernot.mueller@tugraz.at**Keywords:** electroencephalography, magnetoencephalography, motor control, decoding, brain–computer interface, kinematicsSupplementary material for this article is available [online](#)**Abstract**

Objective. One of the main goals in brain–computer interface (BCI) research is the replacement or restoration of lost function in individuals with paralysis. One line of research investigates the inference of movement kinematics from brain activity during different volitional states. A growing number of electroencephalography (EEG) and magnetoencephalography (MEG) studies suggest that information about directional (e.g. velocity) and nondirectional (e.g. speed) movement kinematics is accessible noninvasively. We sought to assess if the neural information associated with both types of kinematics can be combined to improve the decoding accuracy. Approach. In an offline analysis, we reanalyzed the data of two previous experiments containing the recordings of 34 healthy participants (15 EEG, 19 MEG). We decoded 2D movement trajectories from low-frequency M/EEG signals in executed and observed tracking movements, and compared the accuracy of an unscented Kalman filter (UKF) that explicitly modeled the nonlinear relation between directional and nondirectional kinematics to the accuracies of linear Kalman (KF) and Wiener filters which did not combine both types of kinematics. Main results. At the group level, posterior-parietal and parieto-occipital (executed and observed movements) and sensorimotor areas (executed movements) encoded kinematic information. Correlations between the recorded position and velocity trajectories and the UKF decoded ones were on average 0.49 during executed and 0.36 during observed movements. Compared to the other filters, the UKF could achieve the best trade-off between maximizing the signal to noise ratio and minimizing the amplitude mismatch between the recorded and decoded trajectories. Significance. We present direct evidence that directional and nondirectional kinematic information is simultaneously detectable in low-frequency M/EEG signals. Moreover, combining directional and nondirectional kinematic information significantly improves the decoding accuracy upon a linear KF.

1. Introduction

Inferring movement parameters from electrophysiological brain signals during different volitional states has been a central topic in brain–computer interface (BCI) research [1, 2]. BCIs potentially allow individuals with tetraplegia to control computer cursors, robotic arms or neuroprostheses and thereby replace or restore lost or compromised function [3–6]. In nonhuman primates, intracortical

BCIs (iBCIs) typically decode kinematic and kinetic information of executed movements from neural spiking activity in primary motor cortex (M1), dorsal premotor cortex (PMd), primary somatosensory cortex (S1) and posterior parietal cortex (PP) [7–10]. Decoding kinematic parameters from attempted movements has allowed paralyzed individuals, equipped with an iBCI, to control end-effectors with a high accuracy [11–14]. Despite non-invasive functional neuroimaging techniques such

as electroencephalography (EEG) and magnetoencephalography (MEG) have a lower spatial resolution and signal to noise ratio (SNR), they also carry information about movement kinematics and kinetics [15–19]. In this context, low-frequency activity in the range of the movement has been reported to encode kinematic information during different volitional states, such as executed [17, 19, 20], imagined [21–23] and observed movements [20, 23]. Although numerous studies reported that kinematic information is encoded in M/EEG signals, it is not clear with which accuracy a non-invasive BCI can infer movement trajectories.

In studies that decode directional kinematics (e.g. position and velocity) from low-frequency activity, the accuracy of the decoded trajectories is typically quantified by computing correlations between the recorded and decoded trajectories [15, 19, 24]. Correlation is invariant to amplitude mismatches, rendering it insufficient to qualitatively evaluate the accuracy [25]. In fact, linear regression based decoders that minimize the mean squared error (MSE) tend to exhibit amplitude mismatches in discrete reaching [26, 27] and continuous movement tasks [15, 20, 24, 28]. The decoded trajectories are typically estimated too small, with the mismatch increasing as the correlation decreases [29, 30]. Non-linear methods reduce the amplitude mismatch [23], indicating that the low-frequency activity could carry kinematic information that is nonlinearly related to the directional kinematics.

There is evidence that the neural activity carries information about distance (length of the position vector) and speed (length of the velocity vector) [31]. Distance and speed are inherently nondirectional and nonlinearly related to position and velocity. They are also uncorrelated to position and velocity during commonly studied tasks (e.g. center out reaching, pursuit tracking). The nondirectional kinematic information is known to be encoded in neural spiking activity in M1 [31, 32], in low-frequency local field potentials [33] and electrocorticographic (ECoG) activity [34]. Jerbi *et al* were the first to report speed related tuning effects in low-frequency MEG activity [16]. Using a continuous movement task, Hammer *et al* demonstrated that low-frequency ECoG activity simultaneously carries information about velocity and speed [34]. We recently corroborated their findings in low-frequency MEG activity and a 2D pursuit tracking task (PTT) [35].

Due to the nonlinear relationship between directional and nondirectional kinematics, a linear model can not combine the information encoded in the low-frequency M/EEG activity. We surmise that a decoding algorithm that models their nonlinear relation should achieve superior decoding accuracy and reduce the amplitude mismatch. Inspired by models used in iBCIs [32, 36], we use an unscented Kalman filter (UKF) [37] to combine the directional

and nondirectional information during a 2D PTT. In an offline analysis, we compared the UKF decoding accuracy with the one achieved by two linear models, a Kalman filter (KF) [38] and a Wiener filter (WF) [39].

2. Methods

2.1. Participants

In this study we reanalyzed experimental data obtained from two distinct groups of healthy human participants during executed and observed movements. The first group (experiment 1; 15 participants, nine female, six male, mean age of 23.8 years) was previously published in [20, 40], and the second group (experiment 2; 23 recruited participants, 18 male, five female, mean age of 28.5 years) was previously published in [35]. As reported in [35], the data of four participants in the second group were excluded because of incomplete recordings or incorrect positioning in the MEG scanner. In both groups, all participants had normal or corrected to normal vision and self-reported to be right-handed.

The experimental procedure conformed to the Declaration of Helsinki and was approved by the ethics committee of the Medical University of Graz (group 1) and Osaka University Hospital (group 2). After the study participants were informed about the purpose and procedure of the study, they gave their written consent.

2.2. Experimental paradigm

The participants of experiment 1 underwent two experimental conditions (execution and observation) while their EEG activity was recorded. The experimental paradigm and setup have been described in detail in [20]. Figure 1(a) illustrates the sequence of events during a trial (top) and the virtual 2D environment displayed on a computer screen (bottom). In 180 trials (90 per condition, pseudo-randomly distributed), the participants completed a center-out task and a 16-s long PTT. In this study, we analyzed the PTT.

In the execution condition, we instructed the participants to smoothly track a moving target stimulus (large green ball) with a cursor (small gray ball) and their gaze. In the observation condition (blue target), the participants tracked the target only with their gaze; they lost control of the cursor and were instructed to maintain a resting position. In this condition, the paradigm replayed a previous, matching cursor trajectory.

The 2D target trajectories consisted of two independent and identically distributed (iid) components (horizontal and vertical). Each component was sampled from band-limited pink noise (0.3 to 0.6 Hz). The target trajectories were generated offline and were identical for all participants. The trajectory generation procedure ensured that the positions and

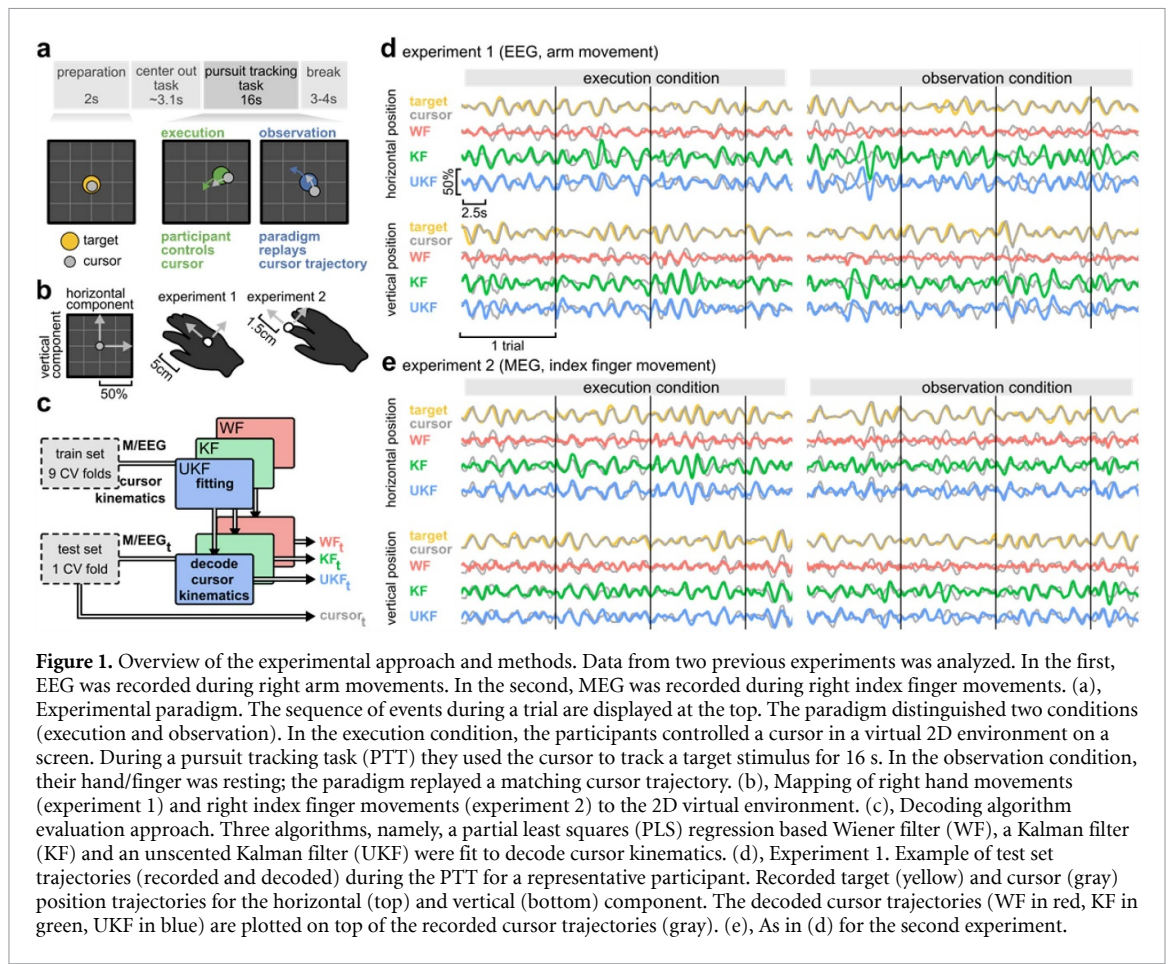


Figure 1. Overview of the experimental approach and methods. Data from two previous experiments was analyzed. In the first, EEG was recorded during right arm movements. In the second, MEG was recorded during right index finger movements. (a), Experimental paradigm. The sequence of events during a trial are displayed at the top. The paradigm distinguished two conditions (execution and observation). In the execution condition, the participants controlled a cursor in a virtual 2D environment on a screen. During a pursuit tracking task (PTT) they used the cursor to track a target stimulus for 16 s. In the observation condition, their hand/finger was resting; the paradigm replayed a matching cursor trajectory. (b), Mapping of right hand movements (experiment 1) and right index finger movements (experiment 2) to the 2D virtual environment. (c), Decoding algorithm evaluation approach. Three algorithms, namely, a partial least squares (PLS) regression based Wiener filter (WF), a Kalman filter (KF) and an unscented Kalman filter (UKF) were fit to decode cursor kinematics. (d), Experiment 1. Example of test set trajectories (recorded and decoded) during the PTT for a representative participant. Recorded target (yellow) and cursor (gray) position trajectories for the horizontal (top) and vertical (bottom) component. The decoded cursor trajectories (WF in red, KF in green, UKF in blue) are plotted on top of the recorded cursor trajectories (gray). (e), As in (d) for the second experiment.

velocities of the horizontal and vertical components were decorrelated, and in addition that the position and velocity of the same component were decorrelated at lag 0 [20].

In experiment 1, the participants controlled the cursor with 2D right arm movements on a table. Figure 1(b) illustrates how arm movements were mapped to cursor movements in the virtual environment on the screen. If the palm of the right hand moved forward (or rightward) by 5 cm from a pre-registered resting position, the cursor moved upward (or rightward) to the edge of the virtual environment (50% of the workspace). The online transformation of hand movements into cursor movements introduced an average delay of 55 ms with a standard deviation (SD) of 1 ms.

The participants of experiment 2 underwent a similar experimental paradigm while their MEG activity was recorded. In this experiment, the participants were lying in an MEG scanner. The experimental conditions, paradigm and setup have been described in detail in [35]. The sequence of events during a trial were identical to experiment 1, except that we omitted the center-out task (figure 1(a)). We recorded 160 trials (80 per condition, pseudo-randomly distributed) per participant.

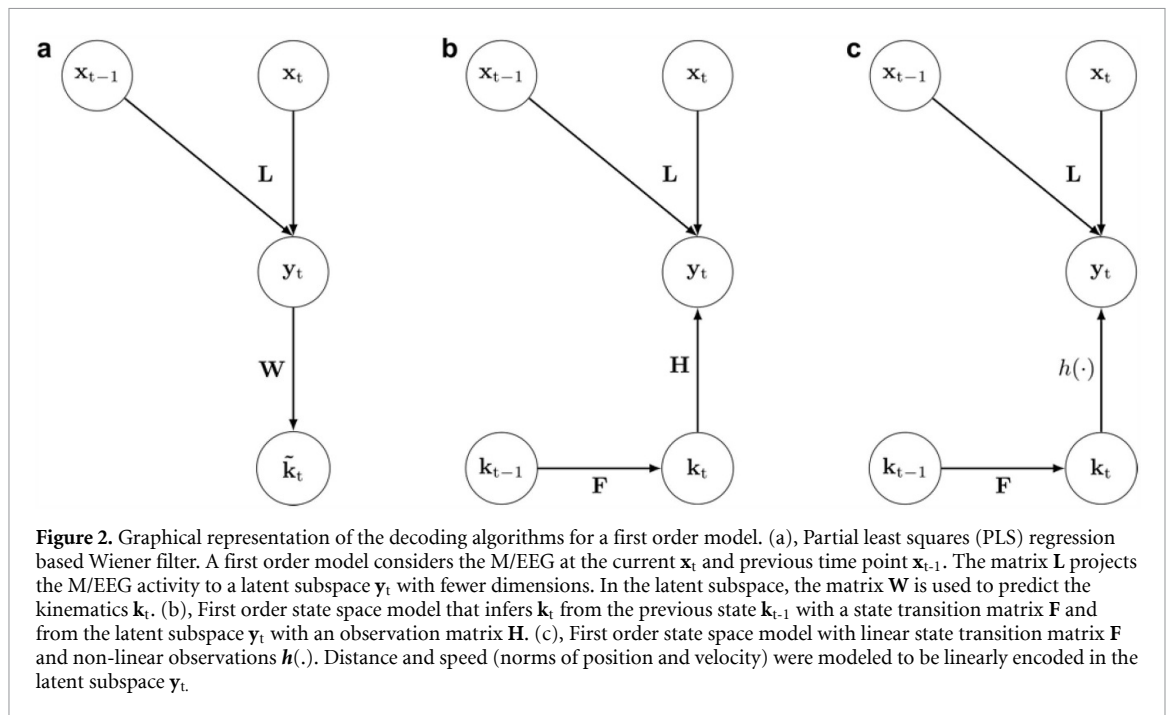
In experiment 2, the participants performed 2D right index finger movements on a planar surface

to the side of their body. If the tip of the index finger moved forward (or rightward) by 1.5 cm from a pre-registered resting position, the cursor moved upward (or rightward) to the edge of the virtual environment (50% of the workspace). We used a custom motion capture system, to transform the index finger movements into cursor movements [35]. The system introduced an average delay of 190 ms.

2.3. Data acquisition

In experiment 1, we recorded EEG activity with 64 active electrodes (actiCAP, Brain Products GmbH, Germany). The electrodes were placed according to the 10–10 system; reference and ground were placed at the right mastoid and AFz. We recorded electrooculographic (EOG) activity with six additional active electrodes, placed next to the outer canthi and above and below both eyes. EEG and EOG signals were amplified and digitized at a rate of 1 kHz with a biosignal amplifier (BrainAmp, Brain Products GmbH, Germany).

In experiment 2, we recorded MEG activity with a 160 channel whole-head MEG system (MEGvision NEO, RICOH Ltd., Japan) housed in a magnetically shielded room. EOG activity was recorded with four electrodes placed at the outer canthi of both eyes, and above and below the left eye. EOG signals were



recorded with a biosignal amplifier (Neurofax EEG 1200, Nihon Koden Corp., Japan). The MEG and EOG signals were recorded synchronously at a rate of 1 kHz. Inside the MEG scanner, the participant's head was resting on a cushion. We asked the participants to avoid head and shoulder movements during the course of the experiment. At the beginning of each run (16 trials), we additionally measured the head position with five marker coils, attached to the forehead.

Visual stimuli (60 Hz sampling rate) and motion capture signals (experiment 1: 100 Hz sampling rate; experiment 2: 60 Hz sampling rate) were recorded with the labstreaming layer protocol [41]. The paradigm was implemented in Python (version 2.7) and the simulation and neuroscience application platform [42].

2.4. Data preprocessing

Offline, we analyzed the data with a custom pipeline implemented in Matlab (version 2015b; Mathworks Inc. USA), EEGLAB toolbox (version 14.1.1) [43], Brainstorm (version 5 June 2018) [44] and R [45, 46]. As a first step, we synchronized the M/EEG and EOG signals with the visual stimuli by aligning impulses captured by a photodiode with the associated markers. We resampled the synchronized signals at a rate of 200 Hz, before we separately preprocessed the cursor kinematics and the M/EEG signals. Supplementary figure 16 (available online at <https://stacks.iop.org/JNE/00/00000/mmedia>) summarizes the M/EEG preprocessing steps in both experiments.

2.4.1. EEG preprocessing (experiment 1)

The EEG and EOG signals were first high-pass (0.25 Hz cut-off frequency, Butterworth filter, eighth order, zero-phase) and notch (49 and 51 Hz cut-off frequencies, Butterworth filter, fourth order, zero-phase) filtered to attenuate drifts and powerline noise. We visually inspected the signals to detect bad channels. A channel was considered as bad, if it was affected regularly by pops, drifts or muscle artifacts. On average, 2.1 channels were marked as bad. The signal of the bad channels was spherically interpolated using EEGLAB. Next, we applied the sparse generalized eye artifact subspace subtraction algorithm (SGEYESUB) to attenuate eye movement and blink related artifacts [47]. SGEYESUB was fit to calibration data recorded at the start and end of the experiment according to the paradigm presented in [48]. After the eye artifacts were attenuated, we excluded the EOG and fronto-temporal channels (FPz, AF7, AF8, AF8, FT9, F7, F8, FT10) from the further analysis and re-referenced the remaining 57 EEG channels to their common average.

2.4.2. MEG preprocessing (experiment 2)

We excluded 31 MEG channels at inferior temporal locations because they were contaminated by technical artifacts. To compensate for small head movements across runs, we spherically interpolated the MEG signals of the remaining 129 channels to their average location across runs. The mean distance of a channel to its average location across runs was 5 mm (0.4 mm SD). After concatenating the signals across runs, we also applied high-pass (0.25 Hz cut-off frequency, Butterworth filter, eighth order,

zero-phase) and notch (59 and 61 Hz cut-off frequencies, Butterworth filter, fourth order, zero-phase) filters. To further attenuate technical and spatially stationary artifacts, we applied independent component analysis [49]. Using the extended Infomax algorithm, we decomposed the MEG signals (high-pass filtered at 0.4 Hz, instead of 0.25 Hz) into independent components (ICs) that explain 99.9% of the variance. We marked 8.6 (0.9 SD) out of 63.5 (0.1 SD) ICs (visual inspection). The marked ICs were then removed from the 0.25 Hz high-pass filtered signals. As in the EEG preprocessing, we applied SGEYESUB to attenuate eye movement and blink related artifacts and excluded the EOG and fronto-temporal channels (RT21, RT22, RT31, RT32, RT33, LT11, LT21, LT22, LT33) from further analysis.

2.4.3. Common M/EEG preprocessing steps

All subsequent processing steps were shared between experiment 1 and 2. The first common step was to attenuate transient drifts and pops in the continuous M/EEG signals with the high-variance electrode artifact removal algorithm [50].

Next, we detected bad epochs [51]. We first epoched the continuous, broadband data into 14 s epochs. Each epoch started 1 s after the beginning of the PTT. An epoch was considered as bad, if the broadband M/EEG activity of any channel exceeded a threshold ($\pm 200 \mu\text{V}$ or $\pm 5\text{pT}$), had an abnormal probability, variance or kurtosis (more than 6 (probability), 5 (variance), 6 (kurtosis) SDs around the mean), the correlation between the EOG and target position signals were improbable (exceeding 4 SDs around the mean), or a tracking error happened (e.g. jerky or no cursor movement). We tested for abnormal probability, variance and kurtosis twice, in order to detect gross outliers in the first iteration and subtle outliers in the second iteration. All criteria combined, a total of 29.5 (9.8 SD) of 180.7 (2.8 SD) epochs were marked for rejection in experiment 1, and 27.3 (8.9 SD) of 152.2 (13.1 SD) in experiment 2.

To extract low-frequency activity, we applied a low-pass filter (2 Hz cut-off frequency, Butterworth filter, sixth order, zero-phase) to the continuous M/EEG signals and resampled the result at 10 Hz. In the last preprocessing step, we extracted the 14 s epochs and rejected the previously marked bad epochs.

2.4.4. Cursor kinematics preprocessing

We used Savitzky–Golay filters [52] (finite impulse response filter, third order polynomial, 21 filter taps, zero-phase) to compute smoothed cursor positions and velocities. The origin of the coordinate system was the center of the virtual 2D environment (figure 1(b)). Similar to the M/EEG signals, we resampled the results at 10 Hz and extracted the 14-s epochs. We computed distance and speed by computing the Euclidean norm of the 2D cursor position and

velocity vectors at each sample t . As a last step, we z-scored the cursor kinematics (2D position, 2D velocity, distance and speed).

2.5. Encoding of cursor kinematics in

low-frequency M/EEG activity

We fitted a general linear model (GLM) with the cursor kinematics as predictors, to identify how the cursor kinematics were expressed in the low-frequency M/EEG activity at 11 lags $l \in [-0.5s, 0.5s]$. In detail, we fitted one GLM per experimental condition and lag l . By concatenating all observations (samples and trials) of one condition, the kinematics could be expressed as a $6 \times n_{\text{observations}}$ matrix \tilde{K}

$$\tilde{K} = \begin{bmatrix} p^{(\text{horz})}; v^{(\text{horz})}; p^{(\text{vert})}; v^{(\text{vert})}; d; s \end{bmatrix} \quad (1)$$

with $1 \times n_{\text{observations}}$ vectors $p^{(\text{horz})}$, $v^{(\text{horz})}$, $p^{(\text{vert})}$, $v^{(\text{vert})}$, d and s coding the horizontal position, horizontal velocity, vertical position, vertical velocity, distance and speed. For each lag l , we defined the GLM as

$$X^{(l)} = A^{(l)} \cdot \tilde{K} + E^{(l)} \quad (2)$$

with an $n_{\text{channels}} \times n_{\text{observations}}$ matrix $X^{(l)}$ containing the EEG activity at lag l , an $n_{\text{channels}} \times 6$ matrix $A^{(l)}$ reflecting the regression coefficients and an $n_{\text{channels}} \times n_{\text{observations}}$ noise matrix $E^{(l)}$. The least squares estimate of $A^{(l)}$ is

$$\hat{A}^{(l)} = \Sigma_{X\tilde{K}}^{(l)} \cdot \Sigma_{\tilde{K}\tilde{K}}^{(l)-1} \quad (3)$$

with an $n_{\text{channels}} \times 6$ cross-covariance matrix $\Sigma_{X\tilde{K}}^{(l)}$ between the low-frequency M/EEG activity and the cursor kinematics, and a 6×6 covariance matrix $\Sigma_{\tilde{K}\tilde{K}}$ between the cursor kinematics. We used analytical shrinkage regularization [53] to estimate $\Sigma_{\tilde{K}\tilde{K}}$.

2.6. M/EEG source imaging

As in [20, 35], we applied M/EEG source imaging [54, 55] to project the regression coefficients $\hat{A}^{(l)}$ to the cortical surface of the ICBM152 template boundary element (BEM) head model [56]. The BEM comprised three layers (cortex, skull, scalp) with relative conductivities (1, 0.008, 1) in experiment 1, and (1, 0, 0) in experiment 2. The cortex layer contained 5011 voxels. We co-registered the BEM and the digitized head points (including EEG and EOG electrode locations) using three anatomical landmarks (nasion, left and right preauricular points). To compensate deviations between participant and template anatomy, we finalized the co-registration by projecting floating EEG electrodes to the scalp layer. OpenMEEG [57, 58] was used to compute the forward model for three orthogonal sources per voxel. sLORETA [59] was used to estimate the inverse solution. To reduce the effect of sensor noise in the inverse solution, resting data (similar preprocessing as the M/EEG data; recorded at the start and end

of the experiments) were used to estimate a sensor noise covariance matrix (shrinkage regularization with 10% of its mean eigenvalue).

After we projected the participant-specific regression coefficients to the cortical surface, we scaled the voxel level regression coefficients with the inverse global field power (GFP) [29]. We estimated the GFP by randomly selecting one sample from all trials, averaging across these samples, and computing the SD across voxels. This procedure was repeated 10 000 times. The final participant-specific GFP estimate was set to the median of the repetitions.

2.6.1. Source space statistics

We first tested for consistent (effect with the same sign across participants) expression of kinematic information at the group level. In detail, we tested the regression coefficients at the voxel level using one-sided permutation tests [60, 61]. We obtained the observed voxel activation by first averaging over participants and then computing the norm across the three voxel components. To reduce the number of tests, we averaged the voxel activations associated with either position, velocity or amplitude (distance and speed) predictors. For example, the voxel activations of the horizontal and vertical positions were averaged. In doing so, we identified voxels that carried information about the vertical and/or horizontal position. Next, we used 10 000 permutations to obtain a random distribution. In each permutation, we randomly flipped the signs of a voxel's regression coefficients before averaging over participants. The p -value was then the fraction of random voxel activations that were larger or equal to the observed voxel activation. We computed tests for all voxels (5011), lags (11), type of kinematic signal (3; position, velocity and amplitude) and condition (2; execution and observation).

In a second test, we compared the two conditions. We specifically tested for voxels with stronger activation in either condition (i.e. consistently higher voxel norm in one condition compared to the other). We computed two-sided, permutation, paired t-tests [60, 61] for all voxels (5011), lags (11) and type of kinematic signal (3).

The total number of tests for consistent activation and difference across participants was 496 089 in both experiments. The significance level of 0.05 was corrected for multiple comparisons in both experiments by controlling the false discovery rate (FDR) [62].

2.7. Cursor kinematics decoding

In a causal sliding window approach, we decoded the cursor kinematics from the low-frequency M/EEG activity. We compared three decoding algorithms, namely, a WF, a KF and an UKF.

2.7.1. Decoding algorithms

figure 2 depicts the models underlying the three decoding algorithms. In all algorithms, we combined

the M/EEG activity x_t at the current time-point t and previous time-points (= lags) as an $n_{channels} \cdot n_{lags} \times 1$ feature vector $\tilde{x}_t = [x_t; x_{t-1}; \dots]$. The number of lags n_{lags} used to create the feature vector defined the model order. For example, if only the previous lag was used, the model order was 1. We then projected the high-dimensional features \tilde{x}_t to a latent subspace y_t

$$y_t = L\tilde{x}_t \quad (4)$$

with an $n_{dim} \times n_{features}$ projection matrix L . As in [20, 22], the SIMPLS algorithm [63] was used to estimate L so that y_t the latent subspace y_t contained the activity of \tilde{x}_t that maximally explained the variance of the z-scored cursor kinematics \tilde{k}_t

$$\tilde{k}_t = \left[p_t^{(horz)}; v_t^{(horz)}; p_t^{(vert)}; v_t^{(vert)}; d_t; s_t \right] \quad (5)$$

In a nutshell, SIMPLS iteratively extracts the 1D subspace that explains most of the variance of the cross-covariance matrix between the predictor \tilde{x}_t and dependent variables \tilde{k}_t . This can be done via iterative singular value decomposition of the cross-covariance matrix, extraction of the dominant singular value and its associated projection vectors, Gram-Schmidt orthogonalization with the previously extracted subspaces and deflating the resulting subspace from the cross-covariance matrix. These steps are repeated until the desired stopping criterion is reached (e.g. a fixed number of latent components n_{dim}).

To reduce collinearity among the features and also the computation time of the KFs, we set $n_{dim} \ll n_{features}$. We fixed n_{dim} so that the latent subspace would explain 70% of the variance in the features. For a first order model, n_{dim} was on average 32 (4 SD) in experiment 1 and 29 (2 SD) in experiment 2. The SIMPLS algorithm was also used to compute the coefficients W of the WF to predict \tilde{k}_t from y_t (figure 2(a)).

The second algorithm was a KF [38]. We used it to infer the cursor kinematics (= state) from the latent subspace y_t and the previous state. Since a KF is a linear state space model (figure 2(b)), we only decoded z-scored positions and velocities k_t

$$k_t = \left[p_t^{(horz)}; v_t^{(horz)}; p_t^{(vert)}; v_t^{(vert)} \right] \quad (6)$$

The KF treats the noise corrupting successive observations y_t as conditionally independent given the hidden state k_t . Combining M/EEG activity at multiple lags \tilde{x}_t into y_t violates this assumption. However, this assumption is already violated for the M/EEG activity at a single lag x_t because some noise sources (e.g. brain sources that do not encode kinematic information) are auto-correlated. In the next steps we outline the fitting procedure for a first order model. For higher order models (multiple previous states), we refer to [36]. The 4×4 state transition matrix

$$F = \sum_{k_t, k_{t-1}} \sum_{k_{t-1}, k_{t-2}}^{-1} \quad (7)$$

can be estimated from the covariance matrix between k_t and k_{t-1} and the covariance matrix of k_{t-1} . We used analytical shrinkage regularization [53] to estimate $\Sigma_{k_{t-1}, k_{t-1}}$ from calibration data. The covariance matrix Σ_{q_t, q_t} of the state transition error can be estimated from the residuals

$$q_t = k_t - Fk_{t-1} \quad (8)$$

The KF also relates the kinematic state k_t with the latent subspace y_t using a $4 \times n_{dim}$ matrix H . H can be determined by minimizing the mean squared error between y_t and its prediction

$$H = \underset{H}{\operatorname{argmin}} \sum_{t=1}^n \|y_t - Hk_t\|^2 \quad (9)$$

After fitting H to calibration data with n observations, we used the residuals r_t defined as

$$r_t = y_t - Hk_t \quad (10)$$

to estimate the measurement noise covariance matrix Σ_{r_t, r_t} .

The third algorithm can be seen as an extension of the KF. We used the linear state transition matrix F from before (figure 2(c)). The key difference was, that we explicitly modelled the nonlinear relationship between position and distance or velocity and speed or both with the function

$$ex(k_t) = \begin{cases} [k_t; \operatorname{zscore}(\|p_t\|_2); \operatorname{zscore}(\|v_t\|_2)] \\ [k_t; \operatorname{zscore}(\|p_t\|_2)] \\ [k_t; \operatorname{zscore}(\|v_t\|_2)] \end{cases} \quad (11)$$

If distance and speed are considered, the function essentially computes the extended kinematics \tilde{k}_t , defined in (5). Next, we utilized the linear encoding of distance and/or speed information in the low-frequency M/EEG signals to predict y_t from $ex(k_t)$

$$H = \underset{H}{\operatorname{argmin}} \sum_{t=1}^n \|Hex(k_t) - y_t\|^2 \quad (12)$$

Using H and (11), the estimated latent subspace \hat{y}_t is

$$\hat{y}_t = h(k_t) = Hex(k_t) \quad (13)$$

As before, we used the residuals to estimate the measurement noise covariance matrix Σ_{r_t, r_t} . After the parameters of the state space models (figures 2(b),(c)) were fitted to calibration data, we used a square root KF [64] to infer the kinematics in test data for the linear model, and a square root UKF [65] for the nonlinear model.

2.7.2. Algorithm evaluation

We fitted and evaluated the algorithms with a ten-fold cross-validation scheme. The model order was fixed to 3 (i.e. M/EEG activity and cursor kinematics of three previous lags). In ten iterations, we used nine folds to fit the parameters, and the held-out fold to test the performance. For the state space models, we estimated the initial state covariance matrix from the calibration data. We then applied the algorithms to each trial within the test set. The KF and UKF required an initial estimate of the state k_0 ; we used the recorded kinematics of the time-points before the first sample in the tested trials. All algorithms decoded the directional kinematics. We used equation (11) to infer the nondirectional kinematics from the directional ones in the test set.

Three metrics were used to test the performance. We first computed Pearson correlation coefficients between the recorded test set kinematics and their decoded estimates. The second metric was the SNR as defined in [36]. For a recorded kinematic signal z_t (e.g. horizontal position) and its decoded estimate \hat{z}_t the SNR is defined as the ratio of the variance of z_t over the mean squared error (MSE):

$$\operatorname{SNR}(z_t, \hat{z}_t) = 10 \log_{10} \left(\frac{\operatorname{var}(z_t)}{\operatorname{mse}(\hat{z}_t, z_t)} \right) \quad (14)$$

The third metric was the decoded signal to signal ratio (DSSR). We defined it as the variance of the decoded signal over the variance of the recorded signal:

$$\operatorname{DSSR}(z_t, \hat{z}_t) = 10 \log_{10} \left(\frac{\operatorname{var}(\hat{z}_t)}{\operatorname{var}(z_t)} \right) \quad (15)$$

The DSSR captures the amplitude mismatch between the decoded and recorded signal. A DSSR of 0 dB indicates that the amplitude range of the recorded and decoded signal match. A negative DSSR indicates a bias of the decoder towards too small amplitudes.

2.7.3. Participant level significance

We assessed the significance of the correlation and SNR metrics at the participant level using a shuffling approach. To break the association between the M/EEG activity and the kinematics, we randomly permuted the kinematics across trials, before we split the data into two folds—one train fold with 90% of the data and one test fold with 10% of the data. The two folds were then used to fit and evaluate the algorithms. The shuffling procedure was repeated 1000 times. We set the p -value to the fraction of random results that were higher than the average cross-validation result. We controlled the FDR for 2 (conditions) * 3 (algorithms) * 4 (kinematics) * 2 (metrics) = 48 tests at a significance level of 0.05 [62].

2.7.4. Group level statistics

We compared the decoding accuracy of the algorithms in terms of correlation, SNR and DSSR

for each experiment, condition and type of kinematic signal (directional, nondirectional). To identify significant differences, we used two-sided, permutation, paired t-tests ($df = 14$, 10 000 permutations, significance level = 0.05). The obtained p -values were FDR adjusted for 3 (metrics) * 3 (algorithms) * 2 (conditions) * 2 (type of kinematic signal) = 36 tests.

3. Results

3.1. Tracking behavior

The tracking behavior during the PTT was inferred by computing cross-correlation curves between the target and cursor positions in the execution condition. At the group level, the target led the cursor position trajectory by 0.15 s (0.02 s SEM) with a correlation of 0.84 (0.02 SEM) in experiment 1. In experiment 2, the target led the cursor trajectory by 0.23 s (0.01 s SEM) with a correlation of 0.91 (0.01 SEM). In figures 1(d), (e) we show target (yellow) and cursor (gray) trajectories for representative participants. The qualitative and quantitative results indicate that the study participants accurately tracked the target stimulus in both experiments.

As reported in [20], the positions and velocities were decorrelated at lag 0 s. For positive and negative lags, the cross-correlations increased and peaked at the lags ± 0.5 s (supplementary figures 14(b), (c), (e), (f)) with average absolute correlations of 0.8 (0.77 in experiment 2). Since the horizontal and vertical components were iid, the cross-correlations between the kinematics of different components were negligible (supplementary figures 14(b), (c), (e), (f)). The cross-correlations between the directional (position and velocity) and nondirectional kinematics (distance and speed) were also negligible (supplementary figures 14(a), (d)). Speed and distance exhibited moderate (below ± 0.5) cross-correlations that slowly varied across lags (supplementary figures 14(a), (d)).

3.2. Neurophysiology

We used the fitted regression coefficients of the GLMs to identify cursor kinematics related effects in the low-frequency M/EEG activity. The low-frequency EEG signals encoded information about the cursor kinematics during the right arm PTT in experiment 1. In figure 3, we show voxels whose activity was significantly tuned to specific cursor kinematics at the group level. Figure 3 displays only activity during negative lags; for example, a significant effect at the lag -0.1 s indicates that the EEG 100 ms ago predicted the current cursor kinematics. Supplementary figures 1 and 2 also include positive lags.

In the execution condition, we observed significant amplitude (distance/speed) related activity (figure 3(a)) in contralateral motor and parietal areas as well as parieto-occipital, occipital and temporal areas of both hemispheres. There was a distinct peak in contralateral primary- and premotor areas at

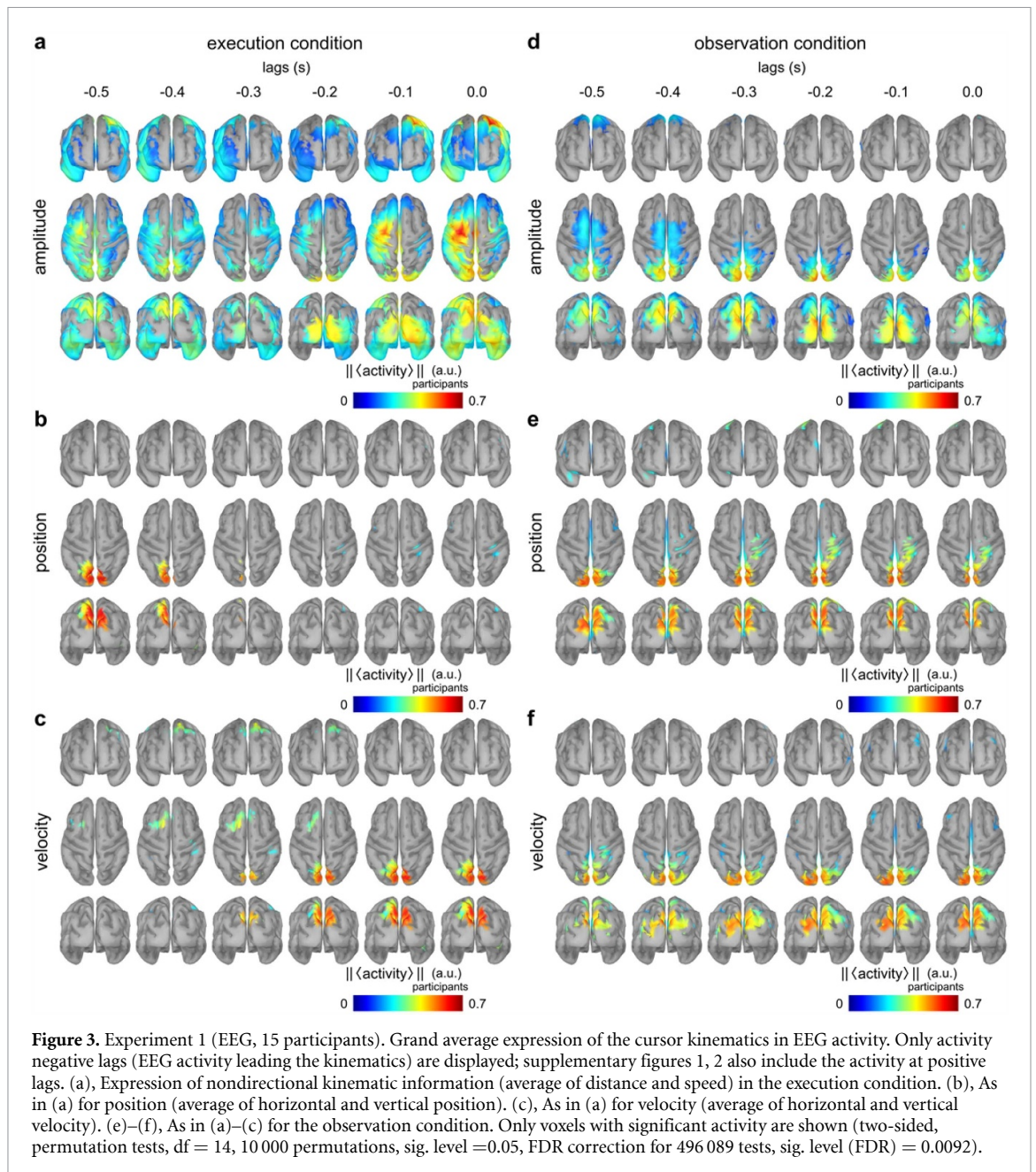
lags -0.1 to 0.0 s. Position (figure 3(b)) and velocity (figure 3(c)) information were consistently expressed in parieto-occipital areas. Due to the large cross-correlations between positions and velocities across lags (supplementary figures 14(b), (c)), we observed similar effects in both kinematic variables at different lags. In the case of velocity, the activity was strongest for the lags -0.1 to 0.0 s. Because the cross-correlation between velocity and position peaked at a delay of 500 ms (supplementary figures 14(b), (c)), we observed a similar effect at the lags 0.4 and 0.5 for position (supplementary figure 1). For an effect to be significant in figure 3, the dipole orientations had to be consistent across participants. If the dipole orientation was allowed to vary across participants, M1, PMd, S1 and PP voxels encoded significant directional information in execution condition (supplementary figure 3).

In the observation condition, parieto-occipital areas also expressed information about position (figure 3(e)) and velocity (figure 3(f)). As before, the effect peaked for velocity at the lags -0.1 to 0.0 s. In contrast to the execution condition, we also observed significant activity at the lags -0.5 to -0.4 s. Regarding amplitude information (figure 3(d)), we also observed significant activity in parieto-occipital and occipital areas. Compared to the execution condition, we neither observed sensorimotor activity at lags -0.1 to 0.0 s, nor activity in temporal areas.

In experiment 2, we also found that low-frequency MEG signals encoded information about the cursor kinematics. Voxels with significant group level activity at negative lags are summarized in figure 4.

In the execution condition, we observed significant amplitude related activity (figure 4(a)) in contralateral sensorimotor areas (peak at lag -0.2 s), and to a weaker extent in occipital, parieto-occipital, parietal and ipsilateral premotor areas. Position (figure 4(b)) and velocity (figure 4(c)) information was consistently expressed in contralateral motor and parietal areas as well as parieto-occipital areas and to a weaker extent in occipital areas. As mentioned before, due to strong cross-correlations between positions and velocities across lags (supplementary figures 14(e), (f)), we observed similar effects in both kinematic variables at different lags. For velocity, the contralateral activity peaked at the lag -0.2 s (figure 4(c)) and consequently for position at lag 0.3 s (supplementary figure 4).

In the observation condition, the kinematics related activity (figures 4(d)–(f)) was generally smaller compared to the execution condition (figures 4(a)–(c)). Amplitude information (figure 4(d)) was expressed strongest in parieto-occipital areas, followed by ipsi- and contralateral sensorimotor areas. Position (figure 4(e)) and velocity (figure 4(f)) related activity was strongest in PP areas.

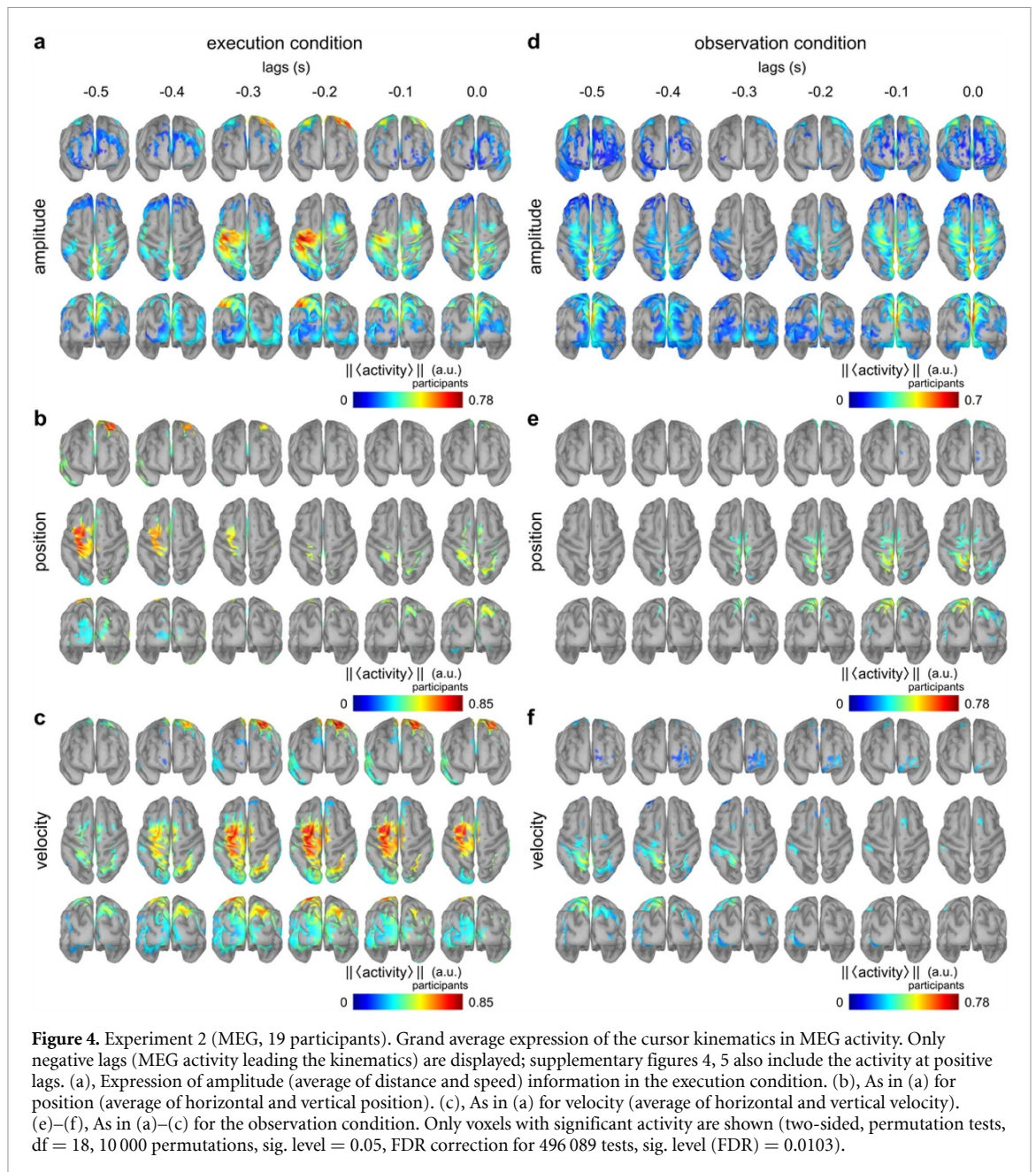


3.3. Cursor kinematics decoding

Figures 1(d),(e) displays recorded and decoded test set trajectories for representative participants. Qualitatively, the UKF decoded trajectories (blue) matched the cursor trajectories (gray) best in terms of time course and amplitude range in the execution condition. The decoded trajectories of the other algorithms were either too small (red, WF) or too large (green, KF). In the observation condition, the congruence between the decoded and recorded trajectories was lower than in the execution condition.

The quantitative participant-level results are listed in supplementary tables 1–6. All three decoding algorithms directly decoded the directional kinematics. To quantify the goodness of fit for the nondirectional kinematics, we converted the decoded position and velocity trajectories into distance and speed

trajectories and compared them with the recorded ones. The correlation and SNR between the recorded and decoded directional kinematics were significantly different from shuffled data for all participants in the execution condition. There were some combinations of algorithm, kinematic signal and condition that were not significant for specific participants. For two participants in experiment 1 the SNR of all algorithms and kinematic signals was not significantly different from chance in observation condition. The WF and KF correlations for distance and speed, inferred from the decoded positions and velocities, were not significantly different from chance for the majority of participants in experiment 1 (execution: 11 participants, observation: 13) and observation condition in experiment 2 (13 participants). Whereas the UKF correlations were not significant



for the minority in experiment 1 (execution: 1 participant, observation: 5) and observation condition in experiment 2 (five participants).

The group level results are summarized in figure 5. The figure shows the performance metrics for each algorithm, condition and experiment. To reduce the number of plots, we grouped the results into directional (2D position, 2D velocity) and non-directional (distance, speed) kinematics. The boxplots in figures 5(a),(d) summarize test set correlations between the recorded and decoded kinematics. The UKF achieved the highest test set correlations across experiments, conditions and kinematics. With regard to the directional kinematics, the UKF correlations in execution and observation condition in experiment 1 were 0.40 ± 0.06 SD and 0.31 ± 0.08 SD (figure 5(a)). The WF correlations were significantly

lower in execution (mean difference: 0.08 ± 0.02 SD) and observation (0.06 ± 0.02 SD) condition compared to the correlations reached by the other algorithms. The results were similar in experiment 2 (figure 5(d)); the UKF correlations in execution (0.56 ± 0.05 SD) and observation (0.40 ± 0.08 SD) condition were significantly higher than the WF correlations. The difference in correlations between the UKF and KF did not reach significance in either experiment and condition. The difference in UKF correlations between experiments was significant (Wilcoxon rank sum tests, execution condition mean difference = 0.16, p -value = 2.1×10^{-7} ; observation condition mean difference = 0.09, p -value = 3.4×10^{-3}). With regard to the nondirectional kinematics, we observed a large gap (mean difference: ≥ 0.1) between the UKF and the other algorithms in both

experiments and conditions (figures 5(a),(d)). Recall that the UKF was the only algorithm that incorporated distance and speed information, encoded in the M/EEG signals, into the predictions of position and velocity.

Figures 5(b), (e) summarize the performance of the algorithms in terms of SNR. The SNR of the UKF was always higher than the SNR of the KF. For the directional kinematics, we observed the highest SNR for the WF. It was on average 0.38 dB (0.16 dB observation) in experiment 1 (figure 5(b)) and 1.08 dB (0.42 dB observation) in experiment 2 (figure 5(e)); it was significantly higher than the SNR of the KF in both experiments and conditions. The difference in SNR between the UKF and WF was significant in experiment 1 (figure 5(b)), and in the observation condition of experiment 2 (figure 5(e)), while the UKF and WF were on a par in execution condition. Regarding the nondirectional kinematics, we observed a large gap (mean difference: ≥ 1 dB) between the UKF and the other algorithms. The differences were significant across experiments and conditions. While there was no significant difference in SNR between the KF and WF in experiment 1 (figure 5(b)), the KF achieved a significantly higher SNR (mean difference: approx. 0.5 dB) in experiment 2 (figure 5(e)).

The DSSR results are summarized in figures 5(c), (f). The differences in DSSR between the algorithms were significant in call cases (kinematic groups, conditions, experiments). Compared to the KF and UKF, the WF DSSR was lower by at least 5 dB. This mismatch in amplitude is clearly visible in figures 1(d), (f). The UKF DSSR was closest to the target value of 0 dB in experiment 1, while in experiment 2 the KF DSSR was closest to 0 dB.

The position, velocity, distance and speed specific group level results are displayed in figure 6 (correlation and SNR) and supplementary figure 11 (DSSR). In experiment 1, the algorithm-specific correlation, SNR and DSSR were generally similar across the directional kinematics (figures 6(a), (b)), supplementary figures 11(a)). In experiment 2, the correlation and SNR were higher for the vertical component (vertical position, vertical velocity) than for the horizontal component (figures 6(c), (d)). We additionally observed that the UKF and KF correlations were higher for the positions than for the velocities (figure 6(c)). The results for distance and speed were consistently lower than the ones for position and velocity (figure 6). Compared to distance, the correlations for speed were similar (figures 6(a), (c)) while the SNR was higher (figures 6(b), (d)).

Next, we evaluated the effect of including only distance or speed or neither in the UKF model. In figure 7, we show the results in terms of correlation and SNR. If we did not consider speed or distance in the UKF model, the associated test set correlation and SNR declined. For example, if we excluded distance

in equation (11), the correlation and SNR for the test set distance trajectories dropped and also to a smaller extent for the position trajectories. If neither distance nor speed was included, the UKF model was equivalent to the linear KF model and achieved a similar accuracy as the KF. Taken together, using distance and speed in (11) resulted in the highest decoder accuracy for the UKF.

4. Discussion

We showed that the low-frequency EEG and MEG activity encoded rich kinematic information during the PTT. At the group level, PP and parieto-occipital (both conditions) and contralateral premotor and primary sensorimotor (execution condition) areas encoded information about directional (position and velocity) and nondirectional (distance and speed) kinematics. Based on the low-frequency M/EEG activity of the current and preceding time-points, the three decoding algorithms could reconstruct the cursor kinematics at the current time-point with moderate congruence. Across experiments and directional kinematics, the correlations of the UKF were 0.49 (0.10 SD) in the execution and 0.36 (0.09 SD) in the observation condition. They were on average 0.08 (0.02 SD) higher than the correlations of the WF. A linear state space model (KF) was sufficient to significantly improve the correlations upon the WF (Δ correlation = 0.06 ± 0.01 SD) at the cost of significantly lower SNR (Δ SNR = -1.5 dB ± 0.6 dB SD). Using information about nondirectional kinematics, encoded within the low-frequency M/EEG activity, the UKF could significantly improve the SNR compared to the KF (Δ SNR = 0.6 dB ± 0.1 dB SD) and at the same time reduce the amplitude mismatch between recorded and decoded trajectories to a minimum (DSSR = -0.3 dB ± 0.5 dB SD).

Despite we observed significantly lower correlations for the WF compared to the state space models (KF, UKF), its SNR was significantly higher for the directional kinematics. The optimization criterion of the WF was to minimize the MSE which is equivalent to maximizing the SNR defined in (14). Whereas the state space models did not directly minimize the SNR; they learned the distribution of the kinematics in the train set (e.g. the amplitude range), and thereby also optimized the DSSR to be close to 0 dB. Intuitively, correlation, SNR and DSSR are related. Since the WF maximized the SNR of the directional kinematics, it achieved the highest SNR at the cost of poor DSSR, while the state space algorithms achieved a DSSR close to 0 dB at the cost of lower SNR for the directional kinematics (figure 5). If the correlations were high, as in experiment 2 (execution condition), the UKF could maintain the same SNR as the WF and at the same time a DSSR close to 0 dB (figures 5(d)–(f)). Knowing that the KF and UKF essentially differed in the sense that the UKF utilized the nondirectional

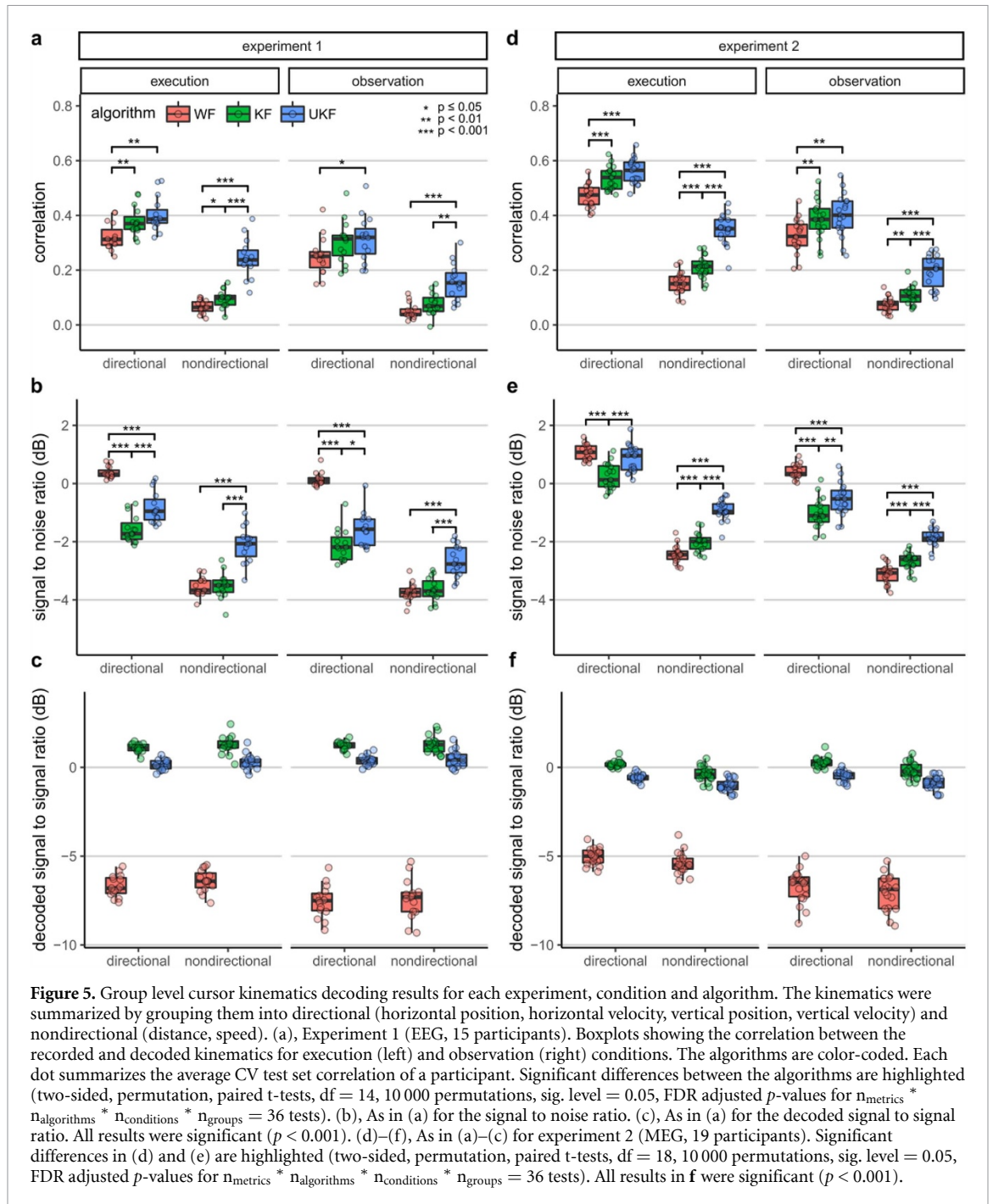
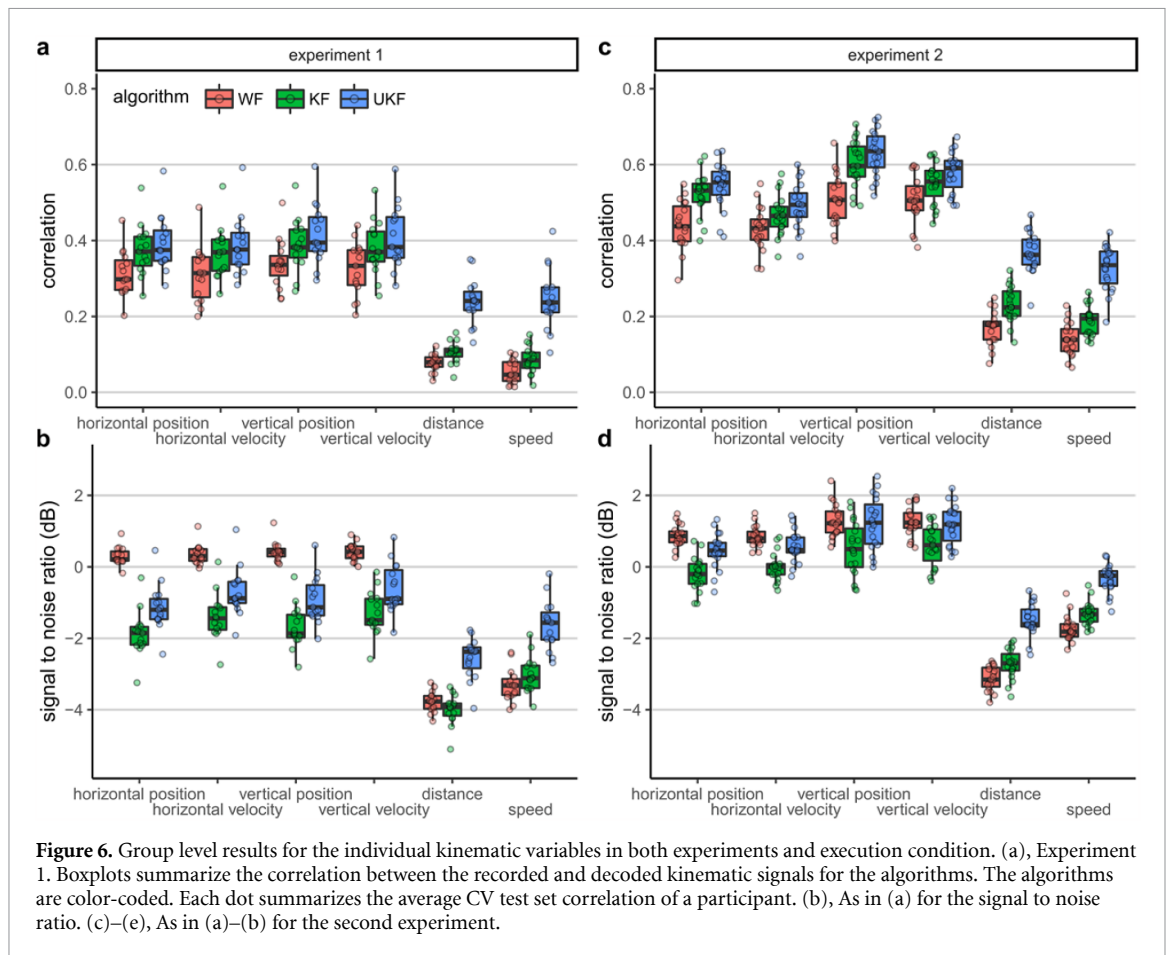


Figure 5. Group level cursor kinematics decoding results for each experiment, condition and algorithm. The kinematics were summarized by grouping them into directional (horizontal position, horizontal velocity, vertical position, vertical velocity) and nondirectional (distance, speed). (a), Experiment 1 (EEG, 15 participants). Boxplots showing the correlation between the recorded and decoded kinematics for execution (left) and observation (right) conditions. The algorithms are color-coded. Each dot summarizes the average CV test set correlation of a participant. Significant differences between the algorithms are highlighted (two-sided, permutation, paired t-tests, $df = 14$, 10 000 permutations, sig. level = 0.05, FDR adjusted p -values for $n_{\text{metrics}} * n_{\text{algorithms}} * n_{\text{conditions}} * n_{\text{groups}} = 36$ tests). (b), As in (a) for the signal to noise ratio. (c), As in (a) for the decoded signal to signal ratio. All results were significant ($p < 0.001$). (d)–(f), As in (a)–(c) for experiment 2 (MEG, 19 participants). Significant differences in (d) and (e) are highlighted (two-sided, permutation, paired t-tests, $df = 18$, 10 000 permutations, sig. level = 0.05, FDR adjusted p -values for $n_{\text{metrics}} * n_{\text{algorithms}} * n_{\text{conditions}} * n_{\text{groups}} = 36$ tests). All results in f were significant ($p < 0.001$).

kinematic information, and that we observed a significantly higher SNR for the UKF across all kinematics, it follows that utilizing the nondirectional information improved the decoder accuracy. In summary, the UKF achieved the highest qualitative (figures 1(d), (e)) and quantitative in terms of correlation and DSSR (figures 5(a), (c), (d), (f)) decoding accuracy among the three algorithms. In terms of SNR, the accuracy of the UKF was on a par with the WF in one case (experiment 2, execution condition) and lower in the other three cases (figures 5(b), (d)).

The UKF was the only algorithm that used distance and speed information to improve the position and velocity estimates. Using either speed or

distance in equation (11), had a negligible effect on the decoder accuracy of the directional kinematics and a negative effect on the nondirectional kinematics (figure 7). If neither distance nor speed were included, the accuracy of the UKF declined to the level of the KF. Yeom *et al* explored a different way to incorporate speed information into the velocity estimates [66]. In an MEG study, they first decoded velocity and speed during center-out movements, then normalized the decoded velocity and multiplied the result with the decoded speed estimate. Compared to linear decoders, their two step approach could slightly, yet significantly improve the accuracy. We also varied the model order to identify how the number of

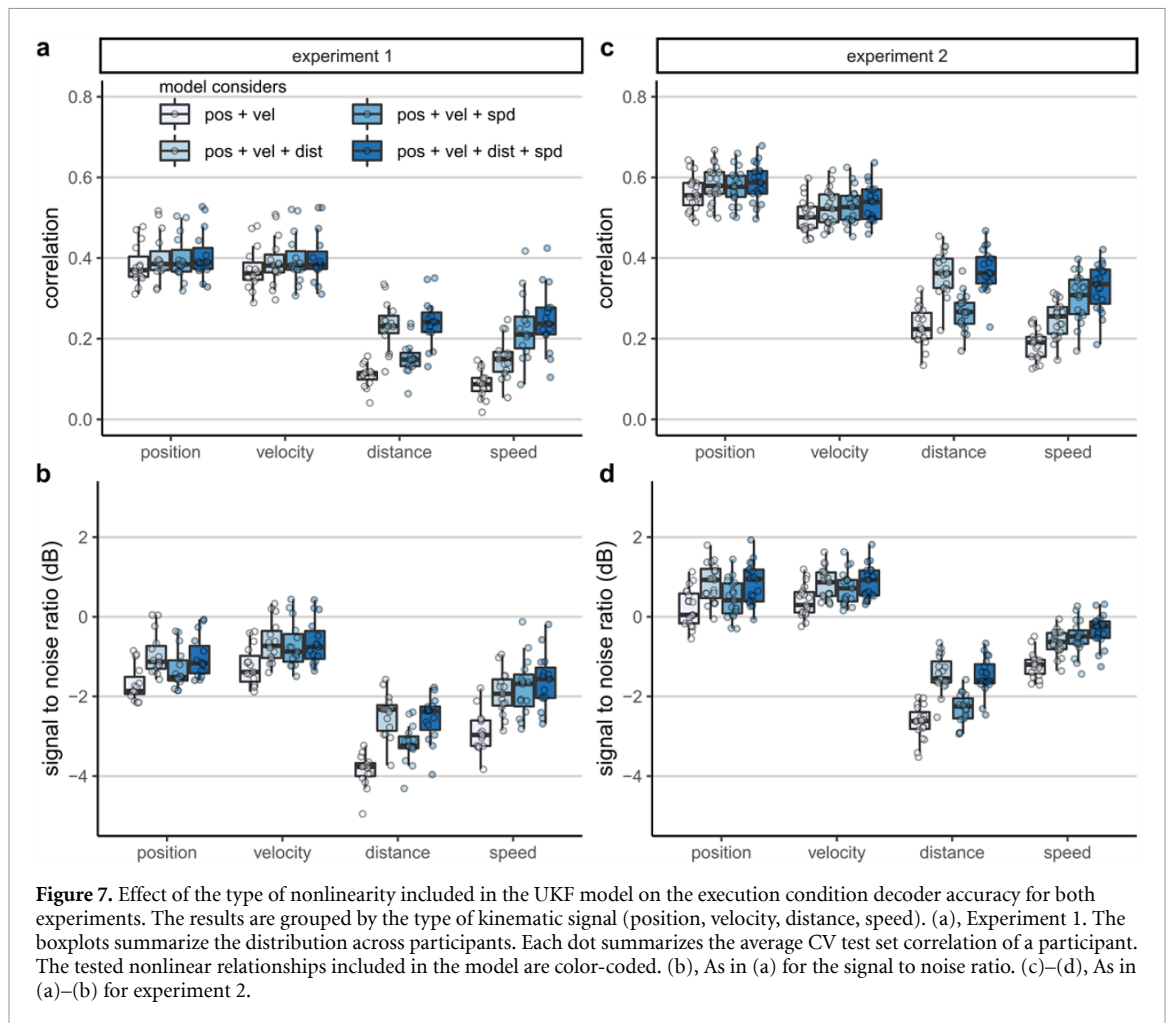


previous lags affected the decoder accuracy (supplementary figure 13). Compared to the third order model (figure 5), the correlations and SNR were marginally smaller for a first order model (Δ correlation = -0.01 ± 0.01 SD; Δ SNR = -0.1 dB ± 0.1 dB SD) and indifferent for a fifth order model (Δ correlation = 0.0 ± 0.01 SD; Δ SNR = 0.0 dB ± 0.1 dB SD). As reported in [20], the WF accuracy increased for higher orders (supplementary figure 13). Despite the increase, the correlations (supplementary figures 13(a), (d)) for a fifth order WF were still lower compared to a fifth order UKF (Δ correlation = 0.05 ± 0.02 SD for the directional kinematics). Taken together, the UKF still outperformed the other algorithms in terms of correlation as the model order increased; higher order models did not improve the accuracy upon a third order UKF.

Since the spectral filter characteristics have a large impact on the performance of low-frequency decoders [66], we tested three low-pass filter cut-off frequencies 0.8 Hz, 2.0 Hz, 5.0 Hz. The results are summarized in supplementary figure 12. With increasing cut-off frequency, the correlations decreased for the directional kinematics (supplementary figures 12(a), (d)); the difference (0.8 Hz–5.0 Hz) was negligible for the UKF (Δ correlation = -0.02 ± 0.01 SD) and high for the WF (Δ correlation = -0.10 ± 0.02 SD).

For the nondirectional kinematics, the correlations increased, since frequencies above 0.8 Hz had a considerable contribution to the power spectral density of distance and speed (supplementary figure 15). Increasing the cut-off frequency had a positive effect on the UKF SNR (0.5 dB directional, 1 dB nondirectional) and DSSR.

Previous works in the context of low-frequency M/EEG kinematics decoding have mainly studied center-out tasks [19, 27, 67–70]. Since correlation and SNR are sensitive to various parameters (e.g. pre-processing, statistical properties of the signals being compared), a direct comparison across studies is not straightforward [25]. Bradberry *et al* were the first to show that velocity trajectories can be decoded from low-frequency MEG [67] and EEG [19] activity during center-out reaching tasks. They decoded 2D velocity trajectories from MEG during a visuomotor adaptation experiment in [67]. Their pre-exposure condition was closest to our execution condition. They obtained average (five participants, two dimensions) correlations of 0.4. In the EEG study [19], they studied 3D self-paced center-out movements and decoded velocities with average (five participants, three dimensions) correlations of 0.3. Kim *et al* decoded continuous, repetitive 3D arm movement trajectories from low-frequency EEG activity with multiple linear regression (MLR) and kernel



ridge regression decoders [23]. After correcting for eye artifacts, they obtained grand average (ten participants, three dimensions) correlations of 0.5 (0.38 MLR) in executed movements and 0.4 (0.3 MLR) in imagined (and observed) movements. Their correlations were in a similar range, compared to our findings in the PTT in experiment 2 (figures 5(d)–(f)). In an even simpler task (rhythmic 2D circular arm movements), Georgopoulos *et al* reconstructed arm movement trajectories from low-frequency MEG activity with high congruence (correlation = 0.85) [15]. Recently we reported slightly lower correlations (correlation = 0.68) for low-frequency EEG activity [29].

In the invasive domain, executed arm movement kinematics have been decoded from ECoG activity of humans [24, 28, 71–73]. Schalk *et al* reported that the low-frequency ECoG activity contributed the most to the decoding of trajectories in a simple, repetitive 2D PTT [24]. Using low-frequency and spectral features, they predicted positions and velocities with correlations of 0.49 (0.10 SD). Using similar features, Pistohl *et al* predicted cursor trajectories with a linear KF (correlation = 0.33 for six participants; correlation = 0.43 for three participants with ECoG grids covering hand/arm areas) in a more complex

2D continuous movement task [71]. Nakanishi *et al* studied a 3D continuous reaching and grasping task in three participants [28]. They decoded wrist and elbow positions and elbow and shoulder joint angles. The average correlation for the 3D wrist position was 0.51 and the average normalized root mean squared error (nRMSE) was 0.29. In a follow up study with three additional participants, they obtained average correlations of 0.62 and a root mean squared error (RMSE) of 55 mm [74]. That is, the M/EEG results in terms of correlation reported here are within the range of those using implanted ECoG grids during continuous, goal-oriented movement tasks, whereas the low nRMSE and RMSE confirm the higher SNR of ECoG compared to M/EEG [75]

Expression of executed arm movement kinematics in neural spiking activity has been studied in non-human primates (NHPs) [8, 31, 36, 76, 77]. An early work by Paninski *et al* studied neural spiking activity during a comparable 2D PTT in three NHPs [77]. They decoded hand positions from the spike rates of few M1 neurons (5 to 19 neurons) with a linear regression model and reported an SNR of 1.3 dB (0.8 dB SD). Our execution condition results for the UKF (−0.8 dB experiment 1; 0.9 dB experiment 2) and WF (0.4 dB experiment 1; 1.1 dB experiment

2) were lower. Later, Li *et al* used neural spiking activity from M1, S1, PMd and PP neurons of two NHPs to decode cursor kinematics during a simple 2D PTT and a center-out task [36]. They applied a similar UKF that used distance and speed information to decode positions and velocities. In the PTT, they reported that a first order UKF decoded positions (correlation = 0.85, SNR = 5.1 dB) and velocities (correlation = 0.52, SNR = 1.5 dB) with high congruence. Our execution condition correlations for velocity were in a similar range, while the correlations for position and the SNRs were lower (figure 6). The discrepancy in correlations could be explained by the task difficulty. Their 2D trajectories were repetitive, while ours were pseudo-random. They also reported results for a WF. In their study, the UKF improved the correlations upon the WF for the positions (Δ correlation = 0.09) and velocities (Δ correlation = 0.06). We also observed significantly higher correlations for the UKF compared to the WF (Δ correlation = 0.06). Recently Makin *et al* compared the UKF proposed by Li *et al* to a recurrent exponential family harmonium (rEFH) filter during a consecutive 2D reaching task to multiple targets [78]. The rEFH filter achieved an SNR of 6 dB compared to 4 dB for the UKF. In a study with two NHPs, Stavitsky *et al* compared the decoder accuracy between population and spiking activity with a linear KF [79]. In a center-out reaching task, they reported similar correlations for the low-frequency population (0.78) and spiking (0.77) activity. Compared to M/EEG, the fine spatial resolution of intracortical electrode arrays enables the reconstruction of movement trajectories with a high accuracy in terms of correlation and SNR.

In both experiments, we studied the PTT in two experimental conditions. Compared to the execution condition, we observed a drop in performance in the observation condition (figure 5). For the UKF the average difference in correlation and SNR was 0.13 (0.08 SD) and 1.1 dB (0.6 dB SD). Kim *et al* also reported lower correlations (Δ correlation = 0.1), if the movements were observed and imagined [23]. Korik *et al* used spectral features to decode repetitive 3D reaching movements from EEG activity [68]. They reported a stronger drop in correlations (Δ correlation = 0.2), if the reaching movements were imagined rather than executed. Using low-frequency EEG activity, Ofner *et al* reported correlations of 0.32 (0.22 SD) for rhythmic movement imaginations [22]. They were substantially lower than the correlations (0.70 ± 0.12 SD) reported earlier in executed 3D movements [80]. The drop in decoding performance could be explained by the brain encoding less kinematic information. A body of work has investigated how cortical areas, involved in movement control, modulate to different volitional states, including executed, imagined, attempted or observed movements [81–85]. In supplementary figures 3 and 6 we compared the group level kinematics related

voxel activations between conditions. In both experiments, voxels in primary sensorimotor cortex (SM1), supplementary motor cortex, PMd and PP encoded significantly more kinematic information in execution condition. Executed movements have been repeatedly shown to activate motor and sensory areas stronger than observed movements [81, 82, 84].

The activity in SM1, PMd, PP and PO simultaneously encodes information about various movement parameters in executed and observed movements [8, 20, 33–35, 73, 86–88]. Our group level encoding results (figures 3 and 4) indicate that directional and nondirectional kinematics were expressed differently across cortical areas. We observed distinct peaks in SM1 for the nondirectional kinematics in both experiments (figures 3(a) and 4(a)), supplementary figures 1, 4, 7, 9). The SM1 activity peaked between lags -0.1 s and 0.0 s in experiment 1 and lags -0.3 s to -0.2 s in experiment 2. Considering the delays between hand/finger and cursor movements (55 ms in experiment 1; 190 ms in experiment 2), the SM1 peak was phase-locked to the executed hand/finger movements. Tuning effects of SM1 to nondirectional kinematics have been reported in ECoG [34], MEG [16, 35, 89] and EEG [18]. We observed that the directional kinematics (position and velocity) were consistently encoded in PO (figures 3(b), (c), (e), (f)) and PP (figures 4(b),(c),(e),(f)) in both conditions. Voxels in contralateral SM1 and PMd also consistently encoded directional information in the execution condition of experiment 2 (figures 4(b),(c)) but not in experiment 1 (figures 3(b),(c)). In figures 3 and 4 we report consistent group level effects. That is, for an effect to be significant, the dipole orientations have to be similar across participants. If only the strength of the effect is considered (= dipole orientations are allowed to vary across participants), SM1, PMd and PP voxels encoded significantly more directional information in execution condition in experiment 1 (supplementary figure 3). This means that the directional information was consistently expressed in PO and PP areas at the group level, and participant specific in PMd and SM1. The less consistent effect in SM1 during experiment 1 could to some degree also be attributed to a lower spatial localization accuracy of EEG source imaging for template head models compared to MEG source imaging [90].

In spite of similar task dynamics (supplementary figure 14) and visual stimuli (figure 1(a)) in both experiments, the movement tasks differed in execution condition; we studied arm movements in experiment 1 and finger movements in experiment 2 (figure 1(b)). The two movement types activate fronto-parietal networks for reaching and grasping [91]. Among the fronto-parietal networks, reaching movements mainly activate the dorsal reach system and grasping movements mainly the lateral grasp system [87, 92–94]. As expected, the kinematic information was encoded strongest in medial areas along

the dorsal stream in experiment 1 (figures 3(a)–(c), supplementary figures 1, 3 and 7) and more lateral areas in experiment 2 (figures 4(a)–(c), supplementary figures 4, 6 and 9). Since the fingers and hand have a stronger representation in SM1 than the elbow and shoulder [95], more kinematic information could have been expressed in experiment 2. This could explain the higher decoding accuracy (Δ correlation(UKF) = 0.16 ; Δ SNR(UKF) = 1.7 dB) in execution condition in experiment 2 (figure 5). In the observation condition the hand/finger was resting. Nonetheless, the decoder accuracy was higher in experiment 2 (Δ correlation(UKF) = 0.09 ; Δ SNR(UKF) = 1.0 dB). This difference could be attributed to the recording modality (EEG in experiment 1; MEG in experiment 2) or the spatial coverage (64 channels in experiment 1; 129 channels in experiment 2).

Despite the promising results, our study suffers from a number of limitations that need to be addressed in future research. The most critical one is that we analyzed the data offline with non-causal filters. Online, the spectral filters would introduce large delays in the order of a second, rendering low-latency control infeasible. If the filter characteristics were relaxed, the decoding accuracy of the WF would drop substantially (supplementary figure 12). Fortunately, the results indicate that the accuracy of the KF and UKF would be marginally affected. In an exploratory closed loop BCI study, we recently demonstrated that a KF decoded arm movements online with low-latency so that healthy individuals could track a target with a robotic arm during a PTT [30]. In [30] we used the KF to smooth the estimates of a WF. As a result we observed a similar amplitude mismatch as for the WF in this study (figures 5(c), (f)); the amplitudes of the decoded position trajectories were three to four times smaller than the ones of the actual movements, rendering feedback training impracticable. We believe that at the start of feedback training, the BCI users prefer larger errors over not being able to produce movements in the same range as during manual control. A second limitation, concerns the transfer to paralyzed individuals. In this study, we decoded executed and observed movements. As the participants were continuously moving in the execution condition, the decoders had access to a mixture of efferent (movement intention) and reafferent (feedback) activity. The reafferent activity is either completely or partially missing in paralyzed individuals. Nonetheless, the observation condition decoding accuracy should transfer to paralyzed individuals. Moreover, we think that if a movement attempt strategy is used rather than mere observation, a similar performance to execution condition should be feasible [84, 85]. Using intracortical BCIs, paralyzed individuals achieved similar decoding accuracy in attempted movements as NHPs in executed movements [6, 96, 97]. Even if the offline results

can be transferred to online experiments, the moderate decoding accuracy obtained here is not sufficient to accurately control an end-effector. Using motor imagery of distinct movements and band power features, Wolpaw and McFarland demonstrated that 2D cursor control could be significantly improved with feedback training [4]. After training for several weeks, the study participants could control a cursor in a 2D center-out task with average correlations of 0.63. Edelman *et al* used a similar control strategy and reported that their participants could improve the control skill significantly faster in a 2D PTT compared to a center-out task [98]. In another online study, Bradberry and colleagues reported that they could decode intended movement trajectories from low-frequency activity with high congruence [99]. Within a single-session experiment the participants could control an end-effector in a center-out movement task. However, they did not report whether the task performance was significant, leading to an inconclusive debate [100, 101]. Although there is evidence that individuals can learn to voluntarily modulate low-frequency activity with feedback training [102], it remains unclear how fast the kinematics decoding accuracy can be improved.

There were also some potential confounding factors that might have affected the presented results. The first one concerns eye movement artifacts. Allowing eye movements enabled us to study similar visuo-motor (and oculomotor) tasks as invasive studies. However, they also give rise to prominent EOG artifacts in low-frequency M/EEG signals [103, 104]. Due to the nature of the PTT, they co-varied considerably with the directional kinematics. We used a state-of-the-art correction algorithm to attenuate these artifacts and maintain brain activity [47]. Although we cannot rule out that residual eye artifacts contributed to the decoding results, the encoding results indicate that the brain activity dominated. If residual eye artifacts had dominated, we would have expected strong activity in prefrontal and anterior temporal cortex (cortical areas closest to the eyes). Across conditions and experiments, the kinematics related activity at prefrontal and anterior temporal areas was much lower compared to cortical areas along the dorsal stream (figures 3 and 4; supplementary figures 1, 2, 4, 5, 7–10). Movement artifacts could have also confounded the execution condition decoding results. Significant activity at the inferior temporal lobe might indicate the presence of an arm movement-related artifact that was phase-locked to the nondirectional kinematics in experiment 1 (figure 3(a)). Alternatively, this activity could have originated in deeper brain structures (e.g. thalamus, cerebellum) which we did not consider in the source imaging model. As in [24, 36], we decoded cursor trajectories and ignored potential effects related to the target stimulus. This raises the question to which extent target related information was utilized by the decoders. During the

PTT, the target and cursor trajectories were highly correlated (figures 1(d),(e)), rendering a disentanglement of cursor and target related effects impracticable. Studying multiple tasks with different dynamics could help to disentangle cursor (arm/finger) and target related effects [105].

5. Conclusion

Previous work suggested that low-frequency EEG and MEG signals encode information about directional (position and velocity) and nondirectional (distance and speed) arm movement kinematics. We found direct evidence that directional and nondirectional kinematic information is simultaneously detectable in low-frequency M/EEG signals. Moreover, movement trajectories could be reconstructed with significantly higher accuracy in terms of correlation and DSSR using an UKF that explicitly models the nonlinear relation between directional and nondirectional kinematics than by using linear Kalman (KF) and WFs which do not combine both types of kinematics. In terms of SNR the UKF outperformed the linear KF in all cases, while it was outperformed by the WF in three out of four cases. Further research is necessary to improve the decoder accuracy, particularly the strengths of the UKF in terms of correlation and DSSR and the WF in terms of SNR should be combined. Apart from improving the algorithms, it is essential to assess how the results transfer to attempted movements in paralyzed individuals and to which extent the accuracy can be improved with feedback training.

Acknowledgments

The authors acknowledge Joana Pereira, Catarina Lopes-Dias, Lea Hehenberger and Hiroaki Hashimoto for their valuable discussions and comments. This work has received funding from the European Research Council (ERC) under the European Union's Horizon 2020 research and innovation programme (Consolidator Grant 681231 'Feel Your Reach'). R J K received additional funding from Graz University of Technology through its research abroad program (Grant Number O-9406000008).

Author contributions

R J K and G R M conceived the study. R J K implemented the algorithms and conducted the analysis. R J K, A I S, V M, M H and G R M interpreted the data. R J K created the Figures and Tables. R J K wrote the draft of the manuscript. R J K, A I S, V M, M H and G R M edited the manuscript.

ORCID iDs

Reinmar J Kobler  <https://orcid.org/0000-0003-4007-279X>

Valeria Mondini  <https://orcid.org/0000-0001-7680-6199>

Gernot R Müller-Putz  <https://orcid.org/0000-0002-0087-3720>

References

- [1] Wolpaw J R, Birbaumer N, McFarland D J, Pfurtscheller G and Vaughan T M 2002 Brain-computer interfaces for communication and control *Clin. Neurophysiol. Off. J. Int. Fed. Clin. Neurophysiol.* **113** 767–91
- [2] Lebedev M A and Nicolelis M A L 2017 Brain-machine interfaces: from basic science to neuroprostheses and neurorehabilitation *Physiol. Rev.* **97** 767–837
- [3] Pfurtscheller G, Guger C, Müller G, Krausz G and Neuper C 2000 Brain oscillations control hand orthosis in a tetraplegic *Neurosci. Lett.* **292** 211–4
- [4] Wolpaw J R and McFarland D J 2004 Control of a two-dimensional movement signal by a noninvasive brain-computer interface in humans *Proc. Natl Acad. Sci.* **101** 17849–54
- [5] Müller-Putz G R, Scherer R, Pfurtscheller G and Rupp R 2005 EEG-based neuroprosthesis control: A step towards clinical practice *Neurosci. Lett.* **382** 169–74
- [6] Hochberg L R, Serruya M D, Friehs G M, Mukand J A, Saleh M, Caplan A H, Branner A, Chen D, Penn R D and Donoghue J P 2006 Neuronal ensemble control of prosthetic devices by a human with tetraplegia *Nature* **442** 164–71
- [7] Wessberg J, Stambaugh C R, Kralik J D, Beck P D, Laubach M, Chapin J K, Kim J, Biggs S J, Srinivasan M A and Nicolelis M A 2000 Real-time prediction of hand trajectory by ensembles of cortical neurons in primates *Nature* **408** 361–5
- [8] Carmena J M, Lebedev M A, Crist R E, O'Doherty J E, Santucci D M, Dimitrov D E, Patil P G, Henriquez C S and Nicolelis M A L 2003 Learning to control a brain-machine interface for reaching and grasping by primates *PLoS Biol.* **1**
- [9] Musallam S 2004 Cognitive control signals for neural prosthetics *Science* **305** 258–62
- [10] Mulliken G H, Musallam S and Andersen R A 2008 Decoding trajectories from posterior parietal cortex ensembles *J. Neurosci.* **28** 12913–26
- [11] Collinger J L, Wodlinger B, Downey J E, Wang W, Tyler-Kabara E C, Weber D J, McMorland A J C, Velliste M, Boninger M L and Schwartz A B 2013 High-performance neuroprosthetic control by an individual with tetraplegia *The Lancet* **381** 557–64
- [12] Wodlinger B, Downey J E, Tyler-Kabara E C, Schwartz A B, Boninger M L and Collinger J L 2015 Ten-dimensional anthropomorphic arm control in a human brain-machine interface: difficulties, solutions, and limitations *J. Neural Eng.* **12** 016011
- [13] Bouton C E et al 2016 Restoring cortical control of functional movement in a human with quadriplegia *Nature* **533** 247–50
- [14] Ajiboye A B et al 2017 Restoration of reaching and grasping movements through brain-controlled muscle stimulation in a person with tetraplegia: A proof-of-concept demonstration *The Lancet* **389** 1821–30
- [15] Georgopoulos A P, Langheim F J B, Leuthold A C and Merkle A N 2005 Magnetoencephalographic signals predict movement trajectory in space *Exp. Brain Res.* **167** 132–5
- [16] Jerbi K, Lachaux J-P, N'Diaye K, Pantazis D, Leahy R M, Garnero L and Baillet S 2007 Coherent neural representation of hand speed in humans revealed by MEG imaging *Proc. Natl Acad. Sci. USA* **104** 7676–81
- [17] Waldert S, Preissl H, Demandt E, Braun C, Birbaumer N, Aertsen A and Mehring C 2008 Hand movement direction decoded from MEG and EEG *J. Neurosci.* **28** 1000–8

Q6

Q7

- [18] Gu Y, Dremstrup K and Farina D 2009 Single-trial discrimination of type and speed of wrist movements from EEG recordings *Clin. Neurophysiol.* **120** 1596–600
- [19] Bradberry T J, Gentili R J and Contreras-Vidal J L 2010 Reconstructing three-dimensional hand movements from noninvasive electroencephalographic signals *J. Neurosci.* **30** 3432–7
- [20] Kobler R J, Sburlea A I and Müller-Putz G R 2018 Tuning characteristics of low-frequency EEG to positions and velocities in visuomotor and oculomotor tracking tasks *Sci. Rep.* **8** 17713
- [21] Wang W, Sudre G P, Xu Y, Kass R E, Collinger J L, Degenhart A D, Bagic A I and Weber D J 2010 Decoding and cortical source localization for intended movement direction with MEG *J. Neurophysiol.* **104** 2451–61
- [22] Ofner P and Müller-Putz G R 2015 Using a noninvasive decoding method to classify rhythmic movement imaginations of the arm in two planes *IEEE Trans. Biomed. Eng.* **62** 972–81
- [23] Jeong-Hun K, Biessmann F and Seong-Whan L 2015 Decoding three-dimensional trajectory of executed and imagined arm movements from electroencephalogram signals *IEEE Trans. Neural Syst. Rehabil. Eng.* **23** 867–76
- [24] Schalk G, Kubánek J, Miller K J, Anderson N R, Leuthardt E C, Ojemann J G, Limbrick D, Moran D, Gerhardt L A and Wolpaw J R 2007 Decoding two-dimensional movement trajectories using electrocorticographic signals in humans *J. Neural Eng.* **4** 264
- [25] Antelis J M, Montesano L, Ramos-Murguialday A, Birbaumer N and Minguez J 2013 On the usage of linear regression models to reconstruct limb kinematics from low frequency EEG signals *PLoS One* **8**
- [26] Yeom H G, Kim J S and Chung C K 2013 Estimation of the velocity and trajectory of three-dimensional reaching movements from non-invasive magnetoencephalography signals *J. Neural Eng.* **10** 026006
- [27] Ubeda A, Azorín J M, Chavarriaga R and Millán J Del R 2017 Classification of upper limb center-out reaching tasks by means of EEG-based continuous decoding techniques *J. NeuroEngineering Rehabil.* **14** 1–14
- [28] Nakanishi Y, Yanagisawa T, Shin D, Fukuma R, Chen C, Kambara H, Yoshimura N, Hirata M, Yoshimine T and Koike Y 2013 Prediction of three-dimensional arm trajectories based on ecog signals recorded from human sensorimotor cortex *PLoS One* **8**
- [29] Kobler R J, Almeida I, Sburlea A I and Müller-Putz G R 2020 Using machine learning to reveal the population vector from EEG signals *J. Neural Eng.* **17** 026002
- [30] Mondini V, Kobler R J, Sburlea A I and Müller-Putz G R 2020 Continuous low-frequency EEG decoding of arm movement for closed-loop, natural control of a robotic arm *J. Neural Eng.*
- [31] Moran D W and Schwartz A B 1999 Motor cortical representation of speed and direction during reaching *J. Neurophysiol.* **82** 2676–92
- [32] Inoue Y, Mao H, Suway S B, Orellana J and Schwartz A B 2018 Decoding arm speed during reaching *Nat. Commun.* **9** 5243
- [33] Mehring C, Rickert J, Vaadia E, Cardoso de Oliveira S, Aertsen A and Rotter S 2003 Inference of hand movements from local field potentials in monkey motor cortex *Nat. Neurosci.* **6** 1253–4
- [34] Hammer J, Pistohl T, Fischer J, Kršek P, Tomášek M, Marusič P, Schulze-Bonhage A, Aertsen A and Ball T 2016 Predominance of movement speed over direction in neuronal population signals of motor cortex: intracranial EEG data and a simple explanatory model *Cereb. Cortex* **26** 2863–81
- [35] Kobler R J, Hirata M, Hashimoto H, Dowaki R, Sburlea A I and Müller-Putz G R 2019 Simultaneous decoding of velocity and speed during executed and observed tracking movements: an MEG study *Proc. of the 8th Graz Brain Computer Interface Conf. 2019* (Graz)
- [36] Li Z, O'Doherty J E, Hanson T L, Lebedev M A, Henriquez C S and Nicolelis M A L 2009 Unscented kalman filter for brain-machine interfaces *PLoS One* **4** e6243
- [37] Wan E A and Van Der Merwe R 2000 The unscented Kalman filter for nonlinear estimation *Proc. of the IEEE 2000 Adaptive Systems for Signal Processing, Communications, and Control Symp. (Cat. No.00EX373)* Symp. on Adaptive Systems for Signal Processing Communications and Control (Lake Louise, Alta., Canada: IEEE) pp 153–8
- [38] Kalman R E 1960 A new approach to linear filtering and prediction problems *J. Basic Eng.* **82** 35–45
- [39] Wiener N 1964 *Extrapolation, Interpolation, and Smoothing of Stationary Time Series* (Cambridge, MA: MIT Press)
- [40] Kobler R J, Kolesnichenko E, Sburlea A I and Müller-Putz G R 2020 Distinct cortical networks for hand movement initiation and directional processing: an EEG study *NeuroImage* **117076**
- [41] Kothe C, Medine D, Boulay C, Grivich M and Stenner T 2019 Lab Streaming Layer (LSL)—A software framework for synchronizing a large array of data collection and stimulation devices
- [42] Kothe C 2012 Simulation and Neuroscience Application Platform (SNAP)
- [43] Delorme A and Makeig S 2004 EEGLAB: an open source toolbox for analysis of single-trial EEG dynamics including independent component analysis *J. Neurosci. Methods* **134** 9–21
- [44] Tadel F, Baillet S, Mosher J C, Pantazis D and Leahy R M 2011 Brainstorm: A user-friendly application for MEG/EEG analysis *Comput. Intell. Neurosci.* **2011**
- [45] R Core Team 2019 *R: A Language and Environment for Statistical Computing* (Vienna, Austria: R Foundation for Statistical Computing)
- [46] Wickham H et al 2019 Welcome to the tidyverse *J. Open Source Softw.* **4** 1686
- [47] Kobler R J, Sburlea A I, Lopes-Dias C, Schwarz A, Hirata M and Müller-Putz G R 2020 Corneo-retinal-dipole and eyelid-related eye artifacts can be corrected offline and online in electroencephalographic and magnetoencephalographic signals *NeuroImage* **218** 117000
- [48] Kobler R J, Sburlea A I and Müller-Putz G R 2017 A comparison of ocular artifact removal methods for block design based electroencephalography experiments *Proc. of the 7th Graz Brain-Computer Interface Conf.* pp 236–41
- [49] Makeig S, Bell A J, Jung T-P and Sejnowski T J 1996 Independent component analysis of electroencephalographic data *Advances in Neural Information Processing Systems* pp 145–51
- [50] Kobler R J, Sburlea A I, Mondini V and Müller-Putz G R 2019 HEAR to remove pops and drifts: the high-variance electrode artifact removal (HEAR) algorithm *Proc. of the 41st Annual Int. Conf. of the IEEE Engineering in Medicine and Biology Society (EMBC)* (Berlin, Germany: IEEE) pp 5150–5
- [51] Delorme A, Makeig S and Sejnowski T 2001 Automatic artifact rejection for EEG data using high-order statistics and independent component analysis *3rd international ICA conference 3rd international ICA conference* pp 9–12
- [52] Savitzky A and Golay M J E 1964 Smoothing and differentiation of data by simplified least squares procedures *Anal. Chem.* **36** 1627–39
- [53] Schäfer J and Strimmer K 2005 A shrinkage approach to large-scale covariance matrix estimation and implications for functional genomics *Stat. Appl. Genet. Mol. Biol.* **4**
- [54] Baillet S, Mosher J C and Leahy R M 2001 Electromagnetic brain mapping *IEEE Signal Process. Mag.* **18** 14–30
- [55] Michel C M, Murray M M, Lantz G, Gonzalez S, Spinelli L and Grave De Peralta R 2004 EEG source imaging *Clin. Neurophysiol.* **115** 2195–222

Q9

Q10

Q8

Q11

- [56] Fonov V, Evans A C, Botteron K, Almlí C R, McKinstry R C and Collins D L 2011 Unbiased average age-appropriate atlases for pediatric studies *NeuroImage* **54** 313–27
- [57] Gramfort A, Papadopoulos T, Olivi E and Clerc M 2010 OpenMEEG: opensource software for quasistatic bioelectromagnetics *Biomed. Eng. Online* **9**
- [58] Kybic J, Clerc M, Abboud T, Faugeras O, Keriven R and Papadopoulos T 2005 A common formalism for the integral formulations of the forward EEG problem *IEEE Trans. Med. Imaging* **24** 12–28
- [59] Pascual-Marqui R D 2002 Standardized low resolution brain electromagnetic tomography (sLORETA): technical details *Methods Find. Exp. Clin. Pharmacol.* **24** 1–16
- [60] Nichols T and Holmes A 2002 Nonparametric permutation tests for functional neuroimaging: A primer with examples *Hum. Brain Mapp.* **15** 1–25
- [61] Maris E and Oostenveld R 2007 Nonparametric statistical testing of EEG- and MEG-data *J. Neurosci. Methods* **164** 177–90
- [62] Benjamini Y and Yekutieli D 2001 The control of the false discovery rate in multiple testing under dependency *Ann. Stat.* **29** 1165–88
- [63] de Jong S 1993 SIMPLS: an alternative approach to partial least squares regression *Chemom. Intell. Lab. Syst.* **18** 251–63
- [64] Bierman G J 1977 *Factorization Methods for Discrete Sequential Estimation* (New York: Academic)
- [65] Van der Merwe R and Wan E A 2002 The square-root unscented Kalman filter for state and parameter-estimation 3461–4
- [66] Garipelli G, Chavarriaga R and Millán J D R 2013 Single trial analysis of slow cortical potentials: a study on anticipation related potentials *J. Neural Eng.* **10** 036014
- [67] Bradberry T J, Rong F and Contreras-Vidal J L 2009 Decoding center-out hand velocity from MEG signals during visuomotor adaptation *NeuroImage* **47** 1691–700
- [68] Korik A, Sosnik R, Siddique N and Coyle D 2018 Decoding imagined 3D hand movement trajectories From EEG: evidence to support the use of mu, beta, and low gamma oscillations *Front. Neurosci.* **12** 1–16
- [69] Toda A, Imamizu H, Kawato M and Sato M 2011 Reconstruction of two-dimensional movement trajectories from selected magnetoencephalography cortical currents by combined sparse Bayesian methods *NeuroImage* **54** 892–905
- [70] Robinson N, Guan C and Vinod A P 2015 Adaptive estimation of hand movement trajectory in an EEG based brain-computer interface system *J. Neural Eng.* **12** 66019
- [71] Pistohl T, Ball T, Schulze-Bonhage A, Aertsen A and Mehring C 2008 Prediction of arm movement trajectories from ECoG-recordings in humans *J. Neurosci. Methods* **167** 105–14
- [72] Ball T, Schulze-Bonhage A, Aertsen A and Mehring C 2009 Differential representation of arm movement direction in relation to cortical anatomy and function *J. Neural Eng.* **6** 016006
- [73] Bundy D T, Szrama N, Pahwa M and Leuthardt E C 2018 Unilateral, 3D arm movement kinematics are encoded in ipsilateral human cortex *J. Neurosci.* **38** 10042–56
- [74] Nakanishi Y, Yanagisawa T, Shin D, Kambara H, Yoshimura N, Tanaka M, Fukuma R, Kishima H, Hirata M and Koike Y 2017 Mapping ECoG channel contributions to trajectory and muscle activity prediction in human sensorimotor cortex *Sci. Rep.* **7** 45486
- [75] Waldert S, Pistohl T, Braun C, Ball T, Aertsen A and Mehring C 2009 A review on directional information in neural signals for brain-machine interfaces *J. Physiol. Paris* **103** 244–54
- [76] Georgopoulos A P, Kalaska J F, Caminiti R and Massey J T 1982 On the relations between the direction of two-dimensional arm movements and cell discharge in primate motor cortex *J. Neurosci.* **2** 1527–37
- [77] Paninski L, Fellows M R, Hatsopoulos N G and Donoghue J P 2004 Spatiotemporal tuning of motor cortical neurons for hand position and velocity *J. Neurophysiol.* **91** 515–32
- [78] Makin J G, O’Doherty J E, Cardoso M M B and Sabes P N 2018 Superior arm-movement decoding from cortex with a new, unsupervised-learning algorithm *J. Neural Eng.* **15**
- [79] Stavisky S D, Kao J C, Nuyujukian P, Ryu S I and Shenoy K V 2015 A high performing brain-machine interface driven by low-frequency local field potentials alone and together with spikes *J. Neural Eng.* **12** 036009
- [80] Ofner P and Müller-Putz G R 2012 Decoding of velocities and positions of 3D arm movement from EEG *Proc. Annu. Int. Conf. IEEE Eng. Med. Biol. Soc. EMBS* pp 6406–9
- [81] Neuper C, Scherer R, Reiner M and Pfurtscheller G 2005 Imagery of motor actions: differential effects of kinesthetic and visual-motor mode of imagery in single-trial EEG *Cogn. Brain Res.* **25** 668–77
- [82] Filimon F, Nelson J D, Hagler D J and Sereno M I 2007 Human cortical representations for reaching: mirror neurons for execution, observation, and imagery *NeuroImage* **37** 1315–28
- [83] Miller K J, Schalk G, Fetz E E, den Nijs M, Ojemann J G and Rao R P N 2010 Cortical activity during motor execution, motor imagery, and imagery-based online feedback *Proc. Natl Acad. Sci.* **107** 4430–5
- [84] Vargas-Irwin C E et al 2018 Watch, imagine, attempt: motor cortex single-unit activity reveals context-dependent movement encoding in humans with tetraplegia *Front. Hum. Neurosci.* **12** 450
- [85] Rastogi A et al 2020 Neural representation of observed, imagined, and attempted grasping force in motor cortex of individuals with chronic tetraplegia *Sci. Rep.* **10** 1429
- [86] Aflalo T et al 2015 Decoding motor imagery from the posterior parietal cortex of a tetraplegic human *Science* **348** 906–10
- [87] Filimon F 2010 Human cortical control of hand movements: parietofrontal networks for reaching, grasping, and pointing *Neurosci. Rev. J. Bringing Neurobiol. Neurol. Psychiatry* **16** 388–407
- [88] Fabbri S, Caramazza A and Lingnau A 2010 Tuning curves for movement direction in the human visuomotor system *J. Neurosci.* **30** 13488–98
- [89] Marty B, Bourguignon M, Jousmäki V, Wens V, Op de Beeck M, Van Bogaert P, Goldman S, Hari R and De Tiège X 2015 Cortical kinematic processing of executed and observed goal-directed hand actions *NeuroImage* **119** 221–8
- [90] Klamer S, Elshahabi A, Lerche H, Braun C, Erb M, Scheffler K and Focke N K 2015 Differences between MEG and high-density EEG source localizations using a distributed source model in comparison to fMRI *Brain Topogr.* **28** 87–94
- [91] Caminiti R, Ferraina S and Johnson P B 1996 The sources of visual information to the primate frontal lobe: a novel role for the superior parietal lobule *Cereb. Cortex* **6** 319–28
- [92] Culham J C and Valyear K F 2006 Human parietal cortex in action *Curr. Opin. Neurobiol.* **16** 205–12
- [93] Gallivan J P and Culham J C 2015 Neural coding within human brain areas involved in actions *Curr. Opin. Neurobiol.* **33** 141–9
- [94] Caminiti R, Borra E, Visco-Comandini F, Battaglia-Mayer A, Averbeck B B and Luppino G 2017 Computational architecture of the parieto-frontal network underlying cognitive-motor control in monkeys *eneuro* **4** ENEURO.0306–16.2017
- [95] Penfield W and Boldrey E 1937 Somatic motor and sensory representation in the cerebral cortex of man as studied by electrical stimulation *Brain* **60** 389–443
- [96] Gilja V et al 2015 Clinical translation of a high performance neural prosthesis *Nat. Med.* **21** 1142–5
- [97] Pandarinath C, Nuyujukian P, Blabe C H, Sorice B L, Saab J, Willett F R, Hochberg L R, Shenoy K V and

- Henderson J M 2017 High performance communication by people with paralysis using an intracortical brain-computer interface *eLife* **6** e18554
- [98] Edelman B J, Meng J, Suma D, Zurn C, Nagarajan E, Baxter B S, Cline C C and He B 2019 Noninvasive neuroimaging enhances continuous neural tracking for robotic device control *Sci. Robot.* **4** eaaw6844
- [99] Bradberry T J, Gentili R J and Contreras-Vidal J L 2011 Fast attainment of computer cursor control with noninvasively acquired brain signals *J. Neural Eng.* **8** 036010
- [100] Poli R and Salvaris M 2011 Comment on 'Fast attainment of computer cursor control with noninvasively acquired brain signals' *J. Neural Eng.* **8** 058001
- [101] Bradberry T J, Gentili R J and Contreras-Vidal J L 2011 Reply to comment on 'Fast attainment of computer cursor control with noninvasively acquired brain signals' *J. Neural Eng.* **8** 058002
- [102] Kübler A, Kotchoubey B, Hinterberger T, Ghanayim N, Perelmouter J, Schauer M, Fritsch C, Taub E and Birbaumer N 1999 The thought translation device: A neurophysiological approach to communication in total motor paralysis *Exp. Brain Res.* **124** 223–32
- [103] Gratton G, Coles M G H and Donchin E 1983 A new method for off-line removal of ocular artifact *Electroencephalogr. Clin. Neurophysiol.* **55** 468–84
- [104] Katila T, Maniewski R, Poutanen T, Varpula T and Karp P J 1981 Magnetic fields produced by the human eye *J. Phys. D: Appl. Phys.* **52** 2565–71
- [105] Gallego J A, Perich M G, Naufel S N, Ethier C, Solla S A and Miller L E 2018 Cortical population activity within a preserved neural manifold underlies multiple motor behaviors *Nat. Commun.* **9** 4233
- [106] Todorova S, Sadtler P, Batista A, Chase S and Ventura V 2014 To sort or not to sort: the impact of spike-sorting on neural decoding performance *J. Neural Eng.* **11** 056005

Q12

Secondary Publications

C

A COMPARISON OF OCULAR ARTIFACT REMOVAL METHODS FOR BLOCK DESIGN BASED ELECTROENCEPHALOGRAPHY EXPERIMENTS

R. J. Kobler¹, A. I. Sburlea¹, G. R. Müller-Putz¹

¹Institute of Neural Engineering, Graz University of Technology, Graz, Austria

E-mail: gernot.mueller@tugraz.at

ABSTRACT: Eye movements and their contribution to electroencephalographic (EEG) recordings as ocular artifacts (OAs) are well studied. Yet their existence is typically regarded as impeding analysis. A widely accepted bypass is artifact avoidance. OA processing is often reduced to rejecting contaminated data. To overcome loss of data and restriction of behavior, research groups have proposed various correction methods. State of the art approaches are data driven and typically require OAs to be uncorrelated with brain activity. This does not necessarily hold for visuomotor tasks. To prevent correlated signals, we examined a two block approach. In a first block, subjects performed saccades and blinks, according to a visually guided paradigm. We then fitted 5 artifact removal algorithms to this data. To test their stationarity regarding artifact attenuation and preservation of brain activity, we recorded a second block one hour later. We found that saccades and blinks could still be attenuated to chance level, while brain activity during rest trials could be retained.

INTRODUCTION

In the last two decades extensive research on the neural encoding of upper limb movement kinematics has been carried out [1]. Experiments on kinematics decoding typically comprise visuomotor (VM) tasks [2–4]. Such tasks inherently involve visual feedback e.g. the distance between a target and an end-effector. Naturally, subjects would foveate between or track objects of interest [5]. This is typically avoided in laboratory conditions by instructing subjects to fixate their gaze to an arbitrary fixation point and reduce blinking to a minimum [2, 3, 6].

We want to emphasize that solely removing frontal channels from the analysis, while allowing eye movements is not sufficient to attenuate ocular artifacts (OAs) [4]. Central and parietal channels would nonetheless exhibit high correlations with saccade directions [7].

If the protocol allows saccades and blinks, literature typically separates between three independent types of artifacts [7, 8]. (1) Corneo-retinal dipole (CRD) artifacts cause signal changes that depend on eyeball rotation size and direction [7]. (2) Eyelid artifacts emerge from blinks, eyelid saccades and post-saccadic eyelid movements [7]. They elicit a large potential and are generated by the eyelid, whose displacement changes the impedance between

positively charged cornea and extraocular skin [8]. (3) The saccadic spike potential (SP) is most prominent on periorbital electrodes and believed to result from contraction of extra-ocular muscles [8].

In future, we plan to apply the methods developed here on decoding kinematics from continuous visuomotor tasks. Previous studies consistently reported significant decoding information in low frequency components (<2 Hz) [2, 3, 6, 9]. We therefore focus on CRD and eyelid movements, since SP artifacts emerge in a frequency range >20Hz [8].

An alternative strategy to OA avoidance is correction. Literature provides numerous offline correction methods. For a recent review see [10]. Most common methods are either source estimation [7, 11, 12] or regression based [13] or a hybrid variant [14]. They all assume a linear mixing model:

$$\mathbf{x}(t) = \mathbf{A}\mathbf{s}(t) = \mathbf{A}^{(b)}\mathbf{s}^{(b)}(t) + \mathbf{A}^{(a)}\mathbf{s}^{(a)}(t) \quad (1)$$

with the scalp recordings $\mathbf{x}(t)$ at time t being a mixture of sources $\mathbf{s}(t)$. The mixing matrix \mathbf{A} is unknown. It can be separated into mixing coefficients $\mathbf{A}^{(b)}$ for brain sources $\mathbf{s}^{(b)}(t)$ and $\mathbf{A}^{(a)}$ for artifact sources $\mathbf{s}^{(a)}(t)$.

Cortical control of an end-effector requires online removal of OAs. One approach is to use adaptive algorithms to iteratively estimate $\mathbf{A}^{(b)}$ [14]. An advantage is that they can track changes of mixing coefficients due to i.e. a changing electrode scalp interface. However, they assume uncorrelated brain activity and artifacts [10]. This does not necessarily hold true for VM tasks. An alternative correction approach proposed in [13] is to use a block based experimental design. In the first block subjects perform voluntary eye artifacts. Thereupon a correction model is learned and applied online in the main block, during which subjects perform the actual task. Here time invariant mixing coefficients are assumed. Consequently, artifacts and brain activity can be correlated during the actual experiment. If the correlated brain activity contributes negligibly to the estimated eye artifact signals, only the artifact fraction is removed.

To our knowledge literature lacks a thorough comparison of how the previously listed correction approaches perform on the described block design. We selected five representatives and assessed their artifact correction performance on held out data. The algorithms are briefly outlined in the remainder of this section.

EYE-REG: A regression based algorithm originally proposed for block design [13]. It requires designated EOG channels to compute vertical and horizontal estimates of eye artifact source signal $\hat{\mathbf{s}}^{(a)}(t)$. The model, defined in equation 1, can be rewritten as

$$\mathbf{x}(t) = \mathbf{A}^{(a)}\mathbf{s}^{(a)}(t) + \mathbf{n}(t) \quad (2)$$

with the brain activity considered as noise $\mathbf{n}(t)$. The authors used the least squares solution to calculate an estimate $\hat{\mathbf{A}}^{(a)}$. The cleaned channels $\mathbf{x}_c(t)$ are then:

$$\mathbf{x}_c(t) = \mathbf{x}(t) - \hat{\mathbf{A}}^{(a)}\hat{\mathbf{s}}^{(a)}(t) \quad (3)$$

If the empiric estimates $\hat{\mathbf{A}}^{(a)}$ and $\hat{\mathbf{s}}^{(a)}$ are close to the unknowns, we can recover the brain activity by inserting equation 2 in 3:

$$\mathbf{x}_c(t) = \mathbf{A}^{(a)}\mathbf{s}^{(a)}(t) + \mathbf{n}(t) - \hat{\mathbf{A}}^{(a)}\hat{\mathbf{s}}^{(a)}(t) \approx \mathbf{n}(t) \quad (4)$$

*MARA*¹: Multiple Artifact Rejection Algorithm (MARA) is an independent component analysis (ICA) based algorithm [12]. ICA is used to estimate an unmixing matrix \mathbf{V} that transforms equation 1 into:

$$\hat{\mathbf{s}}(t) = \mathbf{V}\mathbf{x}(t) = \mathbf{V}\mathbf{A}\mathbf{s}(t) \approx \mathbf{s}(t) \quad (5)$$

and recovers independent components (ICs) $\hat{\mathbf{s}}(t)$. *MARA* then applies a plug-and-play classifier to identify artifactual ICs and rejects them [12].

*EYE-EEG*¹: Here, artifactual ICs are rejected based on a variance ratio metric [7]. An IC's variance is computed during designated saccade and fixation periods². If their ratio exceeds a threshold, the IC is rejected. In [7] an eye tracker was employed to detect saccades and fixations.

*REGICA*¹: Regression-ICA is a hybrid method [14]. The authors showed that artifactual ICs carry more ocular and less brain activity than scalp channels. Hence, they proposed to apply regression to artifactual ICs only.

*EYE-SUB*¹: Artifact subspace subtraction is another approach to correct equation 1 for eye artifacts. Instead of using fixed linear combinations of EOG channels, like for regression, an artifact unmixing matrix $\mathbf{V}^{(a)}$ is computed. It recovers an estimate of the eye artifact signals $\hat{\mathbf{s}}^{(a)}(t)$:

$$\hat{\mathbf{s}}^{(a)}(t) = \mathbf{V}^{(a)}\mathbf{x}(t) \quad (6)$$

In combination with an estimated artifact mixing matrix $\hat{\mathbf{A}}^{(a)}$ equation 3 transforms to:

$$\mathbf{x}_c(t) = \mathbf{x}(t) - \hat{\mathbf{A}}^{(a)}\hat{\mathbf{s}}^{(a)}(t) = (\mathbf{I} - \hat{\mathbf{A}}^{(a)}\mathbf{V}^{(a)})\mathbf{x}(t) \quad (7)$$

The columns of $\hat{\mathbf{A}}^{(a)}$ are computed by finding the subspace which is maximally different between two conditions e.g. up vs. down saccades [11].

¹We used the publicly available eeg-lab extension. Available online: https://scn.ucsd.edu/wiki/EEGLAB_Extensions

²Fixations are defined as periods during which no eye movements happen [7].

MATERIALS AND METHODS

Participants: Five persons, aged 23.6±3.9 years, participated in this study. Three of them were female. All subjects had corrected to normal vision. They had already participated at least once in an EEG experiment before. All signed an informed consent after they were instructed about purpose and procedure of the study. The experimental procedure conformed to the declaration of Helsinki and was approved by the local ethics committee.

Stimulus Presentation: Subjects were seated in a shielded room at 1.4m distance to a computer screen (NEC Multisync 27" IPS TFT, 60Hz refresh rate, FullHD resolution). Stimuli were restricted to a square of 0.32 m x 0.32 m around the center of the screen (~13° x 13° visual angle).

Data Acquisition: EEG and EOG were recorded with a 64 channel ActiCap system connected to a BrainAmp amplifier. It sampled the data at a rate of 1 kHz and applied a first order highpass filter with a cutoff frequency of 0.016 Hz. 58 electrodes were placed at frontal, central, parietal and occipital sites according to the extended 10-20 system. The remaining 6 electrodes were placed on the outer canthi, infra and superior orbital to the left and right eye respectively. Ground and reference were placed on AFz and the right mastoid, respectively.

Experimental Procedure: The paradigm is illustrated in Figure 1. It defines four conditions. REST: subjects were instructed to fixate a blue sphere for 10 s. HORZ/VERT: the sphere moved on a continuous horizontal/vertical trajectory. Subjects were directed to accurately follow it with their gaze. BLINK: The sphere's vertical diameter shrunk 8 times for 0.5 s instructing subjects to blink once each time.

We decided to implement a visually guided paradigm to have control over saccades and blinks. It simplifies splitting the data into corresponding epochs. An eye tracker, originally required by *EYE-EEG*, was not necessary either. Figure 5 (right) illustrates the accordance of the stimulus with subject behavior (EOG derivatives).

The recording time was divided into 3 blocks. The first and last followed the presented paradigm. Both consisted of 27 trials (9 REST, 6 HORZ, 6 VERT and 6 BLINK). The choice of 27 trials and their partition was motivated by the requirements of the algorithms. Recordings of the middle block, lasting roughly 60 minutes, followed a different paradigm and will be published elsewhere.

Preprocessing: The EEG data was first downsampled to 250 Hz. To attenuate 50 Hz line noise, a 2nd order Butterworth bandstop filter was applied. Slow drifts were removed by a zero-phase 4th order Butterworth highpass filter with 0.4 Hz cutoff frequency.

We visually inspected the data for bad channels and flagged 1 to 3 channels across subjects. They were spherically interpolated. We then extracted epochs of 7 s starting 1 s after cue presentation and rejected 1.7±1.2 trials per block by visual inspection.

Three of the five algorithms, that we compare, process

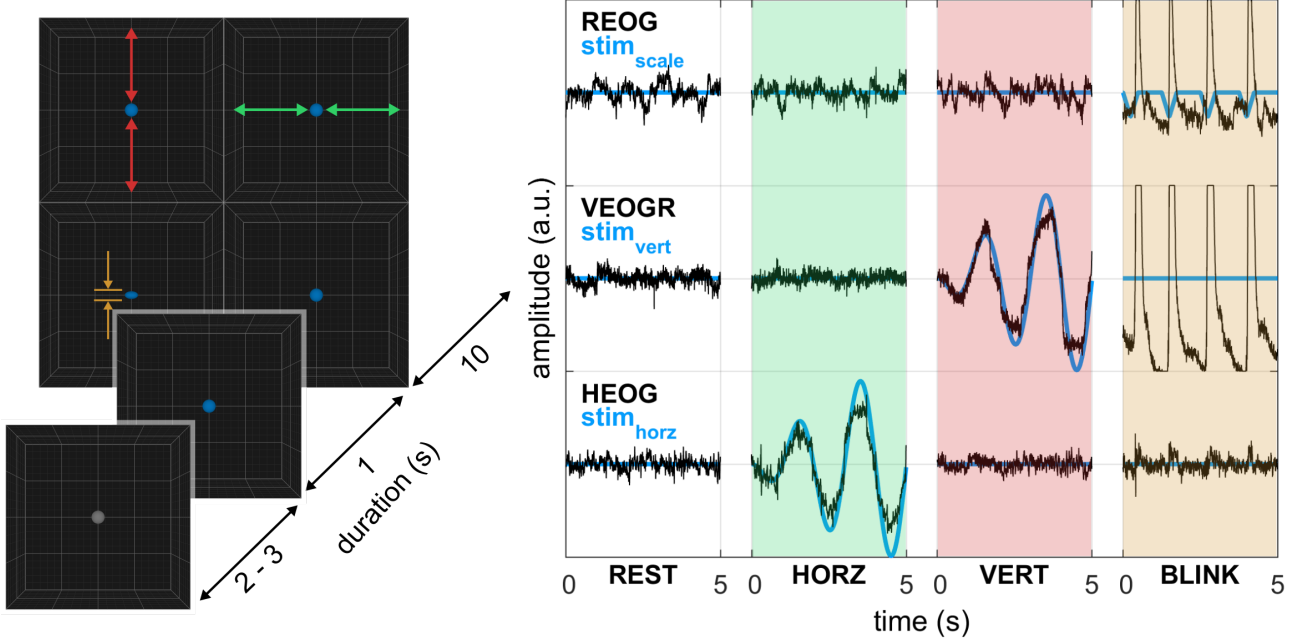


Figure 1: Experimental task. **(left)** The visual stimuli consisted of a 3D grid and a sphere, located in the center of the screen. Every trial started with a break lasting 2 to 3 seconds (uniformly distributed). Thereupon the sphere color changed to blue. After 1 s a condition dependent pattern was presented for 10 s. **(right)** First 5 s of the condition dependent patterns (blue). REST: the sphere remained in the center of the screen. HORZ: it moved along the horizontal plane according to a windowed sinusoid with a frequency of 0.5 Hz. VERT: the same movement but along the vertical plane. BLINK: the vertical diameter of the sphere changed, instructing the subject to blink. Additionally horizontal, vertical and radial EOG derivatives for selected trials of subject 1 are plotted (black).

the data in IC space. Before computing ICA we applied principal component analysis (PCA) on the 64 EEG/EOG channels and retained components explaining 99.9% of the variance. We then applied the extended Infomax algorithm to compute the unmixing matrix \mathbf{V} of equation 5. The regression based algorithms require EOG components as artifact sources $\hat{\mathbf{s}}^{(a)}(t)$. The horizontal EOG (HEOG) derivative was computed as the difference between right and left outer canthi, vertical EOG left/right (VEOGL/R) as the difference between left/right superior and inferior electrode, and the radial EOG (REOG) component as the average of all six EOG electrodes.

Fixation, saccade and blink detection: *EYE-EEG* required separating the data into fixation and saccade periods. Since we asked subjects to avoid eye movements during REST condition, we used REST trials as fixation periods. For saccade detection the HEOG and VEOG³ component were first lowpass filtered (zero-phase Butterworth, 2nd order, 20 Hz cutoff frequency). Horizontal/vertical saccade periods were extracted from HORZ/VERT condition trials if the absolute value of the H/VEOG component was above $10 \mu\text{V}$ for at least 200 ms. The sign was also used to split the data into left/right and up/down saccades.

Blink detection is also based on the lowpass filtered VEOG component. Samples during BLINK trials were set to be blink related if the VEOG amplitude was above $200 \mu\text{V}$. The limits of these periods were expanded by 75 ms to include blink on- and offset.

³VEOG is the arithmetic mean of VEOGR and VEOGL.

EYE-REG: In [13] the authors argue to omit the REOG component, since it also captures considerable brain activity. We, therefore, used only HEOG and VEOGL/R as predictor variables for multiple linear regression.

EYE-SUB: First, penalized logistic regression (PLR) [11] with a regularization factor of 10^{-3} was applied to compute four artifact source signals $\hat{\mathbf{s}}^{(a)}(t)$ (4×1) that have a maximum magnitude difference between either left/right, up/down, blink/up or blink/down conditions. Similar to the regression approach, given $\hat{\mathbf{s}}^{(a)}(t)$, $\hat{\mathbf{A}}^{(a)}$ (64×4) can be computed by the pseudo inverse. The rest data was used to estimate a noise covariance matrix \mathbf{R}_n (64×64). Considering \mathbf{R}_n , the unmixing matrix $\mathbf{V}^{(a)}$ (4×64) can be calculated by the regularized weighted least squares solution [11]:

$$\mathbf{V}^{(a)} = \left(\hat{\mathbf{A}}^{(a)T} \mathbf{R}_n \hat{\mathbf{A}}^{(a)} + \mathbf{\Lambda} \right)^{-1} \hat{\mathbf{A}}^{(a)T} \mathbf{R}_n \quad (8)$$

with $\mathbf{\Lambda} = \lambda \mathbf{I}$ and regularization factor $\lambda = 10^{-4}$.

EYE-EEG: Similar to the original paper we set the threshold for the variance ratio to 1.1 [7].

REGICA: Precomputed ICs were flagged using the correlation between each IC and HEOG, VEOG with a threshold of 0.2. Multiple linear regression was applied to flagged ICs only. We used H/V/REOG as predictor variables.

Evaluation: All algorithms were fitted to the first block of data i.e. computation of ICA, regression weights and fitting of hyper parameters. The second block was solely employed for testing.

To assess artifact attenuation, we computed absolute values of Pearson correlation coefficients $|r|$ between EOG derivatives and each EEG channel. HEOG was used for HORZ, VEOG for VERT and blink periods during BLINK condition, respectively. Bootstrapping was applied to estimate chance level for $|r|$. Thus, we first merged the test trials of all subjects. We then randomly sampled 5 trials⁴ of e.g. HORZ condition and computed $|r|$ with EEG channels of 5 random REST trials. The shuffling was repeated 5000 times for each condition. This yielded a 95%-quantile of 0.11 in every of the three conditions.

Preservation of neural activity was assessed twofold. Firstly, through computing the root mean squared error (RMSE) between cleaned x_c and uncleaned x signals during REST condition trials [14].

$$RMSE(k) = \sqrt{\frac{1}{N_s} \sum_n (x[k, n] - x_c[k, n])^2} \quad (9)$$

with k being the channel index and N_s the total number of samples in the test set.

Secondly, by computing the ratio between power spectral density of cleaned (Pxx_c) and uncleaned (Pxx) signals

$$Pxx_{ratio}(k, f) = \frac{Pxx_c(k, f)}{Pxx(k, f)} \quad (10)$$

for each EEG channel k and frequency bin f [13]. We applied Welch's method to estimate the power spectral density for each trial and averaged across a subject's test trials.

RESULTS

Figure 2 depicts grand average topoplots of the 58 EEG channels after correction. The plots summarize mean test set performance for each metric and algorithm. The first row represents the uncorrected EEG. We observed typical eye artifact patterns for HORZ, VERT and BLINK conditions. Table 1 complements Figure 2. It lists mean and standard deviation across subjects for frontal, central and parietal channel groups.

Regarding the RMSE during REST, all algorithms exhibit a gradient from pre-frontal to occipital regions. *MARA* and *EYE-EEG* removed most activity, whereas *EYE-REG* and *EYE-SUB* achieve lowest RMSE across channel groups.

Figure 2 and Table 1 also summarize the absolute correlation $|r|$ between EEG channels and EOG derivatives after correction. One can clearly see that *MARA* could not identify ICs related to horizontal and vertical eye movements. This results in correlation values of up to 0.28 for frontal regions, which are clearly above the estimated chance level (0.11). The topoplots of the other algorithms show consistent attenuation of horizontal eye movements over scalp regions. Concerning vertical eye movements,

⁴Average number of trials in a subject's test set after rejection.

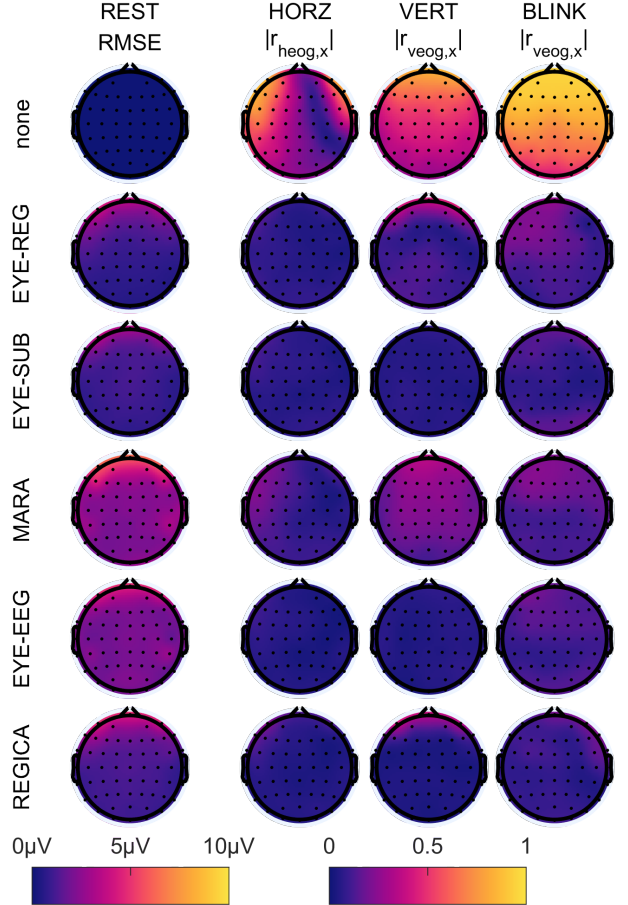


Figure 2: Topoplots (58 EEG channels) summarizing the average test set performance of the algorithms across subjects. (left) RMSE between corrected and uncorrected signal during REST condition, (right) absolute correlation $|r|$ with HEOG/VEOG/VEOG during HORZ/VERT/BLINK conditions.

EYE-SUB, *EYE-EEG* and *REGICA* could attenuate the correlation to similar levels as for horizontal ones. We also found that *EYE-SUB* and *REGICA* could attenuate blinks to chance level for frontal/central and parietal regions.

For visualization purposes, subsequent Figures show only the four algorithms that could attenuate artifact correlations to chance level, namely, *EYE-REG*, *EYE-SUB*, *EYE-EEG* and *REGICA*.

To estimate their performance decrease, we calculated group level means for train and test set. Figure 3 displays them for the average EEG channel. The barplots indicate mean and 95%-confidence interval for each condition and its associated metric. Non-overlapping train and test set confidence intervals, indicate a significant difference. The absolute correlation $|r|$ increased significantly for *EYE-SUB* (HORZ) and *EYE-EEG* (HORZ and BLINK).

The power spectral density ratio Pxx_{ratio} between corrected and uncorrected EEG revealed further differences across algorithms. Group level mean and its 95%-confidence interval are depicted in Figure 4 for frontal, central and parietal regions. *EYE-SUB* had its mean clos-

Table 1: Group level summary of performance metrics for frontal, central and parietal channel groups on the test set. Mean and standard deviation across subjects are stated per metric. The lowest value per metric and channel group is highlighted.

Condition	REST	HORZ	VERT	BLINK
Metric	RMSE	$ r $	$ r $	$ r $
Unit	μV	-	-	-
Frontal (F3, Fz, F4)				
<i>EYE-REG</i>	1.8±0.5	0.06±0.04	0.11±0.07	0.19±0.15
<i>EYE-SUB</i>	1.4±0.1	0.08±0.03	0.06±0.04	0.11±0.08
<i>MARA</i>	3.1±1.0	0.12±0.13	0.28±0.25	0.23±0.08
<i>EYE-EEG</i>	2.3±0.4	0.06±0.02	0.06±0.05	0.15±0.09
<i>REGICA</i>	2.0±0.2	0.07±0.02	0.07±0.04	0.10±0.04
Central (C3, Cz, C4)				
<i>EYE-REG</i>	1.0±0.4	0.06±0.04	0.10±0.04	0.16±0.10
<i>EYE-SUB</i>	1.1±0.4	0.07±0.05	0.06±0.04	0.08±0.05
<i>MARA</i>	2.5±1.0	0.10±0.13	0.24±0.22	0.14±0.09
<i>EYE-EEG</i>	2.2±0.9	0.05±0.02	0.05±0.02	0.12±0.07
<i>REGICA</i>	1.3±0.3	0.05±0.03	0.04±0.03	0.08±0.04
Parietal (P3, Pz, P4)				
<i>EYE-REG</i>	0.7±0.2	0.07±0.04	0.12±0.06	0.12±0.06
<i>EYE-SUB</i>	1.0±0.4	0.06±0.04	0.07±0.04	0.10±0.08
<i>MARA</i>	2.2±1.0	0.10±0.13	0.20±0.21	0.12±0.03
<i>EYE-EEG</i>	2.1±0.8	0.04±0.02	0.06±0.04	0.10±0.08
<i>REGICA</i>	1.2±0.4	0.05±0.02	0.04±0.03	0.09±0.03

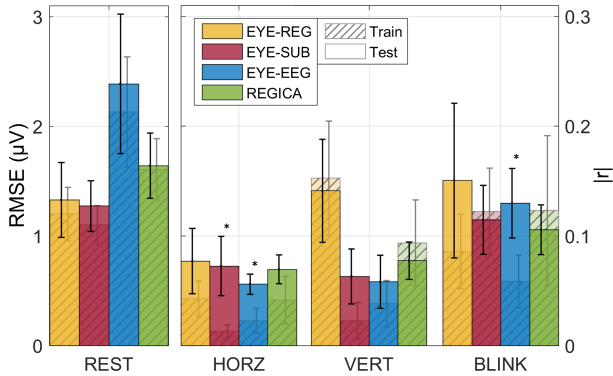


Figure 3: Algorithm performance on the average EEG channel for train (dashed) and test (solid) set. Mean and 95%-confidence interval across subjects are plotted for RMSE (left) and absolute correlation $|r|$ (right). Significant differences between train and test set are marked by *.

est to an ideal ratio of 1 and least variability of the mean across frequencies. *EYE-EEG* showed similar behavior for frontal, but larger attenuation in delta/theta frequency bands for central and parietal areas. *EYE-REG* resulted in largest mean attenuation in frontal areas, closely followed by *REGICA*. This improved considerably for central and posterior areas. We could also observe a larger variance of *REGICA* for the beta frequency band. It peaked in frontal channels.

DISCUSSION

In this work we compared five ocular artifact (OA) removal algorithms with regard to their applicability in a two step block design. We first trained the algorithms on a 5 min block of recordings. We then assessed their

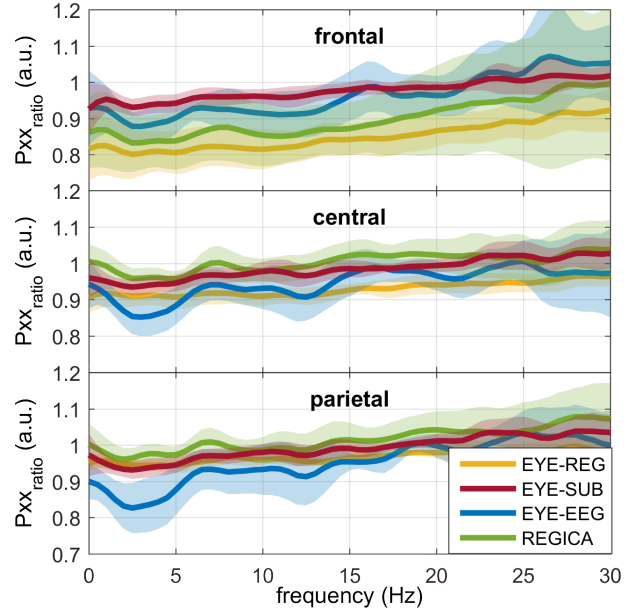


Figure 4: Mean and 95%-confidence interval of the group level power spectral density ratio Pxx_{ratio} for frontal (F3/z/4), central (C3/z/4) and parietal (P3/z/4) channels during REST condition. An ideal algorithm would yield a ratio of 1 for all frequencies.

OA removal quality on a test block recorded 60 minutes later. This approach implies a constant mixing matrix $\mathbf{A}^{(a)}$ for artifact sources. Our results, mainly Table 1 and Figure 3, give evidence that it is a reasonable assumption. We found that correlations for saccades and blinks could be attenuated to chance level, even 60 minutes after training. We emphasize that the difference between train and test set, displayed in Figure 3, captures not only the difference in time but also whether the data was used for parameter estimation. Therefore, we can not rule out if a significant difference was due to changing scalp projections or over-fitting on the train data.

As already pointed out in the introduction, allowing eye movements while only removing frontal channels is insufficient. Average correlations of up to 0.5 for uncorrected central and parietal channels (Figure 2) demonstrate the necessity for correction.

Regarding the algorithms, *MARA*, which did not rely on any label information, achieved lowest performance. While *EYE-SUB*, which required most information (annotated saccade and blink events), could attenuate artifacts to chance level and maintain low RMSE during REST condition. *REGICA* and *EYE-EEG* showed a tendency to achieve better attenuation for saccades and blinks in central and posterior areas but also to remove more brain activity.

The visually guided paradigm allowed us to control artifact occurrence. This simplified an automated annotation of artifact types (e.g. up/down saccades). In general, all algorithms tested here can be applied online. After artifact rejection and model calibration, which takes around 5 minutes, the correction process itself involves only matrix multiplications.

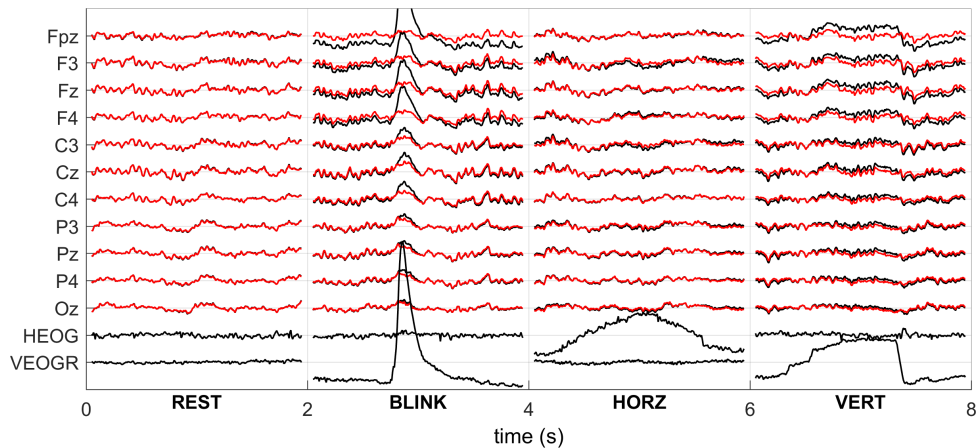


Figure 5: Representative examples in time domain for 2 s windows of selected trials. Displayed are 11 channels before (black) and after correction with *EYE-SUB* (red).

CONCLUSION

Based on the average performance on the test set, we found that *MARA* is not suitable for the investigated block design. Our results indicate, that artifact subspace subtraction (*EYE-SUB*) could achieve the best trade-off between attenuating eye artifacts and maintaining rest brain activity. Figure 5 depicts the difference between corrected and uncorrected EEG for representative trials and channels.

To complement our findings, we plan to analyze the effect on a kinematics decoder. This is a necessary step, since a significant performance drop was reported for a linear decoder after correction for OAs [6]. This demonstrates that eye artifacts were correlated with the dependent variables ($x/y/z$ velocities). Our block design accounts for such a scenario, which encourages further research in this direction.

ACKNOWLEDGMENTS

This work was supported by the ERC Consolidator Grant 681231 "Feel Your Reach".

REFERENCES

- [1] Müller-Putz GR, Schwarz A, Pereira J, *et al.* From classic motor imagery to complex movement intention decoding: The noninvasive Graz-BCI approach. In: Progress in Brain Research, 2016, vol. 228, 39–70.
- [2] Bradberry TJ, Gentili RJ, Contreras-Vidal JL. Reconstructing Three-Dimensional Hand Movements from Noninvasive Electroencephalographic Signals. *Journal of Neuroscience*. 2010;30(9):3432–3437.
- [3] Ofner P, Müller-Putz GR. Using a noninvasive decoding method to classify rhythmic movement imaginations of the arm in two planes. *IEEE Transactions on Biomedical Engineering*. 2015;62(3):972–981.
- [4] Úbeda A, Azoín J, Chavarriaga R, *et al.* Evaluating decoding performance of upper limb imagined trajectories during center-out reaching tasks. In 2016 IEEE International Conference on Systems, Man, and Cybernetics. 2016, 252–257.
- [5] Sailer U, Flanagan JR, Johansson RS. Eye–Hand Coordination during Learning of a Novel Visuomotor Task. *Journal of Neuroscience*. 2005;25(39):8833–8842.
- [6] Kim JH, Bießmann F, Lee SW. Decoding three-dimensional trajectory of executed and imagined arm movements from electroencephalogram signals. *IEEE Transactions on Neural Systems and Rehabilitation Engineering*. 2015;23(5):867–876.
- [7] Plöchl M, Ossandón JP, König P. Combining EEG and eye tracking: identification, characterization, and correction of eye movement artifacts in electroencephalographic data. *Frontiers in Human Neuroscience*. 2012;6(October):278.
- [8] Keren AS, Yuval-Greenberg S, Deouell LY. Saccadic spike potentials in gamma-band EEG: Characterization, detection and suppression. *NeuroImage*. 2010;49(3):2248–2263.
- [9] Waldert S, Preissl H, Demandt E, *et al.* Hand movement direction decoded from MEG and EEG. *Journal of Neuroscience*. 2008;28(4):1000–8.
- [10] Urigüen JA, Garcia-Zapirain B. EEG artifact removal-state-of-the-art and guidelines. *Journal of Neural Engineering*. 2015;12(3):31001.
- [11] Parra LC, Spence CD, Gerson AD, *et al.* Recipes for the linear analysis of EEG. *NeuroImage*. 2005;28(2):326–341.
- [12] Winkler I, Brandl S, Horn F, *et al.* Robust artifactual independent component classification for BCI practitioners. *Journal of Neural Engineering*. 2014;11(3):035013.
- [13] Schlögl A, Keinrath C, Zimmermann D, *et al.* A fully automated correction method of EOG artifacts in EEG recordings. *Clinical neurophysiology*. 2007;118(1):98–104.
- [14] Klados MA, Papadelis C, Braun C, *et al.* REG-ICA: A hybrid methodology combining Blind Source Separation and regression techniques for the rejection of ocular artifacts. *Biomedical Signal Processing and Control*. 2011;6(3):291–300.

HEAR to remove pops and drifts: the high-variance electrode artifact removal (HEAR) algorithm

Reinmar J. Kobler¹, Andreea I. Sburlea¹, Valeria Mondini² and Gernot R. Müller-Putz¹

Abstract—A high fraction of artifact-free signals is highly desirable in functional neuroimaging and brain-computer interfacing (BCI). We present the high-variance electrode artifact removal (HEAR) algorithm to remove transient electrode pop and drift (PD) artifacts from electroencephalographic (EEG) signals. Transient PD artifacts reflect impedance variations at the electrode scalp interface that are caused by ion concentration changes. HEAR and its online version (oHEAR) are open-source and publicly available. Both outperformed state of the art offline and online transient, high-variance artifact correction algorithms for simulated EEG signals. (o)HEAR attenuated PD artifacts by approx. 25 dB, and at the same time maintained a high SNR during PD artifact-free periods. For real-world EEG data, (o)HEAR reduced the fraction of outlier trials by half and maintained the waveform of a movement related cortical potential during a center-out reaching task. In the case of BCI training, using oHEAR can improve the reliability of the feedback a user receives through reducing a potential negative impact of PD artifacts.

I. INTRODUCTION

Electroencephalography (EEG) is a widespread non-invasive functional neuroimaging technique to study electrophysiological activity in the brains of humans [1]. EEG signals are recorded by sampling the voltage between electrodes and a reference electrode at the scalp. During this process, not only brain signals, but also other physiological and non-physiological signals are captured. Other physiological signals such as electromyographic (EMG), electrooculographic (EOG) and electrocardiographic (ECG) signals as well as non-physiological signals such as power-line noise or impedance variations at the electrode scalp interface are typically undesired and classified as artifacts. The impedance variations at the electrode scalp interface manifest as pops and drifts (PD) in the recorded EEG signals. In EEG-based brain-computer interfacing (BCI), transient, high-variance PD artifacts can temporarily deteriorate the control signal and, thereby, impede closed-loop control. It is, therefore, desirable to remove or at least detect PD artifacts.

Key to reduce impedance variations is to properly attach the electrodes to the scalp [2]. To date, the best long-term stability is achieved with sintered Ag/AgCl electrodes and a salty (Cl^-) electrolyte [3]. In this case, the impedance typically stabilizes after approximately 20 to 30 minutes. Nonetheless, transient PD artifacts can arise due to fluctuations of Cl^- concentration in the electrolyte. The change

in Cl^- concentration can be caused by sweating, drying electrolyte, or by liquefaction of a crust of dried electrolyte that covers the electrode.

The variance of transient PD artifacts is typically much higher than the variance of ongoing brain activity. Electrode pops can be described with a step and a subsequent exponential decay. As such, they have a broad-band spectrum with highest spectral power in the lower frequencies. Transient electrode drifts can be described with band-limited, low-frequency – typically $\leq 0.25 Hz$ [4] – noise. As a consequence, BCIs decoding slow processes such as movement related cortical potentials (MRCP) [5] are most prone to PD artifacts.

In recent years, many automatic artifact cleaning methods have been introduced [6]. Some are particularly suitable to remove transient, high-variance artifacts. Offline, it is common practice to detect transient artifacts within trials by visual inspection. Alternatively, outlier trials can be detected automatically using thresholding or high-order statistics [7]. In case of PD artifacts, contaminated trials are rejected or the signals of the affected electrodes interpolated [8].

Kothe and Jung introduced the artifact subspace reconstruction (ASR) algorithm [9]. ASR is a variance-based method and has been shown to improve the quality of independent component analysis decompositions [10]. ASR applies principal component analysis (PCA) in a sliding-windowed approach. The variance of each principal component (PC) is compared to a threshold which is derived from calibration data. Since the orientation of the PCs can change in each new data window, the thresholds are projected to the new PCs. A PC is removed, if its variance is larger than the variance during the calibration data multiplied by a cutoff parameter k . The corrected EEG is computed by back-projecting all clean PCs to the original electrode space.

Another suitable algorithm is robust PCA (RPCA). RPCA was originally designed to partition surveillance videos into transient and stationary segments [11]. A video represented as an $N_{features} \times N_{samples}$ matrix \mathbf{X} would be decomposed into the sum of a sparse matrix \mathbf{S} and a low-rank matrix \mathbf{L} . \mathbf{S} and \mathbf{L} can be estimated by solving the optimization problem

$$\min \|\mathbf{L}\|_* + \frac{\lambda_0}{\sqrt{N_{samples}}} \|\mathbf{S}\|_1 \quad s.t. \quad \mathbf{X} = \mathbf{L} + \mathbf{S} \quad (1)$$

with λ_0 being a regularization parameter that trades-off between the nuclear norm of \mathbf{L} and the L1 norm of \mathbf{S} . In the context of BCIs, RPCA has been used to reduce session-to-session [12] and trial-to-trial [13] variability, and recently

¹Institute of Neural Engineering, Graz University of Technology, Graz, Austria {reinmar.kobler, gernot.mueller}@tugraz.at

²Department of Electrical, Electronic and Information Engineering, University of Bologna, Bologna, Italy

also transient, high-variance artifacts [14]. RPCA is only applicable offline, since it decomposes the entire data at once into corrected EEG signals L and transient artifacts S .

The reported results seem to support the application of ASR and RPCA to remove transient, high-variance artifacts. However, literature lacks a thorough investigation of their performance - specifically with regard to PD artifacts. In this paper, we evaluated the performance of ASR and RPCA on one simulated and one real-world EEG dataset. We compared the results of ASR and RPCA with the high-variance electrode artifact removal (HEAR) algorithm which is introduced in the next section. Unlike ASR and RPCA, HEAR was specifically designed to remove PD artifacts. We hypothesized that all algorithms could improve the SNR during PD artifacts, and that HEAR would be superior to ASR and RPCA since it utilizes the structure of PD artifacts.

II. METHODS

A. High-variance Electrode Artifact Removal (HEAR)

The algorithm is based on two assumptions which are typically met by PD artifacts. First, the variance of each electrode signal can be used to detect periods of PDs. Second, PDs typically appear at single or few electrodes. For a sufficient spatial resolution, the neighboring electrode signals can be temporarily used to estimate the signal of the contaminated electrode.

The detection of PD artifacts based on the electrode variance requires a reference variance $\mu_s^{2(i)}$ for each electrode i . The $N_{electrodes} \times 1$ vector μ_s^2 is computed as the average variance during calibration (e.g., resting) data with no or few PD artifacts. The HEAR algorithm uses an exponential smoothing filter to estimate the instantaneous variances $s^2[n]$ at time n as

$$s^2[n] = \lambda s^2[n-1] + (1-\lambda)x^2[n] \quad (2)$$

with the smoothing factor λ defined as

$$\lambda = (1-p) \frac{1}{t_{est} \cdot f_s} \quad (3)$$

so that the time window t_{est} receives p percent of the weights at the sampling rate f_s . In this paper, we used $p = 0.9$.

Once the reference variances are computed, the HEAR algorithm can be applied to correct new samples $x[n]$. The correction process is implemented in three steps. First, equation (2) is applied to update the estimate of the electrode variances $s^2[n]$. Second, the probability that $s^{(i)}[n]$ was caused by an artifact $p_{art}(s^{(i)}[n]) = p(\text{art} \leq s^{(i)}[n])$ is derived from a normal distribution

$$p_{art}(s^{(i)}[n]) \sim \mathcal{N}(\phi \cdot \mu_s^{(i)}, \xi^2 \cdot \mu_s^{2(i)}) \quad (4)$$

with ϕ and ξ being hyper-parameters to scale the mean and variance. The probabilities for all electrodes are combined to a single diagonal matrix $P[n]$

$$P[n] = \text{diag}(p_{art}(s^{(1)}[n]), \dots, p_{art}(s^{(N_{channels})}[n])) \quad (5)$$

Third, the corrected signal $x_c[n]$ is computed via linear interpolation. $P[n]$ is applied to weigh the amount of linear interpolation so that

$$x_c[n] = P[n] D x[n] + (I - P[n]) x[n] \quad (6)$$

with D containing the relative distances. The relative distances are the inverse Euclidean norm between the 3D position of the target electrode and its $k = 4$ nearest neighbors. They are normalized so that the rows of D sum to 1.

In case of an offline analysis, the filter in (2) can be applied bidirectionally during the calibration and correction procedures. In this paper, we refer to the bidirectionally filtered version as HEAR and the causally filtered version as online HEAR (oHEAR). A reference implementation of (o)HEAR is publicly available at <https://bci.tugraz.at/research/software/#c218405>

HEAR and oHEAR depend on three hyper-parameters $\Theta = \{t_{est}, \phi, \xi\}$. All parameters are intuitive to interpret. The variance estimation duration t_{est} trades-off between smoothness of the estimate and responsiveness to fast events such as pops. The scaling factors of the artifact distribution $\{\phi, \xi\}$ define how often the reference variance has to be exceeded so that the artifact probability is 50% (ϕ), and how quickly the distribution increases (ξ). Hence, ϕ and ξ control the sensitivity of the algorithm.

In this paper, we varied the sensitivity of all correction algorithms by evaluating different hyper-parameter configurations. ASR was evaluated for the cut-off parameter $k = \{20, 40, 80\}$ according to the recommendations in [15], and the default window size (0.5s). Based on [13, 14], RPCA was evaluated for the regularization parameter $\lambda_0 = \{1.0, 1.5, 2.0\}$. We controlled the sensitivity of (o)HEAR by setting $\phi = \{2, 3, 4\}$. Using real data of pilot studies, we set $t_{est} = 0.25$, $\xi = 1$.

We validated the performance of (o)HEAR, RPCA and ASR by applying them to one dataset of simulated EEG and one real-world EEG dataset.

B. Simulated EEG dataset

We generated a simulated dataset specifically for this study with the simulated event-related EEG activity (SEREEGA) toolbox [16] and Matlab 2015b (Mathworks Inc., USA). In detail, we simulated EEG signals at 64 electrodes as linear mixtures of sources on the cortical surface of the ICBM-NY head model template [17] and the EEG electrodes themselves. The 64 electrodes were placed according to the extended 10/20 system. The simulated sources comprised oscillatory brain activity, an MRCP, and noise sources at the electrodes. The noise sources were modeled as stationary white measurement noise and transient PD artifacts.

We simulated 15 participants. For each participant, we used the same head model template, while the source locations and signals were independent and identically distributed (iid). If not explicitly stated, a uniform distribution within a given range was used. For each participant, we simulated two

experimental tasks. During the first task (rest) the oscillatory brain and stationary electrode noise sources were active. We simulated 12 trials, each lasting 15 s. During the second task (reach) all sources were active. We simulated 60 trials, each lasting 15 s.

We modeled the oscillatory brain activity with 40 pink and 40 brown noise sources with amplitudes of $37.5 \mu V$ and $75 \mu V$ respectively. The locations of the 80 sources were picked randomly from 74382 available locations on the template head model.

The location of the MRCP source was picked randomly in a 10 mm radius around the coordinate $[-25, 0, 80]$ mm, which corresponded to the medial end of the pre-central gyrus of the left hemisphere. The waveform of the MRCP was modeled with radial basis function kernels so that the waveform started with a slow negative deflection 7 s after the start of each trial, intensified abruptly after 700 ms, peaked with an amplitude of $-120 \mu V$ after additional 300 ms and subsequently faded within 200 ms. To introduce variability across trials, we randomly varied the location (≤ 10 mm radius), latency ($\leq \pm 200$ ms) and peak amplitude ($\leq \pm 20 \mu V$).

The stationary electrode noise was modeled as white noise at each electrode with a participant and electrode specific amplitude within 0.5 to 1.5 μV .

We modeled pops as single electrode sources. The pop waveform was modeled as a step with an amplitude of $100 \pm 10 \mu V$ and a subsequent exponential decay with a time-constant of $0.25 \pm 0.08 s^{-1}$. To allow multiple pops per trial, we used 10 electrode pop sources that were iid. For each trial every pop source could get active with a 2 % probability at any electrode and time point within the interval [5, 10] s.

Electrode drifts were modeled as transient pink noise that was limited to the [0.1, 0.3] Hz band. The band-limited pink noise was weighted by a Tukey window so that the transient drifts were limited to the interval [3, 12] s. Similar to the pops, we used 10 iid drift sources. For each trial every drift source would get active with a 2 % probability at one of the 64 electrodes.

We added the contribution of each source to the electrodes and stored the result in an EEGLAB dataset [18]. For the reach task, we also saved the clean EEG signals \mathbf{X}_{clean} . I.e., the EEG signals without contributions from the noise sources (electrode noise, pops and drifts). The simulated dataset and the code to generate it are publicly available [19].

We evaluated the algorithms during the interval [5, 10] s by computing the signal to noise ratio (SNR) defined as

$$SNR(M) = \frac{\|\mathbf{X}_{clean} \circ M\|_2}{\|\mathbf{X}_{clean} \circ M - \mathbf{X}_{corrected} \circ M\|_2} \quad (7)$$

with \mathbf{X}_{clean} and $\mathbf{X}_{corrected}$ being $N_{electrodes} \times N_{samples} \times N_{trials}$ arrays of clean and corrected EEG signals. We computed the SNR for PD artifact contaminated or non-artifact contaminated data by applying a $N_{electrodes} \times N_{samples} \times N_{trials}$ mask M . In case of PD artifact contaminated data, M indicated whether an array element was contaminated by a PD artifact.

Applying M on \mathbf{X} extracted a vector of all PD artifact contaminated elements. Complementary to the SNR, we estimated the MRCP by averaging the clean and corrected EEG signals over trials.

C. Real-world EEG dataset

In addition to the simulation, we evaluated the algorithms on one real-world dataset. The dataset consists of EEG recordings of 15 participants, while they performed visuo-motor and oculomotor tasks. The experimental conditions, tasks and equipment is described in detail in [14]. Here, we analyzed the EEG signals during a center-out reaching task. The participants were asked to make a center-out movement with a cursor after a target moved to a specific direction. They operated the cursor by moving their right hand on a 2D surface. In each trial, the target started to move at 2.5 s and stopped at one of four possible positions at 3.0 s. The grand-average cursor movement onset was at 3.2 s.

As in [14], we pre-processed the EEG by resampling the signals of 64 EEG electrodes at 200 Hz, applying a high-pass filter (0.25 Hz cut-off frequency, Butterworth filter, eighth order, zero-phase), a band-stop filter (49 and 51 Hz cut-off frequencies, Butterworth filter, fourth order, zero-phase), spherically interpolating bad channels, correcting eye artifacts and re-referencing to the common average reference (CAR).

The parameters of HEAR and ASR were calibrated to resting data, that were recorded at the beginning of the experiment according to the paradigm outlined in [20]. To ensure clean calibration data, we applied automatic trial rejection criteria. In detail, resting trials were rejected, if the EEG signal of any electrode exceeded a threshold ($\pm 200 \mu V$) or had an abnormal probability/variance/kurtosis ($\geq (6/4/6)$ standard-deviations beyond the mean).

We used two criteria to evaluate the correction algorithms. First, as for the simulated data, we computed the MRCP through averaging the trials during the center-out reaching task. Second, we applied the above defined automatic outlier trial detection criteria (threshold/probability/variance/kurtosis) to the uncorrected and corrected EEG signals. Assuming that the correction algorithms improve the SNR, fewer trials should be marked as outliers for the corrected EEG signals.

III. RESULTS

We present grand-average results which are summarized by the mean across participants. Variability over participants is summarized by the standard-error of the mean, if not specified otherwise.

In the case of the simulated dataset, we had access to all sources. This allowed us to compute the SNR according to (7). Figure 1 depicts the SNR during PD artifact and PD artifact-free periods before and after the correction algorithms were applied. The SNR of the uncorrected signals was -19 ± 0.2 dB and 26.3 ± 0.1 dB during PD artifact and PD artifact-free periods, respectively. Both SNR metrics are informative. If an algorithm overcorrects the signals, the SNR

during artifact-free periods is low. If an algorithm under-corrects the PD artifacts, the SNR during artifact periods is low. The ideal correction algorithm would maximize the SNR during both periods.

Regarding PD artifact periods, all algorithms increased the SNR compared to the uncorrected EEG. The increase depended strongly on the sensitivity parameters of the algorithms. A higher sensitivity lead to higher SNR during artifact periods at the cost of lower SNR during non-artifact periods. For example, ASR (blue color) corrected the PD artifacts almost as good as RPCA (yellow color), but removed more activity during PD artifact-free periods for comparable sensitivities. The best trade-off between over- and under-correction was achieved by (o)HEAR with $\phi = 3$, RPCA with $\lambda_0 = 1.5$ and ASR with $k = 40$.

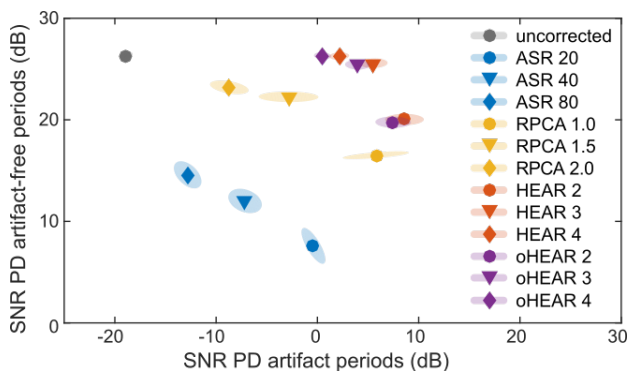


Fig. 1. SNR during PD artifact and PD artifact-free periods for the simulated EEG dataset. Each marker represents the mean across the 15 participants, while the shaded area summarizes the scatter over participants (matrix square root of the covariance matrix). The color indicates the algorithm and the marker the value of the sensitivity parameter (k for ASR, λ_0 for RPCA, and ϕ for (o)HEAR). For example, a blue circle identifies the result for ASR with $k = 20$.

We were not only interested in the impact of the correction algorithms on continuous EEG signals, but also on the simulated MRCP. The grand-average MRCP is displayed in Figure 2. The topographic plots at the peak negativity demonstrate that all algorithms preserved the MRCP waveform. Compared to the MRCP of the clean data (blue contour), RPCA attenuated the peak most (violet contour), with a reduction in peak amplitude of approximately $1 \mu V$. The other algorithms attenuated the peak only negligibly ($\leq 0.2 \mu V$).

Figure 3 displays the grand-average MRCP for the real EEG dataset. All algorithms preserved a clear MRCP waveform. We only observed negligible differences ($\leq 0.2 \mu V$) compared to the uncorrected EEG. The algorithm specific averages were computed after outlier trials were automatically detected and discarded according to the threshold/probability/variance/kurtosis criteria. The fraction of trials that were marked as outliers is displayed in Figure 4. In the case of uncorrected EEG, a median of 18.7% of the trials were marked as outliers. The result did not significantly differ for ASR, while for HEAR, oHEAR and RPCA significantly fewer trials were marked as outliers. The fraction of outlier

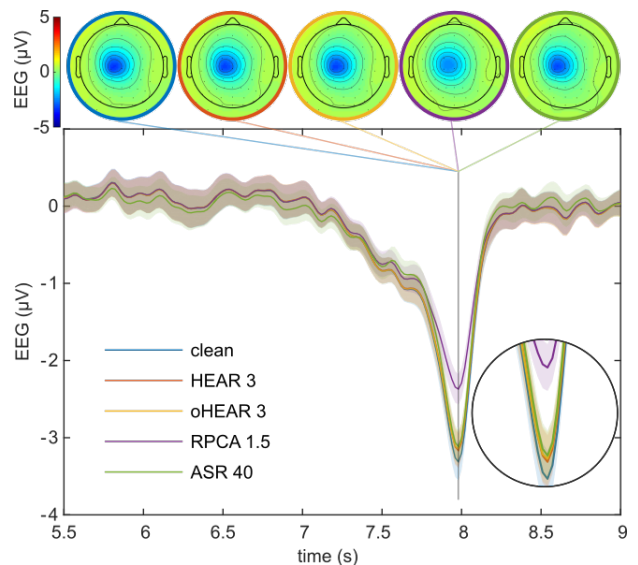


Fig. 2. Grand-average MRCP at electrode C1 for the simulated EEG dataset. The topographic distribution of the potential at the peak negativity is summarized in the top row. The outline color indicates the algorithm. A 100 ms triangular window (zero-phase) was used to smooth the signals before they were plotted. The inset shows a closer view of the differences at peak negativity.

trials did not significantly differ between HEAR (10.1%) and oHEAR (9.9%). Compared to HEAR and oHEAR, RPCA could slightly, yet significantly reduce the fraction to 9.0%.

IV. DISCUSSION

PD artifacts can significantly reduce the number of available trials in an offline analysis, and deteriorate closed-loop BCI control. We proposed HEAR - a simple, yet efficient algorithm to correct transient PD artifacts. The presented simulation results show that HEAR and oHEAR improved the SNR during PD artifacts by approximately 25 dB, and at the same time maintained a high SNR during PD artifact-free periods. State of the art offline (RPCA) and online (ASR) correction algorithms were clearly inferior to (o)HEAR. Compared to uncorrected data, the application of (o)HEAR to real-world EEG signals resulted in a significantly reduced fraction of outlier trials, while slow potentials such as MRCPs could be preserved.

Regarding RPCA, the simulated and real EEG dataset results were not entirely consistent. While RPCA attenuated the simulated MRCP peak considerably stronger than the other algorithms, the difference to the other algorithms was only negligible for the real EEG dataset. The SNR performance of RPCA (Figure 1) was clearly lower compared to HEAR for the simulated data. However, RPCA marginally (1.1%) but significantly reduced the fraction of outlier trials (Figure 4) compared to HEAR for the real EEG dataset. Taken together, it is difficult to generalize the influence of RPCA on the desired brain activity across datasets.

In case of ASR, the SNR (Figure 1) could be only improved at the cost of lower SNR during PD artifact-free

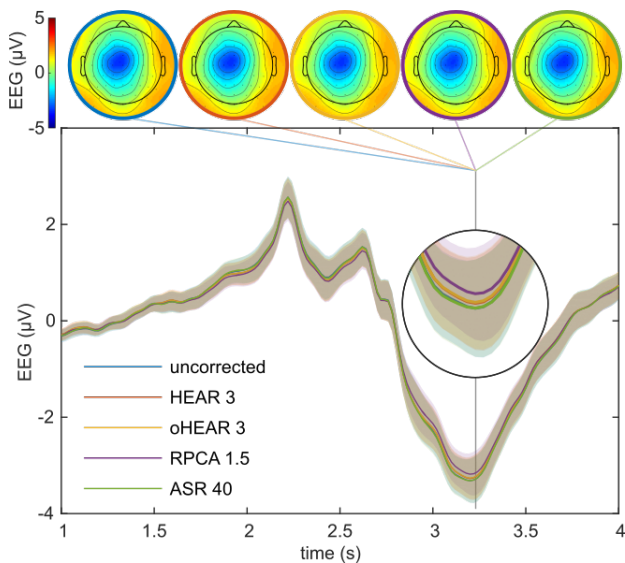


Fig. 3. Grand-average MRCP at electrode C1 for the real EEG dataset. The topographic plots in the top summarize the distribution of the potential at the peak negativity. The outline color indicates the algorithm. We used a 100 ms triangular window (zero-phase) to smooth the signals before they were plotted. The inset shows a closer view of the differences at peak negativity.

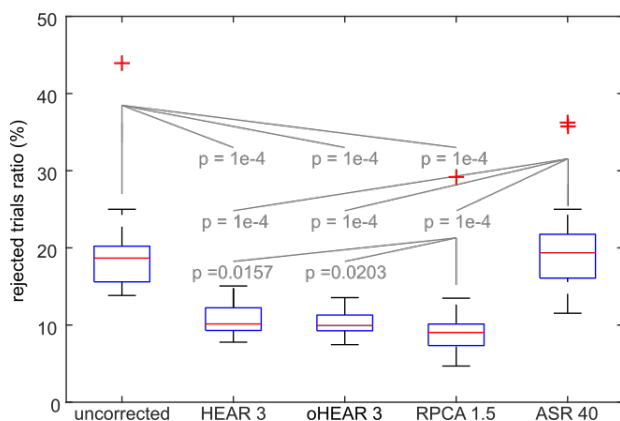


Fig. 4. Boxplots summarizing the fraction of trials marked as outliers across the participants of the real EEG dataset. Trials were automatically marked as outliers according to threshold/probability/variance/kurtosis criteria. Two-sided, paired Wilcoxon sign-rank tests were used to detect significant differences between the algorithms. We controlled the false discovery rate at significance level $\alpha = 0.05$ for 10 tests ($p_{crit} = 0.0203$) [21].

periods. Also, the fraction of outlier trials (Figure 4) could not be significantly reduced by ASR. Since ASR is based on PCA on short time-windows (0.5 s), and PCA is sensitive to drifts, we think that a longer time-window could have improved the correction quality. However, we decided to use the default window size because ASR introduces a processing delay of 0.5 times the window size to achieve the best online correction quality. For the considered window size, ASR introduces a delay of 250 ms. In case of neuro-modulation studies, adding more delay in the detection of transient events such as the onset of movement can be critical [22]. (o)HEAR uses an exponential smoothing filter which

belongs to the class of infinite impulse response filters. As such, the processing delay is frequency specific. For oHEAR with $t_{est} = 0.25$ s it is ≤ 105 ms and declines with rising frequencies.

The correction quality of (o)HEAR depends on the spatial resolution of the electrodes. The higher the spatial resolution (i.e., number of electrodes), the better is the interpolation quality. The presented results demonstrate that 64 equally spaced electrodes were sufficient to outperformed state of the art methods. The interpolation quality could be further improved by using spherical splines instead of Euclidean distances [8, 23].

Online, not only the correction quality, but also the computational complexity matters. For a given electrode configuration, the interpolation matrix D can be pre-computed for k nearest neighbors (k NN). Then, the matrix multiplications in (6) simplify to k element-wise multiplications, which can be computed in $O(k \cdot N_{channels})$. This is considerably faster compared to ASR whose run-time is mainly constrained by PCA which can be computed in $O(\max\{N_{samples} \cdot N_{channels}^2, N_{channels}^3\})$.

We designed (o)HEAR to remove PD artifacts, which are typically active at single electrodes. Other types of transient, high-variance artifacts such as EMG and sweat artifacts typically do not meet this assumption. In that case, the correction quality of (o)HEAR is certainly going to deteriorate. Still, one can compute the probability that a transient, high-variance artifact cannot be corrected by (o)HEAR. If D is applied on $P[n]$, the result is a vector of probabilities that indicate how likely each k NN estimate is contaminated by an artifact. If a threshold is applied, EMG and sweat artifacts can be detected.

ACKNOWLEDGMENT

The authors acknowledge Joana Pereira, Catarina Lopes Dias and Lea Hehenberger for their valuable comments. This work has received funding from the European Research Council (ERC) under the European Union's Horizon 2020 research and innovation programme (Consolidator Grant 681231 'Feel Your Reach'). V. M. received additional funding from a Marco Polo scholarship sponsored by the University of Bologna.

CODE & DATA AVAILABILITY

We encourage a widespread use of (o)HEAR and, therefore, provide an open-source reference implementation of (o)HEAR (<https://bci.tugraz.at/research/software/#c218405>). To support future improvements and ease comparability of algorithms, we also provide the dataset of simulated EEG signals and the code to generate it [19].

REFERENCES

- [1] D. L. Schomer and F. H. Lopes da Silva, *Niedermeyer's Electroencephalography: basic principles, clinical applications, and related fields*. 2011.

- [2] P. Anderer, S. Roberts, A. Schlögl, *et al.*, “Artifact processing in computerized analysis of sleep EEG – a review,” *Neuropsychobiology*, vol. 40, no. 3, pp. 150–157, 1999.
- [3] P. Tallgren, S. Vanhatalo, K. Kaila, *et al.*, “Evaluation of commercially available electrodes and gels for recording of slow EEG potentials,” *Clinical Neurophysiology*, vol. 116, no. 4, pp. 799–806, 2005.
- [4] D. C. Hammond and J. Gunkelman, *The art of artifacting*. Society for Neuronal Regulation, 2001.
- [5] H. Shibasaki, G. Barrett, E. Halliday, *et al.*, “Components of the movement-related cortical potential and their scalp topography,” *Electroencephalography and clinical neurophysiology*, vol. 49, no. 3-4, pp. 213–226, 1980.
- [6] J. A. Urigüen and B. Garcia-Zapirain, “EEG artifact removal—state-of-the-art and guidelines,” *Journal of neural engineering*, vol. 12, no. 3, p. 031001, 2015.
- [7] A. Delorme, S. Makeig, and T. Sejnowski, “Automatic artifact rejection for EEG data using high-order statistics and independent component analysis,” in *Proceedings of the third international ICA conference*, 2001, pp. 9–12.
- [8] F. Perrin, J. Pernier, O. Bertrand, *et al.*, “Spherical splines for scalp potential and current density mapping,” *Electroencephalography and Clinical Neurophysiology*, 1989.
- [9] C. Kothe and T.-P. Jung, “Artifact removal techniques with signal reconstruction,” pat. 14/895,440, 2014.
- [10] L. Pion-Tonachini, S.-H. Hsu, C.-Y. Chang, *et al.*, “Online automatic artifact rejection using the real-time eeg source-mapping toolbox (REST),” in *2018 40th Annual International Conference of the IEEE Engineering in Medicine and Biology Society (EMBC)*, IEEE, 2018, pp. 106–109.
- [11] E. J. Candès, X. Li, Y. Ma, *et al.*, “Robust principal component analysis?” *Journal of the ACM (JACM)*, vol. 58, no. 3, p. 11, 2011.
- [12] P.-K. Jao, Y.-P. Lin, Y.-H. Yang, *et al.*, “Using robust principal component analysis to alleviate day-to-day variability in eeg based emotion classification,” in *2015 37th Annual International Conference of the IEEE Engineering in Medicine and Biology Society (EMBC)*, IEEE, 2015, pp. 570–573.
- [13] P.-K. Jao, R. Chavarriaga, and J. d. R. Millán, “Using robust principal component analysis to reduce EEG intra-trial variability,” in *2018 40th Annual International Conference of the IEEE Engineering in Medicine and Biology Society (EMBC)*, IEEE, 2018, pp. 1956–1959.
- [14] R. J. Kobler, A. I. Sburlea, and G. R. Müller-Putz, “Tuning characteristics of low-frequency EEG to positions and velocities in visuomotor and oculomotor tracking tasks,” *Scientific Reports*, vol. 8, no. 1, p. 17713, 2018.
- [15] C.-Y. Chang, S.-H. Hsu, L. Pion-Tonachini, *et al.*, “Evaluation of artifact subspace reconstruction for automatic EEG artifact removal,” in *2018 40th Annual International Conference of the IEEE Engineering in Medicine and Biology Society (EMBC)*, IEEE, 2018, pp. 1242–1245.
- [16] L. R. Krol, J. Pawlitzki, F. Lotte, *et al.*, “SEREEGA: Simulating event-related EEG activity,” *Journal of Neuroscience Methods*, vol. 309, no. August, pp. 13–24, 2018.
- [17] Y. Huang, L. C. Parra, and S. Haufe, “The New York Head—A precise standardized volume conductor model for EEG source localization and tES targeting,” *NeuroImage*, 2016.
- [18] A. Delorme and S. Makeig, “EEGLAB: An open source toolbox for analysis of single-trial EEG dynamics including independent component analysis,” *Journal of Neuroscience Methods*, vol. 134, no. 1, pp. 9–21, 2004.
- [19] R. J. Kobler and G. R. Müller-Putz, *Simulated electroencephalographic signals contaminated with transient pop and drift artifacts*. DOI: 10.6084/m9.figshare.7718966.
- [20] R. J. Kobler, A. I. Sburlea, and G. R. Müller-Putz, “A comparison of ocular artifact removal methods for block design based electroencephalography experiments,” in *Proceedings of the 7th Graz Brain-Computer Interface Conference*, 2017, pp. 236–241.
- [21] Y. Benjamini and Y. Hochberg, “Controlling the false discovery rate: A practical and powerful approach to multiple testing,” *Journal of the royal statistical society. Series B (Methodological)*, pp. 289–300, 1995.
- [22] N. Mrachacz-Kersting, S. R. Kristensen, I. K. Niazi, *et al.*, “Precise temporal association between cortical potentials evoked by motor imagination and afference induces cortical plasticity,” *The Journal of Physiology*, vol. 590, no. 7, pp. 1669–1682, 2012.
- [23] C. M. Michel, M. M. Murray, G. Lantz, *et al.*, “EEG source imaging,” *Clinical Neurophysiology*, vol. 115, no. 10, pp. 2195–2222, 2004.

SIMULTANEOUS DECODING OF VELOCITY AND SPEED DURING EXECUTED AND OBSERVED TRACKING MOVEMENTS: AN MEG STUDY

R.J. Kobler^{1,2}, M. Hirata^{2,3}, H. Hashimoto^{2,3}, R. Dowaki^{2,4}, A.I. Sburlea¹, G.R. Müller-Putz¹

¹Institute of Neural Engineering, Graz University of Technology, Graz, Austria

²Endowed Research Department of Clinical Neuroengineering, Osaka University, Suita, Japan

³Department of Neurosurgery, Osaka University Graduate School of Medicine, Suita, Japan

⁴Hiroshima University School of Medicine, Hiroshima, Japan

E-mail: mhirata@nsurg.med.osaka-u.ac.jp, {reinmar.kobler, gernot.mueller}@tugraz.at

ABSTRACT: Brain signals carry rich information about voluntary upper-limb movements. Accessing this information to control an end-effector (upper-limb, robotic arm, cursor) has been a central topic in brain-computer interface (BCI) research. To date, non-invasive BCIs based on kinematics decoding have focused on extracting partial information (i.e. single or highly correlated kinematic parameters). In this work, we show that low-frequency magnetoencephalographic (MEG) signals simultaneously carry information about multiple kinematic parameters. Using linear models, we decoded cursor velocity and speed during executed and observed tracking movements with moderate (0.2 to 0.4) correlation coefficients (CCs). Comparing the CCs between executed and observed tracking movements, revealed that the MEG signals carried more information (0.1 higher CCs) about velocity and speed during the executed tracking movements. The higher correlations were mainly explained by increased predictive activity in primary sensorimotor areas. We could, therefore, show that non-invasive BCIs have the potential to extract multiple kinematic signals from brain activity in sensorimotor areas.

INTRODUCTION

Decoding voluntary movement from electrophysiological brain signals has been a central topic in brain-computer interface (BCI) research. In recent years, invasive approaches have demonstrated that individuals who lost control of their upper-limb could successfully control a robotic arm [1] or even regain control of their upper-limb [2]. These invasive BCI systems typically decode various movement parameters from spiking rates of neurons in primary sensorimotor areas [3, 4]. It has long been assumed that non-invasive functional neuroimaging techniques such as electroencephalography (EEG) and magnetoencephalography (MEG) lack the spatial resolution to decode the kinematics of voluntary movements. However, it has been shown otherwise by various studies in the past decade [5–7]. However, the predicted end-effector position of non-invasive decoders typically has a lower signal to noise ratio (SNR) compared to the invasive decoders. We think that the combined decoding of multiple kinematic signals could improve the SNR and, thereby,

elevate the performance of non-invasive decoders.

A myriad of non-invasive studies in this field of BCI research has investigated either directional (e.g. velocity, position) or non-directional (e.g. speed) kinematic signals in isolation [6, 8–10]. Bradberry et al. were the first to show that low-frequency EEG signals carried information about positions and velocities during reaching movements [11]. Complementary, Waldert et al. showed that reach direction can be classified from low-frequency EEG and MEG [12]. Jerbi et al. showed that low-frequency MEG signals are coupled to hand speed during a continuous visuomotor (VM) task [8]. Recent invasive studies using Electrocorticographic (ECoG) signals demonstrated that velocity and speed can be decoded simultaneously from low-frequency brain signals in primary sensorimotor areas [13, 14]. Taken together, we surmise that velocity and speed can be jointly decoded from non-invasive M/EEG signals.

We believe that a pursuit tracking task (PTT) is ideally suited to investigate this question. A PTT is characterized by two stimuli - a target stimulus moving along random trajectories and an end-effector (e.g., cursor). The end-effector is used to track the target stimulus. The PTT has two favorable properties. First, the kinematics vary continuously in a frequency range that can be controlled by the experimenter. Second, the target trajectories can be designed so that specific kinematic signals are jointly uncorrelated. Using a PTT, we showed that the low-frequency EEG originating in premotor and primary sensorimotor areas was preferentially tuned to cursor velocity rather than cursor position [15].

In this study, we investigated the joint decoding of cursor velocity and speed from low-frequency MEG activity during a two-dimensional PTT. Our paradigm separated two conditions. In the first condition (execution), participants tracked the target with their gaze and a cursor. In the second condition (observation), participants tracked the target only with their gaze. This allowed us to address two questions. First, can velocity and speed be decoded simultaneously from non-invasively acquired brain activity during voluntary upper-limb movements? Second, does the decoding performance change if the upper-limb is not involved in the tracking task?

MATERIALS AND METHODS

23 healthy people participated in this study. 5 were female and 18 male. They were 28.5 ± 2.4 (standard-error of the mean; sem) years old, had normal or corrected to normal vision, and self-reported to be right-handed. The experimental procedure conformed to the declaration of Helsinki and was approved by the ethics committee of the Osaka University hospital. We could not complete the experiment for three participants and identified that one participant was positioned incorrectly inside the MEG scanner during the offline analysis. These four participants were excluded from the final offline analysis.

Figure 1a depicts the experimental setup. The participants were lying in a supine position, with the head resting on a cushion inside an MEG scanner. A projection screen fixed in front of their face presented visual stimuli. We used two visual stimuli, a target and a cursor. The cursor could be controlled by the participants through moving their right hand's index finger on a 2D surface. The tip of the index finger was tracked with a custom optical motion capture system.

After each participant found a comfortable position for his/her right arm and hand, the position of the marker was defined as the resting position. The resting position was mapped to the center of the screen. Finger movements, within a 1.5 centimeter radius around the resting position were mapped to cursor movements within a circle confined by the bounds of a virtual grid. Rightward/forward finger movements were mapped to rightward/upward cursor movements.

As in our previous study [15], the experimental procedure consisted of 4 blocks, lasting for about 3 hours in total. In the first block (10 minutes), the participants could familiarize themselves with the paradigm. In the second block, we recorded eye artifacts and resting activity as described in [16] for about 12 minutes (2 runs; each 6 minutes). During the third block, the main experimental task was performed. The fourth block at the end of the experiment was identical to the second one.

Figure 1b outlines the paradigm of the main experimental task. We investigated a PTT in two conditions. A yellow target stimulus indicated the beginning of a new trial. After 2 s of preparation, the target changed its color to green (execution condition) or blue (observation condition).

In the execution condition, the participants were asked to track the target with their gaze and the cursor. In the first experimental block, each participant trained to minimize the distance to the target and to make smooth cursor movements.

In the observation condition, the participants would only track the target with their gaze and keep their finger in the resting position. In order to achieve similar visual input and tracking dynamics in both conditions, we replayed matching cursor trajectories.

The target moved along pseudo-random trajectories, which were generated from pink noise in the [0.3, 0.6] Hz band. The horizontal and vertical components of the target trajectories were independent and identically dis-

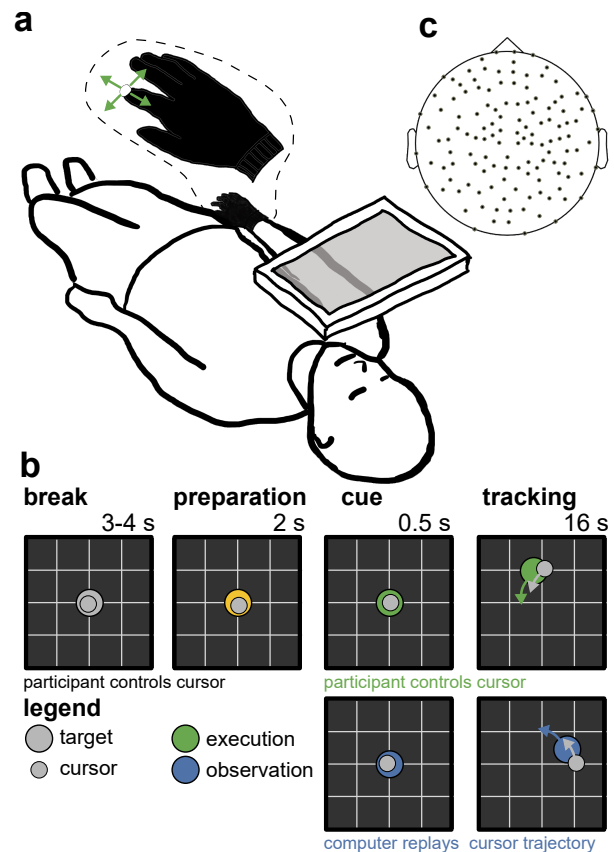


Figure 1: Overview of the experiment. **a**, Experimental setup. The participants were lying in a supine position inside an MEG scanner. They moved their right index finger on a 2D surface to control a cursor on the screen. **b**, Experimental paradigm. Each trial started with a 2 s preparation period. The participants were asked to keep the cursor in the center (i.e. the right index finger in the resting position). After a condition cue, the target stimulus moved along a pseudo-random trajectory for 16 s. In the execution condition (green), the participants tracked the target with both their gaze and the cursor. In the observation condition, they tracked the target only with their gaze. **c**, Topographic distribution of the 129 MEG sensors used in this study.

tributed. This required the participant to control the cursor in 2 dimensions at the same time. The detailed target trajectory generation and cursor trajectory replay procedures are presented in [15].

The paradigm consisted of 160 trials (80 per condition; pseudo-randomly distributed). They were presented in 10 runs (6 minutes each). In between runs, participants could rest for about 2 to 3 minutes. During the experiment, we tested if the finger was in the resting position during the preparation (both conditions) and tracking periods (observation condition). If the position exceeded a threshold, a trial was aborted. On average, 5.2 trials were aborted, resulting in 154.8 complete trials.

Neuromagnetic activity was recorded with a 160 channel whole-head MEG system (MEGvision NEO, Yokogawa Electrip Corp., Kanazawa, Japan) housed in a magnetically shielded room. For this study, we used the signals of 129 sensors (Figure 1c). Electrooculographic (EOG) signals were recorded with 4 electrodes placed at the outer canthi (horizontal EOG) and above/below the left eye

(vertical EOG). The EOG signals were recorded with a 128-channel EEG system (Neurofax EEG 1200, Nihon Kodan Corp., Tokyo, Japan). MEG and EOG signals were recorded synchronously at rate of 1 kHz.

We asked participants to keep their head and shoulder position fixed during the experiment (blocks 2 to 4). We additionally monitored the head position inside the MEG system with five marker coils, attached to the face. Their position was measured at the beginning of each run.

The custom motion capture and visual stimuli signals were recorded at 60 Hz using the `labstreaminglayer` (LSL) protocol¹. We implemented the paradigm in Python 2.7 based on the simulation and neuroscience application (SNAP) platform². Using pilot experiments, we determined the delay between the finger and the cursor movement on the screen. The delays introduced by the hard- and software added up to 190 ms.

We analyzed the recorded data offline with a custom-made pipeline that we implemented with Matlab (Matlab 2015b, Mathworks Inc., USA) and the open source toolboxes EEGLAB [17] (version 14.1.1) and Brainstorm [18] (version 05-Jun-2018). We first synchronized the stimuli and MEG signals by aligning impulses captured by a photodiode. After synchronization, all signals were resampled to 200 Hz. We estimated the cursor velocities by applying a Savitzky-Golay finite impulse response (FIR) differentiation filter (polynomial order 3, 21 filter taps, zero-phase) to the cursor positions.

To compensate small head movements across runs, we spherically interpolated the MEG sensors of all runs (10 tracking, 4 eye) to their average position in relation to the participant's head. If the maximal distance of any channel to the average position was larger than 25 mm, the run was discarded. We discarded 2 runs in total. The grand-average maximal channel distance across accepted runs was 5 ± 0.1 mm (sem). After merging the signals of the tracking runs, we applied high-pass (0.25 Hz cut-off frequency, Butterworth filter, eight order, zero-phase) and band-stop (59 and 61 Hz cut-off frequencies, Butterworth filter, fourth order, zero-phase) filters. To compensate technical and spatially stationary artifacts introduced by equipment, we applied independent component analysis (ICA). In detail, we applied the extended infomax algorithm to decompose the MEG signals (high-pass filter with 0.4 Hz cut-off frequency) into independent components (ICs) that explained 99.9% of the variance. We visually inspected and marked 8.6 ± 0.2 (sem) of 63.5 ± 0.1 (sem) ICs for rejection. They were then removed from the 0.25 Hz high-pass filtered signals. We attenuated eye movement and blink artifacts by applying the artifact subspace subtraction algorithm [15, 16]. To extract the low-frequency MEG signals, we applied a low-pass filter to the broadband MEG signals (2 Hz cut-off frequency, Butterworth filter, sixth order, zero-phase) and resampled all signals at 10 Hz.

We then epoched the continuous data into 14 s trials,

starting 1.5 s after the condition cue. Trials were marked for rejection, if (1) the broadband MEG signal of any sensor exceeded a threshold (± 5 fT), (2) had an abnormal probability, variance or kurtosis ($\geq (6/4/6)$ standard-deviations (stds) beyond the mean), (3) the correlation between the EOG and the target position signals were improbable (≥ 4 stds beyond the mean), or (4) a tracking error happened (i.e., jerky or no cursor movement). All criteria combined resulted in rejecting 26.6 ± 0.4 (sem) of 154.8 trials.

Cursor velocity and speed were estimated with a sliding-window, linear regression approach [11, 15, 19]. At single lags, a partial least-squares (PLS) estimator was used to decode a single kinematic signal (horizontal velocity, vertical velocity or speed) from the pre-processed MEG signals. Similar to [15], the PLS estimator considered 10 latent components. The model was evaluated using a 10 times 5 fold cross-validation (CV) scheme with the evaluation metric being Pearson correlation coefficients (CCs) between the recorded kinematic signals and their neural estimates. We estimated chance level performance by shuffling the kinematic signals across trials of the same condition. We then applied 5 fold CV to the shuffled data and repeated the shuffling and CV evaluation 1000 times. The weights of the linear regression model can be readily transformed to patterns [20]. We computed scaled patterns according to [15].

To ease neurophysiological interpretation, we projected the scaled patterns to the cortical surface of the ICBM152 template boundary element (BEM) head model [21]. We co-registered the template with the head of each participant (and the MEG sensors) by manually fitting the template head model to digitized head points (50 to 60 points per participant) in Brainstorm toolbox. OpenMEEG [22] was applied to compute the forward model for 5011 voxels on the cortical surface. sLORETA [23] was used to estimate the inverse solution for unconstrained sources at the 5011 voxels. The noise covariance matrix was estimated using 5 minutes of resting data (similar preprocessing as the tracking data), recorded during experimental blocks 2 and 4, and applying shrinkage regularization (10% of its largest eigenvalue).

RESULTS

Grand-average results presented here are summarized by the mean and its standard-error across the 19 participants. We assessed the participants tracking behavior by computing CCs between the target and cursor position signals in the execution condition. The CCs peaked at 0.22 ± 0.01 s for the horizontal component and 0.23 ± 0.01 for the vertical component. That is, the target signal lead the cursor by approximately 225 ms on average. The CCs at the peaks were 0.90 ± 0.01 (horz) and 0.92 ± 0.01 (vert). We also assessed the visual tracking behavior in both conditions by computing CCs between the horizontal/vertical target position and horizontal/vertical EOG signals. In the execution condition, the CCs were 0.94 ± 0.01 (horz) and 0.79 ± 0.06 (vert). In the observation condition, they

¹<https://github.com/sccn/labstreaminglayer>

²<https://github.com/sccn/SNAP>

were 0.92 ± 0.01 (horz) 0.70 ± 0.06 (vert).

The auto-/cross-correlation curves in Figures 2a-c demonstrate that during the PTT the three signals of interest (horizontal/vertical cursor velocity and cursor speed) were negligibly correlated. The grand-average cross-correlations were below or equal to 0.1 in both conditions. Similar auto-/cross-correlation curves in both conditions show that the cursor trajectories in observation condition (dashed lines) were similar to the executed ones (solid lines).

Figures 2d-f show the grand-average CV test-set CCs between the decoded and recorded kinematic signals for single-lag, sliding-window, linear regression models. We decoded the cursor velocities and speed from the MEG signals of all 129 sensors at lags ranging from $[-0.5, 0.5]$ s in steps of 0.1 s. The MEG sensor signals lead the cursor signals for negative lags.

We used the CCs of the shuffled data to test if the observed results were due to chance. We controlled the false-discovery rate (FDR) at a significance level $\alpha = 0.05$ for $n_{comparisons} = n_{metrics} \cdot n_{lags} = 3 \cdot 11 = 33$ comparisons per subject [24]. The tables at the bottom of Figures 2d-f list the results.

The horizontal cursor velocity decoding results are summarized in Figure 2d. The decoding model performed above chance level for all lags and participants in the execution condition and almost all participants in the observation condition. The execution condition CCs were larger than the observation condition ones for all lags. The paired difference between conditions (exe-obs) peaked at lag -0.3 s.

The vertical cursor velocity decoding results are summarized in Figure 2e. The CCs were above chance level for all lags and participants. Compared to the horizontal velocity results, we observed higher CCs in the execution condition and similar CCs in the observation condition. As a consequence, the paired difference was higher (peaked at lag -0.1 s).

The cursor speed decoding results are displayed in Figure 2f. All CCs were above chance level in the execution condition. In the observation condition, the results varied across lags and ranged from 14 to 18 participants having CCs above chance level. Compared to the velocities, the CCs were lower by approx. 0.1 in both conditions. However, the effect size of condition was comparable to the velocities (paired difference peak of 0.15 at lag -0.3 s).

To identify the spatiotemporal encoding of information about cursor velocities and speed, we transformed the model weights to patterns at the cortical surface. Figures 2g-i show the grand-average patterns at selected lags for execution condition (top), observation condition (middle) and the paired-difference (bottom). The paired-differences for all three kinematic signals show that the predictive pattern activity in contra-lateral primary-sensorimotor (SM1) areas was larger in execution condition at negative lags. Thus, contra-lateral SM1 activity carried information about the upcoming cursor velocities and speed in the execution condition. The difference was

maximal at lags -0.3 to -0.2 s and varied across the signals of interest (speed > vertical velocity > horizontal velocity).

We also observed that superior parietal and parieto-occipital areas carried predictive information about the three kinematic signals in both conditions (Figures 2g,h top and middle row). The paired-differences indicate that the activity in these areas was similarly predictive for horizontal cursor velocity in both conditions (Figure 2g), more predictive for vertical cursor velocity in execution condition (Figure 2h), and less predictive for cursor speed in execution condition (Figure 2i).

DISCUSSION

We have demonstrated simultaneous decoding of cursor velocity and speed information by means of low-frequency MEG signals during a PTT. The PTT allowed us to study continuous, uncorrelated cursor velocity and speed signals (Figures 2a-c). During executed index finger tracking movements, contra-lateral SM1 activity was simultaneously predictive for cursor velocity and speed, while superior parietal and parieto-occipital activity was also predictive in observed tracking movements.

Linear, single-lag decoding model performance in terms of CCs was above chance level for all participants during execution condition, and almost all participants during observation condition (Figures 2d-f). The range of CCs is in agreement with the results of previous linear M/EEG kinematics decoding studies [11, 15, 25].

Comparing the two conditions, we found that the MEG signals contained more information about the cursor velocities and speed in the execution condition (Figures 2d-f). The average effect of condition was stronger for the vertical cursor velocity than for the horizontal one. This is in accordance with the findings of our previous EEG study [15].

The differences in the decoder patterns (Figures 2g-i; bottom row) indicate that the activity in contra-lateral SM1 carried more information about the uncorrelated velocity and speed signals in the execution condition. The differences peaked at lags -0.3 s (horizontal cursor velocity; Figure 2,g), -0.2 s (vertical cursor velocity; Figure 2,h) and -0.3 s (cursor speed; Figure 2,i) respectively. Since the difference in decoder CCs in Figures 2d-f were modulated by these peaks, the activity in contra-lateral SM1 must have considerably contributed to the larger decoder CCs in the execution condition.

Considered that the cursor movement was the 190 ms delayed index finger movement, the observed peaks are plausible in terms of neurophysiology [26]. Simultaneous decoding of velocity and speed from contra-lateral SM1 has also been demonstrated by recent invasive studies based on spiking activity [27] and low-frequency ECoG signals [14]. Inoue et al. observed that the firing rates of a large fraction of neurons in SM1 were simultaneously tuned to speed and velocity [27]. Hammer et al. reported a stronger encoding of end-effector speed compared to velocity in low-frequency ECoG signals [14]. This in

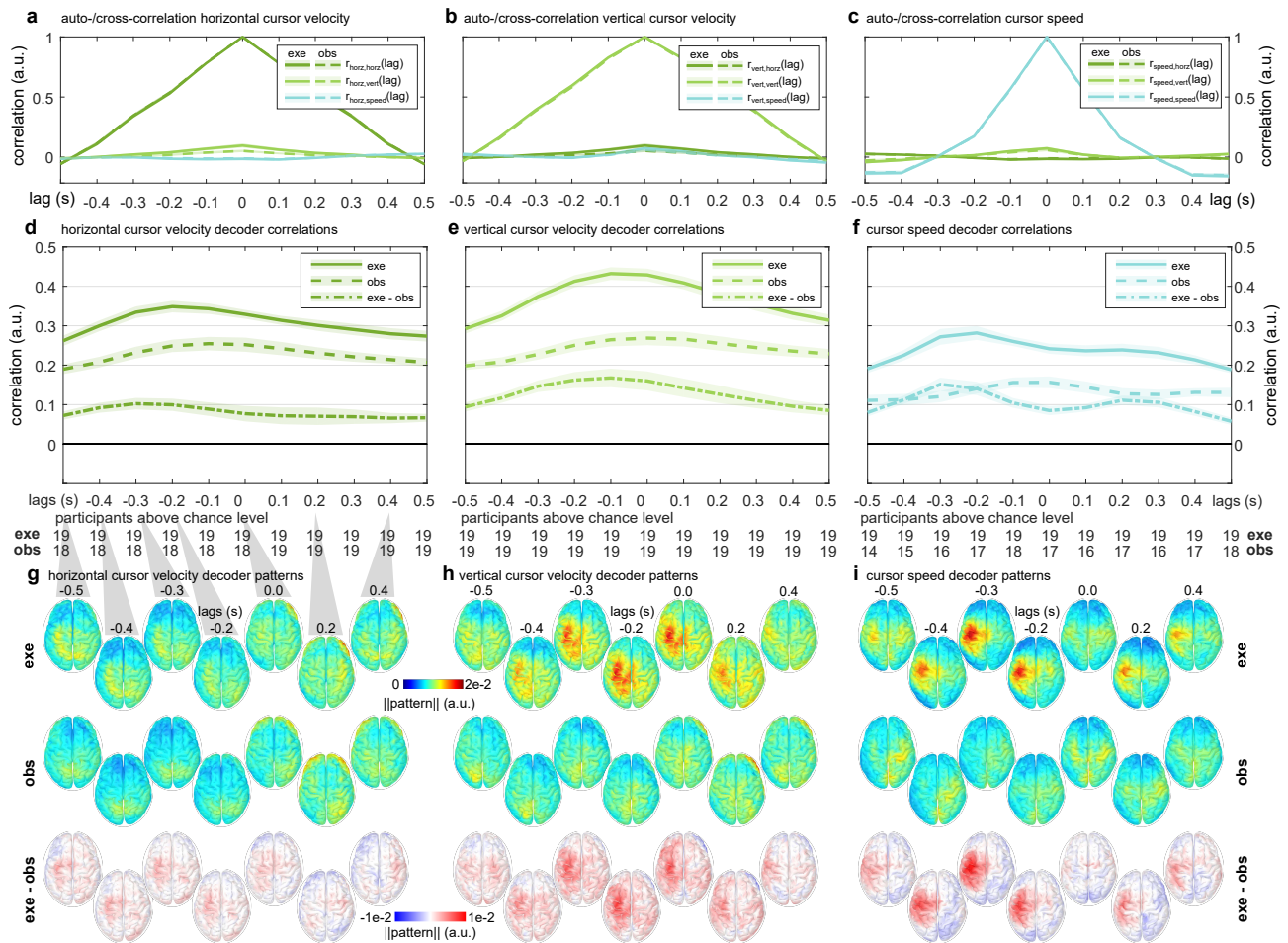


Figure 2: Grand-average results of the experiment. Shaded areas indicate the sem across the 19 participants. **a**, Auto/cross-correlation curves for the three metrics of interest relative to the horizontal cursor velocity. **b,c**, As in **a** for the vertical cursor velocity (**b**) and cursor speed (**c**). **d**, CV Test-set correlations between the recorded horizontal cursor velocity and its decoded estimate for execution condition (solid line), observation condition (dashed line) and their paired difference (dash-dotted line). MEG sensor signals lead the horizontal cursor velocity signal for negative lags. The table below lists the number of participants whose single-lag decoder CCs were above chance level. **e,f**, As in **d** for the vertical cursor velocity (**e**) and cursor speed (**f**). **g**, Horizontal cursor velocity decoder patterns for selected lags. We projected the patterns to voxels of a template BEM head model and averaged their norms across participants. **h,i**, As in **g** for the vertical cursor velocity (**h**) and cursor speed (**i**).

agreement with our results. I.e, in execution condition, the speed decoder patterns in SM1 were larger than the velocity decoder patterns.

The decoder patterns (Figures 2g-i; top and middle rows) showed also common activity in execution and observation condition. In both conditions, superior parietal and parieto-occipital areas were predictive. Their activation in both conditions is in agreement with findings of our previous study [15] and also fMRI studies on executed and observed reaching movements [28, 29].

CONCLUSION AND FUTURE WORK

In this work we have shown that non-invasive MEG signals simultaneously carry information about velocity and speed of executed and observed tracking movements. Linear, single-lag decoders extracted more information originating in contra-lateral SM1 during executed tracking movements. Whereas superior parietal and parieto-occipital areas were informative in executed and observed tracking movements.

Despite the encouraging results presented here, further research is imperative. It needs to be shown that a combined decoding of velocity and speed indeed improves the SNR of the predicted end-points offline and subsequently online. Moreover, studies with humans who lost control of their upper-limb will have to demonstrate whether non-invasive, decoding of imagined body kinematics has the potential to improve their quality of life.

ACKNOWLEDGEMENTS

The authors acknowledge Catarina Lopes Dias, Joana Pereira and Lea Hehenberger for their valuable comments. This work has received funding from the European Research Council (ERC) via the consolidator grant 681231 ‘Feel Your Reach’, from Graz University of Technology via its short-time research abroad scholarship, from the Japan Society for the Promotion of Science (JSPS) program KAKENHI (26282165), from the National Institute of Information and Communications Technology (NICT), from the Council for Science, Tech-

nology and Innovation (Cabinet Office, Government of Japan) program ImPACT, and from a research grant from the Ministry of Internal Affairs (Government of Japan).

REFERENCES

- [1] Collinger JL, Wodlinger B, Downey JE, *et al.* High-performance neuroprosthetic control by an individual with tetraplegia. *The Lancet*. 2013;381(9866):557–564.
- [2] Ajiboye AB, Willett FR, Young DR, *et al.* Restoration of reaching and grasping movements through brain-controlled muscle stimulation in a person with tetraplegia: A proof-of-concept demonstration. *The Lancet*. 2017;389(10081):1821–1830.
- [3] Lebedev MA, Nicolelis MAL. Brain-Machine Interfaces: From Basic Science to Neuroprostheses and Neurorehabilitation. *Physiological Reviews*. 2017;97(2):767–837.
- [4] Branco MP, Boer LM de, Ramsey NF, *et al.* Encoding of kinetic and kinematic movement parameters in the sensorimotor cortex: A brain-computer interface perspective. *European Journal of Neuroscience*. 2019.
- [5] Jerbi K, Vidal JR, Mattout J, *et al.* Inferring hand movement kinematics from MEG, EEG and intracranial EEG: From brain-machine interfaces to motor rehabilitation. *Irbm*. 2011;32(1):8–18.
- [6] Robinson N, Vinod AP. Noninvasive Brain-Computer Interface: Decoding Arm Movement Kinematics and Motor Control. *IEEE Systems, Man, & Cybernetics Magazine*. 2016;2(October):4–16.
- [7] Fukuma R, Yanagisawa T, Saitoh Y, *et al.* Real-time control of a neuroprosthetic hand by magnetoencephalographic signals from paralysed patients. *Scientific Reports*. 2016;6(1):21781.
- [8] Jerbi K, Lachaux JP, N'Diaye K, *et al.* Coherent neural representation of hand speed in humans revealed by MEG imaging. *PNAS*. 2007;104(18):7676–7681.
- [9] Bourguignon M, Jousmäki V, Op de Beeck M, *et al.* Neuronal network coherent with hand kinematics during fast repetitive hand movements. *NeuroImage*. 2012;59(2):1684–1691.
- [10] Marty B, Bourguignon M, Jousmäki V, *et al.* Cortical kinematic processing of executed and observed goal-directed hand actions. *NeuroImage*. 2015;119:221–228.
- [11] Bradberry TJ, Gentili RJ, Contreras-Vidal JL. Reconstructing Three-Dimensional Hand Movements from Noninvasive Electroencephalographic Signals. *Journal of Neuroscience*. 2010;30(9):3432–3437.
- [12] Waldert S, Preissl H, Demandt E, *et al.* Hand movement direction decoded from MEG and EEG. *Journal of Neuroscience*. 2008;28(4):1000–1008.
- [13] Bundy DT, Pahwa M, Szrama N, *et al.* Decoding three-dimensional reaching movements using electrocorticographic signals in humans. *Journal of neural engineering*. 2016;13(2):026021.
- [14] Hammer J, Pistohl T, Fischer J, *et al.* Predominance of Movement Speed over Direction in Neuronal Population Signals of Motor Cortex: Intracranial EEG Data and A Simple Explanatory Model. *Cerebral Cortex*. 2016;26(6):2863–2881.
- [15] Kobler RJ, Sburlea AI, Müller-Putz GR. Tuning characteristics of low-frequency EEG to positions and velocities in visuomotor and oculomotor tracking tasks. *Scientific Reports*. 2018;8(1):17713.
- [16] Kobler RJ, Sburlea AI, Müller-Putz GR. A comparison of ocular artifact removal methods for block design based electroencephalography experiments. In: *Proc. of the 7th Graz BCI Conference*. 2017, 236–241.
- [17] Delorme A, Makeig S. EEGLAB: An open source toolbox for analysis of single-trial EEG dynamics including independent component analysis. *Journal of Neuroscience Methods*. 2004;134(1):9–21.
- [18] Tadel F, Baillet S, Mosher JC, *et al.* Brainstorm: A user-friendly application for MEG/EEG analysis. *Computational Intelligence and Neuroscience*. 2011;2011:8.
- [19] Ofner P, Müller-Putz GR. Using a noninvasive decoding method to classify rhythmic movement imaginations of the arm in two planes. *IEEE Trans. Bio. Eng.* 2015;62(3):972–981.
- [20] Haufe S, Meinecke F, Görgen K, *et al.* On the interpretation of weight vectors of linear models in multivariate neuroimaging. *NeuroImage*. 2014;87:96–110.
- [21] Fonov V, Evans AC, Botteron K, *et al.* Unbiased average age-appropriate atlases for pediatric studies. *NeuroImage*. 2011;54(1):313–327.
- [22] Gramfort A, Papadopoulos T, Olivi E, *et al.* OpenMEEG: Opensource software for quasistatic bioelectromagnetics. *BioMedical Engineering Online*. 2010;9.
- [23] Pascual-Marqui RD. Standardized low resolution brain electromagnetic tomography (sLORETA): technical details. *Methods & Findings in Experimental & Clinical Pharmacology*. 2002;24:1–16.
- [24] Benjamini Y, Hochberg Y. Controlling the false discovery rate: a practical and powerful approach to multiple testing. *J. Royal Stat. Soc. B*. 1995;57(1):289–300.
- [25] Bradberry TJ, Rong F, Contreras-Vidal JL. Decoding center-out hand velocity from MEG signals during visuomotor adaptation. *NeuroImage*. 2009;47(4):1691–1700.
- [26] Miall RC, Wolpert DM. Forward models for physiological motor control. *Neural Networks*. 1996;9(8):1265–1279.
- [27] Inoue Y, Mao H, Suway SB, *et al.* Decoding arm speed during reaching. *Nature Communications*. 2018;9(1):5243.
- [28] Filimon F, Nelson JD, Huang RS, *et al.* Multiple Parietal Reach Regions in Humans: Cortical Representations for Visual and Proprioceptive Feedback during On-Line Reaching. *Journal of Neuroscience*. 2009;29(9):2961–2971.
- [29] Magri C, Fabbri S, Caramazza A, *et al.* Directional tuning for eye and arm movements in overlapping regions in human posterior parietal cortex. *NeuroImage*. 2019;(in press).



PAPER

Continuous low-frequency EEG decoding of arm movement for closed-loop, natural control of a robotic arm

RECEIVED
13 May 2020REVISED
23 June 2020ACCEPTED FOR PUBLICATION
17 July 2020PUBLISHED
11 August 2020Valeria Mondini^{1,2,3} , Reinmar J Kobler^{1,3} , Andreea I Sburlea¹  and Gernot R Müller-Putz¹ ¹ Institute of Neural Engineering, Graz University of Technology, Graz 8010, Styria, Austria² Department of Electrical, Electronic and Information Engineering, University of Bologna, Bologna 40136, ItalyE-mail: gernot.mueller@tugraz.at**Keywords** electroencephalography, brain-computer interface, online decoding, closed-loop control, motor control, kinematics**Abstract**

Objective. Continuous decoding of voluntary movement is desirable for closed-loop, natural control of neuroprostheses. Recent studies showed the possibility to reconstruct the hand trajectories from low-frequency (LF) electroencephalographic (EEG) signals. So far this has only been performed offline. Here, we attempt for the first time continuous online control of a robotic arm with LF-EEG-based decoded movements. *Approach.* The study involved ten healthy participants, asked to track a moving target by controlling a robotic arm. At the beginning of the experiment, the robot was fully controlled by the participant's hand trajectories. After calibrating the decoding model, that control was gradually replaced by LF-EEG-based decoded trajectories, first with 33%, 66% and finally 100% EEG control. Likewise with other offline studies, we regressed the movement parameters (two-dimensional *positions*, *velocities*, and *accelerations*) from the EEG with partial least squares (PLS) regression. To integrate the information from the different movement parameters, we introduced a combined PLS and Kalman filtering approach (named PLSKF). *Main results.* We obtained moderate yet overall significant ($\alpha = 0.05$) online correlations between hand kinematics and PLSKF-decoded trajectories of 0.32 on average. With respect to PLS regression alone, the PLSKF had a stable correlation increase of $\Delta r = 0.049$ on average, demonstrating the successful integration of different models. Parieto-occipital activations were highlighted for the *velocity* and *acceleration* decoder patterns. The level of robot control was above chance in all conditions. Participants finally reported to feel enough control to be able to improve with training, even in the 100% EEG condition. *Significance.* Continuous LF-EEG-based movement decoding for the online control of a robotic arm was achieved for the first time. The potential bottlenecks arising when switching from offline to online decoding, and possible solutions, were described. The effect of the PLSKF and its extensibility to different experimental designs were discussed.

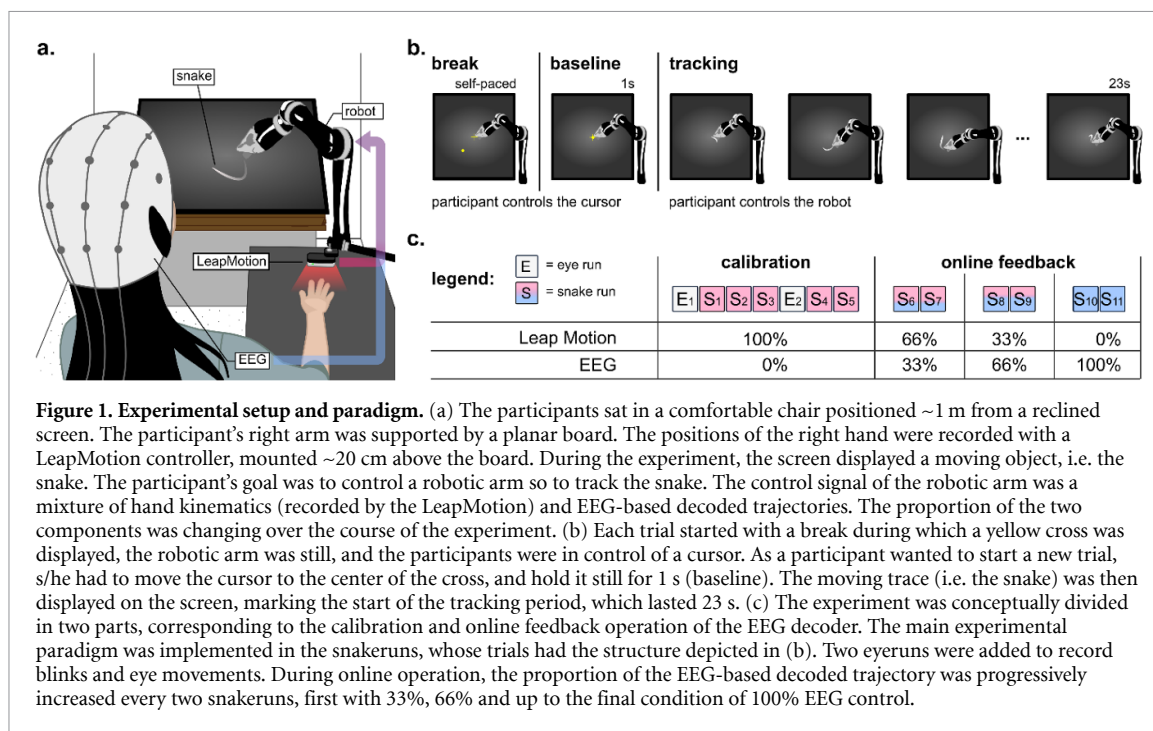
1. Introduction

One of the most recent focuses of brain-computer interface (BCI) research is the reconstruction of movement from neural recordings, to allow for an intuitive and natural control of an actuator, like for example a neuroprosthesis [1–3] or a robotic arm [4]. The ultimate goal of such an approach is the continuous decoding of executed [5] or imagined [6] movements, to use their neural correlates as input for the neuroprosthetic device.

Neural tuning to movement direction has first been shown in monkeys [7–9]. Later, both primate and human studies showed the possibility to decode movement during different volitional states from invasive intracortical [10–15] and electrocorticographic [16–18] recordings. The possibility to access this neural information non-invasively has been proved just recently, first in magnetoencephalographic [19–23] and lately electroencephalographic (EEG) [5, 24–29] studies.

In the EEG, voluntary movement can be reconstructed from the low-frequency (LF) band of the signal (< 3 Hz) [30] and through linear models [31].

³ These authors contributed equally.



Since the first study from Bradberry *et al* [24], reconstructing the three-dimensional velocities of hand movements during center-out tasks, several groups confirmed the possibility to decode the end-effector positions [5, 28, 29] or velocities [24, 29] through linear regression models and from the low-pass filtered EEG signals. Even though it has remained unclear for a while whether positions or velocities were best encoded in the EEG, a recent work from our group [25] could clarify, using a pursuit-tracking-task (PTT) [32] the spatiotemporal tuning of the EEG to each movement parameter.

Although previous studies indicated the possibility to non-invasively reconstruct the movement from LF-EEG, so far, this type of decoding has only been performed offline. In this work, we present a first attempt to translate linear LF-EEG decoding from an offline to an online scenario, and use it for the continuous closed-loop control of a robotic arm.

Since this was the first attempt of EEG-based online decoding, we limited our study to two-dimensional movements, and designed the paradigm to be able to best separate the information of each movement parameter. We therefore designed a PTT, where the participants were asked to track a moving object on a screen by controlling a robotic arm. At the beginning of the experiment, the robotic arm was fully controlled by the participants' hand kinematics. After the EEG-based linear decoding model was calibrated, the robotic arm control was gradually switched from hand kinematics to EEG-based decoded trajectories, first with 33%, then 66%, up to the final condition of 100% EEG-based control.

Given the exploratory nature of the study, a part of this work will be dedicated to describing the

challenges that may arise when switching from offline to online decoding from LF-EEG, and which solutions can be adopted to achieve low-latency, continuous closed-loop control. A second part will be dedicated to the analysis of decoder patterns at cortical level, while a final part will touch upon the impressions and behavioral responses of participants when progressively exposed to closed-loop control based on movement decoding from their LF-EEG.

2. Methods

2.1. Participants

Ten healthy persons, of age 26.5 ± 3.8 yr, took part in this study. All participants had normal or corrected-to-normal vision, five were females, and nine were right-handed (as assessed by the Edinburgh Handedness Inventory [33]). All participants gave their written informed consent to take part in the study, and received compensatory payment for their participation. The data of one participant were excluded from the analysis due to technical problems in the recordings. The experimental procedure conformed to the Declaration of Helsinki and was approved by the ethics committee of the Medical University of Graz.

2.2. Experimental paradigm

The experimental paradigm implemented a pursuit tracking task, where the participants were asked to track a moving object with a robotic arm. A schematic representation of the experimental setup is given in figure 1(a). The participants were comfortably seated in front of a reclined ($\sim 45^\circ$) screen displaying the moving object, which we called snake. An assistive robotic arm (JACO, Kinova Robotics Inc.

Canada) overlaid the screen, and was controlled by the participants through a mixture of hand kinematics and EEG-based decoded trajectories. The right-hand kinematics was recorded using a LeapMotion controller (LeapMotion Inc. USA). The LeapMotion was mounted ~20 cm over a planar board that supported the participant's arm as s/he was performing planar, two-dimensional movements. The electrical brain activity of the participant was meanwhile collected through 64 active EEG electrodes (actiCAP Brain Products GmbH, Germany), placed on the scalp according to the 10–10 system (figure S1) (available online at stacks.iop.org/JNE/17/046031/mmedia). Reference and ground electrodes were placed at the right mastoid and AFz, respectively. Six additional active electrodes were positioned at the inferior, superior and outer canthi of the eyes to record the electro-oculographic signal (EOG) (figure S1, right). The EEG and EOG signals were recorded at 500 Hz through biosignal amplifiers (BrainAmp, Brain Products GmbH, Germany).

The experiment was conceptually divided in two parts, i.e. *calibration* and *online feedback* operation of the EEG-based movement decoder (figure 1(c)). The main experimental paradigm was implemented in the so-called *snakeruns*.

Each *snakerun* consisted of 10 trials and lasted ~5 min. Each *snakerun* trial started with a self-paced *break* (figure 1(b)). During these breaks, a yellow fixation cross was displayed, the robotic arm was kept still, and the participant was in control of a cursor mapping his/her right-hand trajectories. As the participant wished to start a new trial, he/she had to move the cursor to the center of the cross and hold it for 1 s (*baseline* period, figure 1(b)). Thereafter, the cross and the cursor disappeared, the *snake* was displayed and started to move, and the participant gained control over the robot, marking the beginning of the *tracking* period. The *tracking* period lasted for 23 s.

At the beginning of the experiment, participants could choose a comfortable resting position, on the planar board, for their hand; this position was mapped to the origin of the fixation cross, and remained fixed for the whole experiment. In addition, there was no amplitude scaling between robot and hand movement (1:1 scaling). The snake trajectories were generated offline as in [25], and were the same across participants. Twelve trajectories were sampled from band-pass filtered (0.2–0.4 Hz) pink noise [32]. The set of trajectories was extended by rotating (90°, 180° and 270°) and mirroring existing trajectories, leading to a total of 96 trajectories randomly distributed over the trials of the experiment. The procedure ensured uncorrelated positions and velocities across and within horizontal (x) and vertical (y) dimensions [25].

Two *eyeruns* (figure 1(c)), were added to the *calibration* phase to collect the participant's EEG and

EOG activity during rest with eyes open, blinks, horizontal and vertical eye movements, as in [34]. The data from the two *eyeruns* were used to train an eye artifact attenuation algorithm as specified in [35].

As anticipated, the experiment was conceptually divided in two parts (figure 1(c)). In the first *calibration* part, the participants performed five runs where the robot was entirely controlled by their hand kinematics (*snakeruns* 1–5). After the decoding model was fitted to the movement (see the next sections for details), the participant gradually started to receive feedback on his/her decoded movements (*online feedback*). The robotic arm control was gradually switched from hand kinematics to EEG-based decoded trajectories, first with 33% (*snakeruns* 6–7), then 66% (*snakeruns* 8–9), up to the final condition of 100% EEG control (*snakeruns* 10–11).

2.3. Data recording and processing

Data were recorded and synchronized through the lab streaming layer protocol (<https://github.com/scnn/labstreaminglayer>). The presentation of the visual stimulus, the online processing and visualization of data were carried out using custom Matlab scripts (Matlab 2015b, Mathworks Inc. USA) and Psychtoolbox [36–38]. A photodiode was used for off-line synchronization. Offline analysis was carried out in Matlab and EEGLAB (v14.1.1) [39].

2.3.1. Online processing.

The EEG and LeapMotion processing pipelines are outlined in figure 2.

To give an overview of the EEG processing pipelines, the signals were band-pass filtered between 0.18 and 1.5 Hz, the bad channels interpolated, the eye artifacts [35] attenuated and the pops/drifts detected and interpolated [40] after re-referencing (common average reference, CAR). The signals were finally downsampled (20 Hz) and buffered (300 ms) for multi-lag decoding.

In the first processing stage, the EEG was high-pass filtered at 0.18 Hz and downsampled to 100 Hz. To avoid aliasing, the filter was composed as a cascade of i) 1st order IIR high-pass filter at 0.18 Hz, ii) a 2nd order low-pass Butterworth filter at 25 Hz, and iii) two Notch filters at 50 Hz and 100 Hz. The bad channels were identified for each participant (table S1, supplementary material) by visual inspection of the *calibration* runs, and were then linearly interpolated online from the four nearest neighboring channels. The influence of eye movements/blinks was attenuated with the generalized eye artifact subspace subtraction (GEYESUB) algorithm described in [35], which was fitted to the *eyeruns* data. The signals were then re-referenced to the CAR. The electrode pops and drifts were detected online and corrected with the high-variance electrode artifact removal (HEAR) algorithm in [40], which evaluated the probability

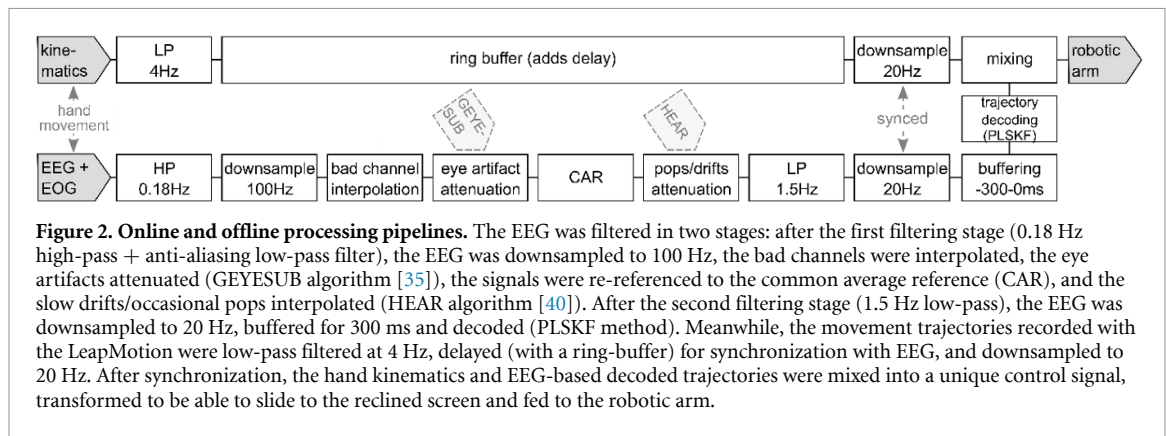


Figure 2. Online and offline processing pipelines. The EEG was filtered in two stages: after the first filtering stage (0.18 Hz high-pass + anti-aliasing low-pass filter), the EEG was downsampled to 100 Hz, the bad channels were interpolated, the eye artifacts attenuated (GEYESUB algorithm [35]), the signals were re-referenced to the common average reference (CAR), and the slow drifts/occasional pops interpolated (HEAR algorithm [40]). After the second filtering stage (1.5 Hz low-pass), the EEG was downsampled to 20 Hz, buffered for 300 ms and decoded (PLSKF method). Meanwhile, the movement trajectories recorded with the LeapMotion were low-pass filtered at 4 Hz, delayed (with a ring-buffer) for synchronization with EEG, and downsampled to 20 Hz. After synchronization, the hand kinematics and EEG-based decoded trajectories were mixed into a unique control signal, transformed to be able to slide to the reclined screen and fed to the robotic arm.

for each sample to be artifactual, and proportionally interpolated it with the four nearest neighboring channels. The second stage filtering (2nd order low-pass Butterworth, 1.5 Hz) and downsampling (20 Hz) was then achieved. To obtain multi-lag decoding of the hand trajectories, the EEG was finally buffered for 300 ms; a partial least squares (PLS) linear model was fitted to the *calibration* data, and used in combination with linear Kalman Filtering (KF) (see the next sections for details).

Right-hand position trajectories, recorded with the LeapMotion, were low-pass filtered at 4 Hz (3rd order low-pass; Butterworth filter), delayed by 165 ms through a ring-buffer, and finally downsampled to 20 Hz. The 165 ms delay was introduced to align the online processed LeapMotion and EEG signals. The estimation of 165 ms was obtained by considering the average processing delay for the EEG (~250 ms) and the LeapMotion (~80 ms), the transmission delay between brain activity and actual movement [41], and the latencies of the recording systems, as depicted in supplementary figure S2.

After alignment, the hand kinematics (LeapMotion) and EEG-based decoded trajectories were weighted according to the run (figure 1(c)), and combined to control the robot. The movement coordinates were transformed with a rotation matrix to make the robot move planarly on the tilted screen, while the amplitude of the movements remained the same (1:1 mapping).

The total delay between the participant's movement and feedback, i.e. the robot reaction, was estimated to be around ~550-650 ms altogether, of which ~250 ms were introduced by the processing pipelines, and 300-400 ms by the inertial displacement of the robot (supplementary figure S2).

2.3.2. Offline processing.

The EEG and LeapMotion data were processed offline following the same pipelines as online (figure 2). At the end of *calibration*, the *snakerun* data were collected, processed and epoched into 23 s trials. These trials were automatically marked for rejection if the EEG signal of any channel exceeded a threshold of

$\pm 100 \mu\text{V}$ or had an abnormal probability or kurtosis (more than five standard deviations from the mean). The procedure was applied twice to detect both gross and subtle outliers. The marked trials were further visually checked to correct, where necessary, the automatic detection. The proportion of rejected trials was 10 out of 50 *calibration* trials on average.

The LeapMotion signals, recording the planar hand trajectories and therefore the sideways (x) and forwards/backwards (y) components of the *positions*, were used as a base to additionally compute *velocities* and *accelerations*. All movement parameters were later used to fit the PLS models and set up the KF (see the next section for details). Velocities and accelerations were estimated with a Savitzky-Golay filter (order 3, 11 taps). The first and last second of each trial were finally excluded to eliminate edge artifacts.

After the experiment, *feedback* runs were processed in the same way as *calibration* runs. The proportion of rejected trials was 10 out of 60 feedback trials on average.

2.3.3. Decoder fitting (PLS).

Likewise previous EEG decoding studies [6, 25], we applied PLS regression [42] to find the linear models linking hand movement parameters (x and y *positions*, *velocities* and *accelerations*) and EEG recordings. PLS is particularly appropriate in situations with strongly collinear predictor variables, as in the case of multi-lag, LF-EEG.

Let X be the $n \times P$ matrix of predictor variables, with n observations and P predictors, here the multi-lag EEG data. Let then Y be the $n \times M$ matrix of response variables with M responses, here the six movement parameters (x and y coordinates of positions, velocities and accelerations).

The predictor variables are then modelled as:

$$X = X_s \cdot X_L^T + E \quad (1)$$

with X_s being an $n \times N_{comp}$ matrix of latent components, X_L being the $P \times N_{comp}$ matrix to relate the predictors X to their latent space, and E being an $n \times P$ matrix of additive independent and identically distributed (iid) noise.

The dependent variables are then modelled as:

$$Y = X_S \cdot Y_L^T + G \quad (2)$$

with Y_L being the $M \times N_{comp}$ matrix relating Y with the predictor components X_S , and G being a matrix of additive iid noise.

The estimates X_L and Y_L may also be combined into a $P \times M$ weight matrix W , to directly predict the dependent from the predictor variables, i.e. the movement parameters from the EEG:

$$\hat{Y} = X \cdot W. \quad (3)$$

In this study, we used the SIMPLS algorithm [43] to estimate X_L , Y_L , and W from the *calibration* data (i.e. the clean trials from *snakeruns 1–5*). Even though eye movement artifacts were strongly attenuated [35], pilot experiments revealed that a subtle residual artifactual activity could sometimes affect the most frontal locations. Therefore, we removed the five most frontal electrodes in the *Fp* and *AF* rows (figure S1, supplementary material), and fitted the model to the remaining 59 channels. Since we considered seven EEG lags (i.e. lag 0, -50 ms, -100 ms, -150 ms, -200 ms, -250 ms and -300 ms), this resulted in $59 \times 7 = 413$ predictor variables. For the latent space, we considered a number of components explaining 99% of the variance in the multi-lag EEG, resulting in $N_{comp} = 85$.

2.3.4. Kalman filter.

The Kalman filter [44] is an algorithm to infer the internal state of a system, given a set of indirect and noisy measurements and the system's underlying model. The Kalman filter is composed of two equations, namely: i) the *process equation*, describing the evolution of the internal state over time and ii) the *measurement equation*, describing the relation between the noisy measures and the state.

In its discrete-time and linear form, the Kalman filter equations can be written as follows:

$$\begin{cases} \theta_{k+1} = F\theta_k + v_k & v \sim N(0, Q) \\ z_k = H\theta_k + w_k & w \sim N(0, R) \end{cases} \quad (4)$$

In the process equation, θ represents the n_θ -dimensional state of the system, F is the $n_\theta \times n_\theta$ transition matrix between the present k and next $k + 1$ time sample, and v is additive Gaussian noise (with zero-mean and covariance matrix Q) modeling the uncertainties and propagation of errors. In the measurement equation, z is the n_z -dimensional vector of measurements, H is the $n_z \times n_\theta$ matrix modeling the linear relation between z and θ , and w is additive Gaussian noise (with zero-mean and covariance matrix R) modelling the measurement and model errors.

In this study, we set up the Kalman filter to estimate the movement parameters, i.e. the status θ , from the noisy measures z , i.e. the multi-lag EEG.

The status θ was therefore defined as:

$$\theta = [p_x v_x a_x p_y v_y a_y]^T \quad (5)$$

and contained the whole kinematic chain from positions to accelerations.

We then adopted for the process equation a general 'zero-jerk' model. This model considers the finite difference integration between positions, velocities and accelerations at sample times k and $k + 1$, while assuming the acceleration to be constant ($a_{k+1} = a_k$) and therefore the variability in the accelerations as a source of noise. Let T be the integration step (in our case $T = 0.05$ s, due to the downsampling to 20 Hz), the F and Q matrices were then defined as:

$$F = \begin{bmatrix} 1 & T & T^2/2 & 0 & 0 & 0 \\ 0 & 1 & T & 0 & 0 & 0 \\ 0 & 0 & 1 & 0 & 0 & 0 \\ 0 & 0 & 0 & 1 & T & T^2/2 \\ 0 & 0 & 0 & 0 & 1 & T \\ 0 & 0 & 0 & 0 & 0 & 1 \end{bmatrix}$$

$$Q = \begin{bmatrix} T^5/20 & T^4/8 & T^3/6 & 0 & 0 & 0 \\ T^4/8 & T^3/3 & T^2/2 & 0 & 0 & 0 \\ T^3/6 & T^2/2 & T & 0 & 0 & 0 \\ 0 & 0 & 0 & T^5/20 & T^4/8 & T^3/6 \\ 0 & 0 & 0 & T^4/8 & T^3/3 & T^2/2 \\ 0 & 0 & 0 & T^3/6 & T^2/2 & T \end{bmatrix} \cdot \frac{1}{10} \cdot \frac{\text{var}(a)}{T} \quad (6)$$

with F modeling the integration process between movement parameters in θ , and Q describing the propagation of noise on the accelerations (i.e. the acceleration variance) to velocities and positions [45].

In the measurement equation, we used the PLS decoder model to estimate the status θ from the EEG. However, to reduce redundancy and increase computation speed, instead of the complete multi-lag EEG in X we considered its projection to the latent space X_S (equation (1)), thus reducing the dimensionality of z from $P = 413$ to the previously defined $N_{comp} = 85$ latent components. As a result of equation (2), the Kalman filter matrix H was therefore:

$$H = \text{pinv}(Y_L). \quad (7)$$

The covariance matrix of the measurement error, R , was obtained by applying its definition, and fitted to the *calibration* data:

$$R = [\text{cov}(z - \hat{z})]_{\text{calibration}} = [\text{cov}(z - H\theta)]_{\text{calibration}}. \quad (8)$$

In equation (8), the 'measured' z were derived by projecting the pre-processed EEG to the latent space X_S (equation (1)), and the 'estimated' were derived by applying the matrix H to the LeapMotion recorded and pre-processed kinematics (θ).

The resulting model, combining the dimensionality reduction properties of PLS regression with the data fusion properties of KF, was used for the online decoding of hand movement from the EEG. We will later refer to this model as PLSKF. The PLSKF model was fitted only once for each participant based on the *calibration* runs; after calibration, the PLSKF decoded hand trajectories were mixed to the LeapMotion recorded and delayed ones (figure 2), with different proportions according to the experimental condition (figure 1(c)).

2.4. Offline evaluation of the decoding performance

2.4.1. Pearson's correlation coefficients.

Even though the PLSKF was the model used online to give feedback during the experiment, its performance was then evaluated offline, and compared to the performance that could have been achieved by using the PLS regression alone, similarly to previous studies [5, 6, 25].

A commonly used measure of similarity between hand kinematics and decoded trajectories is the Pearson's correlation coefficient, r . We evaluated the correlations r between the hand kinematics and PLSKF-decoded trajectories, for each participant, movement parameter (*positions, velocities, accelerations*), and condition (0%, 33%, 66% and 100% EEG control).

We estimated the upper bound confidence interval of the chance level correlations, r_{chance} through a shuffling approach, i.e. by breaking the association between the multi-lag EEG in X and the recorded movement parameters in Y , by randomly shuffling X and Y across trials. After shuffling the data 100 times, fitting each time a new PLS model and evaluating the corresponding correlation r , we estimated the upper bound confidence interval of the chance level, r_{chance} , (with significance $\alpha = 0.05$) as the 95th percentile of the correlations r , taken in absolute value $|r|$.

To evaluate the effect of the Kalman filter on the decoding performance, we computed the correlations r in two cases. In the first case, we estimated the movement parameters using the PLS model only (equation (3)). In the second case, we estimated the correlations using the same PLSKF model as in the online case. We compared the two methods for each participant, movement parameter, and condition, using Wilcoxon signed-rank tests. We ran a total of 24 tests, corresponding to the 6 movement parameters x 4 conditions. We controlled the false discovery rate (FDR), at significance level 0.05, by adjusting the p -values [46, 47].

To avoid overfitting, in the 0% EEG condition (i.e. the *calibration* data) we evaluated r using a leave-one-trial-out cross-validation approach. For each *calibration* trial, we fitted a PLS model (and Kalman filter) to all-but-one trials, evaluated the correlation r on the remaining one, and computed the average r in the end. Regarding the other three conditions of

33%, 66% and 100% EEG control, we evaluated the correlations with the same PLS and Kalman models used online (i.e. the ones fitted to the whole *calibration* data).

2.4.2. Amplitude of hand kinematics and EEG-based decoded trajectories.

To complete the analysis on the decoder output, we evaluated the amplitudes of hand kinematics and EEG-based decoded trajectories for each participant and condition. To quantify the amplitudes, we considered the difference between the 95th and the 5th percentiles of the *position* distributions, for both x and y coordinates.

2.5. Source space analysis

2.5.1. Source imaging.

In order to interpret the decoding models at cortical level, we evaluated the activation patterns A from the weight vectors W , and projected them to the cortex by using EEG source imaging [48, 49]. The activation patterns A were obtained as in [50]:

$$A = \widehat{\Sigma}_X \cdot W \cdot \widehat{\Sigma}_Y^{-1} \quad (9)$$

where $\widehat{\Sigma}_X$ and $\widehat{\Sigma}_Y$ are the sample covariance matrices for the multi-lag EEG (X) and the movement parameters (Y). We estimated $\widehat{\Sigma}_X$ and $\widehat{\Sigma}_Y$ using the *calibration* data, and regularized them through analytical shrinkage regularization [51]. In order to express the patterns A as voltages [52], we *scaled* them by multiplying A with the square root of $\widehat{\Sigma}_Y$. We further normalized these scaled patterns, A_{scaled} , to account for the variability, across participants, of EEG baseline level of activity. For each participant and movement parameter, the baseline level of activity was estimated from the chance level scaled patterns, A_{chance_scaled} . We first evaluated the root mean square (rms) of A_{chance_scaled} over electrodes and lags. These rms values were then averaged over the 100 chance level repetitions. Similarly to [25], the obtained (scalar) values were finally used for the normalization of A_{scaled} .

The normalized, scaled patterns were projected to source space using the open source software Brainstorm [53] (version 22 August 2018). We created the head models by co-registering the ICBM152 boundary element model (BEM) [54] with the recorded electrode positions (ELPOS, Zebris Medical GmbH, Germany) of each participant. The BEM template consisted of three layers (cortex, skull, scalp), whose conductivities were set to (1, 0.008, 1). The electrode positions were registered to the scalp layer using three anatomical landmarks (nasion, left and right preauricular points). In case a participant's anatomy slightly deviated from the template model, we completed the registration by projecting the floating electrodes on the BEM scalp layer. We modelled the cortex with 5001 voxels and computed the forward model, describing the propagation of electrical fields from

the cortex to the scalp with OpenMEEG [55, 56]. We finally used sLORETA [57] to evaluate the corresponding inverse model, and considered 3 unconstrained source components per voxel. We estimated the noise covariance matrix of the EEG, necessary for sLORETA, on the eye-corrected data of the *eyeruns*, and applied analytical shrinkage regularization [51]. We finally computed, for each voxel, the norm of the three x , y and z source components.

2.5.2. Source space statistics, and evaluation of the temporal dependency between movement parameters.

For each movement parameter and time lag, we looked for significant activations in source space by computing the paired difference between each decoder pattern and the corresponding chance level activity (in source space). We computed the chance level by averaging the 100 back-projected, normalized chance level patterns. As in [25], we evaluated significance at eight region of interests (ROIs) associated with movement processing (figure 5(a)), namely the dorsomedial occipital cortex (DMOC), the superior parietal lobule (SPL), the primary somatosensory and motor cortices (SM1) and fronto-central (FC) areas of both hemispheres. We computed the activity of each ROI by averaging its voxels. We assessed the significance through two-tailed non-parametric permutation paired t-tests [58, 59] with 1000 repetitions. We ran a total of 336 tests, corresponding to 8 ROIs \times 7 time lags \times 6 movement parameters. We controlled the FDR by adjusting the p -values at 0.05 significance level [47].

The analysis of significant activations in source space follows from the projection at cortical level of the decoder activation patterns. However, provided that these patterns involve several movement parameters and time lags, the correct interpretation of the results needs to take into account the temporal dependencies between the movement parameters, i.e. the variables to which the decoder is fitted. To investigate this, we evaluated the cross-correlations in the $[-1, 1]$ s time range between *positions*, *velocities* and *accelerations* and between the x and y dimensions. For this analysis, we used the trajectories derived from the LeapMotion in the 0% EEG condition, i.e. the same trajectories to which the linear decoder model was fitted.

2.8. Questionnaires

To collect the participants' impressions during the experiment, we administered a questionnaire at the end of each condition (0%, 33%, 66% and 100% EEG control). The text of the questionnaire is provided at the end of the supplementary material. On the one hand, the questionnaire collected the overall impressions about the experiment, e.g. by asking to what extent the task was intuitive, mentally or physically demanding, complicated and engaging, along with

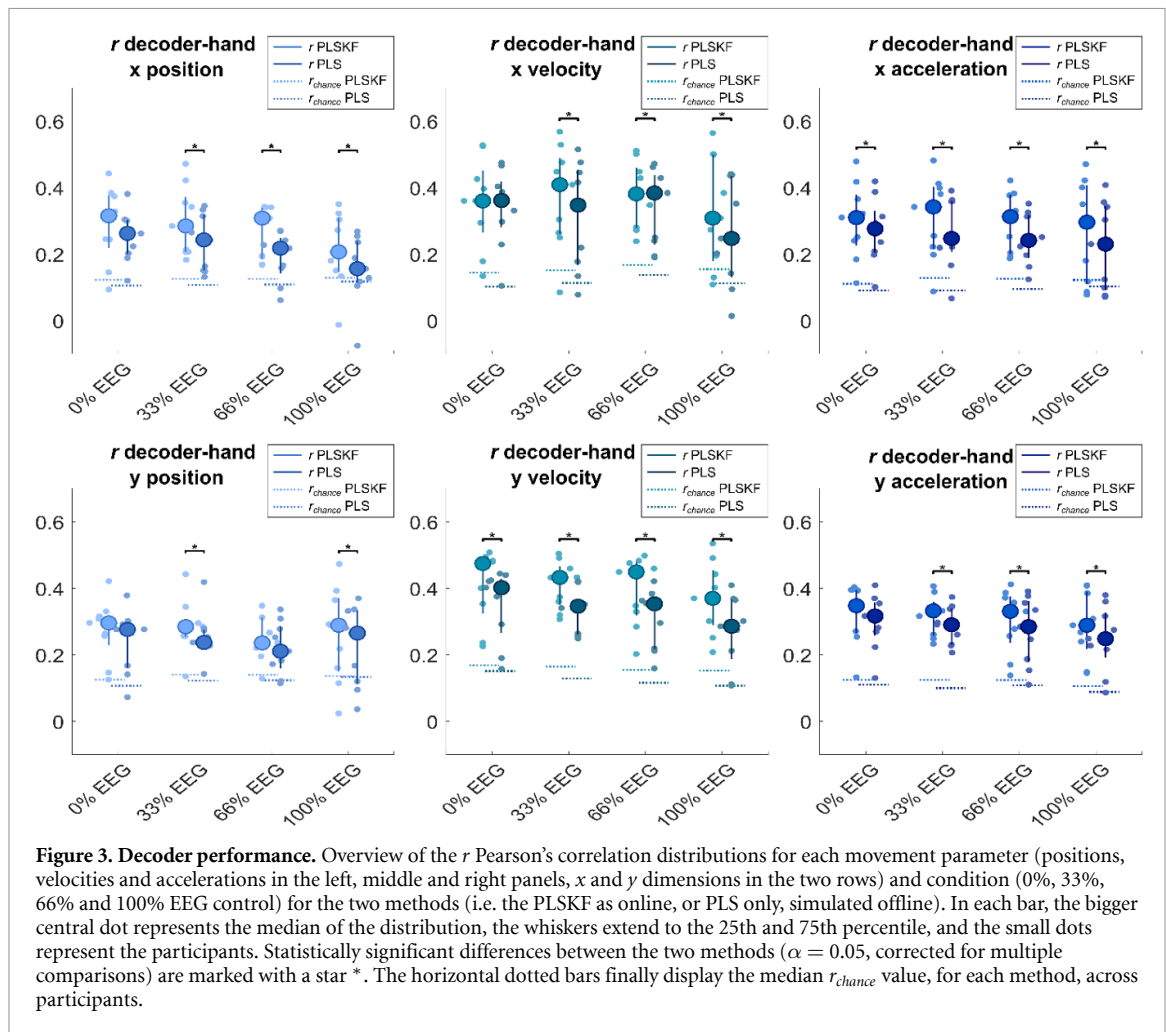
the level of experience with robot usage and whether the participants felt comfortable around the robot. On the other hand, the questionnaire tracked the evolution of the participant during the experiment, by enquiring about the perceived level of control, the perceived delay, the level of attention to the snake, the robot or their hand, and whether the participants had the feeling to be performing smaller or larger movements with respect to the *calibration*. For each question, the participants could quantify their answers by drawing a mark on a visual analogue scale. To analyze the results, we transformed the answers into scores by measuring the distance of each mark from the extremities of the visual analogue scale, and normalized them by the scale length. For the questions regarding the general impressions about the experiments, the scores were mapped between 0 and 1. The score distributions were described by evaluating the median and inter-quartile range (IQR). For the questions regarding the evolution of the participant's state, the decreases/increases with respect to *calibration* were mapped between -1 ('maximum decrease') and 1 ('maximum increase').

After the experiment, we additionally asked the participants whether they perceived (or not) that their ability to control the robot with the EEG-based decoded trajectories could improve with training.

2.9. Task performance and behavioral results

In order to investigate how well the participants could track the snake with their hand, how much the EEG-based decoded trajectories complied with the target, and how well the participants could ultimately control the robot, we performed correlation analysis between three additional pairs of trajectories: i) between snake and hand trajectories (later named 'snake-hand' pair), ii) between the snake and the decoded trajectories ('snake-PLSKF'), and finally iii) between the snake and the robot trajectories ('snake-robot'). For each of the three pairs of trajectories and for each condition (0%, 33%, 66% and 100% EEG control) we evaluated the cross-correlation values in the interval $[-1, 1]$ s (i.e. by shifting one trajectory with respect to the other up to ± 1 s).

Unlike previous analyses, having as an outcome measure the correlation r at lag 0, we decided to consider here the maximum correlation r_{max} in the cross-correlation interval $[-1, 1]$ s. This allowed for a better comparison across participants, considering that the *snake* was a moving trace with a non-negligible length (approximately 1 s of trace was displayed in each moment) and participants could choose to focus on different parts of it (for example, on the head rather than the tail of the snake). Considering r_{max} instead of the correlation r at lag 0 permitted us to evaluate the participant's compliance to the task, independently of which part of the *snake* he/she decided to track.



To estimate the delay between each of the three pairs ('snake-hand', 'snake-PLSKF' or 'snake-robot'), we considered the time-interval between lag 0 and the time point of r_{max} . To finally evaluate whether the correlation r_{max} (or delay) distributions differed among conditions (0%, 33%, 66% or 100% EEG control), we used a Kruskal-Wallis test with significance level $\alpha = 0.05$ and the Tukey's criterion to correct for multiple comparisons.

3. Results

3.1. Decoding performance

3.1.1. Pearson's correlation coefficients.

The results of correlation analysis between hand kinematics and EEG-based decoded trajectories are displayed in figure 3. The diagrams show the distributions of the Pearson's correlations r for each movement parameter (*positions*, *velocities* and *accelerations*) and condition (0%, 33%, 66% and 100% EEG control), and for the two methods (the PLSKF used online, and the PLS alone, simulated offline). The upper bound correlations of the chance level distributions (r_{chance} , with significance $\alpha = 0.05$) are also displayed for each case and method. The corresponding

mean \pm SEM values are detailed in the supplementary table S2.

We obtained moderate yet overall significant correlations r between hand kinematics and EEG-decoded trajectories; the correlations r were significantly ($\alpha = 0.05$) above the chance level r_{chance} in 206 out of 216 cases (considering all 9 participants \times 6 movement parameters \times 4 conditions). For the PLSKF, i.e. the method implemented online, we obtained average correlations of (0.28 ± 0.04 , 0.29 ± 0.03 , 0.26 ± 0.03 , 0.23 ± 0.05 , mean \pm SEM) for the (0%, 33%, 66%, 100%) EEG conditions for the *positions*. The corresponding upper-bound r_{chance} values with significance $\alpha = 0.05$ were (0.14 ± 0.01 , 0.15 ± 0.01 , 0.14 ± 0.01 , 0.13 ± 0.01).

For the PLS model alone, which we simulated offline, we obtained, on average, correlations of (0.25 ± 0.03 , 0.25 ± 0.03 , 0.21 ± 0.03 , 0.19 ± 0.04) for the *positions*, while the corresponding r_{chance} were (0.12 ± 0.01 , 0.12 ± 0.01 , 0.11 ± 0.01 , 0.12 ± 0.01).

In both cases, we observed that the best reconstructed movement parameter was the *velocity* (figure 3, middle).

3.1.2. Effect of the kalman filter.

With respect to the PLS, we could observe two effects introduced by the PLSKF.

The first effect was the moderate yet stable increase in correlation between the PLS and PLSKF. The mean \pm SEM of the correlation r obtained with the two methods, the average increase Δr , and the results of statistical analyses for each movement parameter and condition, are detailed in the supplementary table S3. The grand average increase in correlation due to the Kalman filter was $\Delta r = 0.049$. The increase was consistent over movement parameters and conditions, and statistically significant in the majority (19 out of 24) of the comparisons (figure 3).

The second observed effect was the smoothing of the PLSKF-decoded trajectories with respect to using the PLS model alone. This smoothing effect can be qualitatively appreciated in figure 4(a), displaying an example of decoded trajectories with the two methods.

3.1.3. Amplitude of hand kinematics and EEG-based decoded trajectories.

To complete the analysis of the decoder output, we compared the amplitude of the EEG-based decoded trajectories with the hand kinematics, for each participant and condition. Figure 4(b) depicts the mean and standard deviations for the hand kinematics (recorded with the LeapMotion) and EEG-based decoded trajectories (with KF), across participants, and for each condition. As it can be seen in figure 4(b), the decoded trajectories were generally smaller (~ 5 – 6 cm) with respect to the hand kinematics (~ 15 – 20 cm). In addition, their amplitude remained the same throughout the experiment, even though the participants tended to increase the size of their movement in the 33%, 66% and 100% EEG control conditions.

3.2. Source space analysis

3.2.1. Source imaging and source space statistics.

The results of projecting the decoder patterns to the cortex, and the subsequent statistical analysis in source space, are outlined in figure 5(b) and detailed in supplementary table S4.

Figure 5(b) shows the norm (at each voxel) of the projected activation patterns, averaged across participants, for each movement parameter and at time lag 0. The same results for the other time lags can be found in supplementary figure S3.

The results of the permutation tests for each R (figure 5(a)), time lag and movement parameter are detailed in supplementary table S4. The p -values need to be interpreted according to the critical value from the FDR correction, $p_{crit} = 0.007$. Overall, we found significant activations in the DMOC and SPL areas for the decoded *velocities* and *accelerations*, and over multiple time-lags. No significant activations were found in the FC and somatosensory and motor (SM) areas, or in any region for the decoded *positions*.

3.2.2. Temporal dependency between movement parameters.

The cross-correlation curves between the hand (i.e. LeapMotion) *positions*, *velocities* and *accelerations* and between x and y dimensions are useful to visualize the temporal dependencies between movement parameters and therefore to interpret the multi-lag source analysis results, as displayed in supplementary figure S4.

3.3. Questionnaire results

A visual representation of the questionnaire results can be found in the supplementary figures S5–S7.

Regarding the general impressions over the experiment (figure S5), participants found the task very intuitive (median = 0.75 and IQR = 0.24, within a 0–1 range), very engaging (median = 0.66, IQR = 0.18), and not complicated (median = 0.09, IQR = 0.12). They also found it moderately mentally demanding (median = 0.37, IQR = 0.42), although not physically demanding (median = 0.15, IQR = 0.57). The participants finally varied in terms of previous robot usage experience (median = 0.47, IQR = 0.79), although they generally felt comfortable around the robot (median = 0.91, IQR = 0.46).

Regarding the evolution of the participant's state over time (figures S6 and S7), the participants reported to perceive, after *calibration*, a good baseline level of control (median = 0.79, IQR = 0.38), a moderate delay between movement and feedback (median = 0.48, IQR = 0.56), and reported to focus most of their attention to the snake (median = 0.93, IQR = 0.13) and less to the robot (median = 0.24, IQR = 0.40) or their hand (median = 0.25, IQR = 0.45). Over the course of the experiment (figure S7), their perceived level of control progressively decreased, the perceived delay slightly increased, and the level of attention to the snake, robot and hand also varied. The participants finally perceived to be making larger movements with respect to *calibration*.

Regarding the bonus question, 7 out of 9 participants had the feeling they could improve their control skills with training, 1 participant replied negatively, while the remaining one did not reply.

3.4. Task performance and behavioral results

Figure 6 outlines the behavioral analysis/task performance results, quantifying the participants compliance to the task, the correlation between the target (i.e. the snake) and the EEG-based decoded trajectory, and ultimately the participant's level of control over the robot.

The r_{max} values between snake and hand trajectories, ('snake-hand' panels, figure 6 left), quantifying the participants' compliance to the task, were moderately high (on average 0.68 ± 0.010 and 0.58 ± 0.013 for x and y). The correlations for y were slightly lower

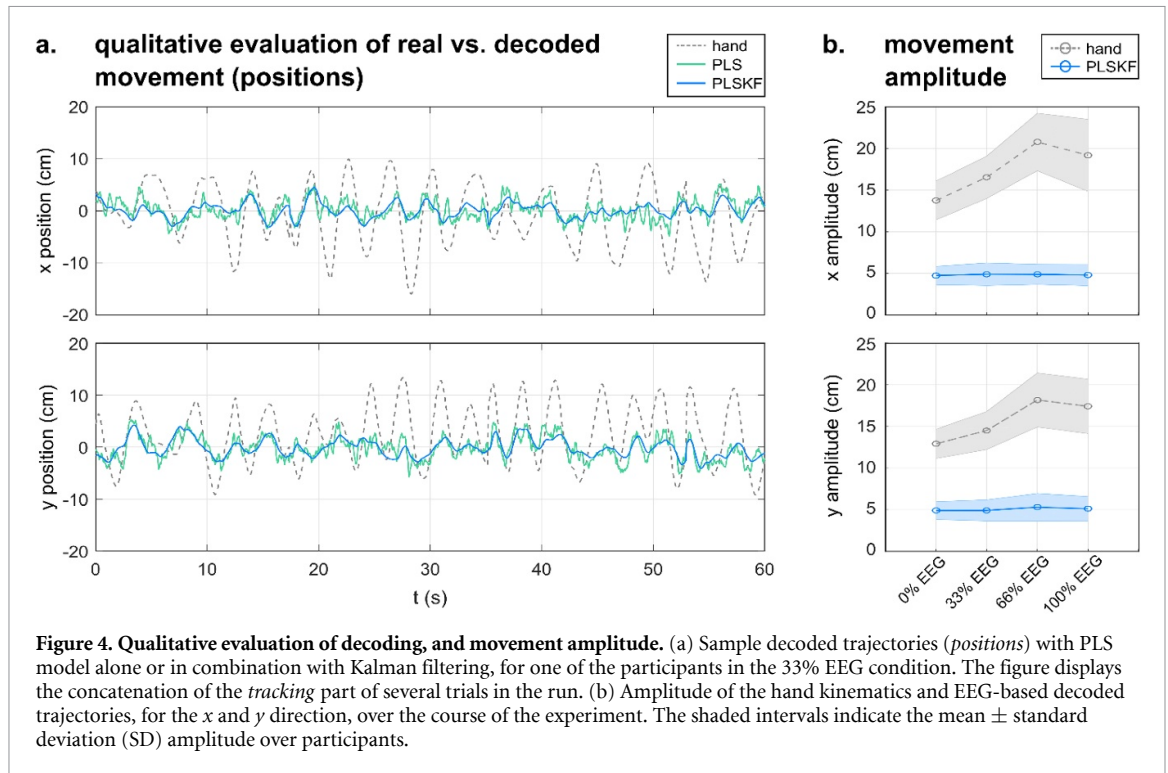


Figure 4. Qualitative evaluation of decoding, and movement amplitude. (a) Sample decoded trajectories (*positions*) with PLS model alone or in combination with Kalman filtering, for one of the participants in the 33% EEG condition. The figure displays the concatenation of the *tracking* part of several trials in the run. (b) Amplitude of the hand kinematics and EEG-based decoded trajectories, for the *x* and *y* direction, over the course of the experiment. The shaded intervals indicate the mean \pm standard deviation (SD) amplitude over participants.

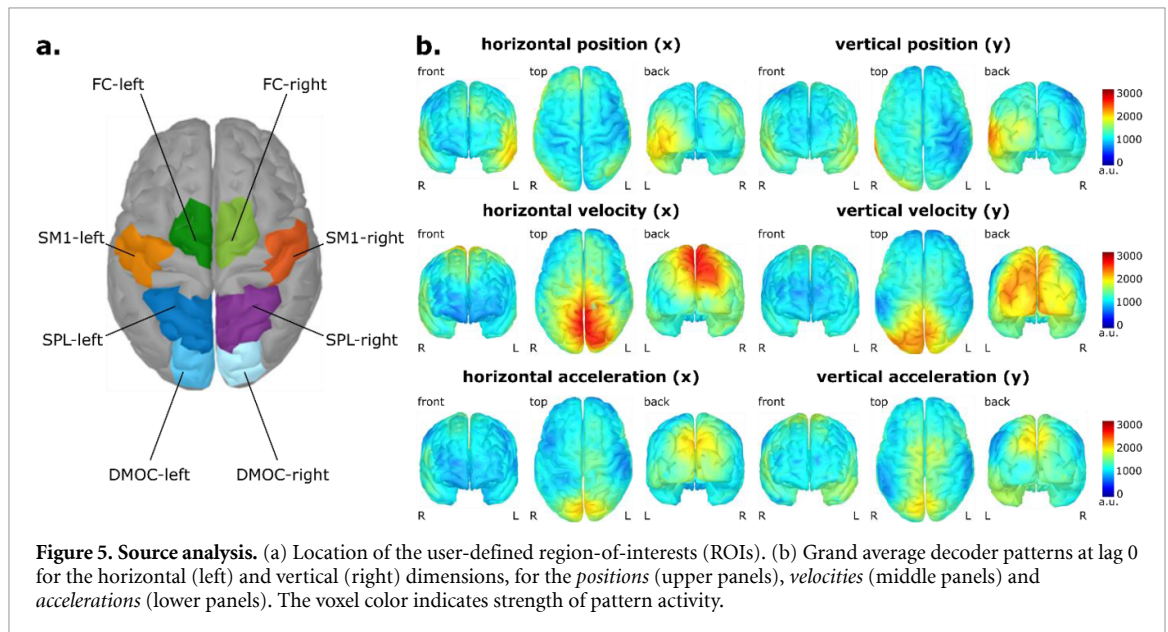


Figure 5. Source analysis. (a) Location of the user-defined region-of-interests (ROIs). (b) Grand average decoder patterns at lag 0 for the horizontal (left) and vertical (right) dimensions, for the *positions* (upper panels), *velocities* (middle panels) and *accelerations* (lower panels). The voxel color indicates strength of pattern activity.

than for *x*, possibly because of a difficulty in evaluating the *y* coordinate, due to the reclining of the screen. In the *x* dimension, we observed significantly lower r_{max} values in the 100% EEG condition with respect to 0% and 33% EEG. However, in this condition the participants had no feedback about their hand position, as the robot was entirely controlled with the EEG.

The middle panel of figure 6 displays the r_{max} correlations between snake and decoded trajectories ('snake-PLSKF'). The correlations were moderate (on average 0.28 ± 0.053 and 0.29 ± 0.046 for *x* and *y*) but above chance level in almost all the comparisons (69 out of 72 comparisons, considering 9 participants x

4 conditions x 2 dimensions). These correlations did not significantly differ among conditions.

The right panel of figure 6 displays the r_{max} correlations between snake and robot trajectories ('snake-robot') quantifying how well, ultimately, the participants could control the robot. It can be noted from the figure that the 'snake-robot' correlations r_{max} are a mixture of the corresponding 'snake-hand' and 'snake-PLSKF' values, reflecting the mixture of hand kinematics and EEG-based decoded trajectories over conditions in the control signal of the robot. In the 0% EEG condition, the distribution of 'snake-robot' correlations r_{max} correspond to the 'snake-hand' case,

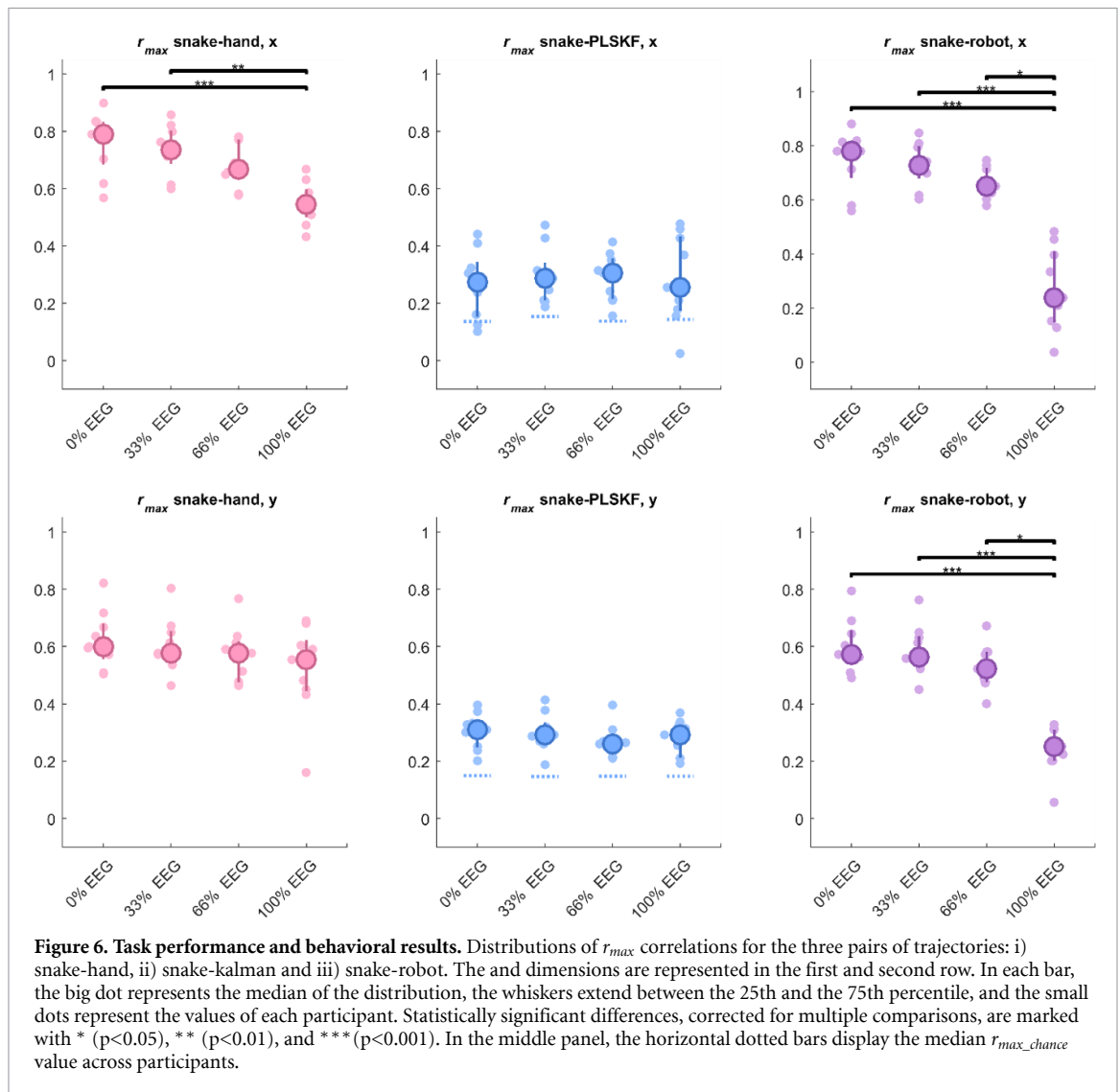


Figure 6. Task performance and behavioral results. Distributions of r_{max} correlations for the three pairs of trajectories: i) snake-hand, ii) snake-kalman and iii) snake-robot. The and dimensions are represented in the first and second row. In each bar, the big dot represents the median of the distribution, the whiskers extend between the 25th and the 75th percentile, and the small dots represent the values of each participant. Statistically significant differences, corrected for multiple comparisons, are marked with * ($p < 0.05$), ** ($p < 0.01$), and *** ($p < 0.001$). In the middle panel, the horizontal dotted bars display the median r_{max_chance} value across participants.

while in the 100% EEG condition, they correspond to the ‘snake-PLSKF’ case. The r_{max} values and therefore the level of control significantly decreased with increasing proportions of decoded EEG to the control. Nevertheless, even in the 100% EEG condition, the r_{max} correlations and therefore the level of control were overall above chance.

The distributions of delays between the three pairs of trajectories are displayed in supplementary figure S8. The delays between snake and hand were on average 120 ± 30 ms and 130 ± 45 ms (mean \pm SEM) for x and y . The corresponding delays between snake and PLSKF-decoded trajectories were 215 ± 80 ms and 290 ± 115 ms. Finally, the delays between snake and the robot were 550 ± 43 ms and 560 ± 51 ms. In all three cases, the delays did not significantly differ across conditions, i.e. they remained constant throughout the experiment.

4. Discussion

Continuous decoding of voluntary movement is desirable for closed-loop, natural control of neuro-

prostheses. Even though recent studies [6, 24, 25, 52] have shown the possibility to infer hand positions and velocities from the LF-EEG, so far, this has only been performed offline. In this study, we made a first attempt to switch to an online scenario, by implementing continuous LF-EEG-based movement decoding for the online control of a robotic arm. We obtained moderate yet overall significant correlations of 0.32 on average over all movement parameters, the PLSKF decoder could significantly improve the performance with respect to PLS regression alone, and the majority of participants reported to feel enough control over the robot to be able to improve it with training.

4.1. Overall decoding performance, potential challenges when switching to an online scenario, and effect of the Kalman filter

In this study, we could show that continuous decoding of voluntary movement from LF-EEG is feasible when switching from an offline to a closed-loop online scenario. The information about the right-hand movement could indeed be decoded above

chance level for almost each participant, movement parameter and condition (figure 3 and supplementary table S2); we obtained a grand average correlation over all movement parameters of 0.32, which is in line with some previous offline EEG studies [26, 27]. The level of robot control was also overall higher than chance even in the 100% EEG condition (figure 6) and, finally, most participants (7 out of 9) reported to feel enough control over the robotic arm to be able to improve with training.

Despite the encouraging results, the translation of linear, LF-EEG-based continuous movement decoding to a closed-loop online scenario presented us some challenges that had to be addressed. These are part of the general bottlenecks that might arise in the translation process. In the following paragraphs, we discuss why the PLSKF model could be an option to overcome these bottlenecks, and how it can be extended to scenarios different than ours.

One of the requirements of closed-loop control is to keep the total delay between the recorded signal and the feedback as small as possible. In the context of LF-EEG-based decoding, one of the main bottlenecks is the delay introduced by the EEG processing pipeline, and particularly by the temporal filtering step. In this type of decoding, the desired movement parameters are indeed obtained through linear combinations of the EEG signals, band-pass filtered in approximately the same frequency band as the movement (i.e. typically between 0.1 Hz and < 3 Hz) [6, 24, 25, 52]. However, if in an offline study processing delays and phase distortions can be eliminated with zero-phase filtering, when switching to an online processing, the introduced delays may render closed-loop control unfeasible. A possible approach to reduce the delays, is to relax the design constraints of the temporal filter. To give an example, if we would have implemented the same filter as in a previous offline study [25], this would have led to an approximately 2 s processing delay, which would be incompatible with closed-loop control. By reducing the filter orders and enlarging the filtered bandwidth, we could reduce the processing delay to ~ 250 ms. The problem with this approach is, however, that the filter attenuation is lower, and therefore higher frequency components may remain in the EEG signal. Provided that linear regression models are only able to relate signals in similar frequency ranges [60], the higher frequency components in the EEG will ultimately transfer to the decoded trajectories (for an example, see the trajectories decoded with PLS regression alone in figure 4(a)), thus deteriorating the quality of decoding.

An additional limitation of previously used linear approaches is that they are typically used to retrieve only one type of movement at a time. For example, some previous studies used linear models to directly decode the *positions* [5, 28, 29], some others only the *velocities* [24, 29]. Using one linear model

at a time would therefore lead to sub-optimal decoding, provided that not all the available sources of information are exploited; in contrast, implementing a method to simultaneously consider the models of all movement parameters, would permit to integrate them and potentially improve the results.

With the introduction of PLSKF, we could address both of the previously identified limitations. First, the method was successful in integrating the linear models of the different movement parameters, as documented by the significant (figure 3 and table S3) increase in correlation with respect to using the PLS decoder alone. Second, the PLSKF had a clear smoothing effect on the decoded trajectories (figure 4(a)), which could finally have a similar frequency content to the actual movement, despite the more relaxed temporal filtering.

Similar Kalman filter approaches had already been introduced in movement decoding studies from invasive recordings, either based on intracortical recordings [10, 14, 15] or electrocorticography [16]. Lv et al [26] used KF with EEG recordings to integrate the information of decoded velocities. However, the filter parameters were fitted to the calibration data not only to regress the velocities from the EEG (matrix H in equation (4)), but also for the process equation (i.e. matrix F), which might lead to overfitting to the task. In addition, although the measurement vector z (equation (4)) was also a multi-lag concatenation of EEG power features, no dimensionality reduction was implemented. In our study, a PLS-based KF (PLSKF) approach was proposed for linear LF-EEG-based decoding. In addition to the dimensionality reduction properties of PLS regression, integrated into the model when using the latent components as measurement vector z instead of the complete EEG (equations (7) and (8)), this version of PLSKF also implements a general zero-jerk model (equation (6)), which means that the process equation is not fitted to the data and, therefore, it is potentially more general. Given the generality of the approach, we believe it could be easily extended to other cases where the decoding models of different movement parameters have to be combined for a better estimation of the trajectories. For example, we recently demonstrated [61, 62] that a non-linear extension of the model with unscented KF can successfully integrate non-linearly related movement parameters (e.g. like velocities and speed [63]) to further improve the estimation of the trajectories.

4.2. Source space analysis: tuning of neural activity to the velocities and activations in the parieto-occipital areas

The source space analysis revealed that i) the strongest activation patterns were the ones relative to *velocities* and *accelerations* and that, in both cases, ii) these patterns were most prominent in parieto-occipital

areas (SPL and DMOC, figures 5(a) and (b), and supplementary table S4). However, given the temporal dependencies between movement parameters, caution should be taken when interpreting these results.

Neural tuning to movement direction has been largely demonstrated in both monkeys and humans, both through invasive and non-invasive recordings [9, 13–16, 20, 22, 24, 25, 29, 32, 63–65]. The significant activations found in our study for the *velocities*, i.e. a parameter related to movement direction, are therefore in line with literature. The localization of the *velocity* activation patterns in the parieto-occipital areas is also consistent with the findings of other studies. Our results are indeed very similar to the ones obtained in the previous offline study of Kobler *et al* [25]. The involvement of posterior parietal areas to decode the *velocities* of the end-effector has finally been demonstrated in [15].

While the neural tuning to *velocities* is quite established in literature, it still remains unclear whether the same can be said for the *accelerations* [15, 63]. The significant activations in the parieto-occipital areas (DMOC and SPL) that we found for the *acceleration* patterns would therefore constitute a novel contribution. However, due to the temporal dependencies between movement parameters, special attention needs to be paid when interpreting these results. Considering the cross-correlation curves in supplementary figure S4, we can indeed see that the correlation between *velocities* and *accelerations* in the -300 to 0 ms time-range (i.e. the time-range in which the decoder patterns were extracted) is moderately high, and that the *accelerations* lead (i.e. anticipate) the *velocities*. Looking at the supplementary figure S3, we can then see that the *acceleration* patterns at previous time lags (e.g. -300 ms) are very similar to the *velocity* patterns at 0 ms, and the same similarities can be found in supplementary table S4. Considering these similarities and the temporal dependency between the two movement parameters, we cannot rule out that the significant ROI activations found for the *accelerations* are actually of the same nature of the *velocities*, i.e. that our experimental paradigm does not permit to disentangle them.

Another question that may arise when looking at the source space results is why the significant ROIs encompassed mostly parieto-occipital areas, but we could not find significant activations in the motor areas. Considering indeed that the task involved voluntary arm movement, a participation of both parietal and motor areas could have been expected [8, 9, 11, 13, 15, 24, 25, 66–68]. It should be considered, however, that the task not only involved voluntary movement, but also visual processing and eye movements. As natural eye movements were allowed during the experiment, participants could track indeed the snake with their gaze, and move their arm accordingly. The presence of eye movements and the additional visual processing may explain why the

activation of parieto-occipital areas was so prominent [68] to mask the contribution of motor areas. This interpretation is also in line with the results of an offline study [25], showing that significant activations in the motor areas, masked during a visuo-motor task, could only be revealed when contrasting between executed and observed movement.

4.3. Amplitude of the decoder output

One important effect that we could observe in this study is that the decoded trajectories were estimated with consistently smaller amplitudes with respect to the hand kinematics. The effect was already present when using the PLS model alone and was not improved by adding the Kalman filter, as it can be observed in the sample decoded trajectories in figure 4(a). The same effect can also be observed in figure 4(b), showing that even though participants were enlarging their movements, this did not influence the amplitude of the decoder output.

Although this amplitude mismatch could also be observed in other non-invasive offline studies [25, 28, 60], it might represent a limitation when translating to closed-loop online control. For example, one related undesired effect in our experiment was that the participants enlarged their movements during the 33%, 66% and 100% EEG condition, to compensate for the smaller amplitudes of the decoded output.

One hypothesis to explain the amplitude mismatch may be that we only included in our model information about movement direction, but not about the corresponding magnitude. This directional information, in our case, was carried by the *position*, *velocity* and *acceleration* x and y components. The corresponding information about the magnitude, however, would have been represented by the distance (for the positions), the speed (for the velocities) and the magnitude of the acceleration vector (for the accelerations). Since previous studies could show that neural activity carries information, for example, about speed [63, 64], including this information in the decoding model might be a possible approach to alleviate the problem of amplitude mismatch. We recently showed that incorporating distance [61] and speed [61, 62] information in the decoding model can lead to a better estimation of the movement amplitude.

4.4. Questionnaire, task performance, effect of feedback and adaptation

One positive aspect of the implemented paradigm is that the participants consistently considered the task to be very intuitive, engaging, and not complicated, according to the analysis of the questionnaire results (supplementary figure S5). Even though these features were suggested to be ideal to improve BCI training [69], we could still observe a gradual loss of

control over the course of the experiment, as documented by both the participants' impressions (supplementary figure S7) and the task performance results (figure 6, right). Even though the level of control shown in figure 6 was above chance level even in the 100% EEG condition, and that the majority of participants (7 out of 9) reported to feel enough control over the robot to be able to improve with training, this surely is an aspect that needs to be improved.

One element that influenced the results of this study is the amplitude mismatch between the hand kinematics and the EEG-based decoded trajectories (figures 4(a) and (b)). Not only this mismatch might have induced changes in the participants' mental state with respect to calibration, but it also changed the participants' behavior, as they naturally tended to enlarge their movements as a compensation strategy (figure 4(b)) with limited awareness of this (supplementary figure S7).

Another indirect effect of the amplitude mismatch was that it probably affected the perception of delays. Although the participants reported to feel increasing delays between movement and feedback (supplementary figure S7), this was not confirmed by the behavioral analysis (supplementary figure S8), showing that the delays were not significantly changing over the course of the experiment. We believe that the increased perception of delay might have been an indirect effect of the amplitude mismatch: since the EEG-based decoded trajectories had smaller amplitudes with respect to the hand kinematics, increasing the proportion of EEG control resulted in a reduced responsiveness of the robot to the movement amplitude, which might have given the impression of larger delays.

A final observation that can be drawn from the questionnaire results, is that the internal state of the participants was changing over time. Although they consistently reported to allocate most of their attention to the *snake* (and less to the robot or their hand) during calibration, their strategies changed over the course of the experiments, and varied among participants (as it can be observed in supplementary figure S7). Switching the attention between the actors (i.e. snake, robot and hand) might also have had an influence on the decoder models, as the proportion of visual processing (e.g. when focusing on the snake) changes with respect to proprioception (e.g. when focusing on the hand). It might be therefore beneficial, to improve the quality of the decoding, by implementing an adaptive scheme that deals with the ongoing changes and progressively adjusts the decoder parameters.

To summarize, we believe that the quality of online control might be improved in two ways. On the one hand, special attention needs to be paid in the future to eliminate amplitude mismatches when giving feedback to the users. On the other hand, the implementation of co-adaptive approaches

(i.e. promoting the simultaneous adaptation of the participant and the decoding model [70]) might help to better deal with the feedback-induced non-stationarities. It might be particularly helpful to deal with changes in the participant's mental state, by adapting the decoder parameters to the changing control strategy.

5. Limitations

One of the main limitations of this study was the presence of residual movement artifacts, visible on the left side of the brain in the position activation patterns (figure 5(b)). However, we believe that the influence of these movement artifacts was negligible for the decoding. If the movement artifacts were contributing, then we should have seen higher correlations in figure 3 for the positions during 33% and 66% EEG control, because in these conditions the movements were larger (figure 4(b)) and the users could still accomplish the task very well (figure 6, left panel). However, since the correlations in figure 3 were not increasing in these conditions, we can conclude that the residual artifactual activity did not have a big effect. One way to overcome this limitation in future studies could be to set a different scaling between hand and robot trajectories (e.g. 1:2), so to have smaller arm movements and therefore reduce the possibility of an artifact.

6. Conclusion

In this study, we could demonstrate for the first time the feasibility of LF-EEG-based decoding for the closed-loop control of a robotic arm. The potential bottlenecks arising when switching from an offline to an online decoding scenario were highlighted, along with possible solutions to address them. A novel possible approach, named PLSKF, was introduced in this sense. In addition to the dimensionality reduction properties of PLS regression, the PLSKF was proved to be suitable for the online decoding and successful in integrating the information from different decoding models (here *positions*, *velocities* and *accelerations*). Although there surely is room for improvement, we could obtain online correlations between hand kinematics and EEG-based decoded trajectories above chance in most of the cases. Source space analysis confirmed the localization in the parieto-occipital areas of the *velocity* decoder patterns, in line with previous literature. An amplitude mismatch between hand kinematics and decoded trajectories was also found. The influence of the amplitude mismatch on the behavioral response of participants was discussed, particularly in the context of shared control like in this study. The behavioral responses and impressions of participants when progressively receiving feedback on their decoded movements were captured and discussed. The level of control of the robot was overall

above chance even in the condition of 100% EEG control. Most participants finally reported to feel enough control over the robot to be able to improve with training.

Altogether, the study takes a first step in the field of continuous EEG-based movement decoding for the closed-loop control of a robotic arm or neuroprosthesis. Other challenges, such as the influence of reinforcement learning over multiple recording sessions, the development of a co-adaptive approach to improve training, or the minimization of the calibration time needed for the decoder, might be of interest in the future.

Acknowledgments

The authors acknowledge Professor Angelo Cappello for his fruitful suggestions and Joana Pereira, Catarina Lopes-Dias, and Lea Hehenberger for their valuable discussions and comments. This work has received funding from the European Research Council (ERC) under the European Union's Horizon 2020 research and innovation programme (Consolidator Grant 681231 'Feel Your Reach'). V. M. received additional funding from a Marco Polo scholarship sponsored by the University of Bologna.

Author contributions

Based on G.R.M-P's conceptual idea, V.M., R.J.K., A.I.S. and G.R.M-P. conceived the study. V.M and R.J.K. implemented the paradigm and performed the acquisition. V.M. and R.J.K. conducted the analysis. V.M., R.J.K., A.I.S. and G.R. M-P. interpreted the data. V.M., R.J.K., A.I.S. and G.R.M-P. wrote and edited the manuscript.

ORCID iDs

Valeria Mondini  <https://orcid.org/0000-0001-7680-6199>

Reinmar J Kobler  <https://orcid.org/0000-0003-4007-279X>

Andreea I Sburlea  <https://orcid.org/0000-0001-6766-3464>

Gernot R Müller-Putz  <https://orcid.org/0000-0002-0087-3720>

References

- [1] Müller-Putz G R, Schwarz A, Pereira J and Ofner P 2016 From classic motor imagery to complex movement intention decoding: the noninvasive Graz-BCI approach *Progress in Brain Research* vol 228, ed D Coyle (Amsterdam: Elsevier) pp 39–70
- [2] Ajiboye A B et al 2017 Restoration of reaching and grasping movements through brain-controlled muscle stimulation in a person with tetraplegia: a proof-of-concept demonstration *Lancet* **389** 10081 1821–30
- [3] Bouton C E et al 2016 Restoring cortical control of functional movement in a human with quadriplegia *Nature* **533** 247–50
- [4] Collinger J L et al 2013 High-performance neuroprosthetic control by an individual with tetraplegia *Lancet* **381** 557–64
- [5] Ofner P and Müller-Putz G R 2012 Decoding of velocities and positions of 3D arm movement from EEG *Conf Proc IEEE Eng Med Biol Soc* vol 2012 pp 6406–9
- [6] Ofner P and Müller-Putz G R 2015 Using a noninvasive decoding method to classify rhythmic movement imaginations of the arm in two planes *IEEE Trans. Biomed. Eng.* **62** 972–81
- [7] Caminiti R, Johnson P B and Urbano A 1990 Making arm movements within different parts of space: dynamic aspects in the primate motor cortex *J. Neurosci.* **10** 2039–58
- [8] Georgopoulos A P, Kalaska J F, Caminiti R and Massey J T 1982 On the relations between the direction of two-dimensional arm movements and cell discharge in primate motor cortex *J. Neurosci.* **2** 1527–37
- [9] Kalaska J F, Caminiti R and Georgopoulos A P 1983 Cortical mechanisms related to the direction of two-dimensional arm movements: relations in parietal area 5 and comparison with motor cortex *Exp. Brain Res.* **51** 247–60
- [10] Black M J, Bienenstock E, Donoghue J P, Serruya M, Wu W and Gao Y 2003 Connecting brains with machines: the neural control of 2D cursor movement *Proc. 1st Int. IEEE/EMBS Conf. on Neural Engineering* pp 580–3
- [11] Carmena J M, Lebedev M A, Crist R E, O'Doherty J E, Santucci D M, Dimitrov D F, Patil P G, Henriquez C S and Nicolelis M A L 2003 Learning to control a brain-machine interface for reaching and grasping by primates *PLoS Biol.* **1** E42
- [12] Hochberg L R et al 2012 Reach and grasp by people with tetraplegia using a neurally controlled robotic arm *Nature* **485** 372–5
- [13] Lebedev M A et al 2005 Cortical Ensemble Adaptation to Represent Velocity of an Artificial Actuator Controlled by a Brain-Machine Interface *J. Neurosci.* **25** 4681–93
- [14] Li Z, O'Doherty J E, Hanson T L, Lebedev M A, Henriquez C S and Nicolelis M A L 2009 Unscented Kalman Filter for Brain-Machine Interfaces *PLOS One* **4** e6243
- [15] Mulliken G H, Musallam S and Andersen R A 2008 Decoding trajectories from posterior parietal cortex ensembles *J. Neurosci.* **28** 12913–26
- [16] Pistohl T, Ball T, Schulze-Bonhage A, Aertsen A and Mehring C 2008 Prediction of arm movement trajectories from ECoG-recordings in humans *J. Neurosci. Methods* **167** 105–14
- [17] Schalk G et al 2007 Decoding two-dimensional movement trajectories using electrocorticographic signals in humans *J. Neural Eng.* **4** 264
- [18] Benabid A L et al 2019 An exoskeleton controlled by an epidural wireless brain-machine interface in a tetraplegic patient: a proof-of-concept demonstration *Lancet Neurol.* **18** 1112–22
- [19] Bradberry T J, Rong F and Contreras-Vidal J L 2009 Decoding center-out hand velocity from MEG signals during visuomotor adaptation *NeuroImage* **47** 1691–700
- [20] Georgopoulos A P, Langheim F J P, Leuthold A C and Merkle A N 2005 Magnetoencephalographic signals predict movement trajectory in space *Exp. Brain Res.* **167** 132–5
- [21] Waldert S et al 2008 Hand Movement Direction Decoded from MEG and EEG *J. Neurosci.* **28** 1000–8
- [22] Yeom H G, Kim J S and Chung C K 2013 Estimation of the velocity and trajectory of three-dimensional reaching movements from non-invasive magnetoencephalography signals *J. Neural Eng.* **10** 026006
- [23] Kobler R, Hirata M, Hashimoto H, Dowaki R, Sburlea A I and Müller-Putz G 2019 Simultaneous decoding of velocity and speed during executed and observed tracking movements: an MEG study *Proc. of the 8th Graz Brain-Computer Interface Conf. 2019: Bridging Science and Application* pp 100–5
- [24] Bradberry T J, Gentili R J and Contreras-Vidal J L 2010 Reconstructing Three-Dimensional Hand Movements from

- Noninvasive Electroencephalographic Signals *J. Neurosci.* **30** 3432–7
- [25] Kobler R J, Sburlea A I and Müller-Putz G R 2018 Tuning characteristics of low-frequency EEG to positions and velocities in visuomotor and oculomotor tracking tasks *Sci. Rep.* **8** 17713
- [26] Lv J, Li Y and Gu Z 2010 Decoding hand movement velocity from electroencephalogram signals during a drawing task *Biomed. Eng. Online* **9** 64
- [27] Úbeda A, Hortal E, Iáñez E, Perez-Vidal C and Azorín J M 2015 Assessing Movement Factors in Upper Limb Kinematics Decoding from EEG Signals *PLOS One* **10** e0128456
- [28] Kobler R J, Almeida I, Sburlea A I and Müller-Putz G R 2020 Using machine learning to reveal the population vector from EEG signals *J. Neural Eng.* **17** 026002
- [29] Úbeda A, Azorín J M, Chavarriaga R and Millán J D 2017 Classification of upper limb center-out reaching tasks by means of EEG-based continuous decoding techniques *J. Neuroeng. Rehabil.* **14** 9
- [30] Waldert S, Pistohl T, Braun C, Ball T, Aertens A and Mehring C 2009 A review on directional information in neural signals for brain-machine interfaces *J. Physiol.* **103** 244–54
- [31] Robinson N and Vinod A P 2016 Noninvasive Brain-Computer Interface: Decoding Arm Movement Kinematics and Motor Control *IEEE Syst. Man Cybern. Mag.* **2** 4–16
- [32] Paninski L, Fellows M R, Hatsopoulos N G and Donoghue J P 2004 Spatiotemporal tuning of motor cortical neurons for hand position and velocity *J. Neurophysiol.* **91** 515–32
- [33] Oldfield R C 1971 The assessment and analysis of handedness: the Edinburgh inventory *Neuropsychologia* **9** 97–113
- [34] Kobler R J, Sburlea A I and Müller-Putz G R 2017 A comparison of ocular artifact removal methods for block design based electroencephalography experiments *Proc. of the 7th Graz Brain-Computer Interface Conf.* pp 236–41
- [35] Kobler R J, Sburlea A I, Lopes-Dias C and Müller-Putz G R 2020 Corneo-retinal-dipole and eyelid-related eye artifacts can be corrected offline and online in electroencephalographic and magnetoencephalographic signals *NeuroImage* **218** 117000
- [36] Brainard D H 1997 The psychophysics toolbox *Spatial Vis.* **10** 433–5
- [37] Kleiner M, Brainard D and Pelli D 2007 What's new in psychtoolbox-3? *Perception* **36** 1–16
- [38] Pelli D G 1997 The VideoToolbox software for visual psychophysics: transforming numbers into movies *Spatial Vis.* **10** 437–42
- [39] Delorme A and Makeig S 2004 EEGLAB: an open source toolbox for analysis of single-trial EEG dynamics including independent component analysis *J. Neurosci. Methods* **134** 9–21
- [40] Kobler R J, Sburlea A I, Mondini V and Müller-Putz G R 2019 HEAR to remove pops and drifts: the high-variance electrode artifact removal (HEAR) algorithm *2019 41st Annual Int. Conf. of the IEEE Eng. Med. Biol. Soc.* pp 5150–5
- [41] Miall R C and Wolpert D M 1996 Forward Models for Physiological Motor Control *Neural Netw.* **9** 1265–79
- [42] Wold S, Sjöström M and Eriksson L 2001 PLS-regression: a basic tool of chemometrics *Chemom. Intell. Lab. Syst.* **58** 109–30
- [43] de Jong S 1993 SIMPLS: An alternative approach to partial least squares regression *Chemom. Intell. Lab. Syst.* **18** 251–63
- [44] Kalman R E 1960 A New Approach to Linear Filtering and Prediction Problems *J. Basic Eng.* **82** 35–45
- [45] Bar-Shalom Y, Li X R and Kirubarajan T 2002 *Estimation with Applications to Tracking and Navigation: Theory, Algorithms and Software* (New York: Wiley)
- [46] Benjamini Y and Hochberg Y 1995 Controlling the false discovery rate: a practical and powerful approach to multiple testing *J. R. Stat. Soc. Ser. B* **57** 289–300
- [47] Yekutieli D and Benjamini Y 1999 Resampling-based false discovery rate controlling multiple test procedures for correlated test statistics *J. Stat. Plan. Inference* **82** 171–96
- [48] Michel C M and Murray M M 2012 Towards the utilization of EEG as a brain imaging tool *NeuroImage* **61** 371–85
- [49] Michel C M, Murray M M, Lantz G, Gonzalez S, Spinelli L and Grave de Peralta R 2004 EEG source imaging *Clin. Neurophysiol.* **115** 2195–222
- [50] Haufe S et al 2014 On the interpretation of weight vectors of linear models in multivariate neuroimaging *NeuroImage* **87** 96–110
- [51] Bartz D and Müller K R 2014 Covariance shrinkage for autocorrelated data *Advances in Neural Information Processing Systems (NIPS)* pp 1592–600
- [52] Ofner P, Schwarz A, Pereira J and Müller-Putz G R 2017 Upper limb movements can be decoded from the time-domain of low-frequency EEG *PLOS One* **12** e0182578
- [53] Tadel F, Baillet S, Mosher J C, Pantazis D and Leahy R M 2011 Brainstorm: a user-friendly application for MEG/EEG analysis *Comput. Intell. Neurosci.* **2011** 8
- [54] Fonov V, Evans A C, Botteron K, Almlí C R, McKinstry R C and Collins D L 2011 Unbiased average age-appropriate atlases for pediatric studies *NeuroImage* **54** 313–27
- [55] Gramfort A, Papadopoulos T, Olivi E and Clerc M 2010 OpenMEEG: opensource software for quasistatic bioelectromagnetics *Biomed. Eng. Online* **9** 45
- [56] Kybic J, Clerc M, Abboud T, Faugeras O, Keriven R and Papadopoulos T 2005 A common formalism for the Integral formulations of the forward EEG problem *IEEE Trans. Med. Imaging* **24** 12–28
- [57] Pascual-Marqui R D 2002 Standardized low-resolution brain electromagnetic tomography (sLORETA): technical details *Methods Finding Exp. Clin. Pharmacol.* **24** 5–12
- [58] Maris E and Oostenveld R 2007 Nonparametric statistical testing of EEG- and MEG-data *J. Neurosci. Methods* **164** 177–90
- [59] Nichols T E and Holmes A 2001 Nonparametric permutation tests for functional neuroimaging: A primer with examples *Hum. Brain Mapp.* **15** 1–25
- [60] Antelis J M, Montesano L, Ramos-Murguialday A, Birbaumer N and Minguez J 2013 On the usage of linear regression models to reconstruct limb kinematics from low frequency EEG signals *PloS One* **8** e61976
- [61] Kobler R J, Sburlea A I, Mondini V, Hirata M and Müller-Putz G R 2020 Distance and speed informed kinematics decoding improves M/EEG based upper-limb movement decoder accuracy *J. Neural Eng.* (submitted)
- [62] Martínez-Cagigal V, Kobler R J, Mondini V and Müller-Putz G R 2020 Non-linear online low-frequency EEG decoding of arm movements during a pursuit tracking task *42nd Annual Int. Conf. of the IEEE Eng. Med. Biol. Soc. (EMBC) in conjunction with the 43rd Annual Conf. of the Canadian Med. Biol. Eng. Soc.* 2981–5
- [63] Hammer J et al 2016 Predominance of movement speed over direction in neuronal population signals of motor cortex: intracranial EEG data and a simple explanatory model *Cereb. Cortex* **26** 2863–81
- [64] Jerbi K, Lachaux J-P, N'Diaye K, Pantazis D, Leahy R M, Garnero L and Baillet S 2007 Coherent neural representation of hand speed in humans revealed by MEG imaging *Proc. Natl Acad. Sci.* **104** 7676–81
- [65] Willett F R et al 2017 Feedback control policies employed by people using intracortical brain-computer interfaces *J. Neural Eng.* **14** 016001
- [66] Culham J C and Valyear K F 2006 Human parietal cortex in action *Curr. Opin. Neurobiol.* **16** 205–12
- [67] Filimon F, Nelson J D, Hagler D J and Sereno M I 2007 Human cortical representations for reaching: Mirror

- neurons for execution, observation, and imagery
NeuroImage 37 1315–28
- [68] Filimon F, Nelson J D, Huang R-S and Sereno M I 2009 Multiple parietal reach regions in humans: cortical representations for visual and proprioceptive feedback during on-line reaching *J. Neurosci.* 29 2961–71
- [69] Lotte F and Jeunet C 2015 Towards improved BCI based on human learning principles *The 3rd Int. Winter Conf. on Brain-Computer Interface* Jan pp 1–4
- [70] Schlögl A, Vidaurre C and Müller K-R 2010 Adaptive methods in bci research-an introductory tutorial *Brain-Computer Interfaces* (Berlin: Springer) pp 331–55

Non-linear online low-frequency EEG decoding of arm movements during a pursuit tracking task

Víctor Martínez-Cagigal, Reinmar J. Kobler, Valeria Mondini, Roberto Hornero, *Senior Member, IEEE*,
and Gernot R. Müller-Putz, *Member, IEEE*

Abstract—Decoding upper-limb movements in invasive recordings has become a reality, but neural tuning in non-invasive low-frequency recordings is still under discussion. Recent studies managed to decode movement positions and velocities using linear decoders, even developing an online system. The decoded signals, however, exhibited smaller amplitudes than actual movements, affecting feedback and user experience. Recently, we showed that a non-linear offline decoder can combine directional (e.g., velocity) and non-directional (e.g., speed) information. In this study, it is assessed if the non-linear decoder can be used online to provide real-time feedback. Five healthy subjects were asked to track a moving target by controlling a robotic arm. Initially, the robot was controlled by their right hand; then, the control was gradually switched until it was entirely controlled by the electroencephalogram (EEG). Correlations between actual and decoded movements were generally above chance level. Results suggest that information about speed was also encoded in the EEG, demonstrating that the proposed non-linear decoder is suitable for decoding real-time arm movements.

I. INTRODUCTION

Current brain–computer interface (BCI) research is gently moving from decoding categorical classes that represent certain actions (e.g., through motor imagery) toward decoding continuous users’ movements [1]. In this sense, imagined upper-limb movements were successfully decoded via invasive recordings [2]; however, the usability of non-invasive methods such as EEG for the same purpose is still under discussion [3–7].

Previous studies demonstrated that kinematic information of executed [3], [6], observed [6], [8] and imagined [5] upper-limb movements is encoded in the low-frequency EEG band, making it possible to decode positions and velocities using linear algorithms, such as partial least squares (PLS) regression [5], [6] or Kalman filters [8–10]. First offline studies assessed whether neural tuning can be retrieved from EEG [3], [5] and studied the locations of the cortical sources [6]. A step further was performed in [10] to develop an online decoder to control a robotic arm by adding a linear Kalman filter based on a kinematic model. Even though this approach demonstrated that a real-time EEG decoding of

upper-limb movements is possible, there was a mismatch in the amplitude range between the decoded and actual movements. This amplitude mismatch has been observed in previous works [4], [6], indicating that linear models were not successful in extracting the amplitude or magnitude of the kinematics (e.g., speed in the case of velocity). We recently showed that non-directional (e.g., speed) and directional (e.g., velocity) kinematics are simultaneously encoded in the magnetoencephalogram [11] and EEG [8], and demonstrated that linear models were not able to combine both kinematic signals due to the non-linear relation [8], in contrast to an unscented Kalman filter (UKF) [12].

The purpose of this study was to implement the UKF in an online system to control a robotic arm and assess if it is possible to decode executed upper-limb movements in real-time. In order to alleviate the amplitude mismatch the UKF decoded not only the positions and velocities, but also the instantaneous speed.

II. MATERIALS AND METHODS

A. Subjects

Five right-handed healthy subjects participated in the study (mean age: 28.2 ± 2.4 years; 2 males, 3 females). The subjects gave their informed written consent and received compensatory payment to participate in the study. The experimental procedure, conforming to the declaration of Helsinki, was approved by the local ethics committee.

B. Experimental setup and paradigm

The experimental setup is depicted in Fig. 1(A). The subject was comfortably seated in front of a screen that depicted a white target trace following a pre-defined trajectory (i.e., “snake”). Three main devices were present: (1) an EEG acquisition system, which monitored the electrical brain activity; (2) a LeapMotion (LM, *LeapMotion Inc., USA*) system, which tracked the position of the user’s right hand (visually occluded); and (3) an assistive robotic arm (JACO, *Kinova Robotics Inc., Canada*).

As in [10], the task of the user was to follow the snake’s trajectory with the gaze and with the JACO. As shown in Fig. 1(B), JACO was initially controlled by the arm movements captured by the LM. That control was progressively substituted by an EEG-based control up to the point of being completely controlled by an EEG-based decoder at the end of the experiment. The EEG decoder was calibrated with 5 snake runs (100% LM, 0% EEG), and then used in snake runs 6–7 (66% LM, 33% EEG), 8–9 (33% LM, 66%

V. M.-C. and R. H. are with the Biomedical Engineering Group, University of Valladolid, Valladolid, Spain; and with the ‘Centro de Investigación Biomédica en Red’ in Bioengineering, Biomaterials and Nanomedicine (CIBER-BBN), Spain (e-mails: victor.martinez@gib.tel.uva.es, robhor@tel.uva.es).

R. J. K., V. M. and G. R. M.-P. are with the Institute of Neural Engineering, Graz University of Technology, Graz, Austria (e-mails: {reinmar.kobler, valeria.mondini, gernot.mueller}@tugraz.at).

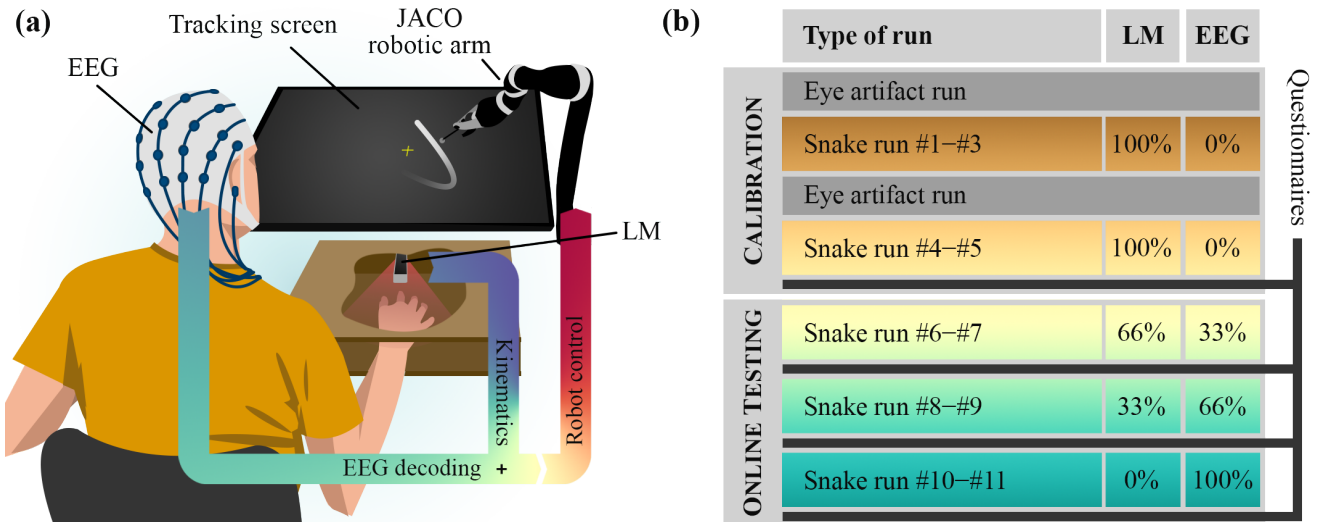


Fig. 1. (a) Experimental setup. The users were seated in front of a screen that depicted a continuous trajectory. The task was to follow the trajectory with the robotic arm (JACO). (b) Paradigm of the study. During calibration, JACO was controlled entirely by the arm movements recorded with a LeapMotion (LM) system. For the feedback runs, the control was reduced until JACO was fully controlled by the EEG.

EEG) and 10–11 (0% LM, 100% EEG). A run typically lasted 5 minutes and was divided into 10 trials. The trials lasted 24 s each and were interleaved with short breaks. Two runs recording eye movements were also performed between calibration blocks. They were used to train an eye artifact correction algorithm according to [13]. After each control condition (100%, 66%, 33% and 0% LM), a questionnaire was fulfilled by the users to collect their impressions.

In order to avoid large movements and consequently motion artifacts, a trial was aborted if the user made movements that were more than 12.5 cm away from the initial position. We additionally decided to map the arm movements to larger movements of JACO; the ratio was 1:2.

The snake’s trajectories were generated offline and were the same across users. Twelve of them were generated by sampling band-pass filtered pink noise (0.2–0.4 Hz) [14]. The final set of trajectories was extended by mirroring and rotating (90°, 180° and 270°) this initial set, obtaining a total of 96 different ones. This procedure assured uncorrelated positions and velocities in both horizontal and vertical components [6].

The EEG was recorded using a total of 60 active electrodes (actiCAP, Brain Products GmbH, Germany), referenced to the left earlobe and using AFz as ground. Four additional channels were placed at the inferior (left), superior (left) and outer canthi (both) of the eyes to record the electrooculogram as well. All electrodes were connected to biosignal amplifiers (BrainAmp, Brain Products GmbH, Germany) with a sampling rate of 500 Hz. Exact locations of the electrodes were initially measured using an ultrasonic positioning system (EPLOS, Zebris Medical GmbH, Germany) for each user.

C. Signal processing pipeline

The signal processing pipeline is shown in Fig. 2. In a nutshell, EEG signals were band-pass filtered (0.18–1.5

Hz), spatially filtered (common average reference, CAR) and down-sampled to 20 Hz. The filter specifications were identical to [10]. Pops and drifts were corrected by a high-variance electrode artifact removal (HEAR) algorithm [15]. Eye movements and blinks were corrected with the sparse generalized eye artifact subspace subtraction (SGEYESUB) algorithm [13]. Then, PLS regression projected the EEG data and reduced the dimensionality [5], [8], leading to the final state decoding with a square-root UKF (SQ-UKF) [12]. Meanwhile, the LM signals were low-pass filtered (< 4 Hz) and down-sampled to 20 Hz. The low-pass filter was used to attenuate occasional jitters and measurement noise. Finally, the real and decoded positions were weighted according to the run and scaled (1:2 ratio) to match the movement range of JACO over the screen.

D. EEG decoding of movements

The decoder aimed at estimating the movement state of the user’s hand by analyzing the EEG. In particular, we focused on decoding 5 different kinematics: positions p_x and p_y , velocities v_x and v_y and speed $\varsigma = \sqrt{v_x^2 + v_y^2}$. The latter was added to include information about the amplitude range of the hand trajectories.

PLS regression was used to reduce the co-linearity of the EEG signals and at the same time maintain kinematic information. In detail, we used it to get an initial estimate of the movement states by simultaneously finding the relation between EEG (i.e., \mathbf{E}) and LM signals, and reducing the dimensionality to $N = 40$ latent components (explaining 70% of variance) [6], [10]. The activity of the latent components is $\hat{\mathbf{L}} = \mathbf{E}\mathbf{W}$; where $\mathbf{E} \in \mathbb{R}^{n \times m}$ denotes the calibration period EEG storing previous lags (n samples, $m = 64$ channels \times 7 lags $\in \{-300 : 50 : 0\}$ ms), and $\mathbf{W} \in \mathbb{R}^{m \times N}$ is the weight matrix. PLS was computed using the SIMPLS algorithm [16]. Afterward, the SQ-UKF, a non-

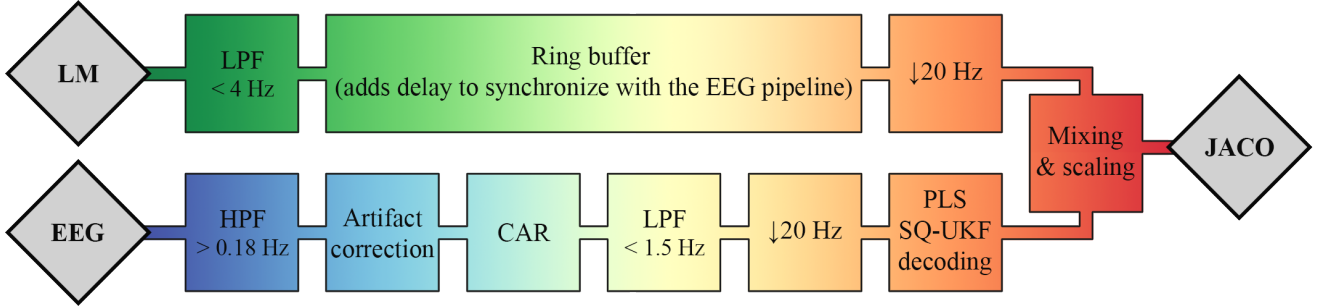


Fig. 2. Online signal processing pipeline followed in this study, in which LM and EEG signals are combined to control the JACO arm.

linear Kalman filter approach, was applied to improve the estimation of the states, assuming that the measurements (i.e., latent component activity) $\hat{\mathbf{L}}$ were noisy. As in [8], the SQ-UKF initial parameters were fitted to the calibration data using an encoding approach:

$$\mathbf{F} = \mathbf{C}_{\mathbf{x}_k \mathbf{x}_{k-1}} (\mathbf{C}_{\mathbf{x}_k \mathbf{x}_k})^{-1}, \quad (1)$$

$$\mathbf{Q} = \mathbf{C}_{\epsilon_q \epsilon_q}, \text{ where } \epsilon_q = \mathbf{F} \mathbf{x}_{k-1} - \mathbf{x}_k, \quad (2)$$

$$h(\mathbf{x}_k) = \mathbf{C}_{\hat{\mathbf{l}}_k \mathbf{x}_k^+} (\mathbf{C}_{\mathbf{x}_k^+ \mathbf{x}_k^+})^{-1} \cdot \begin{bmatrix} \mathbf{x}_k \\ \varsigma(\mathbf{x}_k) \end{bmatrix}, \quad (3)$$

$$\mathbf{R} = \mathbf{C}_{\epsilon_r \epsilon_r}, \text{ where } \epsilon_r = h(\mathbf{x}_k) - \hat{\mathbf{l}}_k, \quad (4)$$

where \mathbf{F} is the state-transition matrix, \mathbf{Q} the process noise covariance, $h(\cdot)$ the observation model, \mathbf{R} the observation noise covariance, and $\mathbf{C}_{a,b}$ denotes the covariance matrix between two signals \mathbf{a} and \mathbf{b} . The state at time k is denoted as $\mathbf{x}_k = [p_x, v_x, p_y, v_y]^T$, becoming $\mathbf{x}_k^+ = [\mathbf{x}, \varsigma]^T$ when speed is included. Note that the non-linearity was included in the measurement equation, whereas the process equation was kept in its linear form. Finally, SQ-UKF returns an estimate of the states $\hat{\mathbf{x}}_k$ in real-time, which is further used to control the JACO arm. In the 100% LM condition, we used a cross-validation approach to simulate the EEG decoder on the calibration data (snake runs 1–5).

III. RESULTS

Fig. 3 depicts the main results concerning the quantitative analysis. Correlations between the SQ-UKF decoded $\hat{\mathbf{x}}_k$ and the actual LM \mathbf{x}_k movement state trajectories are shown for all control conditions, including the upper bound confidence interval of chance level (with significance $\alpha = 0.05$), estimated with a shuffling approach. Moreover, a representative trial is displayed to qualitatively compare the amplitude and shape of LM, PLS and SQ-UKF position trajectories, as well as grand-averaged activation patterns for each kinematic signal. Almost all correlations were above the significance level, except positions and velocities of the Y-axis in the 0% LM condition for some participants. Note that the grand-averaged amplitude ratio between the LM movements and the decoded ones was 1.07 ± 0.09 , indicating that the amplitude mismatch was negligible. The trajectories in Fig. 3(B) also show that the amplitudes of the LM and SQ-UKF trajectories

were in a similar range, whereas the PLS decoded trajectories indicated a large mismatch in amplitudes.

Qualitative analysis results are depicted in Fig 4. As shown, the users found the task engaging and intuitive, and highlighted that the experiment was neither physically nor mentally demanding. From the questionnaires is also revealed that the users paid more attention to the snake, followed by their own hands, and finally to JACO. As expected, the perceived level of control decreased as the control by LM did. Some users' declared that they felt to be in control of the JACO even in the 100% EEG-based control condition.

IV. DISCUSSION AND CONCLUSION

Correlations between the decoded and recorded LM signals indicate that the online EEG-based decoding of continuous arm movements is feasible. Maximal correlations were reached in the 100% LM condition (p_x : 0.63, v_x : 0.68, p_y : 0.51, v_y : 0.55), which progressively decreased as the fraction of EEG-based decoding increased. Nevertheless, maximal correlations for the 100% EEG control (p_x : 0.39, v_x : 0.48, p_y : 0.35, v_y : 0.44) indicate that movement kinematics can still be decoded in a fully EEG-driven BCI. Since the decoder was fitted to 100% LM condition data and its accuracy was moderate (average correlations of 0.45), the users naturally started to compensate erroneous feedback of the EEG decoder in the shared control conditions. Due to the slight difference in the movement behavior a performance decline was expected. Overall, the correlations are comparable with previous offline results [8], and improved the amplitude mismatch upon the linear Kalman filter based online results [10]. It is also noteworthy that the inclusion of JACO entailed an additional delay between hand and robot movements which, although similar across conditions, was perceived by users as higher as the EEG-based control was.

Owing to the nature of the task; i.e., a low and very limited frequency band, the possibility of observing spurious correlations is real. For that reason, the upper boundary of the chance level correlations (with significance $\alpha = 0.05$) were also calculated. Hence, they serve as a landmark to compare with and assure that the decoding states are not due to chance. Note also that the SQ-UKF works ideally for this kind of task and thus, correlations are expected to decay

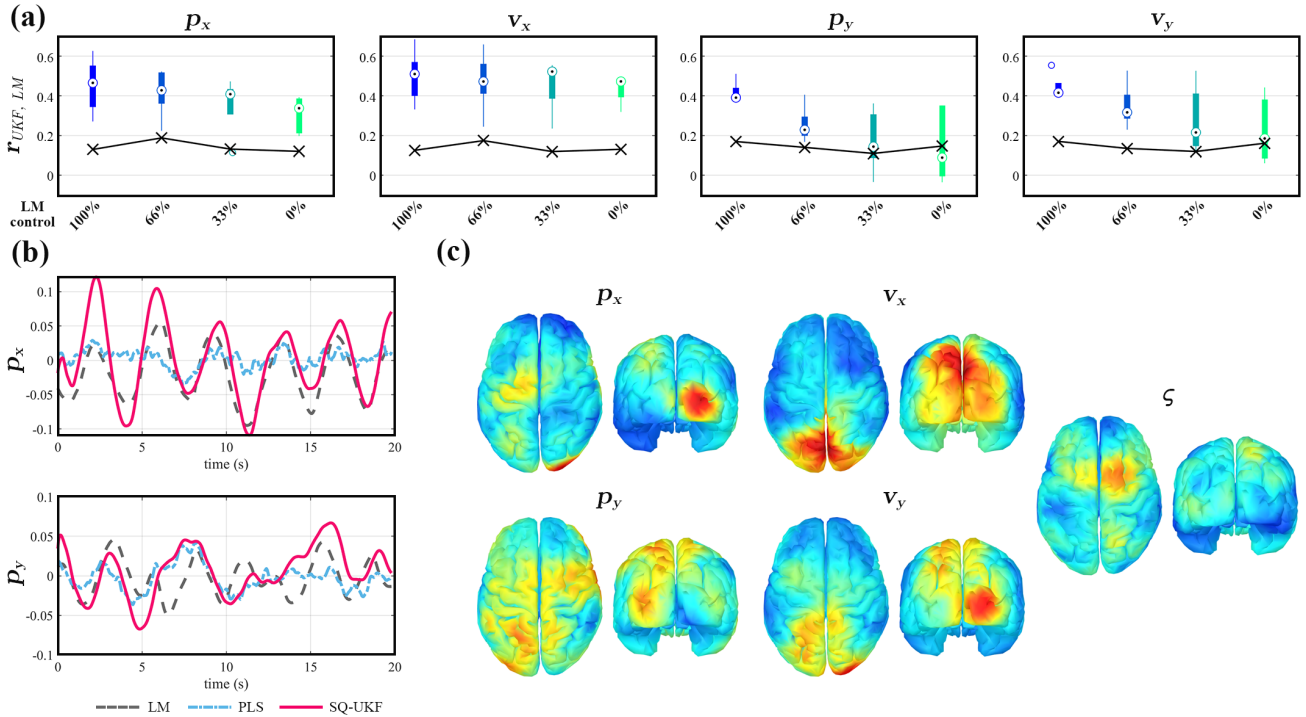


Fig. 3. (a) Feedback runs correlations between the SQ-UKF decoding and the real LM arm movements for each condition and state (chance level is depicted as a black line). (b) Sample trials of 20 s, in which the LM (dashed grey), the PLS decoding (dot-dash blue), and the final SQ-UKF decoding (solid magenta) signals are shown. (c) Averaged activation patterns across subjects in top and back view for each state.

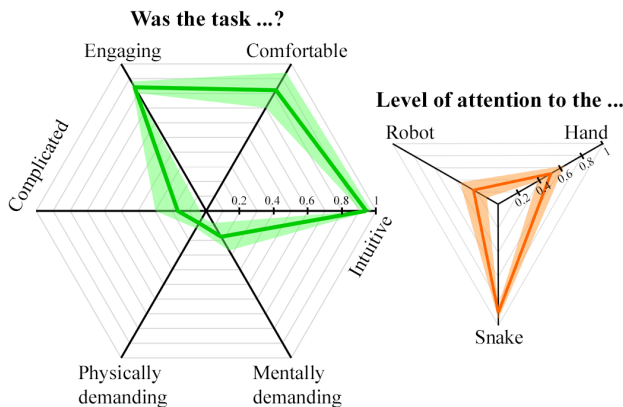


Fig. 4. Normalized questionnaire results regarding (left) the nature of the task and (right) the level of attention users paid to the robot, hand and snake trajectories during the 100% LM condition.

in a “free movement” task, where positions and velocities are not zero-mean or have more variance.

Despite these positive results, we observed that the correlations of the Y-axis kinematics were lower than the X-axis ones. This decrease was especially influential in the 33% and 0% LM condition, leading to correlations near or even at chance level. The rationale could be related to the experimental setup. As shown in Fig. 1(a), the screen was tilted towards the Y-axis to ease the movement of JACO. This leads to a setup in which the perception of vertical move-

ments is ambiguous in comparison with horizontal ones. In other words, to perceive a vertical movement of Δd in Y-axis, JACO needs to move a distance of $d = \Delta d / \sin(\theta)$, where $\theta \sim 45^\circ$ is the vertical angle of the screen (i.e., for the X-axis, $d = \Delta d$). This mismatch could influence the perception of the target snake, hindering the encoding of vertical movements. However, further experiments should be carried out in order to determine the actual cause of the phenomenon, since it was not observed in [10]. A decreasing trend of LM signals in 33% and 0% condition trials was also observed, implying that users began to perform movements slightly shifted from the home position. Hence, they lost the initial reference (i.e., origin of coordinates) due to the unawareness of their own hand position when feedback was almost or entirely EEG-based. This behavior could also influence the final decoding.

One of the drawbacks of previous linear studies was that the amplitude of the decoded EEG signals was lower than the actual arm movements [10], causing the users to enlarge their movements to compensate the decoded trajectories. As shown in Fig. 3(b) and [8], this issue has been alleviated by the inclusion of speed in the state space model, leading to an average amplitude ratio of 1.07. Even though speed is linearly encoded in the EEG signals, its relationship with velocities is non-linear. A non-linear approach like the UKF was successful in combining the information and thereby improve the estimation [8].

Concerning the source analysis of the patterns that effectively contributed to the SQ-UKF decoding, we found

activations over the parieto-occipital areas, especially for the velocities. The patterns for positions seem unfocused, with the exception of a demarcate activation on the right occipital lobe only for p_x , which is likely due to a noisy channel. Both results are in accordance with previous studies that associate neural tuning to velocities [6], [10]. As shown in Fig. 3(c), the main activations for speed were over the anterior part of the frontal cortex, close to the primary motor cortex; which can be viewed as a novel result. Note that this observation is slightly different to [8], where speed-related activations peaked in primary sensorimotor cortex. This difference could also be explained by the limited spatial resolution of the source analysis. The resolution was limited since we used a template head model that we co-registered with the users specific electrode locations.

From the questionnaire results, it was clear that the users were satisfied with the task, reporting that they could feel the control of the JACO, even in 33% and 0% LM conditions. Users reported that the task was engaging, intuitive and easy; which were highlighted to be ideal features for BCI training [17] and make users open to participate in further related studies. In general, the strategy of the users was to focus mainly on the snake, putting less attention to their hands or JACO. By focusing on the trajectory, they could ignore possible unexpected shifts in 66%, 33% or 0% conditions due to the decoder, as well as the delay between LM and JACO. In that way, they also avoided performing movements to compensate inaccurate JACO shifts.

The experimental outcomes not only supported that information about upper-limb positions and velocities are encoded in the EEG [6], [8], [10], but also demonstrates that information about speed is present and can be extracted in real-time to improve the position and velocity decoder accuracy. In conclusion, a non-linear decoder based on SQ-UKF has been proved to be suitable for decoding user movements from non-invasive recordings in real-time, providing moderate correlations.

In spite of these encouraging results, several limitations were identified. Firstly, the users were not aware of their own upper-limb positions when EEG decoding gained importance, leading to shifts from the home position that may influence the final decoding. This issue could be addressed by depicting a pointer that indicates the current LM position on the screen. Secondly, the Y-axis decoding yielded lower correlations than X-axis. Further work is required to investigate the reason and adapt the setup to overcome this limitation. Lastly, the number of users that participated in the study was limited (5 participants). An additional effort to recruit more participants, or even motor-disabled users, is necessary to generalize these results.

V. ACKNOWLEDGMENTS

This study has received funding from the European Research Council (ERC) under the European Union's Horizon 2020 programme (Consolidation Grant 681231 'Feel Your Reach') and from the CIBER-BBN through 'Instituto de Salud Carlos III' and 'European Regional Development

Fund' (FEDER), as well as from projects 'DPI2017-84280-R' of 'Ministerio de Ciencia, Innovación y Universidades' and FEDER, and the project '0378_AD_EEGWA_2.P' (Inter-regional cooperation program VA Spain-Portugal POCTEP 2014-2020) of the European Commission and FEDER. V. Martínez-Cagigal was in receipt of a PIF UVa grant from the University of Valladolid.

REFERENCES

- [1] G. R. Müller-Putz, A. Schwarz, J. Pereira *et al.*, "From classic motor imagery to complex movement intention decoding: The noninvasive Graz-BCI approach," in *Progress in Brain Research*. Elsevier, 2016, vol. 228, pp. 39–70, iSSN: 18757855.
- [2] L. R. Hochberg, D. Bacher, B. Jarosiewicz *et al.*, "Reach and grasp by people with tetraplegia using a neurally controlled robotic arm," *Nature*, vol. 485, no. 7398, pp. 372–375, 2012.
- [3] T. J. Bradberry, R. J. Gentili, and J. L. Contreras-Vidal, "Reconstructing three-dimensional hand movements from noninvasive electroencephalographic signals," *J. Neurosci.*, vol. 30, no. 9, 2010.
- [4] J. M. Antelis, L. Montesano, A. Ramos-Murguialday *et al.*, "On the Usage of Linear Regression Models to Reconstruct Limb Kinematics from Low Frequency EEG Signals," *PLoS ONE*, vol. 8, no. 4, 2013.
- [5] P. Ofner and G. R. Müller-Putz, "Using a noninvasive decoding method to classify rhythmic movement imaginations of the arm in two planes," *IEEE TBME*, vol. 62, no. 3, pp. 972–981, 2015.
- [6] R. J. Kobler, A. I. Sburlea, and G. R. Müller-Putz, "Tuning characteristics of low-frequency EEG to positions and velocities in visuomotor and oculomotor tracking tasks," *Sci. Rep.*, vol. 8, pp. 1–14, 2018.
- [7] A. Korik, R. Sosnik, N. Siddique *et al.*, "Decoding Imagined 3D Hand Movement Trajectories From EEG: Evidence to Support the Use of Mu, Beta, and Low Gamma Oscillations," *Frontiers in Neuroscience*, vol. 12, no. March, pp. 1–16, 2018.
- [8] R. J. Kobler, A. I. Sburlea, V. Mondini *et al.*, "Distance and speed informed kinematics decoding improves M/EEG based upper-limb movement decoder accuracy," *J. Neural Eng.*, in review.
- [9] J. Lv, Y. Li, and Z. Gu, "Decoding hand movement velocity from electroencephalogram signals during a drawing task," *Biomedical engineering online*, vol. 9, no. 1, 2010, iSSN: 1475-925X.
- [10] V. Mondini, R. J. Kobler, A. I. Sburlea *et al.*, "Continuous low-frequency EEG decoding of arm movement for closed-loop, natural control of a robotic arm," submitted.
- [11] R. J. Kobler, M. Hirata, H. Hashimoto *et al.*, "Simultaneous decoding of velocity and speed during executed and observed tracking movements: an MEG study," in *Proc. of the 8th Graz BCI Conference 2019*, Graz, 2019.
- [12] R. Van der Merwe and E. Wan, "The square-root unscented Kalman filter for state and parameter-estimation," in *Proc. of the IEEE ICASP*, 2001.
- [13] R. J. Kobler, A. I. Sburlea, C. Lopes-Dias *et al.*, "Corneo-retinal-dipole and eyelid-related eye artifacts can be corrected offline and online in electroencephalographic and magnetoencephalographic signals," *NeuroImage*, in revision.
- [14] L. Paninski, M. R. Fellows, N. G. Hatsopoulos *et al.*, "Spatiotemporal Tuning of Motor Cortical Neurons for Hand Position and Velocity," *Journal of Neurophysiology*, vol. 91, no. 1, pp. 515–532, 2004.
- [15] R. J. Kobler, A. I. Sburlea, V. Mondini *et al.*, "HEAR to remove pops and drifts: the high-variance electrode artifact removal (HEAR) algorithm," in *Proc. of the IEEE EMBC*, Jul. 2019.
- [16] S. de Jong, "SIMPLS: an alternative approach to partial least squares regression," *Chemom. Intell. Lab. Syst.*, vol. 18, no. 3, 1993.
- [17] F. Lotte and C. Jeunet, "Towards improved bci based on human learning principles," in *The 3rd International Winter Conference on Brain-Computer Interface*. IEEE, 2015, pp. 1–4.